65TH ELECTRONIC MATERIALS CONFERENCE

June 28–June 30, 2023 // University of California, Santa Barbara // Santa Barbara, California

PROGRAM & EXHIBIT GUIDE

PROGRAM & EXHIBIT GUIDE

KANSAS CITY NSC National Security Campus

managed by Honeywell FM&T

DO WORK THAT MATTERS

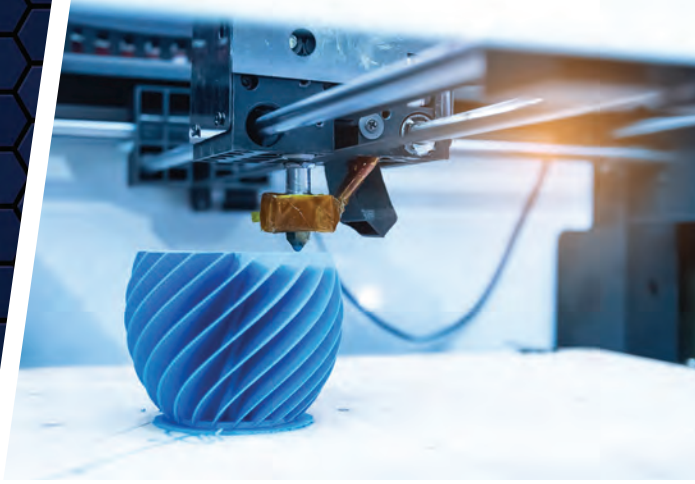

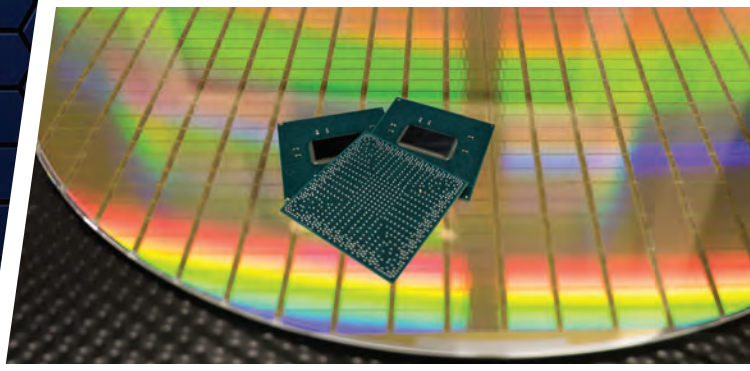

Launch your career in national security.

The Kansas City National Security Campus (KCNSC) is one of eight sites under the Department of Energy's (DOE's) National Nuclear Security Administration (NNSA). KCNSC ensures the safety and security of the nation's nuclear deterrent by providing multi-mission engineering and manufacturing solutions, and by delivering trusted national security products and government services. We develop advanced solutions for complex national security challenges within our three core missions of:

1. **NUCLEAR WEAPON PROGRAMS**
   Maintaining the U.S. nuclear stockpile; providing over 80% of all non-nuclear components in support of the U.S. nuclear deterrence

2. **GLOBAL SECURITY**
   An engineering, manufacturing and operational national asset, safeguarding the nation with products and services that support proliferation deterrence, supply chain assurance and responsiveness to global threats

3. **SUPPLY CHAIN MANAGEMENT CENTER**
   A focused, funded and strategic supply chain program acquisition solution that enables savings across the DOE enterprise and simplifies the buying process

Explore opportunities at kcnsc.doe.gov/careers

U.S. Citizenship Required

The Department of Energy's Kansas City National Security Campus is managed and operated by Honeywell Federal Manufacturing & Technologies, LLC under contract number DE-NA0002839

NNSA National Nuclear Security Administration

WELCOME TO THE CONFERENCE!

It is with great pleasure that we welcome you to the 65th Electronic Materials Conference (EMC 2023) at the beautiful University of California, Santa Barbara. We expect this Conference to follow in EMC's long tradition of offering premier research on the preparation, characterization and use of electronic materials. Below, we have outlined highlights we believe will be of interest to you.

Conference Chair
Lisa Porter
Carnegie Mellon University

Program Chair
Daniel Wasserman
The University of Texas at Austin

CONFERENCE HIGHLIGHTS

The 65th EMC Program

Features over 350 oral/poster presentations and 38 technical sessions focused on Electronic Materials Science and Technology; Energy Storage and Conversion Materials; Nanoscale Science and Technology; Organic Materials, Thin Films and Devices; Oxide Semiconductors and Dielectrics; and Wide Bandgap Semiconductors.

EMC Awards Ceremony & Plenary Session

The 65th EMC kicks off Wednesday morning with the Awards Ceremony & Plenary Session. First, the 2022 Best Student Presentation Award winners will be announced and honored. The Plenary Lecture follows, where **Darrell Schlom,** of Cornell University, will give his presentation, ***Suboxide Molecular-Beam Epitaxy.***

Welcome Reception/Poster Session

Join us for a Welcome Reception on Wednesday evening from 6:00 pm to 8:00 pm in Lagoon Plaza located at the University Center. During this time, poster authors will be available for in-depth discussions at the Poster Session, also located in Lagoon Plaza. Both of these events are great for meeting with longtime colleagues, making new connections and sharing information. Light snacks and refreshments will be served.

Exhibit

Be sure to visit the EMC exhibitors Wednesday and Thursday in Lagoon Plaza. Learn more about the latest products and services in the rapidly evolving world of electronic materials. See page 18 for exhibit hours.

Student Finalists for the Oral Presentation Award

Be sure to check out our first student award finalists on Wednesday at 5:10 pm at the University Center in Lobero and State Street.

Conference Dinner Reception

Don't miss this year's Conference Dinner Reception, Thursday evening from 6:30 pm to 8:30 pm, at the Manzanita Village Las Encinas Quad Lawn. Full Conference registration includes one Dinner Reception ticket. You can purchase additional Dinner Reception tickets at the EMC Registration Desk for $90 per person, subject to availability. This is an outside event on a grassy lawn, so please dress accordingly.

EMC is being coordinated with the Device Research Conference (DRC 2023), held at the University of California, Santa Barbara from June 25 to 28. Badges will be accepted for admittance to both Conferences on Wednesday, June 28.

SPECIAL THANKS!

CONFERENCE SUPPORT

NSF
nsf.gov

REFRESHMENT BREAKS

UMC
umccorp.com

POSTER SESSION SUPPORT

KANSAS CITY NSC National Security Campus
managed by Honeywell FM&T
kcnsc.doe.gov

STUDENT SUPPORT

TMS FOUNDATION
tms.org/foundation

TABLE OF CONTENTS

The 65th EMC has been managed by

MRS CONFERENCE SERVICES
Because the Experience Matters
mrs.org/conference-services

COMMITTEES

Executive Committee

Chair	**Lisa Porter** Carnegie Mellon University
Vice-Chair	**Daniel Wasserman** The University of Texas at Austin
Secretary	**Adrienne Stiff-Roberts** Duke University
Treasurer	**William Wong** University of Waterloo

ELECTRONIC MATERIALS SCIENCE AND TECHNOLOGY

Computational Electronic Materials Discovery

Lauren Garten, Georgia Institute of Technology
Anderson Janotti, University of Delaware
Sriram Krishnamoorthy, University of California, Santa Barbara
Tae-Yeon Seong, Korea University
Patrick Shea, Northrop Grumman Corporation
Angel Yanguas-Gil, Argonne National Laboratory

Contacts to Semiconductor Epilayers, Nanostructures and Organic Films

Leonard Brillson, The Ohio State University
Shadi Dayeh, University of California, San Diego
Suzanne Mohney, The Pennsylvania State University
Lisa Porter, Carnegie Mellon University
Tae-Yeon Seong, Korea University
Jerry Woodall, University of California, Davis

Epitaxial Materials and Devices

Seth Bank, The University of Texas at Austin
Kurt Eyink, Air Force Research Laboratory
Archie Holmes, The University of Texas at Austin
Mihee Ji, U.S. Army Research Laboratory
Sriram Krishnamoorthy, University of California, Santa Barbara
Charles Lutz, Lumentum Operations LLC
Nadeemullah Mahadik, U.S. Naval Research Laboratory
Kyle McNicholas, Lincoln Laboratory, Massachusetts Institute of Technology
Aaron Muhowski, Sandia National Laboratories
Hari Nair, Cornell University
Siddharth Rajan, The Ohio State University
Shadi Shahedipour-Sandvik, State University of New York Polytechnic Institute
Stephanie Tomasulo, U.S. Naval Research Laboratory
Christine Wang, Lincoln Laboratory, Massachusetts Institute of Technology
Dan Wasserman, The University of Texas at Austin
Man Hoi Wong, The Hong Kong University of Science and Technology
Kin-Man Yu, City University of Hong Kong

Hetero-Integration, Interconnects and Packaging

Guohai Chen, National Institute of Advanced Industrial Science and Technology
Mona Ebrish, U.S. Naval Research Laboratory
Daniel Ewing, U.S. Department of Energy's Kansas City National Security Campus
Michael Hamilton, Auburn University
Karl Hirschman, Rochester Institute of Technology
Jamie Phillips, University of Delaware

Materials for Memory and Computation

Alan Doolittle, Georgia Institute of Technology
Susan Fullerton, University of Pittsburgh
Eric Seabron, Howard University
Feng Xiong, University of Pittsburgh
Ke Xu, Rochester Institute of Technology
Angel Yanguas-Gil, Argonne National Laboratory

Materials Processing and Integration

Daniel Ewing, Department of Energy's Kansas City National Security Campus
Mark Goorsky, University of California, Los Angeles
Doug Hall, University of Notre Dame
Karl Hirschman, Rochester Institute of Technology
Karl Hobart, U.S. Naval Research Laboratory
Becky (R.L.) Peterson, University of Michigan
Nate Quitoriano, McGill University
Steve Ringel, The Ohio State University
Robert C. "Chris" Roberts, The University of Texas at El Paso
Patrick Shea, Northrop Grumman Corporation
Jerry Woodall, University of California, Davis

Metamaterials and Materials for THz, Plasmonics and Polaritons

Joshua Caldwell, Vanderbilt University
Kurt Eyink, Air Force Research Laboratory
Rachel Goldman, University of Michigan
Anthony Hoffman, University of Notre Dame
Stephanie Law, The Pennsylvania State University
Aaron Muhowski, Sandia National Laboratories
Eric Seabron, Howard University
Thomas Searles, University of Illinois at Chicago
Berardi Sensale Rodriguez, The University of Utah
Jason Valentine, Vanderbilt University
Daniel Wasserman, The University of Texas at Austin
Huili Grace Xing, Cornell University

Micro-LEDs and -Displays—Materials, Fabrication and Characterization

Steven DenBaars, University of California, Santa Barbara
Karl Hirschman, Rochester Institute of Technology
Joon Seop Kwak, Korea Institute of Energy Technology
In-Hwan Lee, Korea University
Zetian Mi, University of Michigan
Tae-Yeon Seong, Korea University
William Wong, University of Waterloo
Jerry Woodall, University of California, Davis

Nanofabrication and Processing

Bruno Azeredo, Arizona State University
Kris Bertness, National Institute of Standards and Technology
Mona Ebrish, U.S. Naval Research Laboratory
Munho Kim, Nanyang Technological University, Singapore
Xiuling Li, The University of Texas at Austin
Parsian Mohseni, Rochester Institute of Technology
Angel Yanguas-Gil, Argonne National Laboratory

Nano-Magnetic, Magnetic Memory and Spintronic Materials

Hemant Dixit, Wolfspeed
Michael Flatté, The University of Iowa
Cheng Gong, University of Maryland
Michael Hamilton, Auburn University
Roland Kawakami, The Ohio State University
Xinyu Liu, University of Notre Dame
Pawan Tyagi, University of the District of Columbia
Angel Yanguas-Gil, Argonne National Laboratory

Narrow Bandgap Materials and Devices

Ganesh Balakrishnan, The University of New Mexico
Suprem Das, Kansas State University
Shanti Iyer, North Carolina Agricultural and Technical State University
Sanjay Krishna, The Ohio State University
Andrej Lenert, University of Michigan
Kyle McNicholas, Lincoln Laboratory, Massachusetts Institute of Technology
Aaron Muhowski, Sandia National Laboratories
Kunal Mukherjee, Stanford University
Jamie Phillips, University of Delaware
Gregory Triplett, Virginia Commonwealth University
Christine Wang, Lincoln Laboratory, Massachusetts Institute of Technology
Daniel Wasserman, The University of Texas at Austin
Joshua Zide, University of Delaware

Point Defects, Doping and Extended Defects

Andrew Armstrong, Sandia National Laboratories
Ramon Collazo, North Carolina State University
Rachel Goldman, University of Michigan
Karl Hirschman, Rochester Institute of Technology
Lincoln Lauhon, Northwestern University
Kunal Mukherjee, Stanford University
Steve Ringel, The Ohio State University
Shadi Shahedipour-Sandvik, State University of New York Polytechnic Institute
Jun Suda, Kyoto University and Nagoya University
Christian Wetzel, Rensselaer Polytechnic Institute
Jerry Woodall, University of California, Davis

Quantum, Strongly Correlated and Topological Materials

Matthew Doty, University of Delaware
Rachel Goldman, University of Michigan
Anthony Hoffman, University of Notre Dame
Stephanie Law, The Pennsylvania State University
Connie Li, U.S. Naval Research Laboratory
Jeremy Robinson, U.S. Naval Research Laboratory
Thomas Searles, University of Illinois at Chicago
Chakrakpani Varanasi, U.S. Army Research Office—Materials Science Division

ENERGY STORAGE AND CONVERSION MATERIALS

Electrochemical Energy Storage and Conversion

Susan Fullerton, University of Pittsburgh
David Gundlach, National Institute of Standards and Technology
Jung-Hyun Kim, The Ohio State University
Zetian Mi, University of Michigan
Edward Yu, The University of Texas at Austin

Energy Harvesting

Alan Doolittle, Georgia Institute of Technology
Deidra Hodges, Florida International University
Ken Jones, U.S. Army Research Laboratory
Suzanne Mohney, The Pennsylvania State University
Jamie Phillips, University of Delaware
Shadi Shahedipour-Sandvik, State University of New York Polytechnic Institute

Solar Cell Materials and Devices

Geoffrey Bradshaw, Air Force Research Laboratory
Steven Durbin, Western Michigan University
Rachel Goldman, University of Michigan
Mark Goorsky, University of California, Los Angeles
Andrej Lenert, University of Michigan
Steve Ringel, The Ohio State University
Oleg Rubel, McMaster University
Jae-Hyun Ryou, University of Houston
Mike Scarpulla, The University of Utah
Christian Wetzel, Rensselaer Polytechnic Institute
Mark Wistey, Texas State University
Jerry Woodall, University of California, Davis

Thermoelectrics and Thermal Transport

Kris Bertness, National Institute of Standards and Technology
Steven Durbin, Western Michigan University
Samuel Graham, Georgia Institute of Technology
Ferdinand Poudeu, University of Michigan
Xiaojia Wang, University of Minnesota
Yaguo Wang, The University of Texas at Austin
Joshua Zide, University of Delaware

NANOSCALE SCIENCE AND TECHNOLOGY

Graphene, BN, MoS2 and Other 2D Materials and Devices

Thomas Beechem, Purdue University
Kevin Daniels, University of Maryland
Mona Ebrish, U.S. Naval Research Laboratory
James Edgar, Kansas State University
Randall Feenstra, Carnegie Mellon University
Susan Fullerton, University of Pittsburgh
Jyoti Katoch, Carnegie Mellon University
Roland Kawakami, The Ohio State University
Manos Kioupakis, University of Michigan
Rachel Koltun, Guardian Industries
Lincoln Lauhon, Northwestern University
Suzanne Mohney, The Pennsylvania State University
Siddharth Rajan, The Ohio State University
Joan Redwing, The Pennsylvania State University
Eric Seabron, Howard University
Michael Snure, Air Force Research Laboratory
Michael Spencer, Morgan State University
Christine Wang, Lincoln Laboratory, Massachusetts Institute of Technology
Huili Grace Xing, Cornell University
Ke Xu, Rochester Institute of Technology

Low-Dimensional Structures—Quantum Dots, Wires and Wells

Ganesh Balakrishnan, The University of New Mexico
Matthew Doty, University of Delaware
Kurt Eyink, Air Force Research Laboratory
Rachel Goldman, University of Michigan
Lincoln Lauhon, Northwestern University
Minjoo (Larry) Lee, University of Illinois at Urbana-Champaign
Zetian Mi, University of Michigan
Parsian Mohseni, Rochester Institute of Technology
Jamie Phillips, University of Delaware
Paul Simmonds, Boise State University
Daniel Wasserman, The University of Texas at Austin

Nanoscale Characterization—Scanning Probes, Electron Microscopy and Other Techniques

Thomas Beechem, Purdue University
Rachel Goldman, University of Michigan
Lincoln Lauhon, Northwestern University
James LeBeau, Massachusetts Institute of Technology
Anders Mikkelsen, Lund University
Jay Mody, Intel Corporation
Volker Rose, Argonne National Laboratory
Eric Seabron, Howard University
Rainer Timm, Lund University
Heayoung Yoon, The University of Utah
Edward Yu, The University of Texas at Austin

Nanostructured Materials

Kris Bertness, National Institute of Standards and Technology
Matt Brubaker, National Institute of Standards and Technology
Xiuling Li, The University of Texas at Austin
Zetian Mi, University of Michigan
Anders Mikkelsen, Lund University
Parsian Mohseni, Rochester Institute of Technology
Roberto Myers, The Ohio State University
Nate Quitoriano, McGill University
Rainer Timm, Lund University
George Wang, Sandia National Laboratories
William Wong, University of Waterloo

ORGANIC MATERIALS, THIN FILMS AND DEVICES

Flexible, Printed and/or Dissolvable Thin Films or Nanomembranes

Suprem Das, Kansas State University
Daniel Ewing, U.S. Department of Energy's Kansas City National Security Campus
Gerd Grau, York University
Thomas Jackson, The Pennsylvania State University
Thomas Kuech, University of Wisconsin–Madison
Becky (R.L.) Peterson, University of Michigan
Robert C. "Chris" Roberts, The University of Texas at El Paso
Jae-Hyun Ryou, University of Houston
William Scheideler, Dartmouth College
Jung-Hun Seo, University at Buffalo, The State University of New York
Sarah Swisher, University of Minnesota
William Wong, University of Waterloo

Organic and Hybrid Optoelectronic Devices

Alexander Ayzner, University of California, Santa Cruz
David Gundlach, National Institute of Standards and Technology
Diedra Hodges, Florida International University
Tina Ng, University of California, San Diego
Oleg Rubel, McMaster University
Adrienne Stiff-Roberts, Duke University
Wei You, University of North Carolina at Chapel Hill

Organic Devices and Molecular Electronics

Gerd Grau, York University
David Gundlach, National Institute of Standards and Technology
Thomas Jackson, The Pennsylvania State University
David Janes, Purdue University
Ioannis Kymissis, Columbia University
Takhee Lee, Seoul National University
Tina Ng, University of California, San Diego
Curt Richter, National Institute of Standards and Technology
Adrienne Stiff-Roberts, Duke University
William Wong, University of Waterloo

Wearable Electronics and Biosensors

Francesca Cavallo, The University of New Mexico
Buddhadev Paul Chaudhuri, Biolinq Inc.
Tzahi Cohen-Karni, Carnegie Mellon University
Shadi Dayeh, University of California, San Diego
David Estrada, Boise State University
Thomas Jackson, The Pennsylvania State University
David Janes, Purdue University
Robert C. "Chris" Roberts, The University of Texas at El Paso
Jae-Hyun Ryou, University of Houston
Shayla Sawyer, Rensselaer Polytechnic Institute

OXIDE SEMICONDUCTORS AND DIELECTRICS

Dielectrics and Multifunctional Oxides

Alan Doolittle, Georgia Institute of Technology
Doug Hall, University of Notre Dame
Karl Hirschman, Rochester Institute of Technology
Anderson Janotti, University of Delaware
David Lederman, University of California, Santa Cruz
Patrick Lenahan, The Pennsylvania State University
Joseph Ngai, The University of Texas at Arlington
Angel Yanguas-Gil, Argonne National Laboratory

Gallium Oxide and Other Ultra-Wide Bandgap Oxides

Elaheh Ahmadi, University of Michigan
Ramana Chintalapalle, The University of Texas at El Paso
Shizuo Fujita, Kyoto University
Masataka Higashiwaki, National Institute of Information and Communications Technology
Karl Hirschman, Rochester Institute of Technology
Mihee Ji, U.S. Army Research Laboratory
Sriram Krishnamoorthy, University of California, Santa Barbara
Shin Mou, Air Force Research Laboratory
Hari Nair, Cornell University
Becky (R.L.) Peterson, University of Michigan
Lisa Porter, Carnegie Mellon University
Siddharth Rajan, The Ohio State University
Marko Tadjer, U.S. Naval Research Laboratory
Man Hoi Wong, The Hong Kong University of Science and Technology
Huili Grace Xing, Cornell University
Hongping Zhao, The Ohio State University

Oxide Semiconductors—Growth, Doping, Defects, Nanostructures and Devices

Leonard Brillson, The Ohio State University
Steve Durbin, Western Michigan University
Karl Hirschman, Rochester Institute of Technology
Thomas Jackson, The Pennsylvania State University
Anderson Janotti, University of Delaware
Mark Losego, Georgia Institute of Technology
Hari Nair, Cornell University
Becky (R.L.) Peterson, University of Michigan
Shayla Sawyer, Rensselaer Polytechnic Institute
Sarah Swisher, University of Minnesota

WIDE BANDGAP SEMICONDUCTORS

Diamond and Related Materials

Mark Goorsky, University of California, Los Angeles
Andrew Koehler, U.S. Naval Research Laboratory
Nadeemullah Mahadik, U.S. Naval Research Laboratory
Jung-Hun Seo, University at Buffalo, The State University of New York
Patrick Shea, Northrop Grumman Corporation

Group III-Nitrides—Growth, Processing, Characterization, Theory and Devices

Zakaria Y. Al Balushi, University of California, Berkeley
Andrew Allerman, Sandia National Laboratories
Srabanti Chowdhury, Stanford University
Theeradetch Detchprohm, Georgia Institute of Technology
Alan Doolittle, Georgia Institute of Technology
Russell Dupuis, Georgia Institute of Technology
Daniel Ewing, U.S. Department of Energy's Kansas City National Security Campus
Qhalid Fareed, Texas Instruments
Daniel Feezell, The University of New Mexico
Hiroshi Fujioka, The University of Tokyo
Jennifer Hite, U.S. Naval Research Laboratory
Mihee Ji, U.S. Army Research Laboratory
Andrew Koehler, U.S. Naval Research Laboratory
In-Hwan Lee, Korea University
Xiaohang Li, King Abdullah University of Science and Technology
Siddharth Rajan, The Ohio State University
Shadi Shahedipour-Sandvik, State University of New York Polytechnic Institute
Andrei Vescan, RWTH Aachen University
Christian Wetzel, Rensselaer Polytechnic Institute
Jonathan Wierer, North Carolina State University
Man Hoi Wong, The Hong Kong University of Science and Technology
Huili Grace Xing, Cornell University

Silicon Carbide—Growth, Processing, Characterization, Theory and Devices

Joshua Caldwell, Vanderbilt University
MVS Chandrashekhar, University of South Carolina
Sarit Dhar, Auburn University
Michael Dudley, Stony Brook University, The State University of New York
Daniel Ewing, U.S. Department of Energy's Kansas City National Security Campus
Nadeemullah Mahadik, U.S. Naval Research Laboratory
Michael Spencer, Morgan State University
Jun Suda, Kyoto University and Nagoya University

FLOOR PLANS & MAPS

University of California, Santa Barbara

1. MultiCultural Center

Technical Sessions ..... MCC Theater

2. University Center

Main Level

Registration ..... Corwin Lobby
Welcome Reception ..... Lagoon Plaza
Poster Session ..... Lagoon Plaza
Refreshment Breaks ..... Lagoon Plaza
Exhibit ..... Lagoon Plaza
Technical Sessions ..... Corwin East
Technical Sessions ..... Flying A Studios

Lower Level

Technical Sessions ..... Lobero
Technical Sessions ..... Santa Barbara Harbor
Technical Sessions ..... State Street

3. Music Building

EMC Awards Ceremony & Plenary Session .... Lotte Lehmann
Technical Sessions ..... Lotte Lehmann

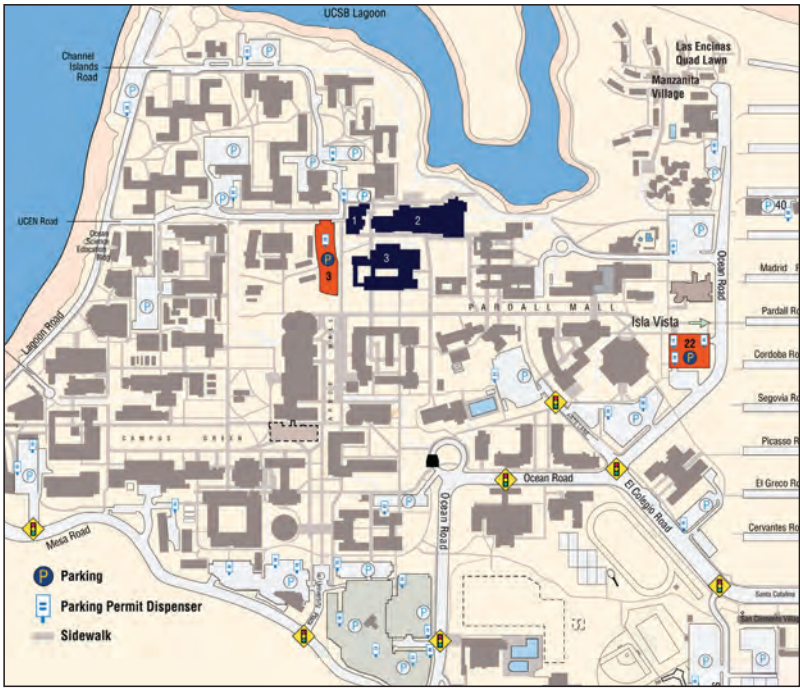

1. MultiCultural Center

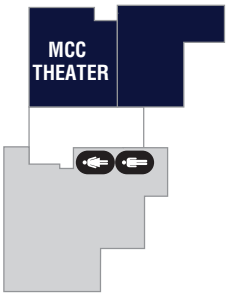

3. Music Building

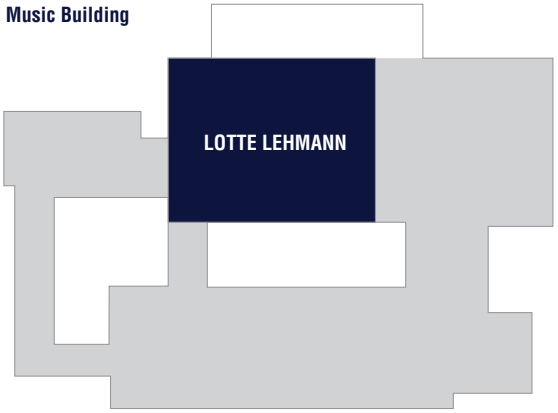

2. University Center
Lower Level

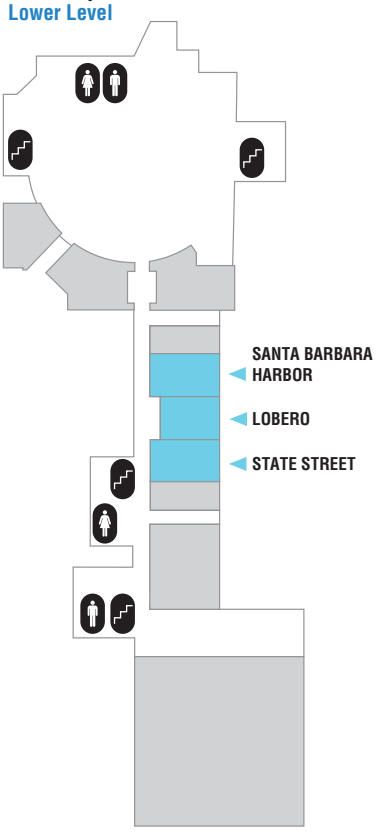

2. University Center
Main Level

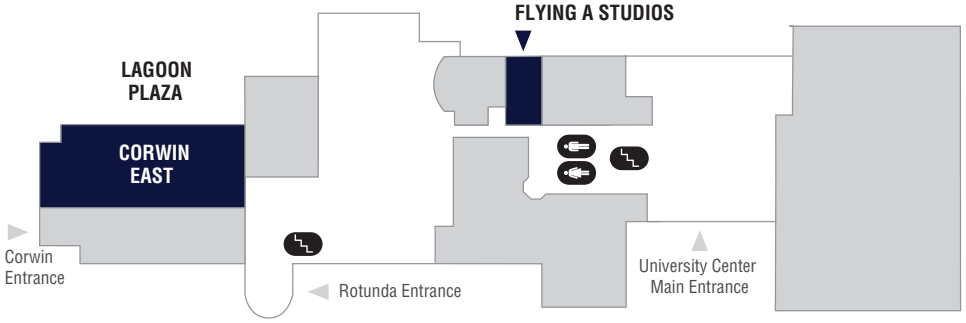

EMC AWARDS CEREMONY & PLENARY SESSION

Wednesday, 8:20 am – 9:20 am
Music Building, Lotte Lehmann

PLENARY SPEAKER

Darrell Schlom
Cornell University

Suboxide Molecular-Beam Epitaxy

Darrell Schlom is the Herbert Fisk Johnson Professor of Industrial Chemistry in the Department of Materials Science and Engineering at Cornell University. After receiving a BS degree from the California Institute of Technology, he completed graduate work at Stanford University receiving a MS degree in electrical engineering and a PhD degree in materials science and engineering. He was then a Postdoc at IBM's research lab in Zurich, Switzerland, in the oxide superconductors and novel materials group managed by Nobel Prize winners J. Georg Bednorz and K. Alex Müller. In 1992, Schlom joined the faculty at The Pennsylvania State University in the Department of Materials Science and Engineering, where he spent 16 years before joining the faculty at Cornell University in 2008. His research interests involve the heteroepitaxial growth and characterization of oxide thin films by reactive molecular beam epitaxy (MBE), especially utilizing a "materials-by-design" approach to the discovery of materials with properties superior to any known. His group synthesizes these oxide heterostructures using MBE. He has published over 500 papers and 8 patents resulting in an h-index of 113 and over 62,000 citations. Schlom has received various awards including a Humboldt Research Award and the MRS Medal, is a Fellow of both the American Physical Society and the Materials Research Society, and is a member of the National Academy of Engineering.

2022 BEST STUDENT PRESENTATION AWARDS

ORAL PRESENTATION

Corey White
The University of Texas at Austin
Growth of InAsSbBi on InSb Towards Lattice-Matched Longwave-Infrared Optoelectronics
Advisor – Seth Bank

POSTER PRESENTATION

Elizabeth Favela
Carnegie Mellon University
Ni/Au and Co/Au Schottky Contacts on β-Ga_2O_3 and Effects of Annealing
Advisor – Lisa Porter

HONORABLE MENTIONS

Emanuel Ber
Technion–Israel Institute of Technology
Reducing Schottky Barrier Height vs Width—Which is Most Effective in Improving Contact Resistance to Atomically Thin Semiconductors?
Advisor – Eilam Yalon

Eamonn T. Hughes
University of California, Santa Barbara
Dislocations Altering the Microstructure and Luminescence of InAs Quantum Dots on Silicon
Advisors – John Bowers, University of California, Santa Barbara and Kunal Mukherjee, Stanford University

Michael Pedowitz
University of Maryland
Growth and Transformation of Mixed Valence Manganese Oxide Nanostructures on Epitaxial Graphene-Silicon Carbide Heterostructures
Advisor – Kevin Daniels

Emma Rocco
State University of New York Polytechnic Institute
N-Polar GaN Photocathodes Stabilized with h-BN
Advisor – Shadi Shahedipour-Sandvik

Nicholas Trainor
The Pennsylvania State University
Kinetics of Wafer-Scale Epitaxial Growth of MoS_2 on Sapphire
Advisor – Joan Redwing

TMS FOUNDATION
Student participation in this Conference is partially supported by a grant from the TMS Foundation

DAILY SCHEDULE OF EVENTS

UC = University Center
MCC = MultiCultural Center

TUESDAY		
Registration	8:00 am – 5:00 pm	UC, Corwin Lobby

WEDNESDAY		
Registration	7:30 am – 5:00 pm	UC, Corwin Lobby
EMC Awards Ceremony & Plenary Session	8:20 am – 9:20 am	Music Building, Lotte Lehmann
Poster Set-up	9:30 am – 3:00 pm	UC, Lagoon Plaza
Refreshment Break	9:20 am – 10:00 am	UC, Lagoon Plaza
A: Group III-Nitrides—Devices	10:00 am – 12:00 pm	Music Building, Lotte Lehmann
B: 2D Materials Properties and Interfaces	10:00 am – 12:00 pm	UC, Corwin East
C: Photonic Devices	10:00 am – 12:00 pm	UC, Flying A Studios
D: Nanoscale Characterization	10:00 am – 12:00 pm	UC, State Street
E: Hetero-Integration, Interconnects and Packaging	10:00 am – 12:00 pm	UC, Santa Barbara Harbor
F: Gallium Oxide Devices	10:00 am – 12:00 pm	MCC Theater
DRC: Session 11: Memory	10:00 am – 12:00 pm	UC, Corwin West
Exhibit	10:00 am – 8:00 pm	UC, Lagoon Plaza
Lunch	12:00 pm – 1:30 pm	(not provided by Conference)
G: Group III-Nitrides—Vertical Power Devices	1:30 pm – 5:10 pm	Music Building, Lotte Lehmann
H: 2D Materials, Devices and Sensors	1:30 pm – 5:10 pm	UC, Corwin East
I: Novel IR Detector Materials	1:30 pm – 3:10 pm	UC, Flying A Studios
K: Energy Materials and Devices	1:30 pm – 4:50 pm	UC, State Street
L: Organic and Hybrid Materials for Optoelectronic Devices	1:30 pm – 3:10 pm	UC, Lobero
M: Group III-Nitrides—Optical Emitters	1:30 pm – 5:10 pm	UC, Santa Barbara Harbor
N: Characterization of Gallium Oxide-Based Materials and Devices I	1:30 pm – 5:10 pm	MCC Theater
DRC: Session 12: Devices for Extreme Conditions	1:00 pm – 2:40 pm	UC, Corwin West
General Poster Viewing	3:10 pm – 3:30 pm	UC, Lagoon Plaza
Refreshment Break	3:10 pm – 3:30 pm	UC, Lagoon Plaza
J: Novel Materials Epitaxy	3:30 pm – 5:10 pm	UC, Flying A Studios
Student Finalists for Oral Presentation Award—Part A	5:10 pm – 6:10 pm	UC, State Street
Student Finalists for Oral Presentation Award—Part B	5:10 pm – 6:10 pm	UC, Lobero
Welcome Reception/Poster Session	6:00 pm – 8:00 pm	UC, Lagoon Plaza

THURSDAY		
Registration	8:00 am – 5:00 pm	UC, Corwin Lobby
O: Group III-Nitrides—Novel Nitride Growth	8:20 am – 12:00 pm	Music Building, Lotte Lehmann
P: 2D Materials Synthesis and Characterization	8:20 am – 11:40 am	UC, Corwin East
Q: Optical Materials on Si	8:20 am – 10:00 am	UC, Flying A Studios
S: SiC Materials Characterization, Processing and Devices	8:20 am – 12:00 pm	UC, State Street
T: Organic Devices and Molecular Electronics	8:20 am – 12:00 pm	UC, Lobero
U: Group III-Nitrides—Contacts and Special Topics	8:20 am – 12:00 pm	UC, Santa Barbara Harbor
V: Growth of Gallium Oxide and Other Ultrawide-Bandgap Oxides	8:20 am – 11:40 pm	MCC Theater
General Poster Viewing	10:00 am – 10:20 am	UC, Lagoon Plaza
Refreshment Break	10:00 am – 10:20 am	UC, Lagoon Plaza
R: Epitaxial Materals Design and Properties	10:20 am – 12:00 pm	UC, Flying A Studios
Exhibit	10:00 am – 4:00 pm	UC, Lagoon Plaza
Lunch	12:00 pm – 1:30 pm	(not provided by Conference)
W: Group III-Nitrides—Late News	1:50 pm – 3:10 pm	Music Building, Lotte Lehmann
X: Group III-Nitrides—Growth and Characterization	1:30 pm – 5:10 pm	UC, Corwin East
Y: Plasmonics, Photonics for Detection and Emission	1:30 pm – 5:10 pm	UC, Flying A Studios
Z: Emergent Materials and Devices for Microelectronics	1:30 pm – 5:10 pm	UC, State Street
AA: Semiconducting Oxide Thin Films and Transistors	1:30 pm – 5:10 pm	UC, Lobero
BB: Group III-Nitrides—P-Type Doping and Characterization	1:30 pm – 4:50 pm	UC, Santa Barbara Harbor
CC: Characterization of Gallium Oxide-Based Materials and Devices II	1:30 pm – 3:10 pm	MCC Theater
General Poster Viewing	3:10 pm – 3:30 pm	UC, Lagoon Plaza
Refreshment Break	3:10 pm – 3:30 pm	UC, Lagoon Plaza
DD: Gallium Oxide Materials Processing	3:30 pm – 5:10 pm	MCC Theater
Poster Tear Down	3:30 pm – 5:30 pm	UC, Lagoon Plaza
Conference Dinner Reception	6:30 pm – 8:30 pm	Manzanita Village Las Encinas Quad Lawn

FRIDAY		
Registration	8:00 am – 12:00 pm	UC, Corwin Lobby
EE: Diamond and Related Materials	8:20 am – 10:00 am	UC, Corwin East
GG: Epitaxy of Structured and Quantum Materials	8:20 am – 12:00 pm	UC, Flying A Studios
HH: Materials Processing and Integration	8:20 am – 12:00 pm	UC, State Street
II: Flexible, Printed and Wearable Electronics and Sensors	8:20 am – 11:40 am	UC, Lobero
JJ: Low-Dimensional Structures—Quantum Dots, Wires and Wells	8:20 am – 10:00 am	UC, Santa Barbara Harbor
LL: Dielectrics, Ferroelectrics, and Multifunctional Oxides	8:40 am – 12:00 pm	MCC Theater
Refreshment Break	10:00 am – 10:20 am	UC, Lagoon Plaza
FF: Group III-Nitrides—Thermal Transport	10:20 am – 11:40 am	UC, Corwin East
KK: Micro-LEDs	10:20 am – 12:00 pm	UC, Santa Barbara Harbor

TRAVEL RESOURCES

The Conference does not endorse or sponsor any of the listings below. Information is provided as a courtesy to attendees.

UNIVERSITY OF CALIFORNIA, SANTA BARBARA SMOKE-FREE AND TOBACCO-FREE POLICY

The entire University of California (UC) system is smoke-free and tobacco-free. Smoking, the use of smokeless tobacco products, e-cigarettes, and unregulated products will not be allowed on UC owned or leased properties.

INTERNET ACCESS

Complimentary Internet access is available through "UCSB Wireless Web" by selecting "Guest Registration" under the credential login. Once you register, you will receive a username and password, which is enabled for a seven-day connection. For more information, please visit the UCSB Visitor's page at https://www.it.ucsb.edu/wifi/visitors-ucsb.

DINING

Attendees staying on campus can enjoy many local dining options: **Starbucks** is located at the University Center next to the Campus store; **Coral Tree Café** offers a hot and cold full coffee bar, breakfast, lunch, prepackaged foods and snacks; **Panda Express** serves quick Asian food; **Santorini Island Grill** has gyros, calamari and other Greek island classics; **Root Burger** makes local, natural and fresh burgers, hot breakfast, wraps and more. Stop by the Registration Desk for a complete list of dining options, hours and their locations during registration hours.

PARKING

Parking ePermits are required at all times when parking at University of California, Santa Barbara. Parking ePermits are issued to the license plate displayed on the vehicle. The license plate must be visible from the drive aisle of the parking lot and are only valid in the lot where the ePermit is purchased.

After purchasing an ePermit, guests may use any green time-restricted parking spaces for the time designated (e.g., 20, 30 or 40 minute green curb spaces) to unload. Guests must have a valid campus ePermit to use one of these loading zones.

The two primary ON-CAMPUS parking locations for conference attendees are **Parking Structures 18 and 22.**

ePermits can be purchased using the ParkMobile app, the ePermit website, or through ePermit Pay Stations/ Dispensers located throughout the parking structures. If purchasing through ParkMobile, use the zone number that is posted where you park.

For multiday permits, be sure to include your arrival day and departure day.

ParkMobile Link/App:

- https://app.parkmobile.io/login
- Primarily for on-campus short-term parking permit purchases.
- Skip the pay station and conveniently pay for parking through your phone!
- Pay Station/Dispenser and ParkMobile permits are only valid in the lot purchased (Structure 18 or 22).

ePermit Portal Link:

- tps.ucsb.edu/epermits
- Scroll to Student & Guest Login at bottom of page.
- Primarily for long-term parking permit purchases.
- Select the Visitor/C permit. If a C ePermit is purchased through the ePermit portal, this will allow you to move your vehicle after 5:00 pm to Lot 3 (unmarked spots), which is closer to University Center. Please reference the campus interactive map and signage at the lot entrance for all guidelines and restrictions (avoid spots marked reserved, restricted, gold, faculty at all times).

PROGRAM AT-A-GLANCE

WEDNESDAY AM

EMC Awards Ceremony & Plenary Session			Music Building, Lotte Lehmann
8:20 am			EMC Awards Ceremony
8:30 am	Darrell Schlom	*PL01	Suboxide Molecular-Beam Epitaxy
9:20 am			BREAK
A: Group III-Nitrides—Devices			**Music Building, Lotte Lehmann**
10:00 am	Yu-Hsin Chen	A01	(Student) High Electron Density AlN/GaN/AlGaN Quantum-Well HEMTs on Al-Polar Single-Crystal AlN Substrates
10:20 am	Joseph Dill	A02	(Student) Measurement of Hole Velocity vs. Electric Field in Polarization-Induced Two-Dimensional Hole Gases in GaN/AlN Heterojunctions
10:40 am	Abdullah Mamun	A03	$Al_{0.64}Ga_{0.36}N$ Channel MOSHFET on Single Crystal Bulk AlN Substrate for Co-Designed Power Electronics
11:00 am	Jiahao Chen	A04	(Student) Record Low Sheet Resistivity (<250 Ω/■) in High Composition (>35%) and Thick (>30 nm) Crack-Free Strain Optimized Barrier AlGaN/AlN/GaN HEMT on Sapphire
11:20 am	Thai-Son T. Nguyen	A05	(Student) Epitaxial Growth and Transport Properties of AlScN/GaN FerroHEMTs
11:40 am	Dawei Wang	A06	(Late News) Reliability Study and Analysis of Vertical GaN Power Devices
B: 2D Materials Properties and Interfaces			**UC, Corwin East**
10:00 am	Mingfei Xu	B01	(Student) Investigation of Dielectric Properties of h-BN/c-BN Nanocomposites
10:20 am	Elisabeth Mansfield	B02	Reliability of Electronics Containing 2D Materials
10:40 am	M. Saifur Rahman	B03	Doping and Damage of MoS_2 Monolayers from Metal Deposition
11:00 am	Zubaer Hossain	B04	Strain-Induced Magnetism in Defective Graphene
11:20 am	Quazi Deen Mohd Khosru	B05	Graphene-Polymar Mono Defect Based Octonacci Quasi-Photonic Dual Narrowband Absorber
11:40 am	Jennifer Elizabeth DeMell	B06	(Student) Temperature Dependent Spin Transport and Thermally Driven Quantum Phase Change in Graphene/$Pb_{0.24}Sn_{0.76}Te$ Heterostructure Two-Dimensional Electron Gas
C: Photonic Devices			**UC, Flying A Studios**
10:00 am	James Bork	C01	(Student) (In)AlBiAs-Based Short-Wave Infrared Avalanche Photodiodes
10:20 am	Subhashree Seth	C02	(Student) Optically Pumped 1200 nm InAs Dot-in-Well (DWELL) Photonic Crystal Surface-Emitting Laser (PCSEL) by Molecular Beam Epitaxy
10:40 am	Jingze Zhao	C03	(Student) Long-Wave Infrared Beam Steering with InAsSb Phased Arrays
11:00 am	Aaron Engel	#C04	(Student) Molecular Beam Epitaxy of Strained Superlattice InAlGaAs/AlGaAs Spin-Polarized Photocathodes
11:20 am	Alexander Timothy Newell	C05	(Student) Sensitivity Optimization in Diffusion-Limited Infrared Detectors
11:40 am	Kevin Kucharczyk	C06	(Student) Development of GaAs Photodetector Arrays for Soft X-Ray Beam Position Monitoring
D: Nanoscale Characterization			**UC, State Street**
10:00 am	Andrey Krayev	D01	TERS Imaging—Unique Nanoscale Technique for Characterization of 2D Materials and Their Lateral/Vertical Heterostructures
10:20 am	Haoxue Yan	D02	Rapid Characterization of Threading Dislocations in Diamond via Coincident Cathodoluminescence and Electron Channeling Contrast Imaging
10:40 am	Carlo Requiao daCunha	D03	Estimating the Background Potential of Quantum Constrictions Using Scanning Gate Microscopy and Machine Learning
11:00 am	Stephen M. Bankson	D04	(Student) Characterization of Surface Morphology and Superconducting Performance of Thin Aluminum Films Deposited via Thermal Evaporation at Tilted Angles
11:20 am	Robert Stroud	D05	TESCAN TENSOR a 4D-STEM for Multimodal Characterization of Challenging and Interesting Specimens
11:40 am	Michael Evan Liao	D06	Investigation of Extended Defects in Single Crystal Calcite Substrates Using High Resolution X-Ray Topography
E: Hetero-Integration, Interconnects and Packaging			**UC, Santa Barbara Harbor**
10:00 am	Muhannad Bakir	E01	Heterogeneous Multi-Die Stitching Enabled by Compressible Microinterconnects (CMIs)
10:20 am	Bilal Azhar	E02	(Student) Quasi-2D Materials for Ultra-Low Resistance Electrical Interconnects
10:40 am	Gangtae Jin	E03	Dimensional Scaling of Topological Metal Nanowires for Interconnect
11:00 am	Kenny Huynh	E04	Stability of Interface Morphology and Thermal Boundary Conductance of Direct Wafer Bonded GaN|Si Heterojunction Interfaces Annealed at Growth and Annealing Temperatures
11:20 am	Bhargav Yelamanchili	E05	(Student) Superconducting Resonators with Closely Spaced Resonant Frequencies for Material Loss Measurements
11:40 am	Rohan Sengupta	E06	(Student, Late News) Improvement of Heterogeneously Integrated InGaAs/GaN Junctions via Post-Bonding Annealing for Next-Generation Transistors
F: Gallium Oxide Devices			**MCC, MCC Theater**
10:00 am	Sushovan Dhara	#F01	(Student) [100] and [010] Oriented β-Ga_2O_3 Trench Schottky Barrier Diodes with Improved On-Resistance Using Low Damage Atomic Ga Etching
10:20 am	Nolan Hendricks	F02	(Student) Forward and Reverse Current Transport of (001) β-Ga_2O_3 Schottky Barrier Diodes and TiO_2/β-Ga_2O_3 Heterojunction Diodes with Various Schottky Metals
10:40 am	Esmat Farzana	F03	Vertical β-Ga_2O_3 Diodes with High Barrier PtOx Contacts and High-k TiO_2 Field Plate on Low-Doped Epitaxy for High Breakdown Voltage
11:00 am	Joseph Spencer	F04	(Student) Platinum Oxide Schottky Contacts to Highly-Doped (-201) β-Ga_2O_3
11:20 am	Takumi Ohtsuki	F05	Application of $(Al_xGa_{1-x})_2O_3$ as Back Barrier in Lateral Ga_2O_3 Radio-Frequency Field-Effect Transistors
11:40 am	Taeyoung Kim	F06	(Student) Demonstration of Gallium Oxide Nano-Pillar Field Emitter Arrays

*Plenary Talk # Student Finalist for Oral Presentation

PROGRAM AT-A-GLANCE

UC = University Center
MCC = MultiCultural Center

WEDNESDAY PM

G: Group III-Nitrides—Vertical Power Devices			Music Building, Lotte Lehmann
1:30 pm	Caleb Glaser	G01	(Student) Improving Electrical Performance of GaN-on-GaN MOS Devices Via Optimized Atomic Layer Deposition of Al_2O_3 Gate Dielectrics
1:50 pm	Dawei Wang	G02	Design and Fabrication of AlGaN/GaN Multiple P-Channel Schottky Barrier Diodes
2:10 pm	Md. Tahmidul Alam	G03	(Student) TCAD-Based Comprehensive Analysis of High Voltage (>600 V) Bidirectional AlGaN/GaN HEMTs
2:30 pm	LeighAnn Sarah Larkin	G04	Alpha Radiation Damage Assessment in GaN by Time-Resolved Luminescence Spectroscopy
2:50 pm	Mina Moradnia	G05	(Student) Crack-Free III-N Epitaxial Growth on Si (111) Substrate Exceeding 1 µm in Thickness
3:10 pm			BREAK
3:30 pm	Zhiyu Xu	G06	(Student) 1.2kV Vertical GaN PIN Rectifiers with Nitrogen-Implanted Floating Guard Rings as Edge Termination and Breakdown Characteristics Correlation Study by Wafer-Level Photoluminescence Mapping
3:50 pm	Henryk Turski	G07	Exploiting Competition Between Built-in Polarization and P-N Junction Field in III-Nitride Heterostructures
4:10 pm	Mona Ebrish	G08	Contacting p-GaN Efficiently—Why the Same Metal Stacks Give Different Results?
4:30 pm	Christopher M. Matthews	G09	(Student) Electrical Characterization of AlN PN Diodes
4:50 pm	Ziyi He	G10	(Student) Effect of Impact Ionization Coefficients on High-Voltage Vertical AlN Power Devices
H: 2D Materials, Devices and Sensors			**UC, Corwin East**
1:30 pm	Juntae Jang	H01	(Student) Reduced Scattering in Remote Surface Charge Transfer Doped MoS_2 Field Effect Transistors
1:50 pm	Ruixue Li	H02	(Student) Electrical Characterization and Contact Resistance to ALD-Deposited $WNbS_2$ Thin Films
2:10 pm	Yun Ping Chiu	H03	(Student) Surface Polarization Engineering Design of 2D Janus MoSSe Complementary Field Effect Transistors
2:30 pm	Daniel Lewis	H04	(Student) Non-Conductive Electron Transport Through a Quasi-Freestanding Epitaxial Graphene-Insulator Heterostructure Towards a Vacuum-Independent X-Ray Source
2:50 pm	Ghanshyam Das Varma	H05	Humidity Tolerant Low Power-Consumption Flexible α-Fe_2O_3/rGO/PANI Ternary Nanocomposite for NO_2 Gas Sensing at Room Temperature
3:10 pm			BREAK
3:30 pm	Saad Bhuiya	H06	(Student) Graphene/III-As Nanosheets—Self-Assembly, Electrical Transport and Potential for THz Generation
3:50 pm	Frances Camille Masim Wu	#H07	(Student) Control of Dark Exciton Dynamics in Suspended WSe_2 Monolayer via Electrostatic Deflection
4:10 pm	Claire Ganski	H08	(Student) Effects of Strain and Local Topography on Electromechanical Coupling in Monolayer Transition Metal Dichalcogenides
4:30 pm	Ying-Chuan Chen	H09	(Student) Studies of 2D Material Resistive Random-Access Memory by Kinetic Monte Carlo Simulation
4:50 pm	Ramesh G. Mani	H10	Electrically Detected Spin Resonance in Graphene
I: Novel IR Detector Materials			**UC, Flying A Studios**
1:30 pm	Charles W. Tu	I01	The Effects of Strain Compensation in Type-II InGaAs/GaAsSb Quantum Wells Grown on GaAs(001) Substrates
1:50 pm	Jingze Zhao	I02	(Student) Minority Carrier Lifetime and Mobility in Bulk InAsSb for High Quantum Efficiency LWIR Detectors
2:10 pm	Rachel Corey White	I03	(Student) Optical and Structural Properties of InSb-Based Dilute-Bismide Alloys Grown by Molecular Beam Epitaxy
2:30 pm	Amberly Ricks	I04	(Student) Bismuth Incorporation in AlInSb for Wide-Bandgap Barriers on InSb
2:50 pm	Fatih Furkan Ince	I05	(Student) MBE Growth of InSb Quantum Well on InAs (100) Using AlInSb Buffer Layer
3:10 pm			BREAK
J: Novel Materials Epitaxy			**UC, Flying A Studios**
3:30 pm	Pooja Donthi Reddy	J01	(Student) Single-Phase Orthorhombic SnSe-PbSe Alloy Thin Films Stabilized on GaAs by Molecular Beam Epitaxy
3:50 pm	Morgan Bergthold	J02	(Student) Photoluminescence Efficiency and Minority Carrier Lifetime of Type-II Superlattices on GaAs Using an Interfacial Misfit Array
4:10 pm	Leland Joseph Nordin	J03	PbSe Mid-Infrared Light Emitting Diodes on III-V Substrates
4:30 pm	Zezhi Wu	J04	(Student) Monolithic III-V on $LiNbO_3$ for Nonlinear Optics Application
4:50 pm	Jarod Meyer	J05	(Student) Room Temperature Photoluminescence at 3–8 µm in Epitaxial PbSe-SnSe Alloy Films on GaAs
K: Energy Materials and Devices			**UC, State Street**
1:30 pm	Etee Kawna Roy	K01	(Student) Photovoltaic Characteristics of PERC-Like CdTe Solar Cells
1:50 pm	Intuon Chatratin	K02	(Student) Compensation Centers in Group-V Doped CdTe
2:10 pm	Arash Takshi	K03	Fiber-Shaped Hybrid Solar Cell and Storage Devices for Wearable Electronics Applications
2:30 pm	Stephen Polly	K04	InGaAs/GaAsP Multiple Quantum Well Enhanced Multijunction Photovoltaics
2:50 pm	Jeffrey Lindemuth	K05	Improved AC Field Hall Measurements Using Hybrid Filters
3:10 pm			BREAK
3:30 pm	Navid Attarzadeh	K06	(Student) Doped Ternary and Quaternary Transition-Metal Chalcogenides Electrocatalyst for Efficient Water Splitting
3:50 pm	Rachael Richards	K07	Influence of Repeat Unit Structure on Exciton Transfer Between Semiconducting Polyelectrolytes
4:10 pm	Luis F. Hernandez Camas	K08	(Late News) Comparing the Effect of TiO_2 and SnO_2 on Efficiency of Perovskite Solar Cells and Development of Efficient Electron Transport Layer for Perovskite Solar Cell
4:30 pm	Doha Mahmoud Sayed Mohammed	K09	Optimized Lithography-Free Fabrication of Sub-100 nm Nb_2O_5 Nanotube Films as Negative Supercapacitor Electrodes: Tuned Oxygen Vacancies and Cationic Intercalation

Student Finalist for Oral Presentation

L: Organic and Hybrid Materials for Optoelectronic Devices			**UC, Lobero**
1:30 pm	Mohammad Ashif Hossain Chowdhury	L01	(Student) Monitoring Stability of Metal-Halide Perovskites Under Combined Stressors of Ion-Beam and Heat
1:50 pm	Jonghoon Lee	L02	(Student) Bulk Incorporation of Organic Molecular Dopants into Two-Dimensional Ruddlesden-Popper Hybrid Perovskite Structures
2:10 pm	Yongsup Park	L03	Direct Measurements of HOMO–LUMO Transport Gaps at the Surface and Interface of Organic Semiconductor Materials Using Direct and Inverse Photoemission Spectroscopies (UPS & IPES)
2:30 pm	Andrew Herzing	L04	(Late News) Structural and Morphological Characterization of Organic Electrochemical Transistors via Four-Dimensional (4D) Scanning Transmission Electron Microscopy
2:50 pm	Shang-Hsuan Wu	L05	(Student, Late News) Climate-Adaptive Thermochromic Perovskite Smart Window Structures
3:10 pm			BREAK
M: Group III-Nitrides—Optical Emitters			**UC, Santa Barbara Harbor**
1:30 pm	Shigefusa F. Chichibu	M01	Short-Term Degradation Mechanisms of 275-nm-Band AlGaN-Based Deep-Ultraviolet Light Emitting Diodes Fabricated on a Sapphire Substrate
1:50 pm	Agnes Maneesha Dominic Merwin Xavier	M02	(Student) Demonstration of AlGaN Tunnel Junction p-Down UV Light Emitting Diodes
2:10 pm	Yuto Ando	M03	Non-Planar Growth of Crack-Free High Al-Mole-Fraction AlGaN Heterostructures on Patterned GaN Substrates for Ultraviolet Light Emitting Diodes and Laser Diodes
2:30 pm	Matt Brubaker	M04	Shadowing Effects in Core-Shell InGaN Quantum Wells Grown on N-Polar GaN Nanowire Arrays by Molecular Beam Epitaxy
2:50 pm	Anand Ithepalli	M05	(Student) Fabrication and Characterization of Epitaxially Grown and Lifted off AlN Membranes
3:10 pm			BREAK
3:30 pm	Mateusz Hajdel	#M06	(Student) III-Nitride Laser Diodes with Wide Quantum Wells: Influence of Built-In Electric Fields on the Light Generation Process
3:50 pm	Gordon Schmidt	M07	Advanced Cathodoluminescence Microscopy of a Cascaded InGaN/GaN LED
4:10 pm	Guangying Wang	M08	(Student) MOCVD of a Novel InGaN/GaN/AlGaN Active Region Design for Ultraviolet Light-Emitting Diodes
4:30 pm	Greg Muziol	M09	Critical Thickness of InGaN Grown by Plasma-Assisted Molecular Beam Epitaxy
4:50 pm	James Loveless	M10	(Student) Demystifying Light Extraction Efficiency in AlGaN Based UV LEDs
N: Characterization of Gallium Oxide-Based Materials and Devices I			**MCC, MCC Theater**
1:30 pm	Hemant Jagannath Ghadi	N01	Evidence of Electron and Hole Photoemission During DLOS Characterization of Nitrogen Implanted β-Ga_2O_3
1:50 pm	Makoto Kasu	N02	Killer Defects Responsible for Leakage Current in HVPE (001) β-Ga_2O_3 SBD Observed by Emission Microscopy and Synchrotron X-Ray Topography
2:10 pm	Takuya Maeda	N03	Photocurrent Induced by Franz-Keldysh Effect in β-Ga_2O_3 Schottky Barrier Diode Under High Reverse Bias Voltage
2:30 pm	Dinusha Herath Mudiyanselage	N04	(Student) Anisotropic Electronic Properties of NiOx/β-Ga_2O_3 p-n Heterojunctions on (-201), (001), and (010) β-Ga_2O_3 Substrates
2:50 pm	Joe F. McGlone	N05	Impact of Radiation Damage and Buffer Charge on Si δ-Doped β-Ga_2O_3 MESFETs
3:10 pm			BREAK
3:30 pm	Kenny Huynh	N06	Origin of Surface Defects in Homoepitaxially Grown (010) β-Ga_2O_3 Films
3:50 pm	Hsien-Lien Huang	#N07	(Student) Atomic Scale Defect Formation and Phase Transformation in Si Implanted β-Ga_2O_3
4:10 pm	Michael Scarpulla	N08	Measuring Diffusion of Al, Sn, and Fe in Ga_2O_3 Using β-$(Al,Ga)_2O_3$/Ga_2O_3 Superlattices
4:30 pm	Minhan Lou	N09	Linearly Polarized UV, Blue and IR Photoluminescence from β-Ga_2O_3
4:50 pm	Cassandra Remple	N10	(Student) Photoluminescence Spectroscopy of Cr^{3+} in β-Ga_2O_3 and $(Al_{0.1}Ga_{0.9})_2O_3$
Student Finalists for Oral Presentation Award—Part A (5:00 pm—6:00 pm)			**UC, State Street**
	Frances Camille Masim Wu	#H07	(Student) Control of Dark Exciton Dynamics in Suspended WSe_2 Monolayer via Electrostatic Deflection
	Sushovan Dhara	#F01	(Student) [100] and [010] Oriented β-Ga_2O_3 Trench Schottky Barrier Diodes with Improved On-Resistance Using Low Damage Atomic Ga Etching
	Ryoya Ishikawa	#S01	(Student) Anisotropic Electron and Hole Mobilities in 4H-SiC Bulk Crystals
	Ashlee Garcia	#GG03	(Student) SiO_2 Surface Planarization for Molecular Beam Epitaxy Selective Area Regrowth of High Aspect Ratio Microstructures
	Hsien-Lien Huang	#N07	(Student) Atomic Scale Defect Formation and Phase Transformation in Si Implanted β-Ga_2O_3
Student Finalists for Oral Presentation Award—Part B (5:00 pm—6:00 pm)			**UC, Lobero**
	Jingxian Li	#Z01	(Student) Origins of Nonvolatility in Resistive Switching Memory
	Aaron Engel	#C04	(Student) Molecular Beam Epitaxy of Strained Superlattice InAlGaAs/AlGaAs Spin-Polarized Photocathodes
	Thomas Leonard	#Z06	(Student) Multi-Weight Magnetic Artificial Synapses with Geometry-Dependent Neuromorphic Functionality
	Mateusz Hajdel	#M06	(Student) III-Nitride Laser Diodes with Wide Quantum Wells—Influence of Built-In Electric Fields on the Light Generation Process
	Saurav Roy	#DD02	(Student) Enhancing the Dielectric Performance of Al_2O_3 on β-Ga_2O_3 Using Temperature Modulated *In Situ* Dielectric Deposition

POSTER SESSION

WEDNESDAY PM | LAGOON PLAZA

General Viewing

Wednesday
3:10 pm – 3:30 pm

Poster Session
6:00 pm – 8:00 pm

Thursday
10:00 am – 10:20 am
3:10 pm – 3:30 pm

Poster Set-up

Wednesday, 9:30 am – 3:00 pm

Poster Tear Down

Thursday, no later than 5:30 pm

Remaining posters will be discarded.

Poster presenters should be standing with their poster.
Student poster presenters must attend from 6:00 pm to 8:00 pm to present poster and answer questions to be eligible for the Best Student Poster Presentation Award.

Presenter	Paper #	Title
Durga Paudyal	PS01	Distinguishing Erbium Dopants in Y_2O_3 by Site Symmetry—*Ab Initio* Theory of Two Spin-Photon Interfaces
Andrew Christopher Grizzle	PS02	(Student) Molecule Spin State and Molecular Structure Impact on Molecular Spintronics Device Properties
Sanghun Lee	PS03	Fabrication of Ohmic Contact on Sulfurized Copper-Doped ZnS
Macarena Maria Santillan	PS04	(Student) Persistent Photoconductivity of Potassium Tantalate $KTaO_3$
Yoshitha Hettige	PS05	(Student) Optical Constants and Lattice Vibrations of Bulk $SrTiO_3$ and $BaSnO_3$ Using Spectroscopic Ellipsometry from 0.03-6.5 eV
Wen-Chang Huang	PS06	Impact of Oxygen Addition on Enhancing Electrochromic Performance of Vanadium Pentoxide Film by Sputtering
Wen-Chang Huang	PS07	Effect of Cu Doping on ZnO Based Thin-Film Sensor for Hydrogen Sensing
M. Jasim Uddin	PS08	Surface Modified $ZnSnO_3$ Hollow Nanorod/PDMS Based Piezoelectric Nano-Generator for Harvesting Mechanical Energy
Efracio Mamani Flores	PS09	Thermoelectric Properties Study on the Ferroelectric Materials $BiFeO_3$ and Bi_2FeCrO_6 via First Principles
Omid Dadras-Toussi	PS10	3D-Printing of Organic Bioelectronics and Biosensors
Wen-Shiung Lour	PS11	Layered Processes for InGaP/GaAs Heterojunction Bipolar Transistors with a Buried-Base Contact
Takashi Tsukasaki	PS12	Suppression of Nitrogen Composition Fluctuation by Beryllium Doping in GaAsN Ternary Alloys
Zinah M Alsaad	PS13	(Student) Optimization of the Event-Based Sensor's Photoreceptor Circuit for Mid-Wave Infrared Photodetection
Enbo Yang	PS14	(Student) Mass Spectroscopic Investigation on Reactions of Tin Tetrachloride and Germane for SiGeSn Chemical Vapor Deposition Growth
Geonwook Yoo	PS15	Reactive-Sputtering and Ferroelectric Switching of Aluminum Scandium Nitride on (-201)β-Ga_2O_3 Substrates
Min-Yeong Kim	PS16	(Student) Imaging Ga_2O_3 Defects and Determining Its Influence on Electrical Properties
Paul Gaurav G. Nalam	PS17	Fabrication and Characterization of High Quality Rutile-Phase GeO_2 Films on MgO(100) for Application in Optoelectronics
Francelia Sanchez Escobar	PS18	Growth Optimization of Sn-Doped Gallium Oxide Thin Films on Sapphire for Deep UV Photodetectors with Ultrafast Response
Sameer Kumar Mallik	PS19	(Student) Thermally-Driven Multi-Level Non-Volatile Memory in Monolayer MoS_2 Field-Effect Transistors
Ramesh G. Mani	PS20	The Effect of Current Annealing on the Transport Properties of CVD Graphene
Changkai Yu	PS21	(Student) Two-Dimensional Hole Gases in N-Polar AlGaN/GaN Heterostructures Grown on GaN Bulk Substrates
Mihee Ji	PS22	Dependence of Compositional Inhomogeneity and Thermal Conductivity on Growth Conditions of High-Al-Content AlGaN Alloys Grown by High Temperature Plasma-Assisted Molecular Beam Epitaxy
Hirandeep Reddy Kuchoor	PS23	Axial Configured GaAsSb Ensemble Nanowire-Based p-i-n photodetectors up to 1.1 µm
A. B. M. Hamidul Islam	PS24	Impact of Current Stress on the Optoelectronic Performances in GaN-Based Micro-LEDs
Nobuo Sasaki	PS25	Motion of a Void Induced by Agglomeration at the Solid-Liquid Interface in the Continuous-Wave Laser Crystallization
Yura Seo	PS26	(Student) Effect of the Atomic Arrangement at the Apex of Tip on AFM Atomic Lattice Images
Dominique Newell	PS27	(Student) Wavelength Dependence of the Verdet Constant Using Visible LEDs and a Modified Pulsed Magnet Station
Jialin Wang	PS28	(Late News) Design and Fabrication of a Fully Epitaxially Grown AlScN FBAR
Rahima Nasrin	PS29	Influence of Cobalt Doping on Surface Morphology, Structural and Optical Behavior of ZnO Nanoparticles Synthesized by CBD Technique
Madison Suzanne King	PS30	(Student) High Dielectric Microdroplet Whispering Gallery Mode Resonators for Opto-Electronics
Pius Suh	PS31	Covalently Connected Single-Molecule Magnets on the Exposed Edges of a Nickel Ferromagnetic Electrode-Based Magnetic Tunnel Junction
Anuj Rajpoot	PS32	DC Modeling for Non-Ohmic Contacts in the Scaled PMMA Dielectric-Based Solution-Processed Organic Thin-Film Transistors
Nurdan Mese	PS33	(Student) Electrochemical and Morphological Properties of PEDOT with Various Boron-Containing Dopants
Julia Isidora Salas Toledo	PS34	(Student) Energy Harvesting with Thermoplastic Polyurethane Nanofiber Mat Integrated with Functionalized Multiwalled Carbon Nanotubes

Presenter	Paper #	Title
Hyerin Jo	PS35	(Student) ZnO TFTs Property with Photoelectric Synaptic Devices
Shea Tonkinson	PS36	(Student) Synthesis and Characterization of $CsPbBr_3$ Perovskites for Radiation Detection Applications
Nolan T. Herbort	PS37	(Student) Synthesis and Characterization of Pulsed-Laser Deposited $Ba(Fe_{0.7}Ta_{0.3})O_3$–δ Thin Films
Hyungwoo Lee	PS38	(Student) Role of Native Defects and Dopants in the Oxygen Evolution Reaction of Heazlewoodite Ni_3S_2
Eyasu Ajebe	PS39	Synergistic Effect of Combining UIO-66 and Mxene Nanosheets in Pebax Mixed Matrix Membranes for CO_2 Capture and Separation
Sherman Peek	PS40	(Student) Femtosecond Laser Processing on Bulk Materials with Water-Assisted Debris Removal
Jeonghum Woo	PS41	Micro Probe System for *In Situ* X-Ray Scattering
Mehrdad Jalali	PS42	Information Visualization in Materials Science through Social Networks Modeling
Seoyeo Park	PS43	(Student, Late News) Metallic Fusion-Induced Flexible Nanocrystal Thin Films for High-Performance Electromagnetic Interference Shielding Materials
Hansel Hobbie	PS44	(Student, Late News) Zirconium Oxide Dielectric Thin Films Fabricated by Water-only Aerosol Jet Printing
Takumi Ikenoue	PS45	(Late News) Epitaxial Growth of Lattice-Matched NiMgZnO Films on MgO Substrate via Mist Chemical Vapor Deposition
Shisong Luo	PS46	(Student, Late News) High-Performance hBN/Graphene/AlGaN/GaN Hot Electron Transistors
Brittany Smith	PS47	(Student, Late News) Realizing 3D Microstructures from Graphene Using Aerosol Jet Printing
Ji-Hyuk Choi	PS48	(Late News) Designing Surface Chemistry of Semiconductor Nanocrystals for High-Performance Thin-Film Transistors
Yi-Kuan Chen	PS49	(Student, Late News) Pyridine-Carbonitriles-Based Thermally Activated Delayed Fluorescence Emitters for High Performance OLEDs
Inseo Kim	PS50	(Student, Late News) Understanding the Oxygen Vacancy Formation in Transition Metal Oxides Using Bond Strength Analysis: A First-Principles Study
Arnold Feutmba	PS51	(Student, Late News) Modeling Effect of Perovskite Layer on Efficiency and Development of Efficient and Stable Perovskite Layer

PROGRAM AT-A-GLANCE

UC = University Center
MCC = MultiCultural Center

THURSDAY AM

O: Group III-Nitrides—Novel Nitride Growth			Music Building, Lotte Lehmann
8:20 am	Matthew Hardy	O01	Epitaxial Growth of High ScN Fraction ScAlN on NbN/SiC and SiC
8:40 am	Ding Wang	O02	Epitaxial Ferroelectric ScAlN—Thickness Scaling to the Nanometer Scale
9:00 am	Naomi Pieczulewski	O03	(Student) Atomic Structure of β-Nb_2N/AlN/ β-Nb_2N Epitaxial Josephson Junction
9:20 am	Swarnav Mukhopadhyay	O04	(Student) First Demonstration of C-Doped Semi-Insulating N-Polar GaN Using Propane Precursor
9:40 am	Vincent E. Meyers	O05	(Late News) Growth of High-Quality Ga-Polar GaN Growth on Mixed-Polarity AlN
10:00 am			BREAK
10:20 am	Alexander Austin Chaney	O06	Metal Modulated Epitaxy Growth of AlN/GaN Short Period Superlattices with Individual Layer Thicknesses Less Than 2 nm
10:40 am	Christopher M. Matthews	O07	(Student) Surface Oxide Removal on AlN Substrates via Low Temperature Aluminum Flashing
11:00 am	Mohammad Hussain	O08	High Figure of Merit Extreme Bandgap $Al_{0.87}Ga_{0.13}N$-$Al_{0.64}Ga_{0.36}N$ Heterostructures Over Bulk AlN Substrates
11:20 am	Clarence Y. Chan	O09	(Student) Mechanism of hv-MacEtch in GaN and III-Nitrides Heterojunctions
11:40 am	Chandrashekhar Prakash Savant	O10	(Student) MBE Growth, Characterization of BAlN Films and 2D Electron Gas in Epitaxial BAlN/GaN Heterojunction
P: 2D Materials Synthesis and Characterization			**UC, Corwin East**
8:20 am	Thomas Virgil McKnight	P01	(Student) Spectroscopic Ellipsometry for *In Situ* Monitoring of MoS_2 Growth at the Sub-Monolayer Limit
8:40 am	Chen Chen	P02	Effects of Growth Temperature on the Properties of Wafer-Scale Epitaxial MoS_2 Monolayers Grown by Metalorganic Chemical Vapor Deposition
9:00 am	Meghan Leger	P03	(Student) MOCVD Growth and Characterization of $MoSe_2$ Nanodots within a WSe_2 Monolayer Matrix
9:20 am	Ramesh G. Mani	P04	Study of Single Crystal Graphene Grown by Chemical Vapor Deposition on Copper
9:40 am	Yeoseon Sim	P05	(Late News) Oxidation Mechanism of 2H-MoTe2 at the Atomic Scale
10:00 am			BREAK
10:20 am	Michael Pedowitz	P06	(Student) Transformation to Alkali Birnessites via Simple Intercalation of Electrochemically Grown 2D-Layered H-Type Manganese Dioxide on Epitaxial Graphene
10:40 am	Shigefusa Chichibu	P07	Ultraviolet Luminescence Dynamics of Hexagonal BN Epilayers Grown by Chemical Vapor Deposition Using Carbon-Free Precursors
11:00 am	Shubham Mondal	P08	(Student) Epitaxial Growth of Wafer-Scale Monolayer Hexagonal Boron Nitride (hBN)
11:20 am	Racha Raman	P09	(Student, Late News) 2D Materials Junction-Templated Photoelectrochemistry
Q: Optical Materials on Si			**UC, Flying A Studios**
8:20 am	Ellie Yilien Wang	Q01	(Student) Growth and Characterization of $Al_xIn_{1-x}As_ySb_{1-y}$ Digital Alloys on InP on Si
8:40 am	Alexandria Ragsdale	Q02	(Student) Synthesis and Characterization of AlSb for Growth on Si and Integrated Circuit Based Radiation Detection
9:00 am	Hyun Uk Chae	Q03	(Student) Defect Filtering at the Interface of MOCVD/TLP Heterogenous Epitaxial III-V on Silicon
9:20 am	Joshua Cooper	Q04	Mechanisms for Solute Incorporation in Highly Mismatched $Ge_{1-x-y}Sn_xC_y$ Alloys
9:40 am	Amanda N. Lemire	Q05	(Student) Doping and Surfactant Behavior of Antimony in Molecular Beam Epitaxy Grown Germanium-Tin
10:00 am			BREAK
R: Epitaxial Materials Design and Properties			**UC, Flying A Studios**
10:20 am	Rithvik Ramesh	R01	(Student) Engineering of the Interband Second Order Optical Nonlinearity with Asymmetric Coupled Quantum Wells
10:40 am	Qian Meng	R02	(Student) Atom Rearrangement in BGa(In)As Alloys Under Annealing
11:00 am	Robert Makin	R03	Design of Epitaxial Material Properties through Engineering of Quantitative Disorder
11:20 am	Subha Prakash Mallick	R04	(Student) The Effect of Group-V "Blow-by" on the Structural and Optical Properties of $Al_xIn_{1-x}As_ySb_{1-y}$ Digital Alloys Grown by Molecular Beam Epitaxy
11:40 am	Mina Moradnia	R05	(Student) Composition Control of Ternary Group-IIIa-IIIb-Nitride Alloy by Hybrid Chemical Vapor Deposition—A Thermodynamic Analysis

Student Finalist for Oral Presentation

CONFERENCE BADGE

Badges must be worn at all times within the Conference venue, including all receptions.

RECORDING/PHOTO POLICY

Recording or photographing Conference presentations, posters or displays is strictly prohibited without prior permission of the presenter.

AMERICANS WITH DISABILITIES ACT (ADA) COMPLIANCE

The Materials Research Society (MRS), its meeting partners and event venues, are responsible for complying with the Americans with Disabilities Act ("ADA") including the "readily achievable" removal of physical barriers to access meeting rooms, sleeping rooms and common areas. This may also include reasonable provisions for auxiliary aids and services when necessary and where achievable without undue burden. MRS will make every attempt to ensure that disabled individuals are accommodated so that they can receive the full benefit of participation in our events, and will modify, where possible, the policies, practices and procedures as necessary to provide goods and services to disabled individuals. On-site needs will be met to the extent possible.

S: SiC Material Characterization, Processing and Devices			UC, State Street
8:20 am	Ryoya Ishikawa	#S01	(Student) Anisotropic Electron and Hole Mobilities in 4H-SiC Bulk Crystals
8:40 am	Zeyu Chen	S02	(Student) Ray Tracing Simulation of Defects of 4H-SiC in 22-4 16 Reflection of Synchrotron Monochromatic Beam X-Ray Topography in Grazing Incident Geometry
9:00 am	Qianyu Cheng	S03	Analysis of Distribution of Threading Edge Dislocation Low Angle Grain Boundaries in 4H-SiC Wafers through Synchrotron X-Ray Topography
9:20 am	Shanshan Hu	S04	Investigation of Defect Formation During Initial Stage of PVT-Grown 4H-SiC Crystals
9:40 am	Scott Galen Criswell	S05	(Student) Nanoscale Spectroscopy of Extended Defects in 4H Silicon Carbide
10:00 am			BREAK
10:20 am	Michael Evan Liao	S06	Mitigation of Basal Plane Dislocation Faulting in 4H-SiC Buffer Layers Using Channeled Vanadium Implantation
10:40 am	Ludovico Megalini	S07	Advanced Carbon Film as a Superior C- Cap for SiC devices
11:00 am	Suman Das	S08	Study of Dopant Activation and Ionization for Phosphorus in 4H-SiC
11:20 am	Jiashu Qian	S09	(Student) A Comparison of Body Diode Degradation in Commercial 1.2 kV SiC Power MOSFETs with the Planar and Trench Structure
11:40 am	Nadeemullah Mahadik	S10	Reliability of Room Temperature vs High Temperature Implantation in 3.3kV SiC MOSFETs
T: Organic Devices and Molecular Electronics			**UC, Lobero**
8:20 am	Pawan Tyagi	T01	Single-Molecule Magnet (SMM) Internal Atomic Configuration Impact of Ferromagnetic Layers of Magnetic Tunnel Junction—A Monte Carlo Study
8:40 am	Brian S. Rolczynski	T02	Understanding Electronic Energy Transport in DNA-Scaffolded Molecular Networks Using Machine-Learning Methods
9:00 am	Libin Liang	T03	(Student) Strain-Enhanced Formation of 1D Coherent Exciton-Polaron States in Small Molecule Semiconductors
9:20 am	Jung Sun Eo	T04	(Student) Effect of Molecular Tilt Configuration in Molecular Heterojunction with Two-Dimensional Semiconductor
9:40 am	Phong Nguyen	T05	(Student) Surface-Confined Brønsted Acidic Doping of Conjugated Polymers Thin Films
10:00 am			BREAK
10:20 am	Anuj Rajpoot	T06	(Student) Probing the Interface Traps in PMMA Gate Dielectric-Based Short Channel Length OTFTs Fabricated Using Bi-Layer Lithography
10:40 am	Chankeun Yoon	T07	(Student) Advantages of Adding a Weak Second Gate in Sub-Micron Bottom-Contact Organic Thin-Film Transistors
11:00 am	Ramin Karimi Azari	T08	(Student) Effect of Thickness and Molecular Weight of Poly (3-hexylthiophene) Film on Ion-Gated Transistor Response Time and Synaptic Functions
11:20 am	Amrita Chakraborty	T09	(Student) Manufacturing of Highly Conductive Organic PEDOT:PSS Films for Electronic Devices
11:40 am	Sarah L. Swisher	T10	(Late News) Transparent, Inkjet-Printed PEDOT:PSS Electrotrode Arrays for Large-Area Multimodal Neural Interfaces
U: Group III-Nitrides—Contacts and Special Topics			**UC, Santa Barbara Harbor**
8:20 am	Shivali Agrawal	U01	(Student) Ohmic Contacts to Homoepitaxial Ultrawide Bandgap n-AlGaN Grown on Bulk AlN Substrates
8:40 am	Amit P. Shah	U02	Evolution of Surface Microstructure of Re-Al-Ni-Au Based Ohmic Contacts on N-Type GaN
9:00 am	Mafruda Rahman	U03	(Student) Ultrawide Bandgap Optoelectronic Properties of Single Crystal Bulk AlN and Sapphire/AlN Templates
9:20 am	Haotian Xue	U04	Structural and Optical Characterization of Thin AlInN Films on c-Plane GaN Substrates
9:40 am	Juergen Christen	U05	Nano-Scale Correlation of Real Structure, Band Bending and Local Electric Fields in the Narrow pn^+ Regions of a GaN Superjunction Using Highly Spatially Resolved STEM-CL Characterization
10:00 am			BREAK
10:20 am	Alireza Lanjani	U06	(Student) Design and Optimization of Room Temperature AlGaN/GaN Multi Quantum Well Infrared Photodetector by MOCVD for Near IR Range
10:40 am	Guangying Wang	U07	(Student) InGaN Films on Crystalline $ScAlMgO_4$ on Al_2O_3 Substrates by MOCVD with up to 123 nm PL Redshift
11:00 am	Geoffrey Foster	U08	Characterization of Optically Modulated Semi-Insulating GaN Photoconductive Semiconductor Switches
11:20 am	Nam-In Kim	U09	Piezoelectric Sensing in Extreme Environments Using Flexible Ultrawide Bandgap III-N Thin Films
11:40 am	Yinxuan Zhu	U10	(Student, Late News) Demonstration of 0.7 Ω.mm MOCVD-Grown Reverse Graded Contacts on $Al_{0.85}Ga_{0.15}N$ Channel
V: Growth of Gallium Oxide and Other Ultrawide-Bandgap Oxides			**MCC, MCC Theater**
8:20 am	Zhuoqun Wen	V01	(Student) Si Doping of β-Ga_2O_3 by Disilane via Hybrid Plasma-Assisted Molecular Beam Epitaxy
8:40 am	Jacob Steele	V02	(Student) Epitaxial Growth of α-$(Al_xGa_{1-x})_2O_3$ by Suboxide Molecular-Beam Epitaxy at 1 μm/h
9:00 am	Brenton A. Noesges	V03	Optimizing Si Dopant Control in n-type β-Gallium Oxide
9:20 am	Abishek Katta	V04	Demonstration of MOCVD Based *In Situ* Ga Etching of β-Ga_2O_3 Using TEGa
9:40 am	Fikadu Alema	V05	Controllable Doping of MOCVD Ga_2O_3 with Nitrogen Using Ammonia Precursor
10:00 am			BREAK
10:20 am	Debabrata Das	V06	Vertically Aligned β–$Ga_{2-X}W_XO_3$ Nanocomposites for Ultrafast Deep-UV Photodetectors
10:40 am	Tianchen Yang	V07	(Student) Investigation of Phase Transition and Bandgap Engineering in $(Mg_xGa_{1-x})_2O_3$ Thin Films Grown by Molecular Beam Epitaxy
11:00 am	Chengyun Shou	V08	(Student) Improving Quality of β–Phase MgGaO Thin Films by Using Low-Temperature Homo-Buffer Layer
11:20 am	Ahmad Matar Abed	V09	(Student) Effect of Post-Deposition Annealing on Crystal Structure of RF Magnetron Sputtered Germanium Dioxide Thin Films

Student Finalist for Oral Presentation

PROGRAM AT-A-GLANCE

THURSDAY PM

W: Group III-Nitrides—Late News			Music Building, Lotte Lehmann
1:50 pm	Emma Rocco	W01	(Late News) Impact of Cap Layer Thickness on Ga- and N-Polar Microstructure Photocathodes
2:10 pm	Md. Irfan Khan	W02	(Student, Late News) Investigation of Si Doping in N-Polar AlN by Plasma Assisted Molecular Beam Epitaxy
2:30 pm	Georgios Doundoulakis	W03	(Late News) Nanometer-Resolution Piezoelectric Probing for Vertical Top-Down GaN Nanowire Field Emitter Devices with Integrated Leveling
2:50 pm	Holger Eisele	W04	(Late News) Characterization of the Space-Charge Region of a GaN *pn*-Junction and *pin*-Drift-Diode Using EBIC and CL
3:10 pm			BREAK
X: Group III-Nitrides—Growth and Characterization			**UC, Corwin East**
1:30 pm	Siddha Pimputkar	X01	Computational Fluid Dynamics Modeling of a Novel High-Pressure Spatial Chemical Vapor Deposition Reactor (HPS-CVD) Design for Growth of Indium-Containing Nitrides
1:50 pm	Yafei Liu	X02	Characterization of Growth Sectors in Patterned HVPE Gallium Nitride Substrate Wafers
2:10 pm	Jack Almeter	X03	(Student) Wing Tilt in ELO-Grown GaN
2:30 pm	Keisuke Motoki	X04	(Student) Structural Analysis and Observation of Tilts, Twists and Crystallographic Orientation of High-Quality, Metal Rich Grown $Sc_{0.2}Al_{0.8}N$
2:50 pm	Andrew J. Winchester	X05	Microscale Surface Electronic Properties of Defects in Gallium Nitride Epitaxial Layers
3:10 pm			BREAK
3:30 pm	Kohei Shima	X06	Luminescence Studies of Bulk GaN Crystals Grown by the Low-Pressure Acidic Ammonothermal Method
3:50 pm	Seokje Lee	X07	(Student) Pulsed-Mode Metalorganic Vapor-Phase Epitaxial Growth of GaN on Graphene/c-Sapphire for Freestanding GaN Thin Films
4:10 pm	Shubham Mondal	X08	(Student, Late News) Molecular Beam Epitaxy and Characterization of N-Polar AlGaN on C-Face 4H-SiC
4:30 pm	Oguz Odabasi	X09	(Student) N-Polar GaN Deep Recess HEMTs with ALD HfO_2 as Gate Dielectric
4:50 pm	Liang Qi	X10	Mechanisms for Polytype Selection During the Growth of Self-Catalyzed GaN Nanowires
Y: Plasmonics, Photonics for Detection and Emission			**UC, Flying A Studios**
1:30 pm	S. Maryam Vaghefi Esfidani	Y01	Critical Coupling in Phonon Polariton Organ Pipe Resonance for Infrared Sensing
1:50 pm	Alexander Ware	Y02	(Student) Decoupling Mid-Wave Infrared Absorption and Long-Wave Infrared Radiative Cooling in Bolometric Elements
2:10 pm	Minho Choi	Y03	Massively Degenerate Coherent Perfect Absorber Using a Single Optic
2:30 pm	Wilder Acuna	Y04	(Student) Property Control of ErAs:InGaAlBiAs Materials for Terahertz Emitters and Detectors Pumped at 1550 nm
2:50 pm	Brandon Swartz	Y05	(Student) Large-Scale Inversely Designed Metasurfaces for Broadband LWIR Optical Edge Detection
3:10 pm			BREAK
3:30 pm	Ashley Blackwell	Y06	(Student) Flexible Metastructure Graded-Index Lens as a Quantum Algorithm Emulator
3:50 pm	Haonan Ling	Y07	(Student) Taming Mid-IR Resonances with Hexagonal Boron Nitride
4:10 pm	Madeline Brown	Y08	(Student) Topological Spin-Valley Coupling in 2D Photonic Crystals
4:30 pm	Abhilasha Kamboj	Y09	(Late News) Localized Phonon Polariton Modes in GaN/AlN Nanowires
4:50 pm	Md. Toriqul Islam	Y10	(Student, Late News) Prospects of Dilute Bismuth in InGaBiAs Alloys for e-SWIR Photodetectors
Z: Emergent Materials and Devices for Microelectronics			**UC, State Street**
1:30 pm	Jingxian Li	#Z01	(Student) Origins of Nonvolatility in Resistive Switching Memory
1:50 pm	Ramin Karimi Azari	Z02	(Student) Controlling Response Time and Synaptic Behavior of Ion-Gated Transistors Through Modulating Different Aspects of Input Biases
2:10 pm	Solomon Amsalu Chekol	Z03	(Student) Effect of the Counter Electrode Material on the SET Kinetics of Ag/HfO_2-Based Diffusive Memristors
2:30 pm	Nithil Harris Manimaran	Z04	(Student) Realizing a Linear Synaptic Weight Update in Electric-Double-Layer Gated Transistors for Achieving Spike-Timing-Dependent Plasticity in Neuromorphic Computing
2:50 pm	Mousam Charan Sahu	Z05	(Student) Highly Stable and Controllable Quantum Conductance States up to 100 G0 in TiO_2 Memristor
3:10 pm			BREAK
3:30 pm	Thomas Leonard	#Z06	(Student) Multi-Weight Magnetic Artificial Synapses with Geometry-Dependent Neuromorphic Functionality
3:50 pm	Marzieh Savadkoohi	Z07	(Student) Impact of Single Molecule Magnets (SMM) on Magnetic Properties of a Cross-Junction-Shaped Magnetic Tunnel Junction
4:10 pm	Finley Haines	Z08	(Student) Vertical Spin Valves Architectures Based on Screw Dislocations in Semiconductor Nanomembranes
4:30 pm	Amrita Chakraborty	Z09	(Student) Methodology for Mitigation of the Reliability of a Resistive RAM Memory Array Caused by Thermal Cross-Talk Between the Memory Cells
4:50 pm	Kuan-Hao Kuan Chiao	Z10	(Student) Micromagnetic Simulations for Deterministic Switching in SOT-MRAM Cell with Additional Heavy Metal Capping Strip

Student Finalist for Oral Presentation

AA: Semiconducting Oxide Thin Films and Transistors			**UC, Lobero**
1:30 pm	Tetyana V. Torchynska	AA01	Optical, Structural and Electrical Properties of Al and in Donor Doped ZnO Films for TCO Applications
1:50 pm	Farida Selim	AA02	Atomic Layer Deposition of Highly Conductive Highly Transparent Indium Gallium Doped Zinc Oxide Thin Films
2:10 pm	Camilo Velez Cuervo	AA03	Atomic Layer Deposition (ALD) and Sol-Gel Techniques Comparison from the Perspective of TiO_2 Thin-Films Fabrication
2:30 pm	Eli Powell	AA04	(Student) Donor Activation in Boron and Phosphorus Implanted Self-Aligned Bottom-Gate IGZO TFTs
2:50 pm	Dong Hyuk Kim	AA05	(Student, Late News) Optimized Heterojunction Metal-Oxide Semiconductor Structures for High Performance Indium-Tin-Oxide TFTs
3:10 pm			BREAK
3:30 pm	Yuchen Zhou	AA06	(Student) Accurate Field-Effect Mobility Estimation with Gate Voltage-Dependent Mobility in Linear Region for IGZO Thin-Film Transistors
3:50 pm	Hongseok Oh	AA07	IGZO Synaptic Thin-Film Transistors Using Embedded AlOx Charge-Trapping Layer
4:10 pm	Reem Alshanbari	AA08	(Student) Tuning Threshold Voltage in Ultrathin Channel Flexible Amorphous InGaZnOx TFTs
4:30 pm	Guoduan Liu	AA09	(Student) Improved Electrical Performance of $InGaZnO_4$ Thin-Film Transistors with UV Ozone Treatment
4:50 pm	William J. Scheideler	AA10	Continuous Liquid Metal Printing of High-Performance 2D Oxide Heterostructures
BB: Group III-Nitrides—P-Type Doping and Characterization			**UC, Santa Barbara Harbor**
1:30 pm	Shashwat Rathkanthiwar	BB01	Achieving Technologically Relevant P-Type Conductivity in Al-Rich (>70% Al) AlGaN Using Impurity Band Conduction
1:50 pm	Cristyan E. Quiñones García	BB02	(Student) Modelling Self-Compensation in Heavily Mg-Doped GaN
2:10 pm	Benjamin McEwen	BB03	MOCVD GaN Co-Doped with Mg and Be
2:30 pm	Masahiro Kamiyama	BB04	(Student) Compensation Mechanism in Mg-Doped N-Polar GaN
2:50 pm	Jia Wang	BB05	Observation of Spontaneous Intercalation of Interstitial Mg into GaN
3:10 pm			BREAK
3:30 pm	Emma Rocco	BB06	Investigation of Diffusion of Be and Mg Acceptor Dopant Implanted in GaN and the Impact of Annealing Method and Temperature
3:50 pm	Shadi Omranpour	BB07	(Student) Photocathode Characteristics Dependency on Mg Incorporation in (N-polar) Semi-Polar and Non-Polar 3D Microstructures by Selective Area Epitaxy
4:10 pm	Kenny Huynh	BB08	Dissolution of Mg Segregated Defects in Mg-Implanted GaN After Ultra-High-Pressure Annealing
4:30 pm	Chandan Joishi	BB09	(Late News) Tunnel Junction Enabled AlGaN/GaN Heterojunction Bipolar Transistor with All n-Type Contacts
CC: Characterization of Gallium Oxide-Based Materials and Devices II			**MCC, MCC Theater**
1:30 pm	Khandakar Aaditta Arnab	CC01	(Student) Temperature-Dependent Calculations of β-Ga_2O_3 Defect Concentrations for Equilibrium, Full Quenching and Generalized Quenching Scenarios
1:50 pm	Kunyao Jiang	CC02	Phase Transformation of β-Ga_2O_3 to Ga_2O_3-Based γ-Phase Spinels on (100) $MgAl_2O_4$ Substrate
2:10 pm	Jacqueline Cooke	CC03	Characterization Analysis of Extended Defects in β-Ga_2O_3 and AGO
2:30 pm	Ariful Islam	CC04	(Student) Temperature Dependence of Bandgap and Anisotropy in Urbach Tails in β-Ga_2O_3
2:50 pm	Kenny Huynh	CC05	Crack Formation in Strained β-$(Al_xGa_{1-x})_2O_3$ Films Grown on (010) β-Ga_2O_3 Substrates
3:10 pm			BREAK
DD: Gallium Oxide Materials Processing			**MCC, MCC Theater**
3:30 pm	Zhenwei Wang	DD01	Improvement of Ga_2O_3 Schottky Barrier Diode Characteristics by Nitrogen Radical Treatment
3:50 pm	Saurav Roy	#DD02	(Student) Enhancing the Dielectric Performance of Al_2O_3 on β-Ga_2O_3 Using Temperature Modulated *In Situ* Dielectric Deposition
4:10 pm	Cameron Anthony Gorsak	DD03	(Student) SIMS Study of the Accumulation of Si on the Surface of Gallium Oxide and Its Mitigation
4:30 pm	Katie Gann	DD04	(Student) Optimizing Si Implantation and Annealing in β-Ga_2O_3
4:50 pm	Alan G. Jacobs	DD05	Silicon Ion Implant Activation in β-$Al_{0.4}Ga_{1.6}O_3$

Student Finalist for Oral Presentation

PROGRAM AT-A-GLANCE

UC = University Center
MCC = MultiCultural Center

FRIDAY AM

EE: Diamond and Related Materials			UC, Corwin East
8:20 am	Dmitry Shinyavskiy	EE01	(Student) Synthesis of Free-Standing Polycrystalline Diamond Nanomembrane
8:40 am	Makoto Kasu	EE02	Characterization of Inch-Sized Diamond Wafer Grown on Misoriented Sapphire
9:00 am	Kaicheng Pan	EE03	(Student) Chemical Mechanical Polishing of Polycrystalline Diamond Films for Integration as High Thermal Conductivity Layers
9:20 am	Michael Spencer	EE04	Electronic and Optical Characterization of Bulk and Epitaxial Single Crystals of Cubic Boron Nitride (cBN)
9:40 am	Lillian Barrett Hughes	EE05	(Student) Two-Dimensional Spin Systems in PECVD-Grown Diamond with Tunable Density and Long Coherence for Enhanced Quantum Sensing and Simulation
10:00 am			BREAK
FF: Group III-Nitrides—Thermal Transport			**UC, Corwin East**
10:20 am	MVS Chandrashekhar	FF01	Thermal Considerations in Co-Designed III-Nitride Transistors
10:40 am	James Spencer Lundh	FF02	Thermal Mapping of AlGaN/GaN High Electron Mobility Transistors Using Mechanically Exfoliated MoS_2 Flakes
11:00 am	Khush Mahendrakumar Gohel	FF03	(Student) Understanding of Multi-Way Heat Extraction Using Peripheral Diamond in AlGaN/GaN HEMT by Electrothermal Simulations
11:20 am	Luke Yates	FF04	Visualizing and Quantifying Thermal Conductance and Strain at Compression Bonded GaN-Diamond Interfaces via Optical Methods
GG: Epitaxy of Structured and Quantum Materials			**UC, Flying A Studios**
8:20 am	Alec Mason Skipper	GG01	(Student) Dark Current Reduction by MBE Selective Area Growth in III-V Semiconductor PIN Photodetectors
8:40 am	Yiteng Wang	GG02	(Student) InP Lateral Epitaxial Overgrowth by Solid-Source Molecular Beam Epitaxy
9:00 am	Ashlee Garcia	#GG03	(Student) SiO_2 Surface Planarization for Molecular Beam Epitaxy Selective Area Regrowth of High Aspect Ratio Microstructures
9:20 am	Mikolaj Chlipala	GG04	(Student) Light-Emitter/Superconducting Stack Within the Nitride Family
9:40 am	J. Andrew McArthur	GG05	(Student) Manipulating the Opto-Electronic Properties of $Al_xIn_{1-x}As_ySb_{1-y}$ Digital Alloys by Adjusting the Period Thickness
10:00 am			BREAK
10:20 am	Brendan Jordan	GG06	(Student) Growth and Characterization of Multigrain SmB_6 Thin Films by Chemical Vapor Deposition
10:40 am	Yuxing Ren	GG07	(Student) Quasi van der Waals Epitaxy of Magnetic Topological Insulator on a GaAs (111) Substrate
11:00 am	Tri Nguyen	GG08	(Student) Electrical and Optical Properties of Sputtered SnTe
11:20 am	Rohit Yadav	GG09	(Student) Self-Limiting Formation of Bismuth-Induced Nanostructures on the InSb(111) Surface
11:40 am	Binghao Guo	GG10	(Student) Magnetotransport Studies of Two-Dimensional Cd_3As_2 Heterostructures
HH: Materials Processing and Integration			**UC, State Street**
8:20 am	Archit Shah	HH01	(Student) Fabrication of SU-8 Microstructures on Bulk Molybdenum Substrates for Cryogenic Applications
8:40 am	Florence A. Nugera	HH02	Growth of Patterned Diamond Using High Seeding Density and Hot-Filament Chemical Vapor Deposition (HFCVD)
9:00 am	Christopher Bishop	HH03	Experimental Characterization and Modification of Silicon Nitride Crystallization Reaction Kinetics for Microelectronics Applications
9:20 am	Eric Blanton	HH04	Investigation of Bonded GaN-Si p-n Junction Interface Properties
9:40 am	Lezli Matto	HH05	(Student) Thin-Film Layer Transfer of 128° Y-Cut $LiNbO_3$ on (0001) Al_2O_3 Through Ion Implantation and Exfoliation
10:00 am			BREAK
10:20 am	Lukas Leonard Janavicius	HH06	(Student) Realization of Vapor-Phase MacEtch: Mechanism, Programmability and Scalability
10:40 am	Abhilasha Kamboj	HH07	(Late News) Substrate-Removed GaAs Photovoltaic Cells for Microscale Energy Harvesting
11:00 am	William J. Scheideler	HH08	(Late News) Anionic Engineering and 3D Integration of 2D $Ti_3C_2T_x$ MXene for Electrocatalysis and Energy Storage
11:20 am	B. Garfield	HH09	(Student, Late News) Development of Sustainable Non-Toxic TiO_2/Sb_2Se_3 Solar Cells for Renewable Energy Applications
11:40 am	Jared Mitchell	HH10	(Student, Late News) Probing Nonstoichiometry and Local Atomic Environments in $GaAs_{1-x-y}N_xBi_y$ Alloys

Student Finalist for Oral Presentation

PROGRAM AT-A-GLANCE

FRIDAY AM

II: Flexible, Printed and Wearable Electronics and Sensors			UC, Lobero
8:20 am	Jung-Bin Ahn	II01	3D Printable Polymer Matrix Synthesis with UV-curable Polyurethane for Wearable Electronics
8:40 am	Annatoma Arif	II02	(Student) Characterization and Fabrication of 3D Inkjet Printed Flexible Copper Electrodes
9:00 am	Jee Young Kwak	II03	(Student, Late News) Carbon Based Omnidirectional Wearable Strain Sensor Arrays with Optimized Multi-Output Neural Networks
9:20 am	Nam-In Kim	II04	Highly Sensitive and Selective Cortisol Detection from Sweat Using Piezoelectric Single-Crystalline Flexible GaN Thin-Film Sensor
9:40 am	Lauren Kelly	II05	(Student) Electrochemical Detection of the LuxR Protein Using the Metabolic Activity of *Shewanella oneidensis* MR-1 for the Development of a Modular Bioelectronic Interface
10:00 am			BREAK
10:20 am	Andrew Bourhis	II06	(Student) Optimizing Dual-Gate IGZO TFTs for Long-Term Flexible Neural Interfaces
10:40 am	Jing Gu	II07	(Student) Integration of ZnO Thin-Film Transistor Array with Surgical Forceps for Minimally Invasive Robotic Surgery
11:00 am	Haein Cho	II08	(Student) Ultrathin Skin-Attachable TiO_2 Synaptic Array Integrated with an Organic Proximity Sensor for Finger Gesture Recognition
11:20 am	Kaori Yamamoto	II09	(Late News) Integrated Graphene FET Array for High Sensitive Detection of New Corona Virus with Automated Solution Exchange System
JJ: Low-Dimensional Structures—Quantum Dots, Wires and Wells			**UC, Santa Barbara Harbor**
8:20 am	Frank Bertram	JJ01	Carrier Capture into Individual InP Quantum Dots Directly Imaged by Nanoscale Cathodoluminescence Microscopy
8:40 am	Ruiqi Hu	JJ02	(Student) Electronic and Structural Properties of Rare-Earth Mono-Pnictide (RE-V) Nanoparticles in III-V Matrices
9:00 am	Yuanchang Zhang	JJ03	MBE Growth for Wafer Scale Uniformity in Low Density InAs Quantum Dots
9:20 am	Chen Shang	JJ04	Quantum Dot Morphology and Defect Configuration Anisotropy for III-V Laser Material Grown on Patterned Si Photonic Wafers
9:40 am	Eamonn T. Hughes	JJ05	(Student) Gradual Degradation via Dislocation Microloop Formation in InAs Quantum Dot Lasers on Si and GaAs
10:00 am			BREAK
KK: Micro-LEDs			**UC, Santa Barbara Harbor**
10:20 am	Sheikh Ifatur Rahman	KK01	(Student) Impact of Barrier Thickness and Doping on the Carrier Transport in MQW P-Down Green LEDs
10:40 am	Xuefeng Li	KK02	(Student) Carrier Dynamics in Blue, Cyan, and Green Commercial InGaN/GaN LEDs Measured by Small-Signal Electroluminescence
11:00 am	Xuefeng Li	KK03	(Student) Trap-Assisted Auger Recombination in Commercial Green InGaN/GaN LEDs
11:20 am	Seonghoon Lee	KK04	The Role of Zn-Precursor in the Formation of Environment-Friendly Highly Luminescent Colloidal Quantum Dots and R/G/B QLEDs with Inverted Structure
11:40 am	Tanay Tak	KK05	(Student, Late News) Electron Emission Microscopy of an Electrically Driven III-Nitride-Based LED: Evidence of Lateral Electron Injection at V-Defect Sidewalls
LL: Dielectrics, Ferroelectrics and Multifunctional Oxides			**MCC, MCC Theater**
8:40 am	Kaveh Ahadi	LL01	Molecular Beam Epitaxy and Strain Engineering of $KTaO_3$
9:00 am	Rainer Timm	LL02	Semiconductor-Oxide Interfaces of InAs-Based Ferroelectric and RRAM Devices
9:20 am	Harish Kumarasubramanian	LL03	(Student) Pushing the Limits of Switching Voltage, Leakage in Ultrathin $BaTiO_3$ Thin Films
9:40 am	Michael Patrick McGarry	LL04	Frequency-Dependent Conductivity of Mo-SiN_x Granular Metals
10:00 am			BREAK
10:20 am	Nicholas C. Strandwitz	LL05	Porous Dielectric Thin Films for Advanced Dielectrics Using Molecular and Atomic Layer Deposition
10:40 am	Tetyana V. Torchynska	LL06	Impact of Annealing Conditions on Structural and Optical Properties of Si-Rich Hafnia-Based Thin Films Doped with Pr Elements
11:00 am	Rajeswari Moolathody Kolagani	LL07	Anion Stoichiometry Modulation and *In Situ* Compositional Analysis of Functional Metal Oxide Thin Films
11:20 am	Subhajit Mohanty	LL08	(Student, Late News) Effect of HfO_2 Dielectric Thickness on the DC-RF Dispersion in N-Polar GaN HEMTs
11:40 am	Pius Suh	LL09	(Late News) Magnetic Tunnel Junction Molecular Spintronics Based Chemical Sensing Device

Student Finalist for Oral Presentation

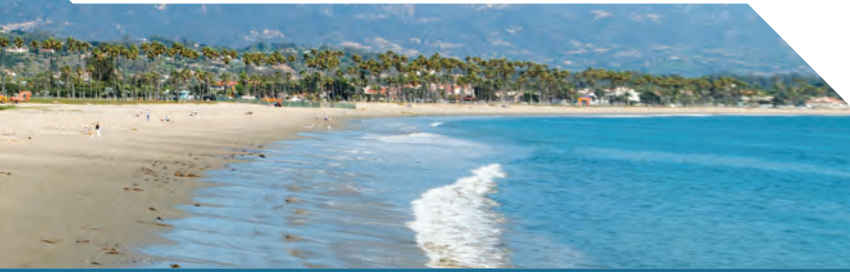

EXHIBITOR PROFILES

LAGOON PLAZA

Wednesday
10:00 am – 8:00 pm

Thursday
10:00 am – 4:00 pm

Klar Scientific, Inc.
klarscientific.com

Key Products: Point-and-shoot confocal spectroscopic microscopes; Scanning autofocus microscopes for mapping photoluminescence and Raman emissions; Wavelength kits for 266nm through 975nm illumination; Thermal kits for 80K-400K scanning; Test and measurement services

Klar Scientific develops compact, affordable instruments designed for scientists who need spectral information with high spatial resolution. Klar microscopes provide photoluminescence (PL) and Raman mapping for excitation wavelengths from the deep-UV to near-IR. Klar also offers measurement services to provide clients with spectral maps of their samples.

k-Space Associates, Inc.
k-space.com

Key Products: kSA BandiT; kSA 400; kSA MOS; kSA ACE; kSA ICE; kSA SpectR; kSA MOS ThermalScan

k-Space is a leading supplier of advanced metrology instrumentation and software used in research and production facilities around the world. Through extensive customer input, close collaboration with its customer base, and a strong commitment to unparalleled technical support, k-Space has developed today's most powerful thin-film and industrial metrology tools.

Lake Shore Cryotronics, Inc.
lakeshore.com

Key Products: Source Measure Systems; Cryogenic Probe Stations; Hall Effect Measurement Systems & Instruments; Modular Characteristic Systems; Electromagnets; Superconducting Magnet Systems; AC/DC Current & Voltage Sources

A leading innovator of solutions for electronic material research, Lake Shore Cryotronics offers modular multichannel lock-in measurement systems for highly synchronized DC, 100 kHz AC, and mixed DC + AC sourcing and measuring; cryogenic probe stations; systems and instruments for fast, highly precise Hall measurements; and modular characterization systems for electronic/electro-transport measurements.

National Institute of Standards and Technology
nist.gov

Key Products: metrology; standards; advanced electronics; quantum science; artificial intelligence; cybersecurity; climate; communications; health and bioscience

NIST is an agency of the US federal government in the Department of Commerce. We run programs in a broad range of technical areas and seek diverse, qualified candidates for positions including applicants for National Research Council postdoctoral fellowships and the Summer Undergraduate Research Fellowship program.

Nextron Corporation
microprobesystem.com

Key Products: MPS-PT, MPS-CH, XRDMPS, Piezo module probe systems

Measurement Solution for Electric, Dielectric, Optic

United Mineral and Chemical Corporation
umccorp.com

Key Products: MBE Source Materials; MBE Equipment; Dopants; PLO systems; PVD systems; Battery material and Chemicals

United Mineral and Chemical Corp. is a leading supplier of ultra-high purity, MBE grade ingots and metal sources including Arsenic, Red Phosphorus, Indium, Gallium, Aluminum, Antimony, Magnesium, Selenium, Silicon and Tellurium. Compounds of III-V materials are offered as well. UMC also represents Dr. Eberl MBE-Komponenten for MBE effusion cells, crackers, doping and sublimation sources as well as ancillary equipment and components. In addition, UMC represents TSST for PLD systems and components used for thin film research.

EMC

65TH ELECTRONIC MATERIALS CONFERENCE

June 28–June 30, 2023 // University of California, Santa Barbara // Santa Barbara, California

WEDNESDAY ORAL PRESENTATIONS

65th Electronic Materials Conference
June 28 - June 30, 2023

* Invited Paper
# Student Finalist for Oral Presentation Award

SESSION EMC Awards Ceremony and Plenary Session
Session Chairs: Lisa Porter and Daniel Wasserman
Wednesday Morning, June 28, 2023
Music Building, Lotte Lehmann

8:20 AM EMC AWARDS CEREMONY

8:30 AM *PL01
Suboxide Molecular-Beam Epitaxy Darrell G. Schlom[1,2,3]; [1]Cornell University, United States; [2]Kavli Institute at Cornell for Nanoscale Science, United States; [3]Leibniz-Institut für Kristallzüchtung, Germany

In this talk I will describe a variant of molecular-beam epitaxy (MBE)—"suboxide MBE"—that makes it possible to deposit many oxide materials with excellent structural perfection at relatively low deposition temperature compared with other epitaxial methods. Examples include:
-type oxide Semiconductors—b-Ga_2O_3, a-$(Al,Ga)_2O_3$, In_2O_3, $BaSnO_3$, $SrSnO_3$
-type oxide Semiconductors—SnO, PbO, $SnTa_2O_6$, $SnWO_4$, Bi_2BaTaO_6
proposed high-T_c Superconductors—$Ba_{n+1}In_nO_{2.5n+1}$ with n=1, 2, ∞
Of these, b-Ga_2O_3, In_2O_3, SnO, PbO, Sr_3SnO, and $SnWO_4$ can all be grown epitaxially at back end of line temperatures. In suboxide MBE the molecular beams consist of pre-oxidized elements (suboxides) that help navigate kinetic pathways. For example, supplying a molecular beam of gallium suboxide (Ga_2O) eliminates the rate limiting step of conventional MBE to the growth of b-Ga_2O_3—the oxidation of gallium to its suboxide—and by skipping this step growth rates exceeding 1 μm/hr with excellent crystallinity, surface smoothness, and at a low growth temperature are achieved. In addition to extensive structural characterization, electrical characterization and working transistors will also be shown.
*This work was performed in collaboration with coauthors from the groups of: K. Ahadi, K. Chabak, K. Cho, S. Datta , R. Engel-Herbert, C.B. Eom, F. Giustino, V. Gopalan, A.J. Green, C. Guguschev, R.T. Haasch, G. Hautier, F.V.E. Hensling, J.T. Heron, A. Hock, D. Jena, M. Jeong, Y. Kim, D. Klimm, K. Lee, Z.K. Liu, S. Mou, D.A. Muller, H.P. Nair, A.T. Neal, T. Onuma, H. Paik, X.Q. Pan, L.F.J. Piper, N.J. Podraza, S. Salahuddin, D.G. Sangiovanni, K.M. Shen, Y.E. Suyolcu, M.O. Thompson, T.E. Tiwald, R. Uecker, P.A. van Aken, P. Vogt, M.D. Williams, C.H. Winter, H.G. Xing, and Q. Zheng.

9:20 AM BREAK

SESSION A: Group III–Nitrides—Devices
Session Chairs: Mihee Ji and Asif Khan
Wednesday Morning, June 28, 2023
Music Building, Lotte Lehmann

10:00 AM A01
(Student) High Electron Density AlN/GaN/AlGaN Quantum-Well HEMTs on Al-Polar Single-Crystal AlN Substrates Yu-Hsin Chen[1], Jimy Encomendero[1], Masato Toita[2], Debdeep Jena[1,1] and Huili Grace Xing[1,1]; [1]Cornell University, United States; [2]Asahi Kasei Corporation, Japan

AlN/GaN/AlN quantum-well (QW) HEMTs have emerged as a promising device technology for high-power applications such as next-generation communication networks and military defense systems [1-2]. Thanks to their strong carrier confinement, high thermal conductivity, and high breakdown electric field of the AlN back barrier, QW-HEMTs are promising for highly scaled high-speed transistors capable of power amplification at high temperatures. Moreover, HEMTs grown on single-crystal AlN substrates would provide higher reliability thanks to their low dislocation densities (~10^4 /cm^2) and the absence of thermal boundary resistance with the substrate in contrast to AlN on SiC, sapphire or other substrates. However, in thin GaN QWs along a crystal polar direction, a strong internal electric field can arise due to large polarization effects. The important consequences of the vertical electric field and compressive strain in the electronic transport of the thin GaN channel is not yet fully understood. Therefore, in this report we present a combined experimental and theoretical study concerning homoepitaxial AlN/GaN/AlGaN QW-HEMTs, in which both the internal electric field as well as the strain in the GaN channel are systematically varied simultaneously.
A series of AlN/GaN/AlGaN QW HEMTs with different QW thickness, ranging from 20 to 200 nm, are grown by molecular beam epitaxy on single-crystal AlN substrates [See Fig. 1(a)]. As the QW thickness increases, the vertical electric field in the GaN channel decreases, resulting in a re-distribution of the electronic wavefunction. These effects can be clearly seen from the self-consistent Schrödinger–Poisson simulations displayed in Fig. 1(b). Structural analysis was performed using atomic force microscopy (AFM) and high-resolution X-ray diffraction (HRXRD). The symmetric ω/2θ diffraction pattern, shown in Fig. 1(c), and the reciprocal space map (RSM) around the asymmetric (-105) reflection, displayed in Fig. 1(d), indicate the relaxation process of GaN layer as the channel thickness increases. The AFM scans, displayed in Fig. 2, reveal smooth surface morphologies with sub-nanometer root-mean-square roughness for all the samples. While clear atomic steps are observed on the HEMT with a 20-nm-thick GaN well, spiral hillocks start to appear on QW HEMTs with thicker GaN layers; this can stem from screw dislocations formed due to GaN relaxation. For both samples featuring a 50-nm-thick GaN well and a 200-nm-thick GaN well, the formation of visible cracks is observed.
To examine the transport properties of the 2DEGs, hall-effect measurements were carried out at room temperature and 77 K. As shown in Fig. 3(a), the electron density increases and saturates with increasing GaN thickness, reaching $4.7x10^{13}$ /cm^2. Meanwhile, a

room-temperature sheet resistance of R_{sh} ~ 340 Ω/sqr was achieved in QW HEMTs with both thin and thick channels. To put these results in context, Fig. 3(b) compares the room temperature transport properties of all the reported 2DEGs in Al(Ga)N/GaN/Al(Ga)N heterostructures. A clear trend relating GaN thickness and mobility is observed. The high mobility HEMTs are achieved in thick and relaxed GaN layers with middle to low carrier densities. Since our samples are located within the high 2DEG density region, there exists room for further mobility improvement by lowering the carrier density in the channel.

[1] Hickman et al. *Semicond. Sci. Technol.* **36** 044001 (2021)
[2] Yaita et al. *IEEE Electron Device Lett.*, vol. 42, no. 11, pp. 1592–1595, Nov. 2021

10:20 AM A02
(Student) Measurement of Hole Velocity vs. Electric Field in Polarization-Induced Two-Dimensional Hole Gases in GaN/AlN Heterojunctions Joseph Dill, Jimy Encomendero, Kazuki Nomoto, Zexuan Zhang, Debdeep Jena and Huili Grace Xing; Cornell University, United States

We present the first-ever measurements of the velocity vs. electric field (v-E) characteristic for a polarization-induced two-dimensional hole gas (2DHG) in gallium nitride (GaN) on metal-polar aluminum nitride (AlN) heterostructures.
The v-E characteristic of a semiconductor aggregates all the scattering mechanisms in that system. It provides the carrier mobility in the low-field regime and the saturation velocity and saturation onset field in the high-field regime. Hence, experimental determination of this characteristic is a common and essential means of benchmarking high-field transport theories. It also aids in high-speed device design as the gate length can be tuned to minimize the source-drain transit time while constraining the peak fields inside the device.
Our sample is grown by molecular beam epitaxy on a single-crystal AlN substrate. It consists of a ~12 nm coherently strained GaN layer grown on AlN to create a high-density 2D hole gas at the interface due to the polarization discontinuity, as verified by Hall-effect measurements. A ~12 nm Mg-doped InGaN cap layer is used only under metal stacks to make ohmic contacts to the 2D hole gas. This InGaN layer is removed from regions not covered by metal.
A pulsed voltage input and four-point measurement of the voltage across and current through a test structure with an etched constriction is used. This style of measurement has previously been performed for a wide variety of semiconductors, including silicon [1,2], graphene [3], silicon carbide [4,5], bulk GaN [6], and two-dimensional *electron* gas in GaN/AlGaN [7,8] and AlGaN/GaN [9] heterostructures. In recent years, our group has realized high-quality GaN/AlN heterostructures with a sizeable polarization-induced 2DHG at the interface (without p-type doping) [10]. Subsequent efforts to fabricate a p-channel finFET using the 2DHG as the conducting channel [11] have motivated performing this v-E measurement to better understand hole transport and to optimize device design.
The fabricated test structure has an etched constriction with micron-scale length, L, and width, W, determined from scanning electron microscope images. The sheet hole density is determined by Hall-effect measurement to be $N_s = +4.92\times10^{13}/cm^2$. A current, I, and voltage, V, across the constriction are measured using a microsecond-width pulsed voltage to minimize heating effects inside the constriction. The measured voltages are also corrected to account for the voltage drop between the metal pads and the constriction edges. The electric field, E, in the constriction and the mean hole velocity, v, are extracted with the equations $E = V/L$ and $v = I/qwN_s$ where q is the electron charge.
The room temperature v-E data are fit by the empirical equation $v=\mu E/[1+(\mu E/v_{sat})^{\alpha}]^{1/\alpha}$ where $\mu = 7.87\ cm^2/Vs$ is the low-field hole mobility, $v_{sat} = 2.45\times10^6$ cm/s is the saturation velocity, and $\alpha = 1.57$ is a fit parameter. These results are lower than, but of comparable magnitude to, previous measurements of hole transport in bulk GaN [12]. The v-E curve fitting suggests that the field to reach saturation velocity is ~3 MV/cm though the highest field measured with our present setup is 0.3 MV/cm.

1) C. Jacoboni et al., Solid State Electron. **20**, 77 (1977).
2) C. Canali et al., IEEE Trans. Electron Devices **22**, 1045 (1975).
3) M. Winters et al., J. Appl. Phys. **113**, (2013).
4) I.A. Khan and J.A. Cooper, IEEE Trans. Electron Devices 47, 269 (2000).
5) W. v. Muench and E. Pettenpaul, J. Appl. Phys. 48, 4823 (1977).
6) J.M. Barker et al., Phys. Status Solidi **190**, 263 (2002).
7) J.M. Barker et al., J. Vac. Sci. Technol. B Microelectron. Nanom. Struct. 22, 2045 (2004).
8) S.A. Vitusevich Semicond. Physics, Quantum Electron. Optoelectron. **9**, 66 (2006).
9) L. Ardaravičius et al., Appl. Phys. Lett. 83, 4038 (2003).
10) R. Chaudhuri et al., Science **365**, 1454 (2019).
11) S.J. Bader et al., IEEE Electron Device Lett. **39**, 1848 (2018).
12) D. Ji et al., IEEE Electron Device Lett. 41, 23 (2020).

10:40 AM A03
$Al_{0.64}Ga_{0.36}N$ Channel MOSHFET on Single Crystal Bulk AlN Substrate for Co-Designed Power Electronics Abdullah Mamun, Mohammad Hussain, Richard Floyd, Md Didarul Alam, MVS Chandrashekhar, Grigory Simin and Asif Khan; University of South Carolina, United States

In this work, we demonstrate a pseudomorphic $Al_{0.87}Ga_{0.13}N/Al_{0.64}Ga_{0.36}N$ metal-oxide-semiconductor HFETs (MOSHFET) on a single crystal bulk AlN substrate with linear ohmic contacts ($R_C \sim 4.3$ Ωmm) enabled by a 30 nm thick reverse composition (x = 87% to 40%) graded contact making $Al_xGa_{1-x}N$ layer using MOCVD. In addition to the thermal benefits, AlN substrates allow the growth of pseudomorphic epilayer structures for extreme bandgap (EBG) $Al_xGa_{1-x}N$ channel HEMT devices (Al-composition > 60%, bandgap > 4.5 eV). The measured threading dislocation densities in our pseudomorphic epilayers were $< 10^4\ cm^{-2}$ which should lead to significantly lower gate-leakage thus promoting device stability.[1] These transistor devices showed Baliga Figure of Merit (BFOM) of 460 MW/cm^2, which to date represents state-of-the-art performance for AlGaN-channel devices with similar composition.
Device fabrication began with mesa isolation using Cl_2-based ICP-RIE followed by Zr-stack metal deposition by e-beam evaporation as source/drain contacts, and rapid thermal annealing at 950 °C for 30 s under N_2 environment. This was followed by an ICP-RIE etch of the graded layer from the access region, 10 nm SiO_2 deposition as the gate oxide, Ni/Au gate, and Ti/Ni/Au probe pads deposition. Finally, the devices were embedded in 400 nm thick SiO_2 film by PECVD to relieve the surface electric field for the breakdown voltage measurements. In addition to the bulk AlN substrates, identical devices were also fabricated where the same epilayer structure was deposited on AlN templates. These innovations enabled MOSHFET devices with on-state peak drain current density 610 mA/mm (at +2V gate bias), on-off ratio (10^7), a three-terminal off-state breakdown field > 3.7 MV/cm, and BFOM of 460 MW/cm^2. Further optimization of surface passivation and edge termination could improve the effective off-state critical breakdown field (E_C) to > 10 MV/cm, as measured in 2-terminal measurements by our team and others.[2,3] Deep scaling of EBG AlGaN power devices is enabled by this high E_C. Compact devices have the additional advantage of reduced capacitance and other parasitics, allowing faster switching. However, the increased power density also leads to thermal limitations in overall system performance, e.g., current droop and premature failure, limiting deep-scaling of III-N power devices, due to poor heat removal through the currently used substrates with poor thermal conductivity (silicon, sapphire, Ga_2O_3).[4] We demonstrate using a novel thermal titration technique that the device on single crystal bulk AlN compared to identical structures on sapphire substrates shows 70% reduction in thermal impedance to 10 K-mm/W, a value that is comparable to SiC and copper heat-sinks. We will show that the improved electrical performance above is due to this enhanced thermal management from the bulk AlN substrate, arising from its intrinsic excellent thermal conductivity and high-temperature stability.[5] These advantages of EBG III-nitrides are attractive for post-GaN

deep-scaled efficient and compact co-designed power electronics with passive thermal management, such as in consumer electronic chargers, and next-generation electric vehicles (EV).[6]
[1] S. Rathkanthiwar, J. Houston Dycus, S. Mita, R. Kirste, J. Tweedie, R. Collazo, & Z. Sitar. Applied Physics Letters, 120(20), 202105 (2022).
[2] K. Hussain, A. Mamun, R. Floyd, M. D. Alam, M. E. Liao, K. Huynh, ... & A. Khan. Applied Physics Express. (2023).
[3] D. Khachariya, S. Mita, P. Reddy, S. Dangi, J. H. Dycus, P. Bagheri, ... & S. Pavlidis. Applied Physics Letters, 120(17), 172106 (2022).
[4] R. L. Xu, M. M. Rojo, S. M. Islam, A. Sood, B. Vareskic, A. Katre, ... & E. Pop. Journal of Applied Physics, 126(18), 185105 (2019).
[5] N. Yafune, S. Hashimoto, K. Akita, Y. Yamamoto, H. Tokuda, & M. Kuzuhara. Electronics letters, 50(3), 211-212 (2014).
[6] T. Kachi. Japanese Journal of Applied Physics, 53(10), 100210 (2014).

11:00 AM A04
(Student) Record Low Sheet Resistivity (<250 Ω/■) in High Composition (>35%) and Thick (>30 nm) Crack-Free Strain Optimized Barrier AlGaN/AlN/GaN HEMT on Sapphire Swarnav Mukhopadhyay, Cheng Liu, Jiahao Chen, Guangying Wang, Shubhra Pasayat and Chirag Gupta; University of Wisconsin–Madison, United States

AlGaN/GaN HEMTs are commercialized currently for high-frequency and high-power operations. Decades of material development allowed researchers to use the GaN HEMTs for high-power operations >500 V in power electronics [1-3]. The major challenge of AlGaN/GaN HEMTs operating at 500 V and beyond is the high gate leakage and soft breakdown. To avoid significant gate leakage at a high E-field and to achieve an improved I_{ON}/I_{OFF} ratio, high composition and thick AlGaN barrier layer is required [4-5]. The material quality degrades with increased thickness and composition of Al in the barrier layer and introduces interface roughness scattering, due to strain [6-7], which is challenging. In this work, we have grown 31 nm $Al_{0.36}Ga_{0.64}N$/AlN/GaN HEMT structure using the metal-organic chemical vapor deposition (MOCVD) process with strain optimization that showed record low room temperature (RT) sheet resistance 249 Ω/■ and very high 2DEG mobility of 7830 cm^2/V.s at 77 K without any cracks in the barrier layer.
AlGaN/AlN/GaN HEMT structure (Figure 1) is grown using MOCVD on a semi-insulating Ga-polar template on c-plane sapphire where tri-methyl gallium (TMGa), tri-ethyl gallium (TEGa), and tri-methyl aluminum (TMAl) were used as metal-organic precursors along with ammonia (NH_3) as the group-V precursor in H_2 ambient at 1210 °C. A controlled growth rate allowed to minimize the strain at the barrier layer and produce a very smooth interface. Different thicknesses of the layers (AlGaN (t_3), AlN (t_2) and GaN channel (t_1)) were explored to analyze the strain in the barrier layer and the characteristics of 2DEG density and mobility. The Al composition was kept constant (36%) throughout the experiments. Growth temperature is also varied from 1210 °C to 1153 °C to understand the effect of carbon incorporation in the channel. Growth parameters are summarized in Table 1. After the growth, the sheet resistance, mobility, and charge were measured using Hall measurement. XRD and AFM measurements are used to analyze the material quality and surface morphology.
In samples 1 and 2 the effect of growth temperature on carbon incorporation is observed (Figure 2), which shows the importance of maintaining low carbon concentration in the channel. XRD result (Figure 3) shows the very high edge dislocation density in sample 2 due to high carbon incorporation. It has been observed in sample 3 that the thickness of the AlN layer (t_2) plays a crucial role to reduce the scattering of the electrons in the channel and the strain in the barrier layer. Increasing the GaN channel thickness (t_1) from 200 nm to 1 μm in sample 4 improved the charge density and mobility by moving the channel/semi-insulating GaN interface away from the 2DEG compared to sample 1. The Hall measurement (Table 2) showed a very low sheet resistance <250 Ω/■ with an RT 2DEG mobility >1700 cm^2/V.s and a charge density >$1.4\times10^{13}/cm^2$ in samples 5 compared to sample 4 while increasing AlGaN thickness (t_3) from 21 nm to 31 nm. Although, a further increase of t_2 from 0.7 nm to 1.2 nm in sample 6 reduced the mobility and the charge compared to sample 5, due to the formation of micro-cracks and causing relaxation shown in Figure 4. Figure 5 compares our result with state-of-the-art HEMT structures grown using MOCVD. These results show that with optimized strain in the barrier layer, high composition thick AlGaN/AlN/GaN HEMT structure can be grown with record low sheet resistances (<250 Ω/■).
Reference: [1] V. Tilak et al., *IEEE EDL*, vol. 22, no. 11, pp. 504-506, Nov. 2001. [2] H. Li, et al., 2016 IEEE 4th WiPDA, Fayetteville, AR, USA, 2016, pp. 23-29 [3] J. G. Kim, et al., *IEEE TED*, vol. 68, no. 4, pp. 1513-1517, April 2021. [4] S. Turuvekereet al., *IEEE TED*, vol. 62, no. 10, pp. 3449-3452, Oct. 2015 [5] Z. Ma et al., 2006 8th *ICSICT Proceedings*, Shanghai, China, 2006, pp. 917-919 [6] A. Yamada, et al., J. Cryst. Growth 560–561 (Apr. 15, 2021) [7] C. R. Elsass et al 2001 *JJAP*. 40 6235.

11:20 AM A05
(Student) Epitaxial Growth and Transport Properties of AlScN/GaN FerroHEMTs Thai-Son T. Nguyen[1], Kazuki Nomoto[1], Joseph Casamento[2], Austin Hickman[1], Huili Grace Xing[1,1,1] and Debdeep Jena[1,1,1]; [1]Cornell University, United States; [2]The Pennsylvania State University, United States

AlScN is the first reported ferroelectric III-nitride material, demonstrated by both sputtering [1] and molecular beam epitaxy (MBE) [2]. Compared to traditional AlGaN/GaN and AlN/GaN high electron mobility transistors (HEMTs), AlScN barriers offer lattice matching capability with GaN for Sc compositions between 10% and 18% [3], enabling polarization-induced 2D electron gas (2DEG) with highly tunable carrier density in AlScN/GaN HEMT heterostructures [4]. MBE-grown AlScN is found to have a high-K with dielectric constants up to 20 [5], suitable for in-situ epitaxial barriers for HEMTs. Moreover, AlScN grown by MBE exhibits coercive fields as low as 1 MV/cm [6], potentially enabling ferroelectric switching in thin barrier AlScN/GaN heterostructures. Fully epitaxial growth of AlScN/GaN HEMT heterostructures is promising to achieve viable AlScN-barrier ferroelectric HEMTs (ferroHEMTs).
In this study, MBE growth and transport properties of ferroHEMT AlScN/GaN heterostructures are investigated. In the first generation, a control AlN/GaN and an AlScN/AlN/GaN ferroHEMT heterostructure with 14% targeted Sc composition were grown directly on 6H-SiC substrates and fabricated into transistors. The as-grown AlScN/AlN/GaN sample exhibited a sheet carrier density N_s = -2.99 x $10^{13}/cm^2$, electron mobility μ = 500 cm^2/V.s, and sheet resistance R_s = 417 Ω/sq. Transistor devices fabricated using this sample demonstrate high on-currents and the highest f_T/f_{MAX} (78 GHz/156 GHz) in AlScN/GaN HEMT devices reported to date [7]. Interestingly, while the control AlN/GaN devices did not show hysteresis, the AlScN/AlN/GaN devices exhibited counterclockwise hysteretic transfer characteristics with memory windows as large as 2 V and sub-Boltzmann switching behavior [7], showing signatures of ferroelectric gating behavior.
In the second generation, AlScN/AlN/GaN and AlScN/GaN heterostructures with 10% targeted Sc composition were grown directly on 6H-SiC substrates using a thinner AlN nucleation layer. Improved sheet carrier density N_s = -3.571 x $10^{13}/cm^2$, electron mobility μ = 1000 cm^2/V.s, and sheet resistance R_s = 174 Ω/sq are achieved in the AlScN/AlN/GaN sample. The enhanced 2DEG transport properties exhibit the lowest sheet resistances reported in AlScN/GaN HEMTs. Without an AlN interlayer, the AlScN/GaN heterostructure showed sheet carrier density N_s = -1.77 x $10^{13}/cm^2$, electron mobility μ = 720 cm^2/V.s, and sheet resistance R_s = 489 Ω/sq. While an AlN interlayer effectively boosts 2DEG mobility [8], it also adds about 1.5 x $10^{13}/cm^2$ to sheet charge density, thereby increasing threshold voltage. Achieving AlScN/GaN heterostructures with comparable 2DEG mobility and lower sheet density will enable

ferroHEMTs with more desirable threshold voltages for device applications.
[1] S. Fichtner *et al*., AlScN: A III-V Semiconductor Based Ferroelectric, J. Appl. Phys. **125** (11), 114103 (2019).
[2] P. Wang *et al*., Fully Epitaxial Ferroelectric ScAlN Grown by Molecular Beam Epitaxy, Appl. Phys. Lett. **118**, 223504 (2021).
[3] D. V. Dinh *et al*., Lattice Parameters of $Sc_xAl_{1-x}N$ Layers Grown on GaN(0001) by Plasma-Assisted Molecular Beam Epitaxy, arXiv:2211.16920v1 (2022).
[4] M. T. Hardy *et al*., Epitxial ScAlN Grown by Molecular Beam Epitaxy on GaN and SiC Substrates, Appl. Phys. Lett. **110**, 162104 (2017).
[5] J. Casamento *et al*., Epitaxial $Sc_xAl_{1-x}N$ on GaN Exhibits High-K Dielectric Properties, Appl. Phys. Lett. **120**, 152901 (2022).
[6] J. Casamento *et al.*, Ferroelectric in Polar ScAlN/GaN Epitaxial Semiconductor Heterostructures, arXiv:2105.10114 (2021).
[7] J. Casamento *et al.*, FerroHEMTs: High-Current and High-Speed All-Epitaxial AlScN/GaN Ferroelectric Transistors, 2022 International Electron Devices Meeting 11.1.1 – 11.1.4 (2022).
[8] J. Casamento *et al.*, Transport Properties of Polarization-Induced 2D Electron Gases in Epitaxial AlScN/GaN Heterojunctions, Appl. Phys. Lett. **121**, 192101 (2022).

11:40 AM A06
(Late News) Reliability Study and Analysis of Vertical GaN Power Devices Dawei Wang, Dinusha Herath Mudiyanselage, Ziyi He and Houqiang Fu; Arizona State University, United States

Wide bandgap GaN holds great promise for high-efficiency power conversion systems due to the excellent physical properties of GaN material. For GaN devices, vertical structure devices have attracted great attention after the lateral GaN-HEMT device since they have high current density, lower peak electric field at high voltage, and immunity to surface-related issues. GaN stability is a serious concern for predictable device behavior in real-world operations. For now, the reliability of vertical GaN devices still needs to be investigated systematically.
In this work, the first comprehensive study of the reliability of GaN vertical P-I-N diode was presented. The device stability and parameter shift under high-temperature stress and current stress have been investigated. The failure mechanism of the device at high power density has been studied. For the high-temperature stress, first, the temperature of devices rising from 25 °C to 400 °C, and the forward curves of the device during temperature stress are shown in Fig.1. The extracted turn-on voltage and On-resistance are shown in Fig.2. At each temperature value, several curves were scanned in case of the transient instability at variable temperature. It shows that the turn-on voltage keeps decreasing with the temperature increase due to the energy band narrowing with increasing temperature. And the turn-on voltage can completely recover after the high-temperature stress is finished. For the On-resistance, it shows that the On-resistance decreases with the temperature increasing from 25°C to 100°C but is stable at each temperature. When the temperature is increased from 125°C to 400 °C, the On-resistance first increases and then decreases. However, the trend is not evident in this experiment. Therefore, another long-time temperature stress testing of 200°C and 400°C was done, as shown in Fig. 3 (forward curves). And the extracted On-resistance is shown in Fig. 4. For the temperature stress of 200°C, the On-resistance first decreases and then increases to larger than the original value. For the stress of 400°C, the On-resistance decreased and then was kept at a constant value. The reason that the device's On-resistance changed during the temperature stress of 200°C is still under investigation. In addition, the On-resistance can recover from high temperatures.
For the current stress testing (turn-on state), first, long-time current stress was finished. It showed that the GaN vertical P-I-N diode is very stable for long-time operation without any degradation. However, at the beginning of the stress, the device is not stable due to trapping behavior and carrier accumulation. As shown in Fig. 5, the current stress at voltages from 4V to 8V and a stress time of the 30s, 60s, 90s, and 120s were applied to a device, respectively. It shows that for the same voltage, the on-resistance (Fig. 6) will decrease to a certain value and then keep constant. This means the filling of the trapped states in the device is voltage-dependent. We also did reverse testing of the recovery of On-resistance at negative voltage stress. After the current stress process of Fig. 5, this device was applied to a negative voltage of -5 V, -10 V, -20 V, and -50 V, respectively. After each reverse voltage stress, the process in Fig. 5 was repeated, as shown in Fig. 7. It was shown that the On-resistance of the device shows voltage level dependent character again after -50 V stress, indicating that the trap and carrier accumulation can be recovered at a higher negative voltage.
Fig. 8 shows the turn-on voltage of the device with different voltage and time stress. The shift of the turn-on voltage is smaller than 0.05 V, indicating that the GaN vertical P-I-N diode has good reliability of turn-on voltage. Fig. 9 shows the forward curve after high power density stress. The failure mechanism is still under investigation.

SESSION B: 2D Materials Properties and Interfaces
Session Chairs: Kevin Daniels and Thomas McKnight
Wednesday Morning, June 28, 2023
UC, Corwin East

10:00 AM B01
(Student) Investigation of Dielectric Properties of h-BN/c-BN Nanocomposites Mingfei Xu, Abhijit Biswas, Shisong Luo, Tao Li, Zhaobo Mei, Jingan Zhou, Robert Vajtai, Pulickel Ajayan and Yuji Zhao; Rice University, United States

Boron nitride (BN), an ultrawide bandgap material, has gained significant attention owing to its excellent structural, electrical, thermal, and mechanical properties. Structurally, BN possesses a variety of polymorphs, including hexagonal BN (h-BN), cubic BN (c-BN), rhombohedral BN (r-BN), and wurtzite BN (w-BN). Among these polymorphs, h-BN has been extensively studied in recent years. It is a 2D layered vdW material with a bandgap of ~5.9 eV, a breakdown field of ~7 MV cm^{-1}, a dielectric constant of ~4, and thermal conductivity of 550 W m^{-1} K^{-1} [1]. Due to its ultrawide-bandgap, and high thermal conductivity, it has become a promising dielectric material for 2D electronic applications. On the other hand, 3D c-BN also has considerable potential in electronics because of its even wider bandgap of ~6.4 eV, a breakdown field of >15 MV cm^{-1}, and a dielectric constant of ~7.1 [2]. Therefore, it is attractive to combine h-BN and c-BN into an h-BN/c-BN nanocomposite form and measure the electronic properties that can facilitate the development of BN-based materials for various electronic applications. To investigate that, here, we have synthesized h-BN/c-BN nanocomposites with different compositional ratios and measured the dielectric properties of nanocomposites by varying frequencies, voltages, and temperatures.
Several h-BN/c-BN-based nanocomposites in a form of a one-inch disk with varying h-BN/c-BN ratios (from 0%/100% to 100%/0%) are made by using the h-BN and c-BN powders, via the solid-state reaction methods. X-ray photoelectron spectroscopy (XPS) shows the characteristic B-N peaks. X-ray diffraction (XRD) shows the presence of both h-BN and c-BN-related peaks throughout the theta-2theta scan range. Fourier-transform infrared spectroscopy (FTIR) spectra further confirm the presence of both h-BN (~1365 cm^{-1}) and c-BN (~1060 cm^{-1}) optical phonon-modes in the composite. Capacitance-voltage (C-V) characteristics are performed for the nanocomposites using Keysight B1505A. The frequency-dependent dielectric constant is extracted within the 1 kHz to 1 MHz frequency range. We found that the frequency-dependent dielectric constant of h-BN/c-BN (50%-50%) nanocomposite increases from ~3.79 (at 1 MHz) to ~5.28 (at 1 kHz). Temperature-dependent C-V measurements are also performed from room temperature to 300 °C. For the temperature-dependent case, it

increases from ~3.79 (at room temperature) to ~4.61 (at 300 °C), for a given frequency of 1 MHz. The structural and dielectric properties of h-BN/c-BN-based nanocomposites with other ratios will be characterized and measured later. These observations are very useful to design and modulate the dielectric properties of novel BN-based nanocomposites and would be beneficial to integrate BN nanocomposites as a robust dielectric material for future nano-electronics.

[1] M. Xu et al., Oxford Open Materials Science 2, itac004, 2022.
[2] M. M. Rahaman et al., Journal of Crystal Growth 593, 126781, 2022.

10:20 AM B02
Reliability of Electronics Containing 2D Materials Elisabeth Mansfield and Jason Holm; National Institute of Standards and Technology, United States

Devices containing electronic-grade 2D materials are gaining ground as researchers learn to manipulate the attractive properties of these materials for new applications. Incorporating these materials into devices on the manufacturing scale requires the relationships between material structure and defects to be well understood to allow for the development of high reliability devices. Factors affecting material reliability include geometry, microstructure, chemistry, dimensional scale, proximity to other materials, and exposure to external stressors. Building upon our publication of defect growth on MoS_2 materials under electrical stress, 2D materials were subjected to traditional challenges for microelectronics to explore degradation procedures. This talk with discuss the conditions that lead towards material failures and the nature of the degradation of these materials under specific conditions. We utilize analytical transmission scanning electron microscopy (STEM in SEM) to identify and highlight defects in materials. The nature of each crystal defect is identified using 4D STEM in SEM and implications of that defect on electronic device functionality will be discussed. The figure shows a defect in InSe with associated diffraction pattern.

10:40 AM B03
Doping and Damage of MoS_2 Monolayers from Metal Deposition Ama Agyapong, M S. Rahman, Chen Chen, Nicholas Trainor, Joan M. Redwing and Suzanne E. Mohney; The Pennsylvania State University, United States

We have employed Raman spectroscopy as a non-destructive method to observe doping and damage induced by metal deposition on monolayer (1L) MoS_2. The monolayers were grown epitaxially by metal organic chemical vapor deposition on sapphire. We probe the single-crystal MoS_2 monolayers after metallization through the transparent sapphire substrates. Low melting point metals (Bi, In and Sn) have recently been exploited for low-resistance ohmic contacts, and we find evidence that these metals can electron dope 1L MoS_2. However, the doping can be inhomogeneous, as signaled by splitting of the first-order out-of-plane vibrational mode in the Raman spectra. Interestingly, the degree of inhomogeneity appears to be dependent on features in the MoS_2 epilayer. In contrast to our measurements of Bi, In, and Sn contacts, we did not find evidence for doping from the Raman spectra of 1L MoS_2 beneath Cu, Pd, and Pt contacts. In this study, we also compared the influence of the metal deposition method (electron-beam evaporation or sputter deposition) on the Raman spectra. Sputter deposition leads to partial or complete suppression of the first-order Raman modes after deposition of the metals, providing evidence that structural damage can occur from metallization.

11:00 AM B04
Strain-Induced Magnetism in Defective Graphene Zubaer Hossain; University of Delaware, United States

Vacancy defects are known to induce magnetization in graphene. However, understanding the effects of defect-defect interaction on magnetization under applied strain remains elusive. This talk will present the effects of symmetry-breaking strain on magnetization in multidefect graphene. We used the density functional theory simulation under the generalized gradient approximation for the exchange-correlation energy to investigate the magnetic consequence of strain applied along different directions relative to the defect pair. Our results show that the spin magnetic moment increases with increasing strain. Decomposition of the total magnetic effects into the individual effects of the orbitals reveals that the p_z orbital dominates the change in the total magnetic moment, while the net change of the local moment in p_x and p_y orbitals are the same but with opposite signs. Nonetheless, for a pair of monovacancies, the strain does not affect the spin magnetic moment when the inter-defect distance reaches a critical value. However, the magnetic moment increases with increasing strain for a longer inter-defect distance, and the combined effects can be well-approximated as a linear superposition of their individual effects. Additionally, if the defects are magnetically isolated, there exists a critical strain whereat each of the defects experiences a second-order Jahn–Teller reconstruction (JTRR) that switches the orientation of the defect and alters the magnitude of the magnetic moment, as shown in the figure. These results are expected to shed new light on controlling the magnetic behavior of a single or multi-defect system as a function of the separation distance and the intensity of mechanical strain.

11:20 AM B05
Graphene-Polymar Mono Defect Based Octonacci Quasi-Photonic Dual Narrowband Absorber Safayat Al Imam, Khandakar Mohammad Ishtiak and Quazi Deen Mohd Khosru; Bangladesh University of Engineering and Technology, Bangladesh

The primary reason for the study of quasi-crystals from a mathematical standpoint is that they exhibit a pattern of self-similarity in their spectrum. Because of their photonic bandgaps and photonic localization characteristics, quasi-photonic crystals (QPCs) may also offer tunable optical responses. Fibonacci, octonacci, dodecanacci quasi periodic, thue-morse systems photonic crystals have also been considered[1,2]. The octonacci substitution method possess better unidirectional absorption comparing other quasi periodic system[3,4]. This article investigates DQPC properties in the vicinity of graphene placed on a poly defect layer to observe the behavior of absorption with electric field dependent octonacci sequential order. With the change in the time period and in the sequential layer generation number of proposed structures, the peak wavelength and the extent of maximum absorption may be adjusted without altering the material thickness. TiO_2 and SiO_2 are the two materials selected for our proposed structure for a specific sequence. In case of defect mode, polystyrene electro optic materials are proposed as defect materials. This work theoretically shows dual ultra-narrowband photonic absorber within the wavelength of near IR range for a graphene based octonacci single defective quasi-photonic crystals (DQPCs) [Figure 2(a, c)]. Electro-optical (EO) material is used as a defect mode under the transfer matrix method in this proposed structure. Sequence coefficients such as generation number, periodicity, utilized in DQPCs are studied to determine the wavelength adjustability of defect state. The wavelength flexibility of the defect mode is determined by sequence coefficients such as generation number, cyclicity, and kind of sequence used in DQPCs. The results indicate that using DQPCs may help enhance absorption and allow for fault mode adjustment when the generation number changes. The findings also show that utilizing DQPCs may assist improve absorption and allow for the modification of the defect mode as its generation number varies. Polystyrene is used as EO-material with octonacci sequence in the proposed structure for narrowband filter design. By adjusting the applied external voltage in EO materials, it is possible to fine-tune graphene-based DQPCs for maximum absorption with a red shift of peak wavelength and for positive voltages, Q-factor of the narrow band absorption filter increases [Figure 2(b)]. Multiple peaks of near perfect absorption can be achieved with a polystyrene based graphene structure under an incident angle within the range of for both TE and TM polarization for suitable voltages [Figure 3(b, c)]. Variance in

defect thickness leads to fine tune the peak absorption [Figure 3(a)]. By changing the chemical potential of the graphene across a specific range, these configurations may achieve increased or dual peak ultra-narrowband absorption [Figure 1(c)]. Such a design could be important in sensor and monochromatic photodetectors design which needs ultra-narrowband absorber.

1. E. F. Silva, M. S. Vasconcelos, C. H. Costa, D. H. A. L. Anselmo, and V. D. Mello, Opt. Mater. (Amst). **98**, 109450 (2019).
2. M. Solaimani, M. Ghalandari, and M. Nejati, AIP Adv. **11**, (2021).
3. M. Zamani, M. Amanollahi, and M. Taraz, Opt. Mater. (Amst). **88**, 187 (2019).
4. S. Guo, C. Hu, and H. Zhang, J. Opt. Soc. Am. B **37**, 2678 (2020).<quillbot-extension-portal></quillbot-extension-portal>

11:40 AM B06
(Student) Temperature Dependent Spin Transport and Thermally Driven Quantum Phase Change in Graphene/$Pb_{0.24}Sn_{0.76}Te$ Heterostructure Two-Dimensional Electron Gas Jennifer E. DeMell[1], Ivan Naumov[2], Gregory Stephen[1], Nicholas Blumenschein[1], Leo Sun[1], Jeremy Robinson[3], Patrick Taylor[4], Pratibha Dev[2], Aubrey Hanbicki[1] and Adam Friedman[1]; [1]Laboratory for Physical Sciences, United States; [2]Howard University, United States; [3]U.S. Naval Research Laboratory, United States; [4]U.S. Army Research Laboratory—Science and Technology at the Energy and Power Division, United States

Quantum phase transitions can provide a low-power switching mode for novel electronic devices for future computing platforms. Heterostructures of novel materials such as topological insulators and two-dimensional (2D) materials possess several unique characteristics, including spin momentum locking, high spin-orbit coupling, and susceptibility to proximity effects. In a previous work[1] we identified the carrier mobility of a $Pb_{0.24}Sn_{0.76}Te$/graphene heterostructure to be nearly 100% greater than the mobility of either constituent $Pb_{0.24}Sn_{0.76}Te$ or graphene. In this work, we fabricate and measure non-local spin valves on a $Pb_{0.24}Sn_{0.76}Te$/graphene heterostructure and calculated spin lifetimes on the order of 2 ns and spin polarization efficiencies up to 10%. We found a spin-split two-dimensional electron gas (2DEG) forms at the 2D-material/topological-insulator interface and observe a quantum phase change near 50 K. Below the transition temperature, the non-local resistance exhibits metallic behavior as the 2DEG dominates the device operation and in the high-temperature regime, we observe semiconducting behavior where the classical Rashba effect dominates. This spin valve has shown to be robust, continuing to operate after a significant time out of vacuum

SESSION C: Photonic Devices
Session Chairs: Abhilasha Kamboj and Joshua Zide
Wednesday Morning, June 28, 2023
UC, Flying A Studios

10:00 AM C01
(Student) (In)AlBiAs-Based Short-Wave Infrared Avalanche Photodiodes James Bork[1], Robert D. Richards[2], Wilder Acuna[1], Xiaofeng Tao[2], Xiao Jin[2], Chee H. Tan[2], John David[2] and Joshua Zide[1]; [1]University of Delaware, United States; [2]The University of Sheffield, United Kingdom

As a class of highly mismatched alloy, the dilute bismuthides (alternatively, dilute bismides) consist of III-V materials with small amounts of bismuth incorporation.[1] Resulting from the large difference in size and electronegativity between Bi and the host material's atoms, the incorporation of bismuth can lead to large bandgap reduction and high spin-orbit splitting. The extension in operating wavelength of III-V devices through Bi incorporation has led to many dilute bismuthide materials having been explored for infrared photodetectors, lasers, and solar energy conversion.[2,3,4] Due primarily to the larger bandgap of the AlAs endpoint compound, Al-containing bismuthide alloys have been comparatively understudied.[5,6] Here we present our work on the application of the Al-containing bismuthide (In)AlBiAs in avalanche photodiodes (APDs) on GaAs and InP. As has been shown previously, the performance of APDs depend heavily on the spin-orbit splitting of the charge multiplication material.[7,8] Through the introduction of bismuth into conventional APD materials, a strong decrease in the hole impact ionization coefficient can be realized, leading to high performance improvement. Additionally, the absorption and multiplication can occur in spatially separated regions, theoretically allowing for the combining of a low bandgap absorber with an Al-containing bismuthide multiplication region. Given the highly performing and well-established use of (In)AlAs-based APDs on GaAs and InP, the study of bismuth incorporation into devices made from these base materials is of great interest.

In our work on InAlBiAs-based APDs on InP (the first InAlBiAs device-type structures ever reported), the introduction of ~2% Bi causes an increase in the cutoff wavelength of the photoresponse of PIN structures by around 100 nm (with an Urbach tail extending it further by 200 nm) compared to InAlAs-based structures. Through measurement of the carrier multiplication, the bismuth incorporation appears to strongly decrease the hole impact ionization coefficient (thereby increasing the ratio of impact ionization coefficient of the electrons to holes at lower electric-fields) by almost an order of magnitude. These preliminary results demonstrate the relevancy of Al-containing bismuthide materials in InP-based optoelectronic devices and motivate their further study. Increasing the bismuth content in these devices (while maintaining high-quality material with few defects) could lead to a stronger effect on the hole impact ionization coefficient.

[1] Crystals 17, 7, 63 (2017) [2] Semicond. Sci. Technol. 27, 094011 (2012). [3] Appl. Phys. Lett. 88, 201112 (2006). [4] J. Cryst. Growth 452, 276 (2016). [5] J. of Appl. Phy. 126, 095704 (2019). [6] J. Vac. Sci. Technol. A 40, 042702 (2022). [7] Optica 10, 2, 147-153 (2023). [8] Sci Rep 8, 9107 (2018).

10:20 AM C02
(Student) Optically Pumped 1200 nm InAs Dot-in-Well (DWELL) Photonic Crystal Surface-Emitting Laser (PCSEL) by Molecular Beam Epitaxy Subhashree Seth[1], Kevin J. Reilly[1], Fatih F. Ince[1], Akhil Kalapala[2], Thomas J. Rotter[1], Zhongue Liu[2], Emma J. Renteria[1], Sadhvikas Addamane[3], Weidong Zhou[2] and Ganesh Balakrishnan[1]; [1]The University of New Mexico, United States; [2]The University of Texas at Arlington, United States; [3]Sandia National Laboratories, United States

Over the past decade, Photonic-crystal surface-emitting lasers (PCSELs) have attracted considerable attention for large area single mode emission while maintaining high output power in a uniformly narrow far-field beam by incorporating a two-dimensional (2D) Photonic Crystal (PhC) resonant cavity. The 2D PhC resonant cavity provides two-dimensional in-plane feedback which will experience multiple Bragg diffraction resulting in a 2D standing wave. When the resonant in-plane light satisfies the vertical diffraction condition, there is a vertical direction emission from the PCSEL surface. Additionally, PCSELs offer single-chip electrically injected light sources, controlling polarization and beam direction. PCSELs with active regions using InAs quantum dots (QDs) have drawn a considerable amount of interest in the 1100 to 1300 nm emission wavelength. Previously, PCSEL devices were fabricated by way of wafer fusion where one wafer containing the active region of the laser device is bonded to the PhC layer. In recent times, epitaxial regrowth has gained popularity due to higher device yield and better device performance.

In this study, we report optically pumped QD PCSEL fabricated by molecular beam epitaxy (MBE). The growth on n-type GaAs substrate started with a 300 nm GaAs n-contact layer, 1360 nm $Al_{0.3}Ga_{0.9}As$ n-cladding, 300 nm GaAs barrier, an active region of three layers of InAs dots-in-well (DWELL), a 110 nm GaAs barrier and finally a 305

nm GaAs PhC region. The growth is interrupted at this stage and a GaAs PhC layer is patterned with an 8 x 8 array of PhC devices with circular voids in square lattice using electron-beam lithography. Based on simulation results we patterned a series of PhC structures by varying the lattice constant 359-373 nm in 2 nm increments along columns to produce a PhC resonance wavelength close to the DWELL peak gain. Photoluminescence is measured from these PCSEL devices. From the simulated and experimental results, we see that the lattice constant and PhC void diameter become critical parameters for diffraction coupling between the PhC structure and the adjacent active region. The PhC layer patterned with sixty-four PCSEL devices in an 8 x 8 array were tested by optical pumping and we present both light input-light output (LL) and spectrum measurements.

1. Imada, Masahiro, Susumu Noda, Hideaki Kobayashi and Gordon Sasaki. “Characterization of a distributed feedback laser with air/semiconductor gratings embedded by the wafer fusion technique.” *IEEE Journal of Quantum Electronics* 35 (1999): 1277-1283.
2. Yoshida, Masahiro, Menaka De Zoysa, Kenji Ishizaki, Yoshinori Tanaka, Masato Kawasaki, Ranko Hatsuda, Bongshik Song, John Gelleta, and Susumu Noda. "Double-lattice photonic-crystal resonators enabling high-brightness semiconductor lasers with symmetric narrow-divergence beams." *Nature materials* 18, no. 2 (2019): 121-128.
3. Ming-Yang Hsu, Gray Lin, and Chien-Hung Pan. "Electrically injected 1.3-μm quantum-dot photonic-crystal surface-emitting lasers." *Optics Express* 25 (2017): 32697-32704.
4. Kevin J. Reilly, Akhil Kalapala, Seuongwon Yeom, Sadhvikas J. Addamane, Emma Renteria, Weidong Zhou, Ganesh Balakrishnan. “Epitaxial Regrowth and Hole Shape Engineering for Photonic Crystal Surface Emitting Lasers (PCSELs)”. *Journal of Crystal Growth* 535 (2020):125531.

This work was performed, in part, at the Center for Integrated Nanotechnologies, an Office of Science User Facility operated for the U.S. Department of Energy (DOE) Office of Science by Los Alamos National Laboratory (Contract 89233218CNA000001) and Sandia National Laboratories (Contract DE-NA-0003525).

10:40 AM C03

(Student) Long-Wave Infrared Beam Steering with InAsSb Phased Arrays Jingze Zhao[1], Jinghe Liu[1], Kevin Kucharczyk[1], Dmitri Donetski[1], Gela Kipshidze[1], Gregory Belenky[1] and Stefan Svensson[2]; [1]Stony Brook University, The State University of New York, United States; [2]CCDC U.S. Army Research Laboratory, United States

Optical phased arrays find many applications including beam steering and beam wavefront correction in imaging and sensing systems. Efficient beam steering in the mid-wave infrared range has been demonstrated with electro-optical and thermal optical effects in arrays of waveguides with phase modulation based on lithium niobate and InGaAs on InP, respectively [1-2]. While lithium niobate-based devices offer ultimate steering rates it application is limited to the mid-wave infrared range due to limited optical transparency. Here we demonstrate the possibility of azimuthal steering with fast scan rates using arrays of InAsSb waveguides realized with modulation of the fundamental absorption by band filling (Moss-Burstein effect). InAsSb alloys are recognized as viable materials for applications in mid-wave and long-wave optoelectronics due to suitable energy band gaps and large fundamental absorption coefficients. The large absorption enables an effective modulation by carrier-induced change of the refractive index in the vicinity of the energy gap [3-4]. The devices were designed to operate at a 10.6-um wavelength of CO2 laser with grating coupling to the phase change section. Various waveguide configurations for optical and electrical carrier injections were considered. For optical carrier injection, we explored the performance of devices based on dielectric waveguides made with InAsSb absorbers grown on GaSb buffers on GaAs platform. For electrical carriers injections, we considered barrier heterostructures (nBp) with InAsSb alloy absorbers on AlInSb and GaInSb graded buffers grown on GaSb platform. The top metal contact of barrier heterostructures served for optical confinement with surface plasmon polaritons (SPP). The dependences of index change, steering angle and optical losses with carrier injection for the waveguide configurations will be discussed.

The project was supported by the Army Research Office award W911NF2010109.

[1] J. Chiles and S. Fathpour, Optica **1**, 350 (2014).
[2] J. Midkiff, K. M. Yoo, J. Shin, H. Dalir, M. Teimourpour, and R. T. Chen, Optica **7**, 1544-1547 (2020).
[3] D. Donetsky, J. Liu, G. Kipshidze, L. Shterengas, G. Belenky, W. L. Sarney, *and* S. P. Svensson, Appl. Phys. Lett., **115**, 081102 (2019).
[4] J. Liu, D. Donetsky, H. Jiang, G. Kipshidze, L. Shterengas, G. Belenky, W. L. Sarney, and S. P. Svensson, J. Appl. Phys. **128**, 083101 (2020).

11:00 AM #C04

(Student) Molecular Beam Epitaxy of Strained Superlattice InAlGaAs/AlGaAs Spin-Polarized Photocathodes Aaron Engel[1], Marcy Stutzman[2], Jason T. Dong[1] and Christopher J. Palmstrøm[1,1]; [1]University of California, Santa Barbara, United States; [2]Thomas Jefferson National Accelerator Facility, United States

Spin-polarized electron beams are a crucial tool in particle physics experiments and electron-in materials characterization techniques. Increasing the electron spin polarization (ESP) and the quantum efficiency (QE) of the photocathodes which produce these beams enhances the overall experimental efficiency. For accelerator applications, high QE is beneficial both in that it enhances operational lifetime and enables high bunch charge (nanoCoulomb and greater) polarized electron beams. The current state-of-the-art spin-polarized photocathodes consist of GaAs/GaAsP strained superlattice quantum wells grown on metamorphic GaAsP virtual substrates on GaAs(001), which consistently produce QE over 1% and ESP around 85%, for a figure of merit (ESP^2QE) of about 0.75. Recently, a seven-fold increase in figure of merit has been achieved by resonantly enhancing the QE to 6.4% by integrating a GaAsP/AlAsP distributed Bragg reflector (DBR) beneath the active region [1].

While the GaAs/GaAsP system is mature, it still faces many limitations. Growth of the relaxed virtual substrate results in a higher density of threading dislocations than there would be in a fully pseudomorphic system, thereby limiting quantum efficiency. In addition, since the As:P ratio controls the lattice constant, band offsets, and band gap, it is difficult to engineer the optimal strain in the well, optimal superlattice bandgap, and optimal band offsets simultaneously.

Here we demonstrate fully pseudomorphic spin-polarized photocathodes based on the InAlGaAs/AlGaAs system grown by molecular beam epitaxy. By switching to these quaternary wells and ternary barriers, we may optimize the material parameters independently. In addition, the fully pseudomorphic structure simplifies growth and reduces the dislocation density in the active region. Through this decoupling, we investigate novel device structures to potentially improve uniformity, QE, and ESP, including a digital alloy active region. Our first test structure using standard photocathode designs yielded polarization over 80%, but a QE of only about 0.3%, giving a reasonable figure of merit around 0.3. We further characterize preliminary AlAs/AlGaAs DBRs and will investigate their integration into photocathode structures.

[1] Wei Liu, Yiqiao Chen, Wentao Lu, Aaron Moy, Matthew Poelker, Marcy Stutzman, and Shukui Zhang, "Record-level quantum efficiency from a high polarization strained GaAs/GaAsP superlattice photocathode with distributed Bragg reflector", Appl. Phys. Lett. 109, 252104 (2016)

11:20 AM C05
(Student) Sensitivity Optimization in Diffusion-Limited Infrared Detectors Alexander T. Newell[1,2], Rigo A. Carrasco[2], Christian P. Morath[2], Chris Hains[2], Julie V. Logan[2], Diana Maestas[2], Zinah M. Alsaad[2], Ganesh Balakrishnan[1] and Preston T. Webster[2]; [1]The University of New Mexico, United States; [2]Air Force Research Laboratory, United States

The performance potential of ideal infrared detectors is fundamentally limited by the thermally generated diffusion and depletion dark currents of the infrared absorbing layer due to its narrow energy gap and consequently large intrinsic carrier concentration. Dark current manifests as shot noise in the detector, which leads to a decrease in sensitivity as the square root of the magnitude of the dark current. Although decreasing the operating temperature is an effective strategy to reduce dark current, active cooling of the device increases system size, weight, and power, which is not tolerable for certain applications. An alternative strategy, utilized to great effect in the *n*B*n* infrared detector architecture, is to hinder the formation of depletion regions in the narrow-gap material and thereby eliminate the depletion current. This can greatly reduce the total dark current as depletion current is proportional to intrinsic carrier concentration, whereas diffusion current is proportional to the equilibrium minority carrier concentration. Unfortunately, despite the ability to minimize the equilibrium minority carrier concentration by increasing the doping concentration, inclusion of donor impurities also increases the Shockley-Read-Hall and Auger recombination mechanisms, which in turn increases diffusion dark current, limiting its reduction via doping. Furthermore, reduction of the minority carrier lifetime decreases the diffusion partial quantum efficiency, which also degrades detector sensitivity. Therefore, a complex trade-off exists between doping density's effects on dark current and minority carrier lifetime which can be balanced to achieve an optimum detector sensitivity. Here, an investigation on the effects of material parameters on minimal attainable shot noise-limited noise equivalent irradiance is performed using models of diffusion current density as well as diffusion partial quantum efficiency derived from carrier continuity equations. The model is then verified using Silvaco TCAD simulations of *n*B*n* devices. Additionally, two mid-wave infrared InGaAs/InAsSb superlattice *n*B*n* detectors grown with different absorber doping densities are characterized and compared to the model results.

11:40 AM C06
(Student) Development of GaAs Photodetector Arrays for Soft X-Ray Beam Position Monitoring Kevin Kucharczyk[1], Jinghe Liu[1], Ricardo Lutchman[1], Jingze Zhao[1], Dmitri Donetski[1], Claudio Mazzoli[2], Christie Nelson[2], Steven Hulbert[2], Christopher Eng[2], Daniel Bacescu[2] and Boris Podobedov[2]; [1]Stony Brook University, The State University of New York, United States; [2]Brookhaven National Laboratory, United States

The fundamental resolution limit for coherent soft x-ray imaging achievable in synchrotron beamlines originates from the finite stability of electron and photon beams. Diagnostics such as X-ray Beam Position Monitors located upstream of the first optical element in a beamline, and thus called "white-beam" are critical for evaluating and controlling photon beams delivered by modern, highly coherent sources. Photoemission-based XBPMs, which typically use metal blades placed into the outside portions of the beam are routinely utilized at the front ends of hard x-ray beamlines. Such XBPMs, however, if installed into coherent beamlines would produce significant wavefront distortion, therefore, novel non-invasive devices with high spatial resolution are needed.
In this work, GaAs photodetector arrays designed for non-invasive monitoring of x-ray beam position in soft coherent beamline front ends in synchrotron light sources will be reported. GaAs and other semiconductors offer greater responsivity in the x-ray range compared to metal since each photon with energy E produces approximately E/4 photoelectrons. At the same time, semiconductor XBPMs should be able to operate under high beam power densities resulting in high photocurrent densities and overheating.
A shallow p-n junction was employed to reduce the device photocurrent density with beam power densities up to 20 W/mm^2, mainly coming from hard x-rays. With this approach, the photocurrent is primarily defined by the excess carriers generated by low-energy x-ray photons absorbed near the detector surface. The p–n junction structures were grown by molecular beam epitaxy and processed into 64-element linear photodiode arrays. The devices were characterized first in the visible range with a high-power 514 nm Ar-ion laser with a maximum power density reaching 200 W/cm^2 and then tested in the soft and hard x-ray regions up to 10 keV at two beamlines of the National Synchrotron Light Source II named CSX 23-ID-1 and 4-ID ISR. The responsivity was measured to be 0.16 A/W at 0.7 keV and 0.05 A/W at 6 keV in agreement with carrier diffusion modeling. At higher x-ray energies the measured responsivity was lower than predicted in the framework of the carrier diffusion model. Modeling of the temperature profile in GaAs photodetectors having a 50-µm wide strip being exposed to an x-ray beam power density of 20 W/mm^2 showed a temperature rise of 40°C above room temperature. The temperature dependence on responsivity of the GaAs photodiodes was characterized with a 635 nm diode laser. The laser photon penetration depth was similar to that of soft-x-ray photons. The responsivity of the GaAs photodiodes was found to increase by 6% up to a temperature of 65°C. This increase was explained by a collection of minority holes from a greater volume due to the increase of the hole diffusion length with temperature. The latter was dominated by an increase of the minority hole carrier lifetime limited by radiative recombination. GaAs/AlGaAs barrier heterostructure devices are being studied for blocking minority hole collection and for improvement of the temperature stability of the device responsivity.
We are grateful for the support of the Accelerator & Detector Research Program of the Scientific User Facilities Division, Office of Basic Energy Sciences, Office of Science of the U.S. Department of Energy (DOE). This research used beamlines 4-ID (ISR) and 23-ID-1 (CSX) of the NSLS-II, a DOE Office of Science User Facility operated for the DOE Office of Science by Brookhaven National Laboratory under Contract No. DE-SC0012704.

SESSION D: Nanoscale Characterization
Session Chairs: Hongmei Dang and Carlo R DaCunha
Wednesday Morning, June 28, 2023
UC, State Street

10:00 AM D01
TERS Imaging—Unique Nanoscale Technique for Characterization of 2D Materials and Their Lateral/Vertical Heterostructures Andrey Krayev; HORIBA Scientific, United States

Since the discovery of graphene Raman spectroscopy and Raman microscopy proved to be indispensable tools for characterization of 2D semiconductors, semimetals and 2D metallic materials. In the same time diffraction limitation of the spatial resolution of conventional Raman microscopy (about 500 nm for visible range) makes it inapplicable for characterization of the nanoscale structural and doping defects in 2D materials and their vertical heterostructures as well as sharp junction lines in their lateral heterostructures.
In this contribution I'll demonstrate how tip enhanced Raman spectroscopy (TERS) which can ultimately enable sub-nm spatial resolution of Raman imaging has been applied for the nanometer-scale characterization of:
Composition-related defects in novel SeMoS Janus monolayers obtained by conversion of MoSe2 crystals grown on the gold substrate.
Alloyed material spatial distribution in the junction lines of MoS_2-WS_2 [1] and WS_2-WSe_2 lateral heteromonolayers.
Spatial distribution of strong coupling in twisted vertical WS_2-WSe_2 heterostructures [2] and twisted bilayer graphene [3].

It will be emphasized that ambient TERS imaging occupies a sweet spot between TEM and conventional Raman microscopy in terms of the spatial resolution routinely achieved and the typical characterization area. In addition, cross-correlation of TERS and other scanning probe microscopy channels like topography, conductivity, surface potential distribution etc, make this nanoscale spectroscopic technique even more powerful.
REFERENCES: Sourav Garg et.al. ACS Nano 2022, 16, 1, 340–350
Alvaro Rodriguez et.al. J. Phys. Chem. Lett. 2022, 13, 25, 5854–5859
Gadelha, A.C., Ohlberg, D.A.A., Rabelo, C. et al. Nature 590, 405–409 (2021).

10:20 AM D02
Rapid Characterization of Threading Dislocations in Diamond via Coincident Cathodoluminescence and Electron Channeling Contrast Imaging Haoxue Yan[1], Alastair Stacey[2], Santiago Gallo[3] and Kunal Mukherjee[1]; [1]Stanford University, United States; [2]Royal Melbourne Institute of Technology University, Australia; [3]Quantum Brilliance Pty Ltd, Australia

Diamond is an attractive wide bandgap semiconductor with application as a host for useful point defects such as the N-V center for solid-state quantum technologies, as well as in diodes and transistors for power electronics and radiation detectors [1]. Synthetic diamond substrates and epitaxial films are commonly grown by chemical vapor deposition (CVD), which often results in crystalline defects like dislocations. To achieve reliable growth of single-crystal diamond wafers and devices, the relationship between CVD process parameters, device design, and the resulting defects (i.e. a processing feedback loop) must be established. While transmission electron microscopy (TEM), x-ray topography, and etch-pit formation methods remain gold standards in defect characterization in diamonds [2, 3, 4], the laborious, destructive, and costly nature of these techniques sacrifice the efficiency of the feedback loop. In this work, we demonstrate dislocation characterization on a single crystal diamond using electron channeling contrast imaging (ECCI) in a scanning electron microscope (SEM) and highlight the applicability of this technique widely used in other semiconductors also to diamond.
As it is challenging to obtain sufficient backscattered electron (BSE) signal from diamond given its low atomic number [5], we optimize microscope conditions to best overcome this challenge. In doing so, we are able to consistently observe features in BSE images with ECCI contrast in a test structure of single crystal (001)-oriented CVD diamond sample with a 2.5 µm homoepitaxial boron doped layer. These features indicate threading dislocations as confirmed by the reversal of their contrast as we move from one edge of the channeling band to the other [6]. Furthermore, we explore the A-band blue luminescence properties of the sample using cathodoluminescence (CL) imaging of the same micron-wide observational regions. In line with literature [4], we find that all observed luminescence connects to dislocations identified by ECCI, whereas the converse was not always true. CL spectra recorded from individual dislocations also revealed a broad peak at the expected 430 nm. Our results highlight the complementary nature of ECCI and CL imaging in diamond where dislocations can be luminescent but also caution against the sole use of CL in high defect density samples as this could lead to an underestimation of the defect density. Hypotheses for non-emitting dislocations will be discussed in the current system. In summary, the statistical study of extended defects in diamond with the convenience of the SEM provides a pathway for an efficient and reliable characterization feedback loop for further development of CVD growth of diamond.
[1] L. Childress and R. Hanson, *MRS Bulletin*, **38**, 134 (2013).
[2] H. Umezawa, et. al., *Diamond and Related Materials*, **20**, 523 (2011).
[3] T. Shimaoka, et. al., *Physica Status Solidi (a)*, **216** (2019).
[4] N. Yamamoto, et. al., *Philosophical Magazine B*, **49**, 609 (1984).
[5] S. Kaboli and P. C. Burnley, *Materials Characterization*, **142**, 154 (2018).
[6] Y. N. Picard, et. al., *Microscopy Today*, **20**, 12 (2012).

10:40 AM D03
Estimating the Background Potential of Quantum Constrictions Using Scanning Gate Microscopy and Machine Learning Carlo R. daCunha[1], David K. Ferry[2] and Nobuyuki Aoki[3]; [1]Northern Arizona University, United States; [2]Arizona State University, United States; [3]Chiba University, Japan

Scanning gate microscopy (SGM) is a powerful imaging technique that allows for the characterization of the coherent electron flow in low-dimensional structures such as quantum constrictions and short quantum wires. The technique utilizes the effect of a charged scanning probe on the electron flow, resulting in a signal that can be related to the local density of states of the device. However, obtaining meaningful information from SGM measurements can be challenging due to the stringent conditions required for the technique to be effective. In this study, we propose a novel approach for using SGM to estimate the disordered background potential of quantum constrictions by utilizing a machine learning-based method. This approach involves matching SGM signals obtained through a weak perturbation approach to a corresponding background potential and then using transfer learning to experimentally obtained SGM images. By studying the potentials that a single electron would experience, this approach enables the characterization of the disordered potentials and their impact on the electron flow in quantum constrictions.
For this study, we performed a comprehensive investigation of the electron flow in a quantum point contact (QPC) fabricated on an InAlAs/InGaAs/InAlAs quantum well. The electron density of the QPC was determined to be 7.2×10^{11} cm^{-2} and the mobility was measured to be 7.4×10^{4} $cm^2/V.s$ by performing Shubnikov-de Haas measurements at a temperature of 280 mK. This corresponds to an electron path of 1.2 um.
On the theoretical side, we employed the non-equilibrium Green's function approach to obtain images of the electron flow in the QPC. In order to estimate the background potential in the QPC, we employed a swarming search algorithm. This algorithm utilized a population of different potentials to compute an SGM signal, and only those potentials that were closest to the experimental measurement were selected for further analysis.
Our results reveal a strong correlation between low conductance values and more granular and rougher potentials. This is consistent with the expectation that low conductance states are associated with Fermi levels closer to the background potential level. To further investigate the properties of the estimated background potential, we have employed clustering analysis. This analysis revealed that the average cluster radius is comparable to the Bohr radius of InGaAs, providing insight into the size and spatial distribution of the potential fluctuations in the quantum constriction. Additionally, we have estimated the static alloy potential of the quantum constriction using our proposed approach. Comparison of the estimated potential with the SGM images showed good spatial agreement, indicating the accuracy of our approach in characterizing the potential landscape of quantum constrictions.
Our results provide insight into the underlying physics of electron flow in low-dimensional systems and demonstrate the potential of combining experimental and theoretical approaches for characterizing quantum point contacts. They also provide a new understanding of the relationship between the conductance of a quantum constriction and the underlying potential landscape and demonstrate the potential of our proposed approach for characterizing the static alloy potential in quantum constrictions.

11:00 AM D04
(Student) Characterization of Surface Morphology and Superconducting Performance of Thin Aluminum Films Deposited via Thermal Evaporation at Tilted Angles Stephen M. Bankson, Chase C. Tillman, John Sellers and Michael Hamilton; Auburn University, United States

Aluminum thin films have many uses in electronic applications. Being a superconducting material, one such application of Al thin films is

their use in superconducting electronics, such as superconducting transmission lines, high Q resonators, and superconducting qubits. Fabrication of Al-based superconducting qubits typically involves a combination of thermal evaporation and shadowing techniques, wherein Al is deposited onto a tilted substrate, to form the components of the qubit. It is critical that films deposited in this manner are high quality, as low-quality Al films may introduce losses into the system and decrease performance overall. Factors such as grain size and surface morphology play an important role in film quality and therefore device quality as well. We present a study of deposition parameter effects on thermally evaporated Al films, deposited at tilted angles. We examine the quality impact of deposition rate, film thickness, and substrate angle during deposition of fabricated Al films. A description of the fabrication process is provided, utilizing a deposition system capable of nano Torr base pressure range and sample rotation manipulation for angled metal depositions. Film surface morphology is characterized using atomic force microscopy and scanning electron microscopy. Metal films are packaged and their critical currents and critical temperatures are measured in a dilution refrigerator with a base temperature of 10 mK. Results from this study help to inform device fabrication process decisions for higher performance devices.

11:20 AM D05
TESCAN TENSOR a 4D-STEM for Multimodal Characterization of Challenging and Interesting Specimens Robert Stroud; Tescan USA, United States

The methodology and design behind TESCAN TENSOR - the world's first Integrated, Precession-assisted, Analytical 4D-STEM will be presented. An advanced (electron diffraction) microscope, with STEM, 4D-STEM and STEM Tomography applications, TESCAN TENSOR will be shown to be the solution of choice for a range of nanoscale applications. These include multimodal characterization of functional materials, semiconductor thin films, and submicron, synthetic and natural particle crystals. Examples including results from battery and semiconductor device applications will be presented. Designed from the ground up to provide quality, throughput, and robustness of 4D-STEM acquisition, analysis, and processing, TESCAN TENSOR has been optimized with state-of-the-art technologies, such as Precession Electron Diffraction (PED), 4D-STEM computing and visualization, electrostatic beam blanking, and ultra-high vacuum at the specimen area. Additionally, TESCAN TENSOR features near real-time, automated data analysis, whereby on-the-fly processing presents first results during acquisition. As a result, TESCAN TENSOR allows the operator to focus on data acquisition and analysis, rather than time consuming manual microscope alignments.
4D-STEM phase and orientation analysis of lithium-ion battery anode materials. A precession-assisted, analytical 4D-STEM, TESCAN TENSOR, provides a solution for nanoscale phase and orientation mapping of phase separations and crystallographic ordering. Precession-assisted 4D-STEM was used to produce maps of $LiTi_2(PO_4)_3$, TiO_2 and $LiTiOPO_4$ phases present in spindle-like battery anode particles. 4D-STEM phase analysis will be presented showing that TiO_2 nanoparticles form a network at the $LiTi_2(PO_4)_3$ sub-particle boundaries, which may provide a more effective diffusion pathway for lithium ions at higher cycling rates.
Due to the fine polycrystalline nature of these networks, conventional phase analysis with TEM selected area diffraction or high-resolution imaging, is not practical. Additionally, the presence of titanium in both $LiTi_2(PO_4)_3$ and TiO_2 phases complicates robust identification of grains with EDX analysis.
Multimodal phase and orientation analysis of complex semiconductor devices. For semiconductor manufacturers, it is desired to have comprehensive analytical capabilities, with the ability to measure chemical and structural properties, complementary to specimen morphology, down to the sub-nanometer scale. This is generally addressed using Energy Dispersive X-Ray (EDX) mapping, defect analysis through diffraction measurements, crystal orientation and phase mapping, and critical dimension imaging. These capabilities are important as the electrical performance of devices depends strongly on the type and distribution of crystalline phases in individual layers. Analytical electron microscopy, incorporating EDX, and phase/orientation analyses is therefore crucial for both process development and failure analysis.
The TESCAN TENSOR analytical 4D-STEM provides a unique workflow interface to facilitate efficient chemical and structural analysis using EDX mapping, and precession-assisted phase and orientation mapping. The alignment and workflow automation enables effortless, automated switching between measurements optimized for STEM imaging, EDX analysis, or analytical 4D-STEM.
While EDX maps are useful for rapid evaluation of elemental distributions, they cannot be used to conclusively determine phase distributions or segregations, this is instead investigated using precession electron diffraction assisted 4D-STEM.
TESCAN TENSOR provides a solution for robust, multimodal, nano-characterization of complex semiconductor devices made up of multiple phases with real-time data analysis and processing for the benefit of process development and failure analysis.

11:40 AM D06
Investigation of Extended Defects in Single Crystal Calcite Substrates Using High Resolution X-Ray Topography Michael E. Liao[1], Nadeemullah Mahadik[2], Katja S. Diaz-Granados[3] and Joshua Caldwell[3]; [1]National Research Council Postdoctoral Fellow at U.S. Naval Research Laboratory, United States; [2]U.S. Naval Research Laboratory, United States; [3]Vanderbilt University, United States

Due to its optical properties in the mid-IR and ability to support surface phonon polaritons, calcite is an appealing material for infrared nanophotonic applications [1,2]. The fundamental understanding of surface phonon polaritons in calcite is still in its infancy. Furthermore, there is a lack of extended defect studies in single crystal calcite. Additionally the influence of these extended defects on their optical properties needs to be investigated. X-ray topography (XRT) is a powerful, nondestructive technique that has been previously used to extensively assess various defects in substrates for other semiconductor materials. However, there has only been one XRT study for calcite reported that examined one type of defect but no dislocations or stacking faults [3]. In this work, we employed high resolution XRT in both transmission and reflection geometry to investigate several extended defects in (0001) oriented and (10$\underline{1}$0) oriented single crystalline calcite substrates.
For this study, we used commercially obtained 10×10 mm^2 calcite substrates. XRT was performed using in-lab Rigaku XRTMicron system equipped with a rotating anode microfocus Cu/Mo dual anode. The incident x-ray beam collimated using a multi-layer mirror for the two x-ray wavelengths. The sample is placed on an automated high precision goniometer capable of both transmission and reflection XRT geometries. The diffraction images were acquired using either a 5.4 mm pixel high sensitivity detector or a 2.2 mm pixel high-resolution detector. The entire sample was imaged by a moving the sample with the automated XY stage through the x-ray beam.
Bragg conditions used in transmission mode were the (30$\underline{3}$0), (20$\underline{2}$2), (02$\underline{2}$4), (11$\underline{2}$0), (11$\underline{2}$3), and (12$\underline{3}$2) planes using Mo Kα radiation. The Bragg reflections used in reflection mode (glancing incident geometry) were the (30$\underline{3}$.12), (11$\underline{2}$.12), and (02$\underline{2}$.16) planes using Cu Kα radiation. The **g●b** criterion, where **g** is the diffraction vector and **b** is the Burger's vector, was used to determine the character of a defect, e.g. if a dislocation is a screw, edge, or mixed dislocation. Some defects found in this study showed contrast when imaged using reflections with a (11$\underline{2}$0) component, but invisible when imaged with reflections that had a (10$\underline{1}$0) component. Identifying and characterizing defects present in substrates is a crucial first step towards understanding their impact on device performance. Other extended defects were also identified, and their microstructural characteristics will be presented. Additionally optical properties will be measured and correlated to the defect maps. The fundamental understanding of defects in calcite would enable the development of

novel nanophotonic mid-IR optical calcite devices.
[1] V. M. Breslin, et al., Light-Matter Interactions Towards the Nanoscale, 251 (2022).
[2] V. M. Breslin, et al., Optics Express, 29(8), 11760, (2021).
[3] C. Jourdan, et al., Phys. Stat. Sol. (a), 3, 343 (1970).

SESSION E: Hetero-Integration, Interconnects and Packaging
Session Chairs: Daniel Ewing and Michael Hamilton
Wednesday Morning, June 28, 2023
UC, Santa Barbara Harbor

10:00 AM E01
Heterogeneous Multi-Die Stitching Enabled by Compressible Microinterconnects (CMIs) Muhannad Bakir; Georgia Tech, United States

A heterogeneous integration technology is demonstrated for seamless stitching of RF and digital chiplets. In this technology, stitch-chips with compressible microinterconnects (CMIs) are used for low-loss and dense interconnection between chiplets. The key features of the CMI technology include: 1) lithographically defined, CMOS-compatible, and simple fabrication; 2) large elastic range of motion to compensate for surface nonuniformity on the attaching substrate, especially for a large die or interposer assembly, and CTE mismatch induced warpage 3) high degree of freedom in interconnect design; 4) pressure based and non-permanent contact mechanism; since CMIs can provide temporary interconnections, they can enable chips, interposers, or packages to be replaced, hence increasing system yield; and 5) since a thermocompression process is not required, the assembly process is simplified as bonding parameters such as temperature need not be considered. To demonstrate the technology, a test sample using fused-silica stitch-chips with integrated CMIs is demonstrated
including modeling, fabrication, assembly, and characterization. RF measurements up to 30 GHz were performed by Cascade Microtech 200 um-pitch G-S-G |Z| probes and a Keysight N5245A PNA-X network analyzer. Short-open-load-thru (SOLT) calibration was used with Cascade Microtech CSR-8 calibration substrate before RF measurements of the test samples. Next, L-sample, 2L-sample, and thru-pads structures were measured. A 500 um-long stitch-chip signal link is measured to have less than 0.4 dB insertion loss for up to 30 GHz. A simulated eye diagram for 1000 um-long stitch-chip signal link has a clear opening at 50 Gbps data rate. Moreover, the S-parameters of CMIs are extracted from this test sample and show less than 0.17 dB insertion loss for up to 30 GHz. To benchmark the stitching technology to silicon interposer technologies, CPWs of similar characteristic impedance are designed and simulated for silicon interposer technologies firstly. Standard silicon (10 S/m conductivity) with 1 um-thick silicon dioxide are selected as substrate material. Solder bumps, instead of CMIs, are implemented as off-chip interconnects at the ends of CPWs. The stitch-chip link improves eye height by 49.4% because of the ultra low-loss signal propagation through the stitch-chip link. In addition, the stitch-chip link's shorter rise/fall time (3.3 ps vs. 8.3 ps for silicon interposer link) implies lower signal latency and link parasitics. The eye diagram with 50 fF ESD capacitors has a clear opening (eye height: 94.1% of logic 1 voltage, eye width: 96.7% of UI) at 50 Gbps data rate. Also note that this performance is achieved without any equalization, which can simplify transceiver circuits design in digital chiplets.

10:20 AM E02
(Student) Quasi-2D Materials for Ultra-Low Resistance Electrical Interconnects Bilal Azhar, Qi Song, Cameron A. Gorsak, Yacob Melman, Darrell G. Schlom and Hari Nair; Cornell University, United States

The dramatic increase in the resistivity of interconnect lines with decreasing dimensions presents a significant bottleneck for further downscaling of integrated circuits.[1] This is because current interconnects use 3-dimensional metals which experience increased interface electron scattering as the interconnect dimensions approach their electron mean free path. A possible solution is to use metals with much lower electron mean free paths such as: W, Mo, and Ru. Metallic delafossite oxides are an alternative solution because of their inherent advantages over traditional metals such as, ultra-low room temperature resistivity, potential mitigation of interface/surface scattering due to their 2D Fermi surface, potentially decreased likelihood of electromigration, and potentially better compatibility with low-K oxide dielectrics. Metallic delafossite can prove to be a disruptive new material for ultra-scaled electrical interconnects. Delafossites are layered oxides with the formula ABO_2 where A is a metal cation that forms 2D sheets separated by the BO_2 transition-metal oxide octahedra. In this study we focus on metallic delafossites $PtCoO_2$ and $PdCoO_2$ because of their ultra-low room temperature resistivity of 2.1 μΩ.cm and 2.6 μΩ.cm, respectively, which is comparable to the current semiconductor industry standard interconnect metal, Cu.[2] The metallic delafossite structure has an anisotropic nature with resistivity along the c-axis a factor of 1000 higher than resistivity within the Pt/Pd sheet. Due to the layered crystal structure, the Fermi surface of the metallic delafossites is cylindrical as for a 2D metal. This quasi-2D crystal structure can potentially mitigate interface and surface scattering since the electron Fermi velocity does not have components perpendicular to the Pd/Pt sheets. This can potentially overcome the resistivity penalty encountered by conventional 3D metals in ultrathin films (< 20 nm). Additionally, the unique Fermi surface topology allows for an electron-phonon coupling constant that is a factor of 3 lower than copper.[3]
In this study we investigate the structural and electrical properties of MBE-grown $PdCoO_2$ delafossite films. High-resolution X-Ray diffraction (HRXRD) confirm that the films are phase-pure. XRD phi scans, however, reveal in-plane twinning in these films, and the lateral size of the rotational twin domains are ~17 nm based on skew-symmetric rocking curves. We measured the resistivity of the films using a van der Pauw geometry and modelled the resistivity scaling with film thickness using Fuchs-Sondheimer (FS) and Mayadas-Shatzkes (MS) model. The upshot is that a 50 nm thick $PdCoO_2$ film has a resistivity of 5 μΩ.cm. Based on our resistivity fitting we find that the twin boundaries have a very low electron reflection coefficient of ~5%. This is extremely encouraging since atomic layer deposition (ALD) which is a back-end-of-the-line (BEOL) compatible synthesis technique will likely yield highly twinned delafossite thin films.
[1] D. Gall, J. Appl. Phys. **127**, 050901 (2020).
[2] V. Sunko, P.H. McGuinness, C.S. Chang, E. Zhakina, S. Khim, C.E. Dreyer, M. Konczykowski, M. König, D.A. Muller, and A.P. Mackenzie, Phys. Rev. X **10**, 021018 (2020).
[3] C.W. Hicks, A.S. Gibbs, A.P. Mackenzie, H. Takatsu, Y. Maeno, and E.A. Yelland, Phys. Rev. Lett. **109**, 116401 (2012).

10:40 AM E03
Dimensional Scaling of Topological Metal Nanowires for Interconnect Gangtae Jin, Hyeuk Jin Han and Judy Cha; Cornell University, United States

The increasing resistance of Cu interconnects for decreasing dimensions is a major challenge in the continued downscaling of integrated circuits as it leads to unacceptable signal delays and power consumption in computing. The resistivity of conventional metals (Cu, Ru, Co) increases due to electron scattering at surfaces and grain boundaries of the interconnects at the nanoscale. Thus, future energy-

efficient computing technologies require breakthroughs in interconnect technologies, particularly in new interconnect materials. Topological semimetals are promising materials for low-dissipation on-chip interconnects as their topologically protected surface electrons are forbidden to backscatter. Here, we demonstrate that the unprecedented resistivity scaling of topological metal nanowires is competitive to those of effective Cu with barrier/liner and barrier-less Ru interconnects, suggesting topological metal (MoP, CoSi, WP) is an attractive alternative for the current scaling challenge of Cu interconnects and atomistic 1D topological material platform.
(Reference) H.J. Han, S. Kumar, G. Jin et al., Topological Metal MoP Nanowire for Interconnect, *Advanced Materials* (2023)
G. Jin et al., Nanoscale size-effects in 1D-confined transformation of tungsten phosphide nanowires, *Submitted* (2023)
(Acknowledgements) G. J and J. C. C. gratefully acknowledge the support by the Semiconductor Research Corporation (SRC) – nCORE IMPACT center. J. C. C. acknowledges support from Betty & Gordon Moore Foundation under the EPiQS Investigator Award.

11:00 AM E04
Stability of Interface Morphology and Thermal Boundary Conductance of Direct Wafer Bonded GaN|Si Heterojunction Interfaces Annealed at Growth and Annealing Temperatures
Kenny Huynh[1], Michael E. Liao[2], Xingxu Yan[3], John Tomko[4], Thomas Pfeifer[4], Viorel Dragoi[5], Nasser Razek[5,6], Eric Guiot[7], Raphael Caulmilone[7], Xiaoqing Pan[3], Patrick Hopkins[4] and Mark Goorsky[1]; [1]University of California, Los Angeles, United States; [2]National Research Council Postdoctoral Fellow at U.S. Naval Research Laboratory, United States; [3]University of California, Irvine, United States; [4]University of Virginia, United States; [5]EV Group, Austria; [6]G-Ray Medical, Switzerland; [7]Soitec, France

The properties of thin (~ 2 mm) GaN templates on a silicon support substrate were studied to assess the stability of the direct wafer bonded GaN / Si interface. EVG® ComBond® equipment was used for bonding under high vacuum (~10^{-8} mtorr) at room temperature by bombarding the GaN and Si surfaces with an Ar ion beam to remove unwanted native surface oxides [1,2]. The [1010] GaN edge was aligned parallel to the Si [110] edge. An X-ray diffraction reciprocal space map of the (004) Si and (0004) GaN revealed that there is a ~0.2° tilt between the GaN and Si layers and is simply due to the relative miscut between the two wafers. The Ar ion bombardment of the surfaces prior to bonding produces an amorphous region at the bonded interface that has been seen in many other bonded systems [3-5]. In the as-bonded sample, high resolution scanning transmission electron microscopy revealed a ~2 nm amorphous region on the Si side of the bonded interface, as confirmed by energy dispersive x-ray spectroscopy (EDX). Subsequent annealing was done in an effort to recrystallize the amorphous interface. Previous work has shown that recrystallization between Si|Si wafer bonded samples occurred when annealed at 450 °C for 12 hours [3]. However, in the GaN|Si system, we found that the amorphous interface did not recrystallize when annealed. Annealing at temperatures up to 450 °C and 120 hours showed only initial stages of interdiffusion and a stable interface. However, after annealing at 700 °C for 24 hours, high resolution EDX revealed the formation of amorphous SiN as well as the diffusion of gallium into silicon.
Preliminary thermal results show that the thermal boundary conductance (TBC) of the as bonded sample is ~140 MW/(m^2K). The TBC results of wafer bonded GaN|Si reported here is higher than previously reported TBC values of epitaxially grown interfaces such as GaN on Si [6-7], GaN on SiC [7-8], and GaN on diamond [9]. The TBC for the annealed interface is degraded by a factor of two compared to the as-bonded interface for the sample that was annealed at 700 °C for 24 hours. These results demonstrate that high TBC can be achieved through wafer bonding of GaN with materials such as silicon and that such interfaces are stable even up to device operation up to 300 °C. However, chemically rough interfaces formed due to high temperature annealing are detrimental to thermal transport across these interfaces.

1. V. Dragoi, et al., ECS Trans., 86(5), 23 (2018)
2. C. Flötgen, et al., ECS Trans., 64(5), 103 (2014)
3. M.E. Liao, et al., ECS Trans., 86(5), 55 (2018)
4. Y. Xu, et al., Ceramics International, 45, 6552 (2019)
5. F. Mu, et al., Appl. Surf. Sci., 416, 1007 (2017)
6. J. F. Ziegler, et al., The Stopping and Range of Ions in Solids vol 1 (Oxford, Pergamon), (1985)
7. L. Yates, et al., ASME InterPACK (2015)
8. J. Cho, et al., Phys. Rev. B, 89, 115301 (2014)
9. H. Sun, et al., APL, 106(11), 111906 (2015)

11:20 AM E05
(Student) Superconducting Resonators with Closely Spaced Resonant Frequencies for Material Loss Measurements
Bhargav Yelamanchili, Chase C. Tillman, Stephen M. Bankson, John Sellers and Michael Hamilton; Auburn University, United States

The demand for precise material loss measurements at cryogenic temperatures increased due to recent developments in packaging and interconnect technologies for cryogenic and quantum systems. A superconducting quantum computer's qubit must use low energy loss materials and fabrication procedures to keep quantum information coherent for reasonable amounts of time. Material losses can vary depending on the type of fabrication methods used, such as photolithography, soft lithography, etching, and bonding. Superconducting microwave resonators have been widely used for qubit readout and for measuring two-level system losses due to their ease of design, fabrication, and sensitivity to loss at low temperatures and photon number. Here we use a long resonating section, which yields very closely spaced frequency resonances to more densely probe the frequency-dependent losses.
Resonators that had previously been used in literature had a finite resonating section that yielded fundamental resonances in the GHz range. We used a 4.17 m long resonating section, which yields a fundamental resonance of approximately 13 MHz to investigate fabrication-induced losses, among other sources. We designed and fabricated Nb shunt microstrip resonators on 200 μm thick, 100 mm intrinsic silicon wafers. Fabricated samples were diced and mounted onto a printed circuit board using silver paint and baked in a vacuum oven at 80 °C to force dry the silver paint and improve the conductivity. The assembly was mounted onto a support board attached to the end of a dip probe used to carry out measurements in liquid helium dewar up to 6 GHz. Material characterization with this close frequency spacing resonances gives a better chance to investigate and connect material losses to different fabrication processes depending on the application. Experimental details, including fabrication, characterization, and a detailed description of the results will be presented.

11:40 AM E06
(Student, Late News) Improvement of Heterogeneously Integrated InGaAs/GaN Junctions via Post-Bonding Annealing for Next-Generation Transistors
Rohan Sengupta[1], Brian D. Little[1], Seiji Mita[2], Keith Markham[1], Shane R. Stein[1], Tim Day[1], Zlatko Sitar[1,2], Fred A. Kish[1] and Spyridon Pavlidis[1]; [1]North Carolina State University, United States; [2]Adroit Materials, Inc., United States

The heterogeneous integration of GaAs/InP technologies, which offer high mobility and efficient doping, with III-Nitrides, which possess large critical electric field and saturation velocity, at the base-collector (B-C) junction of heterojunction bipolar transistors (HBTs) presents a path to boosting output power. Past attempts with wafer bonding have been hampered by current limiting non-idealities [1]. These can arise from fermi-pinning, or junction and contact resistances. Here, we study how post-bonding annealing improves the behavior of p-type InGaAs/n-type GaN junctions to achieve a record current density of 20 kA/cm^2. InP and GaN substrates were bonded using Crystal Heterogeneous Integration (CHI), a novel method that permits engineering of the heterogeneous interface via tuning of the process atmosphere, including H_2, N_2 and Column-V sources. The p-InGaAs

layers are C-doped, while the homoepitaxial GaN layers are Si-doped, as shown in Fig. 1. The InP substrate, buffer layer and etch stop layer were removed via wet etching. Mesa patterning of the p-InGaAs device layer was then conducted. Finally, Ti/Pt/Au and Ti/Al/Ni/Au contacts were made to InGaAs and GaN, respectively, in order to produce vertical heterogeneous InGaAs/GaN PN junction diodes and lateral transfer length method (TLM) structures on bonded InGaAs. In addition, control TLM structures were fabricated on p-InGaAs films on the original epitaxial substrate. To study the role of compensation in these films, especially in InGaAs, we carried out an isochronal annealing study. Fig. 2 shows the TEM cross-section of the InGaAs/GaN junction, which is abrupt. Elemental analysis confirmed the absence of an interface oxide, which is attributed to the use of H_2 during bonding. Fig. 3 shows the I-V measurements performed on a fabricated InGaAs/GaN PN diode. A rectification ratio (RR) of more than 10^4 was extracted at ±3 V. At 3 V, J ~ 2 KA/cm^2, which is >50x higher than the current density measured at the same bias in the aforementioned GaAs/GaN diodes [1]. However, when compared to an analytical model, the measured forward current is less than expected. It was previously reported that this could arise from fermi pinning at the interface due to presence of an oxide layer, but our TEM shows an interface without an interface oxide. Fig. 4 shows the lateral InGaAs TLM results on the bonded wafer, where nonlinear characteristics are clearly observed. The extracted sheet resistance (R_{SH}) is 2.4 KΩ/sq. which is >10x higher than the expected value of our doped p+-InGaAs with [C]=3E19 cm^{-3}. To understand the effect of the CHI conditions on the p- InGaAs film, we also performed TLM measurements on epitaxial p-InGaAs-on-InP that were exposed to the CHI ambient and N_2 ambient separately. As shown in Fig. 5, the H_2-containing CHI ambient leads to the increase in sheet resistance, whereas an N_2 ambient has no significant effect. It is known that C-doped MOCVD InGaAs films are at risk of H-compensation [2]. We hypothesize the same effect occurs in our process. To investigate this, the bonded samples were annealed in N_2 ambient at different temperatures for 10 minutes in an RTA furnace in order to drive-out H_2. Fig. 6 shows the decrease in R_{SH} with increasing annealing temperature, which supports the hypothesis. Furthermore, we observe a decrease in the differential on-resistance of a PN diode annealed at 405 °C, which approaches the case of a GaN Schottky diode on the same wafer. While the use of H_2 during CHI effectively avoids the formation of interface oxides at the InGaAs/GaN interface, H_2 may also compensate C-doped InGaAs. We show that N_2 annealing can be used to increase the conductivity of the InGaAs films, in turn improving the diode's characteristics. Future studies will explore the CHI design space to mitigate compensation.

[1] Kim et al., IEEE Electron Device Lett., doi: 10.1109/LED.2012.2225137.
[2] Watanabe et al. Journal of crystal growth 195.1-4 (1998): 48-53.

SESSION F: Gallium Oxide Devices
Session Chairs: Sriram Krishnamoorthy and Hari Nair
Wednesday Morning, June 28, 2023
MCC Theater

10:00 AM #F01
(Student) [100] and [010] Oriented β-Ga_2O_3 Trench Schottky Barrier Diodes with Improved On-Resistance Using Low Damage Atomic Ga Etching Sushovan Dhara, Ashok V. Dheenan, Sheikh Ifatur Rahman, Nathan Wriedt and Siddharth Rajan; The Ohio State University, United States

β-Ga_2O_3 is a promising material for high-power devices due to its high theoretical breakdown field strength. Due to the lack of p-type doping in Ga_2O_3, there is a need to explore the fabrication of trench Schottky and MOSFET topologies which can avoid premature breakdown at the metal-semiconductor interface by moving the peak electric field into the bulk of the semiconductor. To achieve these trench devices, it is necessary to develop fabrication methods that enable high aspect ratio structures, avoid plasma-induced damage, and are compatible with subsequent deposition of high-quality dielectrics with low interface defects. Previous demonstrations of trench SBDs have shown direction-dependent conductivity due to plasma damage during fin etching[1]. In this work, we demonstrate direction-independent trench SBDs with low on-resistance using atomic Ga etching. The vacuum environment used for this method is also used for subsequent deposition of a dielectric. We show state-of-art breakdown electric field (>5 MV/cm) and power figure of merit (>2 GW/cm^2) using this method.

Devices were fabricated on a 5x10^{16} cm^{-3} Si-doped 10 μm thick (001) β-Ga_2O_3 HVPE epitaxial layer. SiO_2 was deposited by PECVD to form the fin etching mask in the [100] and [010] directions. Etching was performed by exposing the sample to atomic Ga-flux in an MBE chamber[2]. This process resulted in sharply defined vertical structures with a fin height of 1.2 μm. A 92 nm thick layer of Al_2O_3 was deposited with the assistance of O_2 plasma after ex-situ surface cleaning. Al_2O_3 and SiO_2 were removed from the top of the fins to form the Schottky contact by sputtering Ni (50 nm) and subsequent e-beam evaporation of Ni/Au (30/70 nm). The bottom ohmic contact was formed by e-beam evaporation of Ti/Au. For comparison, a planar SBD on the unetched surface and a MOS-capacitor on the etched surface were also fabricated on the same substrate.

The forward I-V measurements of the three SBDs showed a similar turn-on of ~1 V, and C-V measurements of the MOS capacitors showed low hysteresis. The specific on-resistance of all three diodes was estimated (including current spreading effects) to be 1.20mΩ-cm^2, 1.01mΩ-cm^2, and 1.73mΩ-cm^2 for the [010], [100]-oriented fin, and 50 μm diameter planar diode, respectively. Compared to previous SBDs fabricated using ICP-RIE[3], the SBDs fabricated using Ga-flux etching showed similar current densities in [100] and [010]- oriented devices, indicating that atomic Ga etching causes less depletion of charge carriers than plasma etching. MOSCAPs showed a reverse breakdown voltage of 1.53 kV corresponding to a 5.82 MV/cm electric field in the Ga_2O_3. The [100] oriented fin broke down destructively at 1.45 kV(~5.12 MV/cm) and [010] oriented fin showed breakdown at 1.04 kV(4.34 MV/cm). This is significantly higher than the planar SBD which sustained 2.1 MV/cm at 0.25 kV.

TCAD simulation shows the field concentrates near the anode edge of the fin diodes. The electric field along the vertical cutline in the center of the fin shows both the [100] and [010] oriented fins allow the peak field to be moved to the bulk of the epilayer resulting in a lower electric field at the Schottky contact compared to the planar device. The electric field along a horizontal cutline under the Al_2O_3 layer shows the local field concentration at the anode edge is above the theoretical breakdown field of 8 MV/cm. When compared to the previous state-of-the-art Ga_2O_3 SBD, the Ga-flux etched diode showed significantly improved on-resistance and Baliga power figure of merit of 2.08 GW-cm^2.

In conclusion, we have demonstrated a fabrication process for trench SBDs with orientation-independent on-resistance using low-damage Ga-flux etching, resulting in peak electric fields of 5.12 MV/cm in a 0.98 μm wide [100] oriented fin. This work was supported by DOE/NNSA Award No. DE-NA0003921, and AFOSR GAME MURI Award No. FA9550-18-1-0479.

REF: *[1]APL, 2021 [2]APEX, 2019 [3]APL, 2022*

10:20 AM F02
(Student) Forward and Reverse Current Transport of (001) β-Ga_2O_3 Schottky Barrier Diodes and TiO_2/β-Ga_2O_3 Heterojunction Diodes with Various Schottky Metals Nolan Hendricks[1,2], Esmat Farzana[2], Ahmad Islam[1], Daniel Dryden[1], Jeremiah Williams[1], James S. Speck[2] and Andrew Green[1]; [1]Air Force Research Laboratory, United States; [2]University of California, Santa Barbara, United States

β-Ga_2O_3 is an ultra-wide bandgap (~4.8 eV) semiconductor with great potential for power electronics due to its predicted breakdown field of 8 MV/cm, ease of n-type doping, and availability of melt-grown

native substrates. Of great importance is the power diode, which can block large reverse voltage with low forward conduction losses. The TiO_2/β-Ga_2O_3 heterojunction diode (HJD) has been shown to reduce reverse current compared to Schottky barrier diodes (SBDs) due to the high permittivity (ε) of TiO_2 (Fig. 1c) without significantly affecting forward conduction losses due to the negative conduction band offset to β-Ga_2O_3. [1] (Fig. 1b) We report the current transport behavior in forward and reverse bias for Metal/β-Ga_2O_3 SBDs and Metal/TiO_2/β-Ga_2O_3 HJDs with Ni, Pt, Cr, and Ti contacts, showing similar or lower conduction losses in the HJD for all metals and reduced leakage current at higher electric fields in reverse bias.

SBDs and HJDs were fabricated on adjacent die on 8.5 µm Si-doped β-Ga_2O_3 grown by HVPE on a Sn-doped (001) β-Ga_2O_3 substrate. (Fig. 1a) Fabrication of both samples began with backside BCl_3 RIE followed by evaporation of a Ti/Au cathode and RTA at 470 °C for 60 s in an N_2 ambient. A 6.5 nm TiO_2 film was deposited on the HJD sample by plasma-assisted ALD. Circular anode contacts (D=150 µm) were patterned by optical lithography followed by 120 s O_2 plasma ash and 60 s in 1:10 HCl:H_2O. Pt/Au, Ni/Au, Cr/Au, and Ti/Au contacts with thicknesses of 200/1800 Å were deposited in separate lithography steps.

Capacitance-voltage (C-V) characteristics of each device were measured at 1 MHz. Using ε_r=12.4, net donor concentration (N_D-N_A) and Φ_B were extracted from $1/C^2$ (Fig. 2a) and are shown in Table 1. N_D-N_A versus depth is shown for each device (Fig. 2b), with average N_D-N_A ~$1.6x10^{16}$ cm^{-3}. C-V was not measured for the Ti SBD due to large reverse current.

The current-voltage (J-V) characteristics of each device were measured from -5 V to 5 V at 25 °C to 150 °C. (Fig. 3) Richardson plots (Fig. 4) were created from linear fits to ln(J) in the exponential region of each J-V curve, and Φ_B and the Richardson constant (A*) were calculated from slope and y-intercept of each linear regression. The resulting values are tabulated in Table 1. The Ti SBD does not have Richardson plot data because the J-V curve did not exhibit an exponential region. Φ_B extracted for the Ni and Pt HJDs is lower than that of the Ni and Pt SBDs, while it is slightly higher in the HJD than the SBD for Cr. Contrary to the Ti SBD, the Ti HJD showed rectifying behavior. The leakage currents observable above the detection limit at low bias correspond to the thermionic emission (TE) current expected from Φ_B and A* in Table 1. In the linear-scale forward J-V characteristics at 25 °C (Fig. 5), the variation in turn-on voltage corresponds with variation in Φ_B. The differential $R_{on,sp}$ for each device is also shown, and minor differences observed between SBDs and HJDs with the same metal correspond to variation in N_D-N_A.

The reverse J-V behavior of each device at 25 °C was measured up to breakdown. (Fig. 6a) To compare devices with different doping, J_R is plotted against the average electric field at the β-Ga_2O_3 surface (E_{surf}) calculated from N_D-N_A. (Fig. 6b) In all cases, the HJDs saw higher V_{bk} than the SBDs with the same metal. At lower E_{surf}, the leakage current is higher in devices with lower Φ_B as expected from TE. However, at higher E_{surf}, the leakage current is lower in all HJDs than the corresponding SBDs regardless of Φ_B, which is consistent with the expected trend of thermionic field emission (TFE) in the SBDs. [2] TFE current is mitigated in the HJDs due to the higher ε_r of TiO_2 leading to a wider energy barrier for tunneling current. The superior V_{bk} and rectifying behavior of the HJDs despite similar or lower forward conduction losses demonstrates that the TiO_2/β-Ga_2O_3 HJD could be a key to unlocking the potential benefits of β-Ga_2O_3 in power diodes.

10:40 AM F03

Vertical β-Ga_2O_3 Diodes with High Barrier PtO_x Contacts and High-k TiO_2 Field Plate on Low-Doped Epitaxy for High Breakdown Voltage

Esmat Farzana[1], Nolan Hendricks[1,2], Saurav Roy[1], Sriram Krishnamoorthy[1] and James S. Speck[1]; [1]University of California Santa Barbara, United States; [2]Air Force Research Lab, Sensors Directorate, United States

β-Ga_2O_3 is promising for high-power devices due to the unique combination of ultrawide bandgap of ~4.8 eV, high predicted breakdown field of 8 MV/cm, favorable n-type doping, and available melt-grown native substrates for high-quality homoepitaxial films. However, due to the absence of p-type doping, it is difficult to achieve the β-Ga_2O_3 breakdown properties in rectifiers since the breakdown is often dictated by the tunneling leakage with a limited metal/β-Ga_2O_3 Schottky barrier height (SBH) of ~1.5 eV. Moreover, in a Schottky barrier diode (SBD), the edge leakage from high field crowding effects at anode contacts leads to early breakdown. One possible strategy of reducing tunneling leakage is to increase the SBH. The oxidized noble metals, with a higher SBH of > 2 eV (e.g, PtO_x), has been reported to substantially reduce leakage current and improve breakdown voltage in β-Ga_2O_3 SBDs.[1] For vertical SBDs, low background doping in drift layer is also beneficial to have low leakage current and achieve full depletion of the drift layer with a punch-through breakdown. Here, we report vertical Schottky diodes on a low-doped β-Ga_2O_3 epitaxial drift layer fabricated with PtO_x Schottky contacts to have reduced leakage from both Schottky barrier and background doping properties. For the edge leakage management, we implemented extreme permittivity[2] TiO_2 field-plate in the vertical SBDs to have minimal field inside the dielectric from its high dielectric constant properties and further assist in improving the breakdown voltage.

The vertical SBDs were fabricated on halide vapor phase epitaxy (HVPE)-grown (001) β-Ga_2O_3 of ~4 µm epitaxy on Sn-doped substrate. The 1 MHz capacitance-voltage (C-V) measurements extracted a low background doping of 7E15-9E15 cm^{-3} in SBDs of multiple diced pieces across the wafer. The Schottky contacts were co-fabricated with Pt and Pt cap/PtO_x (24 nm) on this low-doped β-Ga_2O_3 epitaxy to have a comparative study on SBH, transport, and breakdown characteristics of Pt and PtO_x contacts. The PtO_x SBDs were also investigated with a TiO_2 field-plate that was formed with reactively sputtered TiO_2 (~110 nm) and an underneath thin Al_2O_3 formed by atomic layer deposition (ALD) to protect the surface from subsequent sputter damage.

The SBHs were characterized on bare SBDs with current density-voltage (J-V) and C-V methods. The forward J-V characteristics showed near unity ideality factor for both contacts and a higher SBH for PtO_x (1.92 eV) compared to Pt (1.51 eV) using the thermionic emission transport. The $1/C^2$-V analysis showed a similar trend of higher SBH for PtO_x (~2.23 eV) compared to Pt (1.88 eV). In reverse J-V, this high SBH of PtO_x enabled to achieve significantly lower leakage (below detection limit) and higher breakdown voltage (-626 V) in the bare SBDs compared to Pt (-374 V). The TiO_2 field-plate further increased the breakdown voltage to ~1.15 kV in PtO_x SBDs from edge leakage management. With a minimum specific on-resistance of 5.16 mΩ-cm^2, the Baliga's figure-of-merit of the field-plate PtO_x SBD was obtained as 0.26 GW/cm^2. The Silvaco simulation in the field-plate SBD showed a punch-through field profile with a peak field of 3.2 MV/cm at the anode center for the 4 µm epitaxy. A peak field of 5.6 MV/cm appears at the low permittivity Al_2O_3 that might have led to its early catastrophic failure. Work is ongoing to integrate edge leakage management in PtO_x SBDs using ALD TiO_2 to minimize the electric field in dielectric by forming a full extreme permittivity dielectric field-plate that will help to maximize the benefit from the low-doped β-Ga_2O_3 epitaxial drift layer in vertical SBDs.

[1] E. Farzana et al., APL Mat 10, 111104 (2022). [2] [11] Z. Hu et al, IEEE Trans. Elec. Dev., 67, 5628, (2020).

11:00 AM F04

(Student) Platinum Oxide Schottky Contacts to Highly-Doped (-201) β-Ga_2O_3

Joseph Spencer[1,2], Alan G. Jacobs[1], Karl Hobart[1], Travis Anderson[1], Yuhao Zhang[2] and Marko Tadjer[1]; [1]U.S. Naval Research Laboratory, United States; [2]Virginia Tech, United States

Ga_2O_3 is an ultra-wide bandgap semiconductor that has gained much interest in the materials and electrical engineering research fields [1,2]. Ga_2O_3 has numerous favorable material properties such as substrate melt and homoepitaxial growth, excellent doping control, low background acceptor concentrations, and the potential for a high critical field strength of ~6 MV/cm. It is these properties and the potential for advancing the field of power electronics beyond SiC and GaN that has spurred interest into Ga_2O_3. The rapidly advancing epitaxial growth methods have resulted in high quality drift regions as thick as 20 µm. However, if such a voltage cannot be obtained in order to fully deplete the drift layer, it only serves as added resistance to a vertical diode. Leakage current over the Schottky contact of both a Schottky barrier diode (SBD) and a junction barrier Schottky (JBS) diode are a common cause of premature breakdown and reduced breakdown voltage that prevent the full depletion of the drift layer from being reached. Ni and Pt are two commonly used Schottky contacts in SBDs with Ni having a lower work function than Pt and thus a lower breakdown voltage [3]. The metallic oxide platinum oxide (PtOx) has a higher work function than both Ni and Pt carrying with it the potential for improved breakdown voltages. In this work, we highlight the increased barrier height (Φ_B) of a PtOx Schottky contact to highly doped Ga_2O_3 and its impact on vertical power diodes.
It is well known that a Schottky contact formed on a highly, or degenerately doped semiconductor will be poor in nature. While Φ_B is defined by the difference between the metal work function (Φ_M) and the electron affinity of the semiconductor (χ), the doping concentration of the semiconductor also influences Φ_B. As E_F becomes closer to the conduction band energy with increased doping, field emission becomes dominant as carriers are able to tunnel through the barrier more readily, thus decreasing the barrier height of the formed Schottky contact ($\Phi_B = \Phi_M - \chi$). Reduced Φ_B contributes to increased reverse leakage current, reducing the blocking voltage capabilities of the rectifier. Thus, one solution is to develop higher work function Schottky contacts to UWBG materials such as Ga_2O_3. This was demonstrated with PtOx and other sputtered oxides recently on low-doped Ga_2O_3 [4]. In this work, we demonstrate that PtOx is an effective Schottky contact to highly conductive Ga2O3:Sn.
Platinum oxide (PtOx) Schottky contacts were deposited using reactive sputtering on highly doped (8×10^{18} cm^{-3}) (-201) β-Ga_2O_3:Sn substrates grown by the edge-defined film-fed method. Electron-beam evaporated Ni and Pt Schottky contacts were deposited as reference. All Schottky metals were capped with evaporated Au. Capacitance-voltage measurements as well as temperature dependent current-voltage measurements were performed in order to extract Φ_B of the PtOx Schottky contact. PtOx was shown to increase Φ_B by 85% and 64% when compared to Ni and Pt Schottky contacts, respectively. At low reverse bias, the leakage current of the PtOx SBDs was 5-6 orders of magnitude lower when compared to the Ni and Pt anodes. These results highlight the increase in Φ_B provided by PtOx as evidenced by the fabrication of a rectifying Schottky contact to highly doped β-Ga_2O_3.

1) Pearton, S. J., et al. "A review of Ga2O3 materials, processing, and devices." *Applied Physics Reviews* 5.1 (2018): 011301.
2) Spencer, Joseph A., et al. "A review of band structure and material properties of transparent conducting and semiconducting oxides: Ga2O3, Al2O3, In2O3, ZnO, SnO2, CdO, NiO, CuO, and Sc2O3." *Applied Physics Reviews* 9.1 (2022): 011315.
3) Wang, Boyan, et al. "2.5 kV Vertical Ga 2 O 3 Schottky Rectifier with Graded Junction Termination Extension." *IEEE Electron Device Letters* (2022).
4) Hou, Caixia, et al. "Oxidized Metal Schottky Contacts on (010) β-Ga2O3." *IEEE Electron Device Letters* 40.2 (2019): 337-340.

11:20 AM F05

Application of $(Al_xGa_{1-x})_2O_3$ as Back Barrier in Lateral Ga_2O_3 Radio-Frequency Field-Effect Transistors

Takumi Ohtsuki[1], Takafumi Kamimura[1] and Masataka Higashiwaki[1,2]; [1]National Institute of Information and Communications Technology, Japan; [2]Osaka Metropolitan University, Japan

β-Ga_2O_3 has great potential as a power semiconductor because it has a large bandgap of 4.5 eV. In addition, its high chemical stability and radiation hardness lead to the application in wireless communication equipment under harsh environments. We have been developing lateral Ga_2O_3 radio-frequency (RF) metal-oxide-semiconductor field-effect transistors (MOSFETs) with a gate length (L_g) of sub-0.1-µm [1]. To further improve the RF characteristics, the issue is to suppress the short-channel effect accompanied by the decrease of L_g. The solution approaches are thinning of the channel layer and the introduction of a back barrier layer. Here, $(Al_xGa_{1-x})_2O_3$ is suitable for the back barrier layer of Ga_2O_3 MOSFETs from the following reasons: $(Al_xGa_{1-x})_2O_3$ can be easily grown on a β-Ga_2O_3 substrate, and a β-Ga_2O_3 layer can be continuously grown on it [2]; the bandgap of $(Al_xGa_{1-x})_2O_3$ is wider than that of Ga_2O_3 [3]. In this study, an $(Al_xGa_{1-x})_2O_3$ back barrier layer was introduced into lateral short-gate Ga_2O_3 MOSFETs for the purpose of suppressing not only drain current (I_d) leakage but also the short-channel effect.
The Ga_2O_3 MOSFETs were fabricated as follows. To begin with, Ga_2O_3(100 nm)/$(Al_xGa_{1-x})_2O_3$ (100 nm, $x \sim 0.12$) bilayers were grown on an Fe-doped β-Ga_2O_3 (010) substrate by ozone molecular beam epitaxy (O_3-MBE). X-ray diffraction (XRD) measurements and atomic force microscopy (AFM) observations suggested that the bilayers were coherently grown with good crystallinity and had atomically flat surfaces. Next, Si ions were implanted into the Ga_2O_3 layer to form a channel (Si concentration of 3.5×10^{18} cm^{-3}) and Ohmic contact regions (Si concentration of 5.0×10^{19} cm^{-3}) with a 60 nm deep box profile. After that, Ti/Au source and drain Ohmic electrodes, an Al_2O_3 gate dielectric (20 nm), and Ti/Pt/Au T-shaped gate electrodes were successively formed. The L_g were 40–1000 nm, and the gate width was 50×2 µm. The source-to-drain distance (L_{s-d}) was 2 µm.
DC and small-signal RF characteristics were measured for the Ga_2O_3 MOSFETs. The DC output characteristics showed a high ON-current density of about 230 mA/mm, and good pinch-off behavior was confirmed. In lateral Ga_2O_3 MOSFETs, the I_d leakage caused by Si accumulation at the interface between the epitaxial layer and the substrate is often problematic [4]. However, the MOSFETs fabricated in this study had a sufficiently low leakage of less than 1 nA/mm. This is considered merit associated with the introduction of the $(Al_xGa_{1-x})_2O_3$ back barrier layer. The current-gain cutoff frequency (f_T) of 10 GHz and maximum oscillation frequency (f_{max}) of 24 GHz were obtained for L_g = 120–150 nm, which were comparable to those for the MOSFETs without an $(Al_xGa_{1-x})_2O_3$ back barrier layer fabricated in our previous work [1]. From the L_g dependences of f_T and f_{max}, it is also suggested that the introduction of the $(Al_xGa_{1-x})_2O_3$ back barrier layer had a certain effect in suppressing the short-channel effect.
We succeeded in suppressing I_d leakage through an epi/substrate interface and the short-channel effect of highly scaled Ga_2O_3 MOSFETs by introducing an $(Al_xGa_{1-x})_2O_3$ back barrier.

Acknowledgement:
This work was supported in part by the Development Program, "Next-Generation Energy-Saving Devices" of the Ministry of Internal Affairs and Communications, Japan (JPMI00316).

References:
[1] T. Kamimura *et al*., Appl. Phys. Lett. **117**, 253501 (2020).
[2] A. Hassa *et al*., J. Phys. D: Appl. Phys. **54**, 223001 (2021).
[3] H. Peelaers *et al*., Appl. Phys. Lett. **112**, 242101 (2018).
[4] S. Kumar *et al*., Appl. Phys. Lett. **117**, 193502 (2020).

11:40 AM F06
(Student) Demonstration of Gallium Oxide Nano-Pillar Field Emitter Arrays Taeyoung Kim[1], Chandan Joishi[1], Zhanbo Xia[1,2], Nidhin Kurian Kalarickal[1,3], Camelia Selcu[4], Tyson Back[5], Jonathan Ludwick[5,6] and Siddharth Rajan[1,1]; [1]The Ohio State University, United States; [2]Navitas Semiconductor, United States; [3]Arizona State University, United States; [4]NanoSystems Laboratory, United States; [5]Air Force Research Laboratory, Wright Patterson Air Force Base, United States; [6]Wright-Patterson Air Force Base, United States

Introduction: We report on the first demonstration of field emission characteristics of β-Ga_2O_3 nano-pillar arrays fabricated using a novel damage-free etching technique. The vacuum field emission characteristics of β- Ga_2O_3 is interesting due to its large theoretical breakdown field strength (8 MV/cm), high mechanical and chemical stability, and resistance to surface oxidation. The current literature on vacuum field emission of Ga_2O_3 is limited to a single nano-pillar fabricated using FIB [2] while β- Ga_2O_3 nanowires made using self-catalytic bottom-up processes display low threshold fields [3].
The β-Ga_2O_3 nano-pillar arrays were fabricated using an *in situ* Ga_2O_3 etching technique in an ultra-high vacuum environment to realize damage free, high aspect ratio nano-pillars with atomic scale etch precision. Electrically conductive Ga_2O_3 nano-pillars with sub-micron widths was realized without the use of e-beam lithography. Field emission characteristics on the nano-pillars displayed an emission current of 10 nA per tip at an electric field of 400 kV/cm. The field emission characteristics were modelled using the Murphy-Good model, and the measurements were validated with a field emission orthodoxy test.
Experimental: A thin SiO_2 sacrificial layer was deposited on a Sn doped (1×10^{18} cm^{-3}) (010) β- Ga_2O_3 substrate as a hard mask for the *in-situ* etch. Circular arrays were patterned using a conventional photolithographic tool on the SiO_2 layer. A portion of the patterned SiO_2 layer was etched using an inductively coupled reactive ion etcher (ICP-RIE), and the remaining SiO_2 was etched in diluted buffered oxide etch to prevent plasma damage to the Ga_2O_3 surface during the dry etch. The Ga_2O_3 etch was carried out at a chamber temperature of 700 ºC and a Ga flux of $5x10^{-7}$ Torr for two hours which resulted in an etch depth of ~960 nm. Formation of nano-pillar arrays, ~240 in diameter was confirmed using a scanning electron micrograph.
Results: The conductive nature of the fabricated nano-pillars was confirmed using conductive atomic force microscope measurements. Field emission characteristics were measured on a wafer with three Ga_2O_3 nano-pillar arrays (a total of 700 nano-pillars). The measurement was carried out in a vacuum chamber with a base pressure of ~$6x10^{-8}$ Pa. The nano-pillar arrays displayed an emission turn-on field ~100 kV/cm, with a field emission current of 19 nA per tip at an applied field of 385 kV/cm. The Murphy-Good plot shows a linear relationship at high electric fields ranging from 250 kV/cm to 385 kV/cm. The field enhancement factor and the 'f_c' value at each voltage were extracted based on the slope at the 1/V value. The orthodox pass dataset was calculated to be in the range, . The measurement data of β- Ga_2O_3 nano-pillar arrays were found to be within the range at high electric fields ranging from 250 kV/cm to 385 kV/cm.
In summary, field emission characteristics of β- Ga_2O_3 nano-pillar arrays were demonstrated and modelled using Murphy-Good equation alongside independent validation using the orthodoxy test. We acknowledge funding from the Air Force Office of Scientific Research (AFOSR) through Award FA9550-19-0349 (Dr. Ken Goretta and John Lungisland). J. Ludwick was supported by the Air Force Research Labs under contract No. FA8650-16-D-5408.
References: [1] Appl. Phys. Lett. **119**, 123503 (2021). [2] Appl. Phys. Lett. **114**, 193101 (2019). [3] J. Phys. D: Appl. Phys. **42**, 185409 (2009).

SESSION G: Group III–Nitrides—Vertical Power Devices
Session Chairs: MVS Chandrashekhar and Geoffrey Foster
Wednesday Afternoon, June 28, 2023
Music Building, Lotte Lehmann

1:30 PM G01
(Student) Improving Electrical Performance of GaN-on-GaN MOS Devices Via Optimized Atomic Layer Deposition of Al_2O_3 Gate Dielectrics Caleb Glaser[1,2], Samantha Rosenberg[1], Robert Kaplar[1], Daniel Feezell[2], Brian Rummel[1] and Joseph Klesko[1]; [1]Sandia National Laboratories, United States; [2]The University of New Mexico, United States

Gallium nitride (GaN) MOSCAPs and MOSFETs are often investigated for high-power applications ranging from electric vehicles to photovoltaic invertors and smart electric grids. The specific material properties of GaN, including its wide bandgap, higher obtainable breakdown voltages, and higher electron mobilities, enable novel advantages not attainable using traditional silicon power devices. Among the many challenges reported for vertical GaN MOSFETs, optimization of the semiconductor/dielectric interface is crucial to improve important parameters such as threshold voltage, leakage currents, and interface trap densities (D_{IT}). Previous work on GaAs has shown the importance of Ga_xO_y mitigation through sequenced TMA purging for improved interfaces but has not elaborated on the impact of this on electrical output characteristics. For GaN, to date little work has been published that analyzes the impact of minimized interfacial Ga_xO_y from optimized ALD techniques and its effect on electrical performance in MOS devices. Minimizing Ga_xO_y formation at the semiconductor-dielectric interface is necessary to obtain optimal performance in GaN MOS structures. The fundamental understanding of the impact of improved oxide deposition techniques for GaN MOSFET gates is critical to accurately describe device performance. Relative improvements to dielectric leakage, D_{IT} distributions, and capacitance-voltage (C-V) trends may be analyzed to understand how each is affected through the elimination of native oxide concentrations at the interface of GaN MOSFET gates.
This study analyzes changes in electrical performance of Al_2O_3 dielectrics fabricated using atomic layer deposition (ALD) techniques on GaN epilayers grown on bulk GaN substrates (GaN-on-GaN). Traditional ALD deposition techniques for aluminum oxide (Al_2O_3) utilize reactions of trimethyl aluminum (TMA) and water to form dielectric films on various substrates. Previous studies have shown that gallium oxide (Ga_xO_y) formation on gallium arsenide (GaAs) can be alleviated by cycling TMA purges during ALD deposition to control oxidation states and mitigate Ga-O and As-O bonding. For GaN, improvements to gate interfaces of high-k dielectrics such as Al_2O_3 are crucial to ensure optimal switching and electrical response of complex vertical GaN MOSFETs. Leakage currents and high densities of interfacial traps have been shown to reduce device performance in previous studies. This work shows improved C-V responses of ALD Al_2O_3 films using quasi-static capacitance measurements. Optimized films were fabricated by the mitigation of Ga_xO_y at the semiconductor/dielectric interface. Films grown on substrates that did not receive a TMA dose prior to the H_2O precursor for ALD growth of Al_2O_3 films show a significantly higher amount of native oxide between the semiconductor and gate dielectric. The relative percentage of native oxide found at the interface is quantified via x-ray photoelectron spectroscopy (XPS) and shows a significant reduction following TMA purges. This improved ALD technique for Al_2O_3 deposition also shows a reduction of mid-gap trap states and hysteresis observed during C-V testing which further indicates improved interface quality and electrical response of the tested

devices. Relative improvement to film quality is dependent upon improved gate dielectric deposition techniques which diminish Ga_xO_y concentration at the semiconductor/dielectric interface. The impact of gate interfaces on GaN MOS devices is directly linked to calculated D_{IT}, leakage currents, and other important electrical characteristics which must be optimized on simple device structures prior to implementation in complex architectures such as vertical GaN MOSFETs.

1:50 PM G02
Design and Fabrication of AlGaN/GaN Multiple P-Channel Schottky Barrier Diodes Dawei Wang, Dinusha Herath Mudiyanselage, Ziyi He and Houqiang Fu; Arizona State University, United States

Wide bandgap GaN holds great promises for high-efficiency power conversion systems. To realize GaN power integrated circuits (ICs), peripheral logic circuits based on GaN are necessary, such as controllers, drivers, protection circuits. By using the AlGaN/GaN high electron mobility transistors (HEMTs) platform, all these components can be integrated on a single chip, dramatically reducing parasitic effects, such as gate ringing and false turn-on of power transistors. Currently, most GaN logic circuits still rely on only n-channel devices. This is because it is challenging to realize high-performance GaN p-channel devices due to much lower hole mobilities and sheet carrier density. Recently, multi-channel heterostructure is proposed to address the tradeoff between carrier mobility and density. But there are still few reports on GaN multi-channel p-type devices partly due to the difficulty in buried p-GaN activation, unknown doping concentration and thickness of the inserted p-GaN layers, and the acceptor-holes separation process. In this work, we perform the design, modeling and fabrication of GaN-based vertically stacked 2DHG (two-dimensional hole gas) multiple p-channel Schottky barrier diodes (SBDs). The schematic of cross-section of an SBD with 5 2DHG-channels is shown in Fig. 1(a), and the energy band structure from the cutline is shown in Fig. 1(b). The device epilayers were grown by metal-organic chemical vapor deposition (MOCVD) on a sapphire substrate, consisting of a thick GaN buffer layer, a 300 nm UID-GaN layer, and multiple layers for p-channels that are composed of a 40 nm p^+-GaN layer, a 20 nm UID-GaN layer, and a 15 nm Al0.2Ga0.8N layer. In order to effectively activate the buried p-GaN layers, trenches with different geometric patterns between the anode and cathode were etched by 400 nm of depth. The devices were then annealed at 800 °C for 1 hour to break the Mg-H bond and allowed the [H] to diffuse to the ambient through the etched sidewall. Moreover, these trenches are also geometrically designed as edge terminations that can eliminate high electric field crowding at reverse bias, which is necessary due to the vulnerability of the etched trenches, as shown in Fig. 2. Finally, the two electrodes and passivation layer were deposited on top of the devices. The distance between the anode and the cathode is from 15 um to 25 um. For the simulation, the impacts of doping concentration and thickness of p-GaN layers and the thickness of UID-GaN layers of the multi-channel heterostructure will be comprehensively investigated. And the ionization energy of [Mg] in GaN was set to be 300 mV. For the forward performance, as shown in Fig. 3(a), the ON-current densities at an anode voltage of -3.5 V for the SBDs with 1, 3, and 5 p-channels were extracted as 0.12, 0.26, and 0.365 mA/mm, respectively. With the thickness of each UID-GaN between p-GaN and AlGaN increasing from 2 to 5, 10, and 20 nm, as shown in Fig. 3(b), the ON-current is also increased from 0.24 to 0.265, 0.3, and 0.365 mA/mm. For the fabrication, as shown in Fig. 4(a) and 4(b), the SBD with 1 2DHG channel and 3 2DEG channels with different doping concentration in p-GaN layers have been fabricated. Compared with the SBD with 1 channel, the SBD with 3 channels and higher concentrations of doping in p-GaN layers has larger current. The performance of these devices needs to be further optimized during the following work. These results can provide critical references for the future development of GaN multiple p-channel devices such as multiple p-channel diodes and FETs for integrated power and logic circuits.

2:10 PM G03
(Student) TCAD-Based Comprehensive Analysis of High Voltage (>600 V) Bidirectional AlGaN/GaN HEMTs Md Tahmidul Alam and Chirag Gupta; University of Wisconsin-Madison, United States

Novel power electronic systems like AC-AC matrix converter [1], multilevel T-type inverter [2], DC-DC dual active bridge (DAB) [3] require current to flow and block voltage in both directions. Unidirectional transistors combination in series and/or parallel type solutions are not ideal for these applications because of high transistor count resulting in an increased form-factor, power consumption, complexity, and reduced speed. Monolithic bidirectional AlGaN/GaN HEMTs can address these concerns [4]. The conventional monolithic bidirectional GaN HEMT consists of two gates to control the current flow and voltage blocking bidirectionally. (Fig.1) [5-7]. Despite the advantages offered by the monolithic bidirectional transistors, detailed and extensive device-level studies have not been performed. **In this work, we have addressed this by performing comprehensive TCAD simulations of this device structure.**
The device structure is set up utilizing a typical AlGaN/GaN material stack. The device consists of two sources at the edge of the device and gates are added close to the sources. Furthermore, two field plates were added near each gate to manage peak electric field on either side of the gate and therefore, maximize the breakdown voltage. The field plate positions were optimized to get almost equal electric field peaks at a horizontal cutline in AlGaN. All the field plates were connected to their nearest ohmic electrode. Since opposite bias voltage is applied to the left-side and right-side field plates, the gap between them was chosen such that the electric field inside the dielectric material (Si_3N_4) never crossed 50% of its critical field (~9 MV/cm) [8].
Unlike conventional unidirectional HEMTs, in this structure electric field accumulated at both source-side (S_1 and S_2) field plates (Fig. 2). This structure allows for electric field or blocking voltage sharing on either side (Fig. 2). **Ideally, bidirectional blocking capability involves 2x increase in the on-resistance compared to a conventional HEMT, however, this voltage sharing reduces the increase in on-resistance from 2x to 1.5x, therefore, making this design very attractive**. For gate-to-gate distances of 4µm, 6µm and 8µm, breakdown voltages were 675V, 915V and 1025V respectively (Fig. 3). The device with two field-plates was optimized for each gate-to-gate length, additional field-plate may be needed to enhance V/µm blocking capability. Bidirectional and symmetric on-state I-V curves were obtained (Fig.4) with a low on-resistance of ~5Ω.mm with a gate bias (both gates) of -3V for a gate-to-gate length of 4 µm.
The capacitance, charge, and energy profiles at the output node (S_2) were simulated at 100kHz with the device in off-state (Fig 5 and Fig.6). The output capacitance was observed to be decreased rapidly with the applied voltage due to 2-DEG depletion. The transient responses of the devices were achieved by applying a step input at the gate from 0V to -15V (Fig.7). With an increase in the channel length, the on-resistance increased linearly, however, output capacitance remained (nominally) constant. Consequently, the device with the smallest L_{gg} resulted in the fastest transient response.
[1] S. Nagai et al. IEEE ISSCC- 2014. [2] C. Kuring et al. International Exhibition and Conference for Power Electronics, Intelligent Motion,
Renewable Energy and Energy Management, 2018. [3] S. Shao et al. IEEE Transactions on power electronics, 2022. [4] T. Morita et al. IEEE International Electron Devices, 2007. [5] M. Wolf et al. IEEE Transactions on Electron Devices-2018. [6] C. Kuring et al. ECCE-2019. [7] S. Musumeci et al. ISIE-2020. [8] I. Sayed et al. Applied Physics Express, Japan, 2019

2:30 PM G04
Alpha Radiation Damage Assessment in GaN by Time-Resolved Luminescence Spectroscopy LeighAnn S. Larkin, Gregory Garrett, Marc Litz, John D. Demaree, Vijay Parameshwaran and Michael Wraback; U.S. Army Research Laboratory, United States

Wide bandgap semiconductors are desirable for α-voltaic energy conversion devices because of both larger open circuit voltage and greater tolerance to radiation damage. A commonly used α source, ^{241}Am, emits radiation at 5.4 MeV, which leads to energy loss by ionization/electron-hole pair creation to a depth of ~ 14 μm. The α particles leave a wake of dislocations and defects with the largest concentration near the final stopping depth, i.e., the "Bragg peak." A well-designed α-voltaic devices will require the isolation of the stopping position outside the active device region, but lower-level damage will still occur throughout the entire ionization region. It is therefore important to determine the fluence threshold at which degradation of electronic properties occurs. To this end, we have irradiated unintentionally doped free-standing GaN substrates grown by hydride vapor phase epitaxy with He ions at 3.7 MeV and fluences of 10^8 – 10^{10} ions/cm^2 that simulate the high energy α source. The profiles of the energy deposition and resulting vacancy profile induced by the radiation were calculated with Stopping and Range of Ions in Matter (SRIM). To determine the effect of these vacancies on the electronic properties, picosecond time-resolved (TR) cathodoluminescence (CL), induced in the GaN by an ultrafast electron pulse created by fs photoexcitation of an electron gun cathode and subsequently accelerated to 30 keV, and photoluminescence (PL) studies, induced with ~100 fs UV pulse excitation spectrally centered at 280 nm, of the near-band edge emission lifetime (~3.4 eV) were performed using time-correlated single photon counting.
The time evolution of the TR-PL and TR-CL is characterized by a more rapid nonexponential initial decay that transitions to an exponential decay. The unirradiated GaN exhibits a TR-PL decay profile with an initial 1/e decay of 440 ps, followed by an exponential decay of 26 ns, while the TR-CL decay a substantially longer 1/e time (7 ns) and subsequent exponential decay (40 ns). The time evolution of TR-PL and TR-CL are governed primarily by the interplay of surface recombination, carrier diffusion, reabsorption of the emission, and the bulk carrier lifetime. The PL excitation results in an absorption depth in GaN of ~ 50 nm, creating a large carrier concentration gradient that results in a decay profile sensitive to all four of these phenomena. On the other hand, electrons accelerated by 30 keV can generate electron-hole pairs much deeper (up to ~ 2 microns) and with a lower carrier concentration gradient, reducing the effect of the surface and diffusion, and providing a better assessment of the bulk lifetime. The significantly longer TR-CL lifetimes relative to TR-PL demonstrate the reduced importance of surface recombination and diffusion, due to the decreased carrier concentration gradient.
At fluences of 10^8 ions/cm^2, the TR-PL decays are indistinguishable from that of the unirradiated material. At 10^9 ions/cm^2, the initial 1/e decay time remains unchanged, but we observe a noticeable drop in the long decay lifetime from 26 to 19 ns. At the highest fluence of 10^{10} ions/cm^2, there was a relatively small change in the 1/e lifetime (from 440 – 366 ps) and a substantial reduction in the exponential decay time down to 14 ns. The TR-PL initial nonexponential decay exhibits less sensitivity to the irradiation fluence than the longer exponential decay. It is evident from the TR-PL lifetimes that the electronic carriers begin to be influenced by the irradiation at fluences of 10^9 ions/cm^2. These results provide a means to assess the impact of α particle-induced damage on GaN α-voltaic energy converter performance as a function of radiation loading while informing the design of these devices.

2:50 PM G05
(Student) Crack-Free III-N Epitaxial Growth on Si (111) Substrate Exceeding 1 μm in Thickness Mina Moradnia, Sara Pouladi, Muhammad Aqib and Jae-Hyun Ryou; University of Houston, United States

A combination of desired properties including excellent thermal and chemical stability, outstanding piezoelectric coefficient as well as high dielectric breakdown voltage, and a bandgap that extends from the infrared to the deep ultraviolet make III-nitride (III-N) materials unique among other semiconductors and a primary candidate for the active area of scientific and technological development. Among III-nitride materials, AlN and GaN have long been of interest for implementation in a wide range of applications from high-temperature and high-power transistors to a solid-state replacement for traditional lighting. However, the growth processing of inexpensive high-quality thick film crack-free of epitaxial III-N material for device applications always faces lots of challenges to achieve. In the epitaxial growth of AlN, difficulty to remove an unintentional partial nitridation of the surface cause problem in the growth process. Therefore, the epitaxial growth of AlN will be prevented or at least severely disrupted in the place where nitridation has occurred. To achieve the device-grade quality of hetero-epitaxially grown AlN on Si, some efforts have been tried to avoid the nitridation of the Si surface, mainly because of the formation of amorphous Si_3N_4 followed by epitaxial growth degradation. Deposition of a first Al layer, typically in the monolayer thickness range before exposing the surface to both the Al and N fluxes is critical to grow an epitaxial AlN buffer layer. Using this Al nucleation step prior to AlN growth substantially improves the crystalline properties of AlN thin films. In the previous efforts on the epitaxial growth of AlN on Si, the metallic interlayer of Al was intended for improvement of the crystalline quality of AlN at limited thickness. Here, we introduce a method to overcome the limitations of existing approaches for the growth of crack-free relatively thick AlN and ultrawide-band gap semiconductor materials with >1μm thickness. We focus on the capability of strain-mediated metal interlayers to diminish the thermal expansion coefficient differences and lattice mismatch between the template and III-N grown layer. Considering different single-crystal metallic interlayers like Aluminum (Al), Gold (Au), and Ytterbium (Yb) with FCC structure or Lanthanum (La), Titanium (Ti), and Terbium (Tb) with HCP structure bring the opportunity of growing crack-free thick layers of high-quality single crystalline semiconductor III-N materials on Si (111) substrate. We have compared the results of our calculations on different possible options (different metallic materials of the periodic table) to find the best combination of interlayers for strain mitigation. Choosing Yb as the first layer of metallic interlayers brings the advantage of epitaxial water lift-off possibility on the samples because Yb can be dissolved in water by the formation of ytterbium (III) hydroxide ($Yb(OH)_3$). Also, the selection of Yb interlayer allows the Si substrate to become a reusable template after AlN thick film growth. In addition, the crack formation issue in the heteroepitaxial growth of thick III-N film on Si due to the induced strain has been reduced when we deposited Yb and Au interlayers rather than using conventionally used Al interlayer based on the previous works. Although Al can be considered for the strain management purpose of AlN thick film growth, more promising metal interlayer candidates like Yb can be employed for simply pilling off the thick film grown because of its water solubility in addition to addressing the lattice mismatch issue. The heteroepitaxial growth of III-N thick film layers on Si substrate which is missing in the previous studies on the III-N growth is of high demand for performance improvement and cost reduction of III-N based devices simultaneously.

3:10 PM BREAK

3:30 PM G06
(Student) 1.2kV Vertical GaN PIN Rectifiers with Nitrogen-Implanted Floating Guard Rings as Edge Termination and Breakdown Characteristics Correlation Study by Wafer-Level Photoluminescence Mapping Zhiyu Xu[1], Matthias A. Daeumer[2], Minkyu Cho[1], Marzieh Bakhtiary-Noodeh[1], Jae Hyuck Yoo[2], Qinghui Shao[2], Ted Laurence[2], Daryl Key[3], Tadao Hashimoto[3], Edward Letts[3], Theeradetch Detchprohm[1], Russell Dupuis[1,1] and Shyh-Chiang Shen[1]; [1]Georgia Institute of Technology, United States; [2]Lawrence Livermore National Laboratory, United States; [3]SixPoint Materials, United States

Gallium Nitride (GaN) is a promising wide bandgap (~3.4eV), material for high-power electronics. GaN devices can sustain a high breakdown voltage (BV) and high temperature operation, providing faster switching frequencies with lower power losses. Compared to lateral devices, vertical rectifiers have larger breakdown voltages and operate in a vertical depletion mode which can mitigate surface breakdown problems. Our prior work has demonstrated that nitrogen-implanted floating guard rings (FGRs) can serve as an effective edge termination technique, as uniform average reverse breakdown above 1.2kV and low turn-on voltage of 3.5V can be achieved. However, even though GaN device technology has made significant advances, remaining material defects have a detrimental impact on device performance. In this study, photoluminescence (PL) imaging was performed after growth and prior to the device processing to evaluate the impact of material quality on the fabricated PIN rectifier performance.
Epitaxial growth on the GaN face of a (0001) ammono-thermally grown bulk GaN substrate was performed in an AXITRON metalorganic chemical vapor deposition reactor equipped with a close coupled showerhead. The device structure consisted of a 0.5µm *n*-GaN:Si ([*n*]=6×10^{18} cm^{-3}), 8.5µm GaN:uid drift layer, a 450nm *p*-GaN:Mg ([*p*]=$1\times10^{18}cm^{-3}$), and a 20nm p^+-GaN:Mg ([Mg]=$1\times10^{20}cm^{-3}$). The device fabrication started with the deposition of Ni/Ag/Ni/Au or Ni/Ag/Pt *p*-GaN ohmic contacts, followed by annealing in dry air for ohmic contact formation. Three-step ion implantation with nitrogen forms the highly resistive device isolation regions as well as the FGR structures in the *p*-GaN layer. Prior to implantation, TCAD simulation was performed to determine the optimum FGR, i.e., widths of 4µm and gaps of 2µm, in order to prevent premature device breakdown and achieve a smooth potential profile along the device surface under reverse bias. After ion implantation, the backside Ti/Al/Ni/Au n-metal contact was formed without annealing.
The *J-V* characteristics of two batches of devices on separate GaN wafers, namely sample A and B, were each measured at 300K with 400 devices within a 1cm×1cm block region consisting of two device groups with mesa diameters of 100µm and 200µm. Sample A had an overall average BV of 1209±229V at 0.01A/cm^2, with 274 out of 400 (68.5%) measured devices reach BV>1.2kV. The average BVs were 1228±190V and 1190±261V for 100µm and 200µm diameter devices on sample A, respectively. Sample B had an overall average BV of 1095V±210V at 0.01A/cm^2, with 241 out of 400 (60.25%) measured devices able to reach BV>1.2kV. The average BVs were 1156±163V and 1033±233V for 100µm and 200µm diameter devices on sample B, respectively.
The distribution of measured BV's as well as the PL image on macro-scale of the measured blocks show a correlation between low BV devices and Mg concentration non-uniformity. The lower PL intensities are related to higher Mg doping concentrations. This is because the PL emission of donor-acceptor pair recombination is suppressed in heavily doped GaN:Mg layers. From the high-resolution PL scanning, it is found that a variety of macro-defects in GaN epi layer, such as cracks, triangular hillocks, particles, and surface roughness induced by step bunching contribute to the increased leakage current density and lower BV of the devices. Dislocations appearing as dot features with dark cores and bright light rings are also observed in PL imaging, and their impact on device performance will be discussed.
Acknowledgements
This work was performed under the auspices of the U.S. Department of Energy by Lawrence Livermore National Laboratory under Contract DE-AC52-07NA27344. R. D. Dupuis acknowledges the support of the Steve W. Chaddick Endowed Chair in Optoelectronics. This work was in part performed in facility supported by the National Nanotechnology Coordinated Infrastructure (NSF Grant ECCS-154217).

3:50 PM G07
Exploiting Competition Between Built-in Polarization and P-N Junction Field in III-Nitride Heterostructures Henryk Turski[1,2], Mikolaj Chlipala[1], Ewelina Zdanowicz[3], Ernest Rogowicz[3], Greg Muziol[1], Marcin Syperek[3], Robert Kudrawiec[3] and Czeslaw Skierbiszewski[1]; [1]" Unipress" Institute of High Pressure Physics PAS, Poland; [2]Cornell University, United States; [3]Wroclaw University of Science and Technology, Poland

The high built-in polarization field is a fingerprint of III-nitride heterostructures. Alloy composition and doping profile significantly affect the magnitude of electric field present in subsequent layers, but sign of the electric field is usually defined by substrate polarity and external bias. As we shown this restriction can be to some extent lifted to realize vertical Ga- and N-polar structures on Ga-polar substrates by the use of buried tunnel-junctions to invert current flow direction [1]. By using plasma-assisted molecular beam epitaxy (PAMBE) such devices can be effectively realized.
Here we propose to utilize acceptor and donor doping concentrations exceeding 10^{20} cm^{-3}, typically used in tunnel junctions, to obtain high junction field that can solely abolish built-in polarization for polar (0001) InGaN/GaN quantum well (QW). By introducing appropriate doping concentration, value of the total electric field in unbiased structure can be controlled. Furthermore, by changing the p- and n-type doped layers ordering, value of the total electric field can be increased from 2.3 MV/cm (for undoped polar structure) to 4 MV/cm in p-i-n structure.
We have used photoluminescence (PL), time-resolved PL (TRPL) and contactless electroreflectance (CER) in order to gain insight into the actual strength of the electric field present in the grown heterostructures. Good match between values estimated by one dimensional Poisson, drift-diffusion, and Schrodinger Solver DDCC-1D [2] and measured electric field values was obtained.
A dramatic decrease in the luminescence lifetime for flat QW was confirmed using TRPL. This low recombination lifetime can be associated with combination of both the higher electron-hole wavefunction overlap and enhanced carrier escape in this case.
Presented results open a way to realize devices that profit from the low built-in field, like photodetectors, using abundant polar substrates.
Funding: This work received funding from the European Horizon 2020 project VISSION (Grant ID:101070622). This research was funded in part by National Science Centre, Poland no. 2021/43/D/ST3/03266, 2019/35/D/ST5/02950, 2019/35/D/ST3/03008, and the Foundation for Polish Science co-financed by the European Union under the European Regional Development Fund within the HOMING POIR.04. 04.00-00-5D5B/18-00 project.
[1] H. Turski, S. Bharadwaj, H. Xing, and D. Jena, Journal of Applied Physics **125**, 203104 (2019).
[2] W. Yuh-Renn, C. Chinghua, C. Cheng-Yu, Y. Peichen, and K. Hao-Chung, IEEE Journal of Selected Topics in Quantum Electronics **15**, 1226 (2009).

4:10 PM G08
Contacting p-GaN Efficiently—Why the Same Metal Stacks Give Different Results? Mona Ebrish[1], Alan G. Jacobs[2], Jennifer K. Hite[2], James C. Gallagher[2], Joseph Spencer[3], Marko Tadjer[2], Karl Hobart[2] and Travis Anderson[2]; [1]Vanderbilt University, United States; [2]U.S. Naval Research Laboratory, United States; [3]Virginia Tech, United States

GaN is a favorable martial for future efficient high voltage power switches. However, GaN has not dominated the power electronics market due to immaturity of several processing technologies. As GaN

attracts attention from foundries as the front runner for future high-voltage switches a fundamental issue such as contact resistance is still a hurdle.[1] Numerous publications have addressed this topic, reporting a wide disparity in the contact resistance values. Contact resistance is traditionally a specified value by the technology specs and this value has implications on the device performance and consequently the whole chip performance. The variation in the reported values from similar structures invites an investigation into the roots of these differences. GaN diodes as an example requires p-type contact whether the diode is vertical PiN or lateral PiN. We are comparing contact resistance from different metal stacks used for p-GaN layer. The n-type contact is less of a concern due to the abundance of elements that function as donors to GaN. Our holistic discussion will focus on whether the issue with the contact resistance stems from the quality of the GaN layer, contact metal stack or a combination of both. The p-GaN layer can be grown epitaxial MOCVD or MBE on a GaN substrate or nonnative substrate. The quality of the p-GaN layer is an important factor in determining the quality of the contact. Nonnative substrates like SiC, Si, or Sapphire led to a higher defectivity level in the grown p-GaN. These defects can be scattering sites that impact the current flow directly or indirectly by the hindering the activation of some of the acceptors in the p-GaN which leads to shallower Fermi-level, and consequently different contact resistance for the same metal work function. [2] Studying the contact metal stack, focuses the choice of the metal work function deposition process, and post deposition annealing which in some cases significantly impacts the contact resistance. [3] Common contact metal stacks such as Ni/Au have been used with the same p-type doping levels, some groups reported contact resistance as low as 0.1 mΩ.cm^2 while others reported values as high as 10mΩ.cm^2. This disparity is an indicative that both the substrate and the metal stack contribute the increase in the metal contact resistance. Our discussion will delve into the combination of both and study the impact each factor has contributed to the total value of the contact resistance. Thus, an analytical or numerical model can emerge and potentially provide recommendations. Ohmic contact with p-GaN is not an issue that concerns only GaN based devices, it is a fundamental issue that will impact all wide and ultra-wide band gap materials. Understanding the roots of the issue and being able to build a model that can predict the contact quality and resistance values will be a revolutionary progress in implementing wide-band gap materials into foundries.

[1] J. Hu, Y. Zhang, M. Sun, D. Piedra, N. Chowdhury, and T. Palacios, "Materials and processing issues in vertical GaN power electronics," *j*, vol. 78, 2018, doi: 10.1016/j.mssp.2017.09.033.
[2] G. Greco, F. Iucolano, and F. Roccaforte, "Ohmic contacts to Gallium Nitride materials," *Appl. Surf. Sci.*, vol. 383, pp. 324–345, 2016, doi: 10.1016/j.apsusc.2016.04.016.
[3] S. Wahid, N. Chowdhury, M. K. Alam, and T. Palacios, "Barrier heights and Fermi level pinning inmetal contacts on p-type GaN," *Appl. Phys. Lett.*, vol. 116, no. 21, 2020, doi: 10.1063/5.0010699.

4:30 PM G09
(Student) Electrical Characterization of AlN PN Diodes
Christopher M. Matthews, Habib Ahmad, Emily N. Marshall, Anusha Krishnan, Sangho Lee, Keisuke Motoki, Huijin Chung and W. Alan Doolittle; Georgia Institute of Technology, United States

In this study we will present thorough electrical characterization of homojunction aluminum nitride (AlN) PIN diodes. Recently, substantial bulk n- and p-doping in AlN as well as AlN homojunction PN diodes were demonstrated, overcoming the longstanding barrier to doping of AlN[1,2]. Current-voltage-temperature (IVT) data from 25 °C to 250 °C is used to investigate these diodes and shows nonstandard behavior in the low forward voltage range. The diodes under study were grown by metal-modulated epitaxy (MME) on AlN templates on sapphire. These quasi-vertical devices consist of 1 μm highly n-type AlN:Si, a lightly Si-doped intrinsic AlN layer with varied thickness, and a 200 nm highly p-type AlN:Be.
Aluminum nitride (AlN) is a material of great interest for high performance power electronics, extreme environment semiconductor devices, radio frequency devices, and deep ultraviolet (DUV) optoelectronics due to its excellent electrical and thermal properties. Compared to other commonly used semiconductors (i.e., Si, SiC, GaN, and β-Ga_2O_3), AlN has the highest critical electric field and theoretical breakdown voltage, which lead to the highest Baliga's and Johnson's figures-of-merit (BFOM & JFOM)[3]. AlN also has the second highest saturation velocity, and thermal conductivity among semiconductors with a commercially available substrate[3]. However, AlN has traditionally only been an insulator without the ability to be converted to a semiconductor via doping. We recently demonstrated substantial bulk doping (carrier concentrations above 10^{18} cm^{-3}) for both p- and n-type AlN using Be and Si dopants, respectively. From these results, we also demonstrated rectification and a 6 V turn-on in AlN PN diodes[1,2].
The substantial bulk doping of AlN is enabled by the combination of the use of a new dopant element (Be) and control of growth kinetics at low growth temperatures enabled by MME. Using MME we are able to reduce the incorporation of compensating impurities and the reconfiguration of metastable defects such as DX centers. This has led to: 1) the first reported bulk p-type AlN (p=3.1×10^{18} cm^{-3}), 2) the highest ever reported bulk Si-doped n-type AlN (n=6×10^{18} cm^{-3}, a nearly 6000 times improvement over previous state-of-the-art), and 3) the first AlN homojunction PN diode[1,2].
Here, we have undertaken further electrical characterization of homojunction AlN PIN diodes to understand their capabilities and identify areas for optimization. IVT measurements from 25 °C to 250 °C in both forward and reverse bias are examined for these purposes. Forward current is presently limited by high series resistance originating from contacts to the etched n-type AlN layer. However, the current increases by ~2 orders of magnitude as temperature increases suggesting thermally stimulated donor activation. Forward current below the turn on voltage shows a kink of unknown origin in the IV characteristics whose voltage onset decreases with increasing temperature. Activation energies of the thermally stimulated processes will be described in the presentation. Contact metallization, surface preparation of the AlN templates, and various device geometry parameters as important areas for future optimization in order to allow AlN diodes to eventually push the limits in the field power electronics.

References

[1] H. Ahmad, J. Lindemuth, Z. Engel, C.M. Matthews, T.M. McCrone, and W.A. Doolittle, *Adv. Mater.* **33**, 2104497 (2021).
[2] H. Ahmad, Z. Engel, C.M. Matthews, S. Lee, and W.A Doolittle, *J. Appl. Phys.* **131**, 175701 (2022).
[3] J.Y. Tsao, et al, *J. A., Adv. Electron. Mater.* **4**, 1600501 (2018).

4:50 PM G10
(Student) Effect of Impact Ionization Coefficients on High-Voltage Vertical AlN Power Devices
Ziyi He[1], Dinusha Herath Mudiyanselage[1], Dawei Wang[1], Yuji Zhao[2] and Houqiang Fu[1]; [1]Arizona State University, United States; [2]Rice University, United States

Aluminum nitride (AlN) is considered a future candidate for the future power electronics applications for its wide bandgap (6.2 eV), high thermal conductivity (340 W/mK), and high breakdown field (~12 MV/cm). However, due to the challenges in material growth and device fabrication, very limited work has been reported on AlN electronics, and the full potential of AlN material is yet to be discovered. The impact ionization (II) coefficients, which determine the blocking limits of AlN power devices is still both experimentally and theoretically imprecise but is under study at present. Here we collected the different II coefficients reported in the literature and analyzed their impacts on the device performance with TCAD Silvaco.
The quasi-vertical AlN Schottky diode is simulated in Silvaco TCAD environment. Selberherr's II model is employed to analyze the breakdown performance of the device as:
$\alpha_{n,p}=a_{n,p}\exp(-b_{n,p}/E)$
Where α is the II coefficients, E is the electric field, and a, b are the parameters need to be determined. 3 II coefficients are collected from

the theoretical results reported, which have a large discrepancy: one calculated from the full-band Monte Carlo model in E. Bellotti *et al.* [1], one calculated from the ensemble Monte Carlo framework in C. Bulutay *et al.* [2], and one in N. Lophitis *et al.* [3]. and another one coefficient is determined by calibration to have a breakdown field of 12 MV/cm. The drift region thickness (W) is set to be 1 mm and the N-type doping concertation (N_d) is set to be 10^{17} /cm^3. A 100 nm SiO2 passivation is employed to optimize the blocking capabilities. The 4 coefficients are applied to the model and their impact on the device performance are analyzed with the simulation.
The breakdown voltages (BV) for the 4 II coefficients are 351, 355, 2090, and 527 V respectively. The discrepancy of the II coefficients also affects the electric field distribution while the breakdown fields for the 4 II coefficients are 8.8, 8.8, 43, and 12 MV/cm respectively. The distribution of the electric field in the devices shows the breakdown occurs due to EF crowding at the anode edge, however, it is alleviated by SiO_2 passivation structure.
[1] J. Appl. Phys. 111, 103711 (2012).
[2] Semicond. Sci. Technol. 17, L59 (2002)
[3] Disruptive Wide Bandgap Semiconductors, Related Technologies, and Their Applications. (2018)

SESSION H: 2D Materials, Devices and Sensors
Session Chairs: Jae-Hyun Ryou and Ke Xu
Wednesday Afternoon, June 28, 2023
UC, Corwin East

1:30 PM H01
(Student) Reduced Scattering in Remote Surface Charge Transfer Doped MoS_2 Field Effect Transistors Juntae Jang[1], Jae-Keun Kim[2], Keehoon Kang[1], Kyungjune Cho[3] and Takhee Lee[1]; [1]Seoul National University, Korea (the Republic of); [2]Max-Planck Institute, Germany; [3]Korea Institute of Science and Technology, Korea (the Republic of)

Two-dimensional (2D) transition metal dichalcogenide (TMDC) semiconductors such as molybdenum disulfide (MoS_2) hold great promise for next-generation electronic devices. From a practical point of view, surface charge transfer doping (SCTD) is known to be an effective method to modulate the electrical properties of 2D semiconductors. However, although SCTD is a facile and non-destructive method, it could also introduce charged impurities that can hinder charge transport [1].
In this study, we overcome the shortcomings of SCTD through demonstrating a remote charge transfer doping by simply inserting a thin hexagonal boron nitride (h-BN) layer (< ~3 nm thickness) between MoS_2 channel and the n-type molecular dopants, benzyl viologen (BV), which was sufficient for achieving a significant charge transfer [2]. First, we characterized the electrical properties of MoS_2 field effect transistors (FETs) with h-BN interlayer (denoted as "remotely doped" device) and without h-BN (denoted as "directly doped" device) before and after doping with temperature-dependent gated four-point probe measurements which can minimizes the effect of phonon scattering and the varying charge injection behaviors due to the BV doping. As a results, we identified a significantly larger enhancement in the mobility of remotely doped device relative to its pristine (un-doped) state than that of directly doped device under similar carrier concentration conditions since the spatial separation of thin h-BN interlayer between BV and the MoS_2 FETs channel suppresses the charged impurity scattering which could be additionally introduced by the SCTD. Next, we conducted the quantitative analysis of the remote doping method in comparison with the conventional direct doping method and our mechanistic study supports the efficient suppression of the dopant-induced charged impurity scattering in the remotely doped MoS_2 channel, corroborated by our theoretical predictions.
Our mechanistic study of the novel doping method promotes the remote charge transfer strategy as a promising way for achieving a wide doping range without compromising the carrier mobility, which is required for high performance emerging electronic and optoelectronic devices based on 2D materials.

1:50 PM H02
(Student) Electrical Characterization and Contact Resistance to ALD-Deposited $WNbS_2$ Thin Films Ruixue Li[1], Jeff J. Schulpen[2], Ageeth Bol[3] and Steven J. Koester[1]; [1]University of Minnesota Twin Cities, United States; [2]Eindhoven University of Technology, Netherlands; [3]University of Michigan–Ann Arbor, United States

Introduction: Two-dimensional transition metal dichalcogenides (TMDs) are promising for use in extreme-scaled metal-oxide-semiconductor field-effect transistors (MOSFETs). However, most TMD films are grown by chemical vapor deposition (CVD) which usually requires deposition temperatures above 800 °C [1], which is much higher than allowed for deposition in the back end of the line (BEOL) [2]. In addition, high contact resistance remains a significant issue for TMD-based MOSFETs, particularly for p-MOSFETs. Atomic layer deposition (ALD) has attracted much interest recently as an alternative deposition technique for BEOL-compatible TMDs, due to its low deposition temperature, controllability, and conformality. ALD also has the potential for incorporation of dopants and selective growth, making it suitable for use as a contact material for 2D MOSFETs [3]. However, to-date, the performance of ALD-deposited TMDs has not been explored extensively, particularly for p-doped materials. In this work, we characterize the electrical properties of p-type $WNbS_2$ deposited by plasma-assisted ALD (PE-ALD) at BEOL-compatible temperatures. We demonstrate low contact resistance and perform preliminary experiments toward realizing p-MOSFETs using ALD-deposited material.
Growth and Device fabrication: The $WNbS_2$ nanolayers were synthesized on 90-nm SiO_2/p-Si substrates using a PE-ALD process previously developed by Balasubramanyam, et al. [4]. The Nb was incorporated into the WS_2 by regularly replacing the W precursor half cycle with an Nb precursor using a so-called supercycle approach. The doping concentration of the film was adjusted based upon the number of Nb half cycles within a supercycle. For the layers used in this study, the film thickness was ~ 3 nm and the deposition temperature was 350 °C. After the ALD deposition, mesas were patterned and etched by SF_6 and O_2 plasma to form a rectangular active region. Next, contacts with varying spacing were formed by patterning and depositing either Ti, Ni or Pd (20nm) / Au (90nm).
Results and analysis: Initial measurements were performed at room temperature on heavily-doped material that used a super-cycle sequence of 6 × (4 ALD cycles WS_2 + 1 ALD cycle NbS_2 + 4 ALD cycles WS_2). Transfer length method (TLM) measurements were used to extract the sheet resistance, R_{SH}, and contact resistance, R_C. For Pd-contacted devices, R_C was found to be 220 Ω-μm and R_{SH} was found to be 83 kΩ/sq. The SiO_2 back gate electrode was used to extract the carrier mobility from the transconductance, g_m. From these measurements, the films were confirmed to be p-type, with hole mobility and concentration of 0.94 cm^2/Vs, and 2.7 × 10^{20} cm^{-3}. No improvement in the contact resistance or mobility was observed after subsequent annealing 300 °C. The effect of contact metal on R_C was also performed and the results showed that Pd provided the lowest resistance contacts, and Ti had the highest R_C, consistent with expectations based upon their relative work functions. Finally, we also performed measurements on lower-doped films (2.8 × 10^{19} cm^{-3}) to assess their suitability for transistor channels. These devices showed clear channel modulation with on/off ratio of ~ 2, but had lower mobility of 0.016 cm^2/Vs and much higher R_C of 1.2 MΩ-μm.
Conclusions: We have demonstrated the low contact resistance and identified the possibilities as transistor channels of ALD growth film. Future work will focus on improving the material quality and further characterizing device performance.
Acknowledgement: This work is supported by Intel Corporation. Portions of this work are carried out in the Minnesota Nano Center which receives partial support from the NSF through the NNCI

program under Award No. ECCS-2025124.
References: [1] T. Schram, et al., ESSDERC, 2017; [2] D. Sun, et al., 2D Mater. **2**, 045014, 2015; [3] V. Vandalon, et al., ACS Appl. Nano Mater. **3**, 10200, 2020; [4] S. Balasubramanyam, et al., ACS Mater. Lett. **2**, 511, 2020.

2:10 PM H03
(Student) Surface Polarization Engineering Design of 2D Janus MoSSe Complementary Field Effect Transistors Yun Ping Chiu, Hsin-wen Huang and Yuh-Renn Wu; National Taiwan University, Taiwan

The 2D TMD-based thin film materials have been believed to be a potential candidate for replacing the Si CMOS technology. Ideally, the 2D material has better device scaling and interface properties. However, contact resistance has been a big issue in the transistor's design due to the difficulties in material doping. It is difficult to dope in 2D material in the contact region to reduce the contact resistance and form an ohmic contact. Hence, most of the work is to find a good metal to adjust the work function. For nMOSFET, a smaller work function material is needed, and a high work function metal is needed for p-MOS. In this work, a new CFET design based on 2D Janus MoSSe material has been proposed based on the polarization field induced by the asymmetric structure. The 2D Janus MoSSe material has been found to have a strong polarization field, which is even larger than the nitride-based polar material because the structure is asymmetric. The p-type and n-type ohmic contact can be formed at the opposite surface by utilizing the asymmetry polarization property of the two opposite surfaces. The positive polar charge surface will attract electrons to form a 2DEG at the surface and make the n-type ohmic contact. The negative polar charge surface will attract holes to form a 2DHG and a p-type ohmic contact. Based on these properties, the n- and p-FET can be produced without doping; combined into a CFET by symmetric structure. In our DFT calculation, the dipole fields are up to 10^6 V/cm order (Table 1) for both MoSSe and WSSe. The DFT calculated projected band structures of 1 and 2-layer-MoSSe/graphene systems with different side contact are calculated to show the p- and n-type contact formation (Fig.1). If graphene makes contact with the Se-side, the 0.2 eV N-type Schottky barrier is formed. And yet, if graphene makes contact with the S-side, we see a 0.3 eV P-type Schottky barrier. In the 2-layer MoSSe case, we find that the N-type barrier for S-side contact is reduced to 0.1 eV, and the Se-side achieves p-type ohmic contact. The intrinsic dipole-induced p- and n-type ohmic contact can also be formed at the metal/MoSSe interface. The DFT extracted data, such as spontaneous polarization and thickness, are further put into the 2D finite difference Poission-Schrödinger solver developed by our lab to design the transistor. Similar to the GaN HEMT devices, this intrinsic dipole in MoSSe material causes band bending, producing 2DEG and 2DHG at the interface region (Fig.2). Thus, the p-FET and n-FET structures are constructed by placing a channel region between two Metal/MoSSe interfaces through attaching contacts to the different faces of JTMD. Then combining p- and n-FET, the CFET structure can be fabricated using a single film. Based on the above-mentioned property, we design the p- and n-FET structure shown in Fig.3 and Fig. 4 and perform the simulation. The double gate structures are used to have better control of the channel. To make the enhanced mode of operation, the HfO_2 material was chosen as the gate dielectrics. The device achieves a smaller SS value (~61 mV/dec) (Fig.5 and Fig. 6). Fig. 7 is the majority carrier density plot with different gate biases, the switching between on and off states can be observed. Furthermore, to make the device fabrication process realistic, we proposed a structure that could be built layer by layer (Fig.8). Based on the I-V curve obtained from the 2D simulation result, we built the model and further performed the circuit simulation by LTspice (Fig.9). Set V_{DD} equals to 1.5V, and the middle plot is Vin to V_{out} of the CMOS inverter. The JTMD materials have a similar transport property as MoS_2 and WS_2. With the built-in polarization field and a proper design, it is possible to make CFET devices in a single thin film without doping.

2:30 PM H04
(Student) Non-Conductive Electron Transport Through a Quasi-Freestanding Epitaxial Graphene-Insulator Heterostructure Towards a Vacuum-Independent X-Ray Source Daniel Lewis and Kevin Daniels; University of Maryland, United States

X-ray radiation has many uses in industry and medical diagnostics. X-rays are generated when electrons are emitted from a source and accelerated by an applied field to a high enough energy that they can experience inelastic collisions with the electrons of a target atom, kicking them to higher energy states which, when they decay, release characteristic X-rays which can be used to analyze samples of arbitrary composition. For such interactions to be possible, the emitted electrons must travel to the target atom with their kinetic energy preserved. In X-ray generation, this is achieved by having the electron source and the anode target separated by a vacuum gap in which the electrons are accelerated by an electric field, impacting the anode, with the X-rays either reflecting off at a known angle (reflection emission) or punching through a thin anode material and emerging on the other side (interaction emission).
We have previously demonstrated controllable electron emission in vacuum at current densities exceeding those of similarly scaled thermionic sources by more than an order of magnitude using patterned quasi-freestanding epitaxial graphene microstructures. In this work, we describe a vacuumless interaction X-ray emission source using these planar, scalable structures. To enable this, the CASINO package was used to model energetic electron behavior and x-ray emission in material stacks. Electrons accelerated by a sufficiently strong electric field can pass through solid materials without needing to interact with an available density of states, instead only experiencing collisions with the electrons and nuclei of the material they pass through. The propensity of the incoming electrons to pass through the material with few enough interactions such that their final energy is close to their initial could be imagined as a kind of ‘electron transparency.’ By layering a thin insulating material with a sufficiently open crystalline lattice to minimize collision probability onto a graphene electron source, the resultant heterostructure can exhibit controllable electron emission within the window of electron transparency allowed by the insulator. This heterostructure could function as two of the components for X-ray generation: an electron source and the interstitial medium, between the source and an anode, that the electrons accelerate through but not as a conduction current. Due to the nature of their construction and operation, a similar process could not be employed on a thermionic or field emission source.
The electron transparency of a material can be classified based on the effect the material has on the emission current density of the substrate graphene electron source. X-ray generation requires that approximately 10^{10} $cm^{-2}s^{-1}$ X-ray photons are generated; with an expected rate of approximately 1% of incoming electrons generating such photons, an electron source should be producing on the order of roughly 0.16 $\mu A/cm^2s$ to be considered an effective source for x-ray generation. Therefore, interstitial materials and necessary thicknesses are presented that can be regarded as sufficiently electron transparent if the resulting heterostructure emitter can still produce emission current densities at or above this threshold. A patterned epitaxial graphene microstructure is used to evaluate the electron transparency of various compositions and thicknesses of insulating materials. The graphene electron emitter is fabricated from hydrogen intercalated quasi-freestanding bilayer epitaxial graphene on silicon carbide, the insulating materials are deposited in incremental layers of discrete thickness via e-beam evaporation, and a capture plate anode in a vacuum measures emission current. For this study, evaluation of the electrons’ final energy distribution is not considered, with the electron transparency of the insulating material instead being given an interim determination based solely on the resultant emission current density.

2:50 PM H05
Humidity Tolerant Low Power-Consumption Flexible α-Fe_2O_3/rGO/PANI Ternary Nanocomposite for NO_2 Gas Sensing at Room Temperature Kshitij Sharma[1], Atul Kumar[1] and Ghanshyam D. Varma[2]; [1]Indian Institute of Technology Roorkee, India; [2]I. I. T. Roorkee, India

Presently, air pollution is among one of the significant global problems caused due to the release of hazardous gases in the environment due to rapid industrial growth. It is becoming harmful to the health of living beings. NO_2 is one of such several pollutant gases which is produced by burning of fuel during combustion in power plants, trucks, buses, cars, and massive engines. The measurement of NO_2 gas is essential for industries, biomedical, technical, and human life. Therefore, it is required to synthesize some advanced sensing materials which is highly selective, sensitive and humidity resistive. For the practical application of room temperature gas sensing, relative humidity (RH) causes critical issues. Here we synthesize a high-sensitive and flexible α-Fe_2O_3/rGO/PANI ternary nanocomposite based NO_2 gas sensor which work at room temperature. Sensor significantly enhances their humidity resistance property at a low operating voltage (0.4 volt) as shown in Fig. (a, b). To fabricate the gas sensing film, a flexible tempered glass (FTG) substrate has been used. Further by using a vacuum coating unit, the silver interdigitated electrodes (IDE) were coated on an FTG substrate. The optimal composite shows a very high 62 % response at 10 ppm NO_2 gas with a very low detection limit (0.25 ppm) depicted in fi Fig. (c). The sensor shows a negligible response for other toxic gases such as C_3H_6O, C_2H_5OH, CO, NH_3, and Cl_2 at 100 ppm, Fig. (d). The enhanced sensing performance can be credited to the development of a unique ternary structure between α-Fe_2O_3/Polyaniline and reduced graphene oxide sheets. Such invention of α-Fe_2O_3/rGO/PANI ternary nanocomposite sensors implies that it is an effective nanohybrid material for the fabrication of low power consumption, humidity tolerant, flexible, and highly selective room temperature NO_2 gas sensor.

3:10 PM BREAK

3:30 PM H06
(Student) Graphene/III-As Nanosheets—Self-Assembly, Electrical Transport and Potential for THz Generation Saad Bhuiya, Carly Strickland, Ruhin Chowdhury, Emma J. Renteria, Thomas J. Rotter, Ganesh Balakrishnan and Francesca Cavallo; University of New Mexico, United States

We report our initial results on the fabrication and characterization of 2D materials/III-As semiconductors heterostructures in a planar and helical geometry. These materials promise to support the generation of cyclotron THz radiation with technologically relevant levels of power density (i.e., between 100s mW/cm^2 and few W/cm^2) under an applied DC bias. An intuitive approach based on a time-of-flight and interference argument shows that radiation frequencies in the THz range are expected from helices with a radius ranging from a few tens to a few hundred nanometers. The exceptional compliance of 2D materials allows them to bend with nanoscale radius curvature without any plastic deformation. A 2D material with high carrier mobility is also required to limit carrier scattering within the helices and thus reduce spectral broadening around the center frequency. h-BN/graphene/h-BN heterostructures will potentially satisfy all the desired attributes to generate cyclotron radiation based on previously reported values of carrier mobility.
We create the helical ribbons via guided self-assembly of graphene-based/GaAs/$In_xGa_{1-x}As$ heterostructures with a thickness of ~2-20 nm. This process enables the fabrication of nanoscale-diameter structures whose dimensions can be precisely manipulated in that they depend on residual strain in a nanosheet, its stiffness, and its geometry in the plane perpendicular to its thickness. These are all parameters that can be readily controlled via top-down processing techniques.
In our work, multi-layer stacks comprising a GaAs/$In_xGa_{1-x}As$ bilayer and an AlAs sacrificial layer are deposited by molecular beam epitaxy on a (001) GaAs substrate surface. Materials combinations and growth conditions are appropriately selected to establish a large strain gradient across the thickness of the III-As bilayer. We then fabricate h-BN/graphene/h-BN heterostructures on the semiconductor bilayer via polymer-assisted release, transfer of the 2D materials, and vacuum annealing in Ar atmosphere to remove the polymer support. X-ray photoelectron spectroscopy characterizes the removal of the polymer during annealing. Next, the 2D materials/GaAs/$In_xGa_{1-x}As$ nanosheets is patterned into ribbons at a non-zero angle with the softest crystallographic direction in GaAs. Selective etching of the AlAs sacrificial layer results in the nanosheet bending and twisting towards the softest crystal direction (i.e., <100>). We have fabricated structures with a scalable diameter between 30 nm and 800 nm, as estimated by scanning electron microscopy.
In addition to illustrating the controlled synthesis of graphene helical ribbons, we present magnetotransport and multi-carrier analysis techniques to characterize mobilities and carrier concentrations in the fabricated heterostructures. A precise knowledge of these parameters will improve our predictive capability of the electromagnetic radiation originated by accelerated charges along the helical path. We fabricate graphene-based/GaAs/$In_xGa_{1-x}As$ Hall bar devices on AlAs-coated substrates and perform variable temperature magnetotransport on a Quantum Design Magnetic Properties Measurement System (MPMS). Multi-carrier analysis techniques are used to shed light on the dominant carrier scattering mechanisms and surface transfer doping of encapsulated graphene on III-As nanosheets.
ACKNOWLEDGEMENT. This work was supported by the U.S. AFOSR/Clarkson Aerospace Corporation through award No. FA9550-21-1-0460/UNM 21-1-0460.

3:50 PM #H07
(Student) Control of Dark Exciton Dynamics in Suspended WSe_2 Monolayer via Electrostatic Deflection Frances Camille M. Wu, Shang-Hsuan Wu, Xintong Li, Jean Anne Incorvia and Edward T. Yu; The University of Texas at Austin, United States

Strain engineering is a powerful tool that strongly influences electronic structure and exciton states in 2D transition metal dichalcogenides (TMDs). Among TMDs, WSe_2 has gained attention as a host for quantum emitters due to its intrinsic ground exciton state–a lowest-lying dark exciton state that hybridizes with defect levels upon strain, giving rise to bright single photon emitters. In particular, the application of uniform biaxial tensile strain to monolayer WSe_2 causes a downshift of the conduction band minima at K and K' valleys which then hybridize with states within the band gap that originate from point defects in WSe_2 such as Se vacancies. This hybridized state allows optical transitions of long-lived dark excitons which are otherwise forbidden for unstrained WSe_2 due to spin and momentum conservation. The high oscillator strength, increased charge and spin lifetime, and long diffusion length of dark excitons allow them to store and transport quantum and classical information which could be beneficial for quantum information processing, sensing, and secure communications. Therefore, the ability to manipulate the emission of dark exciton states is crucial for the design of future quantum emitters based on strained monolayer WSe_2.
Recent advances in spatially localized quantum emitters based on strained WSe_2 utilize strain fields created via transfer of monolayer WSe_2 to prefabricated dielectric nanopillars, metal nanoparticles, etched trenches or holes, or through precise nanoindentation techniques using atomic force microscopy. However, the above-mentioned methods provide low quantum emitter yield due to monolayer piercing, random and uncontrollable quantum emission, limited substrate effects, and restrictions in operating conditions. To realize high purity and tunable quantum emitters, it is necessary to have controllably strained WSe_2 devices operating at cryogenic temperatures. In this study, we demonstrate control of dark exciton dynamics of suspended WSe_2 monolayers via electrostatic deflection at cryogenic temperatures. Our technique implements strain fields which are generated by applying a bias voltage between a suspended

WSe_2 monolayer and an electrode in a back gate geometry. Since the monolayer WSe_2 is grounded and the back gate is positively biased, an electrostatic force is induced between the two surfaces, which in turn results in the deflection of the suspended WSe_2 monolayer membrane. Experimental results revealed a significant monolayer deflection of ~50 nm at 15V gate bias at 300K, corresponding to ~0.3% biaxial tensile strain. Moreover, photoluminescence measurements at 7K showed a ~20 meV shift of dark exciton emission peak from 1.67 eV (0V) to 1.65 eV at (30V), corresponding to approximately 0.2% biaxial tensile strain assuming a redshift of all exciton peaks at a rate of 95meV/%. This strain value is lower than our theoretical result (0.6% strain at 30V) which could be attributed to the change in mechanical constants and built-in strain at lower temperatures. This dark exciton emission shift is an essential step towards the development of controllable WSe_2-based quantum emitters that can be integrated into various optoelectronic systems.

4:10 PM H08
(Student) Effects of Strain and Local Topography on Electromechanical Coupling in Monolayer Transition Metal Dichalcogenides Claire Ganski, Alex De Palma and Edward T. Yu; The University of Texas at Austin, United States

Two-dimensional transition metal dichalcogenides (2D TMDs) have been extensively studied in recent years due to their remarkable electronic, optical, and mechanical properties. Their ability to withstand high levels of strain without fracture makes 2D TMDs attractive candidate materials for devices such as quantum emitters and wearable energy harvesters. This same ability, however, can have pronounced effects on device performance when unintentional sources of strain cause property changes via deformation potentials and electromechanical coupling. One such source of strain is nanobubbles, which are ubiquitous in mechanically exfoliated 2D samples. When using piezoresponse force microscopy (PFM) to measure the flexoelectric effect in 2D TMDs, we observed that nanobubbles showed greatly enhanced electromechanical coupling compared to flat regions, beyond the difference expected due to the absence of substrate pinning. Measurements of flexoelectric moduli in ostensibly flat monolayers may therefore yield overestimates due to the inclusion of nanobubbles in the analyzed area. Our PFM measurements show consistent reduction in the calculated effective flexoelectric coefficient when the data are filtered to exclude nanobubbles, resulting in a more accurate value for unstrained material.
We have also used PFM to characterize the detailed influence of strain, via nanobubbles in exfoliated MoS_2 monolayers, on electromechanical behavior in monolayer TMDs, focusing in particular on strain-dependent enhancement of out-of-plane electromechanical responses. Small bubbles with diameters under 100 nm consistently produce enhanced piezoresponse compared to flat regions. Large bubbles with diameters on the order of hundreds of nanometers exhibit an unexpected PFM profile. Rather than increasing monotonically from perimeter to apex, the piezoresponse amplitude of large bubbles reaches its peak near the perimeter and subsequently decreases toward a local minimum at the bubble center. Combined with the calculation of the strain tensor by representing nanobubbles as thin plates and numerically solving the biharmonic von Karman partial differential equation, these results reveal a correlation between electromechanical response and strain derivatives. We posit that this correlation occurs due to their mutual connection to the local symmetry of the crystal. Within the bubble, the crystal's mirror symmetry is broken, allowing one or more of the out-of-plane piezoelectric tensor elements to become nonzero. The enhanced electromechanical response associated with inhomogeneous strain is likely to have significant implications for a broad range of TMD-based 2D device structures due to the ubiquity of localized strain and the presence of band-edge energy shifts and electrostatic bound charges in those same features.

4:30 PM H09
(Student) Studies of 2D Material Resistive Random-Access Memory by Kinetic Monte Carlo Simulation Ying-Chuan Chen[1], Yu-Ting Chao[1], Edward Chen[2], Chao-Hsin Wu[1] and Yuh-Renn Wu[1]; [1]National Taiwan University, Taiwan; [2]-, Taiwan

This research has studied a resistive random-access memory (RRAM) with different two-dimensional (2D) materials, including experiments and simulations. The physical parameters in the kinetic Monte Carlo (KMC) model have been obtained through data calibration. The model fits well to the I-V characteristics, retention time, and breakdown electric field, On/Off ratio with different 2D layer thicknesses. We built physical models of WS_2, MoS_2, and h-BN RRAM through KMC simulation and experimental data and extracted the physical parameters of the three 2D materials. Through theoretical formulas, we also calculated the retention failure times of WS_2, MoS_2, and h-BN RRAM, which are, respectively , $1.23x10^4$, $3.18x10^4$, and $1.18x10^7$ seconds. Compared with the benchmark device (HfOx RRAM [1]), Our research shows that 2D RRAM has a lower generation activation energy to generate defects at a smaller bias. The diffusion activation energy of ions along the in-plane direction (i.e., X-Y plane) is greater than that of the out-of-plane direction (i.e., Z direction), which means that ions tend to diffuse along the out-of-plane direction. The reason may be due to the polar molecules between the layers. It is caused by the electrostatic attraction (van der Waals force) along the out-of-plane direction and the electromagnetic repulsion force along the in-plane direction of adjacent bonded atoms in the same layer. Under the 2D layered molecular arrangement, the torque perpendicular to the plane is more likely to cause molecular bond breaking to form the defects. Therefore, the set/reset switching voltage of 2D RRAM is lower than that of HfO_x, which means 2D RRAM has a faster resistance switching speed. The simulated results show MoS2 has the shortest switching time. So, MoS_2 is the most suitable for making RRAM devices among the three 2D materials.
To verify the reliability of the KMC model, we will conduct a series of experiments and simulation comparisons for WS_2. For the temperature-dependent analysis, the current characteristics at high bias voltage are more significantly affected by the temperature change. Then, we discussed the physical characteristics of RRAM made of 2D materials obtained by mechanical exfoliation and chemical vapor deposition (CVD) technology. The WS_2 samples obtained by mechanical exfoliation mostly belong to the single crystal structure, and the WS_2 grown by CVD mostly belong to the polycrystalline structure. Therefore, CVD WS_2 has smaller domains and more defects. Each layer has more gaps and vacancies, and the probability of sulfur ion drifting and diffusing between the upper and lower layers is greatly increased. This material property leads to more significant ion transport behavior in the out-of-plane direction than in the in-plane direction. Moreover, the internal electric field of the device in the out-of-plane direction also has a major contribution. Therefore, it is reasonable to adjust only the diffusion activation energy in the out-of-plane direction for data fitting. The results show that 2D materials grown by CVD have better device characteristics and are more suitable for making RRAM. The breakdown electric field of WS_2 as 155 MV/m was obtained with the electrical analysis for different active layer thicknesses. The thickness models for simulation were built to find out the best thickness of WS_2 RRAM, which has the highest On/Off ratio, to avoid bit-read errors. The simulated results show that 40-nm-thickness WS_2 RRAM is the best thickness.
For the development of 2D RRAM, the rapid drift of ions in 2D materials helps to manufacture RRAM devices with faster switching speeds. This advantage can solve the slow switching speed of traditional solid-state disks and the volatile memory property of DRAM. 2D RRAM can make up for the speed gap of the memory hierarchy [2]. To find the faster switching speed RRAM, 2D RRAM can carry out more in-depth experimental and simulated studies on MoS_2 RRAM in the future.

4:50 PM H10
Electrically Detected Spin Resonance in Graphene Ramesh G. Mani; Georgia State University, United States

Graphene is an appealing material for spin-based quantum computing and spintronics due to the predicted long spin lifetimes resulting from the weak spin-orbit interaction and the scarcity of electron-spin-dephasing spin-active-nuclei in natural carbon. However, spin studies of graphene have been constrained because traditional techniques lack the sensitivity to detect the small number of spins in a one- or few atomic layer thick graphene nanostructure. Here, we report on the resistive electrical detection of spin resonance in graphene. Our microwave photo-excited transport study of graphene reveals, surprisingly, a strong microwave response and dual microwave-induced resonances. The results demonstrate resistive detection of spin resonance, identify a remarkable "orbital-cooling-mechanism" in resistive resonance detection, provide a measurement of the g-factor and spin relaxation time, and exhibit a finite splitting in the observed dual resonance transitions even in the limit of a vanishing magnetic field. The last feature has been suggested[1] as a possible manifestation of the quantum spin Hall effect,[2] predicted by Kane and Mele for the graphene system including a weak spin-orbit interaction. Lithographically realized, electrically contacted graphene devices were cooled to liquid helium temperatures inside a superconducting solenoid, and irradiated with microwaves transmitted via waveguides and coaxial cables over the frequency range of $10 \leq f \leq 50$ GHz at a source-power $0.1 \leq P \leq 10$ mW. Measurements are reported for p- and n-type samples. Typically, the observed resonances followed two lines in a excitation frequency vs. magnetic field plot: one set of resonances fit a a first line that satisfied the equation F = 27.2 B, as the second set of resonances fit a second line that satisfied F = 10.8 + 26.9 B. Here, F is in units of GHz and B is in units of Tesla. The observed slopes here suggest a g-factor $g_{//}{}^1 = 1.94$ and $g_{//}{}^2 = 1.92$ for the two branches, respectively, and a zero field splitting $\Delta_0 = 44$ μeV for the observed offset of 10.8GHz between the two spin resonance branches. The two observed resonance branches are thought to correspond[1] to spin resonance at the edge- and within the bulk- of graphene, as the observed zero-field spin splitting is thought to be a direct measure of spin-orbit induced bulk splitting in graphene. In this presentation, we highlight these and other features in observed in our study of electrically detected spin resonance in graphene.
1) J. Sichau et al., Phys. Rev. Lett. 122, 046403 (2019).
2) C. L. Kane and E. J. Mele, Phys. Rev. Lett. 95,226801 (2005).

SESSION I: Novel IR Detector Materials
Session Chairs: Kyle McNicholas and Leland Nordin
Wednesday Afternoon, June 28, 2023
UC, Flying A Studios

1:30 PM I01
The Effects of Strain Compensation in Type-II InGaAs/GaAsSb Quantum Wells Grown on GaAs(001) Substrates Samatcha Voranthamrong[1], Zon .[1], Chao-Chia Cheng[2], Tzu-Wei Lo[1], Zhen-Lun Li[1], Chun-Nien Liu[1], Chun-Te Chiang[3], Li-Wei Hung[3], Ming-sen Hsu[3], Wei-Sheng Liu[4], Jen-Inn Chyi[2] and Charles W. Tu[1]; [1]National Chung Hsing University, Taiwan; [2]National Central University, Taiwan; [3]Epileds, Taiwan; [4]Yuan Ze University, Taiwan

Semiconductor lasers have a wide range of applications in industry and our daily life. Vertical-Cavity Surface-Emitting Lasers (VCSELs), developed from the 1980's, have several advantages, compared to edge-emitting lasers, such as wafer-scale testing, uniformity, scalability, circular beam, single-mode, 2D array, etc. A VCSEL consists of a light-emitting active region sandwiched between a top Distributed Bragg Reflector (DBR) and a bottom DBR.

In 2017, Apple released the iPhone X embedding VCSELs for face recognition. This was a game-changer. The market is expected to reach $1.9 billion in 2027. Current VCSELs on cell phones for facial recognition are based on 940 nm VCSELs consisting of GaAs/AlAs DBRs grown on GaAs(001) substrates.
It is desirable to have longer-wavelength VCSELs, however, because the screen of a smart phone is transparent at longer wavelength (1380 nm) and because of eye safety. The maximum permissible exposure to the retina is higher for wavelength longer than 940 nm. Long-wavelength lasers beyond 1300 nm is commonly fabricated on InP substrates because those wavelengths cannot be accessed by the GaAs/AlGaAs material system. However, it is not practical to grow a DBR on InP because the difference of the index of refraction of InP-based DBR pair, such as InGaAs/InAlAs, is relatively small, compared to that of GaAs/AlAs DBR pair. Thus, many more pairs must be grown to achieve high reflectivity. Also, InP substrates are smaller, more fragile, and more expensive than GaAs substrates. There are several approaches to produce long-wavelength emission from heterostructures grown on GaAs substrates: (1) self-assembled InAs/(In)GaAs quantum dots (QDs), (2) dilute nitride GaInNAs(Sb)/GaAs quantum wells (QWs), (3) wafer bonding of InGaAsP/InP active layers to top and bottom GaAs/AlAs DBRs, and (4) type-II InGaAs/GaAsSb QWs. Each approach has its pros and cons. Here we report on the type-II InGaAs/GaAsSb QWs because QWs have more volume for light amplification than QDs, fewer defects than dilute nitrides, and simpler in processing than wafer bonding. The emission wavelength can be tuned independently by the composition and thickness of the electron and hole quantum wells. There are only a few reports on InGaAs/GaAsSb QWs grown on GaAs substrates. InGaAs and GaAsSb are both compressively strained to GaAs, and tensile-strained GaAsP can be grown to compensate InGaAs and GaAsSb. There is one report of MBE-grown strain-compensated GaAsP/GaAs/GaAsSb VCSELs on GaAs, emitting at 1266 nm. So far, there does not seem to be a report on strain-compensated GaAsP/InGaAs/GaAsSb QWs, let alone VCSELs, on GaAs.
In this talk we report on molecular-beam epitaxy (MBE) and characterization of these QWs, specifically investigating the effects of strain compensation. The compositions and layer thicknesses are measured by high-resolution X-ray rocking curves and compared with simulations. Two series of samples were grown. One series have 3 InGaAs/GaAsSb samples grown in the same day: without the GaAsP strain-compensating layer, with GaP and with $GaAs_{0.8}P_{0.2}$ strain-compensating layers. We found that only the last sample with $GaAs_{0.8}P_{0.2}$ strain-compensating layers shows a strong low-temperature (LT) photoluminescence (PL) at 1100 nm.
The second series also have 3 samples with 2, 4, and 6 nm $In_{0.3}Ga_{0.7}As$ thickness while the corresponding $GaAs_{0.8}P_{0.2}$ thickness is also adjusted to maintain strain compensation and be within its own critical layer thickness. We found that only the 2 nm-thick $In_{0.3}Ga_{0.7}As$ sample shows a strong LT PL at 1050 nm, indicating 4 nm thickness is already larger than the critical layer thickness. These samples do not have room-temperature (RT) PL, but later samples grown with a higher substrate temperature show RT PL.
In conclusion, as expected, strain compensation is beneficial, and we are pursuing longer wavelength emission by adjusting the layer parameters through COMSOL and growth conditions.

1:50 PM I02
(Student) Minority Carrier Lifetime and Mobility in Bulk InAsSb for High Quantum Efficiency LWIR Detectors Jingze Zhao[1], Jinghe Liu[1], Kevin Kucharczyk[1], Dmitri Donetski[1], Gela Kipshidze[1], Gregory Belenky[1] and Stefan Svensson[2]; [1]Stony Brook University, The State University of New York, United States; [2]CCDC U.S. Army Research Laboratory, United States

Sensing and imaging in long-wave infrared (LWIR) range find in various fields [1]. In LWIR range barrier heterostructures with bulk InAsSb absorbers grown on graded GaInSb and AlInSb buffers on GaSb are a viable alternative to InAsSb/InAs strained layer

superlattices (SLS) on GaSb due to strong fundamental absorption and unimpeded hole transport. The fundamental absorption coefficient in bulk InAsSb was found to be up to 3 times greater than in LWIR InAs/InAsSb SLS [2]. It is also worth noting that LWIR InAsSb is produced near the bottom of the bandgap vs Sb composition bowing dependence, meaning that small variations in composition will have marginal effect on the abrupt rise of the absorption above the energy gap [3]. This enables high wavelength reproducibility and uniformity across a wafer. The growth of LWIR InAsSb requires a virtual substrate to reduce the number of threading dislocations that would otherwise form when using a GaSb substrate. Preliminary evaluation of such defects indicates promising numbers in the $1x10^5$ cm^{-2} range [4].

The barrier heterostructures for the LWIR detection were grown by molecular beam epitaxy on n-type GaSb substrates. The unstrained unrelaxed $InAsSb_{0.54}$ absorbers were grown with a 6.28 A lattice constant on GaInSb graded buffers and virtual substrates. All heterostructures had 2 um thick n-type unintentionally doped absorbers and the absorbers doped with tellurium to a $3x10^{15}$ cm^{-3} level. The nBn heterostructures with undoped absorbers had the target cut-off wavelength of 12 um at T =77 K.

The Al-Ga composition of AlGaInAsSb barriers was varied in order to obtain the optimal design experimentally for the lowest bias voltage enabling unimpeded collection of holes in the top contact. Optical characterization included measurements of PL spectra and minority hole lifetime by time-resolved PL with excess carrier concentrations down to a level of low 10^{15} cm^{-3}. The barrier structures with various mesa sizes were processed to determine the hole diffusion length from transient response to a pulsed excitation from the substrate side similar to the approach employed in Ref. 5. The longest minority hole lifetimes of 124 ns and 107 ns at T = 77 K were measured for the structures with undoped and doped absorbers, respectively. It was concluded that the lifetime was limited by Auger recombination due to background carrier concentration. Earlier the minority hole lifetime up of 550 ns was measured in a 10 um energy gap 4.3 nm period $InAsSb_{0.33}$/$InAsSb_{0.55}$ SLS grown on metamorphic buffers and virtual substrates with a 6.2 A lattice constant. In the range from 77 to 125 K the vertical hole mobility in the short period SLS was varied from 40 to 110 cm^2/Vs. The structures with bulk InAsSb absorbers showed the liquid nitrogen temperature hole mobility of 1000 cm^2/Vs. Thus, heterostructures with bulk InAsSb for LWIR absorption offer a factor of 2-3 greater hole diffusion length compared to that for short period SLS and therefore, can be grown with greater absorber thickness to realize the detectors with higher quantum efficiency.

The project was supported by DEVCOM Army Research Laboratory through the Center for Semiconductor Modeling and by Army Research Office award W911NF2010109.

[1] A. Rogalski, R. Ciupa, and W. Larkowski, Solid-State Electronics, **39**(11), 1593-1600 (1996).
[2] I. Vurgaftman, G. Belenky, Y. Lin, D. Donetsky, L. Shterengas, G. Kipshidze, W. L. Sarney, and S. P. Svensson, Appl. Phys. Lett. **108**, 222101 (2016).
[3] Y. Lin, D. Donetsky, D. Wang, D. Westerfeld, G. Kipshidze, L. Shterengas, W. L.Sartney, S.p.Swensson, and G. Belenky,. Electron Mater., **14** (10), 3360 (2015).
[4[N. Mahadik, S. P.Svensson, J. of Appl. Phys. **131**, 184501 (2022).
[5] J. Liu, D. Donetski, K. Kucharczyk, J. Zhao, G. Kipshidze, G. Belenky and S. P. Svensson, Appl. Phys. Lett., **120**, 141101 (2022).

2:10 PM I03
(Student) Optical and Structural Properties of InSb-Based Dilute-Bismide Alloys Grown by Molecular Beam Epitaxy Rachel C. White, Morgan Bergthold, Thomas Leonard, Amberly Ricks, Daniel Wasserman and Seth R. Bank; The University of Texas at Austin, United States

The incorporation of bismuth into traditional III-V alloys enables dramatic reductions in bandgap energy that can be advantageously leveraged for accessing particularly interesting transmission windows for optoelectronic devices. Achieving significant bismuth incorporation in III-V-Bi alloys, though, necessitates a highly optimized growth regime including low substrate temperatures to minimize bismuth desorption and V/III flux ratios near stoichiometry to minimize competition for anion sublattice sites.[1,2] Unfortunately, the utilization of such extreme growth parameters so disparate from the ideal growth conditions for the host matrix has caused the material and optical quality of bismuth-containing alloys to generally lag behind those of traditional III-V alloys. InSb, however, has the coldest ideal growth temperature of any traditional III-V alloy making it a particularly promising host matrix for dilute-bismide alloys. Furthermore, since InSb possesses the smallest bandgap energy of any traditional III-V binary, $InSb_{1-x}Bi_x$ can potentially be grown with long-wave infrared bandgap energies with minimal bismuth incorporation. In this work, we present our progress towards achieving wavelength extension from $InSb_{1-x}Bi_x$ demonstrating photoluminescence (PL) from $InSb_{1-x}Bi_x$ with the highest bismuth concentrations yet reported. Epitaxial $InSb_{1-x}Bi_x$ films were grown by solid-source molecular beam epitaxy on n-type (100) InSb substrates. A low substrate temperature of ~280°C, an Sb/In flux ratio near stoichiometry, and a relatively fast ~1 μm/hr growth rate were employed to promote greater substitutional bismuth incorporation. X-ray diffraction ω-2θ measurements of the $InSb_{1-x}Bi_x$ films suggested bismuth concentrations up to 2.25% in the films with a linear dependence of the bismuth concentration on the bismuth beam equivalent pressure. PL from the $InSb_{1-x}Bi_x$ films demonstrated a significant bismuth-induced bandgap reduction of ~21 meV/% Bi at 83 K, which is in line with previous measurements of high-quality $InSb_{1-x}Bi_x$ films.[3] PL measurements of the sample with the highest bismuth concentration at elevated temperatures showed a decrease in bandgap energy with increasing temperature as expected for an interband transition. Atomic force microscopy measurements of the films' surfaces revealed that the samples exhibited bismuth droplet formation.

As is typically observed for dilute-bismide alloys,[4,5] achieving droplet-free $InSb_{1-x}Bi_x$ surfaces is more challenging at elevated bismuth concentrations. Rather than focusing efforts on avoiding the formation of bismuth droplets during growth, we investigated multiple techniques to remove undesirable bismuth droplets after growth. Three post-processing techniques were performed on an InSb film with large bismuth droplets that possessed an RMS roughness of 23.4 nm as grown. All three techniques resulted in improved RMS roughnesses: 10.8 nm for digital HCl/H_2O_2 etching, 6.3 nm for physical polishing, and 5.9 nm for ion milling under a nonreactive argon beam. Unfortunately, wet etching left behind pits beneath where the bismuth droplets had been, physical polishing resulted in scratches on the sample surface, and ion milling saw remnants of the bismuth droplets still present on the surface. Potentially, a combination of these techniques could result in even further improvement in surface quality after bismuth droplet removal. Studies on the effects of droplet removal on optical quality are underway and will be reported at the conference.

This work was supported by Lockheed Martin, NSF (ECCS-1933836, ECCS-1542159), and an NSF Graduate Fellowship (RCW). The work was performed in part at the University of Texas Microelectronics Research Center, a member of the NNCI.

[1]S. Francoeur et al., *Appl. Phys. Lett.* **82** (2003).
[2]S. Tixier et al., *Appl. Phys. Lett.* **82** (2003).
[3]R. White et al., *Appl. Phys. Lett.* **121** (2022).
[4]A. Ptak et al., *J. Cryst. Growth* **338** (2012).
[5]M. Rajpalke et al., *Appl. Phys. Lett.* **105** (2014).

2:30 PM I04
(Student) Bismuth Incorporation in AlInSb for Wide-Bandgap Barriers on InSb Amberly Ricks[1], Rachel C. White[1], Qian Meng[1,2], Morgan Bergthold[1], Mark Wistey[2], Daniel Wasserman[1] and Seth R. Bank[1]; [1]The University of Texas at Austin, United States; [2]Texas State University, United States

Bi-containing III-V alloys have attracted significant attention over the past few decades due to their suitability for optoelectronic devices operating across the infrared; incorporating small amounts of Bi into

III-V materials offers the ability to decrease the bandgap energy, enabling extended infrared response.1 Current approaches for photodetectors operating in the long-wave infrared, such as HgCdTe and InSb-based devices, suffer from large dark currents.2 While nBn structures can suppress many sources of dark current, the use of AlInSb barriers in InSb-based nBn detectors result in a difficult tradeoff between an undesirably large valence band offset and high barrier layer strain that is difficult to manage.3 A flexible method to mitigate these challenges in InSb-based nBn detectors is to incorporate small amounts of Bi and Al into InSb to independently tune the bandgap of InSbBi absorber regions and AlInSbBi barriers, while simultaneously minimizing strain.

Experimental evidence suggests that the bandgap energy is expected to increase by 24 meV/% Al incorporated into InSb, and to decrease by 29 meV/% Bi incorporated into InSb.4,5 Approximately 55% of the bandgap change from the addition of Bi is expected to manifest in a valence band increase.6 Density functional theory simulations with hybrid functionals (HSE06) were performed using a 54-atom supercell with 1 Al and 1 Bi atom (corresponding to 3.7% Al and Bi). From these calculations, we predict that the direct bandgap energy of Al0.037In0.963Sb0.963Bi0.037 is reduced by ~20 meV from that of InSb. From these projections, roughly 5% Al is required for a sufficiently large conduction band offset and only 1.15% Bi is necessary to minimize the valence band offset. In this work, material properties of AlInSbBi alloys were investigated to evaluate its potential as a barrier layer.

AlInSbBi films were grown by solid-source molecular beam epitaxy on n-type InSb substrates. To promote Bi incorporation, the substrate temperature was maintained at or below 300degC and a low V/III flux ratio of 0.975x was employed. The growth rate chosen was ~1 μm/hr. The Al flux was held constant for each film targeting ~5% incorporation while the Bi flux was varied. X-ray diffraction ω-2θ scans were performed on the films and confirmed ~5% Al incorporation into the AlInSb(Bi). Surprisingly, the films all showed ~0.4% Bi incorporation despite an increasing Bi flux at both 300degC and 270degC substrate temperatures. Atomic force microscopy measurements showed that Bi droplets formed under higher Bi fluxes at 300degC while nanostructures formed at temperatures below 300degC, consistent with results from Rajpalke et al.5 We theorize that only ~0.4% Bi incorporated into all of the AlInSbBi films due to the precipitation of excess Bi into droplets and nanostructures. Optimization of the growth parameters, such as increased growth rate, may be able to mitigate droplet formation and increase Bi incorporation.7 Further growths are underway to increase Bi incorporation and optimize the material's structural and optical quality.

This work was supported by Lockheed Martin and NSF (ECCS-1933836, ECCS-1542159).

*Corresp. Author: afr768@utexas.edu, Phone: 1-512-471-5383

1Y. Gu et al., 'Dilute Bismide Photodetectors' in Bismuth-Containing Alloys and Nanostructures, Singapore: Springer Nature Singapore Pte Ltd., 2019, p. 229-230.
2P. Martyniuk, M. Kopytko, and A. Rogalski, Opto-Electron. Rev. 22, 2014.
3A. Evirgen et al., Elec. Lett. 50, 2014.
4J. Zhang et al., J. Appl. Phys. 126, 2019.
5M. K. Rajpalke et al., Appl. Phys. Lett. 105, 2014.
6M. P. Polak et al., Semicond. Sci. Technol. 30, 2015.
7A. J. Ptak et al., J. Cryst. Growth, 338, 2012.

2:50 PM I05

(Student) MBE Growth of InSb Quantum Well on InAs (100) Using AlInSb Buffer Layer Fatih F. Ince[1], Alexander T. Newell[2], Thomas J. Rotter[1], Subhashree Seth[1], Carter Heinrich[1], Martha McCartney[3], David J. Smith[3] and Ganesh Balakrishnan[1]; [1]The University of New Mexico, United States; [2]Air Force Research Laboratory, United States; [3]Arizona State University, United States

Mid-wave infrared (MWIR) detectors ($\lambda_{cut\text{-}off}$>3μm) are commonly used in medical devices, remote sensing, and spectroscopy [1]. MWIR III-V semiconductors, such as InSb ($\lambda_{cut\text{-}off}$=5.3μm) are more readily fabricated as infrared focal plane arrays (FPA's) because of their weaker ionic and stronger bonding property compared to II-VIs. III-V-based FPA's also have the advantage of spatial uniformity, temporal stability, scalability and affordability. This is particularly true in the case of InSb FPAs.[2] To cover the MWIR spectrum and reach the long wave infrared (LWIR) region, type-II superlattices such as InAs/InAsSb, bulk InAsSb on GaSb and metamorphic buffers are used [3]. Metamorphic buffers allow for better coverage of the MWIR spectrum by allowing for increasing antimony percentage in $InAs_xSb_{1-x}$. However, it is challenging to achieve repeatability in the growth of these thick buffer layers (4μm). Previously, direct growth of GaSb on GaAs has been achieved with a threading dislocation density of 10^8 per cm^3 and further reduction is possible with the use of defect filter layers [4]. In this research, we utilize interfacial misfit dislocations to grow fully relaxed InSb on InAs substrate as well as direct growth of $Al_xIn_{1-x}Sb$ buffer layers on InAs, similar to the GaSb/GaAs system. Developing a fully relaxed, low dislocation density buffer layer will be the basis for developing tunable InAsSb absorbers for MWIR and LWIR applications.

The MBE growth of InSb growth on a InAs substrate starts with the removal of native oxide. To grow a fully relaxed InSb layer using interfacial misfit dislocation arrays, the excess arsenic on the InAs surface must be replaced with antimony. We achieve this by eliminating the Arsenic flux. The surface is monitored using reflection high energy electron diffraction (RHEED). The RHEED pattern turns to 4x2 from 2x4 in the absence of arsenic supply which indicates the transition from a group V rich to a group III rich surface. The process is controlled manually by observation of the RHEED pattern transition, and an extra 30 seconds is added after the transition to achieve uniformity over the substrate. The next step involves growth of 500 nm thick $Al_{0.2}In_{0.8}Sb$ and $Al_{0.1}In_{0.9}Sb$ buffer layers to optimize the buffer layers with different growth temperatures. Finally, InSb quantum wells (QWs) are grown for photoluminescence analysis. Both the directly grown AlInSb and InSb epilayers on InAs substrates are analyzed using HR-XRD ω-2θ scans as well as reciprocal space mapping to quantify the dislocation density of the buffer layers. HR-XRD indicates a relaxation of 99.4% for the direct growth of InSb on InAs, and a slightly reduced value for the $Al_{0.1}In_{0.9}Sb$ and $Al_{0.2}In_{0.8}Sb$ epilayers. By using reciprocal space mapping, we are able to determine the screw and mixed dislocation density for the layers. TEM analysis of the samples shows formation of misfit dislocation arrays at the AlInSb/InAs interface. InSb QWs grown with different AlxIn1-xSb barrier layers are investigated by photoluminescence (PL). We will present a detailed analysis of the buffer layers with respect to threading dislocation density using XRD scans as well as TEM images. We will also present a comprehensive analysis of the InSb QWs on the basis of PL and TRPL results.

[1] W. L. Sarney, S. P. Svensson, Y. Xu, D. Donetsky, and G. Belenky, "Bulk InAsSb with 0.1 eV bandgap on GaAs," J. Appl. Phys., vol. 122, no. 2, p. 025705, Jul. 2017.
[2] A. Rogalski, "Next decade in infrared detectors," in Electro-Optical and Infrared Systems: Technology and Applications XIV, Warsaw, Poland, 2017.
[3] D. Z. Ting et al., "Advances in III-V semiconductor infrared absorbers and detectors," Infrared Phys. Technol., vol. 97, pp. 210–216, Mar. 2019.
[4] A. Mansoori et al., "Reducing threading dislocation density in GaSb photovoltaic devices on GaAs by using AlSb dislocation filtering layers," Sol. Energy Mater. Sol. Cells, vol. 185, pp. 21–27, Oct. 2018.

3:10 PM BREAK

SESSION J: Novel Materials Epitaxy
Session Chairs: Ganesh Balakrishnan and Kurt Eyink
Wednesday Afternoon, June 28, 2023
UC, Flying A Studios

3:30 PM J01
(Student) Single-Phase Orthorhombic SnSe-PbSe Alloy Thin Films Stabilized on GaAs by Molecular Beam Epitaxy Pooja D. Reddy[1], Leland J. Nordin[1], Brian Haidet[2] and Kunal Mukherjee[1]; [1]Stanford University, United States; [2]University of California, Santa Barbara, United States

The IV-VI semiconductor family of PbSe-SnSe alloys spans narrow direct bandgap materials in the Pb-rich cubic rocksalt phase, and indirect bandgap semiconductors in the Sn-rich layered orthorhombic phase. In recent years, there is growing interest in harnessing electronic and photonic properties of these orthorhombic phases that merit their study as epitaxial thin films. Specifically, there is excitement in harnessing in-plane ferroelectricity in SnSe demonstrated in the single or odd number bilayer limit [1]. Additionally, research groups are showing a large contrast in electronic and optical properties for phase-change devices across the orthorhombic to rocksalt structural transition that can not only be driven by temperature but also most by direct application of intense light-fields [2,3]. The development of growth recipes to fabricate high quality thin films of not only SnSe but also $Pb_{1-x}Sn_xSe$ offers new compositional routes to tune these properties. In this work, we synthesize $Pb_{1-x}Sn_xSe$ epitaxial films in the orthorhombic phase across a large composition range by molecular beam epitaxy, on technologically relevant III-V GaAs substrates. Importantly, we find it possible to stabilize metastable single phase compositions beyond what is expected in the bulk.
A Riber Compact 21 MBE system with compound PbSe and SnSe cells is used to grow films. (001)-oriented semi-insulating GaAs substrates are prepared by desorbing the surface oxide under a Se overpressure, followed by PbSe surface preparation steps. We find that smooth, out-of-plane single oriented SnSe films result both from samples grown with a PbSe dose, and samples grown with a PbSe dose and buffer layer.
We expand on the successful growth of SnSe on GaAs and use the identified surface preparation methods to grow orthorhombic *Pnma* space group $Pb_{1-x}Sn_xSe$ alloys on GaAs [4]. The $Pb_{1-x}Sn_xSe$ alloy composition is determined by the relative fluxes of the PbSe and SnSe compound cells. XRD results are used to extract orthorhombic lattice constants as a function of alloy composition, at room temperature. The difference in unit cell volume between alloys around X_{Sn}=0.5 and the predicted unit cell volume of similar composition $Pb_{1-x}Sn_xSe$ alloys in the cubic phase is small, implying a small energy cost to a phase transition at these intermediate compositions. In addition to structural properties, we will be reporting on the optical bandgap as a function of alloy composition.
Based on the bulk phase diagram of the PbSe-SnSe system, we expect alloy compositions from X_{Sn}=0.4-0.8 to be two phase; both cubic and orthorhombic. The X_{Sn}=0.64 sample is phase separated. However, we have managed to grow thin film samples at X_{Sn}=0.55 and X_{Sn}=0.74 which are purely orthorhombic. Moreover, these are not the only metastable sample that we have produced in this materials system. We have synthesized room-temperature stable orthorhombic *Cmcm* phase of $Pb_{1-x}Sn_xSe$, a phase typically only stable above 700 K. We will be exploring the structural properties of these samples further, including temperature cycling experiments to better understand the stability of these phases in the thin film limit.
[1] C. Kai, et al. …S.S. Parkin, *Nano letters*, **20**, 6590,(2020).
[2] T. Katase et al. ... T. Kamiya, *Science advances*, ***7***(12), (2021).
[3] Y. Huang, ... M. Trigo, *Physical Review X*, ***12***(1), (2022).
[4]B. Haidet et al. ... K. Mukherjee, Phys. Rev. Mater., **4,** 033402 (2020).

3:50 PM J02
(Student) Photoluminescence Efficiency and Minority Carrier Lifetime of Type-II Superlattices on GaAs Using an Interfacial Misfit Array Morgan Bergthold, Yadviga Tischenko, Rachel C. White, Seth R. Bank and Daniel Wasserman; The University of Texas at Austin, United States

Type-II superlattice (T2SL) materials have long been investigated for high-performance mid-infrared (mid-IR) optoelectronic device applications due to their bandedge engineering flexibility and large light hole-heavy hole splitting that is predicted to suppress Auger recombination [1]. In particular, they have drawn interest for infrared detector development because i) their effective bandgaps can span the mid-IR wavelength range, ii) the ability to individually engineer their conduction and valence band offsets has enabled their integration with barrier device architectures, and iii) they offer improved growth and fabrication uniformity and reduced toxicity compared to the current state of the art, HgCdTe. The III-V semiconductor T2SLs are all grown using the 6.1 Å family of materials (InAs, GaSb, AlSb, and alloys). These materials offer large type-II band offsets and can be grown lattice-matched to commercially available GaSb or InAs substrates. Unfortunately, focal plane array detector fabrication processes dictate that the constituent pixels be illuminated through the substrate, where below bandgap absorption can significantly reduce the light that reaches the device [2]. Circumventing this problem for 6.1 Å materials usually requires extensive additional fabrication including mechanical lapping, wet-chemical polishing, and wet-chemical etching to thin the substrate to 10s of microns. A more appealing approach to this problem would leverage semi-insulating, transparent substrates such as GaAs. Heterogeneous integration of GaSb onto GaAs is usually accomplished by growth of a thick metamorphic buffer, generally compositionally graded from the lattice constant of GaAs to that of GaSb by slowly adjusting group V fluxes. However, this approach requires extensive additional growth and struggles to bridge the gap between materials with very dissimilar lattice constants. In contrast, the interfacial misfit array, or IMF, approach transitions abruptly between lattice constants such that conversion occurs within a few monolayers of the interface. This method depends on optimizing growth conditions to promote strain relaxation via dislocations propagating along the interface. Since defects propagate parallel to, but not towards, the epitaxial stack grown above the IMF, high material quality can be achieved. This approach has shown improved thermal boundary conductance compared to GaSb/GaAs interfaces grown without the IMF technique [3] and has demonstrated detectors with similar behavior to those grown on native substrates [4]. In this work we investigate InAs/InAsSb mid-wave infrared (MWIR, 3-5 μm) T2SLs grown on highly mismatched GaAs substrates (7.8% lattice mismatch) via the IMF growth mode. We use molecular beam epitaxy to grow two samples each comprised of 500 nm thick MWIR T2SLs lattice-matched to GaSb and located between two 10 nm AlAsSb carrier blocking layers. The first is grown on a native GaSb substrate and the second on a virtual GaSb substrate grown on GaAs using the IMF technique. The optical properties of our materials are characterized by photoluminescence (PL) spectroscopy and the minority carrier lifetime is measured using time resolved photoluminescence (TRPL). The minority carrier lifetime, measured by fitting the exponential decay of the TRPL in the low-injection region of the decay curve, is reduced by 41% for the sample grown on the IMF, from t = 122 ns to t = 72.5 ns, while the peak PL intensity obtained is similar for each sample from 83 to 295 K, indicating suitability for device applications where optical properties play a significant role.
[1] C H Grein, P M Young, and H Ehrenreich, Appl. Phys. Lett. **61**, 2905–2907 (1992)
[2] A Chandola, R Pino, P Dutta, Semicond. Sci. Technol. **20** 886 (2005)
[3] P. Hopkins, J. Duda, S. Clark, C. Hains, T. Rotter, L. Phinney, and G. Balakrishnan, Appl. Phys. Lett. 98, 161913 (2011)
[4] A P Craig, A R J Marshall, Z B Tian, S Krishna, Infrared Phys. Technol., **67** 210-213 (2014)

4:10 PM J03
PbSe Mid-Infrared Light Emitting Diodes on III-V Substrates
Leland J. Nordin, Jarod Meyer, Pooja D. Reddy, Kelly Xiao and Kunal Mukherjee; Stanford University, United States

The mid-infrared (MIR) spectral range is essential for a host of applications. These applications prefer compact high-power sources of light that can operate at room temperature (RT), such as quantum well (QW) lasers or light-emitting diodes (LEDs). III-V semiconductor-based type-I MIR emitters, however, have struggled to achieve efficient RT performance due to fast Auger recombination rates and small band offsets in narrow-bandgap III-V materials [1]. Researchers have developed and commercialized type-II or intersubband III-V semiconductor heterostructures, such as quantum cascade lasers (QCL), interband cascade lasers (ICL), or type-II superlattice light emitting diodes (SLED), to overcome the deleterious characteristics of type-I MIR emitters. Despite being commercially available, QCLs, ICLs, and SLEDs all suffer from growth complexity. Thus, there is a need for MIR devices that are simple to grow, emit efficiently near 4 µm, operate at RT, and, importantly, can be integrated into mature III-V or CMOS fabrication processes. Recently, epitaxial thin films of PbSe grown on III-V substrates have shown remarkably high internal quantum efficiency (>20%) at RT and low growth temperatures (170 °C), [2]. The confluence of these factors suggests that heterogeneous PbSe/III-V devices are a promising candidate for MIR light emitting devices.
In this work, we demonstrate RT MIR light emission from electrically pumped PbSe/III-V devices. Using the large growth temperature window and defect tolerance of PbSe, we extended the crack-free thickness of PbSe films on III-V substrates to grow 308 nm thick n-PbSe/i-PbSe/pGaAs *n-i-p* diodes. The devices were grown on a pGaAs (001) substrate using a Riber Compact 21 molecular beam epitaxy system. The growth began by desorbing the GaAs substrate's native oxide under a Se flux. Following oxide desorption, a PbSe dose procedure was performed, and a PbSe nucleation layer was grown [3]. After the PbSe nucleation layer, the growth temperature was lowered to ~170 °C, and 293 nm of PbSe was grown. Finally, a 15 nm n-doped Sb:PbSe top contact was grown.
Following growth, devices were fabricated using standard photolithography, Ar-based dry etching for mesa delineation (540 µm x 740 µm), and electron beam evaporation of Pd metal for contacts. Figure 1 shows the current-voltage (I-V) measurements of the fabricated devices. The I-V curves display rectifying behavior, but with an abnormally high 8 Ω series resistance. We measured the electroluminescence (EL) of the LEDs using a custom µ-luminescence setup. Figure 2 shows the measured EL signal as a function of drive current. The peak of the devices' EL is at 4 µm MIR, approximately 0.5 µm longer-wave than the devices' peak photoluminescence (PL). This discrepancy between peak PL and EL could be due to band-filling from large photo injection and small electrical injection. In addition, the same µ-luminescence setup showed that the EL signal magnitude is one hundred times smaller than that of the devices' PL, indicating more work is needed on the devices' electronic structure.
We have grown PbSe/GaAs LEDs and measured their electronic and luminescence properties. The LEDs display rectifying behavior and emit MIR light but emit nearly two orders of magnitude less light when electrically pumped. Despite their poor EL, we remain optimistic that straightforward improvements to the electronic structure of the LEDs will dramatically increase EL and thus make MIR LEDs that are competitive with state-of-the-art III-V emitters. Most importantly, however, these LEDs represent a new frontier in dissimilar semiconductor devices, offering an abundance of exciting opportunities for producing new devices with novel properties and important functionalities.
[1] D. Jung, S.R. Bank, M.L Lee, and D. Wasserman, *J Opt .*, **19,** 123001 (2017).
[2] J. Meyer et al. ... K. Mukherjee, *APL Mater.*, **9,** 111112 (2021).
[3] B. B. Haidet et al. ... K. Mukherjee, *Phys. Rev. Mater.*, **4,** 033402 (2020).

4:30 PM J04
(Student) Monolithic III-V on $LiNbO_3$ for Nonlinear Optics Application Zezhi Wu, Hyun Uk Chae, Yiyan Yu and Rehan Kapadia; University of Southern California, United States

III-V materials nowadays are becoming a promising building block for nonlinear optics thanks to their significant nonlinear properties. MBE and MOCVD have been widely used to grow epitaxial films on various substrates. However, the difficulty in lattice matching, the constraint in substrate selection, the issue in epitaxial transfer aligning, and the cost in fabricating, become the barrier to applications. Here, we introduce a new thin-film epitaxial growth method, templated liquid phase (TLP) growth, to directly grow III-V semiconductor film on any substrate with single crystallinity, high uniformity, and high carrier mobility. As a demonstration, we choose lithium niobate (LiNbO3), a promising material widely used in nonlinear optics and acoustoelectric fields, as the substrate to grow patterned InAs layer. With this technology, we grow InAs in line-shape patterns with widths varying from 3 micron to 10 micron and lengths varying from 10 micron to 100 micron. Based on our measurements, the electron mobility reaches ~3500 cm^2/Vs at 100K and ~2400 cm^2/Vs at 300K. In prospect, TLP growth method can construct a platform to fabricate any desired patterns on any substrates in applications of nonlinear optics profit from the superior nonlinear properties of III-V semiconductors.

4:50 PM J05
(Student) Room Temperature Photoluminescence at 3-8 µm in Epitaxial PbSe-SnSe Alloy Films on GaAs Jarod Meyer, Leland J. Nordin and Kunal Mukherjee; Stanford University, United States

Light emitting diodes spanning the 3–12 µm range of the mid-infrared (MIR) portion of the electromagnetic spectrum are critically important for low cost solutions in chemical sensing, biomedical monitoring, and defense.[1] As the emission wavelengths extend deeper into the MIR, traditional LEDs based on III-V semiconductor materials struggle to emit brightly due to high nonradiative Auger recombination rates that quench quantum efficiencies of emission, especially at room temperature.[2] We have recently reported bright photoluminescence (PL) at 4 µm at room temperature from thin films of the IV-VI semiconductor PbSe grown epitaxially on 8% lattice-mismatched GaAs(001) substrates.[3] A high internal quantum efficiency of ~30% was estimated, thanks to the naturally low bulk Auger coefficients of PbSe and a high tolerance to dislocations generated from lattice-mismatched heteroepitaxy.[4] The bandgap energy of IV-VI materials can be further tuned across the entire MIR spectrum by alloying PbSe with SnSe ($Pb_{1-x}Sn_xSe$).[5,6] Thus, understanding the impact of Sn substitution on luminescence and carrier recombination pathways with respect to the good performance of PbSe is critical for the development of IV-VI-based LEDs across the technologically important 3–12 µm range.
In this work, we grow 40 – 110 nm thick $Pb_{1-x}Sn_xSe$ epitaxial films on GaAs (001) substrates by molecular beam epitaxy using compound PbSe and SnSe sources. These films were grown at 280–300 °C, after a GaAs surface pretreatment with PbSe flux at 400 °C to achieve single orientation nucleation,[7] and a PbSe buffer layer. Following $Pb_{1-x}Sn_xSe$ growth, a subset of films were capped in-situ with amorphous GeSe at temperatures below 160°C.
We find the PL intensity of uncapped $Pb_{1-x}Sn_xSe$ films degrades by over an order of magnitude with respect to binary PbSe, even for dilute quantities of Sn ($x < 0.01$). Significantly improved PL in $Pb_{1-x}Sn_xSe$ samples is achieved, however, by in-situ capping with amorphous GeSe and by increasing the PbSe buffer layer thickness to at least 50nm. We measure a monotonic increase in peak PL wavelength in $Pb_{1-x}Sn_xSe$ films from 0 – 30% Sn grown with optimized buffer and cap thickness. For the $Pb_{0.7}Sn_{0.3}Se$ layer, room temperature PL out to a peak wavelength of 8.4 µm is observed. We will present results investigating luminescence and carrier recombination in epitaxial $Pb_{1-x}Sn_xSe$, and explore potential mechanisms for luminescence degradation with respect to binary

PbSe. In addition, we will discuss the origins of the diminishing redshift in emission wavelengths seen in the highest Sn content films.
[1] D. Jung, S. Bank, ML Lee, D. Wasserman, *Journal of Optics* **19** 12 (2017).
[2] J. R. Meyer, C. L. Canedy, M. Kim, CS Kim, C. D. Merritt, W. W. Bewley, I. Vurgaftman, *IEEE Journal of Quantum Electronics* **57** 5 (2021).
[3] J. Meyer, A. J. Muhowski, L. J. Nordin, E. T. Hughes, B. B. Haidet, D. Wasserman, K. Mukherjee, *APL Materials* **9** 111112 (2021).
[4] M. Böberl, W. Heiss, T. Schwarzl, K. Wiesauer, G. Springholz, *Appl. Phys. Lett.* **82** 4065 (2003).
[5] H. Zogg, C. Maissen, J. Masek, S. Blunier, A. Lambrecht, M. Tacke, *Semicond. Sci. Technol.* **5** S49 (1990).
[6] H. Preier, *Appl. Phys.* **20** 189 – 206 (1979).
[7] BB Haidet, E. T. Hughes, K. Mukherjee, *Phys. Rev. Materials* **4** 033402 (2020).

SESSION K: Energy Materials and Devices
Session Chairs: Jamie Phillips and Edward Yu
Wednesday Afternoon, June 28, 2023
UC, State Street

1:30 PM K01
(Student) Photovoltaic Characteristics of PERC-Like CdTe Solar Cells Etee Kawna Roy, Kaden Powell and Heayoung P. Yoon; The University of Utah, United States

Rapid progress has been achieved in thin film CdTe solar cells, reaching a power conversion efficiency of 22.1 %. Researchers demonstrated a short-circuit current density (J_{sc}) of ≈ 31 mA/cm^2 and a fill factor (*FF*) of ≈ 79 %, close to the theoretically calculated maximum values. However, the open-circuit voltage (V_{oc}) remains below 0.9 V, much lower than the estimated V_{oc} of 1.2 V. One strategy to improve the V_{oc} is to implement a passivated back-contact on CdTe that can reduce the recombination by repelling minority carriers at the surface (i.e., electrons in CdTe). An aluminum oxide thin film (Al_2O_3) is an attractive candidate owing to its innate fixed negative charges ($10^{12} \sim 10^{13}$ cm^{-2}).
Here, we use a patterned Al_2O_3 layer on CdTe to produce PERC-like CdTe solar cells (CdTe PERC). This device architecture is similar to a passivated emitter and rear contact (PERC) design, frequently used in high-efficient *Si* solar cells. Samples of a 20 nm Al_2O_3 coated CdTe (dopant: *As*) were provided by First Solar. Before lithography, the samples were thoroughly cleaned with acetone and isopropanol (IPA). We optimized the laser beam doses to pattern the positive photoresist (S1813) on a rough CdTe surface (power: 18 mW, pixel energy: 75 %). The exposed photoresist was developed in a solution (AZ 1:1 developer) for 60 s and soaked in deionized (DI) water. We conducted a selective Al_2O_3 etching in tetramethyl ammonium hydroxide (< 3 % TMAH; AZ 300 MIF) for 20 minutes. The remaining photoresist was stripped off, and the samples were cleaned with acetone and IPA. This selective etching exposes the CdTe surface in a hole array pattern, where the metal can directly contact the surface, collecting hole carriers in the PV operation. Finally, metal contacts (2 mm × 2 mm) were formed using an electron-beam evaporator (3 nm *Cu* / 85 nm *Au*) using a stainless-steel shadow mask.
Statistical analysis of dark/light current-voltage (*I-V*) of our CdTe PERCs reveals notably different trends of V_{oc} compared to I_{sc} and *FF*. The hole diameter of the CdTe PERC is 10 µm, 20 µm, or 40 µm, whereas the pitch (distance between holes) ranges from 10 µm to 320 µm. Each PERC device consists of stacks of CdTe/Al_2O_3/metal and CdTe/metal (i.e., "exposed CdTe"). We observe the I_{sc} increases proportionally to the exposed CdTe area, from ≈ 1.2 µA (0.001256 mm^2) to ≈ 63.1 µA (0.19625 mm^2), and the *FF* increases from 32 % to 49 %. In contrast, the V_{oc} remains relatively constant (600 mV ~ 630 mV), suggesting the Al_2O_3 acts as a passivation layer.
We attempt to understand the role of dopants (*As*) in CdTe PERC operation. Fully completed CdTe PERCs were annealed at 70 °C for two hours while collecting their *I-Vs* every 5 minutes. The I_{sc} increases with time during annealing, indicating activation of part of the dopants in the CdTe absorber. We measure the light *I-Vs* after the annealing and compare them to the initial *I-V* characteristics. Interestingly, the magnitudes of the saturation current (I_s), I_{sc}, and *FF* remain unchanged or show marginal changes after annealing. However, the V_{oc} increases as high as 8 % of its initial value (e.g., 600 mV to 650 mV). This preliminary result suggests that the electrically active Al_2O_3 coupled with the defect chemistry in CdTe could impact the V_{oc} of CdTe PERC. Further investigations are in progress to optimize the PERC structures for CdTe-based solar cells.

1:50 PM K02
(Student) Compensation Centers in Group-V Doped CdTe Intuon Chatratin, Igor Evangelista and Anderson Janotti; University of Delaware, United States

CdTe-based solar cells are an important thin-film technology that is commercially available. Due to the comparably high efficiency but simpler manufacturing process, CdTe thin-film is the most competitive photovoltaic technology against Si-based solar cells. Today efficiency of CdTe solar cells of 22.1% is still far below the theoretical limit of 32%. Further improvement in efficiency relies on increasing hole concentration in the CdTe absorber. Group-V elements, including As, P, and Sb, are the most promising dopants acting as shallow acceptors. However, low doping activation is commonly observed in group-V doped p-type CdTe, and the cause of the compensation is still unclear. In this work, we use hybrid density functional calculations to investigate possible sources of the compensation in group-V doped CdTe. We find that Te vacancies are the most important compensation center acting as a deep donor. Regarding self-compensation from the group-V dopants, the formation of the AX center is unlikely. Instead of the dopant atom moving toward the next nearest Te as the same in the AX center, the group-V dopants pair together, forming V-V bonds and likely limiting the hole density. Using a highly reactive form of doping sources, such as dimer molecules (As_2, P_2 and Sb_2), favors the formation of this pair and increases the compensation centers, especially in the case of As. To avoid the formation of dopant pairs, controlling the doping source and optimizing its concentration is essential.

2:10 PM K03
Fiber-Shaped Hybrid Solar Cell and Storage Devices for Wearable Electronics Applications Arash Takshi[1], Reza Amirabad[1] and Tareq Kareri[2]; [1]University of South Florida, United States; [2]Najran University, Saudi Arabia

In most applications, an energy storage device is required when solar cells are applied for energy harvesting. Instead of integrating a dye-sensitized solar cell and a supercapacitor in one package, we have focused on novel composite materials for developing electrochemical devices with dual properties of energy harvesting and storage. We have studied the application of composite materials of a conducting polymer and dye materials for making electrodes of "photoactive supercapacitors". Devices with an open circuit voltage of 430 mV and storage time longer than 2 hours have been demonstrated. Also, composite gel electrolytes with the ability to conduct both ionic and electronic charges have been studied as a redox-photoactive electrolyte for concurrent energy harvesting and storage. The devised gel electrolyte has been applied as a coating layer on two different conductive threads and then twisted together to make a fiber-shaped hybrid cell for wearable electronics. The results of the study are encouraging to further customize the composite gel for enhancing the energy conversion efficiency and storage capacitance.

2:30 PM K04
InGaAs/GaAsP Multiple Quantum Well Enhanced Multijunction Photovoltaics Stephen Polly[1], Brandon Bogner[1], Anastasiia Fedorenko[1], Subhra Chowdhury[2], Dhrubes Biswas[2] and Seth Hubbard[1]; [1]Rochester Institute of Technology, United States; [2]Magnolia Optical Technologies, Inc., United States

InGaAs quantum wells (QW) grown by MOVPE are used to extend the absorption edge of GaAs photovoltaics into the infrared, increasing the current density with minimal loss in voltage as compared to a bulk GaAs device. GaAsP strain compensation is used to provide a tensile offset to the compressive strain in the wells, allowing growth of 50 pairs of strain balanced wells which did not exhibit detrimental effects of lattice relaxation/defect formation on photovoltaic figures of merit. Significant work was performed to optimize the growth and interfaces of these films to prevent step bunching and poor surface morphology and device performance when grown on offcut substrates, which are necessary for e.g. growth on non-polar germanium for a bottom junction or atomic ordering of InGaP for a top junction. A distributed Bragg reflector (DBR) is incorporated below the device, effectively increasing the optical path through the QWs and nearly doubling their sub-GaAs-bandgap collection per well. Dual-junction InGaP/GaAs devices were designed using a drift-diffusion model incorporating the optical effects of each subcell, connecting tunnel junction, and anti-reflective coating (ARC) along with the expected contribution of a varying number of QWs. These parameters were co-optimized to design control and QW-enhanced designs which were each nominally current-matched under AM0. Dual-junction devices were grown with an InGaP top junction coupled to either a control GaAs bottom cell without quantum wells or to the previously developed 50-QW enhanced GaAs bottom cell. Once fabricated, the QW-enhanced device provided an extra 2.6 mA/cm^2 from sub-gap absorption with a minimal loss in voltage (11 mV) compared to a control device without QWs or DBR, providing an absolute efficiency increase of 3.6% under AM0.

2:50 PM K05
Improved AC Field Hall Measurements Using Hybrid Filters Jeffrey Lindemuth, David Daughton and Emilio Codecido; Lake Shore Cryotronics, United States

Traditional lock-in amplifiers employ a simple IIR filter which can have long measurement times to produce acceptable noise reduction. Using AC field Hall Effect measurements, we demonstrate that a combination of digital lock-in output stage filters, FIR and IIR low pass filters, can produce improved noise reduction and measurement time over the traditional approach of independent IIR filters or FIR filters. We will present step response, equivalent noise bandwidth and autocorrelation times for a n pole IIR filter (n <=4) followed by a filter response of any finite length. We will demonstrate that the performance of the hybrid output filter, with time measured in units of FIR time, depend only on the ratio of the IIR time constant to the FIR time. Finally, we will present criteria for statistically independent samples for the various filter configurations.
AC field Hall Effect characterization is carried out with very low AC field frequency, typically 100 mHz, to avoid inductive pick-up in the measurement. Measurement times for a single voltage reading are as long as 60 seconds. The standard protocol for the Hall effect measurement includes current reversal and two different geometries which increases the number of voltage readings to 6 and results in a 6-minute total observation time to measure a single Hall voltage. Multiple Hall voltage readings are needed to calculate the of standard error of the Hall voltage and increases the measurement time in excess of 1 hour. An effective hybrid filter approach for AC field Hall effect measurement promises shorter measurement times or lower noise in the same observation window.
Because it is a well understood material, an InAs sample was chosen as a model system for performance testing of the hybrid output filter in an AC field Hall effect measurement. Using currents of 10 microamps, the Hall voltage will be on the order of a few microvolts for this InAs sample depending on the field magnitude. In this work, an InAs sample with 6.52e16 cm^{-3} carrier density was first measured in a Lake Shore Cryotronics 8407 using the AC field option of the 8400 system. Using a 10 microamp excitation current and 0.644 T AC field amplitude, the magnitude of the measured Hall voltage was 2.44 microvolts with a 119 nanovolt standard deviation. The measurement electronics were subsequently replaced with the Lake Shore Cryotronics Model M81 Synchronous Source Measure platform equipped with a balanced current source (BCS-10) and voltmeter (VM-10) and the Hall effect measurement repeated with the same magnet and power supply. The M81 lock-in was configured with a hybrid output filter consisting of an IIR filter with a 4 second time constant and 12 dB roll-off combined with a FIR filter with 40 second averaging time which results in a total settle time of the filter of 60 seconds. The measured Hall voltage was 2.47 microvolts with a standard deviation of the Hall voltage of 37 nanovolt – a factor 3.2 improvement in measurement uncertainty over the 8400 system.

3:10 PM BREAK

3:30 PM K06
(Student) Doped Ternary and Quaternary Transition-Metal Chalcogenides Electrocatalyst for Efficient Water Splitting Navid Attarzadeh[1], Debabrata Das[1], Susheng Tan[2], v. Shutthanandan[3] and Ramana Chintalapalle[1]; [1]University of Texas at El Paso, United States; [2]University of Pittsburg, United States; [3]Pacific Northwest National Laboratory (PNNL), United States

The design and development of sustainable and cost-efficient electrocatalysts, specifically those based on transition metal quaternary catalysts, for water-splitting has been of enormous interest in recent years. In the present study, we report on synthesizing sulfurized molybdenum (Mo) phospho-nitride catalysts using a continuous chemical vapor deposition (CVD) process on Mo-mesh. The structural characterization reveals that the crystal structure is a compromise of binary chalcogenide of MoS_2, with a complex mixture of the ternary phase of MoP_xN_{1-x} and a quaternary phase of $MoP_xN_{1-x}S$ with different quantities. The statistical population of formed phases is utilized to understand the effect of CVD-process parameters on phase stabilization. The improved performance of catalysts is achieved by strengthening the intrinsic activity of single/multi-active sites and expanding the active surface area. The best electrocatalyst demonstrates 50 and 120 mV overpotentials to attain current densities of 10 and 100 mA cm^{-2}, respectively. *In-situ* electrochemical impedance spectroscopy (EIS) provides insight into the prolonged stability of the formed quaternary phase during the electrocatalytic activity. Further, EIS studies confirm that quaternary phase formation decreases the charge transfer resistance and accelerates electron exchangeability at interfaces. The results and findings will be discussed in detail.

3:50 PM K07
Influence of Repeat Unit Structure on Exciton Transfer Between Semiconducting Polyelectrolytes Rachael Richards and Alexander Ayzner; University of California, Santa Cruz, United States

The growing global energy crisis demands that we find environmentally benign methods for artificial light harvesting. Aqueous inter-conjugated polyelectrolyte complexes (CPECs) are attractive candidates to serve as artificial energy-transfer antennae in an overarching, water-based light-harvesting system. This potential stems from their extended electronic states, sensitivity to their local environment, and tunable assembly thermodynamics. Electronic energy transfer (EET) between organic semiconductors is often described via the Forster model, which approximates the donor and acceptor chromophores as point-dipoles. However, in proximal extended systems such as CPECs this approximation is expected to break down. This leads to a strong dependence of the EET rate on the precise spatial extent of the excitonic wavefunction and thus the repeat-unit chemical structure of the conjugated polymers. The

aqueous, electrostatically assembled CPEC represents a potentially useful way to probe the foundation of EET between proximal conjugated polymer chains. To probe the dependence of the EET rate on the backbone chemical structure, we synthesized a chemical series of exciton-donor conjugated polyelectrolytes containing a poly(fluorene-*alt*-X) structure, where X is a set of distinct and compact aromatic monomers. We then assembled CPECs with varied X units and all other parameters fixed. In this report, I will first describe the native coil structure of the exciton-donor polyelectrolytes in aqueous solutions. Then, our work interrogating the dependence of the EET rate on the chemical nature of X in identically assembled CPECs with fixed strengths of electrostatic interaction and common exciton-accepting conjugated polyelectrolyte. To do so, we used a combination of ultrafast pump/probe spectroscopy and steady-state photoluminescence excitation.

4:10 PM K08
(LATE NEWS) Comparing the effect of TiO2 and SnO2 on efficiency of perovskite solar cells and development of efficient electron transport layer for perovskite solar cell Luis F. Hernandez Camas and Hongmei Dang; University of the district of columbia, United States

Luis F. Hernandez Camas, Hongmei Dang*, School of Engineering and Applied Sciences Department of Electrical Engineering, University of the District of Columbia

Perovskite solar cells (PSCs) are a promising solar cell with power conversion efficiency that has reached new records greater than 25%. However, the PSCs has not been commercialized due to the short lifetime. Researchers have studied stability and degradation of such PSCs with the goal of making them more reliable and relevant in the commercial market. To improve the performance and stability of PSCs, electron transport layer (ETL) is extremely important. ETL plays an important role as it's in charge of the mobility of electrons in an efficient manner. Therefore, the need for comparison is needed to achieve an optimal PSC structure. Using Solar Cell Capacitance Simulator (SCAPS), a one-dimensional solar cell simulator used in literature, we simulate our PSCs to optimize and improve device performance. Our first PSC consists of three layers Spiro-OMeTAD hole-transport layer (HTL), FAPBI3 perovskite layer and TiO2 electron transport layer (ETL). The second PSC also consists of the same structure layer with the difference of ETL layer being replaced by SnO2 to investigate effect of ETL on solar cell efficiency. The project takes in consideration different components such as thickness, bandgap, electron affinity, hole and electron mobility, and defects. Each of these properties are important to further understand how the perovskite layer interacts with SnO2 and TiO2 ETL layer. Then interlayer between SnO2 ETL and perovskite layer is introduced to further study how the interface states impact perovskite solar cell efficiency in order to understand mechanism of interface defects and minimize the interface recombination and improve open circuit voltage and solar cell efficiency

4:30 PM K09
Optimized Lithography-Free Fabrication of Sub-100 nm Nb_2O_5 Nanotube Films as Negative Supercapacitor Electrodes: Tuned Oxygen Vacancies and Cationic Intercalation Doha M. Mohammed[1,2], Kholood Salem[2] and Nageh Allam[2]; [1]Cairo University, Egypt; [2]American University in Cairo, Egypt

The direct growth of sub-100 nm thin film metal oxides has witnessed a sustained interest as a superlative approach for the fabrication of smart energy storage platforms. Herein, sub-100 nm Zr-doped orthorhombic Nb_2O_5 nanotube films have been synthesized directly on Nb-Zr substrate and tested as negative supercapacitor electrode materials. To boost the pseudocapacitive performance of the fabricated films, supplement Nb^{4+} active sites (defects) have been subtly induced into the metal oxide lattice, resulting in 13% improvement in the diffusion current at 100 m V/s over that of the defect-free counterpart. The defective sub-100 nm film (H-NbZr) exhibits areal and volumetric capacitances of 6.8 mF/cm^2 and 758.3 F/cm^3, respectively. The presence of oxygen deficient states enhances the intrinsic conductivity of the thin film, resulting in a reduction in the bandgap energy from 3.25 to 2.5 eV. The assembled supercapacitor device made of nitrogen-doped activated carbon (N-AC) and H-NbZr (N-AC//H-NbZr) can keep 93, 83, 78, and 66 % of its first cycle capacitance after 1000, 2000, 3000, and 4500 successive charge/discharge cycles, respectively. An eminent energy record of approximately 0.77 Wh/cm^2 at a power of 0.9 mW/cm^2 is achieved at 1 mA/cm^2 with superb capability.

SESSION L: Organic and Hybrid Materials for Optoelectronic Devices
Session Chairs: Deidra Hodges and Adrienne Stiff-Roberts
Wednesday Afternoon, June 28, 2023
UC, Lobero

1:30 PM L01
(Student) Monitoring Stability of Metal-Halide Perovskites Under Combined Stressors of Ion-Beam and Heat Mohammad Ashif Hossain Chowdhury, Yu-Lin Hsu and Heayoung P. Yoon; The University of Utah, United States

Rapid progress has been achieved in perovskite solar cells, improving the efficiency from 3.8 % to 25.7 % in less than a decade. However, the stability of perovskites still need to be improved before commercialization. This study reports the thermal stability of perovskites exposed to an ion beam irradiation. Such combined stressors are seen in atomic/nanoscale microscopy, where a perovskite lamella is characterized using a controlled heating/cooling stage. Focused ion beams (FIBs) are frequently used to section perovskites of interest. Previous studies proposed that high-energy electron beams could cause unexpectedly fast thermal degradation. Alternatively, the perovskite surface may be already altered during FIB processes, accelerating the deterioration.
We use a grazing angle argon ion (Ar^+) beam directly irradiated on methyl-ammonium lead iodide ($MAPbI_3$) to test the impact of ion beams to degradation mechanisms. This perovskite film was spin-coated on a stack of glass / FTO (fluorine-doped tin oxide; 200 nm) / SnO_2 (35 nm). A 4 kV Ar^+ ion beam was injected into a part of the $MAPbI_3$ sample at an angle of 3° for 10 minutes. A strong photoluminescence (PL) peak was observed near 765 nm (1.62 eV) for both samples, attributed to the bandgap emission. However, the PL intensity decreased by 40 % after the Ar^+ polishing. A finite difference time domain (FDTD) simulation estimates an approximately 40 % of the PL excitation (244 nm laser) can be absorbed within ≈15 nm of the $MAPbI_3$ subsurface. This result agrees with the ion-beam penetration depth, calculated by Monte Carlo simulations. The PL analysis and the numerical simulations indicate that the 4 kV ion beam irradiation at an incident angle of 3° introduces an optically inactive "dead layer (≈15 nm)" on $MAPbI_3$. We performed x-ray photoemission spectroscopy (XPS) to investigate possible surface compositional changes of $MAPbI_3$ under Ar^+ polishing. Quantitative XPS analysis shows an apparent reduction of the organic components (e.g., C, O, and N) after the ion beam irradiation. In contrast, XPS signals of the inorganic species (e.g., Pb, I) significantly increase with introducing the doublet metallic Pb (0) near the bonding energy of 137 eV and 142 eV. Overall, the I/Pb ratio decreases from 2.6 (pristine) to 2.1 (polished), suggesting the ion beam irradiation modifies the subsurface of $MAPbI_3$ to be a lead-rich, iodine-deficient layer (< 10 nm).
The impact of the modified subsurface of $MAPbI_3$ on thermal deterioration was qualitatively investigated using a heat lamp at 150 °C. Owing to the partial surface decomposition, we observed the ion-

beam exposed $MAPbI_3$ shows a faster decay than the control under the heating. Apparent deterioration of $MAPbI_3$ (yellow color) on the Ar^+ polished section after applying the heating stressor for 20 minutes. At this stage, the color of the pristine area remains unchanged (dark-brown color). The deterioration of the pristine area began at around 40 minutes. Both sample sections fully deteriorated at 70 minutes. Our experiment confirms that subsurface modification (≈15 nm) can significantly influence the deterioration mechanisms of $MAPbI_3$. This talk will discuss a new method of monitoring the deterioration of perovskites in real-time. A prototype design consists of a patch antenna (≈ 3 cm × 4 cm) and an array of four $MAPbI_3$ solar cells (1 cm × 1 cm). The distance of the adjacent solar cells is set to 1.4 cm in width and 0.6 cm in length. Computer Simulation Technology (CST) simulations display the resonance frequency of the patch antenna changes from 7.13 GHz to 7.07 GHz as the $MAPbI_3$ film decomposes to volatile species and PbI_2. While the shift is small, our pilot design demonstrates the feasibility of wireless monitoring the deterioration of perovskite solar cells. Tailoring antenna design and experimental validations are in progress.

1:50 PM L02
(Student) Bulk Incorporation of Organic Molecular Dopants into Two-Dimensional Ruddlesden-Popper Hybrid Perovskite Structures Jonghoon Lee[1], Kyeong-Yoon Baek[1], Jeongjae Lee[2], Heebeom Ahn[1], Yongjin Kim[3], Hyungbin Lim[1], Yeeun Kim[1], Jaeyong Woo[1], Keehoon Kang[3] and Takhee Lee[1]; [1]Seoul National University, Korea (the Republic of); [2]School of Earth and Environmental Sciences, Korea (the Republic of); [3]Department of Materials Science and Engineering, Seoul National University, Korea (the Republic of)

Organic-inorganic halide perovskites (OHPs) have recently attracted much attention as next-generation semiconducting materials due to their outstanding opto-electrical properties. However, many OHPs critically suffer from relatively poor electrical conductivity, which is challenging to tune with traditional method of bulk atomistic doping. While doping with molecular dopants, a family of versatile dopants for molecular design, has been suggested as a solution to this problem,[1, 2] the action of these dopants was typically restricted to perovskite surfaces, therefore significantly reducing their doping potential. In this study, we report successful bulk inclusion of 'magic blue', a molecular dopant, into two-dimensional (2D) Ruddlesden–Popper perovskites.[3] Our doping strategy of immersing the perovskite film in dopant solution increased the electrical current up to ~60 times while maintaining clean film surface. We provide a full mechanistic picture of such immersion doping, in which the solvent molecule facilitates bulk diffusion of dopant molecule inside the organic spacer layer, based on the optimum solvent processing. The immersion doping method developed in this work which enables bulk molecular doping in OHPs will provide a strategic doping methodology for controlling electrical properties of OHPs for electronic and optoelectronic devices.

References

[1] A. L. Abdelhady et al., J. Phys. Chem. Lett. 7, 295 (2016).
[2] E. E. Perry et al., Adv. Electron. Mater. 4, 1800087 (2018).
[3] J. Lee et al., Chem. Mater. 33, 370 (2021).

2:10 PM L03
Direct Measurements of HOMO–LUMO Transport Gaps at the Surface and Interface of Organic Semiconductor Materials Using Direct and Inverse Photoemission Spectroscopies (UPS & IPES)
Gyuhyeon Lee, Min-Jae Maeng, Kyu-Myung Lee, Jong-Am Hong and Yongsup Park; Kyung Hee University, Korea (the Republic of)

In organic light-emitting diodes (OLEDs) and heterojunction organic solar cells (OSCs), the energy offset between HOMO and LUMO, also called the transport gap (E_{tr}) is substantially different from optical gaps due to the relatively large exciton binding energies. However, the inability to independently measure the LUMO levels makes it hard to elucidate important things like electron injection barrier at the cathode in OLEDs and the voltage loss mechanisms in Voc of OSCs. We have recently developed highly sensitive inverse photoemission spectroscopy (IPES) instrument specifically for the LUMO level measurement of organic semiconductors. In combination with the existing ultraviolet photoemission spectroscopy (UPS) we could determine all the relevant transport energy levels (HOMO, LUMO, Fermi level and vacuum level) in any organic semiconductor surface and interface. In addition, combination of the electron source for IPES and the electron energy analyzer for UPS allowed us to utilize reflection electron energy loss spectroscopy (REELS) to determine both singlet and triplet optical gaps. We first demonstrate that all these measurements can be performed for an identical sample as a function of thickness. We also determine the energy levels at C60/pentacene interface so that the factors affecting the voltage losses that led to observed Voc value of the model planar heterojunction organic solar cells can be evaluated.

2:30 PM L04
(Late News) Structural and Morphological Characterization of Organic Electrochemical Transistors via Four-Dimensional (4D) Scanning Transmission Electron Microscopy Andrew Herzing[1], Lucas Flagg[1], Lee Richter[1], Jonathan Onorato[2], Christine Luscombe[3] and Ruipeng Li[4]; [1]National Institute of Standards and Technology, United States; [2]University of Washington, United States; [3]Okinawa Institute of Science and Technology, Japan; [4]Brookhaven National Laboratory, United States

Organic electrochemical transistors (OECTs) consist of a conjugated semiconducting polymer active layer patterned with source/drain electrodes in contact with an electrolyte solution. Under an external electrical bias, an electrochemical doping process occurs as ions from solution are driven into the polymer thus altering the conductivity of the polymer layer. Because the ion uptake occurs throughout the entire volume of the layer, the devices can convert small changes in ion concentration into large changes in electrical current. This makes them ideal candidates for bio-sensing applications. The performance of these devices is heavily dependent on the structure and distribution of the crystalline and amorphous phases in the polymer active layer. Generally, charge transport occurs more readily within the crystalline domains, while ion uptake scales with increased amorphous content. However, the interplay between ion uptake and electron mobility is complex and not easily predicted. For example, the introduction of polar side-chain species to the backbone of some OECTs has been shown to significantly increase the uptake of ions from the electrolyte. However, there appears to be a complex trade-off between ion uptake and electronic mobility, as in some cases increased crystallinity has been shown to decrease performance. There has been speculation that this behavior can be attributed to the preferential swelling of the amorphous region of the film, however this is difficult to measure experimentally. Moving forward, the ability to spatially resolve the crystalline domains of the polymer is essential to understanding the role of crystallinity and nanoscale morphology on the performance of OECT materials.
Scanning transmission electron microscopy (STEM) is ideally suited to simultaneously revealing the morphological and structural characteristics of materials organized at nanometer length scales and below. However, the high-energy electron beam employed in STEM rapidly destroys the crystal structure in many organic materials. The development of high-sensitivity, direct electron detectors offers one way of surmounting this barrier, as the required data can be collected with a far lower electron dose. Four-dimensional (4D)-STEM, where a full two-dimensional electron scattering distribution is rapidly recorded at every point in an image scan, offers a route to collecting spatially resolved diffraction data from beam sensitive samples using a much lower dose than required using CCD-based cameras. We will discuss the application of 4D-STEM to the characterization of the OECT material poly(3{[2-(2-methoxyethoxy) ethoxy]methyl}thiophene-2,5-diyl) (P3MEEMT). P3MEEMT contains ethylene glycol-based side chains for enhanced ion uptake and exhibits carrier mobilities comparable to state-of-the-art OECTs. 4D-STEM reveals a population of crystalline domains on the order of

(40 to 50) nm with strong Bragg diffraction peaks are observed at q = 3.3 nm^{-1}. A second population of crystals was observed which showed a Bragg peak at q = 17.0 nm^{-1}, corresponding to the (010) π-π stacking in edge-on orientation crystals which are spatially distinct from the face-on crystals. The quantitative characterization of these morphological features as a function of film processing conditions, molecular weight, and heat treatment will be presented.

2:50 PM L05
(Student, Late News) Climate-Adaptive Thermochromic Perovskite Smart Window Structures Shang-Hsuan Wu, Gabriel Cossio, Benjamin Braun, Frances Camille M. Wu and Edward T. Yu; The University of Texas at Austin (J.J Pickle Research Campus), United States

A large portion of energy consumption (50%) in buildings arises from heat transfer to buildings, specifically through windows due to solar illumination. Energy-efficient thermochromic smart windows, which are composed of special materials that enable them to adjust light transmission dynamically based on the ambient temperature, can allow energy demand for building cooling to be reduced. Hybrid halide perovskites are promising candidates for thermochromic smart windows owing to their capability to undergo reversible color and phase transitions between low and high temperatures. Furthermore, a new concept for smart photovoltaic windows has been realized based on inorganic perovskite $CsPbI_{3-x}Br_x$ thin films, which possess both photovoltaic and thermochromic features. However, the perovskite-based thermochromic smart windows require relatively high transition temperatures (>50°C), and this hinders their practical application in buildings since in most places the window temperatures do not reach 50°C in direct sunlight. Therefore, a configuration based on a thermochromic perovskite layer integrated with an external heating source is needed for the activation of thermochromism.
Transparent heaters are a key component in thermochromic smart window devices that employ transparent conductive electrodes (TCEs) to provide electric heating. Low resistance and high optical transparency of TCEs are two essential prerequisites for the fabrication of thermochromic smart windows. Among various TCEs, indium tin oxide (ITO) is most commonly used; but the brittle nature limits its application in flexible optoelectronics, and the scarcity of indium results in high material cost. Transparent and conductive metal nanomesh (NM) films, which are composed of periodic nanostructured metal networks, have gained considerable attention as high-performance TCEs offering several advantages, including excellent mechanical flexibility, high conductivity, tunable transmittance, and low fabrication cost. In this study, we introduce a new class of dielectric/metal/dielectric nanomesh films based on $ZnO/Au/Al_2O_3$ with periodicities of 200 nm and 370 nm which are fabricated using nanosphere lithography. For the metal mesh film design, an Au (15nm) thin film is chosen as the electrode material due to its malleability and high electrical conductivity. Thin layers of Al_2O_3 film (20 nm) and ZnO film (20 nm) are used as high refractive index dielectric layers to induce antireflective effect and suppress surface plasmons. We use relatively smaller metal mesh periodicities of 200 nm and 370 nm as compared to previously reported nanomesh films to create a potential pathway to optoelectronic applications, such as smart windows. As a result, the $ZnO/Au/Al_2O_3$ NM film with a 370-nm periodicity exhibits a transmittance over 90% at 550 nm and sheet resistance lower than 20 Ω/sq. Based on a standard figure of merit, this structure outperforms current state-of-the-art nanomesh films. Moreover, we integrate the $ZnO/Au/Al_2O_3$ NM film into thermochromic perovskite smart windows that operate by inducing a thermochromic transition from transparent to opaque state via electric heating of $ZnO/Au/Al_2O_3$ NM film at 50°C, which can be then maintained solely by 1-sun AM 1.5G solar illumination. This climate-adaptive, low power-activated, and fast-switching smart window structure opens new pathways toward its practical application in the real world.

3:10 PM BREAK

SESSION M: Group III–Nitrides—Optical Emitters
Session Chairs: Theeradetch Detchprohm and Christian Wetzel
Wednesday Afternoon, June 28, 2023
UC, Santa Barbara Harbor

1:30 PM M01
Short-Term Degradation Mechanisms of 275-nm-Band AlGaN-Based Deep-Ultraviolet Light Emitting Diodes Fabricated on a Sapphire Substrate Shigefusa F. Chichibu[1], Kohei Shima[1], Takumi Kasuya[1], Kengo Nagata[2], Koji Okuno[2], Masaki Oya[2], Yoshiki Saito[2], Hisanori Ishiguro[3] and Tetsuya Takeuchi[3]; [1]Tohoku University, Japan; [2]Toyoda Gosei Co. Ltd., Japan; [3]Meijo University, Japan

Steady-state current induced degradation mechanisms of 275-nm-band AlGaN quantum well (QW) deep-ultraviolet (DUV) light-emitting diodes (LEDs) were investigated. The optical output power (P_o) showed an initial rapid decrease by 20-30 % within the aging time (t_{age}) of 100 h and then gradually decreased to about 60 % by t_{age} of 1000 h. For elucidating the causes for the initial and gradual degradations, complementary electrical, time-resolved photoluminescence (TRPL), and impurity characterizations were carried out, making a connection with the junction band profiles. Because the initial degradation of the wells was less significant than the P_o, the short-term degradation is attributed to the reduction in carrier injection efficiency (CIE), not in internal quantum efficiency (IQE) of the wells, most probably due to de-passivation of initially H-passivated vacancy clusters in Mg-doped AlGaN electron blocking layer (EBL) especially close to the multiple QWs. The principal cause for the gradual decrease in P_o is tentatively attributed to a gradual decrease in IQE of the QWs.
(Contents)
Recently, an increasing demand for antivirus has attracted attention for DUV LEDs operating between 200 and 280 nm, because such radiation is known to inactivate bacteria or viruses, including SARS-CoV-2. AlGaN-based 275-nm-band DUV LEDs are suitable for such purposes, and P_o of several manufacturers are increasing. However, simultaneous realization of high power and high quantum efficiency is still difficult and the device lifetime is far less than that of visible and near UV LEDs. With respect to the device lifetime, there is a consensus that the degradation can be divided into two groups: a rapid reduction in P_o within t_{age} below about 100 h and a gradual reduction for $t_{age} \geq 100$ h. The results have been explained to be due to the increase in the number of point defects acting as nonradiative recombination centers (NRCs) in the QWs. However, direct evidence for increased concentration of NRCs has not been given yet. In this presentation, the results of electrical, TRPL, and secondary-ion mass spectrometry (SIMS) measurements carried out on 275-nm-band AlGaN LEDs are shown to define the locations of major degradations. Two sets (lot A and B) of AlGaN DUV LEDs grown on *c*-plane sapphire have been stressed under hard conditions: forward current I_F of 350 mA and junction temperature T_j of 105 °C. Consistent with previous literatures, P_o for the near-band-edge (NBE) emission showed an initial rapid decrease by 20-30 % ($t_{age} < 100$ h) and a gradual decrease to about 60 % by t_{age} of 1000 h. The initial decrease was accompanied by the increases in both I_F below the diffusion voltage (V_D) and reverse leakage current (I_R). For elucidating dominant causes for the degradations, TRPL measurements were carried out using the excitation photon energy below the barrier and above the well to extract pure photoluminescence (PL) lifetimes of the wells. Because the decrease in the room-temperature PL lifetime that represents the nonradiative lifetime was less significant than the P_o, the initial degradation is attributed to the decrease in CIE, not in IQE of the wells. From the energy band diagrams calculated for biases V = -5, 0, 4, and 7 V, both the below V_D and reverse leakages appear to take place in the AlGaN EBL, especially at the interface close to the active region. Because the decrease in H concentration in the EBL to

multiple QW region was confirmed by SIMS measurement, the initial degradation is most probably due to de-passivation of initially H-passivated vacancy clusters (NRCs) in the EBL close to the multiple QWs. The principal cause for the gradual decrease in P_o is tentatively attributed to a gradual decrease in IQE of the QWs.
This work was supported by MOE program for implementation of innovative infection-control and digital technologies with low CO_2 emissions, MEXT Crossover Alliance, an JST SPRING (#JPMJFS2102), Japan.

1:50 PM M02
(Student) Demonstration of AlGaN Tunnel Junction p-Down UV Light Emitting Diodes Agnes Maneesha Dominic Merwin Xavier[1], Arnob Ghosh[1], Sheikh Ifatur Rahman[1], Andrew Allerman[2], Shamsul Arafin[1] and Siddharth Rajan[1]; [1]The Ohio State University, United States; [2]Sandia National Laboratories, United States

Ultra-violet light emitting diodes (UV-LEDs) and lasers based on the III-Nitride material system are very promising since they enable compact, safe, and efficient solid-state sources of UV light for a range of applications. The primary challenges for UV LEDs are related to the poor conductivity of p-AlGaN layers and the low light extraction efficiency of LED structures. Tunnel junction-based UV LEDs provide a distinct and unique pathway to eliminate several challenges associated with UV LEDs[1-4].
In this work, we present for the first time, a reversed-polarization (p-down) AlGaN based UV-LED utilizing bottom tunnel junction (BTJ) design. We show that compositional grading enables us to achieve the lowest reported voltage drop of 1.1 V at 20 A/cm^2 among transparent AlGaN based tunnel junctions at this Al-composition. Compared to conventional LED design, a p-down structure offers lower voltage drop because the depletion barrier for both holes and electrons is lower due to polarization fields aligning with the depletion field. Furthermore, the bottom tunnel junction also allows us to use polarization grading to realize better p- and n-type doping to improve tunneling transport.
The epitaxial structure of the UV-LED was grown by plasma-assisted molecular beam epitaxy (PAMBE) on metal-organic chemical vapor deposition (MOCVD)-grown n-type $Al_{0.3}Ga_{0.7}N$ templates. The transparent TJ was grown using graded n^{++}-$Al_{0.3}Ga_{0.7}N \rightarrow n^{++}$-$Al_{0.4}Ga_{0.6}N$ (Si=3×10^{20} cm^{-3}) and graded p^{++}-$Al_{0.4}Ga_{0.6}N \rightarrow p^{++}$-$Al_{0.3}Ga_{0.7}N$ (Mg=1×10^{20} cm^{-3}) to take advantage of induced 3D polarization charges. The high number of charges at the tunnel junction region leads to lower depletion width and efficient hole injection to the p-type layer. The UV LED active region consists of three 2.5 nm $Al_{0.2}Ga_{0.8}N$ quantum wells and 7 nm $Al_{0.3}Ga_{0.6}N$ quantum barriers followed by 12 nm of p- $Al_{0.46}Ga_{0.64}N$ electron blocking layer (EBL). The active region was grown on top of the tunnel junction. A similar LED with p-up configuration was also grown to compare the electrical performance.
The surface morphology examined by atomic force microscopy (AFM) shows smooth growth features with a surface roughness of 1.9 nm. The dendritic features on the surface are characteristic of high Si doping on the surface. The composition of each layer was extracted from the scan by high resolution x-ray diffraction (HR-XRD). The electrical characteristics of a device show a voltage drop of 4.9 V at 20 A/cm^2, which corresponds to a tunnel junction voltage drop of ~ 1.1 V. This is the best lowest voltage for transparent 30% AlGaN tunnel junctions to-date and is comparable with the lowest voltage drop reported previously on non-transparent (InGaN-based) tunnel junctions at similar Al mole fraction AlGaN. On-wafer electroluminescence measurements on patterned light-emitting diodes showed single peak emission wavelength of 325 nm at 100 A/cm^2 which corresponds to $Al_{0.2}Ga_{0.8}N$, confirming that efficient hole injection was achieved within the structure. The device exhibits a wavelength shift from 330 nm to 325 nm with increasing current densities from 10A/cm^2 to 100A/cm^2.
In summary, we have demonstrated a fully transparent bottom AlGaN homojunction tunnel junction that enables p-down reversed polarization ultraviolet light emitting diodes, and has very low voltage drop at the tunnel junction. This work could enable new flexibility in the design of future III-Nitride ultraviolet LEDs and lasers.
Funding from National Science Foundation under grant number 2034140 is gratefully acknowledged.
References:
[1] Y. Zhang *et al.*, *Applied Physics Letters*, vol. 109, no. 12, 2016
[2] A. Pandey, W. J. Shin, J. Gim, R. Hovden, and Z. Mi, *Photonics Research*, vol. 8, no. 3, 2020
[3] V. Fan Arcara *et al.*, *Journal of Applied Physics*, vol. 126, no. 22, p. 224503, 2019.
[4] K. Nagata *et al.*, *Applied Physics Express*, vol. 14, no. 8, p. 084001, 2021.

2:10 PM M03
Non-Planar Growth of Crack-Free High Al-Mole-Fraction AlGaN Heterostructures on Patterned GaN Substrates for Ultraviolet Light Emitting Diodes and Laser Diodes Yuto Ando, Zhiyu Xu, Theeradetch Detchprohm and Russell Dupuis; Georgia Institute of Technology, United States

Injection laser diodes (LDs) in the III-N alloy system require the growth of heterostructures. Influenced by both lattice mismatch and thermal expansion coefficient mismatch in such structures, the alloy system is restrained from freely allowing full alloy selection for the best device performance. In the case of LDs emitting in the UV-A range, tensile strain limits the growth of adequately thick and/or high Al-mole-fraction AlGaN epitaxial layers on GaN substrates, and the growth of layers having thickness beyond the critical layer thickness results in cracking of the film. The inadequate thickness or index contrast of cladding layer (CL) to the active layer limits the LED or LD device performance due to low optical confinement, while the yield of the devices fabricated on the wafer is significantly reduced by the cracks. In this work, we describe a novel approach employing non-planar growth (NPG) that enables the deposition of crack-free AlGaN layers with relatively thick and high Al-mole-fraction on patterned GaN substrates with rectangular mesas with adequately large area for the fabrication of UV LEDs and injection laser devices.
Cracking of AlGaN layers grown by MOCVD on (0001) GaN substrates with NPG mesas was evaluated. Stripe-shaped NPG mesas were formed on the GaN substrate with conventional dry etching. The direction of the stripe mesas was aligned to be parallel to the *m* axis of GaN. The widths of the NPG mesa were set to be 25 and 100 µm. $Al_xGa_{1-x}N/Al_yGa_{1-y}N$ short period super lattices (SPSLs) were grown on the patterned GaN. The average Al mole fraction and total thickness of the AlGaN SPSL were set to be 0.16 and 1500 nm, respectively. Surface cracking after the growth was not observed on the AlGaN SPSL grown on the top of mesa, while the critical thickness for planar sample without mesa formation was 200 nm. Investigations with AlGaN with different Al mole fractions and thicknesses show that the surface cracking depends on the mesa width and depth. Mesas with narrower widths and/or deeper etching depth are more effective to prevent the cracking than others with either wider widths or shallower depths.[1,2] Additionally, the suppression of the formation of the crack is attributed to an anisotropic relaxation of the strain in the AlGaN SPSL which was enabled by the elastic deformation of GaN layer along the direction perpendicular to the stripe mesa. Our results clearly show that the NPG approach enables us to achieve thick AlGaN layers with high composition contrast to the substrate material with a thickness beyond critical layer thickness by relaxing the tensile stress in the AlGaN layers on the top of mesa. This is especially advantageous for fabrication of UV LDs as these devices require thick CLs with high refractive index contrast to the active layer to lower the lasing threshold.
Using this approach, we have designed and grown a UV-A multiple-quantum-well LD heterostructure. The CL in upper and lower side of the active layers are composed of doped AlGaN SPSLs with average Al mole fraction and combined thickness of 0.16 and 1100 nm, respectively. The surface of the planar reference sample has a high density of cracks along the <11-20> directions while the NPG sample has no cracks on the top surface of several-mm-long NPG mesas. Test

diodes device fabricated on the NPG sample before formation of the laser cavity structure show rectification with no leakage in a DC current-voltage measurement at 300K. Spontaneous light emission in UV-A range was successfully demonstrated by pulsed current injection at 300K. From these results, the NPG approach is proven to effectively suppress the cracking of relatively thick AlGaN layers with high Al mole fraction and thicknesses beyond the critical layer thickness and thus this approach is promising to achieve a high-performance UV-A LD and LEDs.

[1] F. Mehnke *et al.*, J. Appl. Phys. **131**, 073103 (2022).
[2] Y. Ando et al., J. Cryst. Growth **607**, 127100 (2023).

2:30 PM M04
Shadowing Effects in Core-Shell InGaN Quantum Wells Grown on N-Polar GaN Nanowire Arrays by Molecular Beam Epitaxy
Matt Brubaker, Alexana Roshko, Todd Harvey and Kris Bertness; NIST, United States

GaN nanowire arrays present unique opportunities for obtaining color tunability, guided emission, and resonant effects in light-emitting devices. Furthermore, core-shell structures grown on GaN nanowire arrays present a viable route to the increased performance and speed of non-polar quantum wells (QWs) grown on the nanowire sidewalls. In most reported accounts, core-shell structures are obtained on Ga-polar nanowires and are typically grown by MOCVD. This growth polarity leads to semipolar faceting at the nanowire tip (which is the primary source of color tuning) and MOCVD growth often relies on a high silane flux during core growth (which can interfere with uniform shell growth). In this work, we demonstrate core-shell InGaN QWs that avoid these constraints and are grown by MBE on N-polar oriented GaN nanowires. In these structures, the InGaN QW emission properties are dominated by the non-polar sidewalls leading to a low overall color tuning effect and fast recombination. Further, we assess the effects of nanowire-to-nanowire shadowing imposed by the line-of-sight MBE technique on the structure of the core-shell InGaN QWs. We show that low color tuning can be obtained for isolated nanowires, which could be advantageous for applications that require high color purity or decoupling of the emission wavelength from the nanowire dimensions.
Ordered N-polar NW arrays were grown using an MBE-based selective area growth process on N-polar GaN-on-silicon substrates. The Si-doped GaN nanowire cores were grown at high temperature (~860 °C) and resulted in 1.3-1.5 um long nanowires with perfect selectivity. The NW arrays had diameters ranging from 140-310 nm and pitches ranging from 300-3000 nm. A shell consisting of three InGaN QWs was grown at lower temperature (~535 °C) and finally capped with a thin AlGaN passivation layer. Transmission electron microscopy (TEM) was used to characterize the InGaN QW structure on the m-plane sidewalls and the N-face tip. The N-face tips were highly defective but could be removed from many nanowires with mild ultrasonication. In contrast, m-plane QWs were found to be of high quality and had thicknesses that correlated well with flux profiles obtained by numerical simulations of the nanowire shadowing environment during growth. Steady-state and time-resolved photoluminescence (PL) measurements revealed strong luminescence in the InGaN QWs (compared to the GaN bandedge emission) and a short lifetime that is consistent with non-polar QW recombination. The InGaN QW emission wavelength in isolated nanowire arrays was nearly independent of the nanowire diameter. A small blueshift was observed in dense nanowire arrays and is attributed to thinner QWs that result from flux shadowing towards the nanowire base.

2:50 PM M05
(Student) Fabrication and Characterization of Epitaxially Grown and Lifted off AlN Membranes
Anand Ithepalli, Wenwen Zhao, John Wright, Chandrashekhar P. Savant, Eungkyun Kim, Kazuki Nomoto, Debdeep Jena and Huili Grace Xing; Cornell University, United States

In order to integrate high-quality devices like thin-Film Bulk Acoustic Resonators (FBARs), dual-gated High Electron Mobility Transistors (HEMTs) etc., with the existing material systems in fabrication facilities, a process has to be developed to lift the devices off of their native substrates and to transfer them to a desired substrate. The Molecular Beam Epitaxy (MBE) growth of Nitride materials has demonstrated high quality FBARs and HEMTs primarily grown on Silicon Carbide (SiC) and bulk Nitride substrates. There is a growing need to transfer devices grown on these substrates to popular commercial substrates like Silicon. Also, it has been shown that Niobium Nitride (NbN_x) layer can be selectively etched away using Xenon Difluoride (XeF_2) [1]. This makes it possible to grow a seamless device structure using NbN_x as a sacrificial layer. Nb-N binary system has multiple phases, which can be realized by changing the substrate temperature and Nb:N flux ratio during the growth [2]. This work focuses on Aluminum Ntride (AlN) films grown using MBE on c-plane Sapphire and SiC with a NbN_x sacrificial layer. We study the nucleation of AlN on NbN_x grown on Sapphire and show that there is a temperature window where we can get coalesced AlN with low surface roughness. We found that Al and Nb are favoured to form an intermetallic inclusions even in the presence of active Nitrogen atoms from the plasma because the Al-Nb-N ternary phase diagram has no thermodynamically stable ternary phase. The formation of these intermetallics is found to be suppressed by nitrogen-rich nucleation of AlN for a few tens of nanometres followed by metal-rich growth to obtain sub-nm RMS roughness of the as-grown AlN film on NbN_x, the film overall thickness ranges from 300nm to 500nm. These films showed an XRD rocking curve Full Width at Half Maxima (FWHM) of less than 100 arcsecs. However, the nitrogen-rich nucleation results in defective film. In order to be able to nucleate under metal-rich conditions to obtain high-quality AlN film, we experimented with other nitrides as barrier materials between NbN_x and AlN. TiN was the first choice because it can act as an epitaxial electrode and also because there is a ternary phase with Al, Ti and N which might help in preventing the intermetallic inclusions. However, nucleation of AlN on TiN also resulted in intermetallic formation. We also tried to use GaN and ScN as barrier layer to grow AlN under metal-rich conditions.
We studied the effect of XeF_2 on each of the phases of NbN_x we can form on Sapphire substrate and it turns out that when they are exposed directly as-grown without any other layer on them, they all etch away at an equal etch rate. However, when we deposited SiO2 and fabricated some structures before performing the etch test, only the δ phase, which is a rocksalt type cubic structure, was removed completely. So, we tried to use only δ-phase but this had its own challenges as the temperature to produce the highest quality film is slightly higher than the temperature at which we can stabilize the δ-phase. Therefore, there is still room for optimizing the AlN film quality.
We fabricated different shapes and sizes of AlN membranes by etching down the underlying NbN_x layer to create free-standing AlN membranes. It was found that the size of the largest membrane is dependent on the phase of NbN_x, thickness of the NbN_x and chamber temperature during XeF_2 etching. Furthermore, these membranes were transferred on to a different substrate and characterized by various techniques to better understand the surface which was the interface between $NbN_x$and AlN before the lift-off. AFM showed few nanometres of RMS roughness and Raman spectroscopy showed a metallic absorption component and another cycle of XeF_2 etching reduced the intensity of the metallic absoption component indicating that there was some left over NbN_x.

[1] D. J. Meyer et al., IEEE TSM 29, 384 (2016)
[2] J. G. Wright et al., arXiv:2203.14083 (2022)

3:10 PM BREAK

3:30 PM #M06
(Student) III-Nitride Laser Diodes with Wide Quantum Wells—Influence of Built-In Electric Fields on the Light Generation Process Mateusz Hajdel, Krzysztof Golyga, Marcin Siekacz, Anna Feduniewicz-Zmuda, Szymon Stanczyk, Czeslaw Skierbiszewski and Greg Muziol; Institute of High Pressure Physics PAS, Poland

The increasing demand for the illumination in our societies pushed scientist to fight over every bit of the efficiency of the light emitters. Currently the GaN-based emitted such as LEDs and laser diodes (LDs) are taking a leading position in the domestic and industrial light sources [1], mainly because of their extraordinary efficiency and reliability. For most demanding applications like communication systems [2], projection [3] or near absolute zero cooling systems [4], LDs are the best candidates to meet the stringent requirements. Conventional heterostructure of III-nitride emitter consist of the few nanometers thick InGaN quantum wells acting as the active region. One of the issues in this approach is the existence of built-in electric fields in III-nitrides that cause separation of the electron and hole wavefunction and shift of the emission wavelength. Recently, it was shown that also wide InGaN QWs exhibit high oscillator strength thanks to operation on exited states [5-7]. Lack of the wavelength shift mechanism in those structures can potentially allow to realize the integrated RGB emitter on a single, InGaN platform.
In this work, the nature and origin of the stimulated recombination process of the InGaN LDs operating on excited states are studied. The gain spectra of LDs with 2.6, 10.4 and 25nm single QW are extracted from spontaneous and amplified spontaneous emission spectra and compared with those measured by the Hakki-Paoli method. Only by increasing the thickness of the QW sufficiently and without increasing the content of indium, the obtained wavelength of lasing is about 20 nm longer. Due to this red shift, wide QWs are promising candidates for active region in green and red lasers in the GaN material system. Analyzing the measured spectra and the quasi-Fermi level separation we drew a conclusion that the gain must originate from the first exited states, and spontaneously emitted photons from the higher states of the wide QW in the $kAcm^{-2}$ current density regime. The simulation of the wide QW LD band structure was also performed to describe the below threshold behavior. The contributions of individual transition to the total emission showed that the wavelength stable regime of spontaneous emission is due to the state index change from higher excited states to the lower ones. This mechanism occurs, because together with the screening of the built-in electric fields the QW flattens and overlap of the lower excited states increases along with the transition energy. The results reported here reveal true nature of light generation process in the wide QW devices.
[1] J. D. Bergesen et al., Journal of Industrial Ecology 20 (2), 263-275 (2016).
[2] C. Lee et al., Opt Express 23 (12), 16232-16237 (2015).
[3] Y. Nakatsu et al., Proc. SPIE Gallium Nitride Materials and Devices XV 11280 (2020).
[4] Y. Shimada et al., Rev Sci Instrum. 84 (6), 063101 (2013).
[5] G. Muziol et al., Japanese Journal of Applied Physics 61 (2021).
[6] M. Hajdel et.al., Materials 15 (1) (2021).
[7] Z. Zhang et.al., Applied Physics Express 12 (12) (2019).

3:50 PM M07
Advanced Cathodoluminescence Microscopy of a Cascaded InGaN/GaN LED Gordon Schmidt, Frank Bertram, Peter Veit, Konstantin Wein, Juergen Christen, Christoph Berger, Jürgen Bläsing, Armin Dadgar and André Strittmatter; Otto von Guericke Universität Magdeburg, Germany

A possible way to reduce the production cost of GaN-based LEDs is to serially grow several InGaN-GaN multiple quantum well (MQW) structures on the same sapphire substrate and connect these MQW structures with a tunnel junction (TJ). This approach can realize multiple wavelength LEDs covering the same chip area. Furthermore, cascaded LEDs can effectively increase the optical output power per chip area when each MQW section is driven in the low efficiency-droop regime by applying high voltages but low current densities to the whole LED. The complex nature of the growth of cascaded LED requires vertically-resolved structural and optical analytical tools to evaluate the different regions of the stack.
Using nano-cathodoluminescence performed in scanning transmission electron microscope (STEM-CL) as well as electroluminescence (EL) microscopy, we have investigated a cascaded InGaN/GaN LED. The structure has been grown by metal-organic vapor phase epitaxy (MOVPE) in a single growth process on top of a GaN/sapphire template. Three 5-fold InGaN/GaN MQWs are separated by a heavily doped GaN:Mg/GaN:Ge TJ. On top, a GaN:Mg/GaN:Ge TJ was grown as contact scheme completing the cascaded LED structure. The Mg-doped GaN layers were thermally activated by a combination of in- and ex-situ activation steps. Additionally, the cascaded LED was processed by standard UV-lithography, mesa dry-etching and metal deposition.
In the spatially averaged EL spectrum of the processed LED structure, the emission peak is centered at 455 nm modulated by Fabry-Pérot oscillations. The competition between the Fabry-Pérot modes leads to a lateral variation of the EL peak wavelength.
Structural and optical properties have been investigated by highly spatially resolved STEM-CL in cross section. STEM high-angle annular dark field (HAADF) contrast resolves the full structure and the quantum wells with sharp interfaces. The panchromatic CL intensity exhibits highest intensity around 435 nm wavelength at each InGaN/GaN MQW section. Each individual layer of the structure reveals its own characteristic emission in local spectra acting as fingerprint luminescence. In particular, a cross-sectional CL linescan performed at 17 K across the MQW stack reveals the emission evolution in growth direction: all 3 MQW luminescence contributions are spectrally separated shifting from bottom to top to longer wavelengths. In more detail, each individual MQW shows a peak wavelength change in growth direction indicating different structural and/or chemical properties of the individual 5-fold quantum wells.

4:10 PM M08
(Student) MOCVD of a Novel InGaN/GaN/AlGaN Active Region Design for Ultraviolet Light-Emitting Diodes Guangying Wang, Yuting Li, Cheng Liu, Qinchen Lin, Chirag Gupta and Shubhra Pasayat; University of Wisconsin–Madison, United States

UV Light Emitting Diodes (LEDs) have become prevalent in a diverse range of fields, such as medical, scientific, and military industries [1-2]. They are highly valued for their compact, efficient, and eco-friendly properties compared with conventional UV light-emitting sources [3-4]. III-Nitrides material covers the full UV wavelength range from UV-A to UV-C, and in the UV-A range LEDs, InGaN/AlGaN active region design is commonly used [5-8]. The preferred MOCVD growth conditions for InGaN and AlGaN involve N_2 and H_2 as carrier gas (respectively) to prevent the desorption of Indium from InGaN and to obtain high quality AlGaN respectively. However, the transition from InGaN to AlGaN during growth may lead to challenging growth scenarios leading to lower growth control on either InGaN or AlGaN. Further optimization of active region design is also desirable beyond the conventional InGaN/AlGaN active region. This encouraged us to explore a new active region design. In this work, we present a novel InGaN/GaN/AlGaN active region design of high-efficiency UV-A micro-LED with an emission wavelength of 372 nm grown by MOCVD. Additionally, 20 x 20 μm^2 to 100 x 100 μm^2 micro-LEDs were fabricated.
In this InGaN/GaN/AlGaN structure, the GaN interlayer was grown in N_2 and AlGaN was grown in N_2+H_2. This GaN interlayer allowed AlGaN to be grown with higher quality, and the InGaN/GaN combination showed a closer electron and hole wave function compared to InGaN/AlGaN in the simulation. In the simulation, two LED structures were simulated for comparison, InGaN/GaN/AlGaN (Fig.1(a)). and InGaN/AlGaN (Fig.1(b)). The thickness and composition of the InGaN layers were modified to have a similar In

concentration, which ensured the effect of In and the polarization charge in the two structures are relatively the same and granted the fair comparison between the two structures. The bandgap simulation shows that the GaN interlayer in the InGaN/GaN/AlGaN is behaving like a second well in the structure. In comparison with the InGaN/AlGaN structure, InGaN/GaN/AlGaN has a closer electron and hole wave function, which increased the recombination efficiency (Fig.2(a)). Moreover, InGaN/GaN/AlGaN structure showed an improvement in the internal quantum efficiency (IQE) simulation, with >10% improvement in the operating current density range from 0 to 100 A/cm^2 (Fig.2(b).)
The current density (J) versus forward voltage (V) of the fabricated μLEDs at room temperature is shown in Fig.3. The J–V characteristics showed an inverse relationship of injection current density with device size at the same voltage. From 100 x 100 μm^2 device size to 20 x 20 μm^2 device size, the current density increased from 16 A/cm^2 to 63 A/cm^2 at 3.5 V (Fig.4(a)). In comparison with the 100 x 100 μm^2 devices, device size 60 x 60 μm^2 and 40 x 40 μm^2 showed a 20% and 40% increase in relative EQE respectively (Fig.4(b)). This increase may be attributed to improved light extraction efficiency and reduced current crowding in smaller micro-LEDs [9]. Further investigations will be pursued to further increase efficiency. Both simulation and experimental results show the great potential of InGaN/GaN/AlGaN quantum design for high-efficiency UV-A range LEDs.
[1] M. Kneissl et al. III-Nitride Ultraviolet Emitters Technology and Applications (Springer, 2016). [2] Y. Muramoto et al. Semiconductor Science and Technology **29**, 084004 (2014). [3] T.A. Kalajian et al. Scientific Reports **7**, (2017). [4] D. Morita et al. Japanese Journal of Applied Physics **41**, (2002). [5] M. Kneissl et al. Nature Photonics 13, 233 (2019). [6] L. He et al. Optics Letters **43**, 515 (2018).[7] S. Kuo et al. IEEE Journal of Quantum electronics **51**,12 (2015) [8] J.Wu et al. IEEE photonics journal **13** (2021) [9] Y. Yao et al. Appl. Phys. Express **15** 064003 (2022).

4:30 PM M09
Critical Thickness of InGaN Grown by Plasma-Assisted Molecular Beam Epitaxy Greg Muziol, Marcin Siekacz, Marcin Krysko, Anna Feduniewicz-Zmuda, Grzegorz Staszczak and Czeslaw Skierbiszewski; Institute of High Pressure Physics PAS, Poland

InGaN/GaN heterostructures are commonly used in optoelectronic devices such as light emitting diodes and laser diodes (LDs). These layers serve primarily as light emitting active regions. Moreover, thick InGaN layers can be used as waveguides in long wavelength LDs thanks to their high refractive index contrast to GaN. However, the high lattice mismatch between InN and GaN causes significant strain and leads to InGaN relaxation. The critical thickness of InGaN grown by metalorganic vapor phase epitaxy has been extensively studied. It was shown that the thickness is severely limited by relaxation through transition from a planar 2D into a 3D growth mode [1].
In this paper we investigate the critical thickness of InGaN grown by plasma-assisted molecular beam epitaxy (PAMBE) on (0001) bulk GaN substrates. We show that the main mechanism of relaxation of InGaN is different for layers grown by PAMBE. This leads to a higher critical thickness of InGaN heterostructures. We will present x-ray diffraction, cathodoluminescence and atomic force microscopy data of thick InGaN layers and estimate the limit of their thickness. Furthermore, as a proof of concept, we demonstrate AlGaN-cladding free blue LDs, in which the optical mode is confined with extremely wide 300 nm InGaN waveguide with indium composition of 8%. We will discuss the issues arising from realization of LDs with highly strained waveguides, such as mirror fabrication.
References: [1] S. M. de Sousa Pereira et al., Advanced Functional Materials 17, 37 (2007).

4:50 PM M10
(Student) Demystifying Light Extraction Efficiency in AlGaN Based UV LEDs James Loveless[1], Jack Almeter[1], Ronny Kirste[2], Baxter Moody[2], Pramod Reddy[2], Ramón Collazo[1] and Zlatko Sitar[1,2]; [1]North Carolina State University, United States; [2]Adroit Materials, United States

III-nitride LEDs have revolutionized modern lighting through highly efficient blue and white LEDs based on GaN. However, UV LEDs based on high Al-content AlGaN still have relatively low efficiencies due to many compounding factors. One of the largest components is the low light extraction efficiency (LEE), which currently limits the overall efficiency of devices to single digit percentages. The high index of refraction of the LED layers causes total internal reflection (TIR), where generated photons are reflected back into the LED layers where they are ultimately absorbed. Ever more complex surface modifications are proposed to reduce these losses, with limited success. In this study, it is shown that the index of refraction and TIR is not the limiting factor for light extraction but is instead bulk absorption in LED layers and in the substrate.
Ray tracing simulations were developed in MatLab to investigate the effect of several factors on LEE, including the absorption coefficient and index of refraction of LED layers and the substrate, contact reflectivity, and the inclusion or exclusion of a GaN contact layer. These factors were studied in conjunction with the effect of roughening the extraction surface to reduce TIR. The simulation predicts that roughening the surface of an LED with a GaN contact layer will increase the LEE by 40 percent. Further, it was found that through removing the absorptive GaN contact layer and properly minimizing bulk absorption in the substrate, the light extraction efficiency can be improved by more than 10x.
These simulations were verified experimentally for a UV LED grown on a native AlN substrate. A simple wet etch procedure using a KOH solution to roughen the extraction surface is proposed. Since N-polar AlN is selectively etched by KOH with a 900:1 ratio (1), this procedure effectively ensures no damage to the epitaxial surface. Pyramidal structures with dimensions on the order of 1 μm are formed on the extraction surface of the LED to increase photon scattering events and reduce losses due to TIR. After ten minutes of etching, the LEE of the device increased by 50 percent, validating the simulation results for devices with a GaN contact layer. This work points the way to overall efficiencies of greater than 40% in UVC LEDs and definitively shows that low LEE is due to absorption and not the high index of refraction in AlGaN based LEDs.
1. Guo, W. et al. Comparative study of etching high crystalline quality AlN and GaN. Journal of Crystal Growth 366, 20–25 (2013).

SESSION N: Characterization of Gallium Oxide-Based Materials and Devices I
Session Chairs: Alan Jacobs and Nidhin Kurian Kalarickal
Wednesday Afternoon, June 28, 2023
MCC Theater

1:30 PM N01
Evidence of Electron and Hole Photoemission During DLOS Characterization of Nitrogen Implanted β-Ga_2O_3 Hemant J. Ghadi[1], Joe F. McGlone[1], Evan M. Cornuelle[1], Alexander Senckowski[2], Shivam Sharma[3], Man Hoi Wong[4], Uttam Singisetti[3], Aaron Arehart[1] and Steven A. Ringel[1]; [1]The Ohio State University, United States; [2]University of Massachusetts Amherst, United States; [3]University at Buffalo, The State University of New York, United States; [4]The Honkong University of Science and Technology, Hong Kong

Nitrogen (N) is attracting interest as a compensating deep acceptor in beta-phase gallium oxide (β-Ga_2O_3) due to its predicted deep energy levels at 1.3, 1.4, and 2.9 eV below the conduction band. [1] Compared with more common iron (Fe) acceptors, which produce a deep level near E_C-0.8 eV, the larger energies of N states might enable a path to mitigate device instabilities resulting from modulating the Fe charge state that has been observed for lateral device structures grown on a semi-insulating Fe-doped β-Ga_2O_3 substrates.[2] There are a few reports of successful N doping to achieve highly resistive β-Ga_2O_3; the experimental verification of the deep states associated with N doping has not yet been produced. Here, we use Deep-level optical spectroscopy (DLOS) to explore states associated with N doping in β-Ga_2O_3. Information from such measurements can be used to help optimize the use of N doping for β-Ga_2O_3 device applications in the future. This work verifies the dominance of the E_C-2.9 eV state in specially prepared samples but also uncovers a complexity related to the analysis of DLOS data due to the observation of simultaneous electron and hole photoemission. Here we not only prove the presence of both emission processes but also present a solution to this issue so that accurate data can be extracted despite competing emission processes.
Si-doped halide vapor phase epitaxially (HVPE) grown β-Ga_2O_3 epilayers were partially compensated by N-implantation. The conditions were optimized for achieving a uniform N-implantation profile of 2×10^{16} cm^{-3} with an implant layer thickness of approximately 800 nm. Post-implant annealing was done to activate the N dopant, anneal out the implant damage, and achieve the desired co-doped compensated structure. After the anneal, diodes were fabricated with the Ni-Schottky contact on the HVPE epilayer and the ohmic contact (Ti/Al/Ni/Au) on the backside of the substrate. Characterization was done by capacitance-voltage (C-V) characteristics and both single and dual-beam DLOS measurements. C-V revealed that the initial Si-doped epilayer concentration was reduced from 1.2×10^{17} cm^{-3} to 9×10^{16} cm^{-3} after the implantation and anneal. In the DLOS experiment, positive and negative capacitance transients were observed using the same photon energy, which implies the presence of simultaneous electron and hole emission. When the photon energy is greater than half the bandgap, there is always competition between these two processes since both the conduction band (CB) and valence band (VB) can participate. This behavior is well documented for DLOS studies on Mg-doped GaN [2], where photoionization of an electron to CB and hole to VB from the same state is witnessed. A similar process exists here, where we observe a level with a positive transient at E_C-2.9 eV and a negative transient at E_V+1.9 eV, defining a bandgap state that matches the theoretically predicted state for a N atom substituting on the O_{III} site in the β-Ga_2O_3 lattice. A challenge in this situation is an accurate determination of the trap concentration from the steady-state photocapacitance due to the competing emission processes. This was resolved using a dual beam DLOS approach to decouple the electron and hole emission processes by saturating the hole emission with a second (dual) photon source. Once corrected, the measured E_C-2.9 eV state concentration was in agreement with the actual implanted N concentration, obtained using secondary ion mass spectroscopy (SIMS). Separately, dual beam DLOS determined another hole transition at E_V+1.3 eV, which partially contributed to the negative capacitance transient and will be discussed. Temperature-dependent double-beam measurements are underway to understand the thermal stability of the E_C-2.9 eV level and its related hole emission processes.
References:
1. H. Peelaers, APL Mater. 7, 022519 (2019)
2. M. E. Ingebrigtsen et al., APL 112, 4, 042104 (2018)
3. A. Armstrong et al., JAP 103, 063722 (2008).

1:50 PM N02
Killer Defects Responsible for Leakage Current in HVPE (001) β-Ga2O3 SBD Observed by Emission Microscopy and Synchrotron X-Ray Topography Sayleap Sdoeung[1], Kohei Sasaki[2], Akito Kuramata[2] and Makoto Kasu[1]; [1]Saga University, Japan; [2]Novel Crystal Technology, Japan

β-gallium oxide (β-Ga_2O_3) is a promising semiconductor for power device applications owing to its ultra-wide bandgap (4.8 eV) and high breakdown field (8 MV/cm). The high-power performances of the vertical-type Schottky barrier diodes (SBDs) have been demonstrated. However, killer defects are the potential leakage current paths which lowered the off-state voltages and degrade the SBD. [1,2] Therefore, identifying the killer defects and their generation mechanism is essential to enhance the SBD performance. In this talk, we reveal the identification of the killer defects in halide vapor phase epitaxial (HVPE) (001) β-Ga_2O_3 SBDs using ultrahigh sensitive emission microscopy and synchrotron X-ray topography.
The N-type β-Ga_2O_3 epitaxial layer was grown by HVPE on an n-type 4" EFG-grown (001) single-crystal wafer substrate. The net donor doping density, N_D N_A, was ca. 10^{16} cm^{-3}. The epitaxial thickness was approximately 10 μm. Vertical-type SBDs were fabricated. For the ohmic contact, Ti/Au was evaporated on the entire back face. For the Schottky barrier (SB) contacts, Ni/Au was evaporated on the surface. The SBDs were observed by using Synchrotron X-ray topography, emission microscopy, SEM, and STEM.
The current-voltage (I-V) characteristics of the Ga_2O_3 SBD showed that SBD exhibited a leakage current of 0.46 μA at a reverse bias of 100 V. However, emission patterns were observing during the I-V measurements and five emission spots were appeared in the squircle-shaped SBD with the width of 1600 μm (area of 2.37×10^{-2} cm^2). Emission spots are corresponding to the reverse leakage current paths. Further investigation on these emission spots of the crystal using SEM showed a surface defect accompanies (100) cracks with a straight line along [100]. Next, cross-sectional STEM observation was performed. Dislocations were found to be propagated along [100] direction at a depth of 0.5 μm below the surface.
In conclusion, we have found killer defects that act as leakage current paths in HVPE (001) β-Ga_2O_3 SBD. The defects contain (100) cracks and dislocations along [100] direction.
[1] S. Sdoeung, M. Kasu, et al., Appl. Phys. Lett. **120**, 092101 (2022).
[2] S. Sdoeung, M. Kasu, et al., Appl. Phys. Lett. **120**, 122107 (2022).

2:10 PM N03
Photocurrent Induced by Franz-Keldysh Effect in β-Ga_2O_3 Schottky Barrier Diode Under High Reverse Bias Voltage Takuya Maeda[1], Kentaro Ema[2] and Kohei Sasaki[2]; [1]The University of Tokyo, Japan; [2]Novel Crystal Technologies, Inc., Japan

Under high electric field, wavefunctions of electrons and holes leak into the bandgap, then, a semiconductor exhibits the tailing and oscillation in an optical absorption coefficient for below-bandgap (hv < Eg) and above-bandgap (hv > Eg) light, respectively. This is so called the Franz-Keldysh (FK) effect. The FK effect is often used as a powerful tool to investigate physical properties of materials. The

understanding of the optical absorption characteristics under high electric field is very important toward various characterizations. In this study, we investigated the voltage dependence of the photocurrent in a β-Ga_2O_3 Schottky barrier diode under below-bandgap light illumination. Significant increase in photocurrent was observed, which is explained by the electro-absorption induced by the FK effect quantitatively.

Figure 1 shows a schematic cross-section of a β-Ga_2O_3 Schottky barrier diode (SBD) fabricated in this study. The Si and Cl doped 10 µm thick n-type β-Ga_2O_3 layer was grown by hydride vapor phase epitaxy (HVPE) on a single-crystal (001)-oriented Sn-doped β-Ga_2O_3 bulk substrate. The threading dislocation density of the β-Ga_2O_3 substrate was less than10^4 cm^{-2}. The carrier concentration of the substrate is approximately the 1×10^{18} cm^{-3}. After the epitaxial growth, a Ti (50 nm)/Au (200 nm) metal stack was deposited on the surface of the epitaxial layer as Ohmic electrodes, and rapid thermal annealing (RTA) was performed in 450°C N_2 ambient for 1 min. A Ni (20 nm)/Au (500 nm) metal stack was deposited on the surface of the epitaxial layer as Schottky electrodes. The measured device has a circular electrode with a 400 um diameter.

Before the reverse-biased photocurrent measurements, current-voltage (*I-V*), capacitance-voltage (*C-V*) and internal photoemission (IPE) were carried out to characterize the Schottky barrier height of Ni/β-Ga_2O_3 interface. Figures 2, 3 and 4 shows the forward *I-V*, *C-V* and IPE characteristics of the SBD, respectively. The ideality factor of 1.03 was obtained from the *I-V* measurement, suggesting that the device showed nearly ideal thermionic emission transport. From the *C-V* measurement, the net donor concentration of 6.5×10^{15} cm^{-3} and its uniform distribution along the depth were confirmed. From these three measurements, the consistent and reliable barrier height of 1.16-1.17 eV was obtained, indicating that the Schottky interface has very high homogeneity.

Figure 5 shows the reverse voltage dependence of the photocurrent in the β-Ga_2O_3 SBD under the monochromatic illumination with the wavelength of 275-300 nm (the band width is 5 nm). The irradiated light penetrated into β-Ga_2O_3 around top electrodes. The light reached the Schottky interface from the backside through multiple reflection. The light with photon energy higher than the Schottky barrier height causes IPE, resulting the photocurrent. The photocurrent originating from IPE has very small voltage dependence, since the barrier height is lowered by image force with increasing electric field near the Schottky interface. However, the photocurrent showed significant increase with reverse voltage. The increase was more striking as the wavelength approached to the fundamental absorption edge of β-Ga_2O_3. These voltage and wavelength dependences of the photocurrent indicate that the photocurrent is originating from the optical absorption induced by the FK effect. We calculated the photocurrent by considering the optical absorption induced by the FK effect in the depletion layer based on Aspnes's theory. In the calculation, the material parameters of β-Ga_2O_3 were used, which is summarized in Table I. Figure 6 shows the comparison between the experimental data (open circles) and the calculated photocurrent (red broken lines). The calculated curves show excellent agreement with the experimental data. These results are very useful for optical absorption in β-Ga_2O_3 devices under high electric field such as a photomultiplication measurement [1, 2].

2:30 PM N04

(Student) Anisotropic Electronic Properties of NiO_x/β-Ga_2O_3 p-n Heterojunctions on (-201), (001), and (010) β-Ga_2O_3 Substrates

Dinusha Herath Mudiyanselage, Dawei Wang, Ziyi He and Houqiang Fu; Arizona State University, United States

β-Ga_2O_3 as a wide bandgap (WBG) semiconductor has been extensively studied for power, optical, and RF electronics due to its large bandgap of 4.9 eV and high breakdown field of ~ 8MV/cm. β-Ga_2O_3 is an attractive candidate to power electronics that can outperform GaN and SiC counterparts. However, most of the demonstrated β-Ga_2O_3 devices are unipolar due to the lack of p-type Ga_2O_3, such as high electron mobility transistors (HEMTs) and Schottky barrier diodes (SBDs). This is primarily attributed to the absence of shallow acceptors and holes trapped in localized polarons. As, a solution p-NiO_x has been employed to form heterojunction-based p-n diodes with β-Ga_2O_3. Several NiO_x/β-Ga_2O_3 devices, such as p-n diodes and junction barrier Schottky (JBS) diodes have been demonstrated so far with excellent electrical properties such as low on resistance, high ON/OFF ratio, and large reverse blocking voltage. Experimentally it is shown that this heterojunction can withstand 8.2 kV with a 13 µm drift region and a field plate structure[1].

Theoretically, it is investigated to have a 10 kV breakdown voltage with a positive bevel design[2]. These observations indicate the great potential of this heterojunction. However, β-Ga_2O_3 exhibits anisotropic properties along different crystal orientations due to highly asymmetric monoclinic crystal structure. The impacts of different β-Ga_2O_3 crystal orientations on NiO_x/β-Ga_2O_3 p-n heterojunction are still underexplored and needs further investigation.

In this work, we perform a comparative study of NiO_x/β-Ga_2O_3 p-n heterojunctions on (-201), (001), and (001) crystal orientations. The edge-defined film-fed grown β-Ga_2O_3 substrates were acquired from Novel Crystal Technology, Inc Japan with a similar n-type doping concentration of [Sn] ~ 5×10^{18} cm^{-3} and thickness. First, the substrates were cleaned using acetone, isopropyl alcohol (IPA), and DI water. The Ti/Au (20/130 nm) back contacts were deposited by electron beam (E-beam) evaporation followed by rapid thermal annealing at 500 °C in N_2 environment. Then, standard photolithography was performed to define patterns for deposition of NiO_x and the anode. 200 nm NiO_x and the anode Ni/Ti/Au (20/15/100 nm) were deposited using E-beam evaporation, followed by a liftoff process to isolate individual devices. I-V and C-V measurements were performed using a 4200 SCS semiconductor parameter analyzer. All three devices show an excellent rectification with ON/OFF ratio $>10^8$. The I-V measurements indicate a turn-on voltage of 1.9, 2.1, and 2.6 V, an ideality factor of 2.1, 1.9, and 2.9 and an on-resistance of 3.7, 7.4, and 3.9 mΩ.cm^2 for (-201), (001), and (010) devices, respectively. C-V measurements indicated a doping concentration of ~1×10^{17} cm^{-3} indicating similar hole concentrations in the NiO_x layer. The formation of the abrupt NiO_x/β-Ga_2O_3 interface is verified by the transmission electron microscope (TEM) and polycrystalline nature of NiO_x is clearly visible.

These differences in the device electrical properties are attributed to the different atomic configurations, the density of dangling bonds, and conductivity modulated hole injection into β-Ga_2O_3. Anisotropy can arise due to the crystal structure of the materials, impurities, or other factors. In the case of a NiO_x/Ga_2O_3 p-n diode, anisotropy can be observed in the direction of the current flow, the resistance, and the electron mobility, which depends on the orientation of the p-n junction with respect to the crystalline planes of the materials. Further investigation through annealing, temperature-dependent measurements, and reverse recovery of the diodes will reveal more information about the anisotropic nature of NiO_x/β-Ga_2O_3 p-n heterojunctions. This work can be an importance reference for understanding the anisotropic electrical behavior of β-Ga_2O_3 heterojunction based bipolar devices.

[1]*Nat. Commun.* **13**, 3900 (2022).
[2]*ECS J. Solid State Sci. Technol.* **12**, 015001 (2023).

2:50 PM N05

Impact of Radiation Damage and Buffer Charge on Si δ-Doped β-Ga_2O_3 MESFETs

Joe F. McGlone[1,1], Nidhin Kurian Kalarickal[2,1], Ashok V. Dheenan[1], Michael W. McCurdy[3], Enxia Zhang[3], Daniel M. Fleetwood[3], Siddharth Rajan[1] and Steven A. Ringel[1,1]; [1]The Ohio State University, United States; [2]Arizona State University, United States; [3]Vanderbilt University, United States

Gallium oxide has many compelling material properties that have generated a large and growing interest for applications in opto-electronics, power devices, and RF devices. The wide bandgap of ~4.6-4.8 eV leads to a large breakdown field which increases the Baliga and Johnson figures of merit, indicating potentially superior performance in high power and high frequency devices. Additionally,

the large bandgap has a propensity for better radiation hardness due to higher required displacement energies. A targeted application for β-Ga_2O_3 based devices is a harsh radiation environment in space applications. There has been significant work to understand the impact of radiation on the GaN based devices, which degrades device performance due to the introduction of crystal defects. β-Ga_2O_3 has been shown to have higher displacement energies compared to GaN, so it may have improved radiation tolerance.[1] The device studied here is a Si δ-doped β-Ga_2O_3 MESFET, which has already been demonstrated to be highly scalable and has the potential for RF performance with an experimentally measured cutoff frequency of 27 GHz.[2] The impact of neutron and proton irradiation on this device design is explored and monitored by changes in the device characteristics. The device structures are simulated using Silvaco Atlas, informed through bulk radiation studies on β-Ga_2O_3, to model how the radiation damage is influencing the device performance.
The MESFETs were grown by plasma-assisted molecular beam epitaxy (PAMBE) on an (010) EFG Fe-doped substrate. The growth was done with Si being used as the channel dopant and Fe used at the start of the growth to compensate the charge at the growth interface. Throughout this study, multiple buffer thicknesses were used along with different growth conditions. The main change to the growth condition was reducing the plasma power to reduce the amount of unintentional background Si concentration, which has been observed in this study, and in previous work as well.[3] The process for the transistors was done using a regrown ohmic contact to reduce the Ti/Au source and drain contact resistance. A Ni Schottky is used for the gate contact to provide control over the charge in the channel.
This study of the effects of neutron and proton irradiation on MBE grown δ-doped MESFETs has revealed a significant impact of the presence of charge in the UID buffer from background Si contamination during the growth. The changes in the transfer characteristics associated with the buffer charge and the compensation of that charge from irradiation-induced defects has been qualitatively replicated and explained with TCAD simulations. The characteristic changes due to the buffer charge compensation, mainly an improved subthreshold slope and a more abrupt transconductance turn-on is also shown to complicate the extraction of relevant parameters to accurately understand the amount of charge loss in the transistors. Further evidence of the buffer charge impact was directly seen in experimental results which indicated the proton irradiated 675 nm buffer sample with buffer charge converged to similar characteristics as the 225 nm buffer sample that had no indication of buffer charge before irradiation. Finally, an initial comparison between the 225 nm buffer sample, where the effect of buffer charge was not observed, and previously published AlGaN/GaN results under nominally identical proton irradiation conditions indicates great promise for β-Ga_2O_3 devices given the early stage in technology development.[4] As is shown in this work, the impact of the buffer growth and compensation design is an important area of research and optimization for future radiation hard transistor designs.
[1] J. F. McGlone *et al.*, *JAP*, 133, 4, 045702, Jan. 2023.
[2] Z. Xia *et al.*, *IEEE EDL*, 40, 7, 1052–1055, Jul. 2019.
[3] T. J. Asel *et al.*, *JVST A*, 38, 4, 043403, May 2020.
[4] Z. Zhang *et al.*, *JAP*, 119, 16, 165704, Apr. 2016.

3:10 PM BREAK

3:30 PM N06
Origin of Surface Defects in Homoepitaxially Grown (010) β-Ga_2O_3 Films Kenny Huynh[1], Michael E. Liao[2], Marko Tadjer[3], Fikadu Alema[4], James Culbertson[3], Alan G. Jacobs[3], James Lundh[2], Hannah Masten[2], John Gaskins[5], Jennifer K. Hite[3], Michael Mastro[3], Patrick Hopkins[5], Andrei Osinsky[4], Karl Hobart[3] and Mark Goorsky[1]; [1]University of California, Los Angeles, United States; [2]National Research Council Postdoctoral Fellow at U.S. Naval Research Laboratory, United States; [3]U.S. Naval Research Laboratory,, United States; [4]Agnitron Technology, United States; [5]LaserThermal Inc., United States

The origin of surface defects is investigated in homoepitaxially grown (010) β-Ga_2O_3 films. Optical and atomic force microscopy revealed surface pitting distributed nonuniformly across the sample with regions of high and low density of surface defects in a 6 um thick film. The samples are grown via metalorganic chemical vapor deposition with a substrate temperature of 840 °C and 15 Torr pressure. The relationship between the epilayer and substrate defects is studied using x-ray topography and transmission electron microscopy. A recent study observed a threading dislocation at the epilayer-substrate interface that nucleates into the pits that are observed at the surface. This work identifies an alternate source of the surface defects and reports differences in the etch pit defect morphologies.
X-ray topography was used to generate wafer scale tilt maps using the (820) reflection to identify regions of local distortion in the epitaxial layer caused by defects. High defect dense regions in this sample result in highly misoriented domains (>200”) with respect to the surrounding material. Triple axis x-ray diffraction measurements that isolate these regions of low and high defect density show clear differences in the rocking curves with FWHM of 20” and 34” and FW0.001M of 380” and 640” for low defect and high defect dense regions respectively. The nonuniform distribution of defects is further investigated with scanning electron microscopy, which reveals an aggregation of surface pitting that forms a surface morphology similar to a mountain range.
Cross sectional transmission electron microscopy was taken across a single defect as well as within the high defect dense region along the [10$\underline{2}$] zone axis. The cross section taken across the single pit revealed a V-shaped defect with misoriented twinned grains that create a 68° angle, which corresponds to the angle with (830) and ($\underline{8}$30) twinned planes. Additionally, selected area electron diffraction measurements showed that the region between the V-shape twinned grains was oriented the same as the bulk material, suggesting a directional growth to the misoriented defect. In the defect dense region, polycrystalline material was observed with elongated grains in the out of plane direction. This structure is reminiscent of polycrystalline diamond growth, where small, nucleated grains compete during growth and eventually collide leaving one dominant growth direction. In this defect dense region, the epilayer-substrate interface had a roughness of ~18 nm and showed no evidence of a high quantity of threading dislocations originating from the substrate. The high defect density in epitaxial layers does not correspond to a high defect density in the substrates. This suggests that the defects can originate from surface damage (i.e. surface cleaning or polishing) and are not only associated with threading dislocations formed during bulk growth.

3:50 PM #N07
(Student) Atomic Scale Defect Formation and Phase Transformation in Si Implanted *β*-Ga_2O_3 Hsien-Lien Huang[1], Christopher Chae[1], Jared M. Johnson[1], Alexander Senckowski[2], Shivam Sharma[3], Uttam Singisetti[3], Man Hoi Wong[2] and Jinwoo Hwang[1]; [1]The Ohio State University, United States; [2]University of Massachusetts Lowell, United States; [3]University at Buffalo, The State University of New York, United States

β-Ga_2O_3 has emerged as an excellent candidate for power device applications due to its ultrawide bandgap (~4.9 eV), high breakdown field, and potential for high voltage switching. Advancing the

performance of β-Ga_2O_3 electronic devices requires a detailed comprehension of the properties of β-Ga_2O_3, specifically along with the point and extended defects [1,2]. Ion implantation has been known as a highly developed technique to achieve selective doping of β-Ga_2O_3 devices and heterostructures [3,4]. Advantages of ion implantation include the accurate control of dopant distribution and defect engineering. However, crucial aspects of the formation of different types of defects, phase stability, the dependence on defect concentration and implantation dosage, the mechanism of lattice recovery upon annealing, and residual defects or strain accumulation have not been explicitly examined. A systematic analysis of the defect formation in Si ion implantation β-Ga_2O_3 and the lattice recovery upon thermal annealing allows advancing the understanding of ion implantation of β-Ga_2O_3. In this report, we investigated the atomic scale defect formation and phase transformation in Si ion implanted (001) β-Ga_2O_3 using scanning transmission electron microscopy (STEM). Our results indicate the ion implantation generates nanoscale dark spots, resulting from the local lattice distortion due to the phase transformation from β to γ-Ga_2O_3 structure (Fig. 1). We later identified the atomic structure within the dark spot region as a <010> screw dislocation based on the possible slip systems of β-Ga_2O_3 [5]. With the increase of implantation concentration, these nanoscale dislocations form and lead to a γ phase inclusion. The density of γ phase inclusion increases as a function of the implantation dose, resulting in the γ-Ga_2O_3 crystal structure with planar defects occupying the implantation volume with the peak Si concentration over 10^{20} cm^{-3} determined by SIMS profiles. *In-situ* and *ex-situ* annealing of implanted β-Ga_2O_3 were performed up to 1,100 °C, and the defective γ phase changed back to the β phase but left a high concentration of dislocations within the *b* phase. The formation of dislocations after lattice recovery is associated with the inhomogeneous distribution of Si atoms and has implications for material properties. In summary, our findings provide crucial insights to precisely control the dopant dosage, distribution, and defects induced by ion implantation for the future developments of β-Ga_2O_3 power electronic devices with better performance and practical applications. We acknowledge support from the Department of Defense, Air Force Office of Scientific Research GAME MURI Program (Grant No. FA9550-18-1-0479). **Reference**

[1] J. M. Johnson, Z. Chen, J. B. Varley, C. M. Jackson, E. Farzana, Z. Zhang, A. R. Arehart, H. L. Huang, A. Genc, S. A. Ringel, C. G. Van De Walle, D. A. Muller, and J. Hwang, *Unusual Formation of Point-Defect Complexes in the Ultrawide-Band-Gap Semiconductor β-Ga_2O_3*, Phys. Rev. X **9**, 041027 (2019). [2] J. M. Johnson, H. L. Huang, M. Wang, S. Mu, J. B. Varley, A. F. M. A. Uddin Bhuiyan, Z. Feng, N. K. Kalarickal, S. Rajan, H. Zhao, C. G. Van de Walle, and J. Hwang, *Atomic Scale Investigation of Aluminum Incorporation, Defects, and Phase Stability in β-$(Al_xGa_{1-x})_2O_3$ Films*, APL Mater. **9**, 051103 (2021). [3] M. H. Wong, K. Sasaki, A. Kuramata, S. Yamakoshi, and M. Higashiwaki, *Anomalous Fe Diffusion in Si-Ion-Implanted β-Ga_2O_3 and Its Suppression in Ga_2O_3 Transistor Structures through Highly Resistive Buffer Layers*, Appl. Phys. Lett. **106**, 032105 (2015). [4] M. H. Wong, H. Murakami, Y. Kumagai, and M. Higashiwaki, *Enhancement-Mode β-Ga_2O_3 Current Aperture Vertical MOSFETs with N-Ion-Implanted Blocker*, IEEE Electron Device Lett. **41**, 296 (2020). [5] H. Yamaguchi, A. Kuramata, and T. Masui, *Slip System Analysis and X-Ray Topographic Study on β-Ga_2O_3*, Superlattices Microstruct. **99**, 99 (2016).

4:10 PM N08

Measuring Diffusion of Al, Sn, and Fe in Ga_2O_3 Using β-$(Al,Ga)_2O_3$/Ga_2O_3 Superlattices Nathan D. Rock[1], Michael Scarpulla[1], Haobo Yang[1], Aviva Levin[1], Arkka Bhattacharyya[2], Sriram Krishnamoorthy[2], Michael Walker[3], Wei Zhao[4] and Ming K. Cheng[4]; [1]University of Utah, United States; [2]University of California, Santa Barbara, United States; [3]Colorado School of Mines, United States; [4]EAG Eurofins Laboratory, United States

Gallium oxide has rapidly advanced as a material for high-power electronics and optically blind photodetectors, due not only to its wide band gap and availability of melt-grown substrates, but also its dopability with n-type doping being demonstrated from 10^{14} cm^{-3}-10^{22} cm^{-3}. However, numerous reports have shown dopant compensation when annealing in temperatures greater or equal to 1000 ºC. To further device development, it is critical to understand the compensation mechanism, and to study defect formation and diffusion. It is of course difficult to study the diffusion of native defects such as gallium vacancies (V_{Ga}); typically isotope diffusion experiments are conducted. It is also of high interest to investigate the mechanisms by which native defects are introduced; does the material generate them homogeneously in its bulk or are they generated at surfaces? Do vacancies diffuse alone or as complexes with other defects? We sought an alternate method to determine the introduction and diffusion of Ga vacancies. We began with the hypothesis that Al could be used as a tracer for cation vacancy diffusion because of the assumption that Al would diffuse primarily substitutionally via cation vacancies. We designed superlattices of alternating epitaxial layers of $Al_{0.1}Ga_{1.9}O_3$ / Ga_2O_3 deposited on both Sn- and Fe-doped (010) β-Ga_2O_3 substrates. The presence of many repeated layers diffusing during the same experiment can be used to reveal gradients in the diffusion constant vs depth and time, which in turn can indicate the direction of vacancy flux from the source. Dynamic Secondary Ion Mass Spectrometry (D-SIMS) profiles were collected before and after annealing in O_2 at 1000-1100 ºC. A novel transient simulation of vacancy- mediated diffusion was developed in Matlab to model the evolution of Al profiles under different scenarios of transient vacancy diffusion. A surprising finding is that there was no evidence of vacancy injection from the free surface, but that a large flux of vacancies flows into the superlattices from Sn-doped substrates. In the case of superlattices on Fe-doped substrates, no such flux is detected and the diffusion constant of Al is uniform and much smaller in depth, consistent with smaller uniform vacancy concentrations or other non-vacancy-mediated diffusion mechanisms. We present our results for the diffusion constant of VGa or its dominant complex mediating Al diffusion as well as the diffusivity for Al by the vacancy mechanism. The role of macroscopic crystallographic defects on the diffusion results was explored via ToF-SIMS 3D reconstructions and shown to be negligible under well-chosen conditions. Meanwhile, we also investigated the diffusion of Sn and Fe from the wafers into the superlattices. We provide a lower bound for the Sn diffusion coefficient, and discuss the strong possibility that it retards the diffusion of V_{Ga} by complexation. Fe profiles are very complex and evolve via multiple diffusion channels. We provide the diffusion coefficient for the slower channel, and model the faster surface pile-up by interaction with surface potential.

4:30 PM N09

Linearly Polarized UV, Blue and IR Photoluminescence from β-Ga_2O_3 Minhan Lou[1], Jacqueline Cooke[1], Michael Scarpulla[1,1], Arkka Bhattacharyya[2], Sriram Krishnamoorthy[2], Xueling Cheng[1], Yunshan Wang[1] and Berardi Sensale Rodriguez[1]; [1]The University of Utah, United States; [2]University of California, Santa Barbara, United States

An ultra-wide bandgap of 4.8 eV makes β-Ga_2O_3 a promising material for high-power devices and ultra-violet (UV) optoelectronic devices such as UV-transparent electrodes and solar-blind photodetectors [1]. It is well-known that the optical absorption of β-Ga_2O_3 is anisotropic, having different threshold energies for different incident linear polarizations. Due to its low-symmetry, the polarization of the emitted photoluminescence (PL) of β-Ga_2O_3 should also be polarized; but this phenomenon which could allow distinguishing between point defects based on their structure has received much less attention. Polarized emission has been predicted and measured to be strongly related to self-trapped holes (STHs) involving O displacements, impurities, and doping [2-4]. The reported typical β-Ga_2O_3 PL is composed of UV, blue, green, and red main emission bands [5,6]. Previously-reported PL has not shown a high degree of polarization (DOP; difference of power fraction carried by maximum and minimum polarization component), which we suspect is due to low sample or surface quality, doping, and impurities. To our knowledge, the highest previous DOP for PL emission under one-photon absorption in β-Ga_2O_3 is 0.88 [7].

Herein we report that, in high-crystalline-quality melt-grown [-201]-oriented bulk β-Ga_2O_3 (1.9×10^{17} cm^{-3} unintentional doping (UID)), and with 240 nm excitation wavelength, we observed pure linearly polarized PL (along [102]) with DOP of about 0.975 in UV, blue and IR regions and linear polarization ratio (PR) of about 80 (PR defined as the intensity ratio of maximum to minimum polarization components). The PR is almost independent of excitation polarization, indicating that it is primarily related to the STH or defect structure rather than initial absorbing states. The PR is much lower in the green and red regions, which can be attributed to the mixed weak green and red band PL originating possibly from oxygen interstitials [4] and unintentionally doped transition metals such as Cr [6]. We observed a pure linearly polarized IR PL band peaking at ~1.57 eV different from the known emissions from Cr, which typically peak at ~1.75 eV (709 nm) [8]. Since the IR PL energy is close to the STH energy and shows same DOP as the UV and blue band PL, we suspect that the IR PL band is related to the optical transitions between STH states and valance band [9]. Under 266 nm (4.66 eV) excitation wavelength (which is below b-axis and above the a,c plane optical transitions band gap energy), the PL shows smaller PR (~55). The penetration depth of the excitation light is larger at 266 nm wavelength than at 240 nm wavelength and the refractive index of β-Ga_2O_3 is highly anisotropic (especially for polarization parallel to b-axis vs the a,c-plane). As a result, higher proportion of the collected PL is generated at deeper places from the surface and undergo longer paths inside the sample, which makes the collected PL polarization more elliptical .
PL from Sn-doped [-201]-oriented bulk β-Ga_2O_3 shows smaller PR (~40), stronger incident polarization-dependence and higher proportion of green-band emission. PL in the Sn-doped [010]-oriented bulk β-Ga_2O_3 shows highly linear polarization (PR~32) along c-axis and almost no excitation polarization dependence. In all above-mentioned samples, blue band is the dominating emission and the IR band is the second strongest PL band.

[1] X. Chen, et al., *Photon. Res.* **2019**, *7*, 381.
[2] M. Yamaga, et al., *Phys. Status Solidi C* **2011**, *8*, 2621.
[3] N. Zhang, et al., *Opt. Express* **2021**, *29*, 18587.
[4] Q. D. Ho, et al., *Phys. Rev. B* **2018**, *97*, 115163.
[5] J. Cooke, et al., *Sci Rep* **2022**, *12*, 3243.
[6] G. Naresh-Kumar,et al., *Phys. Status Solidi B* **2021**, *258*, 2000465.
[7] J. B. Cho, et al., *J. Phys. Chem. C* **2021**, *125*, 1432.
[8] C. Remple, et al., *Journal of Vacuum Science & Technology A* **2023**, *41*, 022702.
[9] S. Marcinkevičius, et al., *Appl. Phys. Lett.* **2020**, *116*, 132101.

4:50 PM N10
(Student) Photoluminescence Spectroscopy of Cr^{3+} in β-Ga_2O_3 and $(Al_{0.1}Ga_{0.9})_2O_3$ Cassandra Remple, Lauren Barmore, Jani Jesenovec, John S. McCloy and Matt D. McCluskey; Washington State University, United States

Alloying β-Ga_2O_3 with Al_2O_3 to create $(Al_xGa_{1-x})_2O_3$ enables ultra-wide bandgap material suitable for applications deep into the ultraviolet. In this work, photoluminescence (PL) spectra of Cr^{3+} were investigated in monoclinic single crystal β-Ga_2O_3:Cr, and 10 mol.% Al_2O_3 alloyed with β-Ga_2O_3, denoted β-$(Al_{0.1}Ga_{0.9})_2O_3$ or AGO. Temperature-dependent PL properties were studied for Cr^{3+} in AGO and β-Ga_2O_3 from 295 K to 16 K. For both materials at room temperature, the red-line emission doublet R_1 and R_2 occurs at 696 nm (1.78 eV) and 690 nm (1.80 eV), respectively, along with a broad emission band at 709 nm (1.75 eV). The linewidths for AGO are larger for all temperatures due to alloy broadening. For both materials, the *R*-lines blue-shift with decreasing temperature. The (lowest energy) R_1 line is dominant at low temperatures due to the thermal population of the levels. For temperatures above ~50 K, however, the ratio of R_2 to R_1 peak areas is dominated by nonradiative combination. Additionally, Hall effect measurements were taken at low and elevated temperatures which demonstrated n-type behavior. Two different activation energies were identified, 57 meV associated with the Cr level, and 26 meV associated with an impurity band at lower temperatures.

Student Finalists for Oral Presentation Award—Part A
Moderator: Kevin Daniels
Wednesday Afternoon, June 28, 2023
5:10 pm – 6:10 pm
UC, State Street

#H07
(Student) Control of Dark Exciton Dynamics in Suspended WSe_2 Monolayer via Electrostatic Deflection Frances Camille M. Wu, Shang-Hsuan Wu, Xintong Li, Jean Anne Incorvia and Edward T. Yu; The University of Texas at Austin, United States

Strain engineering is a powerful tool that strongly influences electronic structure and exciton states in 2D transition metal dichalcogenides (TMDs). Among TMDs, WSe_2 has gained attention as a host for quantum emitters due to its intrinsic ground exciton state–a lowest-lying dark exciton state that hybridizes with defect levels upon strain, giving rise to bright single photon emitters. In particular, the application of uniform biaxial tensile strain to monolayer WSe_2 causes a downshift of the conduction band minima at K and K' valleys which then hybridize with states within the band gap that originate from point defects in WSe_2 such as Se vacancies. This hybridized state allows optical transitions of long-lived dark excitons which are otherwise forbidden for unstrained WSe_2 due to spin and momentum conservation. The high oscillator strength, increased charge and spin lifetime, and long diffusion length of dark excitons allow them to store and transport quantum and classical information which could be beneficial for quantum information processing, sensing, and secure communications. Therefore, the ability to manipulate the emission of dark exciton states is crucial for the design of future quantum emitters based on strained monolayer WSe_2. Recent advances in spatially localized quantum emitters based on strained WSe_2 utilize strain fields created via transfer of monolayer WSe_2 to prefabricated dielectric nanopillars, metal nanoparticles, etched trenches or holes, or through precise nanoindentation techniques using atomic force microscopy. However, the above-mentioned methods provide low quantum emitter yield due to monolayer piercing, random and uncontrollable quantum emission, limited substrate effects, and restrictions in operating conditions. To realize high purity and tunable quantum emitters, it is necessary to have controllably strained WSe_2 devices operating at cryogenic temperatures. In this study, we demonstrate control of dark exciton dynamics of suspended WSe_2 monolayers via electrostatic deflection at cryogenic temperatures. Our technique implements strain fields which are generated by applying a bias voltage between a suspended WSe_2 monolayer and an electrode in a back gate geometry. Since the monolayer WSe_2 is grounded and the back gate is positively biased, an electrostatic force is induced between the two surfaces, which in turn results in the deflection of the suspended WSe_2 monolayer membrane. Experimental results revealed a significant monolayer deflection of ~50 nm at 15V gate bias at 300K, corresponding to ~0.3% biaxial tensile strain. Moreover, photoluminescence measurements at 7K showed a ~20 meV shift of dark exciton emission peak from 1.67 eV (0V) to 1.65 eV at (30V), corresponding to approximately 0.2% biaxial tensile strain assuming a redshift of all exciton peaks at a rate of 95meV/%. This strain value is lower than our theoretical result (0.6% strain at 30V) which could be attributed to the change in mechanical constants and built-in strain at lower temperatures. This dark exciton emission shift is an essential step towards the development of controllable WSe_2-based quantum emitters that can be integrated into various optoelectronic systems.

#F01

(Student) [100] and [010] Oriented β-Ga_2O_3 Trench Schottky Barrier Diodes with Improved On-Resistance Using Low Damage Atomic Ga Etching Sushovan Dhara, Ashok V. Dheenan, Sheikh Ifatur Rahman, Nathan Wriedt and Siddharth Rajan; The Ohio State University, United States

β-Ga_2O_3 is a promising material for high-power devices due to its high theoretical breakdown field strength. Due to the lack of p-type doping in Ga_2O_3, there is a need to explore the fabrication of trench Schottky and MOSFET topologies which can avoid premature breakdown at the metal-semiconductor interface by moving the peak electric field into the bulk of the semiconductor. To achieve these trench devices, it is necessary to develop fabrication methods that enable high aspect ratio structures, avoid plasma-induced damage, and are compatible with subsequent deposition of high-quality dielectrics with low interface defects. Previous demonstrations of trench SBDs have shown direction-dependent conductivity due to plasma damage during fin etching[1]. In this work, we demonstrate direction-independent trench SBDs with low on-resistance using atomic Ga etching. The vacuum environment used for this method is also used for subsequent deposition of a dielectric. We show state-of-art breakdown electric field (>5 MV/cm) and power figure of merit (>2 GW/cm^2) using this method. Devices were fabricated on a 5x10^{16} cm^{-3} Si-doped 10 µm thick (001) β-Ga_2O_3 HVPE epitaxial layer. SiO_2 was deposited by PECVD to form the fin etching mask in the [100] and [010] directions. Etching was performed by exposing the sample to atomic Ga-flux in an MBE chamber[2]. This process resulted in sharply defined vertical structures with a fin height of 1.2 µm. A 92 nm thick layer of Al_2O_3 was deposited with the assistance of O_2 plasma after ex-situ surface cleaning. Al_2O_3 and SiO_2 were removed from the top of the fins to form the Schottky contact by sputtering Ni (50 nm) and subsequent e-beam evaporation of Ni/Au (30/70 nm). The bottom ohmic contact was formed by e-beam evaporation of Ti/Au. For comparison, a planar SBD on the unetched surface and a MOS-capacitor on the etched surface were also fabricated on the same substrate. The forward I-V measurements of the three SBDs showed a similar turn-on of ~1 V, and C-V measurements of the MOS capacitors showed low hysteresis. The specific on-resistance of all three diodes was estimated (including current spreading effects) to be 1.20mΩ-cm^2, 1.01mΩ-cm^2, and 1.73mΩ-cm^2 for the [010], [100]-oriented fin, and 50 µm diameter planar diode, respectively. Compared to previous SBDs fabricated using ICP-RIE[3], the SBDs fabricated using Ga-flux etching showed similar current densities in [100] and [010]- oriented devices, indicating that atomic Ga etching causes less depletion of charge carriers than plasma etching. MOSCAPs showed a reverse breakdown voltage of 1.53 kV corresponding to a 5.82 MV/cm electric field in the Ga_2O_3. The [100] oriented fin broke down destructively at 1.45 kV(~5.12 MV/cm) and [010] oriented fin showed breakdown at 1.04 kV(4.34 MV/cm). This is significantly higher than the planar SBD which sustained 2.1 MV/cm at 0.25 kV. TCAD simulation shows the field concentrates near the anode edge of the fin diodes. The electric field along the vertical cutline in the center of the fin shows both the [100] and [010] oriented fins allow the peak field to be moved to the bulk of the epilayer resulting in a lower electric field at the Schottky contact compared to the planar device. The electric field along a horizontal cutline under the Al_2O_3 layer shows the local field concentration at the anode edge is above the theoretical breakdown field of 8 MV/cm. When compared to the previous state-of-the-art Ga_2O_3 SBD, the Ga-flux etched diode showed significantly improved on-resistance and Baliga power figure of merit of 2.08 GW-cm^2. In conclusion, we have demonstrated a fabrication process for trench SBDs with orientation-independent on-resistance using low-damage Ga-flux etching, resulting in peak electric fields of 5.12 MV/cm in a 0.98 µm wide [100] oriented fin. This work was supported by DOE/NNSA Award No. DE-NA0003921, and AFOSR GAME MURI Award No. FA9550-18-1-0479. REF: *[1]APL, 2021 [2]APEX, 2019 [3]APL, 2022*

#S01

(Student) Anisotropic Electron and Hole Mobilities in 4H-SiC Bulk Crystals Ryoya Ishikawa[1], Hajime Tanaka[1,2], Mitsuaki Kaneko[1] and Tsunenobu Kimoto[1]; [1]Kyoto University, Japan; [2]Osaka University, Japan

The mobility in 4H-SiC exhibits anisotropy because of its hexagonal crystal structure [1,2], and determination of the mobility considering its anisotropy is strongly required for accurate simulation and designing of SiC devices. However, knowledge of the mobility anisotropy in SiC has been extremely limited because of the unavailability of SiC wafers other than SiC(0001). In this study, we prepared special SiC(11-20) single crystals with various doping concentrations, and determined the mobility anisotropy of both electrons and holes by Hall effect measurements over a wide range of temperature. The origin of the temperature-dependent anisotropy in mobility was also discussed, and the anisotropy was quantitatively explained by the effective mass anisotropy taking account of the energy distribution of carriers. Hall bar structures shown in Figs. 1(a) and (b) were fabricated on n-type and p-type 4H-SiC(11-20) epitaxial layers to measure the electron and hole mobilities, respectively. Two kinds of Hall bar structure were formed on a sample side by side, which are oriented along 〈0001〉 and 〈1-100〉 directions for measuring the mobilities parallel and perpendicular to the *c*-axis ($\mu_{H,//}$ and $\mu_{H,\perp}$), respectively. The mobilities were extracted by Hall effect measurement at temperatures (*T*) from 140 to 600 K. Figure 2 shows the doping concentration dependences of $\mu_{H,//}$ and $\mu_{H,\perp}$ at room temperature, indicating that $\mu_{H,//}$ is about 12-18% higher than $\mu_{H,\perp}$ for electrons ($\mu_{H,//} < \mu_{H,\perp}$), which is opposite to the case for the hole mobility ($\mu_{H,//}$ is 8-12% lower than $\mu_{H,\perp}$). We determined the relationship between $\mu_{H,//}$ and doping concentration using the Caughey-Thomas equation as depicted by solid lines in Fig. 2. Next, we discuss the anisotropy of μ from the resistivity ρ ratio ($\mu_{//}/\mu_\perp=\rho_\perp/\rho_{//}$) to eliminate the effect of the Hall scattering factor. Figure 3 shows the μ ratio as a function of the temperature, indicating $\mu_{//}/\mu_\perp$= 1.0-1.3 for electrons while $\mu_{//}/\mu_\perp \sim 0.9$ for holes. In principle, the anisotropy of μ originates from that of the effective mass (m^*) and/or the average relaxation time ($\langle\tau\rangle$) since μ is given by $\mu=e\langle\tau\rangle/m^*$. Using the reported values of m^* at the band edges [3], $m^*_\perp/m^*_{//}$ is obtained to be 1.21 for electrons and 0.38 for holes as shown by dashed lines in Fig. 3. The μ ratio cannot be simply explained by the m^* ratio at the band edges, indicating that m^* at higher energies than the band edges should be taken into account for a more precise analysis because the number of carriers with higher energy increases at higher temperatures (Figs. 4(a) and 5(a)). Figures 4(b) and 5(b) show the relationship between m^* and the energy of carriers obtained from the first-principles calculation using ABINIT. Based on this relationship, the averaged effective mass (m^*_{ave}) was calculated by using the energy distribution as a weighting function for each temperature as depicted by Fig. 4(c) and Fig. 5(c) [4]. Note that we considered the whole first Brillouin zone for the calculation of m^*_{ave} of holes because the valence band structure is not isotropic as shown in Fig. 5(d) [4]. As a result, it was found that the m^*_{ave} ratios depicted by the solid lines in Fig. 3 show good agreement with the μ ratio for both electron and hole mobilities. In summary, we presented the complete set of the electron and hole mobilities along the *c*-axis in 4H-SiC over wide ranges of doping concentration and temperature. In addition, the mobility anisotropy could be quantitatively explained by the m^* anisotropy considering the energy distribution of carriers for both electrons and holes based on the first-principles calculation.

#GG03

(Student) SiO_2 Surface Planarization for Molecular Beam Epitaxy Selective Area Regrowth of High Aspect Ratio Microstructures Ashlee Garcia, Alec M. Skipper, Morgan Bergthold and Seth R. Bank; The University of Texas at Austin, United States

A molecular beam epitaxy (MBE) approach to selective area epitaxy (SAE) of III-V semiconductors could enable the seamless integration

of metals, dielectrics, and high-quality crystalline semiconductors. This technique has the potential to advance novel optoelectronic structures, such as high-contrast photonics, site-controlled quantum emitters, stacked pixel detectors, and photonic integrated circuits. While SAE by metal organic chemical vapor deposition has been widely successful due to its high material deposition selectivity, an SAE MBE method could enable further advances through its high layer precision and access to non-equilibrium growth conditions[1,2]. SAE is difficult to achieve with conventional MBE due to III-V nucleation on the amorphous mask even at temperatures as high as 700°C. As a result, Allegretti et al. developed periodic supply epitaxy (PSE), a method to inhibit polycrystal formation by cycling group III deposition under a constant group V flux[2,3]. Combined with high growth temperatures and low growth rates, PSE enables SAE by mitigating the nucleation of poly-GaAs through increased Ga adatom diffusion to seeding windows and desorption off the mask surface[3-4]. While this all-MBE approach has been demonstrated to achieve selective growth and embedding of features up to ~2 µm wide and ~300 nm tall, applications requiring larger dielectric features such as mid- and long-wave infrared high-contrast photonics[5] and aspect ratio trapping of threading dislocations for metamorphic growth[6], are more difficult to access due to increased surface roughness of micron-scale features.[7] Increased roughness and defects on the mask surface lowers the barrier for nucleation further restricting the selective growth regime.[8] Hydrogen silsesquioxane (HSQ) is an inorganic flowable oxide that has been utilized to create high quality planar SiO_2 interfaces that are vacuum and high temperature stable once cured.[9,10] In this study, we explore the use of HSQ surface planarization and curing process to restore the surfaces of micron-scale films for fabrication of high aspect ratio SiO_2 features with surfaces comparable to that of thin films. Integrating surface planarization with a 100 nm layer of HSQ in the fabrication of 1.5 µm tall features demonstrated a significant decrease in film roughness from a root-mean-square roughness of 3.95 nm to 0.75 nm. Furthermore, selectivity studies on cured HSQ films have demonstrated selectivity equivalent to that of SiO_2 deposited by plasma-enhanced chemical vapor deposition. Experiments are underway to utilize the surface planarization technique to achieve MBE selective area growth of high aspect ratio microstructures. [1] D.J. Ironside et al., *J. Cryst. Growth* (2019). [2] A.M. Skipper et al., 2019 MRS EMC. [3] F.E. Allegretti et al., *J. Cryst. Growth* (1995). [4] S.C. Lee et al. *J. of Appl. Phys.* (2002). [5] Jun Wang *et al.* 2017 *Laser Phys. Lett.* 14 125801. [6] J.Z. Li et al. Appl. Phys. Lett. 91 (2) (2007). [7] M. R. Amirzada et al. *Appl Nanosci* 6, 215–222 (2016). [8] M. Ohring, The Material Science of Thin Films, *Academic Press* (1992). [9] F. Salmassi et al, *Applied Optics*, Vol. 45, No. 11 (2006). [10] C.-C. Yang and W.-C. Chen, J. *Mater. Chem.*, 2002,12, 1138-1141 This research was partly done at the Texas Nanofabrication Facility (NSF grant NNCI-1542159) and was supported by Lockheed Martin and NSF via the UT CDCM: an NSF MRSEC under Cooperative Agreement DMR-1720595, as well as CCF-1838435, DMR-1839175 and ECCS-1926187.

#N07

(Student) Atomic Scale Defect Formation and Phase Transformation in Si Implanted β-Ga_2O_3

Hsien-Lien Huang[1], Christopher Chae[1], Jared M. Johnson[1], Alexander Senckowski[2], Shivam Sharma[3], Uttam Singisetti[3], Man Hoi Wong[2] and Jinwoo Hwang[1]; [1]The Ohio State University, United States; [2]University of Massachusetts Lowell, United States; [3]University at Buffalo, The State University of New York, United States

β-Ga_2O_3 has emerged as an excellent candidate for power device applications due to its ultrawide bandgap (~4.9 eV), high breakdown field, and potential for high voltage switching. Advancing the performance of β-Ga_2O_3 electronic devices requires a detailed comprehension of the properties of β-Ga_2O_3, specifically along with the point and extended defects [1,2]. Ion implantation has been known as a highly developed technique to achieve selective doping of β-Ga_2O_3 devices and heterostructures [3,4]. Advantages of ion implantation include the accurate control of dopant distribution and defect engineering. However, crucial aspects of the formation of different types of defects, phase stability, the dependence on defect concentration and implantation dosage, the mechanism of lattice recovery upon annealing, and residual defects or strain accumulation have not been explicitly examined. A systematic analysis of the defect formation in Si ion implantation β-Ga_2O_3 and the lattice recovery upon thermal annealing allows advancing the understanding of ion implantation of β-Ga_2O_3. In this report, we investigated the atomic scale defect formation and phase transformation in Si ion implanted (001) β-Ga_2O_3 using scanning transmission electron microscopy (STEM). Our results indicate the ion implantation generates nanoscale dark spots, resulting from the local lattice distortion due to the phase transformation from β to γ-Ga_2O_3 structure (Fig. 1). We later identified the atomic structure within the dark spot region as a <010> screw dislocation based on the possible slip systems of β-Ga_2O_3 [5]. With the increase of implantation concentration, these nanoscale dislocations form and lead to a γ phase inclusion. The density of γ phase inclusion increases as a function of the implantation dose, resulting in the γ-Ga_2O_3 crystal structure with planar defects occupying the implantation volume with the peak Si concentration over 10^{20} cm^{-3} determined by SIMS profiles. *In-situ* and *ex-situ* annealing of implanted β-Ga_2O_3 were performed up to 1,100 °C, and the defective γ phase changed back to the β phase but left a high concentration of dislocations within the *b* phase. The formation of dislocations after lattice recovery is associated with the inhomogeneous distribution of Si atoms and has implications for material properties. In summary, our findings provide crucial insights to precisely control the dopant dosage, distribution, and defects induced by ion implantation for the future developments of β-Ga_2O_3 power electronic devices with better performance and practical applications. We acknowledge support from the Department of Defense, Air Force Office of Scientific Research GAME MURI Program (Grant No. FA9550-18-1-0479). **Reference** [1] J. M. Johnson, Z. Chen, J. B. Varley, C. M. Jackson, E. Farzana, Z. Zhang, A. R. Arehart, H. L. Huang, A. Genc, S. A. Ringel, C. G. Van De Walle, D. A. Muller, and J. Hwang, *Unusual Formation of Point-Defect Complexes in the Ultrawide-Band-Gap Semiconductor β-Ga_2O_3*, Phys. Rev. X **9**, 041027 (2019).
[2] J. M. Johnson, H. L. Huang, M. Wang, S. Mu, J. B. Varley, A. F. M. A. Uddin Bhuiyan, Z. Feng, N. K. Kalarickal, S. Rajan, H. Zhao, C. G. Van de Walle, and J. Hwang, *Atomic Scale Investigation of Aluminum Incorporation, Defects, and Phase Stability in β-$(Al_xGa_{1-x})_2O_3$ Films*, APL Mater. **9**, 051103 (2021).
[3] M. H. Wong, K. Sasaki, A. Kuramata, S. Yamakoshi, and M. Higashiwaki, *Anomalous Fe Diffusion in Si-Ion-Implanted β-Ga_2O_3 and Its Suppression in Ga_2O_3 Transistor Structures through Highly Resistive Buffer Layers*, Appl. Phys. Lett. **106**, 032105 (2015).
[4] M. H. Wong, H. Murakami, Y. Kumagai, and M. Higashiwaki, *Enhancement-Mode β-Ga_2O_3 Current Aperture Vertical MOSFETs with N-Ion-Implanted Blocker*, IEEE Electron Device Lett. **41**, 296 (2020). [5] H. Yamaguchi, A. Kuramata, and T. Masui, *Slip System Analysis and X-Ray Topographic Study on β-Ga_2O_3*, Superlattices Microstruct. **99**, 99 (2016).

Student Finalists for Oral Presentation Award—Part B
Moderator: Angel Yanguas-Gil
Wednesday Afternoon, June 28, 2023
5:10 PM – 6:10 PM
UC, Lobero

#Z06
(Student) Multi-Weight Magnetic Artificial Synapses with Geometry-Dependent Neuromorphic Functionality Thomas Leonard, Samuel Liu, Mahshid Alamdar, Harrison Jin and Jean Anne Incorvia; The University of Texas at Austin, United States

Spintronic devices offer a more efficient hardware-based alternative to digitally simulated neural networks (NNs) on conventional CMOS devices[1]. This is because spintronic devices have the potential to emulate individual biological neurons and synapses which allows for one-to-one hardware mapping of NNs[2]. Domain wall (DW) based magnetic tunnel junction (MTJ) devices offer a highly tunable way to emulate many neuromorphic functionalities on a monolithic platform. The device relies on the switching of a MTJ to change state. The MTJ is composed of a fixed ferromagnetic (FM) layer and a freely switching FM layer separated by a thin tunnel barrier[3]. The resistance across the barrier is low when the magnetizations of the FM layers are parallel (P) and high when the magnetizations are antiparallel (AP). We have previously shown that if the free layer is replaced with an DW track, the device can be switched by moving the DW back and forth with current[4]. Now, we present prototypes demonstrating the tunability of these devices for neuromorphic functionalities.
The logic devices had a long DW track and a small MTJ along the track. As the DW passed under the MTJ, the resistance through the junction would switch. However, artificial synapses benefit from a higher number of states. To open more resistance states between P and AP, the MTJ was lengthened and pinning notches were patterned in the DW track beneath it. This allows for the DW to be caught under the MTJ, such that the junction is in a mixture of P and AP states. The DW can be depinned by current pulses or left in a nonvolatile state to store a weight. This allows the devices to be efficiently set during NN training and remember their weights during NN inference.
Two prototypes were explored here, a rectangular and a trapezoidal DW track[5]. The rectangular device had 5 lithographically defined pinning locations along the DW track, 3 of which were under the MTJ. This allowed for 5 repeatable and stable resistance states using one MTJ. For the trapezoidal device the asymmetry of the track allows for directional switching. Higher input current is required for wider regions to maintain current density. This allows for distinct switching voltages, since each notch has a different depinning energy depending on its location in the track. When the DW is pushed from the narrow end to the wide end, stronger pulses are needed to depin it from each notch. Pushing the DW from the wide end to the narrow end is not MW, since the DW starts in the notch with the strongest depinning energy. This behavior was shown by pushing the DW back and forth for 3 complete write/reset cycles without reinitialization.
We performed simulations of NN training and inference using experimental device data. To take advantage of the state-dependence of the trapezoidal device, a stream-learning task was implemented, where the FMNIST training dataset was separated into 60 subsets of 1000 images. The NN is then trained on one subset at a time for 30 epochs. For standard full-batch training on FMNIST, the trapezoidal device performed worse than a rectangular linear device, but when the information was provided in subsets the trapezoidal device outperformed the linear device. The trapezoidal device network was also able to reach the full accuracy of 85.6% for both training types. For inference, CIFAR-100 was used to evaluate the rectangular device, accounting for the experimental variability and stability of the states. Near-ideal accuracy was achieved, though quantization due to notches limits the attainable accuracy. Future advances for the DW-MTJ platform can enable tunable and efficient neuromorphic computing on the edge.

[1]J. Grollier et al., *Nat. Electron.* **3** (2020).
[2]A. Kurenkov et al., *Adv. Mater.* **31** (2019).
[3]S.Z. Peng et al., *Magnetic Tunnel Junctions for Spintronics: Principles and Applications.* (2014).
[4]T. Leonard et al., *Appl. Phys. Lett.* **118** (2021).
[5]T. Leonard et al., *Adv. Electron. Mater.* **8** (2022).

#Z01
(Student) Origins of Nonvolatility in Resistive Switching Memory Jingxian Li, Anirudh Appachar, Wei Lu, Wenhao Sun and Yiyang Li; University of Michigan–Ann Arbor, United States

Resistive memory or memristor is a highly potential memory and computing unit for next-generation information storage, in-memory computing, and neuromorphic computing. Valence change memory (VCM) is a promising memristor using transition metal oxides, and changes electronic resistance by moving oxygen vacancies under applied electric fields and joule heating to form or break the conducting filaments. Amorphous TaO_X ($0<X<2.5$) has been widely used in the VCM due to its outstanding performance of fast switching, high endurance and long retention time. The LRS retention failure is consistent with the standard Fickian diffusion model that oxygen vacancies in the conducting filaments will diffuse out, which cannot explain the HRS retention failure results.
In this work, we show that the Fickian diffusion model is inadequate and fails to account for “uphill” diffusion against the concentration gradient in VCM. To do so, we combine experimental measurements and first-principles thermodynamic calculations to investigate phase separation in amorphous TaOX. Experimentally, we use reactive sputtering to deposit TaOX thin-film bilayers with different oxygen:metal ratios (X). We use Auger depth profiling to measure how the thickness and composition (X) of the two layers evolve after annealing at 300C. Our results show that, while the composition and thicknesses of each layer changed during annealing, the bilayer interface persists even after long annealing times and one phase composition is ~$TaO_{1.9}$. We complement the experimental measurements with ab initio thermodynamic calculations of the amorphous formation energies, and identify the two stable phases are $TaO_{1.9}$ and Ta. The 1D phase field simulation with chemical potential from the calculated formation energy matches the Auger depth profile results to further confirm the phase separation in the amorphous Ta-O system. We also build a 2D phase separation model to simulate the retention behavior of TaO_X VCM devices, which confirms that retention failure types can be modulated by the filament width and gaps. Our results reconcile unexplained discrepancies and enable predictive design of key performance indicators such as retention stability.

#DD02
(Student) Enhancing the Dielectric Performance of Al_2O_3 on β-Ga_2O_3 Using Temperature Modulated *in situ* Dielectric Deposition Saurav Roy, Arkka Bhattacharyya, Carl Peterson and Sriram Krishnamoorthy; University of California, Santa Barbara, United States

We report on the growth and characterization of in-situ Al_2O_3 on (010) β-Ga_2O_3 deposited using metalorganic chemical vapor deposition (MOCVD) to enhance the dielectric quality and lifetime. The growth of Al_2O_3 is performed after the growth of β-Ga_2O_3 without breaking the vacuum in an Agnitron MOVPE reactor with far injection showerhead design using Trimethylaluminum (TMAl) and Oxygen as precursor gas. The interfacial dielectric layer (First 5 nm) is grown at 800 °C to crystallize the interface to have reduced interface trap density and the rest of the dielectric (17 nm) is grown at 600 °C. Thickness of the grown Al_2O_3 layer was extracted to be ~22 nm using Xray reflectivity measurements. Grazing incident Xray diffraction analysis was performed and polycrystalline inclusions were observed in the grown Al_2O_3 films. The dielectrics grown at 600 °C exhibited higher interface trap densities ($D_t = 3.2\times10^{12}$ cm^{-2}) and lower breakdown fields (E_{BR}=6 MV/cm) when compared to the dielectrics

grown at 800 °C (E_{BR}= 10 MV/cm, D_t=5.4×10^{11} cm^{-2}) as is evident from the hysteresis and the trap density vs energy characterization which were determined using deep-UV assisted CV measurements and the current-voltage characteristics of the MOS capacitor test structures. The temperature-modulated dielectric sample (interfacial layer grown at 800 °C, and the bulk dielectric grown at 600 °C) has higher breakdown strength (E_{BR}=7.7 MV/cm) and lower trap density (D_t = 1.1×10^{12} cm^{-2}) compared to the dielectric grown at 600 °C. This is possibly due to the interfacial crystallization of the hybrid dielectric due to the initial growth at higher temperature. Time dependent dielectric breakdown (TDDB) (current vs stress time) was performed to characterize the long-term reliability of the grown dielectrics. From the Weibull distribution plots of the time to breakdown for four different TDDB stress conditions, a shape factor of $\beta > 1$ is observed which indicates good statistical uniformity and intrinsic breakdown behavior. The TDDB distribution is much tighter (higher β value) for the 600 °C dielectric, compared to the 800 C grown dielectric. This is possibly due to the short-range ordering of the 800 °C dielectric compared to the 600 °C dielectric, which reduces the long-term reliability of the dielectric. However, for the hybrid dielectric, the time to breakdown is found to be more tightly distributed when compared to both 600 °C & 800 °C dielectric. Based on the E-model (field-based model), the lifetime of the 800 °C can be extended to 10 years if the dielectrics are stressed at 0.7 MV/cm, whereas the lifetime of the hybrid dielectric can be extended to 10 years if it is stressed at 3.1 MV/cm. Thus although the static breakdown voltage and trap densities of the hybrid dielectric are a little inferior compared to the 800 °C dielectric, the long term reliability of the hybrid dielectric is much superior. This approach of in-situ dielectric deposition on β-Ga_2O_3 can pave the way for promising robust gate dielectrics for future β-Ga_2O_3 based high performance MOSFETs due to its promise of improved interface and bulk quality and long-term reliability compared to other conventional dielectric deposition techniques.
We acknowledge funding from AFOSR MURI program under Award No. FA9550-21-0078 (PM: Dr. Ali Sayir).

#M06
(Student) III-Nitride Laser Diodes with Wide Quantum Wells—Influence of Built-In Electric Fields on the Light Generation Process Mateusz Hajdel, Krzysztof Golyga, Marcin Siekacz, Anna Feduniewicz-Zmuda, Szymon Stanczyk, Czeslaw Skierbiszewski and Greg Muziol; Institute of High Pressure Physics PAS, Poland

The increasing demand for the illumination in our societies pushed scientist to fight over every bit of the efficiency of the light emitters. Currently the GaN-based emitted such as LEDs and laser diodes (LDs) are taking a leading position in the domestic and industrial light sources [1], mainly because of their extraordinary efficiency and reliability. For most demanding applications like communication systems [2], projection [3] or near absolute zero cooling systems [4], LDs are the best candidates to meet the stringent requirements. Conventional heterostructure of III-nitride emitter consist of the few nanometers thick InGaN quantum wells acting as the active region. One of the issues in this approach is the existence of built-in electric fields in III-nitrides that cause separation of the electron and hole wavefunction and shift of the emission wavelength. Recently, it was shown that also wide InGaN QWs exhibit high oscillator strength thanks to operation on exited states [5-7]. Lack of the wavelength shift mechanism in those structures can potentially allow to realize the integrated RGB emitter on a single, InGaN platform.
In this work, the nature and origin of the stimulated recombination process of the InGaN LDs operating on excited states are studied. The gain spectra of LDs with 2.6, 10.4 and 25nm single QW are extracted from spontaneous and amplified spontaneous emission spectra and compared with those measured by the Hakki-Paoli method. Only by increasing the thickness of the QW sufficiently and without increasing the content of indium, the obtained wavelength of lasing is about 20 nm longer. Due to this red shift, wide QWs are promising candidates for active region in green and red lasers in the GaN material system. Analyzing the measured spectra and the quasi-Fermi level separation we drew a conclusion that the gain must originate from the first exited states, and spontaneously emitted photons from the higher states of the wide QW in the $kAcm^{-2}$ current density regime. The simulation of the wide QW LD band structure was also performed to describe the below threshold behavior. The contributions of individual transition to the total emission showed that the wavelength stable regime of spontaneous emission is due to the state index change from higher excited states to the lower ones. This mechanism occurs, because together with the screening of the built-in electric fields the QW flattens and overlap of the lower excited states increases along with the transition energy. The results reported here reveal true nature of light generation process in the wide QW devices.
[1] J. D. Bergesen et al., Journal of Industrial Ecology 20 (2), 263-275 (2016).
[2] C. Lee et al., Opt Express 23 (12), 16232-16237 (2015).
[3] Y. Nakatsu et al., Proc. SPIE Gallium Nitride Materials and Devices XV 11280 (2020).
[4] Y. Shimada et al., Rev Sci Instrum. 84 (6), 063101 (2013).
[5] G. Muziol et al., Japanese Journal of Applied Physics 61 (2021).
[6] M. Hajdel et.al., Materials 15 (1) (2021).
[7] Z. Zhang et.al., Applied Physics Express 12 (12) (2019).

#C04
(Student) Molecular Beam Epitaxy of Strained Superlattice InAlGaAs/AlGaAs Spin-Polarized Photocathodes Aaron Engel[1], Marcy Stutzman[2], Jason T. Dong[1] and Christopher J. Palmstrøm[1,1]; [1]University of California, Santa Barbara, United States; [2]Thomas Jefferson National Accelerator Facility, United States

Spin-polarized electron beams are a crucial tool in particle physics experiments and electron-in materials characterization techniques. Increasing the electron spin polarization (ESP) and the quantum efficiency (QE) of the photocathodes which produce these beams enhances the overall experimental efficiency. For accelerator applications, high QE is beneficial both in that it enhances operational lifetime and enables high bunch charge (nanoCoulomb and greater) polarized electron beams. The current state-of-the-art spin-polarized photocathodes consist of GaAs/GaAsP strained superlattice quantum wells grown on metamorphic GaAsP virtual substrates on GaAs(001), which consistently produce QE over 1% and ESP around 85%, for a figure of merit (ESP^2QE) of about 0.75. Recently, a seven-fold increase in figure of merit has been achieved by resonantly enhancing the QE to 6.4% by integrating a GaAsP/AlAsP distributed Bragg reflector (DBR) beneath the active region [1].
While the GaAs/GaAsP system is mature, it still faces many limitations. Growth of the relaxed virtual substrate results in a higher density of threading dislocations than there would be in a fully pseudomorphic system, thereby limiting quantum efficiency. In addition, since the As:P ratio controls the lattice constant, band offsets, and band gap, it is difficult to engineer the optimal strain in the well, optimal superlattice bandgap, and optimal band offsets simultaneously.
Here we demonstrate fully pseudomorphic spin-polarized photocathodes based on the InAlGaAs/AlGaAs system grown by molecular beam epitaxy. By switching to these quaternary wells and ternary barriers, we may optimize the material parameters independently. In addition, the fully pseudomorphic structure simplifies growth and reduces the dislocation density in the active region. Through this decoupling, we investigate novel device structures to potentially improve uniformity, QE, and ESP, including a digital alloy active region. Our first test structure using standard photocathode designs yielded polarization over 80%, but a QE of only about 0.3%, giving a reasonable figure of merit around 0.3. We further characterize preliminary AlAs/AlGaAs DBRs and will investigate their integration into photocathode structures.
[1] Wei Liu, Yiqiao Chen, Wentao Lu, Aaron Moy, Matthew Poelker, Marcy Stutzman, and Shukui Zhang, "Record-level quantum efficiency from a high polarization strained GaAs/GaAsP superlattice photocathode with distributed Bragg reflector", Appl. Phys. Lett. 109, 252104 (2016)

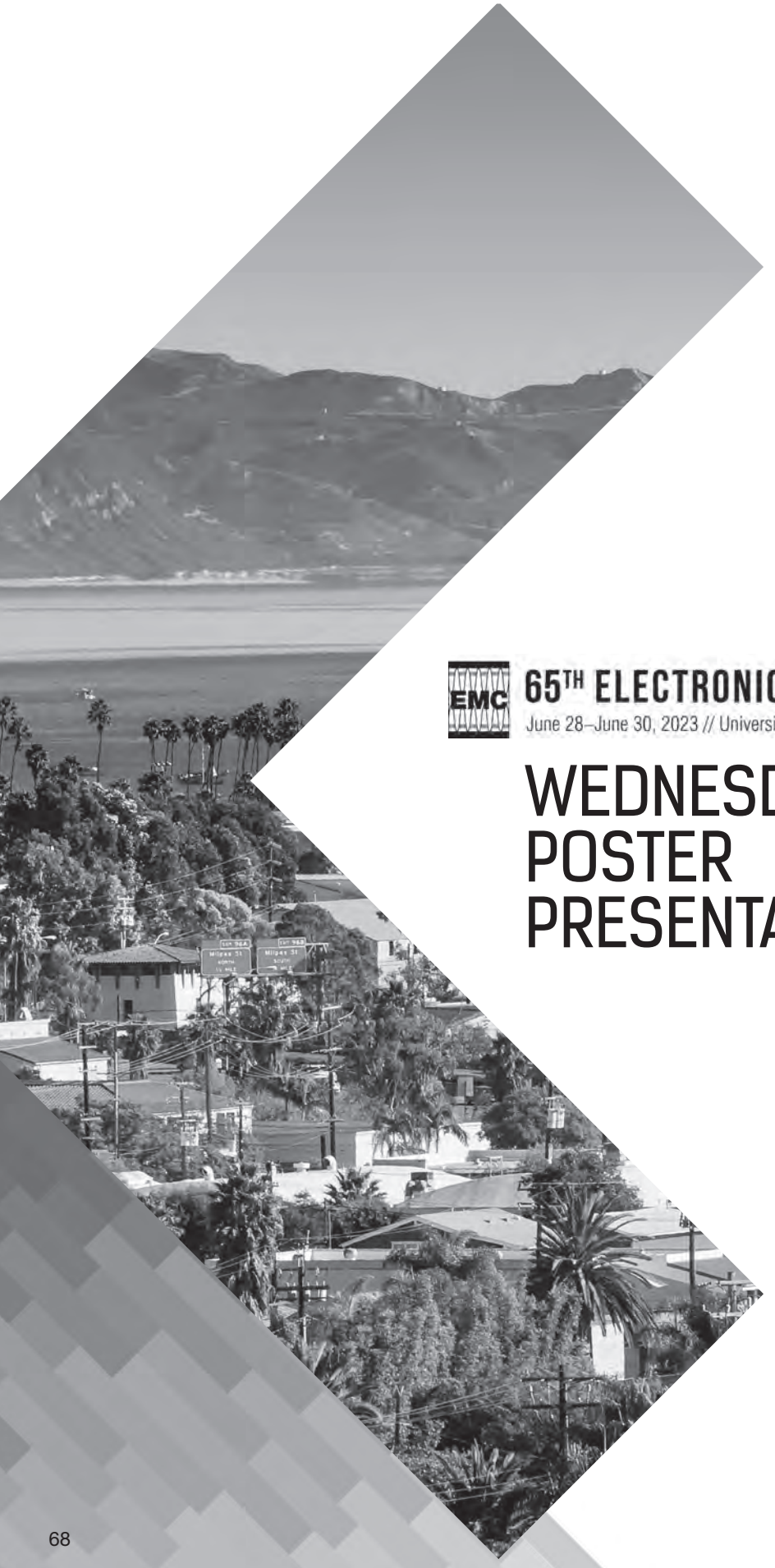

65TH ELECTRONIC MATERIALS CONFERENCE

June 28–June 30, 2023 // University of California, Santa Barbara // Santa Barbara, California

WEDNESDAY POSTER PRESENTATIONS

SESSION PS: Poster Session
Wednesday Afternoon, June 28, 2023
6:00 PM - 8:00 PM
UC, Lagoon Plaza

PS01
Distinguishing Erbium Dopants in Y_2O_3 by Site Symmetry—*Ab Initio* Theory of Two Spin-Photon Interfaces Churna Bhandari[1], Cüneyt Sahin[2], Michael Flatté[3,4] and Durga Paudyal[1,5]; [1]Ames National Laboratory, United States; [2]Bilkent University, Turkey; [3]University of Iowa, United States; [4]Eindhoven University, Netherlands; [5]Iowa State University, United States

We present a first-principles study of defect formation and electronic structure of erbium (Er)- doped yttria (Y_2O_3). This is an emerging material for spin-photon interfaces in quantum information science due to the narrow linewidth optical emission from Er dopants at standard telecommunication wavelengths and their potential for quantum memories. We calculate formation energies of neutral, negatively, and positively charged Er dopants and find the charge neutral configuration to be the most stable and consistent with the experiment. Of the two substitutional sites of Er for Y, the C_2 and C_{3i}, we identify the former (with lower site symmetry) as possessing the lowest formation energy. The electronic properties are calculated using the Perdew–Burke-Ernzerhof (PBE) functional along with the Hubbard U parameter and spin orbit coupling (SOC), which yields the orbital ($\sim$6 μ_B) and spin ($\sim$3 μ_B) magnetic moments, and occupancy (11 electrons) of Er 4*f* confirming the formation of Er^{3+}. The standard DFT provides incorrect occupied and unoccupied bands, which along with occupied 4*f* split states to some degrees are improved in the single particle level by the inclusion of onsite Coulomb and SOC. To further understand the strong electron correlation and overcome the underestimate of the PBE+U band gap of the host as well as the splitting of 4*f* -states, we perform screened hybrid functional (HSE) calculations. The standard HSE06 (mixing parameter, $\alpha = 0.2$ and screening parameter, $w = 0.25$ Å^{-1}) produces the correct band gap of the host material; however, it pushes unoccupied 4*f* -states above the band gap leading to resonant states. Although the $4f - 4f$ splitting is significantly improved using $\alpha = 0.2$ and $w = 0.2$ Å^{-1} in the HSE, it reduces the band gap of the host. Interestingly, standard HSE06 + negative U for 4*f* -states improves the localization of 4*f* -valence states, $4f - 4f$ and $4f - 5d$ splittings, and the band gap.
Work done at the Ames Laboratory was conducted for the US-DOE under its contract with Iowa State University, Contract No. DE-AC02-07CH11358. MEF and CS acknowledge support from NSF DMREF under Award No. DMR-1921877. We acknowledge fruitful conversations with Tian Zhong, University of Chicago.

PS02
(Student) Molecule Spin State and Molecular Structure Impact on Molecular Spintronics Device Properties Andrew C. Grizzle, Christopher D'Angelo and Pawan Tyagi; University of the District of Columbia, United States

Molecular spintronics devices (MSDs) are formed by connecting two ferromagnetic (FM) electrodes with molecular channels. Utilizing a magnetic tunnel junction (MTJ), molecular magnets create a strong molecular channel between the FM electrodes, resulting in a magnetic tunnel junction-based molecular spintronics device (MTJMSD). Prior experimental investigations showed that the molecular magnet-based MTJMSDs generated unprecedentedly strong anti-ferromagnetic coupling between the FM electrodes, resulting in unique electrical, optical, and magnetic device characteristics. Although isolated molecular magnets' structure and spin states have been experimentally confirmed, it is difficult to measure their states when coupled to two FM electrodes. Here, we demonstrate the variable Heisenberg Exchange coupling (Jm) within an analogous cubic molecule and its effect on the MTJMSD equilibrium properties and response to the external magnetic field. We have utilized cubic-shaped molecules in the Monte Carlo simulations(MCS) to explore and explain the experimental MTJMSD studies performed with Octametallic cube-shaped molecules. In our MCS study, we have varied the nature of interatomic molecular coupling to produce different spin states in the same molecule. Cube-shaped molecules were connected between the first and second FM electrodes of the MTJMSD from different corners of the molecules to investigate many possibilities for forming molecular bridges. For all the situations, cube-shaped molecules were studied in a state where they produced overall robust anti-FM coupling between two FM electrodes. We examined the devices' temporal and spatial magnetic moments as a function of Jm strength and thermal energy using MCS and similar 11x50x50 3D Heisenberg models of the MTJMSD. We also demonstrate the effect of the molecules on the spatial correlation factor, heat capacity, and magnetic susceptibility of MTJMSDs. Our findings indicate that the amplitude of the molecular exchange coupling has a considerable influence on the magnetic characteristics of the MTJMSD. Additionally, we saw that Jm hastened the stabilizing process.

PS03
Fabrication of Ohmic Contact on Sulfurized Copper-Doped ZnS Sanghun Lee[1,2], Gye-Jung Lee[1,2], Ji-Won Jeong[1,2], Sung-Tae Kim[1,2] and Jae-Hyung Jang[2,2]; [1]Gwangju Institute of Science and Technology, Korea (the Republic of); [2]KENTECH, Korea (the Republic of)

Wide bandgap Zinc-sulfide(ZnS) related materials is one of the potential candidates in various optoelectronics devices such as solar cells, light-emitting diodes (LEDs), and transparent electron devices for display backplane. ZnS exhibits a wide bandgap of 3.72eV for zinc blende and 3.77eV for wurtzite crystal structures. Zinc-oxide (ZnO) materials have similar optical characteristics with ZnS and they have been utilized for the above applications. However, compared to zinc-oxide(ZnO). However, ZnS has not been widely utilized for the real devices due to several technical difficulties including material growth and device processing.
In this study, we explored the fabrication of ohmic contacts on top of copper-doped ZnS which have been reported to exhibit p-type semiconductor properties. To realize high-performance electron devices using copper-doped ZnS, it is imperative to find a method to make ohmic contact on top of the active channel materials. However, it has been very difficult to obtain ohmic contact on top of p-type ZnS due to its large work function and surface Fermi-level pinning. It is reported that the ohmic contact formation is facilitated when Cu_2S layer is formed between the metal and manganese-doped ZnS. Additional sulfurization process is included in the ohmic contact fabrication process to form Cu_2S layer on top of copper-doped ZnS layer before the metallization process.
A 50-nm-thick copper-doped ZnS was deposited using a radio frequency magnetron sputtering at an RF power of 70W to achieve better conductivity than ZnS. Subsequent sulfurization process was executed to form Cu_2S layer between copper-doped ZnS and copper/gold metal bilayer electrode because Cu_2S layer facilitates to form an ohmic contact between metal and Cu-doped ZnS. The sulfurization process was carried out with the 60-mg sulfur powder (99.9% purity) in a graphite box placed inside a thermal chemical vapor deposition chamber. The temperature was elevated to 500°C, and the sulfurization process was carried out for 30 minutes. Bilayer metallization consisting of 50-nm-thick copper and 150-nm-thick gold was deposited using an electron beam evaporation and then annealed at 750°C for 2 minutes in N_2 ambiance. The specific contact resistivity, which were obtained using the transmission line method, is 2.28×10^{-5} Ωcm^2.

PS04
(Student) Persistent Photoconductivity of Potassium Tantalate $KTaO_3$ Macarena M. Santillan and Matt D. McCluskey; Washington State University, United States

Persistent photoconductivity is a phenomenon in which the conductivity of a material increases upon light exposure and remains high without the source of exciting illumination. Potassium tantalate $KTaO_3$ (KTO) is a cubic perovskite semiconductor with a wide bandgap of 3.6 eV. Grown by Czochralski methods, this novel material is a subject of interest due to its possible applications in electronic and storage devices.
KTO crystals have been annealed in a silica ampoule filled with hydrogen gas and a piece of tantalum wire, creating an oxygen-poor environment and thus oxygen vacancies. After exposing the crystals to 340 nm light-emitting diode (LED) light, evidence of persistent photoconductivity (PPC) was observed as well as a color change. Two-point electrical measurements show a decrease in resistance of one to two orders of magnitude that last for several weeks. Moreover, the PPC effect can be reversed by an open-air anneal and re-induced by repeating the irradiation. Hall effect experiments determined the charge carriers to be electrons with low mobility. UV-visible measurements show the transmittance of the irradiated samples to decrease relative to as-grown samples. IR spectra of KTO before and after the heat treatment indicate that the O-H peaks vanish in annealed samples, likely due to hydrogen occupying oxygen vacancy sites. Conductive paths were also attempted by focused LED irradiation between two contacts.

PS05
(Student) Optical Constants and Lattice Vibrations of Bulk $SrTiO_3$ and $BaSnO_3$ Using Spectroscopic Ellipsometry from 0.03-6.5 eV Yoshitha Hettige[1], Stefan Zollner[1], Suyeong Jang[2], Agham B. Posadas[2] and Alexander A. Demkov[2]; [1]New Mexico State University, United States; [2]The University of Texas at Austin, United States

We measured the ellipsometric angles Ψ and Δ for bulk $SrTiO_3$ (STO) before and after cleaning (isopropanol cleaning, ozone cleaning at 150°C, and ozone cleaning after isopropanol) on a J. A. Woollam Variable Angle Spectroscopic Ellipsometer (VASE) from 0.5 to 6.6 eV with 0.01 eV steps at four angles of incidence from 60° to 75° with a step size of 5°. We found that ozone cleaning is a better cleaning method than isopropanol cleaning. We calculated the thickness of the remaininng surface layers considering the $<\epsilon_2>$ below the band gap of STO as 19.7 Å.
Then we measured the ellipsometric angles Ψ and Δ for ozone cleaned bulk STO on a J. A. Woollam IR VASE MARK II Ellipsometer (VASE) from 250 to 8000 cm^{-1} steps at four angles of incidence from 60° to 75° with a step size of 5° at 8 cm^{-1} resolution. The lattice vibrations of STO were described using three anharmonically broadened Lorentzians with two Gaussian oscillators. A Lowndes model with four Gaussians gives almost same results. We developed a VASE model for bulk STO using the obtained surface layer thickness to describe the UV/VIS optical constants of STO and an IR VASE model to describe the lattice vibrations of STO.
We are interested in $BaSnO_3$ (BSO), since it can be used for structuring quantum wells due to its low effective mass, which allows us to have an easily tunable quantum well by varying the thickness of the BSO layer. These quantum wells can be used for optoelectronic devices. When structuring the quantum well, the BSO layer is used as the well (having smaller band gap) and Al_2O_3 is used as the barrier (larger band gap). We grew a thin BSO layer on STO (100) by molecular beam epitaxy. The layer thickness is measured as 136 Å from X-ray reflectance (XRR). The BSO/STO sample was ozone cleaned and we measured the ellipsometric angles Ψ and Δ under the same conditions as for STO on both ellipsometers. Ozone cleaning removes most of the water and chemical molecules attached to the BSO surface. The UV VASE model developed for the STO substrate and the XRR thickness of the BSO layer were used to find the surface layer thickness as 11.7 Å and optical constants of BSO. The band gap of BSO is found as 3.4 eV from both a Tauc plot and the UV VASE model. We are expecting one BSO phonon mode (TO energy related to O vibrations) in our IR range for a reasonable broadening of 10-20 cm^{-1} and a layer thickness of 136 Å. This phonon was not observed, possibly because the broadening was larger than expected.

PS06
Impact of Oxygen Addition on Enhancing Electrochromic Performance of Vanadium Pentoxide Film by Sputtering Wen-Chang Huang, Tien-Chai Lin and Bai-Jhong Jheng; Kun Shan University, Taiwan

The electrochromic performance of vanadium pentoxide (V_2O_5) thin films on ITO glass substrate with different pressure ratios of O_2/Ar during sputtering deposition as ionic storage layer of electrochromic device is presented in the study. The pressure ratio of the O_2/Ar is 0, 0.05, 0.07, 0.10 and 0.20, respectively. The RF power toward V_2O_5 ceramic target is 120 W, the power toward Ni target is 10 W, working pressure is 5 mtorr, Ar gas flow is 5 sccm and the deposition time is 3 hrs. For the Ni:V_2O_5 thin film, the power toward Ni target is 10 W and the deposition time is 2 hrs.
The surface morphology was examined by a field-emission scanning electron microscope (FE-SEM). The topographical property of the film was characterized by atomic force microscopy (AFM). The optical properties of the film were recorded by a UV-Vis to show the difference in the film's transparency between colored and bleached states. A cyclic voltammetry (CV) method was used to measure the electrochromic properties of the films.
The deposition rate of the film decreased with the increase of oxygen partial pressure, and it also made a rougher of surface morphology. This is due to "target poison effect" with the increase of oxygen flow during sputtering deposition. For the electrochromic property of the film, a large transparent difference, $\triangle$T between colored/bleached states of 43.8 % is found at the sample of O_2/Ar pressure ratio is 0.07 and it accompanies with a high charge storage capacity of 64.43 mC/cm^2. Both two values of electrochromic property are better than that of the sample without oxygen partial pressure. The improvement of the performance is due to the roughness of surface morphology and loose structure by oxygen addition to the film. And it promotes the amount of Li^+ ion intercalate into (de-intercalate from) the V_2O_5 thin film. Similar effects also been observed in the Ni:V_2O_5 thin film as ionic storage layer of electrochromic device, the charge capacity increased to 57.53 mC/cm^2 as the O_2/Ar pressure ration is 0.07.

PS07
Effect of Cu Doping on ZnO Based Thin-Film Sensor for Hydrogen Sensing Wen-Chang Huang, Tien-Chai Lin and Zhao-Hong Yang; Kun Shan University, Taiwan

High sensing response for hydrogen gas based on the copper doped ZnO thin film (Cu:ZnO) sensor is presented in the research. The Cu:ZnO thin film was deposited by co-sputtering with various powers toward Cu target for the study of the Cu doping effect on the hydrogen sensing property. The RF power toward ZnO ceramic traget was constant at 120 W and the power toward Cu target was varied as 0, 10, 15, 20, and 25 W, respectively. Structural, morphological and hydrogen sensing behaviour were excused to observe the enhancement of sensibility of the Cu:ZnO thin film. It is found that the Cu:ZnO thin film with power of 20 W toward Cu target exhibits highest H_2 gas response and as compared to the undoped ZnO sensor resulting in a ~5 fold enhancement in the gas response. The sensing response value is defined as $S\%=[(I_g-I_a)/I_a]100\%$, where I_a is the current of the sensor in the air and I_g is the current in the presence of certain H_2 concentration. The sensing response of the undoped ZnO sensor is 58.3%, while a high sensing response of 299.8% is obtained at the 20 W deposited-Cu:ZnO sensor at 500 ppm hydrogen concentration at 300 °C. Also, both a short response time of 9 sec and a good sensing repeatability during the sensing cycle was found at the 20 W deposited-Cu:ZnO thin film sensor. The improvement of sensing response of the Cu:ZnO thin film is due to the modification of ZnO grain size by Cu doping

and leads to increase of the specific surface area for chemisorbed oxygen and hydrogen on the surface of the sensor.

PS08

Surface Modified $ZnSnO_3$ Hollow Nanorod/PDMS Based Piezoelectric Nano-Generator for Harvesting Mechanical Energy Tamanna Zakia, Christopher Munoz, Cristian Alaniz and M. Jasim Uddin; University of Texas Rio Grande Valley, United States

Piezoelectric materials are comparatively new among other alternative energy sources. Harvesting waste mechanical energy through these materials can be a potential solution of the increasing energy demand. In response to applied mechanical stress, piezoelectric materials accumulate electric charges on their surface. Upon connecting with a circuit, accumulated charges can flow and generate electricity. Based on this hypothesis piezoelectric nano-generator has been fabricated. Binary semiconducting oxides such as ZnO, TiO_2 and SnO_2 have attracted immense interest as they have unique properties of electron mobility. However, there is always a need for specially designed semiconductors to better match with the properties. This interest has turned the research focus in search of suitable ternary oxide semiconductors known as perovskite. Among other perovskite compounds, $ZnSnO_3$ has attracted the attention due to its high electrical conductivity. In this study, we reported crystal growth of hexagonal hollow $ZnSnO_3$ nanorod and investigated the piezoelectric properties for different concentration of $ZnSnO_3$-PDMS film. Hydrothermal synthesis was carried out for the formation of $ZnSnO_3$. We explored different variables (temperature, pH and reaction time) to observe the morphology and surface structure. Variation in reaction time showed significantly distinct structure of nanorod. XRD, XPS, EDX, SEM have been carried out to characterize the material. Piezo-potential has been measured for different frequencies. Maximum 40 V open circuit voltage and 23 µA short-circuit current produced under 120 BPM.

Reference: Sk Md Ali Zaker Shawon, Zaida D. Carballo, Valeria Suarez Vega, Chen Lin, Muhammad Sufian Rafaqut, Andrew Xu Sun, J. James Li, M. Jasim Uddin, 2022, Surface modified hybrid ZnSnO3 nanocubes for enhanced piezoelectric power generation and wireless sensory application, Nano Energy, (92) 106653.
Yun Chen, Huihua Ye, Xusheng Wang, Yanxia Li, Xi Yao, 2020, Grain size effects on the electric and mechanical properties of submicro BaTiO3 ceramics, Journal of the European Ceramic Society (40), 391-400.
G. Wang, Y. Xi, H. Xuan, R. Lui, X. Chen, L. Cheng, 2015, Hybrid nanogenerators based on triboelectrification of a dielectric composite made of lead- free ZnSnO3 nanocubes, Nano Energy, Nano Energy (18) 28-36.

PS09

Thermoelectric Properties Study on the Ferroelectric Materials $BiFeO_3$ and Bi_2FeCrO_6 via First Principles Efracio M. Flores[1], Mauricio J. Piotrowski[2], Julio Ricardo Sambrano[3] and Mario lucio Moreira[2]; [1]UNJBG, Peru; [2]UFPEL, Brazil; [3]University of São Paulo State–UNESP, Brazil

This study analyses the electronic, structural and thermoelectric properties of $BiFeO_3$ and Bi_2FeCrO_6 using density functional theory (DFT). Bismuth ferrite (BF) has gained significant attention in recent years due to its environmentally friendly and promising thermoelectric properties. The thermoelectric properties of the materials are computed using BoltzTraP code, covering a temperature range of 200-800 K, yielding room temperature figures of merit (ZT) of 0.96 and 1.1 for $BiFeO_3$ and Bi_2FeCrO_6, respectively, making them suitable for waste heat to electricity conversions. The structural and electronic properties of bismuth ferrite in both the ferroelectric hexagonal phase and electric orthorhombic phase are also investigated through ab initio DFT calculation.
Acknowledgements: This study was financed in part by the project "Study of ferroelectric materials ($BiFeO_3$ and Bi_2FeCrO_6) and their application in solar cells" of the Universidad Nacional Jorge Basadre Grohmann, approved by rectoral resolutions N 10164-2022-UN/JBG, for their support, which we thank.

PS10

3D-Printing of Organic Bioelectronics and Biosensors Omid Dadras-Toussi, Milad Khorrami, Sheereen Majd and Mohammad Reza Abidian; University of Houston, United States

3D printing has emerged as the focal point of research and innovation, particularly in the field of organic bioelectronics and biosensors. Two-Photon Polymerization (TPP) based on direct laser writing is an exclusive 3D printing technique, owing to its capability to fabricate 3D architectures in sub-micron resolution with high temporal and special control. Herein, we have directly incorporated organic semiconductor poly(3,4-ethylenedioxythiophene)-poly(styrenesulfonate) (PEDOT:PSS) in a TPP-compatible resin, conductive bioink, for fabrication of highly conductive and bioactive microstructures.
Figure 1 displays the components of conductive bioink and the fabrication process. As shown in Figure 1-A, the conductive bioink contained polymer crosslinker poly(ethylene glycol) diacrylate (PEGDA), organic semiconducor (PEDOT:PSS), photo-initiator ethyl (2,4,6-trimethylbenzoyl) phenylphosphinate, and miscible agent dimethyl sulfoxide. Bioactive proteins, i.e. laminin and glucose oxidase, were also directly incorporated into the resin for biomedical engineering applications. Microstructures were constructed through 3D movement of XYZ stages and irradiation of 130 femtosecond laser pulses, which solidified the resin at it's focal point (Figure 1-B). Current-voltage measurements revealed that conductivity of microstructures fabricated by non-conductive resin dramatically improved from 3.4 ± 0.8 S m^{-1} to 24248 ± 929.7 S m^{-1} (n=5) by incorporation of 0.5 wt% PEDOT:PSS in the resin.
Fabrication and characterization of various conductive microstructures such as printed circuit boards, micro capacitors and micro resistors were successfully demonstrated. *In-vitro* cell studies revealed that presence of laminin protein (100 mg ml^{-1}) in the resin significantly enhanced cellular adhesion and proliferation on microstructures (337 ± 20 cells mm^{-2}) compared to control structures (8 ± 13 cells mm^{-2}). Multi-material neural microelectrodes (combination of conductive sites, interconnects and pads with non-conductive isolation coverage) were fabricated, which exhibited high charge storage capacity and low impedance at their conductive sites. High performance biosensors were also developed via direct incorporation of glucose oxidase enzyme (3.5 KU ml^{-1}) into the resin, which detected glucose at low operating potential, i.e. 300 mV through an oxygen-independent electron transfer pathway due to presence of PEDOT:PSS. It is worthy of note that within the linear range of 0.1 – 1 mM of glucose, microbiosensors showed high sensitivity (232.9 ± 22.5 mA mM^{-1} cm^{-2}), low limit of detection (0.03 mM), fast response time (4 s), high precision (4%), and excellent specificity against interference agents, namely acetaminophen. Successful demonstration of 3D-printed multi-functional microstructures sets the sights high for development of next-generation organic bioelectronic devices and biosensors.

PS11

Layered Processes for InGaP/GaAs Heterojunction Bipolar Transistors with a Buried-Base Contact Shih-Wei Tan[1], Hao Lo[2], Chieh Lo[3], Chia-Hua Huang[4], Chih-Hsiang Hwu[1] and Wen-Shiung Lour[1]; [1]National Taiwan Ocean University, Taiwan; [2]University of Minnesota, United States; [3]Taiwan Semiconductor Manufacturing Company, Taiwan; [4]National Dong-Hwa University, Taiwan

Breakdown characteristics of InGaP/GaAs single heterojunction bipolar transistors (SHBTs) with a buried-base contact were studied. There are 8 epitaxial layers in our SHBT structure grown by a metal organic chemical vapor deposition system. Important parameters of the layered structure are (i) an unintentionally-doped GaAs collector layer (L4) doped to 1×10^{16} cm^{-3} was grown as thick as 3.1 mm for an expected high voltage; (ii) a 100 nm GaAs base layer (L5) is extremely high doped to $p^{+}=5\times10^{19}$ cm^{-3}; and (iii) a 40 nm InGaP layer

(L6) doped to 3×10^{17} cm^{-3} is used as the emitter. In experiments, they are compared with those of SHBTs with a non-alloyed base which were also fabricated by using the same layered structure. After active device mesas, fabrication of SHBTs starts with the emitter mesa. Two different etching depths were implemented. One is to expose the L5 for the non-alloyed base and the other is to expose the L6 for the buried base. AuZn was deposited as the base metal. Two- (emitter-base-junction, EBJ and collector-base-junction, CBJ) and three-terminal (Gummel-plot and common-emitter, CE) characteristics of the HBTs with a non-alloyed base were addressed in advance. Then, verification and processing manufacture of the buried-base contact evaluated by real-time measurements of the EBJ and the CBJ characteristics while performing post deposition annealing (PDA) treatments were reported in this work. Experimental results reveal that an appropriate PDA time is $t_B = 220$ s at a PDA temperature of $T_B = 340^oC$. Measured turn-on voltage and resistance, ideality factor, and scaling current of the EBJ (CBJ) are 1.08 (0.9) V and 14Ω (15.3Ω), 1.01 (1.92), and 9.97×10^{-20} (1.84×10^{-9}) mA for the buried-base HBT while they are 1.07 (0.92) V and 14.5Ω (21.6Ω), 1.04 (1.96), and 2.36×10^{-19} (9.27×10^{-10}) mA for the non-alloyed-base HBT. Common-emitter characteristics of the SHBTs measured during PDA treatments were indicative of (i) normal transistor actions were observed after $t_B = 30$ s; (ii) a collector current of $I_C = 2.256$ mA at an $I_B = 40$ mA, resulting a $\beta_{DC} \approx 56$; and (iii) no obvious improvement was found after $t_B = 160$ s. Corresponding I_Cs measured at an $I_B = 40$ mA are 2.295 and 2.287 mA. Both calculated dc current gains are $\beta_{DC} \approx 57$. Thus, the buried base was verified to be achieved by the PDA treatment. Temperature dependence of breakdown properties of fabricated SHBTs with a non-alloyed and a buried base was addressed to consider their applications for high-speed power devices. The buried-base (non-alloyed-base) HBT exhibits open-emitter CBJ breakdown voltages in range from 70.4 to 78 (62.67 to 69.33) V at temperature (T) increases from 20°C to 120°C with a positive temperature coefficients of 0.080 (0.067) V/°C. Accordingly, degraded breakdown due to effects of etched edges produced by wet-etch was not found. Besides, open-base collector-emitter breakdown voltages achieved can be expressed as $BV_{CEO} = 36.375 + 0.08554T$ ($36.12 + 0.05543T$) V. Note that the buried metal forms conformal-like passivation on the base surface. Thus, the enhanced temperature coefficient of 0.08554 V/°C to 0.05543 V/°C is considered being due mainly to the base layer that is totally passivated by the InGaP layer.

PS12

Suppression of Nitrogen Composition Fluctuation by Beryllium Doping in GaAsN Ternary Alloys

Takashi Tsukasaki[1], Takumasa Tsunoda[1], Ko Inoue[1], Miki Fujita[2] and Toshiki Makimoto[1]; [1]Waseda University, Japan; [2]NIT, Ichinoseki College, Japan

The GaAsN ternary alloy has been receiving increasing attention owing to its drastic band gap reduction property in a dilute nitrogen composition [1]. Therefore, the GaAsN system alloys have been expected to be employed in devices such as a multi-junction solar cell using InGaAsNSb and as a tunnel diode using InGaAsN inserted to a multi-junction solar cell with GaAs system alloys [2, 3]. However, transfer of photogenerated electrons have concerns to be interfered in these devices using the GaAsN system alloys because they are trapped at localized levels induced by nitrogen atoms [4]. Herein, nitrogen atoms have been indicated to be mainly coordinate as N at an As site (N_{As}) and interstitial N (N_i) in GaAsN. Nitrogen composition at the As site ([N_{As}]) fluctuates due to the large miscibility gap in GaAsN [5]. Then, electrons are localized at a high [N_{As}] region because N_{As} reduces the bottom of conduction band for GaAs [1]. Meanwhile, electron traps could be formed from N_i in GaAsN [6]. These two types of localized levels in GaAsN have been actively discussed using electrical and optical measurement [5, 7]. Therefore, in this study, these localized levels are discussed in another respect of structural characteristics especially for Be-doped p-type GaAsN ternary alloys. Undoped GaAsN layers were grown by radio-frequency plasma-assisted molecular beam epitaxy on semi-insulating GaAs (001) substrates using nitrogen RF plasma with different nitrogen gas flow rates. Be-doped GaAsN layers were also grown by the same procedure for undoped GaAsN layers except for a nitrogen gas flow rate which was fixed for all of them, and the Be impurity concentrations ([Be]) were designed at 1×10^{19}, 6×10^{19}, and 3×10^{20} cm^{-3}. Fluctuation of a lattice constant was evaluated by reciprocal space maps (RSMs) around (004) plane with a high-resolution X-ray diffraction system for undoped and Be-doped GaAsN. Thicknesses of all undoped and Be-doped GaAsN layers were confirmed to be thinner than the critical thickness [8, 9].

Considering a lattice strain, a lattice constant was evaluated by a diffraction peak of (004) plane for undoped GaAsN. Here, a lattice constant of undoped GaAsN was reported to be little affected by N_i compared with N_{As} which decrease the GaAs lattice constant, according to the theoretical calculation [10]. Therefore, [N_{As}] could be evaluated by the Vegard's law. In an RSM measurement for undoped GaAsN, a diffraction peak for (004) plane was broadened to (001) plane direction with increasing [N_{As}], meaning that fluctuation of a lattice constant increases with increasing [N_{As}]. This result indicates that fluctuation of [N_{As}] increases with increasing [N_{As}] for undoped GaAsN because only N_{As} is considered to modulate the GaAs lattice constant as mentioned above.

Meanwhile, in an RSM measurement for Be-doped GaAsN, a diffraction peak for (004) plane was narrowed to (001) plane direction with increasing [Be], meaning that fluctuation of a lattice constant decreases with increasing [Be]. Here, Be-N complexes could be formed at a Ga site in Be-doped GaAsN, according to the theoretical calculation [11]. Therefore, these Be-N complexes could reduce fluctuation of a lattice constant for Be-doped GaAsN, suggesting that fluctuation of [N_{As}] decreases with increasing [Be] in Be-doped GaAsN compared with undoped GaAsN.

References

[1] W. G. Bi and C. W. Tu, APL, 70 (1997) 1608.
[2] R. Isoaho *et al*., SEMSC, 195 (2019) 198.
[3] D. E. Mars *et al*., APL, 84 (2004) 2560.
[4] W. Yanwachirakul *et al*., JJAP, 56 (2017) 08MA04.
[5] M. C. Hsieh *et al*., JAP, 110 (2011) 103709.
[6] K. Laaksonen *et al*., JPCM, 20 (2008) 235231.
[7] T. Tsukasaki *et al*., Physica B, 625 (2022) 413482.
[8] J. W. Mattews and A. E. Blakeslee, JCG, 27 (1974) 118.
[9] R. People and J. C. Bean, APL, 47 (1985) 322.
[10] W. Li *et al*., APL, 78 (2001) 2864.
[11] H. Komsa *et al*., PRB, 79 (2009) 115208.

PS13

(Student) Optimization of the Event-Based Sensor's Photoreceptor Circuit for Mid-Wave Infrared Photodetection

Zinah M. Alsaad[1,2], Julie V. Logan[1], Diana Maestas[1], Zachry Theis[1], Peter N. McMahon-Crabtree[1], Christian P. Morath[1], Preston T. Webster[1] and Payman Zarkesh-Ha[2]; [1]Air Force Research Laboratory, United States; [2]University of New Mexico, United States

Neuromorphic imaging is being considered for space surveillance applications where it can perform sensing and tracking functions with reduced downstream datalink demands and power consumption. In contrast to the conventional framing camera which produces images by essentially counting the electrons produced by light incident on each pixel's photodetector, the event-based camera's read-out is designed to only be sensitive to changes in the signals it receives from the photodetector, which results in a datastream of events indicating where and when changes in illumination occur. These types of cameras are commercially-available with silicon-based detectors for visible wavelength applications, however, much work remains to enable the event-based read-out to effectively operate with smaller bandgap photodetectors to extend the utility of event-based sensing into the mid- and long-wavelength infrared.

The event-based read-out circuitry that fundamentally interacts with the photodetector is called the photoreceptor stage. Here, DC and AC characterizations of the event-based sensor photoreceptor circuit are performed as a function of mid-wave infrared detector parameters to assess the performance and potential limitations of using the pixel

circuitry for longer wavelength infrared detection. Detailed analysis of the circuit provides insight into the sensitivity of the photodetector bias stability, temperature-dependence of the dynamic range, and practical limitations to the dynamic range limits that arise with the use of longer-wavelength photodetectors. This work is being conducted to produce a basic event-based sensing circuit tuned for mid-wave infrared photodetection, to enable characterization of prototype mid-wave event-based sensors and evaluate which mid-wave infrared detector properties the event-based sensor's performance characteristics are most sensitive to.

PS14

(Student) Mass Spectroscopic Investigation on Reactions of Tin Tetrachloride and Germane for SiGeSn Chemical Vapor Deposition Growth Enbo Yang[1], Joshua Grant[1], Alexander Golden[1,1], Wei Du[1,1], Baohua Li[2] and Shui-qing Yu[1,1]; [1]University of Arkansas, Fayetteville, United States; [2]Arktonics LLC, United States

SiGeSn has gained intensive research interest as a novel semiconductor material since it was proposed [1]. To better understand the growth mechanism of GeSn on Si (100) substrate in the Chemical Vapor Deposition (CVD) process, we used a differential vacuum pumping system equipped with a Residual Gas Analyzer (RGA) isolated from the CVD reactor to investigate the species generated in the vacuum chamber after introducing the gases of Tin tetrachloride ($SnCl_4$), Germane (GeH_4), and the mix of them, respectively. In this paper, we report our latest results of the mass spectra of $SnCl_4$ and GeH_4 and their mix. We have obtained the whole mass spectra of $SnCl_4$ and GeH_4 with all expected from our spectra compared to the available data published [2]. Preliminary results suggest that at room temperature, a reaction has occurred with $SnCl_4$ and GeH_4 at the pressure of several Torrs. It will enable us to understand better the surface chemistry and the thermodynamics for the GeSn CVD growth. Future experiments include more systematic studies varying the parameters such as temperature, pressure, reaction time, and so forth for the mass spectroscopic scans before incorporating the RGA system into the CVD growth process, enabling us to make an *in-situ* growth diagnostics and optimize the growth recipes to get higher material quality.

Acknowledgments: The work is supported by the Air Force Office of Scientific Research (AFOSR) (Grant No.: FA9550-19-1-0341, FA9550-20-1-0168). We thank Sylvester Amoah and Steven Akwabli from Electrical Engineering at the University of Arkansas for assistance with the experimental setup maintenance.

References: [1] Shui-Qing Yu et al., SiGeSn Technology for All-Group-IV Photonics, 2022 Device Research Conference (DRC). [2]https://webbook.nist.gov/cgi/cbook.cgi?ID=C7646788&Mask=200, retrieved Jan. 17, 2023.

PS15

Reactive-Sputtering and Ferroelectric Switching of Aluminum Scandium Nitride on (-201)β-Ga_2O_3 Substrates Seung Yoon Oh[1], Seokgi Kim[2], Jeong Yong Yang[1], Gyuhyung Lee[1], Sungkyu Kim[2] and Geonwook Yoo[1]; [1]Soongsil University, Korea (the Republic of); [2]Sejong University, Korea (the Republic of)

Aluminum scandium nitride (AlScN) is an emerging ferroelectric material that has a significantly high remanent polarization and can be prepared using mature deposition techniques. It can be deposited using reactive sputtering below 400 °C and exhibits a high remanent polarization of up to 115 μC/cm^2 depending on the Sc concentration and crystallization quality. These features are intriguing for exploiting their feasibility with wide bandgap semiconductors such as gallium nitride and gallium oxides. In particular, beta-gallium oxide (β-Ga_2O_3), which is promising for next-generation power device applications owing to its enhanced electrical properties, has not been investigated as a ferroelectric film. Furthermore, the integration of the ferroelectric AlScN on β-Ga_2O_3 is yet to be reported. In this study, for the first time, we integrate an $Al_{0.7}Sc_{0.3}N$ film on a β-Ga_2O_3(-201) substrate with an Al_2O_3 insulator layer added by atomic layer deposition. To fabricate the MFIS and MFS capacitors, a Ti/Au (20/80 nm) electrode was deposited via an e-beam evaporator. Subsequently, rapid thermal annealing was performed in N_2 ambient for 80 s at 470 °C for ohmic contact. An interlayer dielectric Al_2O_3 (~4 nm thick) was deposited for the MFIS through ALD using trimethylaluminum and an ozone precursor at a stage temperature of 430 °C for 50 cycles (0.9 Å/cycle). The $Al_{0.7}Sc_{0.3}N$ (40 nm) film was deposited by the reactive sputtering method from an $Al_{0.57}Sc_{0.43}$ metal alloy target in an Ar/N_2 mixed gas at a stage temperature of 350 °C. The content of Al and Sc was measured by energy dispersive X-ray spectroscopy (EDS). A Ni (50 nm) was formed as a top electrode for all capacitors. Next, we investigate ferroelectric switching properties and memory effects for the metal-ferroelectric- insulator-semiconductor (MFIS) capacitor. Remanent polarization of about 60 μC/cm^2 was obtained at 3.8 MV/cm from metal-ferroelectric-metal. A ferroelectric memory window (MW) of 1.7 V was achieved for the MFIS, which is a record value of MOS sturucture. The results show the potential of the $Al_{0.7}Sc_{0.3}N$/β-Ga_2O_3(-201) metal-oxide-semiconductor structure for ferroelectric-based β-Ga_2O_3 devices.

PS16

(Student) Imaging Ga_2O_3 Defects and Determining Its Influence on Electrical Properties Min-Yeong Kim[1,2,3], Ory Maimon[1,3], Sang-Mo Koo[2], Qiliang Li[3,1] and Sujitra Pookpanratana[1]; [1]National Institute of Standards and Technology, United States; [2]Kwangwoon University, Korea (the Republic of); [3]George Mason University, United States

β-gallium oxide (β-Ga_2O_3) semiconductors are considered a key material for next generation high power electronics owing to their excellent material properties, such as an ultra-wide bandgap of 4.7-4.9 eV, a high theoretical breakdown field of 8 MV/cm which in turn gives it a higher Baliga's figure of merit for power devices in comparison with those developed using silicon (Si), silicon carbide (SiC), and gallium nitride (GaN). In addition, the Ga_2O_3 is expected to surpass the trade-off relationship between breakdown voltage (BV) and on resistance ($R_{on,sp}$) that other materials have. From the viewpoint of crystal growth, a low-cost single-crystal substrate of β-Ga_2O_3 can be synthesized with a high growth rate using various melt growth techniques, such as Czochralski, vertical Bridgeman, and edge-defined film-fed growth (EFG). Among these methods, the EFG has shown promise for the bulk growth of Ga_2O_3 with a large bulk size (4 inch) and high growth rate (15 mm/h).

Crystal defect control is an important issue in the development of a substrate for power devices, as defects in the substrate impact the power device performance. In order to achieve high-performance and high-reliability devices, it is pivotal to eliminate various defects in bulk crystal as well as those in thin films. Especially, isolating failure mechanisms at the source rather than relying on backend test is important for the successful proliferation of Ga_2O_3 power devices and cost reduction. To visualize nanoscale defects and determine their electronic impact, photoemission electron microscopy (PEEM) is used. PEEM is based on the photoelectric effect and is a non-destructive analysis method where light is used to excite and eject electrons from the sample surface and these electrons are analyzed. From PEEM measurements, the topography and electronic structure could be obtained.

In this study, we perform the comprehensive analysis of defects on epitaxy β-Ga_2O_3 on EFG (010) Ga_2O_3. The sample was obtained commercially, where the epitaxy was formed by using the hydride vapor phase epitaxy (HVPE) method with a target doping of 1×10^{18} cm^{-3} on the (010) semi-insulating Ga_2O_3 wafer (010). We have identified elongated structures on the HVPE Ga_2O_3 epi-layer via PEEM, and they appear in multiple instances of the sample surface and in a parallel configuration. These same features cannot be identified by confocal microscopy which suggests that these features may not be topographic in origin. We are performing ongoing work to identify this feature as a microscopic defect. For understanding the electrical influence of these elongated features on the HVPE epi-layer, we will analyze the surface of Ga_2O_3 with conductive atomic force microscopy (c-AFM) to measure electrical properties on defect and

non-defect surfaces. Together, we will present a discussion on the nature of these distinct features and their implication on device performance.

PS17
Fabrication and Characterization of High Quality Rutile-Phase GeO_2 Films on MgO(100) for Application in Optoelectronics Paul Gaurav G. Nalam, Debabrata Das and Ramana Chintalapalle; The University of Texas at El Paso, United States

Ultra-wide bandgap materials (UWBG) with energy bandgaps ~4eV or larger are currently of immense interest for the development of devices for high-power electronics, deep-ultraviolet (DUV) optoelectronics, energy harvesting, electrocatalysis and quantum information processing. In this context, the functional metal oxide GeO_2 is important for its large bandgap (4.5-6.0 eV), ambipolar dopability and large thermal conductivity. GeO_2 exists primarily in two crystalline polymorphs: the rutile / tetragonal (*r*) phase and the *α*-quartz / hexagonal (*h*) phase. Both polymorphs exhibit interesting and useful optical and opto-electronic properties. However, since it exists in multiple metastable phases with similar formation energies, isolated synthesis of multiple polymorphs with high crystal quality is challenging and has hindered its adoption into advanced optoelectronic applications. Here, we employed radio-frequency magnetron sputtering, which is a relative cost effect method, to deposit r-GeO_2 thin films on MgO (100) substrates in a controlled oxidation environment. The lower degree of interfacial lattice mismatch between r-GeO_2 and MgO enabled to tune the degree of epitaxy of the thin film based on the oxidation environment. The surface morphology, growth mechanism, optoelectronic properties, crystallography, and chemical stoichiometry of these thin films are studied in detail using atomic force microscopy, UV-Vis, Photoluminescence spectroscopy, Ellipsometry, X-ray diffraction, Transmission electron microscopy and X-ray photoelectron spectroscopy.

PS18
Growth Optimization of Sn-Doped Gallium Oxide Thin Films on Sapphire for Deep UV Photodetectors with Ultrafast Response Francelia S. Escobar, Debabrata Das and Ramana Chintalapalle; The University of Texas at El Paso, United States

Gallium oxide (Ga_2O_3), an ultra-wide band gap material, has the potential for integration into next-generation electronic, optoelectronic, photonic, and sensing devices. High physical/chemical stability and stoichiometric phase stabilization along a wide temperature range also attract applicability in extreme environmental conditions. Despite the potential for numerous technologies, there are few fundamental problems, such as asymmetric thermal energy distribution, partial oxidation of dopant source during the growth process, and poor p-type conductivity, still exists. In this work, we optimized the growth conditions to demonstrate highly Sn dope Ga_2O_3 (Sn-Ga_2O_3) thin films for deep-UV (DUV) photodetectors. The Sn-Ga_2O_3 targets were prepared using solid-state synthesis and deposited on sapphire substrates by the pulsed laser deposition (PLD) technique with precisely controlled growth parameters. X-ray diffraction, atomic force microscopy, UV-visible spectrophotometry, and spectroscopic ellipsometry were employed to understand the structure-property correlation. Metal-semiconductor-metal type devices were fabricated using Ti-Ag metal contact. Detailed device characteristics affirmed a drastic increment in responsivity and external quantum efficiency with ultrafast transient response time in the optimized Sn-Ga_2O_3 sample. The findings of the current study can be carried forward to realize the the low-cost and highly efficient DUV photodetectors with ultrafast response.

PS19
(Student) Thermally-Driven Multi-Level Non-Volatile Memory in Monolayer MoS_2 Field-Effect Transistors Sameer K. Mallik[1,2], Roshan Padhan[1,2], Mousam C. Sahu[1,2], Gopal K. Padhan[3], Prasana K. Sahoo[4], Saroj P. Dash[5] and Satyaprakash Sahoo[1,2]; [1]Institute of Physics, India; [2]Homi Bhabha National Institute, India; [3]KIIT Deemed to be University, India; [4]Indian Institute of Technology Kharagpur, India; [5]Chalmers University of Technology, Sweden

Ultrahigh data storage density is imperative for smarter computing platforms and vigorous information processing applications. Strenuous efforts have been spurred to realize in-memory operations with a high density of data storage capabilities towards the development of alternatives to von Neumann architectures.[1] With the advent of the Internet of Things and Big data, vivacious data processing and storage are obligatory in a single chip with high packing density arrays and low power consumption. Additionally, the scaling down of transistors and integration of memory functionalities insinuate brain-inspired computing and sensing capabilities. Owing to the physical limits of silicon-based metal oxide field effect transistors, the quest for alternative prospective materials has been the focus of intensive research to improve storage capacity. Multifunctional 2D layered semiconductors, in particular, Molybdenum disulfide (MoS_2) beget incessant technological evolution and has deeply permeated the fabric of low-power electronic applications. With the growing packing density of FET arrays on a single wafer, high-performance integrated circuits (ICs) can reach an operating temperature as high as 500K,[2] making it important to understand and exploit novel properties of 2D materials-based devices at high temperatures. Thermally-driven memory is one of the applications where locally generated heat can be ventured to aid the memory functions with multi-level storage capabilities. In this pursuit, we have proposed and demonstrated a novel monolayer MoS_2 mem-transistor for multi-level non-volatile memory applications. The device portrays novel mechanisms and unique functionalities that drive to a highly geared intrinsic transistor behavior with linear output characteristics and high field-effect mobilities at room temperature and exhibits a multi-level memory cell above room temperature. an avant-garde phenomenon is illustrated by temperature-dependent hysteresis inversion which is attributed to the active cation migration and additional charge injection to the channel interface. The thermally-driven cation migration emulates low-cost multi-level non-volatile memory applications using a single FET device. The transient drain current analysis provides an elementary route to understand subsequent intermediate mechanisms at different time scales that alter with temperature under the application of positive bias at the gate terminal. The charge trapping process is more favorable at room temperature which is quenched by the migration of cations near the channel-dielectric interface at high temperatures. The accumulation of cations enroute the memory capabilities with large switching windows in monolayer MoS_2 FETs. Furthermore, we explore the pulse gate voltage-controlled memory behavior, where the multi-level memory cycles are expanded to different programming pulsed width measurements that are ascribed to distinct conductance states based on several pulses. The multi-level WRITE and ERASE operations in our devices show exceptional pulse control of charge injection and release providing a complete yet simplest suite to achieve large-scale data storage capabilities. Additionally, the proposed mechanisms based on energy band diagrams adequately explain the single and multi-level memory effects arising in our MoS_2 FETs. Considering advanced materials for future computing, 2D materials such as MoS_2 are dominating the race owing to their superior electronic mobility, mechanical strength, extraordinary photo-response, and low energy consumption. The high-temperature applications of 2D transistors pave the way for next-generation techno-electronic applications in making high-performance wafer-scale integrated circuits with larger packing densities.

Reference

[1] M. C. Sahu, S. Sahoo, S. K. Mallik, A. K. Jena, S. Sahoo, *Adv. Mater. Technol.* **2022**, 2201125.
[2] D. K. Schroder, J. A. Babcock, *J. Appl. Phys.* **2003**, *94*, 1.

PS20

The Effect of Current Annealing on the Transport Properties of CVD Graphene Udagamage K. Wijewardena[1], Tharanga Nanayakkara[1,2], Rasanga Samaraweera[1,3], Annika Kriisa[1], Rameshwor Poudel[1] and Ramesh G. Mani[1]; [1]Georgia State University, United States; [2]Brookhaven National Laboratory, United States; [3]Uva Wellassa University, Sri Lanka

Graphene is a promising material for future nanoelectronics, as well as flexible electronics applications. The materials challenge here, therefore, lies in producing large area, high quality, pristine graphene suitable for device development. The chemical vapor deposition (CVD) method has proved useful for producing large area graphene. However, it has been difficult to realize high carrier mobility in part due to utilization of many chemicals and steps in the isolation of this CVD graphene onto a suitable substrate. It turns out that lab-grown CVD graphene often exhibits p-type behavior due to the presence of surface adsorbates and impurities, and such material often shows a significant hysteresis effect in gate voltage dependent measurements, with the graphene on a silicon/silicon dioxide substrate. One approach to increasing the quality of CVD graphene relies upon applying a "large" current through the specimen. Such current annealing turns out to be an effective in-situ cleaning technique for CVD graphene samples. Here, we report on the impact of current annealing on the material properties and examine the limitations of such a current annealing process.

In our investigation, we employed CVD graphene Hall bar devices on a silicon/silicon dioxide substrate, with a back gate electrode on the conducting silicon substrate, to study the evolution of the resistance hysteresis versus gate voltage as a function of current annealing in CVD graphene at T=35K. Thus, the sample was cooled down to a temperature of 35K from room temperature in a closed-cycle refrigerator, with a back-gate bias applied during the annealing process. The specimen was annealed at several progressively larger currents. Transport properties were measured using standard low frequency lock-in techniques, and the data were examined to understand the impact of current annealing on the sample's hysteresis and transport properties. Measurements indicated that the charge neutrality point, which was initially at a large positive voltage, moved towards vanishing gate voltage with increased current of the current anneal, suggesting that the sample becomes less p-type with time. However, the hysteresis between the traces obtained in the upsweep – and the downsweep- of the gate voltage increased as the CNP shifted towards zero gate voltage. In this presentation, we provide a qualitative model to help understand these observed features in experiment.

PS21

(Student) Two-Dimensional Hole Gases in N-Polar AlGaN/GaN Heterostructures Grown on GaN Bulk Substrates Changkai Yu, Zexuan Zhang, Huili Grace Xing, Debdeep Jena and YongJin Cho; Cornell University, United States

N-polar three-nitride heterostructures and devices have been a subject of intense recent investigation, as the inverted polarization fields provide unique advantages over the metal-polar devices. N-polar devices with outstanding performance have been demonstrated, such as MIS-HEMTs [1], resonant tunneling diodes [2], p-n diodes [3]. Specifically, output power above 8 W/mm at a frequency of 94 GHz has been achieved in N-polar GaN/AlGaN MIS-HEMTs [1]. From the MBE growth point of view, however, obtaining p-type conductivity in Mg-doped N-polar heterostructures is challenging: apart from the high activation energy of Mg acceptor in GaN, unintentional O donor incorporation is higher but Mg incorporation is lower for N-polar growth compared to metal-polar counterpart, both by roughly an order of magnitude [4, 5]. Polarization-induced doping provides an alternate route for p-type conductivity [6]. However, direct observation of two-dimensional hole gases (2DHGs) in N-polar AlGaN/GaN heterostructures has not been reported yet.

We report the observation of 2DHGs in N-polar AlGaN/GaN heterostructures grown by plasma-assisted MBE. AlGaN/GaN heterostructures were grown on N-polar semi-insulating GaN bulk substrates with a dislocation density of 10^6 cm^{-2}. The structure was grown at a constant thermal couple temperature of 670 °C under metal-rich conditions. 2 nm thick AlN nucleation layer was first grown under N-rich conditions to suppress unintended n-type conductivity induced by impurities present at the growth interface. 300 nm thick GaN:Mg buffer layer with Mg concentration of ~1×10^{19} cm^{-3} was then grown, where the Mg doping is used to compensate for the unintentional background n-type conductivity. Typical sheet resistivity of such GaN:Mg structures exceeds 600,000 Ω/sq at room temperature. Following the buffer layer, 5 nm thick nominally undoped GaN channel and $Al_{0.26}Ga_{0.74}N$ barrier were grown. In-situ reflection high-energy electron diffraction shows a well-resolved (3×3) reconstruction, confirming the N-polarity of the samples. Smooth surface morphology was observed with rms roughness of 0.86 nm using atomic force microscopy.

Hall-effect measurements were performed on two samples with different AlGaN barrier thicknesses (45 nm and 26 nm) in the van der Pauw configuration. Both samples exhibit p-type conductivity at room temperature and 77 K. Sheet resistivity, sheet carrier density, and Hall mobility of the 45 nm AlGaN barrier sample at room temperature are 24,700 Ω/sq, $+1.52\times10^{13}$ cm^{-2}, and 16.6 $cm^2/(V.s)$, respectively. At 77 K, its sheet carrier density decreases to $+1.01\times10^{13}$ cm^{-2} and its mobility increases to 102 $cm^2/(V.s)$. The high mobility of holes at 77 K indicates the existence of 2DHG at the AlGaN/GaN interface. The observed decrease in hole density cannot be simply explained by carrier freeze out, and similar phenomena have been observed in 2DHGs in undoped metal-polar GaN/AlN heterostructures [7, 8]. Sheet hole density and mobility of the 26 nm AlGaN barrier sample are $+8.25\times10^{12}$ cm^{-2} and 19.4 $cm^2/(V.s)$ at room temperature and $+6.76\times10^{12}$ cm^{-2} and 124 $cm^2/(V.s)$ at 77 K, respectively. Hole density of this sample is lower due to the smaller barrier thickness. A possible explanation for the increased mobility is that 2DHGs with lower density is pushed farther away from the AlGaN/GaN interface, becoming less vulnerable to interface roughness scattering and alloy scattering. Detailed temperature-dependent scattering mechanisms of such 2DHGs will be discussed.

1. S. Wienecke et al., IEEE Electron Device Letters 38, 359 (2017). 2. Y. J. Cho et al,. Applied Physics Letters 117, 143501 (2020). 3. K. Nomoto et al., Applied Physics Express 15, 064004 (2022). 4. A. J. Ptak et al., Applied Physics Letters 79, 2740 (2001). 5. A. J. Ptak et al., Applied Physics Letters 78, 285 (2001). 6. J. Simon et al., Science 327, 60 (2010) 7. Z. Zhang et al., Applied Physics Letters 119, 162104 (2021). 8. R. Chaudhuri et al., Science 365, 1454 (2019).

PS22

Dependence of Compositional Inhomogeneity and Thermal Conductivity on Growth Conditions of High-Al-Content AlGaN Alloys Grown by High Temperature Plasma-Assisted Molecular Beam Epitaxy Mihee Ji[1], LeighAnn S. Larkin[1], Wendy Sarney[1], Asher Leff[2], Yuanping Chen[1], Gregory Garrett[1], Michael Wraback[1] and Anand Sampath[1]; [1]U.S. Army Research Laboratory, United States; [2]General Technical Services, United States

AlGaN with nanoscale compositional inhomogeneities (NCI) grown by plasma-assisted molecular beam epitaxy (PAMBE) has been shown to have high room temperature (RT) radiative efficiency in the ultraviolet (UV) [1, 2], despite higher defect density heteroepitaxy on sapphire, and without the need for commonly employed multiple quantum well (MQW) active regions, which can further exacerbate the already low thermal conductivity inherent in the ternary alloy. For high Al content AlGaN, previous studies [1] have linked the formation of NCI to III/V>>1 growth conditions employing excess gallium in a manner more representative of liquid phase epitaxy, at moderate growth temperature T_g ~ 770 °C. In this study, high-Al-content $Al_xGa_{1-x}N$ epitaxial layers ($0.6 < x < 0.8$) were grown 200-250 nm-thick on 3-µm-thick AlN templates on c-plane (0001) sapphire substrates under relatively high growth temperatures ranging between 800 °C < T_g < 950 °C by PA-MBE and III/V>1 growth conditions. Before the

material growth, AlN/sapphire substrates were cleaned by standard solvent and acid cleaning procedures and outgassed at 600 ˚C. Detailed structural properties were investigated by transmission electron microscopy (TEM) and X-ray diffraction (XRD), and photoluminescence (PL) spectra were collected at different temperatures to analyze optical properties. In addition, time-domain thermoreflectance (TDTR), an optically based pump-probe technique, was used to monitor the thermal conductivity of the $Al_xGa_{1-x}N$ epitaxial layers.
As the growth temperature is raised from 800 ˚C to 900 ˚C, an additional peak in the PL spectrum appears at ~275-280 nm that is strongly red shifted from both the near band edge peak at 235-240 nm and another peak at ~250-255 nm that may be correlated with oxygen impurities in the films. The strong RT PL at ~ 275 nm in the film grown at 900 ˚C is characterized by an internal quantum efficiency (IQE) as high as 40 %, obtained by comparison of low and RT PL. TEM images of this film showed a microstructure characterized by an oscillating compositional inhomogeneity between 79% and 86% Al content in the growth plane with a periodicity of ~ 12 nm, as measured by EDS. TEM images of the film grown at 800 ˚C show that this behavior is suppressed, as is the PL peak at 275-280 nm. Since the lateral modulation of the AlGaN band structure and resultant strain due to these compositional inhomogeneities are not commensurate with the observation of the PL peak at 275-280 nm, these results suggest that they may play a different role in channeling the electrons and holes to emitting states at the periodic interfaces of the lateral heterostructure, perhaps related to small lateral electric fields created by the in-plane projection of the polarization field due to stepped terraces associated with the substrate miscut [3]. In addition, the thermal conductivity of relatively thin $Al_xGa_{1-x}N$ epitaxial layers ranging from 50-250 nm with this type of lateral compositional inhomogeneity was found to be around 12 W/mK, measured by TDTR. This value was only slightly lower than the thermal conductivity of bulk compositionally homogeneous $Al_xGa_{1-x}N$ layers with similar Al content, while significantly higher than representative MOCVD AlGaN MQW structures commonly employed to enhance UV emission, for which a thermal conductivity of 3 W/mK was measured. These results may open new avenues for codesign of light emitting and thermal properties in AlGaN UV emitters.
Detailed structural, optical, and thermal properties of $Al_xGa_{1-x}N$ layers under different growth conditions and their relation to the emission mechanism will be further discussed in the conference.
[1] A. Bhattacharyya, *et al.*, Appl. Phys. Lett. 94, 181907 (2009).
[2] C.J. Collins, *et al.*, App. Phys. Lett. 86, 031916 (2005).
[3] N. Woodward, *et al.*, Phys. Status Solidi C 11, No. 3–4, 686 (2014).

PS23
Axial Configured GaAsSb Ensemble Nanowire-Based p-i-n photodetectors up to 1.1 µm Hirandeep Reddy Kuchoor, Shisir Devkota, Kendall D. Dawkins, Jia Li and Shanthi Iyer; North Carolina Agricultural and Technical State University, United States

In this work, we present a systematic design of self-catalyzed molecular beam epitaxially grown GaAsSb heterostructure axial p-i-n nanowires (NWs) on p-Si <111> for the ensemble photodetector (PD) application in the near-infrared (NIR) region. A systematic study has been performed to realize a high-quality p-i-n heterostructure by exploring several growth methods for better insight to mitigate the growth challenges, which impacts on the NW electrical and optical properties. The successful growth approaches are (i) suppression of p-type nature in the intrinsic GaAsSb segment by Te-dopant compensation, (ii) growth interruption for interface strain relaxation, (iii) decreased substrate temperature to enhance supersaturation and minimize the reservoir effect, (iv) higher bandgap compositions of the n-segment of the heterostructure relative to the intrinsic region for boosting the absorption, and (v) the high-temperature ultra-high vacuum in-situ annealing to reduce the parasitic radial overgrowth. The efficacy of these methods is supported by enhanced photoluminescence (PL) emission, suppressed dark current, photosensitivity, and a reduced low-frequency noise level. The PD fabricated utilizing the optimized GaAsSb axial p-i-n NWs exhibited the longer wavelength cutoff at ~ 1.1 µm with a significantly higher responsivity of ~ 120 A/W (@-3 V bias) and a detectivity of 1.1×10^{13} Jones operating at room temperature. Frequency and the bias independent capacitance in the pico-Farad (pF) range and substantially lower noise level at the reverse biased condition, show the prospects of p-i-n GaAsSb NWs PD for high-speed optoelectronic applications.

PS24
Impact of Current Stress on the Optoelectronic Performances in GaN-Based Micro-LEDs A B M Hamidul Islam[1], Tae Kyoung Kim[1], Yu-Jung Cha[1], Jae Won Seo[1], Jiun Oh[1], Dong-Soo Shin[2], Jong-In Shim[2] and Joon Seop Kwak[1]; [1]Korea Institute of Energy Technology, Korea (the Republic of); [2]Hanyang University ERICA, Korea (the Republic of)

With the advantages of low power consumption, fast frequency response, and high contrast ratio, GaN-based micro light-emitting diodes (µ-LEDs) have attracted interests for various applications including optogenetics, visible-light communications (VLC), and portable micro-sized displays. Micro-displays for augmented reality (AR) and virtual reality (VR) require high contrast ratio, high brightness (> 10,000,000 cd/cm^2), high pixel per inch (> 5000), and small chip size (< 100 µm). Many works have been conducted and proposed for improving the efficiency by reducing the surface leakage caused by the recombination of carriers via sidewall defects. As is well known, the decrease in efficiency by the sidewall defects becomes more severe with decreasing size of the µ-LEDs. In the big-sized LEDs, it was found that the injection of electrons by a forward-current stress at 100 A/cm^2 and the application of high ambient temperature by thermal stress could cause various effects such as formation of Mg-H complexes in the p-GaN layer, modification of the ohmic contact, defect generation inside the active region, changes in carrier injection inside the active region, and modification of the local indium concentration. In the case of µ-LEDs, however, the works on the degradation mechanisms have not been as extensive as the large-sized LEDs. Therefore, it is essential to investigate the aging behaviors of µ-LEDs for identifying the degradation of performances caused by the current stress.
In this study, we fabricated an InGaN/GaN multiple-quantum-well blue µ-LED sample with the mesa size of 80×80 µm^2. The µ-LED sample was bonded on a flip-chip package by the Ag paste. In an enclosure with uniform temperature, a current stress at 75 A/cm^2 was applied on the sample for 200 h. To observe the variation of performances during stress, different kinds of optoelectronic performances such as the reverse leakage current, the forward voltage, the forward capacitance, the light-emission distribution at low and high currents, the light output power (LOP), the external quantum efficiency (EQE), and the electroluminescence spectrum were measured carefully at every 25 h.
It is found that the series resistance (R_s), dominated by the p-GaN and p-contact resistances, slowly reduces with aging time, which is synchronous with the current injection. The current injection improves at a given voltage (>2.6 V) due to the reduction of R_s. Thus, the LOP and the EQE are increased with aging. The decrease in R_s is due to reduction of p-GaN resistance caused by the dissociation of Mg-H complex. The increase in peak of forward capacitance reveals the improvement of current injection inside the active region. The forward (<2.3V) and the reverse leakages also increase a little compared to without aging. However, these leakages have no effect on the radiative recombination. Moreover, the minimum value of ideality factor and S-parameter at low current are decreased with aging time. It indicates that increase in radiative recombination due to decrease in defects inside active region and p-GaN layer. During the presentation, we will discuss both theoretical and experimental backgrounds of this work in more detail.

PS25
Motion of a Void Induced by Agglomeration at the Solid-Liquid Interface in the Continuous-Wave Laser Crystallization Nobuo Sasaki[1,2], Satoshi Takayama[2], Rikuto Sasai[2] and Yukiharu Uraoka[2]; [1]Sasaki Consulting, Japan; [2]NAIST, Japan

This paper studies straight-line-shaped grooves of 2~3 μm width observed in the Si thin films obtained by the scanning continuous-wave-laser crystallization (CLC) at the laser power above the optimum power of CLC condition. The CLC grows {100}-oriented grain-boundary (GB) free Si thin films at the power around the threshold of lateral growth [1-3]. The CLC has been demonstrated on substrates of quartz [1], glass [1], or polyimide [2], and isotropic TFT mobilities of ~ 700 cm^2/Vs have been realized [3]. The GB-free Si TFTs are candidates for monolithic 3D integrations, system flat-panel-displays (FPDs), CMOS wearable electronics, etc.
We used two kinds of sample structures for the crystallization: (A) a 110 nm-thick SiO_2 cap / a 60 nm-thick undoped a-Si / quartz, and (B) a 337 nm- thick SiO_2 cap / a 50 nm-thick undoped a-Si / a 500 nm-thick SiO_2 buffer / glass. After the dehydrogenation annealing at 550 °C for 1 h in N_2, the a-Si was crystallized by unseeded single-scanning CLC with a DPSS Nd:YVO_4 laser at a wavelength of 532 nm keeping the substrate at room temperature in air. A highly-uniform line beam was used [1-3]. The spot size was 492 μm × 8 μm with a beam shape of top-flat for the long-axis and Gaussian for the short-axis. Scans were performed perpendicular to the long-axis at a velocity V of 1~15 mm/s and a laser power P of 2.0~3.3 W. High speed movie camera FASTCAM was used for in-situ observation of the crystallization. Frame rate was 4000 FPS.
The crystallized films show accidental generations of straight lines with an angle θ to the scan direction at the laser power above the optimum power of CLC for both samples on quartz and glass. Atomic-force-microscope (AFM) observation discloses that these lines consist of grooves of 2~3 μm width and vertically formed in the Si film to the underlying substrate. The observed angle θ of the groove lines are almost constant in the same CLC film. In-situ observations of the melt zone during the crystallization with the high-speed camera reveal that this groove originates at a void. The void is generated by agglomeration and is moving along the solid-liquid interface in the melt zone. The void moves at a constant velocity V_{void} perpendicular to the laser scan direction, and the melt zone itself moves at the laser scan velocity V parallel to the scan, resulting that a straight line of the groove is formed as the void trace in the crystallized film. The angle θ of the groove to the scan direction is given by $\tan(\theta) = V_{void} / V$.
The obtained constant value of θ in the same CLC results in the same void velocity V_{void} along the solid-liquid interface in the same CLC. If the void happens to generate at an edge of the melt zone and travel to another edge, one straight groove line is formed across the crystallized region. If a void generates at an intermediate point of the melt zone and splits into two voids, they run to opposite directions resulting in a chevron pattern. When V is as low as 1 mm/s at 3.2 W, the groove line becomes almost perpendicular to the scan direction. The void velocity V_{void} along the solid-liquid interface varies in proportion to $1 / V^{1/2}$.
The agglomeration will be suppressed by optimizing the interface tensions at the top and bottom interfaces of the melted-Si.
In conclusion, straight agglomeration grooves with 2~3 μm width are observed at a laser power above the optimum power of CLC. The groove originates at the void generated by agglomeration at the solid-liquid interface in the melt zone. The void moves in the melt zone perpendicular to the scan direction at a constant velocity and melt zone in the same time moves to the scan direction, resulting in a groove straight line with an angle θ to the scan direction. The angle θ depends on the scan velocity V.
[1] N. Sasaki, et al., crystals, Vol. 10, p. 405 (2020).
[2] N. Sasaki, et al., J. Electronic Materials, Vol. 50(6), p. 2974 (2021).
[3] N. Sasaki, et al., crystals, Vol. 13, p. 130 (2023).

PS26
(Student) Effect of the Atomic Arrangement at the Apex of Tip on AFM Atomic Lattice Images Yura Seo, Jeahun Lim and Suenne Kim; Hanyang University, Korea (the Republic of)

Atomically sharp tips are recommended when using atomic force microscopy (AFM) to obtain atomic lattice images of crystalline solids. In order to maintain the sharpness of the tip, it is important to avoid tip damage due to the well-known jump-to-contact effect during the approach. Liquid environments or tips with highly elastic carbon nanotubes (CNTs) have been used for this purpose, although these approaches are either costly or difficult to implement. More recently, a few research groups have acquired atomic lattice images even with blunt tips.
AFM tip experiences a periodic potential as it moves on the surface of a crystalline sample due to the regular arrangements of sample atoms. The tip prefers to stay at positions of potential minima. As a result, the tip continuously sticks and detaches during sliding. This phenomenon is known as atomic stick-slip and is the origin of atomic resolution. Here we model the apex of the tip with different atomic configurations and drag each tip along the zigzag direction of monolayer graphene to obtain respective potential profiles. Based on our calculations, we discuss how the change in stick-slip behavior and the possibility of acquiring atomic-lattice images depend on the atomic arrangement at the tip-sample interface.
*This work is supported by the National Research Foundation of Korea (NRF) grant funded by the South Korean government (2021R1F1A1062731).

PS27
(Student) Wavelength Dependence of the Verdet Constant Using Visible LEDs and a Modified Pulsed Magnet Station Dominique Newell[1], Victoria Adebayo[2], Zizwe A. Chase[1], Oleksiy Drachenko[3], Jean Leotin[3] and Thomas A. Searles[1]; [1]University of Illinois at Chicago, United States; [2]Howard University, United States; [3]Laboratoire National des Champs Magne tiques Intenses, France

The Faraday Rotation is a well-known magneto-optical effect that connects the fields of electromag- netism and optics. Etienne Malus first observed that natural light could be polarized when reflected off a glass surface. In 1845 Michael Faraday observed this rotation when he passed linearly polarized light through an optical material while inducing an external magnetic field. The resulting rotation is a function of the Verdet constant, magnetic field, and the length of a material. In this work, we modify TeachSpin's Faraday Rotation apparatus to operate in a pulsed magnetic field reaching up to 500mT in comparison to the current limit of 20mT. The ap- plied oscillating pulsed magnetic field allows for field reversal during the long duration of the single magnet shot supplied by a capacitor current source. This capacitor supplies the discharge current to the wrapped coils of the apparatus. This modification allows for the direct measurement of the faraday rotation and the magnetic field.
Figure 1(a) shows a comparison of experimental values to theoretical values of normalized light inten- sity to rotation angle. It shows that our apparatus gives reproducible results. The Faraday rotation was scanned in the linear range of the Malus's photocurrent response as shown by the results in Figure 1(b). The charged device produced a sweep from 0T to the maximum magnetic field while simultaneously measuring the intensity coming out of the material. By having this information under these conditions, the change in polarization and the magnetic field were plotted. Relating the normalized light intensity through the Malus Law, we were able to determine the Verdet constant of 19 rad/T/m. The Verdet constant matched closely to that of previous results from literature.[1,2] This new approach showcases the validity of the measurements compared to the current techniques used but adds more safety, lower cost, and the capability of higher sensitivity measurements.

PS28
(Late News) Design and Fabrication of a Fully Epitaxially Grown AlScN FBAR Jialin Wang, Mingyo Park and Azadeh Ansari; Georgia Institute of Technology, United States

The development of next-generation communication networks heavily relies on the improvement of both the operating frequency and device performance of acoustic resonators and filters. Thinning down the thin film is a convenient method to increase the operating frequency, making epitaxially grown films, such as AlScN, an excellent choice due to their precise thickness control and high film quality. However, one of the drawbacks of epitaxial growth is the native oxide layer that forms on the thin film surface when the piezoelectric stack is exposed to air after deposition [1,2]. This leads to a decrease in the electric mechanical coupling coefficient (k_t^2) of the FBARs. Currently, the most effective methods to remove the native oxide are through diluted Hydrofluoric acid (HF) solution or argon (Ar) plasma, but these techniques also increase the surface roughness, resulting in decreased device performance [3]. In this study, we designed and fabricated an AlScN-based film bulk acoustic resonator (FBAR) with a fully epitaxy-grown stack to prevent native oxide from forming between the metal/piezoelectric interface.
In this study, an $Al/Al_{0.8}Sc_{0.2}N/Mo/Sc_2O_3$ stack with a thickness of 40/120/40/40nm film was epitaxially grown with molecular-beam epitaxy (MBE) by Prof. Zitian Mi's group from the University of Michigan in the same run to ensure the oxide-free metal/piezoelectric contact. The fabrication of the FBAR, illustrated in figure 1, began with the deposition of a thin Mo layer (5nm) to protect the highly reactive Al metal during processing. The top metal consisting of Mo/Al was then patterned and etched with RIE with SF_6 etchant. Next, the substrate was patterned with a thick photoresist, which acts as the etching mask. The AlScN thin film was subsequently etched with ICP (inductively coupled plasma) with $BCl_3 + Cl_2$ etchant. Then the bottom Mo layer was patterned and etched with RIE to isolate each FBAR. A SiO_2 layer of 200nm was deposited onto the AlScN/Mo edge with the E-beam evaporator to isolate the top and bottom electrodes. Next, the Sc_2O_3 layer was etched down to the Si substrate with ICP to reduce the parallel capacitance between the electrode pads. The electrode pad layer consisting of Ti/Au was then sputtered with Unifilm Sputter to ensure conformal coating from the top Al electrode to the Si substrate. Finally, the release hole was etched with ICP, and the FBAR was released with XeF_2 Si etcher. Figure 2 shows the scanning electron microscopy (SEM) image of the fabricated FBARs. Several design approaches were used to improve the performance of the FBAR. Firstly, the active region was shaped as an off-angle pentagon to minimize the reflection wave from each corner. Additionally, the active region for both FBAR and cascaded FBAR (C-FBAR) was designed to match the impedance of the measurement probe, utilizing the lower sheet resistance of the epitaxially grown metal (figure 3) to precisely determine the dimension of the top metal. The C-FBAR was particularly designed to improve the resonator's power handling and precise impedance matching due to its larger surface area. Finally, the dimension of the electrode pads was chosen to minimize the noise of the frequency response. The frequency response (Y11) of the fabricated single FBAR and C-FBAR were measured with a PNA network analyzer. The C-FBAR exhibited a k_t^2 of 8.85% at 16.6GHz with Q_{bode} around 81, whereas the single FBAR demonstrated a k_t^2 of 6% at 16.4GHz with Q_{bode} around 170. The reduction in k_t^2 for the single FBAR was due to the change in top electrode size for impedance match, leading to a long distance between the active region and the release holes for a single FBAR. Table I summarizes the compassion of k_t^2, Q_{bode}, and resonant frequency of the fabricated FBARs in this work and previous work, highlighting that this work exhibits one of the highest k_t^2 values among other FBARs operating at similar resonant frequencies.

PS29
Influence of Cobalt Doping on Surface Morphology, Structural and Optical Behavior of ZnO Nanoparticles Synthesized by CBD Technique Rahima Nasrin; University of Barishal, Bangladesh

Nanosize particles have received considerably more attention in the past era owing to their outstanding optical, structural, electrical and thermal properties [1,2]. Semiconductor nanoparticles (NPs) are presently an active subject of research in nanoscience and nanotechnology due to its potential applications in different arena, such as gas sensors, solar cells, light emitting devices, photocatalyst, transparent conductor, UV electronics, spintronic devices, etc. [3,4]. In order to understand the influence of doping concentration on the properties of ZnO NPs, in this research pure and Co:ZnO NPS with different Co contents were efficaciously synthesized using a cost-effective, and environmentally friendly chemical bath deposition (CBD) method. Field emission scanning electron microscopy (FESEM), AFM, XRD and UV-Vis spectroscopic analysis has been executed to study the morphology, structural and optical properties of the Co:ZnO NPS , respectively. SEM images depicted a homogenous flower-like shaped for the undoped ZnO. After 10% Co-doping the olive-like structure changed in flower-like structure. XRD results displayed that the structure of the material attained is hexagonal wurtzite ZnO. It was also observed that the estimated crystalline size of ZnO NPS depends on doping concentration. UV spectroscopy presented a slightly shift on the absorption edges with an increasing in the molar content of Co. The highest E_g was obtained for the pure ZnO. As the Co-doping concentration increased up to 10 % , the E_g value decreases to 2.54 eV in comparison to pure ZnO.
1. K.Gherab,Y.Al-Douri,C.H.Voon,U.Hashim,M.Ameri,A.Bouhemadou, Results in Physics, 7, 1190-1197 (2017).
2. L.G. Valluzzi, M.G. Valluzzi, G. N. Darriba, M. Meyer, L.C. Damonte, J. Alloys and Compounds, 829, 154488 (2020).
3. R. Bekkaria, L. laânaba, D. Boyerb, R. Mahioub, B. Jaberc, Materials Science in Semiconductor Processing 71, 181–187 (2017)
4. F.B. Dejene, M.O. Onani , L.F. Koao, A.H. Wako, S.V. Motloung, M.T. Yihunie, Physica B, 480, 63-67 (2016).

PS30
(Student) High Dielectric Microdroplet Whispering Gallery Mode Resonators for Opto-Electronics Madison S. King[1], Parker Awerkamp[2], Gregory Nordin[2], Stephanie Hurst[1] and Ryan Camacho[2]; [1]Northern Arizona University, United States; [2]Brigham Young University, United States

Due to their mode stability and high quality (Q) factors; whispering gallery mode (WGM) resonators have a wide range of applications from biological sensing to lasing to quantum electro-optical devices [1]. A variety of geometries and materials, including liquids, can be used to create WGM resonators [2]. There are several existing preparations for microdroplet resonators including suspending a drop on a glass stem [3,4] or suspending a droplet in another liquid [5,6]. These methods range in complexity, preparation time, and accessibility. The fabrication of 3D-prints is easy, quick, and accessible but their inherent surface roughness makes them less than ideal for optical applications. Due to this roughness, 3D-prints result in low-quality WGM resonators and can better serve as mounts for microdroplets. In this work a variety of different liquids were characterized as WGM microdroplet resonators. Microdroplets with high dielectric constants are of special interest due to the potential for controlling their geometries, and thus their resonant frequencies, with an external electric field [7].
[1] Vahala, K. J. Optical Microcavities. *Nature* **2003**, *424* (6950), 839–846.
[2] Cai, L.; Pan, J.; Zhao, Y.; Wang, J.; Xiao, S. Whispering Gallery Mode Optical Microresonators: Structures and Sensing Applications. *physica status solidi (a)* **2020**, *217* (6), 1900825.
[3] R. Dahan, L. L. Martin, and T. Carmon, "Droplet optomechanics," Optica **3**(2), 175–178 (2016).

[4] M. Gaira and C. Unnikrishnan, "Integrated table-top facility for the study of whispering gallery modes in dynamic liquid micro-cavities coupled to sub-micron tapered fibers," arXiv preprint arXiv:1911.01187 (2019).
[5] S. K. Tang, R. Derda, Q. Quan, M. Lončar, and G. M. Whitesides, "Continuously tunable microdroplet-laser in a microfluidic channel," Opt. Express **19**(3), 2204–2215 (2011).
[6] S. Maayani and T. Carmon, "Droplet raman laser coupled to a standard fiber," Photonics Res. **7**(10), 1188–1192 (2019).
[7] Humar, M.; Ravnik, M.; Pajk, S.; Muševič, I. Electrically Tunable Liquid Crystal Optical Microresonators. *Nature Photonics* **2009**, *3* (10), 595–600.

PS31

(Student) Covalently Connected Single-Molecule Magnets on the Exposed Edges of a Nickel Ferromagnetic Electrode-Based Magnetic Tunnel Junction Pawan Tyagi[1], Marzieh Savadkoohi[1], Pius Suh[1] and Jose Martínez Lillo[2]; [1]University of the District of Columbia, United States; [2]Instituto de Ciencia Molecular (ICMol) Universitat de València, Spain

The single-molecule magnet (SMM) is one of the most exciting classes of molecules possessing tunable spin states for a wide range and exhibited Berry phase-like quantum mechanical phenomenon. However, further advancement in producing SMM-based molecular devices will require an efficient and mass fabrication approach to connect the metallic leads to this type of molecular system. Here we report a method of connecting SMM to the ferromagnetic electrodes. We utilized a nickel (Ni)-AlOx-Ni magnetic tunnel junction with the exposed side edges as a test bed. In the present work, we utilized SMM with a hexanuclear $[Mn_6(\mu_3\text{-}O)_2(H_2N\text{-}sao)_6(6\text{-}atha)_2(EtOH)_6]$ [H_2N-saoH = salicylamidoxime, 6-atha = 6-acetylthiohexanoate] complex core that is attached to alkane tethers terminated with thiols. SMMs were electrochemically bonded between the two Ni electrodes of an exposed edge tunnel junction that was produced by the lift-off method. SMM-treated magnetic tunnel junction exhibited current enhancement and transitory current suppression at room temperature. Magnetic field further enhanced the current level significantly. Magnetic force microscopy and Ferromagnetic resonance study were performed to investigate the effect of SMMs on the ferromagnetic electrode.

PS32

DC Modeling for Non-Ohmic Contacts in the Scaled PMMA Dielectric-Based Solution-Processed Organic Thin-Film Transistors Anuj Rajpoot and Soumya Dutta; Indian Institute of Technology Madras, India

In recent years, solution-processed organic thin film transistors (OTFTs) have proven their potential for inexpensive flexible electronic circuit applications (Xu *et al.*, 2020). Aggressive device scaling and analytical assessment of device characteristics are important to the adoption of OTFTs for circuit applications. However, the presence of non-linear contact resistance in short-channel solution-processed OTFTs is critical in modeling the device. In this work, for the first time, we have successfully fabricated short-channel solution-processed OTFTs employing pristine PMMA as a gate dielectric layer in the most preferred BG-BG configuration. A novel bi-layer lithography (Rajpoot and Dutta, 2017) is used to achieve hi-resolution photo-lithography for source and drain patterning on pristine polymer gate dielectric by eliminating the constraint of using complex polymer cross-linking. P3HT OTFTs were fabricated using 460 nm thick (spin-coated) pristine PMMA gate dielectric in BG-BC configuration. P3HT was spin-coated (3000 rpm, 5 mg/ml DCB solution) over lithographically patterned S/D (Cr/Au) contacts over PMMA gate dielectric layer, realized on gate metal/glass substrate.
PMMA offered a high-quality interface with P3HT as per the expectations due to a smooth, hydrophobic, and (-OH) group-free surface (Shi *et al.*, 2013). However, we also observed an S-shaped curve in the output characteristics of the fabricated short-channel OTFTs which is the indicative of dominant contact effect for short channel lengths below 10 µm. Here, an attempt is made to model this effect of non-ohmic contacts in fabricated OTFTs by using a modified Shichman-Hodges (mSH) model (Marinov *et al.*, 2009) and a reverse-biased Schottky-diode model. In this approach, intrinsic OTFT parameters are extracted from the measured output characteristics for different V_{GS} by assuming an extended channel length ($L_{ch} + L_{ch'}$) instead of the intrinsic channel length (L_{ch}) to include the effect of source contact resistance. For reliable extraction of the intrinsic parameters, the analysis is carried out in the saturation region as the drain current is not affected by drain contact resistance in the saturation region, leaving the effect of non-ohmic source contact (Fischer *et al.*, 2017). This approach does not require TLM or four-probe contact resistance measurement to evaluate the contact resistance. The intrinsic-OTFT-model parameters (μ_0, n, λ and α) for 4 µm channel length OTFT are extracted by fitting model equations to the measured output characteristics, considering $L_{ch'}$ and L_{ch} to be 1.5 µm and 4 µm respectively. The extracted intrinsic parameters are observed to be in good agreement with the measured values. The electrical characteristics of the OTFT are simulated using the Quite Universal Circuit Simulator (QUCS) software. The simulated results are in good agreement with experimental results both in linear and saturation regions for low V_{GS}. However, for larger V_{GS}, there is a deviation in the linear region due to the effect of drain resistance, which has not been accounted for in this study.
References:
-Fischer, A. *et al.* (2017), *Physical Review Applied*, 8(5), p. 054012. Available at: https://doi.org/10.1103/PhysRevApplied.8.054012.
-Marinov, O. *et al.* (2009), *IEEE Transactions on Electron Devices*, 56(12), pp. 2952–2961. Available at: https://doi.org/10.1109/TED.2009.2033308.
-Rajpoot, A. and Dutta, S. (2017). Available at: https://patents.google.com/patent/WO2019008602A1/en.
-Shi, W. *et al.* (2013), *Applied Physics Letters*, 102(11). Available at: https://doi.org/10.1063/1.4798368.
-Xu, T. *et al.* (2020), *Applied Physics Letters*, 116(2), pp. 5–10. Available at: https://doi.org/10.1063/1.5135043.

PS33

(Student) Electrochemical and Morphological Properties of PEDOT with Various Boron-Containing Dopants Nurdan Mese, Yuhang Wu, Peter Sitarik, Junghyun Lee, Quintin Baugh and David C. Martin; University of Delaware, United States

Poly(3,4-ethylenedioxythiophene) (PEDOT) is a promising electroactive polymer of interest for a variety of applications including capacitors, biosensors, and electrochromic devices. The choice of doping agents used during electrochemical polymerization is a crucial factor affecting the ultimate performance of PEDOT thin films. Although polystyrene sulfonate (PSS^-), perchlorate (ClO_4^-), and hexafluorophosphate (PF_6^-) are commonly used counterions, it is worthwhile utilizing alternative dopants with variations in size, nucleophilicity, and solubility. Boron-containing dopants, including organic and inorganic borate salts as well as boron clusters, are a versatile group of materials that make it possible to convenient tune film properties according to the needs of particular applications. Here, we investigated how such boron-containing dopants affect the structure and electrochemical properties of electrodeposited PEDOT. The utilized dopants were sodium tetrafluoroborate ($NaBF_4$), sodium tetrakis[3,5-bis(trifluoromethyl)phenyl]borate (NaTFPB), and sodium tetraborate ($Na_2B_4O_7$, Borax). We compared these dopants with the more commonly utilized lithium perchlorate ($LiClO_4$). According to the results of electrochemical impedance spectroscopy (EIS) taken between 10^{-1} to 10^5 Hz, the low-frequency impedances of all types of PEDOT-coated electrodes were at least one order of magnitude lower than those of bare electrodes. Bumpy PEDOT film surfaces were confirmed by scanning electron microscopy (SEM) images. Among these interfaces, PEDOT/BF_4 and PEDOT/ClO_4 exhibited similar and the lowest impedances, about 110 times lower than that of bare electrodes at a frequency of 1 Hz. We also quantified the areal-

specific capacitances (C_A) of PEDOT-coated electrodes using linear cyclic voltammetry (CV) and galvanostatic charging/discharging (GCD). PEDOT/BF_4 and PEDOT/ClO_4 coated electrodes had similar areal-specific capacitances C_A, which were 5.7×10^{-3} F/cm^2 and 6.0×10^{-3} F/cm^2, respectively. On the other hand, PEDOT/TFPB and PEDOT/Borax had much smaller capacitances compared to PEDOT/BF_4 and PEDOT/ClO_4. While PEDOT/BF_4 and PEDOT/ClO_4 had CV graphs with quasi-rectangular shapes, representing their nearly ideal capacitive behaviors, the CV voltammograms of PEDOT/TFPB and PEDOT/Borax deviated significantly from regular rectangular shapes for the voltage interval between 0.0 V and 0.5 V. We also performed morphological characterization of these surfaces by SEM and AFM. Compared to PEDOT/ClO_4 and PEDOT/BF_4, with relatively small size counterions, much smoother surface structures were generated when the relatively bigger TFPB counterion was used as the dopant. Since PEDOT/ClO_4 and PEDOT/BF_4 provided better coverage on the electrodes, we compared their roughness quantitatively using power spectral density (PSD), which provides length-scale dependent measures of the surface roughness fluctuations, and root-mean-square (RMS) roughness at different length scales. Our observations confirm that the choice of dopant is an important factor that needs to be examined in detail for optimizing PEDOT film performance.

PS34

(Student) Energy Harvesting with Thermoplastic Polyurethane Nanofiber Mat Integrated with Functionalized Multiwalled Carbon Nanotubes Julia I. Salas Toledo; The University of Texas, Rio Grande Valley, United States

In recent years, triboelectric nanogenerator (TENG) has been received great attention to fabricate flexible and stretchable energy harvester that can convert mechanical energy to electrical energy. This paper studied poly(vinylidene fluoride) (PVDF) and thermoplastic polyurethane (TPU) nanofiber membranes based flexible TENG. Both PVDF and TPU nanofiber (NF) triboelectric functional layers were synthesized by Forcespinning (FS) technique. To improve the performance of the TENG, the TPU NFs were decorated with multiwalled carbon nanotubes (MWCNT) that are functionalized with fluorine, amide, and carboxylic groups with variable time (6, 12 and 24 hours) of exposure and concentration. The TPU nanofibers demonstrated a stronger interaction with the carboxylic functionalized multiwall carbon nanotube (c-MWCNT) as depicted by its electrical performance when compared to the non-modified fibers. The maximum open circuit voltage (V_{oc}) recorded at a 4 Hz hand tapping frequency for modified TNEG was ~252 V, which 152% higher than basic TPU/PVDF TENG. Furthermore, the c-MWCNT functionalized TPU/PVDF TENGs were evaluated with varied compressive force applied by a pneumatic cylinder and the maximum alternating voltage and current outputs were obtained of 158 V and 170 μA at 30 psi pressure. To demonstrate the potential of harvesting human motion into charging small electronic device, the modified TENG showed that it can charge 3.03 V connected with 1 μF capacitor by hand tapping motion at 4 Hz load frequency for only 25 seconds, suggesting the prospect of our as fabricated TENG has the capability as self-charging flexible energy harvester.

Keywords: Forcespinning, Functionalized multiwall carbon nanotubes, Thermoplastic polyurethane nanofibers, Poly (vinylidene fluoride) nanofibers, Triboelectric nanogenerator.

PS35

(Student) ZnO TFTs Property with Photoelectric Synaptic Devices Hyerin Jo and Hongseok Oh; Soongsil University, Korea (the Republic of)

We report the fabrication of ZnO thin-film transistors (TFTs) as neuromorphic devices with photo-sensing properties that can be used in advanced high-energy efficiency applications. Synaptic devices that mimic the operation of the biological nervous system, such as synapses in the human brain, are gaining intensive attention as a new type of power-efficiency next-generation device. Mainly, a single synaptic transistor can perform control and signal propagation separately from its 3-terminals configuration. This feature allows us to achieve reduced integration complexity and enhanced power efficiency. However, most research focused on electrically driven operations. The strong photocurrent response of the ZnO can allow us to achieve optically driven synaptic transistors, where excitation or depression of the device can be performed by the light pulses. Moreover, a combination of electrical and optical stimulation will lead to a continuous, reversible, highly-linear synaptic response. Here, we report the fabrication of ZnO TFTs and their application to photoelectric synaptic transistors.

In this device, ZnO thin films were deposited using radio-frequency magnetron sputtering and utilized as a channel layer of the TFT. The structural characteristics and the surface properties of the deposited ZnO channel layer, as a function of deposition temperature, were investigated by synchrotron-radiated X-ray diffraction and reflectivity. The basic output and transfer characteristics and the photocurrent properties of the fabricated TFT were investigated as well. More importantly, our devices exhibited good synaptic properties when the electrical pulse was used, and improved synaptic response was observed when UV illumination was added. Further tailoring electrical and optical synaptic response by pulse engineering will allow us to achieve synaptic transistors with highly linear or customizable activation functions that can lead to high-performance, next-generation electronic synaptic devices.

PS36

(Student) Synthesis and Characterization of $CsPbBr_3$ Perovskites for Radiation Detection Applications Shea Tonkinson[1], Maya Kutty[1], Mega Frost[1], Melvin Foster[1], Alexandria Ragsdale[1], Charles Han[2], Thomas J. Rotter[1], Alexander Barzilov[2], Adam Hecht[1] and Ganesh Balakrishnan[1]; [1]UNM Center for High Technology Materials, United States; [2]University of Nevada Las Vegas, United States

In recent years, lead halide perovskites ($APbX_3$) such as $CsPbBr_3$ (E_g=2.3eV) have emerged as an attractive candidate for ionizing radiation detection over the established CdZnTe due to their: (i) high Z compound with effective atomic number (Z_{eff}=65.9) leading to high photon interaction probabilities in the photoelectric region (< 500keV); (ii) high defect tolerance giving rise to high radiation damage tolerance; (iii) large mobility-lifetime ($\mu\tau$) product; (iv) low density of defects; (v) tunable bandgap and (vi) facile, low-cost synthesis and processing of large crystal sizes from melt as well as solution.

In this study, we report growth and characterization of $CsPbBr_3$ perovskite crystals. Our starting components included 49.6 grams of Lead Nitrate ($Pb(NO_3)_2$) , 35.7 grams of Potassium Bromide (KBr), and 150 mL of Deionized water (DI). In separate beakers, 0.15 mol of Pb(NO3)2 and 0.3 mol of KBr was dissolved in 100 mL and 50 mL of boiling water, respectively. The KBr solution was added to the $Pb(NO_3)_2$ solution, stirred for 15 minutes and then cooled at RT. Vacuum filtration and a wash with DI water was used to collect the $PbBr_2$ solution and it was then dried under a vacuum overnight. In our next step of the growth process, we started with 7.31 grams of $PbBr_2$, 4.26 grams of Cesium Bromide (CsBr), 30 mL of Hydrobromic acid (HBr) 30 mL, and 10 mL of DI water. 0.02 mol of $PbBr_2$ was dissolved in 30 mL of 48% aqueous HBr. In a separate beaker, 0.02 mol of CsBr was dissolved in 10 mL of boiling water and then added to the $PbBr_2$ solution and cooled at RT. Next, $CsPbBr_3$ was collected by vacuum filtration and washed with absolute ethyl alcohol. To grow the crystal, we used the Bridgman method. With a mortar and pestle, 6 grams of $CsPbBr_3$ was finely ground, placed in a quartz tube and flame sealed. The ampoule was lowered into a 3-zone vertical furnace with a translation speed of 0.2 cm/h undergoing four phase transitions, arriving at an orthorhombic crystal at RT.

Extensive surface analysis and compositional analysis of the crystals was also performed using Nomarski optical contrast microscopy and using SEM/EDS. The presence of phase segregation in the growth of the perovskite crystals was observed and this was also correlated to

the photoluminescence emission. The pitted/cracked, uneven surface, and varying color of the perovskites can be seen in the Nomarski images shown in Fig. 3. This may be due to the cooling process. In the EDS analysis shown in Fig. 4, we confirm that the perovskites are $CsPbBr_3$.
The photoluminescence spectra of the three perovskite samples in the range of 450-1050 nm was measured at room temperature using a setup based on a lock in amplifier. For excitation a blue diode laser with emission at ~448nm was used.
This material is based upon work supported by the Department of Energy/National Nuclear Security Administration under Award Number DE-NA0004008.

PS37
(Student) Synthesis and Characterization of Pulsed-Laser Deposited $Ba(Fe_{0.7}Ta_{0.3})O_{3-\delta}$ Thin Films Nolan T. Herbort, Debabrata Das and Ramana Chintalapalle; The University of Texas at El Paso, United States

Research and development activities in the topical area of semiconducting metal oxides (SMO) for application in a wide variety of sensors for utilization in domestic and industrial sectors is continually raising. The strong, continued interest in SMOs primarily driven by the increased market size of sensors for consumer and industrial applications. Optimization of many industrial processes to eliminate emissions that deteriorates the air quality to reduce pollution requires reliable and rapid response sensors to monitor and control a wide variety of hazardous chemicals. Recently, $Ba(Fe_{0.7}Ta_{0.3})O_{3-\delta}$ (BFTO) has been evolved as an efficient oxygen sensor material with a functionality over a broad temperature and oxygen partial pressure range. However, efforts directed to understand the fundamental scientific aspects of crystal chemistry and phase stabilization, especially as a function of variable thermochemical synthetic conditions, in BFTO materials is meager. In this context, in the present work, we focused our efforts on the synthesis and characterization of bulk and thin film $Ba(Fe_{0.7}Ta_{0.3})O_{3-\delta}$ [BFTO30] materials. The BFTO compounds were synthesized using the conventional high-temperature solid-state chemical reaction method. The structure and phase stability of the BFTO bulk materials studied in order to optimize the bulk target, which was used to fabricate thin films by pulsed-laser deposition (PLD). The BFTO films were made by PLD by varying the deposition temperature and oxygen pressure. The effect of these thermodynamic parameters on the structure, composition, and optical properties is established.

PS38
(Student) Role of Native Defects and Dopants in the Oxygen Evolution Reaction of Heazlewoodite Ni_3S_2 Hyungwoo Lee and Minseok Choi; Inha University, Korea (the Republic of)

The discovery and design of materials, exhibiting high catalytic performance toward oxygen evolution reaction (OER), are currently key requirement for the development of water splitting catalysts. Although IrO_2 and RuO_2-based materials have reported promising OER activities, the high cost of Ir and Ru metals (10,000-55,000 USD/kg in Shanghai Metals Market) is one of obstacles for enabling practical applications. Recently, it has been reported that the heazlewoodite Ni_3S_2, composed of much lower cost Ni elements (13.9 USD/kg in Federal Institute for Geosciences and Nature Resources), shows comparable or higher OER activity, and the activity can also be controlled by changing the defect concentration and by adding dopants. For examples, H. M. A. Amin and U.-P. Apfel observed that as defect increases activation site and dopants that are substitution or incorporation of other metals or heteroatoms improve catalytic activity, the OER performance get increased [1]. Several experiments also reported that cobalt and nitrogen doping and rich sulfur vacancies in heazlewoodite Ni_3S_2 improve OER performance [2,3]. In this work, we attempt to address the role of native defects in the Ni_3S_2 OER performance and propose further improvement of OER activity by Sn and Co dopants [4,5]. Through density functional theory (DFT) + *U* calculations, electronic properties and energetics of native defects and dopants in Ni_3S_2 are examined, and the role of each defect and dopant in the OER activities is addressed. Our DFT+*U* results are compared with experimental reports.
[1] H. M. A. Amin and U.-P. Apfel, Eur. J. Inorg. Chem. **2020**, 2679 (2020).
[2] X. Du, G. Ma, and X. Zhang, Dalton Trans. **50**, 8955 (2021).
[3] S.-C. Sun *et al*., Sustain. Energy Fuels. **4**, 3326 (2020)
[4] D. Kim *et al*, J. Alloys Compd. **914**, 165305 (2022)
[5] W. Y. An, H. Lee *et al*., Under review

PS39
Synergistic Effect of Combining UIO-66 and Mxene Nanosheets in Pebax Mixed Matrix Membranes for CO_2 Capture and Separation Eyasu Ajebe; NTUST, Taiwan

Membrane separation systems have received much attention in the field of gas separation due to their low cost, high efficiency, and environmental benefits. Poor filler-matrix interactions and aggregation of highly loaded fillers in mixed matrix membranes limit the benefit of overcoming the trade-off limitation between permeability and selectivity. In this work, the hybrids of Mxene ($Ti_3C_2T_x$) nanosheets and UIO-66 nanoparticles were prepared and used as dual fillers with Pepax-1657 polymer matrix to synthesize mixed matrix membranes. As-prepared MMMs were used to capture CO_2 The large surface area and porosity of UiO-66 served as a highway to enhance permeability, and Mxene nanosheets were used as selective channels to achieve high selectivity via the terminal polar surface groups of MMMs. The controllable surface functionality of UIO-66 and fluidic nanochannels in lamellar mxene not only enhanced selectivity of CO_2 from N_2 and O_2 but also increased the solubility and diffusivity via the carboxylate group of UIO-66 and narrow channels provided by Mxene nanosheets. As a result, the MMMs containing the dual fillers ($Ti_3C_2T_x$/UiO-66) show not only high CO_2 permeability but also high CO_2/N_2 selectivity. Pebax-based MMMs incorporated with 10 wt% of $Ti_3C_2T_x$ nanosheets/UIO-66 hybrid provide CO_2 permeability of 248.591 barrers and CO_2/N_2 selectivity of 141.253. The as-prepared MMMs showed an enhancement of 400% and 500% increment in CO_2 permeability and CO_2/N_2 selectivity respectively, compared to pristine Pebax membrane. The upper limit of Robeson separation has been successfully exceeded, indicating that mixed matrix membranes have potential for CO_2 capturing applications. This work provides a roadmap to fabricate highly selective composite gas separation membranes to capture CO_2 and reduce environmental pollution.
***Keywords*:** Mxene nanosheets, UiO-66, Pebax, MMM, Gas Separation

PS40
(Student) Femtosecond Laser Processing on Bulk Materials with Water-Assisted Debris Removal Sherman Peek, Jacob Ward, Grant Gleason, John Sellers and Michael Hamilton; Auburn University, United States

Laser processing is an increasingly popular method of subtractive manufacturing. The ability to process complex geometries with higher resolution as compared to mechanical cutting is a primary benefit of laser manufacturing. Furthermore, by utilizing femtosecond laser pulses, thermal damage to surrounding areas of irradiation is minimal when compared to longer pulse widths. Additionally, shorter pulse durations allow for higher overall peak powers delivered to the work piece, enabling a more efficient cutting process. A challenge in laser processing arises when processing bulk work pieces with high aspect ratio. To maintain high resolution, a trade-off of focal depth is usually needed which leads to a layer-by-layer cutting approach for bulk work pieces. This can be further problematic due to insufficient delivered energy densities into deep cuts from photoablation residue accumulation. Solutions to this challenge exists, where simply increasing the delivered average power of the laser (thus increasing the overall pulse energy) is sufficient. This solution can be costly or inaccessible since replacing a laser source is not economic. Additionally, increasing laser power can lead to excess

heating/damage of the work piece. Methods to remove laser processed residue have been explored previously. For example, compressed inert gas can be used to apply positive pressure to aid in extracting debris from the laser site. In addition, argon chambers are commonly used to remove debris in an inert environment. Argon chambers can be costly to setup and requires appropriate facilities to house the gas. An alternative approach is to use a water tank to remove debris from the laser site with laminar water flow; however, thin work pieces (thickness, t < 200 µm) are generally the target for this method. We present a use-case of the water tank concept that allows for improved bulk substrate (thickness, t > 500 µm) processing times to create more complex cutouts than with typical mechanical dicing methods. Examples of samples cut, the processing parameters, and the overall processing benefits are discussed. Limitations of using water-aided debris removal are also considered. Results of this work aim to enable more efficient laser processing that is easily accessible to the laser operator.

PS41

Micro Probe System for *In Situ* X-Ray Scattering Joonhyuck Lee[1], Jeonghum Woo[2], Yeongdeuk Mun[1], Hyunjung Kim[1], Jinhyeong Cho[3], Hakbeom Moon[2] and Hyungjeen Jeen[1]; [1]Pusan National University, Korea (the Republic of); [2]Nextron Corporation, Korea (the Republic of); [3]Busan National University, Korea (the Republic of)

Simultaneous electrical and structural measurements provide necessary information for dynamics of structural and electronic phase transition or modulation. In this poster, we would like to present a new platform of next-generation micro probe system, which combine functionality of conventional environmental-controlled micro probe system and x-ray scattering technique. The light weight and compact design are suitable for lab-based and synchrotron x-ray scattering experiments. In addition, it can easily create extreme environments: high temperature as high as 1000°C, high vacuum as low as 0.9 x 10^{-4} Torr, and oxidizing/reducing condition with different gases. With an oxygen sponge $SrFe_{0.8}Co_{0.2}O_x$, the apparatus was tested in a lab x-ray diffractometer and a synchrotron-based diffractometer. Redox-driven structural change was clearly reproduced as demonstrated previously[1]. In addition, simultaneous *dc* transport results clearly support associated modulation in its resistivity. Thus, the system can be applied not only for electrochemical experiments but also field-driven phase transitions in the controlled environments. [1] J. Lee et al., Phys. Rev. Applied 10, 054035 (2018)

PS42

Information Visualization in Materials Science through Social Networks Modeling Mehrdad Jalali; Karlsruhe Institute of Technology, Germany

Information visualization in materials science widely utilizes graphical and interactive techniques to ?display and analyze data related to materials properties, such as chemical composition, structure, ?physical and mechanical behavior, and others. Since Social networking can help identify patterns and ?relationships within the data, allowing materials scientists to gain new insights into the structure and ?behavior of social networks created on the materials data. Information visualization techniques used in ?materials social networks can provide a more straightforward and intuitive understanding of the ?materials data, making it easier to predict material properties and anomalies and even discover new ?materials.? By creating social networks on materials data, interactive information visualization tools allow ?researchers to zoom in, pan out, and explore the data more engagingly and dynamically, providing a ?more immersive experience and deeper understanding of the materials. Furthermore, information ?visualization with social networking can help inform better analysis and improve machine-learning ?processes. By automating the data analysis and visualization process, social networking can increase ?the efficiency and speed of data analysis and reduce the time and resources required to gain insights ?from the materials. The goal is to provide a more straightforward process to create social networks on ?material data and help researchers make more precise knowledge by deploying information ?visualization techniques. Community detection, Network centrality measures, Link prediction, ?Influencer identification, and Network evolution are social network analysis techniques where ?information visualization techniques can be used to represent the analysis results more understandably. ?For instance, some information visualization techniques include node-link diagrams with different ?colors or shapes to represent different communities, heat maps to show ?the strength of connections ?within and between communities, or force-directed layouts to highlight the ?structure and boundaries of ?the communities. ? This work describes two social networks created on metal-organic framework (MOFs) and high-entropy alloys (HEAs) materials data. As a first demonstration of MOFs materials, we construct a social network called MOFSocialNet from geometrical MOFs descriptors in the CoRE-MOFs database. The MOFSocialNet is an undirected, weighted, and heterogeneous social network; following the construction of this graph, a set of social network analysis processes is conducted to extract valuable knowledge from the MOFs data using graph machine learning algorithms. Community detection in MOFSocialNet can extract the most similar MOFs, which information visualization techniques can represent for a better understanding of MOFs relations.
Furthermore, node centrality algorithms were applied to discover the most representative MOF and visualize those nodes. As a second demonstration, we attempted to build interaction networks based on HEAs descriptors to discover HEAs communities with similar functionalities. In addition, specific HEAs characteristics, such as phase composition, could be predicted by extracted communities. The results indicate that information visualization in materials social networks can precisely improve ?the understanding of the material properties and the relation between them.?

PS43

(Student, Late News) Metallic Fusion-Induced Flexible Nanocrystal Thin Films for High-Performance Electromagnetic Interference Shielding Materials Seoyeon Park[1,2] and jihyuk Choi[2]; [1]Korea University, Korea (the Republic of); [2]Korea Institute of Geoscience and Mineral Resources, Korea (the Republic of)

Wearable smart electronics with the extensive use of electrical equipment have aroused major concerns about the electromagnetic interference (EMI) issue. Hence, flexible electrodes with EMI shielding capable of various modifications are more required. In general, metal-based, carbon, and conductive polymer materials having excellent conductivity have been studied. Among these, metal-based materials having high electrical conductivity have been widely used as EMI shielding materials. However, metal powders in which silver, copper, and nickel are mixed in a diluent, have the disadvantages of weak binding force and non-uniformity of power. These lead to low EMI shielding efficiency, restricting its further development. In addition, the metal sheets are not only inconvenient for extensive deformation due to lack of mechanical flexibility but also are made by vacuum deposition or sputtering required high energy. Recently, inorganic colloidal nanocrystals (NCs) are good candidates for solution-processable materials because of their useful physical and chemical properties. Furthermore, the NCs films can be fabricated by low-cost solution processes such as spin-coating, inkjet printing, and spray-coating, which are compatible with flexible substrates. In this study, we developed highly conductive and flexible thin films with superior EMI shielding properties that can be produced at room temperature using colloidal Ag NCs. The Ag NCs thin films were prepared through a simple solution process of the Layer-by-Layer method including ligand exchange and reduction steps. A ligand-exchange process substantially induced intensive metallic fusion of the Ag NCs, resulting in large-scale three-dimensional interconnected conductive pathways. The sequential reduction process leads to eliminating nonmetallic compounds that improve efficient charge transport in the resultant Ag NC films. With the advantages of easy processing, resultant Ag NC thin films exhibited a maximum

EMI SE of ~60 dB with a thickness of ~1.3 μm and excellent mechanical stability under various mechanical deformations.

PS44
(Student, Late News) Zirconium Oxide Dielectric Thin Films Fabricated by Water-only Aerosol Jet Printing Hansel Hobbie, Brittany N. Smith, Paolo Maccarini and Aaron D. Franklin; Duke University, United States

The potential for realizing complex electronics using printing techniques and solution-processable electronic materials is accelerating. Performance of these printed devices critically depends on the physical and electrical properties of each conductor, dielectric, and/or semiconductor used. Despite considerable progress in refining semiconducting and conducting inks for printed electronics, the development of fully printed dielectrics with high performance capabilities has been limited. An encouraging option that has received little attention for printability is zirconium oxide (ZrO_2/zirconia) – a ceramic material that has often been used in electronic devices for its advantageous properties as a high-*k*, low-loss dielectric. As a ceramic metal oxide, zirconia also offers unique physical properties like extreme heat tolerance, high chemical/corrosion resilience, biocompatibility, and non-toxicity to the environment. While zirconia is certainly a powerful material to exploit, it is often limited in its utilization because of costly fabrication and high-temperature post-processing, which constrains material choice and process integration. In this work, we developed a water-based ink of zirconia nanoparticles and water-soluble polymeric binders, and by fabricating with aerosol jet printing (AJP), we were able to form high-*k* thin films of zirconia. With AJP, we printed thin zirconia dielectric layers with only a 280 °C post-bake required to remove the polymeric binders. To achieve a solution-processable ink suitable for AJP, we combined commercially-purchased zirconia nanoparticles in an aqueous suspension with water-soluble polymers, polyethylene glycol (PEG) and hydroxypropyl methylcellulose (HPMC) at a ratio 10:3:0.2, respectively. The resulting ink formulation possesses a nearly identical viscosity to water that makes it easy to aerosolize, and with the added polymeric binders the deposition is continuous and uniform with no major print defects like coffee-staining or egregious overspray. Though the polymeric binders aid in the printing process, by removing the binders through a post-bake treatment a pure zirconia film is achieved, which improves dielectric performance and reduces the risk of redispersion in multilayer printing. Using thermal gravimetric analysis (TGA) we found that the binders in the printed films begin thermally degrading at 180 °C. To ensure full binder removal, we used a 280 °C post-printing bake for 2 hours and confirmed the absence of the polymeric binders through x-ray photoelectron spectroscopy (XPS). The monoclinic crystalline structure of the resultant zirconia was also confirmed via x-ray diffraction (XRD). A single layer of the printed zirconia is less than 250 nm thick with good uniformity and only mild surface roughness due to the particulate nature of the film. We analyzed the electrical properties of the printed zirconia film using parallel-plate capacitors with 1-4 layers of zirconia. As verified by the different thicknesses and corresponding capacitances, the relative dielectric constant of the zirconia was $\varepsilon = 16.1$ at 1 kHz. This value far exceeds what other nonionic printed dielectrics exhibit and places this AJP zirconia material as one of the best printed dielectrics currently available. These encouraging dielectric properties, combined with the simple fabrication process, reveal significant promise for considering printed zirconia for low-cost and eco-friendly printed electronics.

PS45
(Late News) Epitaxial Growth of Lattice-Matched NiMgZnO Films on MgO Substrate via Mist Chemical Vapor Deposition Takumi Ikenoue[1,2], Shintaro Iida[1], YongJin Cho[2], Vladimir Protasenko[2], Bennett J. Cromer[2], Chandrashekhar P. Savant[2], Masao Miyake[1], Tetsuji Hirato[1], Michael O. Thompson[2], Debdeep Jena[2] and Huili Grace Xing[2]; [1]Kyoto University, Japan; [2]Cornell University, United States

Gallium nitride (GaN) and gallium oxide (Ga_2O_3) are wide bandgap semiconductor materials with broad applications. The bandgap can be widely varied by alloying across the Al-Ga-In-N and $(Al\text{-}Ga\text{-}In)_2O_3$ composition space. However, composition changes also lead to changes in the lattice constant resulting in significant increases in the lattice mismatch with potential substrates. For high quality crystal growth and/or strain control, a ternary or quaternary system with minimal lattice mismatch is highly desired.
Therefore, we focus on the NiZnMgO system exhibiting the rock salt structure. MgO has a bandgap of 7.8 eV, and inexpensive single-crystal substrates are commercially available. NiO has a bandgap of 3.7 eV and exhibits p-type conductivity, which is rare among wide bandgap oxides. Both MgO and NiO also have the rock salt structure at room temperature. While ZnO has the wurtzite structure at room temperature, it can also adopt the metastable rock salt structure. Because the lattice constant rock salt structure ZnO is slightly larger than that of MgO, NiZnMgO can be expected to be lattice-matched with MgO. We previously conducted a study on the growth of NiO or NiMgO on MgO substrates using mist chemical vapor deposition (CVD), an oxide growth technique that utilizes solution sources under atmospheric pressure and is known for its high quality and productivity. Herein, we report the growth of lattice-matched NiMgZnO films on MgO (001) substrates using the mist CVD method.
Prior to growth, MgO substrates were ultrasonically cleaned with acetone and methanol. Acetylacetonate salts of Ni, Zn, and Mg were used as precursors. Our previous studies have shown that $Ni_xZn_yMg_{(1-x-y)}O$ films with a Ni and Zn composition ratio *x*/*y* of approximately 2.0 are lattice-matched with the MgO substrate. Therefore, the composition of the lattice-matched NiZnMgO film can be expressed as $Ni_{2x}Zn_xMg_{(1-3x)}O$. $Ni_{2x}Zn_xMg_{(1-3x)}O$ films with various *x* values were grown with the Mg composition (1-3*x)* of the films controlled between 0 and 0.8. In order to obtain these composition films, two solutions were used for deposition. The first was a DI solution with dissolved Mg precursors at a concentration of 0.020 mol/L. The second was a DI solution with Ni and Zn precursors dissolved at concentrations of 0.0133 mol/L and 0.0067 mol/L, respectively. The composition of the thin film was controlled by the carrier gas rate which supplies each solution. The growth temperature was set at 600 °C.
From XRD, peaks from $Ni_{2x}Zn_xMg_{(1-3x)}O$ (002) overlapping MgO (002) peaks were observed, confirming that completely lattice-matched $Ni_{2x}Zn_xMg_{(1-3x)}O$ films were obtained. This result is also supported by the fact that the reciprocal lattice map of $Ni_{2x}Zn_xMg_{(1-3x)}O$ (113) diffraction has peaks only at the position of MgO (113). Absorbance spectroscopy revealed that the bandgap of $Ni_{2x}Zn_xMg_{(1-3x)}O$ thin films increased to 3.8–4.7 eV with increasing Mg composition. In addition, the RMS roughness, measured by AFM, was below 1 nm. These results demonstrate that the bandgap can indeed be controlled without changing the lattice constant, leading ultimately to strain- and stress-free heterojunction formation.

PS46
(Student, Late News) High-Performance hBN/Graphene/AlGaN/GaN Hot Electron Transistors Shisong Luo[1], Xiang Zhang[1], Zhaobo Mei[1], Mingfei Xu[1], Ziyi He[2], Tao Li[1], Jingan Zhou[1], Pulickel Ajayan[1] and Yuji Zhao[1]; [1]Rice University, United States; [2]Arizona State University, United States

Introduction Wide band gap AlGaN/GaN heterostructures are promising candidates to build RF power devices, mainly due to the high-density two-dimensional electron gas (2DEG) at the

$Al_xGa_{1-x}N$/GaN interface and the high critical field of $Al_xGa_{1-x}N$ and GaN. As Schottky contracts are the basic block for these devices, the transport properties at metal/semiconductors contracts on AlGaN/GaN heterostructures are important. Since graphene (Gr) enables ballistic electron transit in the transversal direction and excellent in-plane transport within monolayer thickness, Gr/AlGaN/GaN Schottky contracts are attracting more interest, especially for hot electron transistors with theoretical > 1 THz cutoff frequency [1]. Due to its atomic thickness and high breakdown electric field, hBN is a promising choice for hot electron transistors (HETs) [2]. However, there is a lack of reports for HETs based on hBN/Gr/AlGaN/GaN.
Experimental Process In this work, AlGaN/GaN epitaxial layers were grown on Si substrate by MOCVD. Lateral isolation of the AlGaN/GaN active area (~5×10^{-5} cm^2) was achieved after GaN etch by RIE and SiO_2 deposition by E-beam evaporation. Monolayer Gr was grown by CVD on Cu foils and transferred to the target and the Gr active area is patterned by RIE. Similarly, hBN was transfer to Gr surface and is patterned by RIE. Metal stacks of Ti/Al/Ti/Au for Ohmic contacts were deposited by E-beam evaporation, followed by rapid thermal annealing at ~ 850 ºC for 30 s under N_2 ambient. A schematic cross-section of the hBN/Gr/AlGaN/GaN HET is illustrated in Fig. 1. Fig.2 shows the top view optical micrograph and Raman spectrum of hBN/Gr at the active region, which could demonstrate that hBN and Gr have been successfully transferred to the AlGaN/GaN substrate.
Devices Results Fig.3 (a) shows the measured collector current at various applied collector-base voltages, V_{CB}, in common base measurement, which could obtain the maximum current density ~ 30 A/cm^2 by dividing the active region's area. Fig.3 (b) presents the corrected collector current ( ), which is the difference between the original collector current (I_C ($V_{BE} \neq 0$)) and the collector current at zero V_{BE} (I_C ($V_{BE} = 0$)) to extract the leakage current from the base to the collector. It is apparent that the I_C' increases with a rising positive V_{CB}, which confirms that the applied V_{CB} can effectively lower the filter potential barrier width of the collector-base filter junction. One of the important parameters for a HET is its common base current gain, which is calculated as to take into account. In Fig.3c, gets closer to 0.9994 and maintains a certain value at an applied bias greater than 1.0 V. Fig. 4 (a) shows I_C tuned by V_{CE} at varying input base current (I_B). In Fig. 4 (b), the common-emitter current gain ( ) as a function of V_{CE} is shown, demonstrating a stable β* of around 0.6. Here, the is a value of pure hot electrons which is the difference between the original collector current (I_C ($I_B \neq 0$)) and the collector current at zero I_B (I_C ($I_B = 0$)) to extract the leakage current from the emitter to the collector.
Conclusion In this work, hBN/Gr/AlGaN/GaN HETs were fabricated, and their common base and common emitter I-V characteristics were measured. These devices exhibit a high current density (~ 30 A/cm^2), high common base current gain (~ 0.9994), and moderate common emitter current gain (~ 0.6). Our proposed HET could be a promising candidate for a high current gain DC amplifier and high-speed transistor working at radio frequency.
Acknowledgements This research is supported as part of ULTRA, an Energy Frontier Research Center funded by the US Department of Energy (DOE), Office of Science, Basic Energy Sciences (BES), under Award No. DE-SC0021230.
Reference [1] F. Giannazzo *et al.*, *ACS Applied Electronic Materials*, vol. 1, no. 11, pp. 2342-2354, 2019.
[2] B. W. Liang *et al.*, *ACS Nano*, vol. 15, no. 4, pp. 6756-6764,7 2021.

PS47
(Student, Late News) Realizing 3D Microstructures from Graphene Using Aerosol Jet Printing Brittany N. Smith, Peter Ballentine, James L. Doherty, Ryan Wence, Hansel A. Hobbie, Nicholas X. Williams and Aaron D. Franklin; Duke University, United States

Graphene has shown promise as a sensor electrode material for all-carbon electronics due to its high mechanical strength, electrical conductance, and surface area. While a broad range of sensors have used 2D printed graphene electrodes, additively manufactured 3D microstructures have gained recent attention with the promise of performance improvement without increasing the electrode aerial footprint. However, these methods typically rely on structural supports and/or lengthy post-print processing to achieve uniform and functional 3D microstructures, increasing cost and complexity. In this work, we develop a versatile and robust aerosol jet printing (AJP) approach to fabricating 3D graphene microstructures without the use of post-processing, hazardous chemicals, or support structures. We identified several key factors that must be followed for the AJP of 3D graphene: 1) have a high weight percent of graphene in water (2.3 wt. %); 2) print at elevated substrate and ink temperatures (120 °C and 50 °C, respectively) for rapid water evaporation; 3) successively deposit circles directly atop one another to create vertical pillars, or slightly shifted laterally to create leaning pillars or trusses; and 4) manually finetune the ultrasonic atomizer current to balance the amount of graphene deposition with water. To assess the effect of print speed on pillar height, 60 layers were deposited at print speeds from 0.1 mm/s to 2 mm/s, highlighting that a decrease in print speed in turn corresponds to an increase in pillar height, with heights as high as 0.9 mm achieved with only a 100 μm diameter. Without tilting the nozzle or platen, the minimum achievable angle a 3D pillar could be printed with respect to the substrate is 36.6°, which is comparable to 3D extrusion-based printers. Truss structures were printed and characterized for conductivity, revealing a high (~10^9 Ω) resistance at the base (i.e., the overspray from the print) compared to a reasonably low 2.87 kΩ on the graphene truss itself. Importantly, this conductivity was achieved in as-printed 3D structures with no baking or other post-processing, which may be used to further reduce the resistance. To demonstrate their utility in sensors, 3D graphene pillars and trusses were printed on the electrodes of impedimetric humidity sensors. The control sensor (printed graphene with no 3D structures), exhibiting minimal resistance drift over 15 hours, yielded an average sensitivity of 3.4 %Ω / %RH (relative humidity), which was decreased to 3.2 %Ω / %RH with the addition of pillars due to their shielding of current-carrying pathways – this indicates that simply increasing surface area of the electrode is not sufficient for boosting sensing performance. However, the sensitivity rose to 5.2 %Ω / %RH with trusses, which added a parallel current-carrying pathway to increase the active graphene sensing surface. This AJP approach to realizing 3D graphene microstructures that are conductive and mechanically robust provides a simple path to enhancing sensing electrodes and realizing a variety of other additively manufactured structures.

PS48
(Late News) Designing Surface Chemistry of Semiconductor Nanocrystals for High-Performance Thin-Film Transistors Seoyeon Park[1,2], Soon Ju Oh[2] and Ji-Hyuk Choi[1]; [1]Korea Institute of Geoscience and Mineral Resources, Korea (the Republic of); [2]Korea University, Korea (the Republic of)

The field of colloidal semiconductor nanocrystal (NC) technology has made tremendous advancements in recent years, with a particular focus on the development of high-performance thin-film transistors (TFTs). One key area of interest is the surface chemistry of semiconductor NCs, as it plays a critical role in the electronic properties of the films constructed from semiconductor NCs. Various strategies such as ligand exchange, surface passivation, and doping have been explored to improve the electronic properties of semiconductor NCs. In this study, we report a simple, solution-based, and postsynthetic process for halide ligand exchange and simultaneous doping of CdSe NCs, and highlights the key properties that are critical for achieving high-performance TFTs. The optimized TFTs exhibited high mobility of over 10 $cm^2 V^{-1} s^{-1}$, an on/off ratio of over 10^7, and negligible hysteresis. Overall, we discuss in detail the influence of surface chemistry on the device performances, including carrier mobility, on/off ratio, and threshold voltage.

PS49

(Student, Late News) Pyridine-Carbonitriles-Based Thermally Activated Delayed Fluorescence Emitters for High Performance OLEDs Yi-Kuan Chen[1], Tien-Lin Wu[1] and Chien-Hong Cheng[1,2]; [1]National Tsing Hua University, Taiwan; [2]Department of Chemistry, National Sun Yat-sen University, Kaohsiung, 80424, Taiwan, Taiwan

In recent years, the 3rd generation emitters of Organic Light Emitting Diodes (OLEDs) which exhibit thermally activated delayed fluorescence (TADF) characteristics draw great attention due to the high internal quantum efficiency (IQE) of nearly 100% in the electroluminescent device, and the triplet-harvesting capability from the reverse intersystem crossing (RISC) process. However, there is the trade-off between the fast RISC and the high photoluminescent quantum yield (PLQY) for TADF molecules, and the conventional TADF emitters suffer from the instability problem.
In this work, our team develop a series of pyridine-carbonitriles-based (PPC) TADF emitters, and they exhibit high PLQYs of 76% to 100% in doped films, good thermostabilities, and the large dihedral angles to prevent intermolecular aggregation. By introducing xylene groups between the electron donor and the acceptor, the energy-splitting between the singlet and the triplet states are minimized, which accelerates the endothermic RISC process. In addition, with the donor effect and the acceptor modulation design strategies, the degree of charge transfer (CT) is controlled, resulting in color-tuning from sky-blue, green to orange red. The resulting devices of PPC emitters as dopants exhibit high external quantum efficiencies and small turn-on voltages. The highest device efficiency of 39.8% appears to be record-breaking among the TADF-based OLEDs to date. In addition, the TPAmPPC-based device shows superior operation lifetime and high-temperature resistance. It is worth noting that the PPC-based materials have excellent optical properties and the potential for making them strong candidates for TADF practical application.

PS50

(Student, Late News) (Late News) Understanding the Oxygen Vacancy Formation in Transition Metal Oxides Using Bond Strength Analysis: A First-Principles Study Inseo Kim and Minseok Choi; Inha university, Korea (the Republic of)

The oxygen vacancy is crucial to the various properties of oxides. Therefore, although numerous efforts have been made to identify the factors that determine the vacancy formation in oxides [1-3], accurate prediction of the vacancy formation and property still remains a challenge. In this study, we attempted to link the formation energy of the oxygen vacancy to the fundamental bond characteristics such as covalency and ionicity [4,5]. Density functional theory $+U$ calculations were performed to investigate the electronic and structural properties of the vacancy in various binary transition metal oxides, and the crystal orbital Hamiltonian population method was used to analyze the oxygen-metal bond nature [6-8]. Subsequently, the correlation between the vacancy formation energy and the covalent and ionic bond strength was examined. Finally, the results were compared and discussed with the bond-valence theory.
[1] A. M. Deml *et al*., J. Phys. Chem. Lett. **6**, 1948 (2015).
[2] A. A. Emery and C. Wolverton, Sci. Data **4**, 1 (2017).
[3] Y. Hinuma *et al*., J. Phys. Chem. C **122,** 29435 (2018).
[4] I. Kim, H. Lee, and M. Choi, J. Appl. Phys. 131, 075106 (2022).
[5] I. Kim and M. Choi, in preparation
[6] R. Dronskowski and P. E. Bloechl, J. Phys. Chem. **97**, 8617 (1993).
[7] V. L. Deringer, A. L. Tchougreff, and R. Dronskowski, J. Phys. Chem. A **115**, 5461 (2011).
[8] P. C. Müller *et al*., J. Phys. Chem. C **125**, 7959 (2021).

PS51

(Student, Late News) Modeling Effect of Perovskite Layer on Efficiency and Development of Efficient and Stable Perovskite Layer Arnold K. Feutmba, Stephanie Rouamba and Hongmei Dang; university of the District of Columbia, United States

Solar power is an essential source of renewable energy that can help to reduce greenhouse gas emissions. Halide-based perovskite has shown great promise in solar cell technology, with an impressive efficiency of 25.5%. However, there are still several challenges that need to be addressed, such as thermal instability, degradation, and defects of the perovskite layer.
Perovskite is a promising material for photovoltaic devices composed of a large organic cation, a metal cation, and a halide anion. The advancement of perovskite material largely depends on material engineering in order to improve both its performance and stability. The organic cation utilized in perovskite is known to cause thermal instability but incorporating formamidinium (HC(NH2)2+= FA) into the structure can result in a more durable and sturdy perovskite material. However, depositing a uniform and dense FAPbI3 layer is challenging, and achieving complete surface coverage can be difficult, leading to less efficient performance in FAPbI3-based perovskite solar cells than in MAPbI3-based perovskite solar cells.
To address these issues and improve efficiency and stability, two possible approaches will be considered: first, the performance and stability of FAPbI3 perovskite will be numerically investigated using the SCAPS-2D software package. The suggested structures will be evaluated on SCAPS-2D through dark and light I-V characterization. This will serve as a baseline experiment, with SnO2 used as the electron transport layer. Second, the design of (FAPbI3)-x(MAPbBr3)x perovskite layer will be optimized, and its performance and stability will be numerically investigated. The optimal (FAPbI3)x(MAPbBr3)x compound will be determined by simulation based on absorption, defect density, carrier lifetime and mobility to provide foundation for fabrication of highly efficient and stable perovskite solar cells. Comparing the data of the optimized perovskite with the baseline experiment under the same conditions will help to clarify and enhance the performance of perovskite solar cells based on FAPbI3

EMC

65TH ELECTRONIC MATERIALS CONFERENCE

June 28–June 30, 2023 // University of California, Santa Barbara // Santa Barbara, California

THURSDAY ORAL PRESENTATIONS

SESSION O: Group III–Nitrides—Novel Nitride Growth
Session Chairs: Mona Ebrish and Christian Wetzel
Thursday Morning, June 29, 2023
Music Building, Lotte Lehmann

8:20 AM O01
Epitaxial Growth of High ScN Fraction ScAlN on NbN/SiC and SiC Matthew Hardy, Andrew C. Lang, Eric Jin, Neeraj Nepal, Brian Downey, Vikrant Gokhale, Scott Katzer and Virginia Wheeler; U.S. Naval Research Laboratory, United States

ScAlN thin films have attracted significant attention due to their factor of five increase in piezoresponse over AlN for $Sc_xAl_{1-x}N$ compositions of $x = 0.43$ [1], leading to potential applications in 5G filters and RF electronics. Integration of metallic epitaxial NbN with ScAlN using molecular beam epitaxy (MBE) enables a pathway towards a highly conductive lower electrode while preserving high crystal quality even in relatively thin ScAlN films suitable for use at or above X-band frequencies. For example, epitaxial GaN/NbN/SiC high-overtone bulk acoustic resonators have recently demonstrated record f × Q of 7×10^{14} Hz [2]. Maintaining phase-pure and high crystal quality $Sc_xAl_{1-x}N$ at high x is critical to improve resonator bandwidth and reduce insertion loss.
In this work, we show the importance of layer nucleation—both an AlN interlayer, and the initial ScAlN layer—to the final crystal quality of MBE-grown ScAlN films on SiC and NbN/SiC. Very thin AlN layers, grown at standard molecular beam epitaxy growth conditions have a large impact on both the surface evolution as observed though reflection high-energy electron diffraction (RHEED) and in the final X-ray diffraction (XRD) 0002 reflection full-width at half maximum (FWHM). AlN layers grown on SiC show streaky, narrow RHEED patterns, indicating a smooth, well-ordered surface, for film thicknesses as low as 5 nm. With the inclusion of a 5-nm AlN interlayer, the $Sc_{0.32}Al_{0.68}N$ XRD FWHM decreases from 7200 arcsec to 4100 arcsec. An AlN interlayer is also critical to growth of ScAlN on NbN thin films. A two-step AlN growth process can effectively encapsulate the NbN layer while providing a smooth surface on which to nucleate ScAlN growth.
In addition to the AlN interlayer, the initiation steps used for the ScAlN layer also has a strong impact on the final quality of the film. Previously we demonstrate elimination of cubic RHEED features by starting with a $Sc_{0.32}Al_{0.68}N$ layer before growth the $Sc_{0.40}Al_{0.60}N$ layer. Instead of a two-step ScAlN growth, initiation using a linear composition grade from $Sc_{0.32}Al_{0.68}N$ to $Sc_{0.40}Al_{0.60}N$ over 100 nm leads to further improvements in the RHEED pattern, including a narrowing of the spots early in the growth, as well as elimination of remaining ring-like character in the final RHEED pattern after an additional 40 nm of growth, and a XRD FWHM as low as 4400 arcsec for ScAlN films grown on SiC. The graded sample has the same average ScN fraction and thickness as the two-step sample. The grade thickness can be reduced to 25 nm (with the remaining 125 nm $Sc_{0.40}Al_{0.60}N$) without degrading the XRD FWHM or RHEED pattern, increasing the average ScN fraction from 0.373 to 0.393. Finally, a 500-nm-total-thickness sample (100 nm $Sc_{0.32}Al_{0.68}N \rightarrow Sc_{0.40}Al_{0.60}N$, 400 nm $Sc_{0.40}Al_{0.60}N$) was grown to show the impact of defect annihilation in thicker films, resulting in a reduction of XRD FWHM to 3190 arcsec. Employing the same 25-nm grade followed by 125-nm of $Sc_{0.40}Al_{0.60}N$ grown on AlN/NbN/SiC enables a measurable XRD peak with a FWHM of 7100 arcsec. The improved layer initiation shows that more gradual changes in chemical composition (surface energy) and strain reduces the nucleation of undesirable anomalous cubic grains, and may point to a general strategy for elimination of anomalous grains in high ScN fraction ScAlN.
[1] M. Akiyama, K. Kano, and A. Teshigahara, *Appl. Phys. Lett.*, **95**, 162107 (2009).
[2] V.J. Gokhale, B.P. Downey, J.A. Roussos, D.S. Katzer, and D.J. Meyer, *IEEE T. Ultrason. Ferr.*, (2021).

8:40 AM O02
Epitaxial Ferroelectric ScAlN—Thickness Scaling to the Nanometer Scale Ding Wang, Ping Wang, Shubham Mondal, Mingtao Hu, Danhao Wang, Yuanpeng Wu and Zetian Mi; University of Michigan–Ann Arbor, United States

Ferroelectrics functioning at reduced dimensionality have long been pursued for the rich physics behind, including domain wall motion and energy transfer, charge compensation, phase stability, strain and interface coupling, as well as the devices enabled for highly scaled, energy efficient, multifunctional memory/sensing/computing devices and architectures. The emergent nitride ferroelectrics, including ScAlN and ScGaN, have been proposed as promising ferroelectrics with wide and tunable bandgap, large polarization and high tunable coercive field, with potentially high compatibility with both GaN and Si technology. For this new class of ferroelectrics, the ferroelectric wurtzite phase is energetically stable at room temperature, making it highly possible to maintain ferroelectric order in nitride ferroelectrics even at extremely reduced dimensionality.
In this work, the thickness scaling down behavior of ScAlN thin films in the thickness range of 100 nm to 5 nm, has been studied to reveal the ferroelectric order in nitride ferroelectrics at reduced dimensionality. The ScAlN samples were grown by molecular beam epitaxy (MBE) on CMOS-compatible Mo/Si substrates. Reflection high energy electron diffraction (RHEED), X-ray diffraction (XRD), and scanning transmission electron microscopy (STEM) confirmed the wurtzite structure of the as-grown films. The ferroelectric properties of the as-grown films have been confirmed and investigated by capacitance-voltage (C-V) loops and positive-up-negative-down (PUND) measurements. An increase in the coercive field and a significant reduction of remnant polarization are found when the ferroelectric layer is scaled down to below 20 nm. Significantly, a switching voltage of 2-3.8 V, and a saturated remnant polarization of ~23 μC/cm^2 are measured in ~ 5 nm thick ScAlN. X-ray diffractions and transmission electron microscopy studies suggest that the increase in the coercive field and diminishment in switchable polarization can be attributed to the naturally formed surface oxide and the compressive strain in ultrathin ScAlN films due to a larger in-plane lattice constant of ScAlN compared to Mo (011). Our work sheds light on the fundamental thickness-scaling properties of epitaxial ferroelectric ScAlN thin films and paves the way for next-generation compact and power-efficient devices and applications based on nitride ferroelectrics.

9:00 AM O03
(Student) Atomic Structure of β-Nb_2N/AlN/ β-Nb_2N Epitaxial Josephson Junction Naomi Pieczulewski[1], John Wright[1], Anand Ithepalli[1], Danqing Wang[2], Hong Tang[2], David Muller[1], Huili Grace Xing[1] and Debdeep Jena[1]; [1]Cornell University, United States; [2]Yale University, United States

Transition metal nitrides (TMNs) bring complex electronic properties such as ferroelectricity, magnetism, and superconductivity to the GaN and AlN semiconductor families. For example, recent developments in epitaxial growth of single phase, atomically smooth β-Nb_2N have confirmed superconductivity at critical temperature $0.35<T_c<0.6$K.[1,2] Hexagonal β-Nb_2N and wurtzite AlN are structurally similar with only 1.8% lattice mismatch. Especially in qubits where the quality of interfaces significantly affects the phase-coherence of Rabi oscillations, the lattice and symmetry matching open the door for epitaxial integration of superconductors into semiconductor heterojunction devices.
Here, we demonstrate a TMN epitaxial Josephson junction (JJ) with a β-Nb_2N/AlN/ β-Nb_2N trilayer structure grown by plasma-assisted molecular beam epitaxy (MBE) on c-plane sapphire. The JJ consists of 1-2nm AlN layer sandwiched between two β-Nb_2N film grown at a high substrate temperature around 1100°C in N-rich conditions to approximately 50nm each. The JJ structure was confirmed by X-ray reflectivity (XRR) measurements sensitive to thickness below 1nm. X-ray diffraction (XRD) symmetric scan exhibited Pendellosung

fringes indicative of sharp and smooth interfaces. The JJ also demonstrates non-linear I-V characteristics.
The β-Nb_2N/AlN/ β-Nb_2N JJ interfaces were further investigated by high-angle annular dark-field scanning transmission electron microscopy (HAADF-STEM). High crystallinity phase pure β-Nb_2N was confirmed with no secondary NbN_x phases. The AlN layer on β-Nb_2N is imaged to be metal-polar, opposite to the sputtered films studied.[3] Interestingly, the upper and lower AlN interfaces exhibit different interface roughness. The lower β-Nb_2N/AlN interface is atomically sharp, while the upper AlN/ β-Nb_2N interfaces shows greater interfacial roughness. Stacking sequences of atomic planes in all three layers confirm hexagonal close packed cation sublattice and is replicated across the lower β-Nb_2N/AlN interface. However, the ABAB sequence in the upper AlN/ β-Nb_2N interface is disrupted in some regions of the film due to the presence of some disorder. The interfacial atomic configuration was further quantified by a two-dimensional Gaussian fitting of the atom columns in Atomap[4] to determine interfacial distances, and distances between Nb and Al cations.

1. Wright, J., Xing, G., Jena, D., (Preprint) arXiv:2203.14083v1, March 2022.
2. Kobayashi, A., Kihira, S., Takeda, T., Kobayashi, M., Harada, T., Ueno, K., Fujioka, H., Crystal-Phase. Adv. Mater. Interfaces 2022, 9, 2201244.
3. Kobayashi, A., Kihira, S., Akiyama, T., Kawamura, T., Maeda, T., Ueno, K., Fujioka, H., ACS Applied Electronic Materials, 2023, 5, (1), 240-246.
4. Nord, M., Vullum, P.E., MacLaren, I. et al, Adv Struct Chem Imag 3, 9 (2017).

9:20 AM O04
(Student) First Demonstration of C-Doped Semi-Insulating N-Polar GaN Using Propane Precursor Swarnav Mukhopadhyay, Guangying Wang, Surjava Sanyal, Chirag Gupta and Shubhra Pasayat; University of Wisconsin–Madison, United States

N-polar GaN-based electronic devices are showing immense potential in high-power and high-frequency domains of operation. The material development process of N-polar GaN of more than a decade has enabled device researchers to unleash its true potential. N-polar GaN not only broke records in high-frequency electronic devices but also turned out to be a crucial candidate in power electronics as well as optoelectronics devices [1-3]. For obtaining high performance the material quality should be significantly high with low dislocation density along with low surface roughness. Generally, N-polar GaN grown with metal-organic chemical vapor deposition (MOCVD) growth process is known to contain very high background impurities such as O_2 (unintentional n-type dopant), which can cause high dislocation density, reduced breakdown voltage, excessive leakage current, and RF losses [4-6]. Controlling the background carrier concentration is challenging in N-polar GaN compared to Ga-polar GaN due to its high affinity towards O_2 [7-8]. The background carrier concentration can be controlled by either doping with iron (Fe) or carbon (C). To avoid the memory effect of Fe, in this work we have demonstrated the use of propane as a gaseous carbon precursor to compensate for the background carrier concentration in N-polar GaN grown in MOCVD.
The N-polar GaN layer is grown with trimethylgallium (TMGa), and ammonia (NH_3), as the precursor for gallium and nitrogen, while H_2 and N_2 are used as carrier gases at 1270 °C and 100 mbar pressure for all different experiments. The epitaxial layer is shown in Figure 1. Propane is used as a carbon precursor and inserted at different stages of growth such as 50 nm away from the coalescence layer (S_1), starting from the coalescence layer (S_2) and beginning from the nucleation layer (S_3), alongside TMGa and NH_3. The propane concentration is also varied as 2.4 mmol/min, 1.2 mmol/min, and 0.6 mmol/min to check the propane incorporation efficiency in N-polar GaN.
We have found that 2.4 mmol/min of propane provided semi-insulating behavior, which was introduced 50 nm away from the coalescence layer (S_1). The background carrier concentration was reduced by 3 orders of magnitude compared to UID N-polar GaN. The 1.2 mmol/min and 0.6 mmol/min propane showed 6 times and 2 times reduction in background carrier concentration respectively, while injected at S_1. We restricted the use of 2.4 mmol/min of propane in S_2 and S_3 to avoid degradation of material quality. Propane injection from S_2 of 1.2 mmol/min and 0.6 mmol/min reduced the background concentration further by 2.4 and 1.3 times compared to S_1. Although propane introduction from the nucleation (S_3) didn't change the background carrier concentration much. The data are summarized in Table 1. The XRD (Figure 2) and AFM (Figure 3) result shows that with propane incorporation the material quality and the surface morphology remain reasonably good for fabricating N-polar GaN HEMTs. Further extensive studies will be done to understand the behavior of propane incorporation in N-polar GaN in the future. These results show the great potential of propane precursor towards achieving semi-insulating behavior as well as the possibility to control the background carrier concentration of N-polar GaN without degrading material quality.

References: [1] B. Romanczyk et al., IEEE TED. 65, no. 1 (Jan. 2018): 45–50. [2] O. S. Koksaldi et al., IEEE EDL. 39, no. 7 (July 2018): 1014–17. [3] Z. Zhuang et al., Opt. Express 28, 30423-30431, 2020 [*4*] B.C. Chung, et al., JAP. 72, no. 2 (Jul. 15, 1992): 651–59. [*5*] S. Keller et al 2014 SST. 29 113001. [*6*] C Mauder et al 2021 SST. 36 075008. [*7*] N. A. Fichtenbaum, et.al., J. Cryst. Growth 310, no. 6 (Mar. 15, 2008): 1124–31. [*8*] T. Tanikawa et al., PSS. (b) 254, no. 8, 2017: 1600751.

9:40 AM O05
(Late News) Growth of High-Quality Ga-Polar GaN Growth on Mixed-Polarity AlN Vincent E. Meyers[1], Emma Rocco[1], Benjamin McEwen[1], Alireza Lanjani[1], Helen Zhao[2], Michel Khoury[2], Philippe Vennegues[3] and Fatemeh (Shadi) Shahedipour-Sandvik[1]; [1]State University of New York Polytechnic Institute, United States; [2]Applied Materials, Inc., United States; [3]Université Côte d'Azur, France

The (Al)GaN material system holds tremendous importance in high power and high- and radio-frequency electronics, optoelectronics, and sensing applications. The system's common wurtzite crystalline structure lacks inversion symmetry in the *c* direction, causing it to exhibit polarity along this direction. Material characteristics depend on whether the film exhibits metal- (+*c*) or N- (-*c*) polarity. Incorporation of impurities during growth, surface diffusion, and heterointerface polarization field all exhibit strong polarity-dependence [1]. The ability to control both polarity and the strain resulting from heteroepitaxial growth is therefore critical for higher-performing future power electronics and optoelectronics. Recent studies of 2D AlN/GaN grown by metalorganic chemical vapor deposition (MOCVD) utilize pre-growth surface treatments [2] and *in-situ* growth approaches [3] to determine uniformly Al-polar AlN or N-polar GaN growth, respectively. However, to the best of our knowledge, no inducement of 2D metal-polar MOCVD (Al)GaN growth on a mixed-polarity AlN has been demonstrated.
In this work, we show that MOCVD growth of GaN on polycrystalline AlN deposited by physical vapor deposition (PVD) exhibits growth in the Ga-polar direction when an oxygen plasma pre-growth treatment is applied. In the absence of this treatment, GaN exhibits mixed polarity, as determined by atomic-scale transmission electron microscope imaging. Combination of a plasma pre-treatment with strain-engineered buffer layers of composition-graded $Al_{0.65–0.3}Ga_{0.35–0.7}N$ prior to GaN growth induces high-quality epitaxy at the growth surface. This combination of PVD AlN, pre-growth treatment and strain engineering is applied to a technologically-relevant 300 mm Si substrate. The substrate-agnostic PVD process expands the potential applicability of this approach to a wide variety of alternative substrate materials heretofore considered unsuitable for GaN heteroepitaxy.
References
[1] Fichtenbaum, N. A., *et al.* J. Crystal Growth 310.6 (2008)
[2] Stolyarchuk, N., *et al.* Sci. Rep. 8.1 (2018)
[3] Hite, J., *et al.* physica status solidi a 208.7 (2011)

10:00 AM BREAK

10:20 AM O06
Metal Modulated Epitaxy Growth of AlN/GaN Short Period Superlattices with Individual Layer Thicknesses Less Than 2 nm
Alexander A. Chaney, Cynthia Bowers, Krishnamurthy Mahalingam, Shin Mou, Kent Averett and Thaddeus J. Asel; Air Force Research Laboratory, United States

In this work we show the capability of metal modulated epitaxy (MME) in realizing self-assembled AlN/GaN short period superlattices (SPSLs) with individual layer thicknesses less than 2 nm. During MME, the supplied group III metal flux is modulated via the periodic opening and closing of its corresponding shutter. When done without interruption of the N flux, and under nominally metal rich conditions, the resulting growth oscillates between regimes of metal accumulation and consumption. It is possible to leverage this behavior to generate AlN/GaN short period superlattices (SPSLs) through the addition of a constant Ga overpressure during the MME growth of AlN. Samples grown using this technique, at a substrate temperature of 825 ºC, were found to have AlN/GaN SPSLs for Ga fluxes of $5x10^{-7}$ Torr or higher. Analysis of x-ray diffraction (XRD) coupled scans found the GaN layer thickness was determined by the supplied Ga flux. The highest Ga beam flux of $1x10^{-6}$ Torr produced a GaN layer thickness of 4 ML as determined by XRD coupled scan fitting. AlN layer thicknesses were consistently 6 nm. In order to reduce the AlN layer height, the shutter oscillation period used during the MME process was drastically shortened with the intent of growing only 4 ML of AlN per cycle. Additionally, the substrate temperature was lowered to 790 ºC in order to limit Ga desorption, resulting in increased Ga adatoms at lower flux values. Coupled XRD scans of the first growth done with these alterations showed peaks associated AlN, the Al_2O_3 substrate and an AlGaN alloy with accompanying Pendelosung fringes, typically indicative of high quality SPSLs. TEM analysis of the sample showed strong interfacial intermixing between the GaN and AlN layers, resulting in an almost random distribution of the GaN layers. The lack of definitive AlN and GaN layers likely explains random alloy AlGaN behavior seen in XRD (i.e. no superlattice satellite peaks). It is believed that the presence of Ga during the final stages of Al consumption is the cause for this strong layer intermixing. In order to improve the abruptness of the AlN/GaN interfaces, shutter conditions were modified in order to limit the Ga and Al interaction. Coupled XRD scans of both samples showed a combination of superlattice satellite peaks and a random alloy peaks along with the AlN and substrate peaks. Examination of the layer structure via TEM found that the reduced Al/Ga interaction had indeed resulted in significantly improved interface abruptness, with intermixing being limited to a single atomic layer at best. Unfortunately this improvement came the cost of a reduction in the AlN layer thickness uniformity vertically across the entire structure. One of the samples also showed 3 distinct vertical regions of different SPSL uniformity, varying from highly uniform to almost completely randomized. As with the previous sample, these layer structures help to explain the presence of multiple AlGaN peaks seen in XRD. AFM imaging showed deep pits (> 14 nm) on the surface, indicating that there was a lack of complete coalescence in some regions, a sign of a poorly optimized growth. Based on these results, we believe that through careful optimization of growth parameters, highly ordered AlN/GaN SPSLs with a sub 4 nm period are possible using the MME process. This will enable us to realize high quality AlGaN digital alloys.

10:40 AM O07
(Student) Surface Oxide Removal on AlN Substrates via Low Temperature Aluminum Flashing
Christopher M. Matthews, Habib Ahmad, Zachary Engel, Keisuke Motoki, Sangho Lee, Emily N. Marshall, Huijin Chung, Anusha Krishnan and W. Alan Doolittle; Georgia Institute of Technology, United States

Recently, substantial bulk n- and p-doping in aluminum nitride (AlN) as well as AlN homojunction PN diodes were demonstrated, overcoming the longstanding barrier to doping of AlN[1]. Highly crystalline material is a pre-requisite for semiconducting AlN films and devices, but the well-known formation of surface oxides on AlN can result in a dense layer of stacking faults that create dislocations at the growth interface. These dislocations could be detrimental to the performance of any semiconductor devices fabricated from the AlN thin films. High temperature aluminum flashing (Al-flashing) has shown promise for improving AlN film quality but is exceedingly time consuming, and difficult to perform in a standard MBE[2]. In this study, we show that regrown AlN films can be obtained with threading dislocation densities matching that of the substrate by using a low-temperature Al-flashing process.
Surface oxides readily form on polar III-nitride surfaces, but the stability of these oxides varies, with aluminum oxides being much more stable than their gallium-based counterparts[3,4]. This results in the unavoidable presence of stubborn surface oxides on AlN substrates and templates, making regrowth of highly crystalline AlN difficult. Removal of surface oxides is an important process for gallium nitride (GaN) films and devices, but the methods used for the less stable gallium oxides (e.g., ex situ chemical cleaning and in situ thermal annealing) are ineffective for removing aluminum oxides from AlN. Recently, an in situ Al-assisted surface cleaning process has been reported to remove the surface oxides from AlN substrates[2]. However, the reported method requires high temperature annealing of the AlN substrates, which could prove detrimental to subsequent efforts to dope the regrown AlN films[1]. It is also time consuming and requires high temperatures, both things that may prove to be commercially unviable. Using a hydrogen plasma to remove surface oxides from AlN has also been shown to work, but this process is expensive and the introduction of hydrogen to the AlN surface could hinder the doping of AlN, especially since the interaction of H and Be in AlN is unknown. Ga-flashing has been widely used to successfully remove surface oxides from GaN surfaces and operates on the same principle as the reported Al-assisted surface cleaning process[2] but takes considerably less time. Hence, we modified our established Ga-flashing process to create a low temperature Al-flashing procedure in an attempt to quickly remove AlN surface oxides before regrowth without overheating the sample.
In this study we examine the effectiveness of the low-temperature Al-flashing procedure. Reflection high-energy electron diffraction analysis shows the surface evolution during the Al-flashing and provides useful feedback on the status of the Al-flashing process (i.e., when the surface has reached a stable AlN configuration). X-ray diffraction and transmission electron microscopy show regrown AlN films without Al flashing have stacking faults and many threading dislocations while films with Al flashing have quality matching the substrate. Secondary ion mass spectroscopy allows the concentrations of contaminant species (oxygen, carbon, and hydrogen) to be compared between the substrates, the regrowth interface, and the regrown films. A residual gas analyzer is used to perform desorption mass spectroscopy during Al-flashing and will also be presented.
References
[1] H. Ahmad, Z. Engel, C.M. Matthews, S. Lee, and W.A Doolittle, *J. Appl. Phys.* **131**, 175701 (2022).
[2] Y.J. Cho, C.S. Chang, K. Lee, M. Gong, K. Nomoto, M. Toita, L.J. Showalter, D.A. Muller, D. Jena, and H.G. Xing, *Appl. Phys. Lett.* **116**, 172106 (2020).
[3] L. Brewer and A.W. Searcy, *J. Am. Chem. Soc.* **73**, 11, 5308 (1951).
[4] P. Vogt and O. Bierwagen, *Appl. Phys. Lett.* **108**, 072101 (2016).

11:00 AM O08
High Figure of Merit Extreme Bandgap $Al_{0.87}Ga_{0.13}N$-$Al_{0.64}Ga_{0.36}N$ Heterostructures Over Bulk AlN Substrates Mohammad Hussain, MVS Chandrashekhar and Asif Khan; University of South Carolina, United States

Extreme bandgap (EBG) semiconductors such as $Al_xGa_{1-x}N$ (x>0.6, bandgap energy E_G > 4.88 eV) are ideal for high power, high voltage, and high temperature power electronics. Their critical breakdown field (Ec) in lateral devices scales as $E_G^{2.5}$, leads to an estimated value of the Baliga's Figure of Merit (BFOM) significantly higher than that for GaN[1],[2],[3],[4] For achieving high BFOM, in addition to a large breakdown voltage (V_{BR}), a simultaneous low device specific ON-resistance($R_{ON,SP}$) is also required. For the EBG $Al_xGa_{1-x}N$ channel HEMTs to have a low $R_{ON,SP}$, a 2-dimensional electron gas (2DEG) concentration >1x10^{13} cm^{-2} is needed, requiring a barrier $Al_xGa_{1-x}N$ layer with x > 0.80. At such high value of "x", it is challenging to make linear ohmic contacts due to large Schottky barrier height between metal-AlGaN interface.
To solve these issues, we demonstrate EBG *n*-$Al_{0.87}Ga_{0.13}N$-$Al_{0.64}Ga_{0.36}N$ heterostructures over bulk AlN substrate grown by Low Pressure-MOCVD. To facilitate ohmic contact formation, highly doped reverse-graded AlGaN layer(x=0.87 to 0.40) was grown *in-situ.* Reciprocal Space Map(105) and AFM analysis revealed pseudomorphic epilayers with step-flow morphology and RMS roughness ~0.18 nm. X-Ray Topography estimation of control sample gave us a TDD ~ 7 x 10^3 cm^{-2}, indicating the high quality of our pseudomorphic epilayers. A planar Zr-based metal stack was deposited and subsequent removal of the reverse graded *n*-$Al_xGa_{1-x}N$ layer in the access region gave linear ohmic contacts, R_C~4.3 Ω-mm. Additionally, planar metal-oxide-semiconductor (MOS) diodes were fabricated and 2-terminal gate-source breakdown measurement was performed. A V_{BR} of 739 V was measured at metal flashover point for 0.65 μm gate-source spacing, giving an electric field value ~ 11.37 MV/cm. From the breakdown data and the $R_{ON,SP}$ (~2.4 × 10^{-4} Ω-cm^2) value, we estimate the BFOM for our EBG *n*-$Al_{0.87}Ga_{0.13}N$-$A_{0.64}Ga_{0.36}N$ heterostructures to be as high as 2.27 GW/cm^2. This, to the best of our knowledge is the highest reported value to date for an extreme bandgap $Al_xGa_{1-x}N$ (x>0.6) channel heterostructure.[5]

References

[1] B. J. Baliga, IEEE Electron Dev. Lett., **10**, 455 (1989).
[2] R. J. Kaplar, A. A. Allerman, A. M. Armstrong, M. H. Crawford, J. Ray Dickerson, A. J. Fischer, A. G. Baca, and E. A. Douglas, ECS J. Solid State Sci., **6**, Q3061 (2016).
[3] T. Nanjo, A. Imai, Y. Suzuki, Y. Abe, T. Oishi, M. Suita, E. Yagyu, and Y. Tokuda, IEEE Trans. Electron Devices, **60**, 1046 (2013).
[4] N. Yafune, S. Hashimoto, K. Akita, Y. Yamamoto, H. Tokuda, and M. Kuzuhara, Electronics Lett., **50**, 211 (2014)
[5] K. Hussain et al., Appl. Phys. Express (2023)

11:20 AM O09
(Student) Mechanism of hv-MacEtch in GaN and III-Nitrides Heterojunctions Clarence Y. Chan[1], Aadil Waseem[2], Xihang Wu[2], Yixin Xiao[3], Andy Xie[4], Zetian Mi[3] and Xiuling Li[2,1]; [1]University of Illinois at Urbana-Champaign, United States; [2]The University of Texas at Austin, United States; [3]University of Michigan–Ann Arbor, United States; [4]Qorvo, Inc., United States

III-nitride (GaN, In GaN, and AlGaN) compound semiconductors form the building blocks of a wide variety of devices for applications in optoelectronics as well as high frequency and power electronics. Current methods to produce micro and nanostructured devices such as trenches and mesas typically employ reactive ion etching (RIE). It is well known that plasma damage is incurred in RIE-etched material with different degrees dependent on process conditions. A post-RIE damage-repair step involving material removal is typically required to reduce the said plasma damage in order to recover device performance.
Photo-assisted metal-assisted chemical etching (hv-MacEtch) is a plasma-free anisotropic etching method that has been shown to effectively etch GaN with rates similar to that of RIE [1]. While this technique has been studied (both in its open-circuit MacEtch as well as photoelectrochemical etching forms) as a function of etching chemistry [2-3] and semiconductor doping types [4-5], a clear overarching picture of the ensemble effects of MacEtch components on etch rate and morphology have never been presented such that both etching and structure design optimizations can be taken into account of in tandem to mitigate undesired process outcomes.
In this study, we present MacEtch of GaN and its heterojunctions from the fundamental perspective of a photoelectrochemical process, governed by both carrier transport and extraction in the semiconductor as well as solution chemistry. This is broken into three key aspects of MacEtch. The first relates the change in basic semiconductor properties such as doping type, concentration, and resultant band energy level alignment between semiconductor-etchant junctions with implications for heterojunctions. The second depicts the tuning of metal electrodes not only with consideration for the catalyst-semiconductor junction energy alignment but also its distribution with respect to the semiconductor anode with potential effects on scalability and packing density of features as shown in Fig. 1. Finally, the third discusses the properties of the solution ranging from acid-base chemistries to concentration and temporal evolution of the solution induced by experimental procedure which ultimately affects the consistency and replicability of III-N MacEtch. In addition to the above we will extend discussion pertaining to the production of 3D device structures consisting of multi-heterojunction epitaxial layers.
This work is supported in part by an ARL MURI Program #W911NF2110337.
[1] C. Y. Chan, S. Namiki, J. K. Hite, M. A. Mastro, S. B. Qadri, X. Li, *Journal of Vacuum Science & Technology A.* **39**, 053212 (2021).
[2] J. A. Bardwell, J. B. Webb, H. Tang, J. Fraser, S. Moisa, *J Appl Phys.* **89**, 4142–4149 (2001).
[3] D. M. Dryden, R. J. Nikolic, M. S. Islam, *J Electron Mater.* **48**, 3345–3350 (2019).
[4] C. Youtsey, G. Bulman, I. Adesida, *J Electron Mater.* **27**, 282–287 (1998).
[5] A. C. Tamboli, A. Hirai, S. Nakamura, S. P. Denbaars, E. L. Hu, *Appl Phys Lett.* **94**, 151113 (2009).

11:40 AM O10
(Student) MBE Growth, Characterization of BAlN Films and 2D Electron Gas in Epitaxial BAlN/GaN Heterojunction
Chandrashekhar P. Savant, Kazuki Nomoto, Thai-Son T. Nguyen, Yu-Hsin Chen, Ryan Page, Joseph Casamento, Huili Grace Xing and Debdeep Jena; Cornell University, United States

In this work, epitaxial wurtzite phase BAlN films were grown by nitrogen plasma molecular beam epitaxy on different wurtzite phase substrates (e. g. nitrided sapphire, β-Nb_2N film, GaN template). Effect of different growth parameters on composition of BAlN films was explored. B incorporation was found to increase with decreasing substrate temperature and with increasing B flux. In-situ electron diffraction and ex-situ x-ray diffraction measurements confirm the growth of wurtzite BAlN films at 30^0 in plane orientation with sapphire substrate and at 0^0 orientation with bottom Nb_2N films. With increasing boron content in BAlN films, the c-parameter decreases while the a-parameter shows a non-monotonic trend. Ferroelectricity (with remnant polarization of ~16 μC.cm^{-2} and coercive field of ~1.45 MV.cm^{-1}) and high dielectric constant (of ~18 at 500 kHz) were also observed in these BAlN films. A slight reduction in bandgap is seen with increasing boron content in BAlN films (from ~6.12eV for AlN films to ~5.95eV for $B_{0.15}Al_{0.85}N$ film). This work also reports the first demonstration of polarization-induced two-dimensional electron gas (2DEG) in the epitaxial BAlN/GaN heterojunctions. Observation of ferroelectricity with low coercive field, remnant polarization (lower than the sputtered BAlN [1] and comparable to MBE grown AlScN films [2]) and high-k, makes BAlN an attractive barrier in GaN high electron mobility transistors (HEMTs). Therefore, BAlN/GaN

heterostructures were grown on 2” and 3” wafers; showing polarization-induced 2DEG with good sheet resistance of ~650 ohm/sq, ~400-500 cm^2/V.s mobility (400-500 cm^2/V.s), and 1.4-1.8 e13 cm^{-2} charge. The results presented in this paper demonstrates MBE growth of BAlN films and heterostructures with interesting properties that would enable new electronic devices. These films could be useful for combining memory and logic functionalities in digital electronics and to mingle epitaxial ferroelectric and high-k barrier technology into RF and mm-wave power electronics. For instance, a new class of ferroelectric HEMTs devices can be formed by integrating epitaxial ferroelectric, high-k nitride barrier with III-V nitride semiconductors [3].

SESSION P: 2D Materials Synthesis and Characterization
Session Chairs: Chen Chen and Suzanne Mohney
Thursday Morning, June 29, 2023
UC, Corwin East

8:20 AM P01
(Student) Spectroscopic Ellipsometry for *In Situ* Monitoring of MoS_2 Growth at the Sub-Monolayer Limit Thomas V. McKnight[1,1], Elizabeth Houser[2], Lorenzo Tamez[1], Frank Peiris[2] and Joan M. Redwing[1,1]; [1]The Pennsylvania State University, United States; [2]Kenyon College, United States

The ability to monitor the growth rate of transition metal dichalcogenide (TMD) monolayer and few-layer films in situ is an area of great interest to achieve tight control of layer number and to gain insight into the fundamental mechanisms of film growth. Optical characterization techniques such as laser reflectivity are widely used for real time measurements of growth rate during thin film deposition by metalorganic chemical vapor deposition (MOCVD) but cannot be readily extended to the growth of 2D materials which require sensitivity in the sub-monolayer regime. Spectroscopic ellipsometry (SE), on the other hand, is widely used to measure the dielectric function and thickness of thin films and is a powerful in situ technique for atomic layer deposition providing information on film thickness per cycle and insight into the initial mechanisms of nucleation.
In this study, we investigate the use of SE as an in situ technique to monitor the growth of MoS_2 monolayer and few-layer films by MOCVD on c-plane sapphire substrates. The studies were carried out in a vertical cold wall MOCVD reactor equipped with a J.A. Woollam M2000XI ellipsometer with a spectral range of 210 – 1687 nm, integrated using purged optical ports on the reactor. Molybdenum hexacarbonyl ($Mo(CO)_6$) and hydrogen sulfide (H_2S) were used as precursors with H_2 as the carrier gas. Initial studies were carried out by keeping growth parameters constant at 100 Torr reactor pressure, 1050°C substrate temperature, $Mo(CO)_6$ flow rate of 8.6 $x10^{-3}$ sccm, S/Mo ratio of ~46700 and varying growth time (5 – 40 min) to develop a series of samples with varying surface coverage. After each growth, SE was performed as a function of temperature during cooldown to room temperature under H_2S. Atomic force microscopy (AFM) and field emission scanning electron microscopy (FE-SEM) were used to measure the film coalescence and quantify monolayer and bilayer surface coverage. An optical model of the layer structure was developed assuming an interfacial layer between the film and substrate and using an effective medium approximation to consider partial film coverage where the effective medium is a variable combination of void and the MoS_2 film. The models were first used to fit the room temperature data to extract the dielectric function of MoS_2, which compared favorably to prior literature reports. The optical model was then used to predict the variation in the ellipsometric parameters (Ψ and Δ) as a function of surface coverage demonstrating sensitivity in the sub-monolayer regime down to ~40% coverage. Additional studies are underway to determine the temperature dependence of the dielectric function in order to refine the models to accurately measure film coverage at growth temperature. The features of the ellipsometric curves soften at elevated temperatures compared to room temperature measurements and marked differences are observed when comparing samples of varying coverage, expounding the potential for SE to discern sub-monolayer coverages at growth temperatures. The optical models will then be applied to monitor MoS_2 film growth in situ, demonstrating the effectiveness of SE to allow precise control of film thickness and properties in real time through layer-by-layer tailoring of film deposition conditions.

8:40 AM P02
Effects of Growth Temperature on the Properties of Wafer-Scale Epitaxial MoS_2 Monolayers Grown by Metalorganic Chemical Vapor Deposition Chen Chen[1], Nicholas Trainor[1,1], Shalini Kumari[1], Henrik Myja[2], Tilmar Kummell[2], Thomas V. McKnight[1], Andrew R. Grave[1], Gerd Bacher[2] and Joan M. Redwing[1,1]; [1]The Pennsylvania State University, United States; [2]University of Duisburg-Essen, Germany

Two-dimensional (2D) transition metal dichalcogenides (MX_2, with M being a transition metal and X a chalcogen) have potential application in next-generation optoelectronics, electronics, chemical sensing and quantum technologies.
Epitaxial growth of single crystal TMD monolayers at the wafer-scale is of significant interest for device applications. Metalorganic chemical vapor deposition (MOCVD) is a promising approach for TMD growth as it enables the use of high substrate temperatures (900-1000ºC) and chalcogen/metal ratios (10^3-10^5) which are beneficial for epitaxy. In addition, the flow rate of precursors can be modulated during growth to enhance the surface diffusion of metal-containing species and control the lateral growth rate of TMD domains. Sapphire has emerged as a promising substrate for wafer-scale TMD monolayers and few layer films due to its crystallographic compatibility and commercial availability. Despite the broad interest in wafer-scale 2D TMDs, the fundamental understanding of how the growth conditions, e.g. growth temperature, impacts the epitaxial growth and properties of 2D TMDs has rarely been investigated.
In this study, MOCVD growth of wafer scale MoS_2 monolayer was carried out in a horizontal cold-wall reactor that includes an induction-heated rotating SiC-coated graphite susceptor and separate gas inlets for the metal and chalcogen precursors. Molybdenum hexacarbonyl ($Mo(CO)_6$) and hydrogen sulfide (H_2S) were used as precursors in a H_2 carrier gas. A 2” c-plane sapphire substate was used for all MoS_2 growths. The growth temperature was varied as 900ºC, 950ºC, and 1000ºC. The flow rate of the molybdenum precursor used in this work ranged from 0.001 to 0.003sccm while the H_2S flow rate was maintained at 400 sccm. Growths were carried out with a moderate reactor pressure of 50 Torr using H_2 as the carrier gas. Using these conditions, growth of fully coalesced monolayer MoS_2 was achieved in 10-30 minutes across the 2” substrate. AFM and FESEM were used to characterize the surface coverage and morphology of the layers and in-plane X-ray diffraction was used to assess the epitaxial quality. Spatially resolved Raman and photoluminescence spectroscopy were carried out to assess the uniformity of the monolayer and along with variable temperature photoluminescence measurements.
A coalesced monolayer of MoS_2 was achieved on 2” c-plane sapphire over the temperature range from 900ºC to 1000ºC. The surface coverage (growth rate) was found to be only weakly dependent on the growth temperature and scaled roughly linearly with $Mo(CO)_6$ flow rate indicating that the growth is limited by mass transport rather than reaction kinetics. In-plane XRD phi-scans confirm that the films are epitaxially oriented with respect to the sapphire over the temperature range (900ºC to 1000ºC) with the (1120) of MoS_2 aligned with the (1120) of α-Al_2O_3. The FWHM of the phi-scan peak of MoS_2 decreases with increasing growth temperature, indicating a reduction in in-plane rotational misorientation of the MoS_2 domains at higher growth temperature. The MoS_2 monolayer sample grown at 1000ºC

exhibits strong photoluminescence at room temperature centered around 1.9 eV and defect-related emission which dominates at low temperature of 6 K. PL measurements also reveal an increase in the intensity ratio of the A exciton to trion emission with increasing growth temperature indicating a reduction in defects. Additional results correlating the structural and optical properties of the MoS_2 monolayers to the transport properties of field-effect devices will be reported.
The results of this work provide a deeper understanding of the epitaxial growth of MoS_2 monolayers grown by MOCVD and the impact of defects on the optical and electrical properties of the layers.

9:00 AM P03
(Student) MOCVD Growth and Characterization of $MoSe_2$ Nanodots within a WSe_2 Monolayer Matrix Meghan Leger[1,1], Benjamin Huet[1], Saiphaneendra Bachu[1], Gwangwoo Kim[2], Nasim Alem[1,1], Deep Jariwala[2] and Joan M. Redwing[1,1]; [1]The Pennsylvania State University, United States; [2]University of Pennsylvania, United States

Single photon emitters (SPEs) in 2D transition metal dichalcogenides (TMDCs) offer a compelling solution to create bright, spectrally narrow quantum emitters with high photon-extraction efficiencies. Quantum emitters in TMDC monolayers are typically associated with point defects or strain in engineered structures. Another potential avenue for SPEs is the formation of lateral heterostructures in which a TMDC nanodot is embedded in a matrix comprised of a wider bandgap TMDC. The nanodot can capture excitons from the surrounding matrix and may also host quantum states. Despite these intriguing prospects, there have been few studies focused on nanodot formation in TMDC monolayer material.
In this work, we report on the synthesis of $MoSe_2$ nanodots embedded within a WSe_2 monolayer matrix via metal-organic chemical vapor deposition (MOCVD). MOCVD growth was carried out at 800-1000 °C in a cold-wall reactor using $Mo(CO)_6$ and $W(CO)_6$ as metal precursors and H_2Se as the chalcogen source. C-plane sapphire was used as the substrate with H_2 as the carrier gas. A three-step process was employed whereby a short nucleation step was initially used to form nanoscale $MoSe_2$ domains followed by a ripening step in which the $Mo(CO)_6$ was switched out of the reactor and the sample was annealed under H_2Se. $W(CO)_6$ was then introduced resulting in lateral growth of a WSe_2 matrix surrounding the $MoSe_2$ domains. The nucleation time was varied to change the size of the $MoSe_2$ nanodots and the duration of ripening was modified to control the interfacial abruptness. Raman spectroscopy of the monolayers confirmed the presence of both the A_{1g} peaks for WSe_2 and $MoSe_2$ at 247 cm^{-1} and 239 cm^{-1}, respectively. High resolution scanning transmission electron microscopy (STEM) and energy dispersive spectroscopy (EDS) revealed the presence of triangular $MoSe_2$ nanodots with edge lengths on the order of 10-100 nm embedded within a continuous WSe_2 matrix. Variable temperature photoluminescence (PL) measurements were carried out on monolayer samples removed from the sapphire growth substrate and encapsulated in hBN. At room temperature, PL peaks were observed at 1.65 eV and 1.57 eV which correlate with exciton-related emission from WSe_2 and $MoSe_2$, respectively. As the temperature was decreased from 280K to 80K, the $MoSe_2$ PL intensity increased relative to the WSe_2 emission which is suggestive of charge transport from the WSe_2 matrix to the $MoSe_2$ nanodots.

9:20 AM P04
Study of Single Crystal Graphene Grown by Chemical Vapor Deposition on Copper Tharanga Nanayakkara[1,2], Udagamage K. Wijewardena[1], Annika Kriisa[1], Rasanga Samaraweera[1,3], Rameshwor Poudel[1] and Ramesh G. Mani[1]; [1]Georgia State University, United States; [2]Brookhaven National Laboratory, United States; [3]Uva Wellassa University, Sri Lanka

Graphene, which is a single two-dimensional layer of carbon atoms organized in a hexagonal structure, has attracted great interest due to its intriguing electronic properties and its promise of living up to expectations as a material of choice for critical future electronics applications. Several methods of graphene growth have been employed, including exfoliation from graphite, epitaxial growth on SiC, chemical vapor deposition (CVD) and the reduction of graphite oxide. Among these methods, the CVD technique has attracted considerable interest since it is a promising method for producing comparatively large-scale, high-quality graphene at a relatively low cost.
Graphene growth by CVD on copper starts with the formation of stable nuclei, these nuclei grow into grains and the grains coalesce at the grain boundaries, resulting in the polycrystalline graphene over 100 micron length scales. The polycrystalline morphology degrades the mechanical and electrical properties of graphene, which is undesirable for graphene applications. Thus the development of growth techniques to reduce the density of two-dimensional grain boundaries, and ultimately produce large single crystals of graphene, is a topic of interest in graphene growth.
In this work, we utilized low pressure CVD (LPCVD) technique to produce graphene single crystals. The chemical vapor deposition (CVD) growth of single-crystal graphene on polycrystalline copper foils is a complex process affected by thermodynamics, kinetics, and growth conditions. These factors lead to the diversity of island shapes of single crystal graphene. Here, we present an experimental atomic force microscopy (AFM) study of the different shapes of single-crystal graphene grown on the inner surface of copper enclosures using the low pressure CVD technique. Most remarkably, this study indicates that graphene single crystal appears to form below the adjacent copper foil surface. This feature is revealed in cross sectional AFM scans of the height, which indicate that the graphene surface lies below the neighboring foil surface by ~15- 30 nm.
Our results also show that an impurity assisted growth mechanism governs the growth of single crystal graphene via isotropic diffusion, producing two-fold, four-fold, and six-fold symmetries in the resulting flakes. In addition, single crystal graphene produced via anisotropic diffusion is also present here, but they do not exhibit signs of an impurity assisted growth mechanism. Finally, we find that strain relaxation in two-fold and four-fold symmetric graphene structures via isotropic diffusion are more complicated than the six-fold structures via isotropic diffusion, which results in multiple steps orientations in low symmetry structures.

9:40 AM P05
(Late News) Oxidation Mechanism of 2H-$MoTe_2$ at the Atomic Scale Yeoseon Sim[1], Se-Yang Kim[1], Soon-Dong Park[2], Jung Hwa Kim[1], Seunguk Song[1], Daeyong Kim[2], Jingsung Kwak[3], Zonghoon Lee[1], Sung Youb Kim[1] and Soon-Yong Kwon[1]; [1]Ulsan National Institute of Science and Technology, Korea (the Republic of); [2]Korea Institute of Materials Science, Korea (the Republic of); [3]Changwon National University, Korea (the Republic of)

Defects can occur during the growth of two-dimensional (2D) transition metal dichalcogenide (TMD) crystals. Exposure to these defects in 2D TMD to air and harsh conditions initiates the reaction of exposed transition metal atoms with active species such as O_2 and H_2O molecules, triggering an oxidation process. Understanding the oxidation behavior of 2D TMDs is crucial for their practical applications in electronics, optoelectronics, and electro-/photocatalysis because any structural deformation under ambient conditions directly affects their unique properties. As 2D semiconductor, 2H-$MoTe_2$ is highly susceptible to air, it has the potential to control the conversion between p- and n-type characteristics. Nevertheless, previous research has been conducted on macroscopic scale oxidation, there is limited understanding of the oxidation behavior at the atomic level. It is imperative to explore the oxidation behavior of 2H-$MoTe_2$ in greater detail to effectively modify its properties.
In this study, we provide a detailed investigation on the oxidation of 2H-$MoTe_2$ under various environmental conditions and insights for oxidation control. Exposure of synthesized 2H-$MoTe_2$ flakes to air at room temperature for 17 months led to two striking morphological changes: 1) Hexagonal or triangular etching was observed from

defects such as screw dislocations, crystal edges, and grain boundaries, resulting in the preferential oxidation and formation of pits with an average lateral size of several micrometers. 2) After a relatively slow reaction, triangular protruding oxide layer consisting of a stable MoO_2 hillocks were formed on the basal plane of $MoTe_2$, as confirmed by surface and structure characterization using scanning electron microscope (SEM), transmission electron microscope (TEM) and Raman. Experiments monitoring at the oxidation process at 230 °C for 3 h and TEM analysis showed that the substrates and active species have a significant effect on oxidation mechanism. Interestingly, under an O_2 atmosphere, MoO_2 layers was formed on the entire surface of 2H-$MoTe_2$, while in a H_2O atmosphere, most of the surface remained intact but oxidation etching occurred at defects in the basal plane. Furthermore, using theoretical calculations, we investigated the reaction of the surface Te atoms of defective 2H-$MoTe_2$ with O_2 and H_2O molecules, which provide volatile TeO_2 and H_2Te and create a Te vacancy in the 2H-$MoTe_2$ basal plane. It was found that, although O_2 dissociation in the basal plane of 2H-$MoTe_2$ with a Te vacancy is energetically favored over H_2O dissociation, the subsequent reaction involving H is a dominant mechanism in forming Te vacancies than reactions involving an O atom. More importantly, when TeO_2 volatilizes, the additional adsorbed O atom suppresses the lattice reconstruction around TeO_2, resulting in an increased kinetic barrier (~2.22 eV) to volatile TeO_2. This finding is consistent with the TEM analysis results of the monitoring experiment, which demonstrated the formation of a stable oxide film under an O_2 atmosphere. Our study provides valuable insight into the oxidation dynamics of 2H-$MoTe_2$ at the atomic level and can inspire a new approach to improve the reliability and durability of TMD-based 2D devices.

10:00 AM BREAK

10:20 AM P06
(Student) Transformation to Alkali Birnessites via Simple Intercalation of Electrochemically Grown 2D-Layered H-Type Manganese Dioxide on Epitaxial Graphene Michael Pedowitz[1,1], Jennifer E. DeMell[2,1,1], Daniel Lewis[1,1] and Kevin Daniels[1,1]; [1]University of Maryland, United States; [2]Laboratory for Physical Sciences, United States

Mixed valence manganese oxides (MnO_x) have attracted significant interest in recent years due to the easily reversible redox reactions between manganese oxidation states (Mn^{+2}, Mn^{+3}, and Mn^{+4})[1], which has enabled applications in catalysis[2], energy storage[3], and gas sensing[4]. Manganese dioxide (MnO_2), in particular, has demonstrated tunable structural properties, due to its wide variety of synthesizable structural polymorphs ((α, β) tunnel[5], (γ) spinel[5], and (δ) layered[5]) which allow for control over its available surface area and the reactive properties. Among these structural polymorphs, the α and δ phases exhibit strongly mixed-valence character, with Mn^{+3} defects found throughout the crystal structure[5], which is desirable due to it being a highly active site[6]. Water-stabilized hexagonal δ-MnO_2 ($HMnO_2$) contains many Mn^{+3} ions as the interlayer contains $Mn^{+2/+3}$ ions to neutralize the layer charge from Mn^{+3} lattice defects[7]. However, the direct synthesis of $HMnO_2$ has not been reported extensively in the literature, as most synthesis routes rely on permanganate salts[1], which leads to the synthesis of ion intercalated δ-MnO_2 and a reduction in Mn^{+3} defects in the lattice[9].
In our previous work, we presented the synthesis of high Mn^{+3} content $HMnO_2$ via electrodeposition on epitaxial graphene/silicon carbide (EG/SiC) substrates[4]. In this work, we extend upon this by transforming also these as-grown films via intercalating with ions to form alternate birnessites and controlling the growth via patterning. The electrodeposition was carried out by a three-pulse deposition in a three-electrode electrochemical cell, as described previously[4]. The resulting δ-MnO_2 thin films were then characterized through Raman spectroscopy, scanning electron microscopy (SEM), and atomic force microscopy(AFM). Raman spectroscopy confirmed the formation of δ-MnO_2 as the peaks were consistent with the literature[4,8]. The AFM indicated that the surface was made up of nanofibrous nanoparticles, which SEM confirmed and indicated that the deposition on EG/SiC was made up of microplates larger than 40 μm x 40 μm in size. After this characterization, the resulting films were exfoliated mechanically and analyzed with AFM to determine if the films were epitaxial. This exfoliation generated 6-layer MnO_2 nanoplates, indicating we can reach the 2D limit and confirm epitaxial growth. The resulting films were intercalated with alkali metals (Na^+) via cyclic voltammetry in a similar three-electrode cell to the deposition, using a 2 M metal nitrate solution. Optical Analysis of the film indicated two distinct regions formed in the film, large multicolored regions, and small blue and black islands. Raman analysis of these regions found that the islands were unintercalated MnO_2 but the colored regions were Na-type birnessite due to their Raman shifts which are consistent with the literature[8]. Believing ion diffusion resistance to be impeding the intercalation we patterned δ-MnO_2 into 100 μm ribbons and attempted additional intercalation. Optical analysis of the film post patterned intercalation revealed two regions, a brown and blue region. Raman spectroscopy of these two regions indicated that both were Na-type birnessite. However, differing peak intensities indicate the crystallinity of the two regions is different. This demonstrates that we have successfully grown and transformed the H-type birnessite to Na-type birnessite with 100% efficiency on EG/SiC, allowing for additional fine-tuning of its properties and expanding its application in energy storage to Na^+ and K^+ chemistries.
References: [1]L. Spinelle et al. *Sensors* 17(7), 2017 [2] F. Cheng et al. *Chem. Mater* 22(3), 2010 [3] Y.J. Huang et al. *Electrochim Acta* 99, 2013 [4] M. Pedowitz et al. *J. Microelectromech Syst* 29(5), 2020 [5] Z. Chang et al. *Proc Natl Acad Sci USA* 115(23), 2018 [6] Julien et al. *Spectrochim Acta A* 60, 2004 [7] Drits et al. *Am Mineralogist* 82, 1997 [8] Julien et al. *Solid State Ionics* 159, 2003

10:40 AM P07
Ultraviolet Luminescence Dynamics of Hexagonal BN Epilayers Grown by Chemical Vapor Deposition Using Carbon-Free Precursors Takumi Kasuya[1], Kohei Shima[1], Kazuhiko Hara[2] and Shigefusa F. Chichibu[1]; [1]Tohoku University, Japan; [2]Shizuoka University, Japan

Hexagonal (h) BN is an ultrawide bandgap semiconductor built from layers of sp^2-bonded honeycomb structure. Although hBN has an indirect bandgap with the energy of 6 eV, hBN is expected to be used in deep-ultraviolet light-emitting devices because of its high quantum efficiency for the indirect exciton (iX) emissions at around 5.8 eV. Very recently, accidental formation of graphitic bernal (b) BN, which is one of the polytypes of hBN, has been reported for the solution growth of BN under specific growth conditions where carbon or more precisely graphite existed in the growth environments. Because theoretical and experimental studies have pointed out that bBN has a direct bandgap and the spontaneously formed bBN segment [1] exhibited a direct exciton (dX) emission at 6.035 eV at low temperature, the research scope for BN was greatly expanded. On another front, the research group led by Hara has been growing hBN epilayers on *c*-plane sapphire by low-pressure (LP) chemical vapor deposition (CVD) using carbon-free precursors. In some of their LP-CVD hBN films, the authors' group has detected an inclusion of bBN segments that exhibited the dX emission at 6.035 eV, in addition to significant phonon replicas of iXs of hBN. In this presentation, structural and optical properties of hBN films grown by LP-CVD using the new cold-wall reactor with limited carbon sources in the growth environment will be shown to discuss how to control a bBN incorporation.
Approximately 0.6 to 1.4-μm-thick hBN films were grown on a *c*-plane sapphire at 1300 °C for 60 min by LP-CVD at 15 kPa using a BCl_3-NH_3-N_2 gas system. The molar flow rate ratio of group V to group III precursors (V/III ratio) and supply timing of BCl_3 and NH_3 were varied in the following three manners. (i) V/III=2500 and BCl_3 was supplied 10 s prior to NH_3, (ii) V/III=3000 and BCl_3 and NH_3 were supplied simultaneously, and (iii) V/III=1250 and BCl_3 and NH_3 were supplied simultaneously. X-ray diffraction (XRD) measurements

were carried out using a Bruker D8 DISCOVER diffractometer. Wide-area cathodoluminescence (CL) spectra were recorded at 12.5 K using a homemade CL system with an acceleration voltage of -3.5 kV, giving an electron beam diameter of about 750 μm. The probe current was 68 μA, resulting in a probe current density of 15 mA/cm^2.
In the XRD spectra, a 002 diffraction peak of hBN was observed at 2θ=26.7 ° regardless of growth conditions, while the peak at around 2θ=44.3 °, which was assigned as 101 diffraction of bBN, was not detected. However, the emission peak at 6.035 eV peculiar to bBN was detectable in all the films. These results imply sufficiently high quantum efficiency of the dX emission of bBN. Nevertheless, fractions of integrated spectral CL intensities for the bBN emission (5.96–6.10 eV) to the entire spectral range (2.5–6.5 eV), I_{bBN} / $I_{overall}$, of the present films were approximately an order of magnitude lower than the previous film grown at 1400 °C in a hot-wall reactor. From these results, higher growth temperature and/or the use of a hot-wall reactor, which potentially enhances parasitic reactions in the gas phase, seem effective in enhancing bBN formation in our growth package. We note that in the present films, CL intensities for the iX peaks of hBN (5.77–5.96 eV) were lower than that of the 5.5-eV band that originates from certain stacking errors. In addition, $I_{overall}$ of the present films were lower than the hBN film grown using the old hot-wall reactor. These results indicate higher concentrations of midgap recombination centers, which decrease the quantum efficiency of iX emissions, in the present films than the previous one due presumably to the lower growth temperature. Carrier dynamics of iXs in the present hBN films will be presented onsite.
This work was supported by Crossover Alliance, JSPS KAKENHI (#18K04231, #20K20993, #22H01516), Tsukuba Innovation Arena "kakehashi," JST SPRING (#JPMJFS2102), Japan.
[1] Rousseau *et al*., ACS Nano **16**, 2756 (2022).

11:00 AM P08
(Student) Epitaxial Growth of Wafer-Scale Monolayer Hexagonal Boron Nitride (hBN) Shubham Mondal, Ping Wang, Ding Wang, Danhao Wang, Mingtao Hu, Yuanpeng Wu and Zetian Mi; University of Michigan–Ann Arbor, United States

As silicon-based electronics approaches its dimensional scaling limit, two-dimensional (2D) materials have emerged to be promising candidates for the next generation of semiconductor technology. In this context, monolayer hexagonal boron nitride (hBN) has been widely considered a fundamental building block for 2D van-der Waals heterostructures and devices. Being isostructural to graphene but with alternating B and N atoms arranged in a monolayer honeycomb structure, 2D hBN is highly stable with a wide bandgap of 6-8 eV, making it one of the thinnest materials for future electronic and optoelectronic devices. Owing to the lack of a scalable growth approach, recent developments in 2D hBN heterostructures are mostly based on a top-down exfoliation and stacking process, which limits the technological potential of 2D hBN. Intensive efforts are underway for developing a scalable growth process for 2D hBN, wherein the lattice mismatch between the substrate and the grown overlayer is a critical factor. Owing to the compatible lattice symmetry and small lattice mismatch of hBN with graphene (~ 1.6%), highly oriented pyrolytic graphite (HOPG) and epitaxial graphene have emerged as promising substrates for the epitaxy of monolayer hBN as well as hBN/G heterostructures. Our recent studies have shown that the initial nucleation of h-BN happens only along the atomic edges of the HOPG substrate, giving rise to defect-free hBN nanoribbons, which could be extended laterally with increasing growth time. In this work, we further propose a unique approach for promoting precise hBN nucleation that can lead to, for the first time, wafer-scale epitaxy of defect-free 2D hBN. Large area, single domain, monolayer hBN is achieved by employing high-temperature growth in a plasma-assisted Molecular Beam Epitaxy (MBE) system. Scanning Electron Microscopy (SEM) images show the morphological evolution of discrete hBN islands coalescing to form large-area monolayer hBN on HOPG substrate which eventually form multi-layer hBN with prolonged growth. Photoluminescence characterization of the epitaxially grown sample reveals a sharp peak at ~ 201 nm corresponding to the band-edge emission of hBN (~6.1 eV), which confirms the presence of monolayer hBN. Moreover, the Raman spectra show a clear E_{2g} corresponding to hBN (~ 1360 cm^{-1}) whereas the D peak corresponding to graphene (1580 cm^{-1}) is observed in both samples. Further studies on this work are currently underway and will be reported. This work promises to resolve the fundamental bottleneck in the epitaxy of 2D materials for the development of highly uniform, wafer-scale monolayer hBN that can support the next generation of electronic and optoelectronic devices.

11:20 AM P09
(Student, Late News) 2D Materials Junction-Templated Photoelectrochemistry Radha Raman[1,2,3], Ya-Ping Hsieh[2] and Mario Hofmann[3]; [1]National Central University, Taiwan; [2]Academia Sinica, Taiwan; [3]National Taiwan University, Taiwan

In recent years, the development of lateral junctions between 2D materials has enabled a new class of nanostructures with precise transitions in electronic structure. In this study, we have utilized the unique carrier transport properties of lateral junctions to conduct electrochemistry with unprecedented spatial resolution and dynamic controllability. By electrostatically confining electrons within the junction, we were able to localize electrochemical reactions with nanometer precision in their lateral position. We have also developed a scalable process for the formation of graphene pn-junction networks that is compatible with various materials and techniques, including dielectrophoretic deposition. The high spatial selectivity of the deposition process allowed us to create complex 1D fractal-shaped nanostructures with ultrahigh Raman enhancement.
Furthermore, we have extended our study to utilize MoS2 junctions to photodeposit gold nanoparticles. The incorporation of MoS2 lateral junctions facilitated the deposition of gold nanoparticles with high spatial resolution. The resulting nanostructure morphology can be used for various applications including surface-enhanced Raman spectroscopy and nanoelectronics.
These results offer exciting possibilities for the assembly of a new type of neural network based on axon-like guided growth of interconnected neurons. Such a network could have significant applications in the development of evolvable, brain-like future electronics. The potential of this technology highlights the importance of continued research in the field of photoelectrochemically deposited nanostructures on 2D material lateral junctions.

SESSION Q: Optical Materials on Si
Session Chair: Kunal Mukherjee
Thursday Morning, June 29, 2023
UC, Flying A Studios

8:20 AM Q01
(Student) Growth and Characterization of $Al_xIn_{1-x}As_ySb_{1-y}$ Digital Alloys on InP on Si Ellie Y. Wang[1], J. A. McArthur[1], Adam A. Dadey[2], Matthew Fetters[3], Amy W. Liu[3], Joel M. Fastenau[3], Joe Campbell[2] and Seth R. Bank[1]; [1]The University of Texas at Austin, United States; [2]University of Virginia, United States; [3]IQE Inc., United States

$Al_xIn_{1-x}As_ySb_{1-y}$ (referred to as AlInAsSb) grown as a digital alloy lattice-matched to GaSb substrates has been shown to have characteristics useful for avalanche photodetectors (APDs) operating at near- to mid-IR wavelengths. In addition to a broadly tunable bandgap over a wide compositional range, the material system has favorable band offsets, with most of the bandgap change occurring in the conduction band, and exhibits low excess noise due to impact ionization coefficient ratios as low as k = 0.01 [1]. The digital alloy method of growing thin binary layers to form extremely short-period

superlattices allows for finer control over compositional gradings in the growth of complex heterostructures compared to analog growth [2]. In some cases, the technique also improves the noise characteristics of the material— for example, the lattice-matched extremes of the AlInAsSb quaternary on InP, $Al_{0.48}In_{0.52}As$ and $AlAs_{0.56}Sb_{0.44}$, exhibit lower impact ionization ratios when grown as digital alloys instead of random alloys, suggesting the potential of the system as a low-noise multiplier on InP [3-5].
We have previously demonstrated the growth of AlInAsSb digital alloys lattice-matched to InP across its compositional range, overcoming the phase separation challenging random alloy growth [6, 7]. Combined with the availability of commercial InP-on-Si templates, this introduces the ability to integrate the quaternary onto silicon, allowing for AlInAsSb-based APDs operating in the mid-IR compatible with the established silicon manufacturing and photonic integrated circuit infrastructure.
Here we present the first growths of AlInAsSb as a lattice-matched digital alloy on InP-on-Si substrates. AlInAsSb digital alloys of different aluminum compositions were grown using the molecular beam epitaxy (MBE) growth approach described in [8], where x is calculated as the sum of the number of AlAs and AlSb monolayers divided by the total number of monolayers. Each composition was strain-balanced to InP by adjusting the AlAs/AlSb thickness. Lattice matching of AlInAsSb controls to InP was verified by X-ray diffraction, and nominally identical films were then grown on an InP-on-Si template. Reflection high-energy electron diffraction (RHEED), atomic force microscopy (AFM), and photoluminescence (PL) measurements were performed on AlInAsSb on InP-on-Si with Al compositions of x = 0.60 and x = 0.70 to verify structural, optical, and surface quality. During the growths, we observed initial spotty RHEED patterns that smoothed out into streaks in the AlInAsSb digital alloy layers. AFM showed a rougher surface for the samples on InP-on-Si, with an RMS roughness of ~5.7 nm compared to ~3.5 nm on InP— this is likely partially due to the rougher substrate, which has an RMS roughness of ~2.9 nm compared to ~0.4 of InP. Room temperature PL was observed for the samples grown on InP-on-Si, showing optical emission at wavelengths of ~1.24 μm (x = 0.60) and ~1.04 μm (x = 0.70), comparable to control samples grown on InP. Further work to characterize the electrical properties of AlInAsSb on InP-on-Si is underway, as is growth on improved InP-on-Si templates, and these will be reported at the conference. This work was supported by a Multidisciplinary University Research Initiative from the Air Force Office of Scientific Research (AFOSR MURI Award No. FA9550-22-1-0307).
[1] S. R. Bank, et al. *JSTQE* (2018). [2] A. J. Muhowski, et al. *JVST* (2021). [3] A. K. Rockwell, et al. *Appl. Phys. Lett.* (2018). [4] X. Yi, et al. *Nat. Pho.* (2019). [5] J. Xie, et al. *IEEE TED* (2012). [6] S. Tomasulo, et al. *J. Cryst. Growth* (2020). [7] E. Y. Wang, et al. *64th EMC.* (2022). [8] S. J. Maddox, et al. *Cryst. Growth Des.* (2016).

8:40 AM Q02
(Student) Synthesis and Characterization of AlSb for Growth on Si and Integrated Circuit Based Radiation Detection Alexandria Ragsdale, Shea Tonkinson, Maya Kutty, Mega Frost, Melvin Foster, Thomas J. Rotter, Adam Hecht and Ganesh Balakrishnan; The University of New Mexico, United States

High resolution, room temperature radiation detection is of utmost importance, with applications in national security, nuclear nonproliferation, and medical physics. A typical high-resolution solid-state detector crystal, Ge, has a high carrier mobility (μ) and lifetime (τ) for both electrons and holes, and a small band gap ~ 0.6 eV which increases the counting statistics and improves energy resolution, but requires operation at cryogenic temperatures to reduce thermal noise. High energy resolution room temperature solid state detectors allow much more ease of use by removing the cooling constraints. The leading solid state room temperature detector material is CdZnTe (CZT), with a band gap of ~ 1.6 eV (depending on composition), which eliminates cooling needed to reduce thermal noise, but still has reasonable counting statistics for good resolution. The μ and τ values are lower than for Ge and, very importantly, the μτ product for holes is ~1000 times poorer, leading to an asymmetric charge induction efficiency across a CZT based detector. While this can be compensated for by multiple electrode arrangements, this is still a fundamental material issue and reduces counting statistics vs. a dual carrier detector.
AlSb crystals have similar band gap and electron properties compared to CZT and are expected to have similar electron and hole mobility and lifetime, making this a dual carrier material and increasing the total number of charge carriers which should improve resolution. Efforts to characterize AlSb have been met with challenges due to the high reactivity of Al with oxygen, and Sb and molten AlSb being extremely volatile, reacting to almost all crucible materials. Additionally, AlSb oxidizes rapidly in air, further complicating handling.
To avoid the issues others experienced with bulk growth, we applied molecular beam epitaxy (MBE) to grow high quality, low impurity, potentially detector-grade AlSb crystals. Additionally, the group has previously grown AlSb on Si and are studying high purity growth. This involves relaxation of an interfacial misfit dislocation layer, as seen for example with AlSb on GaAs in Fig. 1, and could open the door to fully integrated IC based detectors.
Three micrometer samples of AlSb were grown on semi-insulating GaAs via MBE for preliminary studies, Fig 2. In undoped samples, an average Hall mobility of 1200 cm^2/Vs, Hall carrier concentration of 10^{10} cm^{-3}, and resistivity of 10^6 Ω-cm were found. Samples used the GaAs substrate for n-type and GaSb for p-type cap layers to study Te and Be compensation doping concentration effects. Crystal diffraction, Fig. 3, shows a very good AlSb crystal quality. Alpha-particle radiation detection was achieved, and spectra were produced for Am-241 and Pu-239 sources, Fig. 4. Gamma rays are detected, and purity and compensation are being studied to achieve gamma radiation spectroscopy.

9:00 AM Q03
(Student) Defect Filtering at the Interface of MOCVD/TLP Heterogenous Epitaxial III-V on Silicon Hyun Uk Chae, Juan S. Vazquez and Rehan Kapadia; USC, United States

Integrating III-V semiconductors on silicon has been a long desire to realize the advanced electronics and photonics application for the future 'extended' Moore's Law regime. Transfer methods have been developed to integrate the III-V layer onto silicon, which is limited by the costive epitaxial wafer and alignment issue. Direct growth is, an alternative method to realize heterogeneous integration, which is necessary to use lattice-matching buffer layers. This imposes a significant growth challenge: thick lattice-matching buffer layers for each material must be grown with nanometer spacing, a significant challenge considering. As such, enabling high-quality growth without the use of lattice matching layers would provide a clear path toward direct growth of III-V CMOS. Here, we propose a defect-filtering growth technique to enable high-quality III-V growth on silicon by combining conventional growth with templated liquid phase growth to ensure the quality and uniformity of the grown material. Critically, this approach enables the growth and manufacturing of high-quality crystalline materials on silicon without requiring a nearly lattice-matched substrate, potentially impacting a wide range of fields, including electronics, photonics, and energy devices.

9:20 AM Q04
Mechanisms for Solute Incorporation in Highly Mismatched $Ge_{1-x-y}Sn_xC_y$ Alloys Joshua Cooper[1], Thales Borrely[1], Tuhin Dey[2], Augustus Arbogast[2], Mark Wistey[2] and Rachel S. Goldman[1]; [1]University of Michigan–Ann Arbor, United States; [2]Texas State University, United States

Due to the indirect to direct bandgap transitions predicted and observed in $Ge_{1-y}C_y$ and $Ge_{1-x}Sn_x$, $Ge_{1-x-y}Sn_xC_y$ alloys are promising candidates for Si-compatible optoelectronics. For example, dilute GeSn alloys have been utilized for electrically-injected lasers

operating at cryogenic temperatures and ultra-dilute GeC alloys with narrowing in the direct bandgap have been reported. Due to the opposing strain effects of Sn and C in Ge, the alloy compositions are difficult to discern using x-ray diffraction measurements, and the mechanisms for Sn and C solute incorporation remain unknown. Here, we report on channeling ion beam analyses of C and Sn incorporation into ~200 nm thick $Ge_{1-x-y}Sn_xC_y$ alloy films grown by molecular-beam epitaxy on Ge substrates. To quantify the Sn composition, we conducted Rutherford backscattering spectrometry (RBS), using a 3 MeV α beam to enable energetically distinct Sn and Ge backscattering yields. Channeling RBS (RBS/c) reveals an increase in the fraction of non-substitutional Sn from 13% to 16% and a decrease in the fraction of displaced Ge atoms from 7% to 5%, as the substrate temperature is increased from 160°C to 200°C. To quantify the C composition in the alloys, we conducted nuclear reaction analysis (NRA) using the $^{12}C(d,p)^{13}C$ reaction. Taking advantage of the energy resonance at 1.2 MeV and the energy stopping power of a 700 nm Ge cap layer, we were able to distinguish the C yields associated with the $Ge_{1-x-y}Sn_xC_y$ films from those of the surface hydrocarbons. In this case, channeling NRA reveals an increase in χmin from 0.2 to 0.5 as the substrate temperature is increased from 160°C to 200°C, suggesting a corresponding increase in non-substitutional C incorporation. Monte Carlo-Molecular Dynamics simulations of the channeling ion beam analyses of $Ge_{1-x-y}Sn_xC_y$ alloy films will also be discussed.

9:40 AM Q05
(Student) Doping and Surfactant Behavior of Antimony in Molecular Beam Epitaxy Grown Germanium-Tin Amanda N. Lemire, Kevin A. Grossklaus and Thomas E. Vandervelde; Tufts University, United States

The bandgap of germanium-tin ($Ge_{1-x}Sn_x$) alloys can vary from ~0.8 eV into the far-IR as the Sn composition increases, and transition from indirect to direct bandgaps between 6 and 17 at% Sn depending on strain. Consequently they are being developed for a range of thermal and multijunction photovoltaic (PV) cells, thermal imaging, and photonic data transmission applications. However, at useful Sn contents these alloys are metastable and require low epitaxial growth temperatures and can only be grown to limited thickness; otherwise films may experience Sn segregation and defect formation. Growing below ideal temperatures for Ge can also induce defects, reducing electrical conductivity. PV cell design is harder to optimize for performance if the absorbing layer is limited in thickness by material considerations. One mitigation strategy for non-optimal growth conditions is to deposit and maintain on the growth surface a thin coverage of an additional atomic species, which acts as a surfactant to modify adatom interactions. Surfactants change the surface energy of the growth front, which controls the mobility of adatoms and affects the rate of positional exchange between buried and surface layers. A surfactant that preferentially moves to the growth surface could thus increase the incorporation of Sn into deeper layers and reduce defects due to growth at low temperatures. Additionally, the filling of partial growth layers by surfactant atoms tends to reduce islanding and therefore suppresses surface roughness.
In this work, antimony is applied as an *n*-type dopant and surfactant in the growth of GeSn alloys to potentially improve the crystallinity of Ge and GeSn films grown by molecular beam epitaxy. Sb has a high vapor pressure at low temperatures, which is ideal for minimizing radiative heating of the substrate during low-temperature growths. Pairs of GeSn samples are deposited without and with the codeposition of Sb. The growth temperature, film thickness, and Sn content are varied to investigate the impact of Sb on Sn incorporation and film critical thickness. Depending on growth conditions, varying amounts of Sb will be incorporated into the growing film, so this study also provide data on the retention of Sb as a dopant during low-temperature GeSn growth. Sn content and film quality are characterized by X-ray diffraction, photoluminescence spectroscopy, Raman spectroscopy, spectroscopic ellipsometry, and optical microscopy. Electrical properties are determined by Hall effect measurement. Results will be discussed in terms of how the Sb surfactant has modified the kinetics of the growth process and considered with design of a GeSn based photodiodes and thermophotovoltaic (TPV) cells in mind.

10:00 AM BREAK

SESSION R: Epitaxial Materials Design and Properties
Session Chairs: Sadhvikas Addamane and Aaron Muhowski
Thursday Morning, June 29, 2023
UC, Flying A Studios

10:20 AM R01
(Student) Engineering of the Interband Second Order Optical Nonlinearity with Asymmetric Coupled Quantum Wells Rithvik Ramesh[1], Teddy Hsieh[1], Alec M. Skipper[1], Qian Meng[1], Kevin Wen[1], Mark Wistey[2], Farbod Shafiei[1], Michael W. Downer[1], Jacob Khurgin[3] and Seth R. Bank[1]; [1]The University of Texas at Austin, United States; [2]Texas State University, United States; [3]Johns Hopkins University, United States

Semiconductor platforms exhibiting high second-order optical nonlinearities are of great interest as they can improve device performance and simplify chipscale integration compared with traditional nonlinear materials. While it has been shown that strong and engineerable nonlinearities are achievable using intersubband transitions, transition energies are limited by the possible heterojunction band offsets, restricting operation to mid-IR and longer wavelengths [1]. By contrast, leveraging interband transitions can extend these optical nonlinearities to the near-IR and even visible by utilizing the transitions between conduction and valence band states [2]. This work aims to enhance the interband second-order optical nonlinear susceptibility, $\chi^{(2)}$, using multiple asymmetric coupled AlGaAs/GaAs quantum wells (QWs). The asymmetric coupled QW structures are two quantum wells of different widths (~5-10 nm) separated by a 1 nm barrier that couples the electron or hole wavefunctions in the two wells. By tuning structure parameters, such as the alloy compositions, asymmetry of the quantum well widths, and tunneling barrier thickness, the energy level spacing of the states and the dipole matrix elements between them can be optimized for $\chi^{(2)}$. To evaluate $\chi^{(2)}$ for an arbitrary structure using the density matrix formalism, the wavefunctions and energy levels of the first two bound electron and heavy hole states were determined using a Schrodinger-Poisson solver [3], [4]. The interband Bloch function matrix element was determined from density functional theory (DFT) using Vienna Ab initio Simulation Package (VASP) with HSE06 hybrid functionals. The second-order susceptibility was calculated for the case of second harmonic generation (SHG) with input photon energy adjusted to be 75 meV below resonance to mitigate absorption losses.
We found that enhanced optical nonlinearity can be accessed in unexpected regions of the design space. When using wavefunctions and energy levels determined by linear combination of atomic orbitals (LCAO) theory and only considering one set of transitions corresponding to SHG, the dimensionless SHG coefficient versus QW asymmetry matched literature predictions [5]. However, using more rigorous wavefunction calculation methods and including all possible transitions contributing to SHG, a strong peak in susceptibility was observed at low QW asymmetry (~10%) in addition to the known peak around 50% QW asymmetry. Varying the total QW width and barrier composition can tune the resonant susceptibility for SHG across the technologically important S, C, and L optical fiber communication bands (1.5 - 1.7 μm). Based upon these findings, a series of AlGaAs/GaAs asymmetric coupled QWs have been grown using molecular beam epitaxy. SHG measurements are underway, and results will be reported at the conference. This work paves the way to

design multi-QWs, type-II superlattices, and digital alloys with enhanced second-order optical nonlinearities that can be tailored for particular applications.

This research was supported by a Multidisciplinary University Research Initiative from the Air Force Office of Scientific Research (AFOSR MURI Award No. FA9550-22-1-0307).

[1] M. M. Fejer *et al.*, "Observation of extremely large quadratic susceptibility at 9.6 – 10.8 μ m in electric-field-biased AlGaAs quantum wells," *Phys. Rev. Lett.*, Feb. 1989, doi: 10.1103/PhysRevLett.62.1041.

[2] J. Khurgin, "Second order susceptibility of asymmetric coupled quantum well structures," *Appl. Phys. Lett.*, Dec. 1987, doi: 10.1063/1.98960.

[3] N. Bloembergen, *Nonlinear optics*, 4. ed., Repr. Hackensack, N.J.: World Scientific, 2010.

[4] S. Birner *et al.*, "nextnano: General Purpose 3-D Simulations," *IEEE Trans. Electron Devices*, Sep. 2007, doi: 10.1109/TED.2007.902871.

[5] J. Khurgin, "Second order nonlinear effects in asymmetric quantum-well structures," *Phys. Rev. B*, Aug. 1988, doi: 10.1103/PhysRevB.38.4056.

10:40 AM R02

(Student) Atom Rearrangement in BGa(In)As Alloys Under Annealing Qian Meng[1], Rachel C. White[1], Rasha El-Jaroudi[1], Tuhin Dey[2], Seth R. Bank[1] and Mark Wistey[2,2]; [1]The University of Texas at Austin, United States; [2]Texas State University, United States

The incorporation of small size boron into conventional III-V alloys provides a method for strain engineering of near-infrared, direct-bandgap alloys that can be lattice-matched to silicon[1] and other[2,3] substrates. In other highly-mismatched alloys (HMAs) such as dilute-nitrides and dilute-bismides, dilute amount of nitrogen or bismuth changes the lattice constant and perturbs the host band structure, reducing the bandgap though often at the expense of degraded optical properties. The advantage of incorporating boron is a higher predicted solid solubility, which suggests that less degradation of material properties can be expected than for other HMAs.[4] However, B-III-V alloys remain underexplored in both theory and experiment.

Thermal treatment is often employed to recover the optical properties of HMAs, but is typically accompanied by an undesirable blueshift in emission wavelength from changes in the nearest-neighbor bonding configuration.[5] A blueshift in emission wavelength and modest improvement in photoluminescence (PL) has been observed with *in situ* and *ex situ* thermal annealing of BGaInAs films,[2] while the converse is observed from BGaAs.[6] Here we report the effects of atomic rearrangement on the band structure and optical properties of B-III-V alloys to understand this dichotomy.

BGa(In)As films were grown by solid-source molecular beam epitaxy on (100) semi-insulating GaAs substrates. Samples were progressively annealed by rapid thermal annealing for 1 minute in 50°C steps from 550°C to 900°C and then characterized by room-temperature PL. Experimental results were then compared to *ab initio* simulations obtained with the density functional theory (DFT) package VASP using HSE06 hybrid functionals. A set of BGaInAs structures were simulated varying numbers of In atoms in the first group-III nearest neighbor positions around B atom, as well as BGaAs structures with varying distances between B atoms.

We found an increase in bandgap with increasing numbers of B-In bonds and the most energy-favorable $B_{0.037}Ga_{0.663}In_{0.3}As$ structure was that with the highest number of B-In bonds. This suggests In atoms tend to be in the first nearest neighbor position of B under thermally stable conditions, contributing to a blueshift during annealing. We used an elevated In concentration for BGaInAs calculations compared with experimental data to both sweep a larger number of B-In bonds and investigate bandgap energies closer to the technologically significant 1.3 and 1.55 µm emission wavelengths. Further studies of rearrangement in BGaInAs with low In concentration are in progress. In contrast, the calculated bandgap differences, and energetic driving force due to different B-B distances in $B_{0.03}Ga_{0.97}As$ were much smaller than for In-containing alloys, suggesting BGaAs alloys are not likely to show a strong blueshift upon annealing. This is consistent with the minimal, ~5 meV shift in peak PL energy observed experimentally from $B_{0.03}Ga_{0.97}As$ with annealing. While the intrinsic matrix element strength of BGaInAs increased by about 30% from no B-In bonds to most B-In bonds in our calculations, it can explain a portion of the improvement in optical quality observed with annealing. Since improvement in PL intensity was observed from both BGaAs and BGaInAs, we suspect the removal of the defects played a significant role. Studies of the In concentration on the magnitude of blueshifting in BGaInAs, specifically targeting 1.3 and 1.55µm emitters, are in progress and will be reported at the conference.

This work was supported by the National Science Foundation (Award Nos. ECCS-1933836, DMR-1508646, and CBET-1438608). The authors also acknowledge the LEAP cluster at Texas State University for computing resources.

1 McNicholas et al. Cryst. Growth. Des. (2021)
[2] El-Jaroudi et al. Appl. Phys. Lett. (2020)
[3] El-Jaroudi et al. Cryst. Growth. Des. (2022)
[4] Hart et al. Phys. Rev. B. (2000)
[5] Lordi et al. Phys. Rev. B. (2003)
[6] White et al. 62nd EMC (2020)

11:00 AM R03

Design of Epitaxial Material Properties through Engineering of Quantitative Disorder Robert Makin[1], Andrew Messecar[1], Steve Durbin[1], Nancy Muyanja[2], R.F Martinez-Gazoni[3], Kate Wislang[3], Roger Reeves[3] and Martin Allen[3]; [1]Western Michigan University, United States; [2]University of Michigan, United States; [3]University of Canterbury, New Zealand

In the context of epitaxial semiconductor layers prepared for electronic devices, disorder is frequently an important consideration. One well-known model for quantifying disorder was developed by Bragg and Williams in the early 1930s, who were concerned with accurately describing the varying degrees of atomic ordering in metal alloys [1]. In their formulation, a numerical order parameter (S) is defined as having a value between 0 (fully randomized lattice) and unity (fully ordered lattice). Traditionally this order parameter is measured using x-ray diffraction techniques, but we have recently demonstrated that electron diffraction, Raman spectroscopy and electron microscopy are equally viable experimental methods [2,3]. Following the approach of Laks, Wei and Zunger [4] as applied to semiconductor alloys, it is possible to employ spin-based modeling in conjunction with cluster expansion theory (out to pair-interaction terms) to express a material property P as $P(x,S) = [P(x=0.5, S=1) – P(x,S=0)]S^2 – P(x,S=0)$, provided that P is dominated by pair interactions. Here, S is the Bragg-Williams order parameter, and x represents the composition (e.g. $x = [Ga]/([Ga]+[N])$). Consequently, the expectation is that some properties may exhibit a linear dependence on S^2 provided that composition is properly accounted for; in fact, this is what has been observed in the case of a number of different semiconductor materials [2,3].

In the present study, 44 Ga_2O_3 and 28 GaN samples were considered. Ga_2O_3 layers were grown either by plasma-assisted molecular beam epitaxy or a sol-gel method; GaN was grown by plasma-assisted molecular beam epitaxy. Additional Ga_2O_3 samples from the literature grown by other techniques were also included. The Bragg-Williams order parameter was measured using either in-situ reflection high-energy diffraction, Raman spectroscopy, or electron microscopy image analysis, with several samples characterized by multiple techniques (with S typically agreeing to three decimal places). For the GaN samples measured, S^2 ranged from approximately 0.02 to 0.52, with both nitrogen-rich and gallium-rich compositions in addition to stoichiometric material included. For Ga_2O_3, experimentally-determined values of S^2 ranged from 0.08 to 0.53. As would be expected, a range of band gap energies was measured for the GaN samples, including evidence of inverted bands for some gallium-rich samples as indicated by the observed temperature dependence. In the case of Ga_2O_3, only stoichiometric samples were included in the initial

study, with a range of measured band gap energy between 3.2 eV at S^2 = 0.53 to 5.0 eV at S^2 = 0.08. For the GaN samples, Hall effect mobility values were also measured, with a linear relationship between mobility and S^2 and higher mobility values for Ga-rich samples at the same value of S^2. Extrapolation of the experimental points suggests that further tuning of S could lead to slightly higher mobility values than what have been reported for undoped epitaxial layers. There are several ways to tune S in a plasma-assisted molecular beam epitaxy process, with a weak dependence on temperature and a stronger dependence on plasma conditions. In contrast, for Ga_2O_3 grown by PLD, a strong dependence of S^2 on oxygen partial pressure is observed, with a weaker dependence on sapphire substrate plane. For Ga_2O_3 grown by dehydoxylation of GaOOH, a linear relationship between temperature and S^2 is observed. Consequently, process parameters can be tuned during epilayer growth to achieve a specific value of S and composition (x), and thereby engineer a desired value of band gap and potentially mobility.

[1] W.L. Bragg and E.J. Williams, Proc. Roy. Soc. London 145 A, 699-730 (1934).
[2] R.A. Makin, et al., Phys. Rev. Lett. 122, 256403 (2019).
[3] R.A. Makin, K. York, S.M. Durbin and R.J. Reeves, Phys. Rev. B 102, 115202 (2020).
[4] D.B. Laks, S.-H. Wei and A. Zunger, Phys. Rev. Lett. 69, 376 (1992).

11:20 AM R04
(Student) The Effect of Group-V "Blow-by" on the Structural and Optical Properties of $Al_xIn_{1-x}As_ySb_{1-y}$ Digital Alloys Grown by Molecular Beam Epitaxy

Subha P. Mallick[1], J. A. McArthur[1], Chaojie Du[2], Ellie Y. Wang[1], Stephen March[1], Xiaoqing Pan[2,2,3] and Seth R. Bank[1]; [1]The University of Texas at Austin, United States; [2]University of California-Irvine, United States; [3]University of California-Irvine, Irvine, United States

$Al_xIn_{1-x}As_ySb_{1-y}$ alloys offer numerous advantages for optoelectronic devices in the near- and mid-infrared, including widely tunable direct bandgap, large conduction band offsets, nearly single carrier-initiated impact ionization, and tunable second-order optical nonlinearity through wavefunction engineering. To avoid the miscibility gap of AlInAsSb, high-quality alloys across the entire composition range can be grown by molecular beam epitaxy (MBE) using the digital alloying technique where films are comprised of repeat units of the constituent binary materials: AlAs, AlSb, InAs, and InSb [1-2].

Here, we study the effects of group-V blow-by during the MBE growth process, which leads to the unintentional incorporation of group-V elements in the various binary constituents [3]. Digital alloy growth is very sensitive to the shutter positioning in the MBE cell pocket, growth temperature, and the group-V flux emitted behind the closed shutter. High volatile unintentional group-V elements can sneak around a closed group-V cell shutter and reach the sample surface, resulting in dilute-ternary digital alloy layers. To study the effects of this blow-by, we first quantified this unintentional incorporation. High-angle Annular dark field scanning transmission electron microscopy (HAADF STEM) and energy-dispersive X-ray spectroscopy (EDS) of AlInAsSb digital alloys showed well-defined interfaces and were used to measure the spatial distribution of the constituent elements. The average mole fraction of each group-V blow-by species was calculated by integrating the EDS line scans. Consequently, the blow-by of As and Sb were estimated to be 12 at% and 14 at%, respectively, and were corroborated with high-resolution X-ray diffraction (HR-XRD) experiments. Dynamical simulations of (004) ω-2θ scans using these blow-by values agreed well with measurements and were far better than those assuming simple binary digital alloy layers. To investigate the effects of blow-by on the optical properties, room temperature photoluminescence (PL) measurements were performed on AlInAsSb films with Al% of 60% and 70% strain-balanced to InP substrates and compared against simulated PL spectra with and without blow-by of group-V species. The bandgaps and PL emission for different Al fractions of AlInAsSb digital alloys were calculated with a self-consistent single-band Schrödinger-Poisson solver accounting for strain effects. Excellent agreement with the measured PL spectra and bandgaps was only achieved when the measured levels of group-V blow-by incorporation were used in the calculations. Work is underway to study blow-by effects across the full compositional range of AlInAsSb alloys and will be reported at the conference.

This research was supported by a Multidisciplinary University Research Initiative from the Air Force Office of Scientific Research (AFOSR MURI Award No. FA9550-22-1-0307).

References

[1] L.G. Vaughn, et al., Physics and Simulation of Optoelectronic Devices XIII 307 (2005).
[2] S. J. Maddox, S. D. March, S. R. Bank, "Broadly tunable AlInAsSb digital alloys grown on GaSb." *Cryst Growth des.* 2016; 16(7): 3582- 3586.
[3] Z.R. Wasilewski, S.J. Rolfe, R.A. Wilson, "Contamination in molecular beam epitaxy: the role of arsenic drag effect," J. Cryst. Growth, vol. 175-176, pt. 2, pp. 1270, May 1997.

11:40 AM R05
(Student) Composition Control of Ternary Group-IIIa-IIIb-Nitride Alloy by Hybrid Chemical Vapor Deposition—A Thermodynamic Analysis

Mina Moradnia, Sara Pouladi and Jae-Hyun Ryou; University of Houston, United States

Exceptional properties of ultra-wide band gap (UWBG) materials in chemical/thermal stability, spontaneous electric polarization, low dielectric permittivity, high sound velocity, high biocompatibility, and high mechanical flexibility cause increasing attention to UWBG materials as great candidates for wide range of piezoelectric applications. However, compared to those of currently dominant piezoelectric materials such as lead zirconate titanate (PZT), the piezoelectric coefficients of III-N materials are relatively low. Nevertheless, these lead-free materials have a great potential to replace the PZT because of their operational performance in high temperature and pressure conditions. Also, the biocompatibility of III-N materials makes them a promising candidate to overcome the critical limitation of PZT in epidermic and implantable sensors and electronics. Therefore, we introduce a hybrid chemical vapor deposition (HybCVD) as a new thin-film growth technique for Group-IIIa-Group-IIIb-Nitride alloy to significantly improve the piezoelectric properties in group-IIIa-N (III-N) materials such as wurtzite AlN, by group-IIIb transition metals including scandium (Sc) and yttrium (Y). In this study, we focus on the thermodynamic analysis of precursor reaction chemistry and solid-phase formation, including growth temperatures, input V/III ratios, and input carrier gas ratios in different parts of source zones and mixing/growth zone. The main reason for our calculations comes from the necessity of control on the alloy composition depending on various precursors and deposition conditions. For YGaN alloys, there is not a linear relationship between the input cation precursor ratio, R_Y, and composition, x_Y: the x_Y is always higher than R_Y, indicating significantly higher driving force for the formation of YN in the ternary phase. Also, higher growth temperature (700 → 900 °C), more H_2 in the carrier gas (0 → 100 Pa), and lower V/III ratio (200 → 100) result in higher x_Y by further decrease in driving force of GaN deposition. In contrast, R_Y vs. x_Y is nearly linear for YAlN alloys. When the effects of temperature, carrier gas mixture, and V/III ratio on x_Y are marginal, ScAlN showed the same trend as YAlN in different growth parameters' changes. The new growth technique offers the potential to produce well-controlled, uniform, and high-quality piezoelectric films based on transition-metal-alloyed III-N materials which is critical to obtain high performance piezoelectric devices based on this material.

SESSION S: SiC Material Characterization, Processing and Devices
Session Chairs: Hemant Dixit and Nadeemullah Mahadik
Thursday Morning, June 29, 2023
UC, State Street

8:20 AM #S01
(Student) Anisotropic Electron and Hole Mobilities in 4H-SiC Bulk Crystals Ryoya Ishikawa[1], Hajime Tanaka[1,2], Mitsuaki Kaneko[1] and Tsunenobu Kimoto[1]; [1]Kyoto University, Japan; [2]Osaka University, Japan

The mobility in 4H-SiC exhibits anisotropy because of its hexagonal crystal structure [1,2], and determination of the mobility considering its anisotropy is strongly required for accurate simulation and designing of SiC devices. However, knowledge of the mobility anisotropy in SiC has been extremely limited because of the unavailability of SiC wafers other than SiC(0001). In this study, we prepared special SiC(11-20) single crystals with various doping concentrations, and determined the mobility anisotropy of both electrons and holes by Hall effect measurements over a wide range of temperature. The origin of the temperature-dependent anisotropy in mobility was also discussed, and the anisotropy was quantitatively explained by the effective mass anisotropy taking account of the energy distribution of carriers.
Hall bar structures shown in Figs. 1(a) and (b) were fabricated on n-type and p-type 4H-SiC(11-20) epitaxial layers to measure the electron and hole mobilities, respectively. Two kinds of Hall bar structure were formed on a sample side by side, which are oriented along 〈0001〉 and 〈1-100〉 directions for measuring the mobilities parallel and perpendicular to the *c*-axis ($\mu_{H,//}$ and $\mu_{H,\perp}$), respectively. The mobilities were extracted by Hall effect measurement at temperatures (*T*) from 140 to 600 K.
Figure 2 shows the doping concentration dependences of $\mu_{H,//}$ and $\mu_{H,\perp}$ at room temperature, indicating that $\mu_{H,//}$ is about 12-18% higher than $\mu_{H,\perp}$ for electrons ($\mu_{H,//} < \mu_{H,\perp}$), which is opposite to the case for the hole mobility ($\mu_{H,//}$ is 8-12% lower than $\mu_{H,\perp}$). We determined the relationship between $\mu_{H,//}$ and doping concentration using the Caughey-Thomas equation as depicted by solid lines in Fig. 2.
Next, we discuss the anisotropy of μ from the resistivity ρ ratio ($\mu_{//}/\mu_{\perp}=\rho_{\perp}/\rho_{//}$) to eliminate the effect of the Hall scattering factor. Figure 3 shows the μ ratio as a function of the temperature, indicating $\mu_{//}/\mu_{\perp}$= 1.0-1.3 for electrons while $\mu_{//}/\mu_{\perp} \sim 0.9$ for holes. In principle, the anisotropy of μ originates from that of the effective mass (m^*) and/or the average relaxation time ($\langle\tau\rangle$) since μ is given by $\mu=e\langle\tau\rangle/m^*$. Using the reported values of m^* at the band edges [3], $m^*_{\perp}/m^*_{//}$ is obtained to be 1.21 for electrons and 0.38 for holes as shown by dashed lines in Fig. 3. The μ ratio cannot be simply explained by the m^* ratio at the band edges, indicating that m^* at higher energies than the band edges should be taken into account for a more precise analysis because the number of carriers with higher energy increases at higher temperatures (Figs. 4(a) and 5(a)). Figures 4(b) and 5(b) show the relationship between m^* and the energy of carriers obtained from the first-principles calculation using ABINIT. Based on this relationship, the averaged effective mass (m^*_{ave}) was calculated by using the energy distribution as a weighting function for each temperature as depicted by Fig. 4(c) and Fig. 5(c) [4]. Note that we considered the whole first Brillouin zone for the calculation of m^*_{ave} of holes because the valence band structure is not isotropic as shown in Fig. 5(d) [4]. As a result, it was found that the m^*_{ave} ratios depicted by the solid lines in Fig. 3 show good agreement with the μ ratio for both electron and hole mobilities.
In summary, we presented the complete set of the electron and hole mobilities along the *c*-axis in 4H-SiC over wide ranges of doping concentration and temperature. In addition, the mobility anisotropy could be quantitatively explained by the m^* anisotropy considering the energy distribution of carriers for both electrons and holes based on the first-principles calculation.

8:40 AM S02
(Student) Ray Tracing Simulation of Defects of 4H-SiC in 22-4 16 Reflection of Synchrotron Monochromatic Beam X-Ray Topography in Grazing Incident Geometry Zeyu Chen[1], Yafei Liu[1], Qianyu Cheng[1], Shanshan Hu[1], Balaji Raghothamachar[1], Reza Ghandi[2], Stacey Kennerly[2] and Michael Dudley[1]; [1]Stony Brook University, The State University of New York, United States; [2]GE Global Research, United States

Silicon Carbide (SiC) is a wide bandgap semiconductor, which has been widely applied to power electronics due to its excellent properties of wide band gap, high break down voltage and thermal stability. However, defects, such as threading edge dislocations (TEDs), threading screw dislocations (TSDs) and basal plane dislocations (BPDs), can limit the performance of the devices [1,2], so characterization of those defects becomes a critical aspect to improve the quality of 4H-SiC wafers. Synchrotron monochromatic beam X-ray topography (SMBXT) is a powerful technique to characterize the defects with the advantages of large field of view and clear contrast of the defects. SMBXT in 11-28 reflection has been widely used, however, the penetration depth, around 17um [3], appears to be shallow to characterize device with deep PN junction. Therefore, a new reflection with deeper X-ray penetration depth and clear contrast on the defects has been sought for. 22-4 16 reflection, the harmonic reflection of 11-28, shows better contrast on the defects, higher strain sensitivity and deeper X-ray penetration.
Contrasts from the same defect of 4H-SiC with 24 um epilayer in 11-28 and 22-4 16 reflections are compared as shown in Fig. 1. From 11-28 SMBXT, BPD segments near the surface of the wafer can be observed, as shown in the blue arrows in Fig 1(a), but contrasts of the segments lying deeper in the crystal are blurred as shown in the green boxes. On the other hand, in 22-4 16 SMBXT (Fig 1(b)), the contrasts of the full BPDs can be clearly seen and the contrasts of BPD segments lying deeper in the crystal are highlighted in green boxes to compare with contrasts in 11-28 reflection. This result also proves that the penetration depth of 22-4 16 SMBXT is deeper than that of 11-28 SMBXT. Previously we have simulated images of defects in 11-28, 0008 and 000 12 using the principle of ray tracing, showing good correlation with the topograph[4,5]. In this paper, we apply the ray tracing principle to simulate defect images in the 22-4 16 topograph and compare and discuss the contrast for the different defect types.
Reference:
[1] K. Konishi, R. Fujita, Y. Mori and A. Shima, Semiconductor Science and Technology 2018 Vol. 33 Issue 12
[2] W. Gao, G. Yang, Y. Qian, X. Han, C. Cui, Xi. Pi, D. Yang and R. Wang, Frontiers in Materials, Jan 2023, DOI:10.3389/fmats.2023.1022878
[3] Q. Cheng, H. Peng, S. Hu, Z. Chen, Y. Liu, B. Raghothamachar and M. Dudley, Materials Science Forum 1062, 366-370
[4] H. Peng, Z. Chen, Y. Liu, B. Raghothamachar, X. Huang, L. Assoufid and M. Dudley, J. Appl. Crystallogr. 55 (2022) 544-550.
[5] H. Peng, Z. Chen, Y. Liu, Q. Cheng, S. Hu, X. Huang, L. Assoufid, B. Raghothamachar and M. Dudley

9:00 AM S03
Analysis of Distribution of Threading Edge Dislocation Low Angle Grain Boundaries in 4H-SiC Wafers through Synchrotron X-Ray Topography Qianyu Cheng, Yafei Liu, Zeyu Chen, Shanshan Hu, Balaji Raghothamachar and Michael Dudley; Stony Brook University, The State University of New York, United States

Silicon carbide is a wide bandgap semiconducting material that is playing an important role in the fabrication of high-frequency, high-power electronic devices nowadays. Its superior properties such as high thermal conductivity, high saturation velocity, and high breakdown field enables its excellent performance in various application fields including transportation, communication, and

bioelectronics. However, the device performance and long-term reliability is highly depended on the quality of SiC substrate and epitaxial material as the deleterious defects within can induce device degradation and failure. Therefore, the availability of large-scale high-quality single crystals is a key issue in the development of the full potential of SiC-based device technology. In bulk SiC crystal, low angle grain boundary (LAGB) is a commonly observed planar defect that prevents the implementation of large size ($\geq$ 1 cm^2) SiC devices [1]. LAGBs have been shown to replicate during the epitaxial growth in both 6H and 4H-SiC [2], which can raise critical issue that triggers device degradation. The presence of LAGBs in commercial wafers can lead to increased leakage currents during reverse-bias operation of devices [3]. Besides, the existence of prismatic tilt boundaries is usually accompanied with aggregation of edge type basal plane dislocations (BPDs) [4], which cause severe degradation in SiC bipolar devices [5] as BPD segments can dissociate into partials and form stacking faults in between [6].
In this study, a distinct distribution pattern of LAGBs is observed on physical vapor transport (PVT) grown off-axis 4H-SiC wafers. Synchrotron X-ray topographs in both transmission and grazing geometry reveal the presence of three sets of LAGBs on one side of the wafer, away from the facet position, each set contains numerous LAGB arrays. The approximate location of each LAGB set is indicated in Figure 1 (a). As the grazing-incidence topographs shown in Figure 1 (b), The LAGB sets located at the upper and lower region of the wafer consist of white contrast threading edge dislocations (TEDs) extending from the inner area towards the edge approximately along 60° and 120° direction, respectively. The LAGB set located at the middle region of the wafer consist of dark contrast TEDs extending from the inner area towards the edge approximately along 90° direction. All individual TED arrays in each LAGB set extends along the <1-100> directions, with identical Burgers vectors perpendicular to the array direction. The white and dark contrast of TEDs corresponds to tilt in opposite directions. White contrast TEDs are with Burgers vectors of 1/3[2-1-10] and 1/3[1-210], dark contrast TEDs are with Burgers vectors of 1/3[-2110] and 1/3[-12-10]. Such TED LAGBs are identified as pure tilt boundaries that accommodate the rotational misorientation between two adjacent regions. Therefore, across the entire wafer, the net disorientation due to these TED arrays should be zero for a flat wafer but a non-zero net misorientation will lead to instability and likely contribute to the curvature of the (0001) plane. A systematic analysis is being carried out across several wafers and this relationship between the distribution of TED arrays and lattice curvature will be discussed.
Reference:
[1] N. Ohtani et al. *Journal of Crystal Growth* **237–239**, 1180–1186, (2002).
[2] C. Hallin et al, *J. Cryst. Growth* **181**, 241 (1997).
[3] R. Singh and M. Pecht, *IEEE Industrial Electronics Magazine*, **2**, 19-31, (2008).
[4] Y Chen et al, *Materials Science Forum* **556**, 231-234 (2007).
[5] T. Kimoto, et al., *Proc. IEEE Int. Rel. Phys. Symp.*, 2A-1.1–2A-1.7, (2017).
[6] M. Dudley, et al, *Materials Science Forum*, **600-603**, 261-266 (2008).

9:20 AM S04
Investigation of Defect Formation During Initial Stage of PVT-Grown 4H-SiC Crystals Shanshan Hu, Yafei Liu, Qianyu Cheng, Zeyu Chen, Balaji Raghothamachar and Michael Dudley; Stony Brook University, The State University of New York, United States

Silicon Carbide, typically 4H-SiC, due to its excellent electrical and thermal properties, has been replacing conventional silicon materials, which are considered to have reach their limit, for high power and high frequency applications[1]. Nevertheless, high quality SiC wafers with low defect density are still in urgent need for automotive and energy saving applications. During the PVT growth of 4H-SiC bulk crystals, the initial stage of crystal growth is critical as most defects are nucleated at this stage. Nucleation of TEDs and TSDs at the initial growth stage in PVT-grown SiC is revealed by Sanchez et al[2]. Behaviors of TEDs, TSDs/TMDs, and BPDs across the seed/newly grown layer interface in PVT-grown 4H SiC are demonstrated by Ailihumaer et al[3].
However, more detailed investigations are required for PVT grown 4H-SiC crystals during initial stage of growth as a function of growth conditions to map the parameter space systematically. In this study, 4° off-axis 4H-SiC initial-stage growth wafers are prepared with physical vapor transport (PVT) method under different growth conditions. Synchrotron X-ray topography (XRT) was used to image the wafers on both the seed and as-grown side using grazing incidence geometry. Topography reveals that the seed and as-grown side of these initial-stage growth wafers are characterized by dramatically different defect distribution across the seed/newly grown layer interface (Figure 1). In the facet region, dislocations are observed lying along <11-20> directions on basal plane to form rhombus shapes bounding Shockley stacking faults. (Figure 2). Additional statistical analysis will be performed on defect distributions across the seed/newly grown layer interface and discussed. Nomarski optical microscopy (NOM) and Raman Spectroscopy will be applied to deduce the formation mechanism of the stacking faults and other defects across the seed/newly grown layer.
References:
1. G. Dhanaraj, K. Byrappa, V. Prasad and M. Dudley, Springer handbook of crystal growth, edn. (Springer, 2010)
2. E. Sanchez, J. Liu, M. De Graef, M. Skowronski, W. Vetter and M. Dudley, Nucleation of threading dislocations in sublimation grown silicon carbide, J. Appl. Phys., 91, (2002).
3. T. Ailihumaer, H. Peng, Y. Liu, B. Raghothamachar, M. Dudley, G. Chung, I. Manning and E. Sanchez, Synchrotron X-ray Topography Studies of Dislocation Behavior During Early Stages of PVT Growth of 4H-SiC Crystals, J. Electron. Mater., 50, (2021).

9:40 AM S05
(Student) Nanoscale Spectroscopy of Extended Defects in 4H Silicon Carbide Scott G. Criswell[1], Nadeemullah Mahadik[2], Jason Valentine[1] and Joshua Caldwell[1]; [1]Vanderbilt University, United States; [2]U.S. Naval Research Laboratory, United States

Nano Fourier Transform InfraRed (nanoFTIR) spectroscopy is a powerful non-destructive characterization technique offering nanoscale spatial resolution combined with spectroscopic information. In this work we apply the combination of nanoFTIR and finite dipole modeling to characterize and identify the polytype of in-grown stacking faults (IGSF) in 4H silicon carbide. The results of stacking fault identification are verified using the established techniques of confocal Raman spectroscopy and ultraviolet photoluminescence spectroscopy.
Results from one IGSF consisting of a double layered 3C inclusion will be reported. Results from additional IGSF exhibiting other polytypes are expected as the work continues in upcoming months, with the goal of identifying an IGSF with 8H polytype and extracting the dielectric function using nanoFTIR. 8H stacking faults are common, but the dielectric function of 8H is yet unmeasured due to the lack of commercially available 8H wafers.

10:00 AM BREAK

10:20 AM S06
Mitigation of Basal Plane Dislocation Faulting in 4H-SiC Buffer Layers Using Channeled Vanadium Implantation Michael E. Liao[1], Nadeemullah Mahadik[2], Geoffrey M. Foster[3], Andrew D. Koehler[2], Robert E. Stahlbush[2], Rachael L. Myers-Ward[2], Karl Hobart[2] and Travis Anderson[2]; [1]National Research Council Postdoctoral Fellow at U.S. Naval Research Laboratory, United States; [2]U.S. Naval Research Laboratory, United States; [3]Jacobs Inc., United States

For high voltage pulsed power applications that require rapid high current pulses, SiC bipolar devices offer >100x lower resistance than

Si devices. However, stacking faults (SF) expansion due to basal plane dislocations (BPDs) in SiC cause forward voltage device degradation [1]. Several efforts have almost eliminated BPDs in SiC drift layers and converted them to threading edge dislocations within a buffer layer. However, BPDs within the buffer layers can fault during very high current injection resulting in device failure [2]. It was also reported that their faulting in the buffer layers could be mitigated by quenching carrier lifetimes in the buffer layer [2]. While carrier lifetime can be lowered via electron irradiation [3], subsequent high temperature device processing steps can recover the carrier lifetime. On the other hand, Vanadium doping during epitaxial growth has been shown to quench and retain a lowered carrier lifetime even after complete device fabrication [4]. In this work, novel channeling ion implantation of V^{51} ions was performed in SiC buffer layers to selectively control lifetime for inhibiting SF expansion as well as tailoring carrier lifetime in device structures to optimize on-state resistance.

Vanadium ions were implanted into 100-mm 4H-SiC wafers using a ~4° channeling angle, determined by X-ray diffraction, towards the [11$\bar{2}$0] direction with ion energies of either 350 keV or 700 keV. Channeling enables deeper ion projected ranges to be achieved compared to traditional ion implants without channeling. Vanadium implantation using channeling was reported to penetrate as far as ~500 nm with 100 keV implant energies [5]. For this study, we implanted V^{51} ions into SiC using channeling to achieve an implant depth of ~1 mm with 700 keV energy while inducing negligible lattice damage. Prior to implantation, a 6.6 mm thick SiC epitaxial layer with $3x10^{18}$ cm^{-3} n-type doping was grown using standard chemical vapor deposition. The implant doses varied from $1.5x10^{8}$ cm^{-2} - $1.5x10^{10}$ cm^{-2} at each ion energy. High-resolution X-ray rocking curves showed negligible changes in the peak widths before and after implantation for both the 350 keV and 700 keV implants, indicating the channeled implantation induces minimal lattice damage. This is significant in order to grow subsequent epitaxial device active layers. Interference fringes associated with the thickness of the implanted region were resolved using a Hypix position-sensitive area detector along the 2θ direction for the symmetric (0008) reflection. The average thicknesses for the 350 keV and 700 keV implanted samples were measured to be 586 ± 13 nm and 977 ± 23 nm, respectively. These depths were ~2 times deeper than what is expected from conventional ion implantation without channeling. Furthermore, higher energies for deeper non-channeled implants will induce severe lattice damage. Following the implant, low-doped device drift layers were grown on V^{51} implanted as well as on non-implanted control buffer layers. BPD faulting is being investigated using high carrier injection using high intensity UV laser excitation and SF imaging. These studies will be presented to demonstrate the effectiveness of V^{51} implantation to achieve robust pulsed power SiC devices. Following device fabrication, the impact of V^{51} concentration on BPD faulting density will be assessed and directly correlated with device performance.

[1] J. P. Bergman, et. al., Mater. Sci. Forum 353-356, 299 (2000)
[2] N. A. Mahadik, et. al. Appl. Phys. Lett., 100, 042102 (2012)
[3] K. Danno, et. al., Appl. Phys. Lett., 90, 202109 (2007)
[4] T. Miyazawa et. al., Appl. Phys. Exp., 9, 111301 (2016)
[5] M. K. Linnarsson, et. al., Semicon. Sci. Tech., 34, 115006, (2019)

10:40 AM S07

Advanced Carbon Film as a Superior C- Cap for SiC devices

Ludovico Megalini, Yi Zheng, Ricky Fang, Jang seok Oh, Jinghe Yang, Jiao Yang, Xiao Chen, Bryan Turner, Fengshou Wang, Pratim Palit, Aswin Prathap Pitchiya, Stephen Krause, Raghav Sreenivasan and Michael Chudzik; Applied Materials, Inc., United States

SiC is replacing the more common Si in several high-power devices due to its attractive material properties such as a wide-bandgap (3X larger), a high-E_{bd} (10X higher), a superior thermal conductivity (3X bigger). The availability of large and low defective native substrates (up to 200 mm) makes it also appealing from an economic standpoint for a large-scale manufacturing. However, the exploitation of its full potential requires to address some key-processing challenges – unique to SiC – including the protection of SiC surface, either planar or patterned, during the high-temperature processing. Annealing temperature T_{anneal} exceeding 1650°C for tens of minutes is required to activate the implanted *p*- and *n*- species as well as to restore the lattice from implant damages; however, this process leads to SiC surface roughening (*step bunching*) due to Si evaporation, with detrimental consequences to the device performance and reliability. For that, a protective surface C-cap is adopted, typically made via a carbonized photo-resist (PR). However, this solution presents several drawbacks including: (a) PR outgassing, (b) relatively low-throughput due to ~hour-long pyrolysis step, and (c) potential film cracking and delamination due to PR extreme shrinkage at such high-T anneal process. To address those disadvantages, we propose the use of *Advanced Patterning Film* (*APF*), a PECVD C_xH_y-based film family deposited via Applied Materials *Producer*. As-deposited this film presents already some graphitization degree, further tunable by the film chemistry and deposition conditions, in contrast to the PR case, even after hard-baking it at 180°C for 2 hours (**Fig. 1**). At the typical SiC post-implant annealing temperature range, the *D* (disorder), *G* (graphite) and *2D* peaks emerge more clear from the Raman spectra (**Fig. 2a** and **2b**). **Fig. 3** shows a plot of the *D* and *G* intensity peaks ratio: according to Tuinstra and Koenig model, the ratio , and (the graphite crystallite size) is ~ 40Å and 50Å for the APF and PR case, respectively. Those graphite peaks result from the films shrinkage, an effect relatively small for the APF film, but extremely severe for PR (**Fig. 4**). This is relevant because such material loss can cause severe contamination load downstream in the high-T furnaces, hence requiring frequent furnace parts cleaning and consequently a decrease of the throughput in high volume manufacturing of SiC devices. The ability to preserve the SiC surface fidelity of the APF is equivalent to (or better than) the PR cap as monitored by AFM scans of the as-grown, as-implanted, and annealed (after stripping the C-cap) samples (**Fig. 5)**. SIMS analysis suggests that APF can better prevent Al (not shown) & P dopants out-diffusion (**Fig. 6a** and **6b**). This can help reducing devices electrical parameters variation and improve production yield, as well as it may enable next-generation devices requiring an extremely tight doping control, like SiC super-junctions. The SIMS analysis of **Fig. 7** shows the detailed profile of the P- atoms *out*- diffusing from the P-implanted SiC surface into the PR during t_{anneal}, the high-temperature anneal process time needed to activate the P dopants. The local flux of P- dopants can be modelled by the 2nd Fick's law as . Assuming the diffusion coefficient *D* as a constant, and the boundary conditions and where is P- implanted total dose per unit area, the concentration profile of the P- dopants *out*-diffused for a length into the PR is . For a t_{anneal} at 1700°C, *D* is estimated to be Finally, the APF is also capable to protect the SiC trench sidewall with a tunable step-coverage as high as 86% (**Fig. 8a and 8b**).

In short, we demonstrated the use of a PECVD a-C:H film as an effective way to protect the SiC surface and apt for mass-manufacturing highly efficient SiC devices with a tighter processing control.

11:00 AM S08

Study of Dopant Activation and Ionization for Phosphorus in 4H-SiC

Suman Das, Daniel Lichtenwalner, Hemant Dixit, Steven Rogers, Andreas Scholze and Sei-Hyung Ryu; Wolfspeed, A Cree Company, United States

Ion implantation is the most useful technology for doping of 4H silicon carbide to fabricate power devices. For n-type doping, nitrogen is the most common element used in device fabrication due to its low atomic mass and proven applicability in epitaxial n-type SiC. Phosphorus can be an alternative to nitrogen (N) for providing a lower sheet resistance, although the research on phosphorus as a dopant is limited [1-3] in range of doping and activation temperatures. A rigorous study comprising different doping concentrations would help to verify the activation percentage and ionization energies and will lead to a better understanding of the properties of dopants other than N, to take advantage of any underlying benefits.

In this work, phosphorus is implanted in different concentrations on

150 mm Si-face 4H SiC (0001) of 4 degree off-axis wafers and activated above 1600 ºC. To study the electrical characteristics, circular van der Pauw structures were made. Deep p-well implants were performed to isolate the phosphorus doped region from the n-type substrate. Nickel contacts were deposited using evaporation and post-annealed at high temperature to get ohmic contacts. The samples were then placed on a 1cm x 1cm PCB board with 4 contacts at the corners, and wire bonding from sample to board was performed. Following that, 4-point probe resistance and Hall measurements were conducted to obtain resistivity, carrier concentration, and Hall mobility for different doping levels. Thereafter, dopant activation percentage and ionization energy levels are calculated.
Figure 1 shows typical IV characteristics of the fabricated van der Pauw samples that indicate linear or ohmic behavior of the contacts. Figure 2 shows the temperature-dependent variation of resistivity for different doping levels. From 150 to 300 K the resistivity drops as temperature increases, while above room temperature a small increase of resistivity can be observed. An increase in the carrier concentration versus temperature is shown in Fig. 3, for doping less than $9x10^{19}$ cm^{-3}. The sample with a doping concentration of $9x10^{19}$ cm^{-3} behaves like a semimetal for which the carrier concentration is almost constant with changing temperature. A small upshoot in carrier concentration at very low temperature (~150 K) might be caused either by a change of effective implant thickness with temperature, or p-well dopant freeze out effects underneath the n-wells. Figure 4 shows mobility versus temperature for different Phosphorus implanted concentrations. At lower temperatures mobility drops due to increased ionized impurity scattering. Mobility reaches a peak value near room temperature and drops again as temperature increases due to increased phonon scattering owing to enhanced lattice vibrations. Figure 5 shows the carrier concentrations as modeled in hexagonal and cubic lattice sites (50:50 distribution assumed) with assigned specific ionization energies. For example, for the sample with implanted doping concentration of $4x10^{18}$ cm^{-3}, the ionization energies are extracted to be 48 and 110 meV for hexagonal and cubic lattice positions from the model fit. The values of activated dopants are also calculated here from this analysis and plotted as a function of doping concentrations as shown in figure 6. It is clear that the phosphorus activation is well below 100%.
The extracted activation percentages and dopant ionization levels will be shown for all samples, and compared to literature values, in the full manuscript. The activation percentages and ionization energies, extracted from the data, will be useful for calibration of Technology Computer Aided Design (TCAD) models for electrical simulations of 4H-SiC based devices.
[1] M.A. Capano et al., J. Electron. Mater. 29, 210 (2000).
[2] J. Gardner et al., J. Appl. Phys. 83, 5118 (1998).
[3] T. Kimoto, J.A. Cooper, Fundamentals of Silicon Carbide Technology (2014).

11:20 AM S09
(Student) A Comparison of Body Diode Degradation in Commercial 1.2 kV SiC Power MOSFETs with the Planar and Trench Structure Jiashu Qian[1], Dongyoung Kim[2], Michael Jin[1], Shengnan Zhu[1], Limeng Shi[1], Atsushi Shimbori[3], Woongje Sung[2] and Anant K. Agarwal[1]; [1]The Ohio State University, United States; [2]State University of New York Polytechnic Institute, United States; [3]Ford Motor Company, United States

Motivation
To reduce the device cost, body diode is expected as the freewheeling diode for commercial trench SiC power MOSFETs in the high frequency applications. Therefore, it is necessary to investigate the reliability of body diodes. This study compares the body diode degradation of commercial 1.2 kV planar and trench SiC power MOSFETs from several vendors listed in Table 1. Besides, 1.2 kV planar SiC power MOSFETs are fabricated with the nominal and deep JFET. The deep JFET extends down from the nominal JFET into the drift layer, and part of the additional n^+ layer is in contact with p-body. We assume that the deep JFET enhances the recombination of the injected minority carriers from p-body. This leads to the suppression of body degradation by reducing the recombination energy provided to expand SFs. These two different JFET structures are presented in Fig. 1.
Results
Fig. 2 compares the average degradation ratio of V_F, R_{ON}, and forward leakage current in the blocking mode (I_L) on the commercial 1.2 kV planar SiC power MOSFETs from Vendors E, I, and C. Decline in device performance from body diode degradation is at negligible or acceptable levels for all these three vendors. **It can be concluded that body diode degradation is not a big issue in most commercial 1.2 kV planar SiC power MOSFETs**.
In Fig. 3, commercial trench DUTs from Vendor K have more significant average body diode degradation than planar DUTs. Trench DUTs from Vendor D have no obvious degradation. However, the influence of body diode degradation on I_L is not reflected as expected. This may be due to the fact that devices are breaking down in the termination area where no SFs exist, as opposed to the active area. As shown in Fig. 4, 7 of 10 DUTs from Vendor K have reached the degradation criterion while there's no significant body diode degradation in 8 DUTs, apart from the 2 dead devices, for Vendor D. This can be explained in Fig. 5 that the deep p^+ contact by the Al implantation with high dose and energy is required to shield the electric-field-crowded corner of the trench gate, which creates many BPDs around the p^+ contact in the trench structure from Vendor K. Although the p^+ contact with the heavy dose is still needed for Vendor D, it is implanted after the dummy trench formed by RIE. That means the p^+ contact can be shallow which significantly reduces the new BPDs. In the planar structure, high density of new BPDs around the implanted regions is hard to create because of light-dose and shallow p-type contact, as well as many improved designs and processes that have already minimized the BPDs arising from the SiC substrate wafer and epitaxial growth. In addition, Vendor D not only has the Gen 3 trench structure mentioned above, but also has the Gen 4 trench structure as shown in Fig. 6. In the Gen 4 trench structure, the Al implantation with the high energy and dose for the deep p^+ contact is performed before the RIE for the trench dummy. Therefore, this new trench structure is expected to have significant body diode degradation as that of Vendor K. The body diode degradation test on the Gen 4 DUTs from Vendor D is still in progress.
Furthermore, Fig. 7 compares the body diode degradation of the fabricated 1.2 kV SiC power MOSFETs with the nominal and deep JFET. It can be observed that there is increasing average body diode degradation in the DUTs with the nominal JFET during the stress. However, for the DUTs with the deep JFET under the same process, there is no average body diode degradation during the stress. It is also reflected that the breakdown voltage of the DUTs with the nominal JFET decreases due to the increasing leakage current while there is no variation for the DUTs with the deep JFET. **This confirms the assumption that body diode degradation in commercial 1.2 kV SiC power MOSFETs, especially in the trench devices, is mainly caused by the new BPDs around the p-type contacts introduced by the deep Al implantation with heavy dose.**

11:40 AM S10
Reliability of Room Temperature vs High Temperature Implantation in 3.3kV SiC MOSFETs Nadeemullah Mahadik[1], Michael E. Liao[2,1], Elias M. Kallon[3], Robert E. Stahlbush[1], Jake Soto[4] and Bruce Odekirk[4]; [1]Naval Research Laboratory, United States; [2]National Research Council, United States; [3]University of Maryland, United States; [4]Microchip Inc, United States

Generation of basal plane dislocations (BPDs) in 4H-silicon carbide (SiC) epitaxial layers due to ion implantation was reported by Stahlbush et. al. [1]. These BPDs formed loops that were generated at the epitaxial layer surface within the implanted layer and propagated towards the substrate interface. Such BPD generation was observed when high dosage Al ion implantation was carried out at room temperature (RT) for typical contact formation. With recent advances in device processing, several of these newly generated BPDs have

been mitigated either by high temperature (HT) ion implantation or by other processing techniques such as post implant oxidation [2]. It is, however, desirable to perform ion implantation at RT to reduce high temperature fabrication steps, which could affect wafer yield due to less thermal induced stress in the wafer. It is also unclear in device layers with differently doped regions if the BPDs would result in stacking fault (SF) formation and if the typical carrier injection conditions would cause SF expansion. In this work, we investigate SF expansion from potential BPDs generated by ion implantation in SiC epitaxial layers that had both RT and HT ion implantation and compare their robustness using high carrier injection using high intensity ultraviolet (UV) laser excitation.

For this work, MOSFET device structure with 30 mm drift layers were fully fabricated on 4 commercial 150 mm diameter SiC wafers at a commercial foundry. Two of the wafers had a RT implant for the high Al dose contact layer and two remaining wafers had a HT implant performed at approximately 600 ºC. Several of the device dies were removed from each of the four wafers and their metal layers were stripped to observe the generation of defects. UV photoluminescence (UVPL) imaging using a 355nm laser and a microscopy setup was performed with typical (10-20 W/cm^2) excitation power on all the 4 samples. This was followed by high intensity (500 W/cm^2) UV carrier injection. Sequence of images were collected to study progression of SF formation.

The UVPL images obtained using typical excitation power did not introduce any BPDs in either the RT or the HT implanted samples even after exposure for several minutes. Upon UV excitation at 500 W/cm^2, SF expansion from BPDs were observed in the RT implanted samples near the edge of the termination regions and not in the active areas within 8 secs. UV excitation generates carriers with an exponential depth decay uniformly across the device region, which is different from current injection that depends on background doping. Hence, in highly doped regions, UV excitation simulates significantly higher minority carrier generation responsible for SF generation compared to current injection. A comparison of UV excitation power with current injection conditions will be presented. The active device region did not show SF expansion, which is likely due to fast recombination of electrons from the implanted region due to depletion in the p-well. Details of the mechanisms will be presented. In the HT implanted samples, no SFs were observed even after 96 secs of high intensity UV exposure, indicated no generation of new BPDs. Even though SF expansion was not observed in active regions of the RT samples, BPD are likely formed in the contact layers and pose a reliability issue for long term device operation, especially if surge current conditions are expected during switching.

[1] R. E. Stahlbush, N. A. Mahadik, Q. Zhang, et. al., Mater. Sci. Forum 821-823, 389 (2015)

[2] Y. Bu, H. Yoshimoto, N. Watanabe, et. al., J. Appl. Phys., 122, 244504 (2017)

Acknowledgement: Author Kallon's research was sponsored by the Office of Naval Research NREIP program.

SESSION T: Organic Devices and Molecular Electronics
Session Chairs: Andrew Herzing and William Scheideler
Thursday Morning, June 29, 2023
UC, Lobero

8:20 AM T01

Single-Molecule Magnet (SMM) Internal Atomic Configuration Impact of Ferromagnetic Layers of Magnetic Tunnel Junction—A Monte Carlo Study Christopher D'Angelo, Pawan Tyagi, Andrew C. Grizzle and Pius Suh; University of the District of Columbia, United States

Metamaterials formed by placing paramagnetic molecules between two ferromagnetic layers have opened a new field for composite magnetic metamaterials. Several forms of paramagnetic In our experimental studies, single-molecule magnets (SMMs) interacting with the ferromagnetic electrodes of a magnetic tunnel junction (MTJ) produced unconventional magnetic and transport characteristics. The properties and future scope of new systems differ dramatically from the properties of isolated molecules and ferromagnets. However, it is unknown how far deep in the ferromagnetic electrode the impact of the paramagnetic molecule and ferromagnet interactions can travel for various levels of molecular spin states. Our prior experimental studies showed two types of paramagnetic SMMs, the hexanuclear Mn_6 [1] and octanuclear Fe-Ni molecular complexes[2], covalently bonded to ferromagnets produced unprecedented strong antiferromagnetic coupling between two ferromagnets at room temperature leading to a number of intriguing observations [2]. This paper reports the Monte Carlo Simulations (MCS) study focusing on the impact of the molecular spin state and internal configuration on cross junction shaped MTJ-based molecular spintronics device (MTJMSD). Our MCS study focused on the Heisenberg model of MTJMSD and investigated the impact of various molecular coupling strengths, thermal energy, and molecular spin states. To gauge the impact of the molecular spin state on the region of ferromagnetic electrodes, we examined the spatial distribution of molecule-ferromagnet correlated phases. Our MCS study shows that under a strong coupling regime, the molecular spin state should be ~30% of the ferromagnetic electrode's atomic spins to create long-range correlated phases.

8:40 AM T02

Understanding Electronic Energy Transport in DNA-Scaffolded Molecular Networks Using Machine-Learning Methods Brian S. Rolczynski[1], Sebastian Diaz[1], Youngchan Kim[1], Divita Mathur[2], Igor Medintz[1] and Joe Melinger[1]; [1]US Naval Research Laboratory, United States; [2]Case Western Reserve University, United States

Molecular electronics are being developed as materials for light-harvesters and -emitters, sensors, and quantum technology. The themes for optimizing these systems are miniaturization and improved precision, which increasingly moves these materials into the quantum-mechanical regime. Natural systems like photosynthetic pigment-protein complexes have shown that vast improvements to functional bottlenecks like energy-transport can be achieved, if the structural and energetic properties are finely controlled. In that spirit, we are developing modular molecular networks whose structures are controlled by DNA scaffolds. This approach controls the network's structural, energetic, and dynamic properties.

However, this increased control presents new needs and challenges. We must know what the ideal parameters are for optimal function. In turn, that optimization requires a better understanding of the molecular-scale characteristics of the systems. Another challenge is that these characteristics often include many degrees of freedom, especially for large chemical networks, so an approach must be developed to treat large amounts of data efficiently, yet thoroughly.

Here, we describe approaches to address these challenges. By combining machine-learning tools with experimental spectroscopies and computational models (Figure 1), we can simultaneously understand and map the sample characteristics on the molecular scale, the energy transport characteristics on the mesoscale, and the material performance on the bulk scale. We will discuss how we have used these tools to predicted optimal system configurations for energy-transport, and how they reveal the interchromophore effects in chromophore arrays.

9:00 AM T03
(Student) Strain-Enhanced Formation of 1D Coherent Exciton-Polaron States in Small Molecule Semiconductors Libin Liang[1,2] and Madalina Furis[3]; [1]University of Vermont, United States; [2]Intel Corporation, United States; [3]The University of Oklahoma, United States

Organic molecules, such as pentacene, rubrene and phthalocyanine are at the forefront of materials research, due to their desired electric, excitonic and mechanical properties. They represent the feasible alternative to traditional silicon-based semiconductor applications for flexible electronics platforms, where materials in flexible devices will experience complex strain environment. Octabutoxy phthalocyanine (H_2-OBPc) is a soluble derivative of the Phthalocyanine (Pc). It has π-conjugated systems and large directional intermolecular interactions, which allow the formation of molecular crystal with well-defined structure like J-aggregate, where molecules are stacked in a head-to-tail fashion (Fig.1a). [1, 2] In this quasi one-dimension system, the Frenkel exciton can couple with lattice and intramolecular vibrations to form exciton-polarons which are delocalized along the molecular aggregates. The formation of these one-dimensional delocalized exciton-polaron states grants H_2-OBPc the potential for efficient excitation energy transport in the coherent exciton regime. [3-6]
In this work, H_2-OBPc polycrystalline thin films were prepared using a solution-based pen-writing deposition technique. These ordered thin films with macroscopic grain size (Fig.1b, millimeter scale) uniquely offer the opportunity to spatially explore optical and excitonic properties within a single crystalline grain, free from the influence of grain boundaries or static disorder (Fig.1b). Temperature-dependent absorption and photoluminescence (PL) experiment points to the existence of red-shifted bandgap when temperature T < 175 K (Fig.2c and d). This new bandgap at low temperature is the result of the formation of exciton-polaron states, where the molecular Frenkel excitons couple with intermolecular low energy phonon modes (i.e. dynamic disorder fluctuations), leading to the wavefunction spreading over the π-stacked molecular chain (Fig.1a). These delocalized exciton-polaron states have robust emission properties and they are potentially coherent. [6]
The critical role played by low-energy phonons (25-300 cm^{-1}) [7] in the formation of delocalized, 1D coherent exciton-polaron states is explored using an externally applied uniaxial mechanical strain (example of the tensile strain geometry is shown in Fig.2a). Strain-dependent absorption (Fig.2b), PL microscopy (Fig.2c), and confocal Raman measurements (Fig2.e) reveal the strain-induced softening (red shift) of the phonon modes favors the survival of the coherent exciton-polaron states at room temperature (A2 peak in Fig.2b and P2 peak in Fig.2c). Remarkably, **an 80% enhancement in PL intensity is observed with a uniaxial tensile strain of 4.7% applied at room temperature** (Fig.2c), which is equivalent to lowering the temperature to 200K for the unstrained film. [8] Time-resolved transient absorption (TA) spectroscopy confirms the behavior of the exciton-polaron state as a function of strain.
Reference
(1) Rawat, N.; Pan, Z.; Manning, L. W.; Lamarche, C. J.; Cour, I.; Headrick, R. L.; Waterman, R.; Woll, A. R.; Furis, M. I. *J. Phys. Chem. lett.* **2015,** 6, (10), 1834-1840.
(2) Manning, L. W.; Rawat, N.; Lamarche, C.; Waterman, R.; Headrick, R. L.; Furis, M. *J. Phys. Chem. C* **2016,** 120, (22), 11966-11976.
(3) Ghosh, R.; Spano, F. C. *Acc. Chem. Res.* **2020,** 53, (10), 2201-2211.
(4) Spano, F. C. *Acc. Chem. Res.* **2010,** 43, (3), 429-439.
(5) Yamagata, H.; Spano, F. C. *J. Phys. Chem. lett.* **2014,** 5, (3), 622-632.
(6) Liang, L.; Burrill, K.; Furis, M. I. *J. Phys. Chem. C* **2021,** 125, (51), 27966-27974.
(7) Fornari, R. P.; Aragó, J.; Troisi, A. *J. Phys. Chem. C* **2016,** 120, (15), 7987-7996.
(8) Liang, L.; Czar, K.; Furis, M. I. *J. Phys. Chem. C* **2022,** 126, (20), 8889-8896.

9:20 AM T04
(Student) Effect of Molecular Tilt Configuration in Molecular Heterojunction with Two-Dimensional Semiconductor Jung Sun Eo, Jaeho Shin and Gunuk Wang; Korea University, Korea (the Republic of)

There have been studies of understanding and controlling the charge transport through molecular junction wince it gives fundamental grounds that helps to gain a novel idea to realize numerous potential molecular functional devices. [1,2] There are some key factors considered in molecular charge transport, such as molecular barrier which is directly related to molecular orbital levels, coupling strength, asymmetric factor, and molecular configuration and conformation. Much research has been reported to obtain deeper insights of such key factors under certain controlled conductions with the effect of the external stimuli applied on the molecular junction such as light irradiation [3], electrochemical gating [4], electrical field [5], and mechanical stress such by tip loading force [6]. Molecular heterojunction with two-dimensional (2D) semiconductor provides various key factors for the charge transport through the heterojunction; however, the effect of molecular tilt configuration on the molecular heterojunction have never been studied. Here, we present the effect of molecular tilt configuration on the molecule/mono-layer (1_L) 2D semiconductor heterojunction by tip loading force with conductive atomic force microscopy (C-AFM) technique. With various tip loading force (1-30 nN), the molecular tilt configuration affects differently for the three different interfaces in Au/molecule/1_L-2D semiconductor/Au heterojunction that the transition voltage spectroscopy (TVS), which is a conventional tool to analyze charge transport through molecular junction, rectification ratio (*RR*), non-linearity (N_L) and possible array size are demonstrated. Molecule/2D semiconductor heterojunction system has been reported as molecular diode (with *RR*) and selector (with N_L) and it is a novel platform owning so much various potential in, that understanding the charge transport by the effect of external stress on the heterojunction will help developing such future molecular scale functional devices.
[1] L. A. Bumm, J. J. Arnold, M. T. Cygan, T. D. Dunbar, T. P. Burgin, L. Jones, D. L. Allara, J. M. Tour, P. S. Weiss, *Science* 271, 1705 **(1996)**,.
[2] H. Song, Y. Kim, Y. H. Jang, H. Jeong, M. A. Reed, T. Lee, *Nature* 462, 1039 **(2009)**.
[3] G. Reecgt, C. Lotze, D. Sysoiev, T. Huhn, K. J. Franke, *ACS Nano* 10, 10555 **(2016)**.
[4] R. A. Wong, Y. Yokta, M. Wakisaka, J. Inukai, Y. Kim, *Nat. Commun.* 11, 4194 **(2020)**.
[5] J. Shin, S. Yang, Y. Jang, J. S. Eo, T.-W. Kim, T. Lee, C.-H. Lee, G. Wang, *Nat. Commun. 11*, 1 **(2020)**.
[6] G. Wang, T. -W. Kim, G. Jo, T. Lee, *J. Am. Chem. Soc.* 131, 5980 **(2009)**.

9:40 AM T05
(Student) Surface-Confined Brønsted Acidic Doping of Conjugated Polymers Thin Films Phong Nguyen, Rachel Segalman and Michael Chabinyc; UC Santa Barbara, United States

Many semiconductor devices (*e.g.*, light emitters and photovoltaics) utilize heterojunctions of doped and undoped layers or depend on gradients of electronic doping to control charge transport. Doping of conjugated polymers requires the introduction of small molecules

dopants which undergo charge transfer reactions with the polymer. The rate of the doping reaction and diffusion of the dopant controls the overall doping level. Conjugated polymers can be electrically doped by strong acids, but the details of the reaction mechanism and subsequent stability are not understood. Here, we show a clear kinetic isotope effect in the doping of thin films of poly(3-hexylthiophene) (P3HT) by bis(trifluoromethane)sulfonimide (HTFSI) from solution indicating that this doping process is limited by proton transfer to the polymer. The subsequent charge transfer reaction occurs rapidly between polymer segments in the solid state, thus circumventing the need to match redox potentials of dopants and conjugated polymers. Dynamic secondary ion mass spectrometry (DSIMS) of doped films show that H/D is retained in doped films after the doping process. Complementary X-ray photoelectron spectroscopy and DSIMS depth profiling of dopant concentrations show definitive evidence of enrichment at the P3HT surface. These surface-limited concentration profiles suggest that diffusivity of dopants vary inversely with dopant concentration due to doping-induced changes to the structure of the conjugated polymer.

10:00 AM BREAK

10:20 AM T06
(Student) Probing the Interface Traps in PMMA Gate Dielectric-Based Short Channel Length OTFTs Fabricated Using Bi-Layer Lithography Anuj Rajpoot and Soumya Dutta; Indian Institute of Technology Madras, India

In recent years, solution-processed polymer-based organic thin film transistors (OTFTs) have shown considerable performance improvement. These OTFTs are the potential building block for flexible and low-cost electronics applications like flexible sensors and switching circuits due to their low temperature and low-cost processing (Guo *et al.*, 2017), (García De Arquer *et al.*, 2017). Meanwhile, choosing the suitable polymer gate dielectric to realize short-channel OTFTs in the most preferred BG-BG configuration is critical for good operational stability and easy circuit integration. In this regard, the choice of an ideal low-cost polymeric gate dielectric PMMA which offers a smooth, hydrophobic, and (-OH) group-free surface is critical in achieving a high-quality interface with the polymer semiconductor (Shi *et al.*, 2013). However, the incompatibility of PMMA with photo-lithography and organic solvents poses severe challenges in realizing solution-processed PMMA gate dielectric-based OTFTs.
This study discusses the interface quality and device stability of the PMMA gate dielectric-based, solution-processed short-channel OTFTs (L < 10 µm). A spin-coated layer of pristine PMMA with a thickness of 400 nm is used as a preferred gate dielectric employed in BG-BC configuration. These short-channel lengths (up to L = 2 µm) devices are realized using novel bi-layer lithography (Rajpoot and Dutta, 2017) with PMGI and S1813 resists, specifically developed to perform conventional photo-lithography on pristine polymer dielectrics without using complex polymer cross-linking methods. OTFTs with high mobility polymer semiconductor DPP-DTT are fabricated successfully to demonstrate high performance of the solution processes OTFTs. The µ, on/off ratio, and switch-on voltage (V_0), is estimated to be 8.5×10^{-2} cm^2/Vs, $10^{7,}$ and -3.5 V respectively for DPP-DTT-based OTFTs. To evaluate the interface trap states and operational stability, standard RR-P3HT polymer semiconductor-based OTFTs are fabricated. Low effective interface trap density (N_{trap}) of the order of 10^{11} $eV^{-1}cm^{-2}$ and V_0 of 0 V with negligible threshold voltage shift in P3HT OTFTs during continuous bias stress application verifies the quality semiconductor-dielectric interface.
References:
García De Arquer, F.P. *et al.* (2017) 'Solution-processed semiconductors for next-generation photodetectors', *Nature Reviews Materials*. Nature Publishing Group. Available at: https://doi.org/10.1038/natrevmats.2016.100.
Guo, X. *et al.* (2017) 'Current Status and Opportunities of Organic Thin-Film Transistor Technologies', *IEEE Transactions on Electron Devices*, 64(5), pp. 1906–1921. Available at: https://doi.org/10.1109/TED.2017.2677086.
Rajpoot, A. and Dutta, S. (2017) 'Bi-layer resist approach of photolithographic patterning over pmma based polymer dielectrics'. Available at: https://patents.google.com/patent/WO2019008602A1/en.
Shi, W. *et al.* (2013) 'Performance enhancement of poly(3-hexylthiophene) organic field-effect transistor by inserting poly(methylmethacrylate) buffer layer', *Applied Physics Letters*, 102(11). Available at: https://doi.org/10.1063/1.4798368.

10:40 AM T07
(Student) Advantages of Adding a Weak Second Gate in Sub-Micron Bottom-Contact Organic Thin-Film Transistors Chankeun Yoon, Yuchen Zhou and Ananth Dodabalapur; The University of Texas at Austin, United States

Several studies have reported on the advantages of dual gate architecture in thin-film-transistors (TFTs) with organic/polymer and thin-film inorganic semiconductors. These advantages include improved gate control, higher on-currents, reduced sub-threshold swing, and reduced contact resistance. In some of these studies, both gates contribute to the total channel charge; or in other words, the capacitances per unit area of both gate insulators are roughly comparable in magnitude. In this presentation, it is demonstrated that a "weak" second gate can also result in a substantial improvement in the electrical performance of TFTs. Weak gates pertain to dual gate TFT configurations in which the insulator capacitance per unit area of one gate/gate insulator combination is much less than that of the other gate/gate insulator combination. The dominant gate (or strong gate) induces most of the channel charge; however, the weak gate, while not contributing much to the channel charge, can nevertheless improve device performance by a surprisingly large degree.
For the work reported here, the material system examined is ZrO_2/Dinaphtho[2,3-b:2′,3′-f]thieno-[3,2-b]thiophene (DNTT)/CYTOP. Two DNTT TFTs with different source electrode shapes were analyzed: one has a source consisting of an array of three nanospike electrodes and the other has a conventional flat-edge source electrode. While high-k dielectrics can be used to lower the operating voltage of organic thin film transistors (OTFTs), they often result in reduced mobility and other device performance metrics when in direct contact with the organic semiconductor channel, as is the case in the TFTs reported in this work. The use of a second gate is a new approach to alleviate the degradation in electrical performance characteristics that result in OTFTs with high-k/organic semiconductor TFT interfaces. In dual gate TFTs with a weak top gate, the primary role of the top gate is not to induce additional charges, but to cause the charge induced by the strong bottom gate to move away from the trap-filled interface with the gate dielectric. This results in less impact from the interface and in an improvement in various electrical properties such as threshold voltage (and the turn-on voltage, which are both reduced in magnitude), decreased sub-threshold swing, and substantially higher carrier mobilities and velocities. The movement of charges away from the interface with the high-k dielectric also reduces Frohlich polaron effects that may be present. The mobility/velocity is increased by up to a factor of 3 by the synergistic action of the weak top gate with the bottom gate. This large increase represents a substantial recovery in TFT electrical parameters that are otherwise diminished by the effects of the high-k interface in a single gate TFT device. The experimental results indicate that: (a) The use of a weak second gate and (b) The use of nanospike array shapes source electrodes, independently result in substantial improvements in electrical characteristics such as carrier velocity/mobility, contact resistance, sub-threshold swing and threshold voltage. When these two techniques are used together, the combined benefits result in the best overall performance characteristics. This strongly suggests that for sub-micron and nanoscale organic TFTs, a combination of a dual gate architecture and nanospike shaped source electrodes is a very promising design for improved performance. While symmetric or near symmetric dual gate designs have obvious advantages, this work shows that when

symmetric gates are difficult to realize due to experimental constraints, asymmetric dual gate designs with one weak gate and one strong gate can have substantial performance advantages over single gate TFTs. The benefits of a weak top gate in a dual gate configuration will are likely to be beneficial for a range of materials combinations, involving organic as well as thin-film inorganic semiconductors.

11:00 AM T08
(Student) Effect of Thickness and Molecular Weight of Poly (3-hexylthiophene Film on Ion-Gated Transistor Response Time and Synaptic Functions Ramin Karimi Azari and Clara Santato; Polytechnique Montréal, Canada

The von Neumann architecture was designed for serial processing tasks.
The amount of data produced in the present *intelligent* era renders this architecture unable to keep up. As a result, new solutions such as neuromorphic parallel computing are being developed to increase data storage and processing speed. There are concerns, however, about the sizes of the chips composed of synaptic transistors and their parallel computing capacity.
In this work, we present the effect of poly (3-hexylthiophene) (P3HT) film thickness on the synaptic behavior and response time of bio-inspired organic ion-gated transistors (IGTs). The P3HT film thickness varies from 50 to 300 nm. The drain-source current, I_{ds}, and charge carrier mobility increase with thickness. The changes in the thickness lead to the development of a larger number of ordered P3HT aggregates in the films. The presence of such ordered aggregates increases the de-doping time (time to remove anions) of the p-type P3HT transistors. In turn, this increases the transistors' response time and permits to achieve the transition from short-term plasticity (STP) to long-term plasticity (LTP). Further, increasing the thickness of the channel increases the plasticity and paired-pulse facilitation (PPF) index.
The molecular weight (MW) is another parameter that we considered to control the synaptic functions and response time of P3HT IGTs. The XRD patterns of films obtained from three different MW, low (24 kDa), intermediate (42 kDa), and high (91 kDa), show the crystallinity decreases with increasing MW. This is expected to strongly affect ion permeability, and therefore the advancement of doping and redistribution time of anions, in the P3HT IGTs. We, therefore, propose a methodology to control the response time and synaptic functions of IGTs with changing P3HT MW in a constant thickness of the film.
<quillbot-extension-portal></quillbot-extension-portal>

11:20 AM T09
(Student) Manufacturing of Highly Conductive Organic PEDOT:PSS Films for Electronic Devices Marius Orlowski, Amrita Chakraborty and Payton Fallen; Virginia Tech, United States

The paper reports on a novel process flow to manufacture conductive organic electrodes from highly conductive doped PEDOT:PSS polymer films that can be patterned and display good adhesion to oxidized Si wafers as well as to flexible substrates, such as Mylar. It is shown that multiple depositions of PEDOT:PSS increase the electrical conductivity by more than two orders of magnitude without increasing the film thickness of PEDOT:PSS significantly. An exponential dependence between sheet resistance and the number of PEDOT:PSS coatings is found. Additional coatings, in excess of 6 coatings provide diminishing returns to the lowering of the sheet resistance. The dependence of the sheet resistance $R_{sq}(n)$ as function of the number of PEDOT:PSS coatings, n, can be described by the formula $R_{sq}(n)=230\times\exp[-(n-1)\times1.28]$ kΩ. The multiple coating methods can be further optimized by selecting a low spinning speed (e.g. 1500 rpm) for the initial coatings and a high spinning speed (e.g. 3000 rpm) for the final coatings. The reason for the decrease in the sheet resistance is the densification of the conductive PEDOT ribbons at the bottom part of the PEDOT:PSS layer. The electrical conductivity of PEDOT:PSS can be increased by another two orders of magnitude by doping it with Cu nanoparticles (Cu NP) when coated on the surface of a soft-baked PEDOT:PSS film. However, if Cu NP are dispersed in the aqueous solution of PEDOT:PSS then the impact on the sheet resistance is nil. It is found that both kinds of conductivity enhancement are not additive. The doping with Cu nanoparticles is desirable, as it provides the surface of an organic electrode with readily ionized copper ions useful for several applications including Cu filament formation in organic switching layers of a resistive RAM (ReRAM) memory cell. Adhesion of PEDOT:PSS to oxidized Si wafers and to BoPET (Mylar) has been ensured by applying an oxygen plasma cleaning step prior to spin coating. The manufactured high conductivity PEDOT:PSS film can be patterned using a sacrificial metal layer with subsequent etching of PEDOT:PSS in oxygen plasma, followed by the removal of the patterned segments of the sacrificial metal layer in an aqueous acid solution on both Si wafers and flexible Mylar substrates. A single PEDOT:PSS layer has a thickness of around 60 nm depending on the spinning speed and has sheet resistance (R_{sq}) of 230 kΩ. The same deposition applied 6 times results in a PEDOT:PSS layer of 90 nm thickness (instead of 6×60 nm=360 nm) and R_{sq}=980 Ω. A surface doping of 1xPEDOT:PSS with Cu NP lowers the sheet resistance from 230 kΩ to 60 kΩ, whereas in the case of multiple coatings, the 6xPEDOT:PSS with the same Cu doping lowers the R_{sq} from 980 Ω to 6.2 Ω. Thus, with reference to one PEDOT:PSS layer, the sheet resistance has been reduced by a factor of 4×10^4. The methods described above can be further combined with the methods of in situ doping of PEDOT:PSS with inert metal NP such as Ag and Au NP, that are largely immune to the oxidation reactions in the aqueous solutions, and with acid treatment such as nitric or phosphoric acid. It has been found that all the various methods to increase the conductivity mentioned above are not additive and, in some cases, work at cross-purposes with one another. Therefore, a tailored optimum combination of the available methods requires a detailed understanding of their respective mechanisms. Careful morphological analysis performed by dint of optical microscope picture and surface roughness plots by AFM reveals a close interplay between the thickness of the PEDOT:PSS film, the density of the PEDOT:PSS particles - here controlled by the multiple coatings -, and the size of the Cu NP. The size of Cu NP should be smaller than the film thickness, and the density of PEDOT:PSS particle should be neither too small nor too high to accommodate the Cu NP in the PSS spaces between the conductive PEDOT ribbons to achieve the lowest sheet resistance.

11:40 AM T10
(Late News) Transparent, Inkjet-Printed PEDOT:PSS Electrotrode Arrays for Large-Area Multimodal Neural Interfaces Sarah L. Swisher; University of Minnesota, United States

Electrocorticography (ECoG) is a critically important neuroscientific tool for recording neural activity in the cerebral cortex. Advances in recent years have produced high-resolution ECoG arrays, which have enabled brain-machine interface (BMI) applications such as speech and motor intention decoding systems. Alternatively, cortical activity can be studied using optical tools such as genetically encoded calcium indicators (GECIs) and optogenetics. Optical access to the brain is typically achieved with a small craniotomy covered by a transparent window. Electrophysiology and optical imaging provide complementary neural sensing capabilities: electrophysiological recordings have high temporal resolution, while optical imaging allows recording of genetically-defined populations at high spatial resolution. Combining these two modalities for simultaneous large-scale, multimodal sensing of neural activity across multiple brain regions can be very powerful. To this end, many research groups have developed transparent ECoG arrays that can be used simultaneously with optical recording methods in small rodents and nonhuman primates. These devices are made possible by using transparent conductive materials such as graphene or indium tin oxide (ITO). Alternatively, poly(3,4-ethylenedioxythiophene) polystyrene sulfonate

(PEDOT:PSS) is a biocompatible transparent organic conductor which is routinely used to coat chronic neural interfaces in order reduce the interfacial impedance of the contact site.
We have developed inkjet-printed transparent PEDOT:PSS microelectrodes which use a novel ring-shaped geometry to reduce interfacial impedance and improve charge injection. [1] This is accomplished by taking advantage of the volumetric capacitance in PEDOT:PSS. Ring-shaped microelectrodes with diameters ranging from 300 µm to 550 µm were fabricated by inkjet-printing PEDOT:PSS, encapsulating with Parylene C, and then exposing a contact site that is much smaller than the microelectrode outer diameter. This unique structure allowed the encapsulated portion of the microelectrode volume surrounding the contact site to participate in signal transduction, which reduced impedance and enhanced charge storage capacity. For the same size contact site, increasing the outer diameter of the encapsulated electrode from 300 to 550 µm reduced the impedance from 294 ± 21 to 98 ± 2kΩ, respectively, at 1 Hz. Similarly, the charge storage capacity was enhanced from 6 to 21 mC cm^{-2}. The PEDOT:PSS microelectrodes provide a low-haze, high-transmittance optical interface, demonstrating their suitability for optical neuroscience applications. They remained functional after a million 1 V stimulation cycles, up to 600 µA of stimulation current, and more than 1000 mechanical bending cycles.
We have integrated these inkjet-printed PEDOT:PSS electrodes into transparent cranial windows for multi-modal recording of activity from the cortex.[2] Implanted on transgenic mice expressing the Calcium (Ca2+) indicator GCaMP6f in excitatory neurons, these "eSee-Shells" provide a robust opto-electrophysiological interface for over 100 days. eSee-Shells enable simultaneous mesoscale Ca2+ imaging and electrocorticography acquisition from multiple brain regions covering 45 mm^2 of cortex under anesthesia and in awake animals. These eSee-Shells allow either mesoscale imaging across the entire field of view (FOV) or random-access cellular level imaging of small FOVs throughout ≈45 mm^2 of the cerebral cortex, an area that is an order of magnitude larger than previous transparent ECoG electrode arrays.
[1] P. D. Donaldson and S. L. Swisher, *Physica Status Solidi (a)* **2022**.
[2] P. D. Donaldson et al., *Adv. Healthcare Mater.* **2022**.

SESSION U: Group III–Nitrides—Contacts and Special Topics
Session Chairs: Ramón Collazo and James Spencer Lundh
Thursday Morning, June 29, 2023
UC, Santa Barbara Harbor

8:20 AM U01
(Student) Ohmic Contacts to Homoepitaxial Ultrawide Bandgap n-AlGaN Grown on Bulk AlN Substrates Shivali Agrawal, Joseph Dill, Jimy Encomendero, Len van Deurzen, Kazuki Nomoto, Huili Grace Xing and Debdeep Jena; Cornell University, United States

We present vanadium (V) based ohmic contacts to high composition n-AlGaN grown on single crystal bulk aluminium nitride substrates by plasma-assisted molecular beam epitaxy (PAMBE).
Metal-semiconductor contacts are integral for the performance of electronic devices such as transistors, light-emitting diodes (LEDs), lasers and photodetectors [1,2]. Low-resistance Ohmic contacts have proven difficult to achieve on n-AlGaN epilayers grown on single crystal bulk AlN substrates as compared to the ones grown on AlN-on-sapphire templates [3]. This is because the large density of threading dislocations allow for conduction pathways [4]. While the low dislocation density of the films grown on bulk substrates reduce optical losses, it also makes low resistance ohmic contacts difficult due to lack of such conduction channels.
Since the bandgap of AlGaN increases with increasing Al composition, it is difficult to find suitable metals with low work functions for a low energy barrier in the conduction band. Therefore, an alternate way to make ohmic contacts to wide bandgap semiconductors is to heavily dope the semiconductor layers to thin down the depletion enough to enable tunneling of electrons.
A Ti-based metal stack has been shown to work for low resistance ohmic contacts to low composition n-AlGaN [5]. More recently, vanadium based ohmic contacts have been achieved on entire AlGaN composition grown on sapphire wafers [6]. It is hypothesised, that through annealing, vanadium nitride (VN) forms at the junction and has a work function of 3.56 eV [7].
In this work we demonstrate V-based Ohmic contacts on Si-doped $Al_{0.7}Ga_{0.3}N$ grown by PAMBE on bulk AlN. Degenerately doped AlGaN layers with Silicon doping concentrations [Si] = 3e19/cm^3-9e19/cm^3 were used. The metal-polar single-crystal AlN substrates were cleaned ex-situ using solvents and acids, as well as in-situ by Al-assisted cleaning [8,9]. A 500 nm thick buffer layer was grown in Al-rich conditions to separate the AlGaN layer from the substrate. Then a 400-440 nm thick AlGaN layer was grown in metal-rich conditions. Atomic steps were observed in the coherently strained epilayers that have an energy bandgap of 4.8 eV as measured by room temperature photoluminescence.
The samples were blanket etched 70 nm using chlorine-based reactive ion etching to emulate the n-AlGaN contacts as required for a light-emitting diode or laser diode. Two metal stacks were explored. Bottom-up, they consist of V(20n m)/Al(80 nm)/V(40 nm)/Au(100 nm) and V(20 nm)/Al(80 nm)/Ni(40 nm)/Au(100 nm). They were deposited using an e-beam evaporator and annealed by rapid thermal annealing (RTA) for 30 seconds at 800ºC in N_2 ambience. Linear transfer length method (TLM) analysis was done to determine the specific contact resistance and sheet resistance for which the results are shown in Figure 2.
Successive annealing steps were performed to explore the effect of annealing time on the contact resistance. We found that a 30 second anneal is enough to make a low resistance ohmic contact. For both samples V/Al/V/Au contact gave a lower specific contact resistance than the V/Al/Ni/Au contact. We find that only a very high doping (9e19/cm^3) results in low resistance ohmic contacts in the 10^{-4} ohm.cm^2 range. These optimised doping conditions and metal stacks are now available to be used for ultrawide bandgap photonic and electronic devices on homoepitaxial AlGaN.
References:
[1] AIP Advances 12, 035023 (2022)
[2] Appl. Phys. Lett. 121, 222103 (2022)
[3] Appl. Phys. Lett. 114, 113501 (2019)
[4] Journal of Applied Physics 117, 245702 (2015)
[5] Sampath, A., et al. "Metal Contacts to n-$Al_xGa_{1-x}N$." MRS Online Proceedings Library (OPL) 482 (1997)
[6] Appl. Phys. Lett. 90, 062115 (2007)
[7] Fomenko, V. S. (2012). Handbook of thermionic properties. Springer Science & Business Media
[8] Applied Physics Letters 116.17 (2020): 17210
[9] Applied Physics Letters 116.26 (2020): 262102

8:40 AM U02
Evolution of Surface Microstructure of Re-Al-Ni-Au Based Ohmic Contacts on N-Type GaN Amit P. Shah, Bhagyashree A. Chalke, Jayesh B. Parmar, Manish B. Ghag and Arnab Bhattacharya; Tata Institute of Fundamental Research, India

Low specific contact resistivity ohmic contacts ($\rho_c \sim 10^{-6}$ Ω-cm^2) with thermal and chemical stability play an important role in III-nitrides based devices. A Ti-Al-Ni-Au multilayer metallization is the most commonly used scheme and requires high temperatures (>800ºC) to form reliable ohmic contacts. There are a few reports on the surface microstructures and chemical composition of the Ti-Al based contacts [1-2]. The low contact resistivity has been explained via the formation of TiN and $TiAl_3$ phases along with Al-Ni agglomerates surrounded by alloys of Al-Au, mainly $AlAu_2$, Al_2Au_5 and $AlAu_4$.

We have investigated low ρ_c ohmic contacts ($\rho_c \sim 10^{-7}$ Ω-cm^2) formed on n-GaN using a Re-Al-Ni-Au multilayer stack annealed at 650-700ºC [3]. In this work, we report the effect of Re layer thickness and annealing temperature on the microstructure of these contacts. Several samples with Re thickness (10, 30, 60 nm) were prepared and annealed at 450ºC—800ºC temperatures. The ρ_c was estimated using C-TLM measurements while AFM, GIXRD and SEM equipped with EDS were used to analyze the chemical composition and microstructures of the contacts.

AFM images show surface microstructures as a function of annealing temperatures in the range of 500—800ºC in steps of 50ºC for 30 nm Re samples. The metals form almost a continuous film with signs of segregation into small clusters at an annealing temperature up to 500ºC. The films show more extensive segregations into separate islands, forming larger agglomerates and the density of these islands keeps on reducing, with a concomitant increase in height with increasing temperature. The RMS roughness increases linearly with annealing temperature.

AFM images of the surface microstructures as a function of Re thickness for the annealing temperature where lowest ρ_c is observed; (a) 10 nm at 650ºC and (b) 30 and 60 nm at 700ºC; shows that as the Re thickness increases, the size of the agglomerates increases, with the corresponding reduction in the density. The RMS surface roughness also increases with Re content. For contacts with 10 nm Re, the RMS roughness starts increasing slowly with increasing temperature from 450ºC with a faster rate of increase beyond 600ºC. For contacts with 30 nm Re, the surface roughness increases linearly over the entire temperature range 500—800ºC. However, in case of contacts with 60 nm Re, the surface roughness starts increasing initally and then saturates around at ~170 nm.

EDS elemental scans for Re, Al, Ni and Au for samples with Re thickness 10, 30 and 60 nm, annealed at temperatures for which ρ_c is minimum, shows that the Ni layer disintegrates to form isolated islands and also Al-Ni agglomerates. There is a thin continuous layer of Al over the entire surface with a few isolated patches devoid of aluminum. A continuous layer of Re underneath is observed across the surface. The dark spots observed in the Re scan are due to the thick agglomerates which absorb the signal from the underlying Re layer. The gold layer seems to get accumulated around the agglomerates.

Glancing angle SEM image of the surface of 60 nm Re sample annealed at 650ºC shows hills formed due to the Al-Ni agglomerates covered by Al-Au films spread across entire surface. A cross section view of one of the agglomerates shows a thick lump of Al-Ni in the centre of the hill, while rest of the surface is covered by an Al-Au layer. The Re layer is delineated from the top structure. The Re layer may form intermetalic phases of Re-Ni-Al in the center, while the different phases of Al-Re are formed on the entire surface. The combinations of phases of Al-Re, Re-Al-Ni, Al-Au along with a thin layer of Re-N formed between the Re and GaN interface gives the low ρ_c of this material system.

[1] S. Ruvimov, et al., *Appl. Phys. Lett.*, **69**, 1556 (1996).
[2] W. Macherzynski et al., *Optica Applicata*, **XLIII**, 67 (2013).
[3] A. P. Shah, et al., *J. Appl. Phys.*, **132**, 075701 (2022).

9:00 AM U03

(Student) Ultrawide Bandgap Optoelectronic Properties of Single Crystal Bulk AlN and Sapphire/AlN Templates Mafruda Rahman[1], Abdullah Mamun[1], Mohammad Hussain[1], Md Didarul Alam[2], Richard Floyd[1], Grigory Simin[1], MVS Chandrashekhar[1] and Asif Khan[1]; [1]University of South Carolina, United States; [2]Intel Corporation, United States

Optoelectronic performance parameters of III-nitrides are sensitive to low concentrations of electrically active defects and enable epitaxial crystal growers to optimize for extremely high quality material. As the push for ultra-wide bandgap (UWBG) power electronics emerges, the crystalline structure quality improves and the concentration of defects decreases, with threading dislocation densities (TDD) < 10^4cm^{-2} for $Al_{0.87}Ga_{0.13}N/Al_{0.64}Ga_{0.36}N$ pseudomorphic hetereostructures on AlN bulk substrates routinely measured on our structures, although the role of trapping endemic to the nitrides has not been examined in detail. The goal of this paper is to compare the optoelectronic properties of identical heterostructures grown on bulk AlN and sapphire/AlN templates. By focusing on low current operation near threshold, the influence of thermal effects is eliminated, thus providing a clear insight into the role of traps in off-state performance for power devices. We will show photoresponse measurements through a 3-terminal metal-oxide-semiconductor HFETs (MOSHFET) structure near threshold, and compare this with 2-terminal control metal-semiconductor-metal structures (MSM) on insulating AlN to eliminate epitaxial interfaces and identify the location of electrically active defects.

Under top-side illumination, $Al_{0.87}Ga_{0.13}N/Al_{0.64}Ga_{0.36}N$ MOSHFETs near threshold (V_{th}~-15V) showed responsivity increasing at ~260-270 nm corresponding to the $Al_{0.64}Ga_{0.36}N$ channel band edge, indicating the wide bandgap $Al_{0.87}Ga_{0.13}N$ barrier is a low-loss window. Responsivities (normalized to the area of the source-drain spacing) as high as 10^6A/W are seen at V_{GS}=-13V, indicating that photoconductive gain due to trapping may be present[1]. The devices on bulk AlN (TDD<10^4cm^{-2}) and sapphire/AlN (TDD~10^8cm^{-2}) showed similar behavior, indicating that point defects are responsible, given the large difference in TDD between the 2 samples. These point defects may be generated due to thermal cycling of highly strained pseudomorphic structures during growth[2] as has been observed in DX-center formation even with homoepitaxial AlN[1]. This is further supported by the relatively low solar rejection ~10^2, as well as non-zero photoresponse at longer wavelengths ~700nm. For wavelengths with energy below the $Al_{0.64}Ga_{0.36}N$ channel band edge, the photocurrent magnitude turns negative. While measurements were taken from long wavelength (low energy) to short wavelength (high energy), the role of persistent photocurrent (PPC) from previous measurement cycles cannot be ruled out.

To eliminate growth interfaces and test whether deep centers in AlN[3] are responsible for the photoconductive gain and low solar rejection, we will present preliminary photoresponse results on control MSM structures on AlN that have been fabricated. The hypothesis is that high lateral electric fields at short distances <5um separate photogenerated e-h pairs quickly as a function of applied voltage, minimizing the influence of trapping, although again the role of PPC may play a role if a deep trap is present. These optoelectronic measurements will provide insight to growers as well as device designers in UWBG power electronics, particularly in vertical/quasi-vertical device architectures for high current handling.

References:

Jewel, M. U., Alam, M. D., Mollah, S., Hussain, K., Wheeler, V., Eddy, C., ... & Khan, A. (2019). Trap characterization in ultra-wide bandgap Al0. 65Ga0. 4N/Al0. 4Ga0. 6N MOSHFET's with ZrO2 gate dielectric using optical response and cathodoluminescence. *Applied Physics Letters*, *115*(21), 213502.

Hussain, K., Mamun, A., Floyd, R., Alam, M. D., Liao, M. E., HUYNH, K., ... & Khan, A. (2023). High figure of merit extreme bandgap Al0. 87Ga0. 13N-Al0. 64Ga0. 36N heterostructures over bulk AlN substrates. *Applied Physics Express*.

Ahmad, H., Engel, Z., Matthews, C. M., Lee, S., & Doolittle, W. A. (2022). Realization of homojunction PN AlN diodes. *Journal of Applied Physics*, *131*(17), 175701.

9:20 AM U04

Structural and Optical Characterization of Thin AlInN Films on c-Plane GaN Substrates Haotian Xue[1], Elia Palmese[1], Renbo Song[2], Md. Istiaque Chowdhury[2], Nicholas C. Strandwitz[2,2] and Jonathan J. Wierer[1]; [1]North Carolina State University, United States; [2]Lehigh University, United States

III-nitride (AlInGaN) semiconductors have had wide success in optoelectronic and electronic devices. Of the ternary compounds, $Al_{1-x}In_xN$ is arguably the least explored. It is of interest because it has a large bandgap tuning range (6.21 eV – 0.675 eV), and it can be lattice-matched or polarization-matched to InGaN and AlGaN. The possible uses of AlInN in III-nitride devices include in barrier layer in high-

electron-mobility transistors (HEMTs), distributed Bragg reflectors (DBRs), drift layer in GaN power diodes, and claddings for laser diodes. A relatively new development is the demonstration of oxidizing AlInN at shallow or significant depths to create oxide/III-nitride structures.
There is a wide variation in the measured optical properties of AlInN [1-5]. The growth on different substrates results in different lattice constants for the AlInN, and any relaxation of the films will modify the lattice constants further. Since the lattice constant factors into the properties, particularly the bandgap energy, these diverse data sets often do not agree. What is missing is a set of AlInN films that are pseudomorphic to GaN substrates and can provide clear trends of optical properties. This information is technologically vital because device structures using AlInN grown on GaN will need to be pseudomorphic to avoid defect formation and its adverse impacts on properties such as mobility and radiative recombination.
In this work, the structure and optical characteristics of thin (~30 nm) wurtzite AlInN films grown pseudomorphic on free-standing, c-plane GaN substrates are presented. The $Al_{1-x}In_xN$ layers are grown by metalorganic chemical vapor deposition, resulting in films with varying In content from x = 0.142 to 0.225 and thicknesses of ~30 nm. They are measured using atomic force microscopy, X-ray diffraction, reciprocal space mapping, and spectroscopic ellipsometry (SE). The pseudomorphic AlInN layers provide a set where optical properties can be determined without the additional variability caused by lattice relaxation, a crucial need for designing devices. They have smooth surfaces (RMS < 0.29 nm) with minimum pit densities when the In content is near lattice-matched to GaN. As expected, the SE shows the refractive index increases and bandgap energy decreases with increased In-content. Plots of bandgap energy versus In content are fitted with a single bowing parameter of 3.19 eV when using bandgap energies for AlN and InN pseudomorphic to GaN, which is lower than previous measurements and closer to theoretical predictions.
[1] T. Onuma *et al.*, "Recombination dynamics of localized excitons in Al1-xInxN epitaxial films on GaN templates grown by metalorganic vapor phase epitaxy," *Journal of Applied Physics*, vol. 94, no. 4, pp. 2449-2453, 2003.
[2] W. Walukiewicz *et al.*, "Structure and electronic properties of InN and In-rich group III-nitride alloys," *Journal of Physics D: Applied Physics*, vol. 39, no. 5, p. R83, 2006.
[3] E. Iliopoulos, A. Adikimenakis, C. Giesen, M. Heuken, and A. Georgakilas, "Energy bandgap bowing of InAlN alloys studied by spectroscopic ellipsometry," *Applied Physics Letters*, vol. 92, no. 19, 2008.
[4] T. Aschenbrenner *et al.*, "Optical and structural characterization of AlInN layers for optoelectronic applications," *Journal of Applied Physics*, vol. 108, no. 6, 2010.
[5] M. Miyoshi, M. Yamanaka, T. Egawa, and T. Takeuchi, "Microstructure variation in thick AlInN films grown on c-plane GaN on sapphire by metalorganic chemical vapor deposition," Journal of Crystal Growth, vol. 506, pp. 40-44, 2019.
[6] J. F. Carlin et al., "Progresses in III-nitride distributed Bragg reflectors and microcavities using AlInN/GaN materials," Status Solidi B 242, no. 11, pp. 2326-2344, 2005.

9:40 AM U05
Nano-Scale Correlation of Real Structure, Band Bending and Local Electric Fields in the Narrow pn^+ Regions of a GaN Superjunction Using Highly Spatially Resolved STEM-CL Characterization Juergen Christen[1], Gordon Schmidt[1], Frank Bertram[1], Peter Veit[1], Konstantin Wein[1], Holger Eisele[1], Arne Debald[2,3], Michael Heuken[2,3], Thorsten Zweipfennig[2], Holger Kalisch[2], Andrei Vescan[2], Patrik Stranak[4] and Lutz Kirste[4]; [1]Otto von Guericke Universität Magdeburg, Germany; [2]RWTH Aachen University, Germany; [3]AIXTRON SE, Germany; [4]Fraunhofer Institute for Applied Solid State Physics, Germany

GaN has become the semiconductor of choice where energy density, energy efficiency, and the size of systems are of paramount concern. In detail, Gallium-nitride based power devices switch faster and have lower on-resistance than conventional silicon and even silicon-carbide based devices. Significant progress on GaN-based power devices has been achieved on the way to approach the unipolar limit of breakdown voltage and on-resistance of GaN material.
The superjunction concept, based on charge compensation in the drift region by fully balanced n- and p-regions, is intended to break the tradeoff between breakdown voltage and on-resistance and further improve GaN-based device performance. In this study, a pn^+ superjunction was investigated by scanning transmission electron microscope cathodoluminescence microscopy (STEM-CL). The GaN superjunction structure was grown by metal organic vapor phase epitaxy (MOVPE) on top of a GaN/sapphire template with an n-doped GaN buffer layer. The subsequently grown 10 nm thick $Al_{0.23}Ga_{0.77}N$ film is used as marker layer. The 9-fold superjunction was epitaxially deposited and is composed of alternating 91 nm thick GaN:Mg and 23 nm thick GaN:Si layers. Finally, the structure was capped by an n-GaN layer of 91 nm thickness. The Mg-doped GaN layers were thermally *in-situ* activated for 900 s at 850°C.
The Mg as well as Si doping concentrations were analyzed by secondary ion mass spectrometry (SIMS). Investigated by 1 keV Cs ions, the SIMS profile for Si varies between n^+ and p-layers by more than one order of magnitude. For the n^+-doped layers, the Si concentration increases monotonously from 5.9×10^{18} cm^{-3} to 8.5×10^{18} cm^{-3} at the top most n^+-GaN and drops down to 1×10^{17} cm^{-3} in p-doped layers. In contrast, the atomic Mg concentration modulates only slightly between n^+-GaN (6×10^{17} cm^{-3}) and p-GaN (7×10^{17} cm^{-3}).
Spatially averaged STEM-CL spectra from the superjunction region exhibit three recombination channels at T = 16 K: the donor (D^0,X) and acceptor bound exciton (A^0,X), as well as the donor-acceptor-pair DAP emission with its phonon replica. Compared to the broad (D^0,X) emission from the GaN buffer, a distinct differentiation between excitons bound to neutral Si and O can be resolved indicating the commonly known unintentional oxygen incorporation during MOVPE process. The DAP emission arises typically in partially compensated Mg-doped GaN layers and gives insight into the Mg incorporation and possible compensation effects.
In monochromatic CL intensity profiles the bound exciton and DAP recombination signals exhibit a complementary modulation in the superjunction region, which clearly illustrates the compensation effects in the superjunction layers. DAP dominates across the whole superjunction, however its intensity is increased in the n-doped GaN region due to the high background Mg concentration verified by SIMS. In contrast, (A^0,X) as well as (D^0,X) show higher intensity in p-doped GaN due to higher [Mg] and drastically reduced Si concentration. Here, even the oxygen bound exciton becomes more prominent compared to (Si^0,X).
At room temperature, electrons / excitons dissociate from shallow donors leading to free exciton emission FX and deep donor acceptor pair recombination DAP. Additionally, yellow luminescence YL becomes more prominent compared to low temperature. In contrast to the low-temperature results, an intensity modulation is only observed for DAP in the superjunction region. The intensity of FX remains almost constant.

10:00 AM BREAK

10:20 AM U06
(Student) Design and Optimization of Room Temperature AlGaN/GaN Multi Quantum Well Infrared Photodetector by MOCVD for Near IR Range Alireza Lanjani[1], Benjamin McEwen[1], Emma Rocco[1], Vincent Meyers[1], David Hill[2], W. K. Chan[2] and Fatemeh (Shadi) Shahedipour-Sandvik[1]; [1]SUNY Polytechnic Institute, United States; [2]SRI International, United States

Quantum well infrared photodetectors (QWIP) based on III-Nitrides are a subject of increasing interest due to their potential for applications in telecommunications, optical gas sensors, military, and imaging. These detectors rely on intersubband transitions (ISBTs) of an electron (hole) between the ground state and the first excited state in the conduction (valance) band. Large conduction band offset (CBO)

of nearly 2 eV [1], [2] and valance band offset (VBO) of nearly 0.85 eV [3] in AlN/GaN QWIPs make this material system suitable for a wide range of ISBTs depending on Al composition and specifically in the spectral regions where GaAs-based QWIPs are limited due to their smaller bandgap offsets. Also, the longitudinal-optical (LO) phonon energy of GaN (92 meV) is more than two times higher than GaAs [4], which makes this material an ideal choice for room temperature detection application. By employing GaN-based QWIPs, ISBT energies can be tuned from a few meV to 2 eV based on QWIP design, allowing for full NIR to IR band tunability within a single material system.

While III-N materials can be grown in cubic zincblende structure, only hexagonal wurtzite structure is thermodynamically stable. In this structure, lack of inversion symmetry along the (growth) c-axis, generates a spontaneous polarization (P_{sp}) along this axis [5]. Additionally, at AlGaN/GaN heterointerface, the lattice mismatch causes strain leading to piezoelectric polarization [6]. The discontinuity of polarization at heterointerfaces results in an uncompensated sheet charge at the interface. Further due to the polarization selection rule, normal incidence absorption is not allowed in n-QWIPs [7], requiring a light coupler and adding to design complexity. To circumvent this issue, p-QWIPs are being considered. In this work, we report on the growth of 5 periods Mg-doped $Al_{0.4}Ga_{0.6}N$/GaN QWIP, by metal organic chemical vapor deposition (MOCVD) on c-plane sapphire for a target 1.55 µm absorption. Critical to the performance of the QWIP are high controllability of layer thicknesses and composition in superlattice and interface quality. Sub-nanometer control of layer thicknesses is challenging in MOCVD growth due to the high temperature and the relatively poorer control of precursor flux on the sample surface, compared to other methods such as MBE. To overcome this, a pulsed growth method was used to achieve higher control of growth rate [8]. A TCAD-based physics model was implemented in the commercial Synopsys Sentaurus to model the energy band diagram, electric field and calculate the band offsets between $Al_xGa_{1-x}N$/GaN heterointerfaces by considering polarization charges. Based on the CBO and VBO in the QW, layers thicknesses and compositions can be adjusted to achieve desired absorption wavelength. X-ray diffraction and transmission electron microscope (TEM) are used to assess strain, interface quality, layer thicknesses, and aluminum composition. Transmission/reflection measurement is used to determine the absorption spectrum of the QWIP.

[1]D. Cociorva *et al.*, 'Quasiparticle calculations of band offsets at AlN–GaN interfaces', *Solid State Commun*, 2002
[2]A. N. Westmeyer *et al.*, 'Determination of energy-band offsets between GaN and AlN using excitonic luminescence transition in AlGaN alloys', *J Appl Phys*, 2006
[3]G. Martin *et al.*, 'Valence-band discontinuities of wurtzite GaN, AlN, and InN heterojunctions measured by x-ray photoemission spectroscopy', *Appl Phys Lett*, 1996
[4]K. Ahi, 'Review of GaN-based devices for terahertz operation', *Optical Engineering*, 2017
[5]H. Ünlü *et al.*, 'Band offsets in III-nitride heterostructures', *J Phys D Appl Phys*, 2002
[6]S. Nicolay *et al.*, 'Strain-induced interface instability in GaN/AlN multiple quantum wells', *Appl Phys Lett*, 2007
[7]B. F. Levine, 'Quantum-well infrared photodetectors', *J Appl Phys*, 1993
[8]P. Suvarna *et al.*, 'Design and growth of visible-blind and solar-blind III-N APDs on sapphire substrates', *J Electron Mater*, 2013

10:40 AM U07
(Student) InGaN Films on Crystalline $ScAlMgO_4$ on Al_2O_3 Substrates by MOCVD with up to 123 nm PL Redshift Guangying Wang, Yuting Li, Jeremy Kirch, Yizhou Han, Jiahao Chen, Samuel Marks, Swarnav Mukhopadhyay, Rui Liu, Cheng Liu, Paul Evans and Shubhra Pasayat; University of Wisconsin–Madison, United States

The group III-nitride material system has enabled numerous electronic and optoelectronic device technologies. For InGaN-based LEDs, a high In content in the quantum well is required for longer emission wavelengths. One of the most difficult aspects of the InGaN material synthesis is the 11 % lattice mismatch between GaN and InN [1]. Such high lattice mismatch results in high strain, causing defect generation in the crystalline structure [1,2]. $ScAlMgO_4$ (SAM) is lattice-matched with $In_{0.17}Ga_{0.83}N$, making it a suitable candidate for hetero-epitaxial growth of III-nitride materials [3-5]. The high substrate cost of bulk SAM substrates of $9k USD for 2 in. substrates, is quite limiting for academic research. The solid phase epitaxy (SPE) of amorphous SAM on sapphire followed by crystallization is a cost-efficient way to solve this issue. A problem associated with the crystallization of SAM on sapphire is the appearance of scandium-deficient regions due to unoptimized annealing conditions on the surface, leading to undesirable spinel phase $MgAl_2O_4$ formation [6]. In this work, an improved crystallization method for SAM layers on sapphire and present MOCVD growth of InGaN layers on the same. The amorphous SAM layer was deposited using on-axis radio frequency (RF) magnetron sputtering at room temperature. SAM layers were crystalized by annealing in a pre-heated furnace at different temperatures (850-950°C) for different durations (20-30 h). In the series of annealing experiments, the effect of pre-annealing, SAM film thickness, annealing duration, and temperature were studied. After SAM crystallization, InGaN layers were grown using MOCVD with triethylgallium (TEGa), trimethylindium (TMI), and ammonia (NH_3) (Fig 1). 100 nm and 400 nm thick InGaN layers were grown with the calibrated composition of x_{In}=0.14, on both SAM on sapphire and reference GaN on sapphire templates (Fig.2).

We have discovered the pre-annealing the substrate prior to the SAM deposition at 1400 °C resulted in a higher quality material. A low spinel (311) to SAM (0009) peak-to-background intensity ratio, by optimizing various crystallization annealing parameters mentioned above, was the key parameter for improving crystallinity and lowering surface roughness. For InGaN film depositions, Samples A-C with 75 nm thick SAM, with spinel to SAM ratios of 0.177, 0.453, and 0.446, respectively were chosen, having AFM roughness between 2- 2.5 nm (fig. 3). Sample D had 40 nm thick SAM with this ratio at 0.263. InGaN films were successfully deposited on SAM on sapphire (100 nm InGaN for Samples A and B, 400 nm InGaN, for C and D) (Fig.4(a),4(b)), along with reference GaN templates. Higher PL intensities (upto 2 times higher for 100 nm InGaN and 6 times higher for 400 nm InGaN) and longer emission wavelengths (~123 nm for 100 nm InGaN and ~37 nm for 400 nm InGaN) were observed than those on co-loaded GaN templates (Fig.5(a),5(b)). Although sample A showed 123 nm redshift, a lower intensity than the GaN on sapphire was observed, sample D with 37 nm red shift and B with 80 nm redshift, both showed a higher PL intensity compared to co-loaded GaN template. This is one of the highest reported redshifts for any relaxed InGaN pseudo-substrate technology so far and one of the few wherein the redshift is accompanied by an increased emission intensity [7]. Further investigations will be pursued to study the InGaN layers and will be presented at the conference. These results demonstrate the potential of SAM on sapphire substrates as a viable candidate to achieve thick high Indium concentration InGaN layers for long wavelength emitters.

Refs:[1]. P. Rinke et al. APL. **89**, 161919 (2006) [2]. R. Kour et al. JSS. **9** 015011 (2020) [3]. T. Ozaki et al. APEX. **7**, 091001 (2014) [4]. T. Ozaki et al. APEX **8**, 062101 (2015) [5]. R. Takahashi et al. APL. **120**, 142102 (2022) [6]. Y. Chen et al. Cryst. Growth & Des., **20**, 9, 6001–6007 (2020) [7]. S. S. Pasayat et al. APL. **116**, 111101 (2020).

11:00 AM U08
Characterization of Optically Modulated Semi-Insulating GaN Photoconductive Semiconductor Switches Geoffrey Foster[1,2], Andrew D. Koehler[2], Karl Hobart[2], Sadab Mahmud[3], Samuel Atwimah[3], Raghav Khanna[3] and Travis Anderson[2]; [1]Jacobs Inc., United States; [2]U.S. Naval Research Laboratory, United States; [3]The University of Toledo, United States

Photoconductive semiconductor switches (PCSSs) have the potential to outperform conventional unipolar semiconductor power devices.

PCSS devices operate using photoconductivity, wherein the material becomes conductive after the absorption of light. Traditionally, silicon switches have been used[1]. However, in recent years, wide bandgap photoconductive semiconductor switches, such as GaN PCSSs, have gained attention due to high critical electric field strength, high electron saturation velocity, and the ability to provide high power ultrafast devices. The limits of the conventional, unipolar, power semiconductor devices are constrained by the size of the drift layer, which is required for voltage hold-off. This drift layer creates a conduction path where there is an inherent tradeoff between specific on-state resistance ($R_{ON\text{-}SP}$) and breakdown voltage (V_{BR}),

$R_{ON\text{-}SP}$ μ $V_{BR}^2/(\mu\, e\, E_C^3)$ (1)

where μ, ε, and E_C are mobility, permittivity, and critical field. In traditional power devices, higher voltage operation has required having thicker drift layer thickness increasing $R_{ON\text{-}SP}$. A PCSS can overcome the on-resistance vs. breakdown voltage limits of the drift layer in a unipolar power device by optically modulating the conductivity of the entire drift layer through high-density free-carrier injection. This mechanism of modulating channel-conductivity by injecting charge facilitates fast switching speeds while inherently providing optical isolation to the gate driver control circuitry. The high photo responsivity of the PCSS will enable small $R_{ON\text{-}SP}$ with high V_{BR}.

Four microns of GaN was grown on a silicon carbide (SiC) substrate by metal organic chemical vapor deposition (MOCVD), with a carbon doping concentration of 5 x 10^{17} cm^{-3}. Ti/Al/Ni/Au contacts were deposited, using a lift off technique with an 800C rapid anneal, varying the distances between the two contacts. Devices were then characterized using photoionization spectroscopy with a monochromatic light source. A strong photoresponse, with eight orders of magnitude on/off current, is seen at bandgap, and at 3.1eV, indicating a response from carbon-related defects. A COTS 365 nm LED is used to produce a photoresponse several orders of magnitude greater than the monochromatic light. The increase in optical power density results in an increase in generated free carriers, corresponding to a proportional reduction of R_{ON}. A 1mm wide device with a gap of 20 microns was characterized using a COTS 365 nm LED source while modulating the intensity of the LED. The resulting family of curves illustrates decreasing resistance with increasing power density of photons. The on-resistance is 334.1Ω at LED intensity of 33.33 mW/cm^2, and is 193.2Ω at LED intensity of 191.67 mW/cm^2. CTLM structures were measured to extract values for sheet resistance, transfer length, contact resistivity, and contact resistance using high illumination (191.67 mW/cm^2) and low illumination (91.67 mW/cm^2). All of these values decrease with increasing optical power density from the LED. Off-state breakdown values, measured from CTLM structures, ranging from 2760V at a gap of 50 microns to 8444V at a gap of 250 microns. In order to characterize the transient on/off switching times, a custom circuit will need to be developed. A double pulse testing (DPT)[2] circuit that would be used to characterize transient switching behavior for the device under test (DUT) while eliminating thermal effects.

References

[1] A. D. Koehler *et al.*, "High Voltage GaN Lateral Photoconductive Semiconductor Switches," *ECS J. Solid State Sci. Technol.*, vol. 6, no. 11, pp. S3099–S3102, 2017, doi: 10.1149/2.0231711jss.

[2]A. J. Sellers *et al.*, "An automated model tuning procedure for optimizing prediction of transient and dispersive behavior in wide bandgap semiconductor FETs," in *IEEE Transactions on Power Electronics*, vol. 35, no. 11, Nov. 2020, pp. 12252 – 12263, doi: https://doi.org/10.1109/TPEL.2020.2986928

11:20 AM U09

Piezoelectric Sensing in Extreme Environments Using Flexible Ultrawide Bandgap III-N Thin Films Nam-In Kim, Miad Yarali, Muhammad Aqib and Jae-Hyun Ryou; University of Houston, United States

Piezoelectric sensors are particularly promising in various industries such as automotive, plant, and biomedical due to their advantages such as high sensitivity, fast response time, ease of manufacturing, reliable operation, lightweight, and low power consumption. One of the essential characteristics of extended applications is flexibility. For example, in a closed gas inlet or outlet network, flexible sensors attached to membranes can be used to measure gas pressure. Flexible piezoelectric sensors using various materials have been reported for use in typical situations. However, there is a shortage of sensor materials at ultra-high temperatures above 500°C. The most common piezoelectric material, lead zirconate titanate (PZT), has high piezoelectric coefficients that allow for increased output voltage generation, but because of its low Curie temperature, T_c, it cannot operate at high temperatures. Another impediment to sensing at high temperatures exists for piezoelectric materials based on zinc oxide (ZnO) and polyvinylidene fluoride (PVDF). As the temperature increases, ZnO is said to increase oxygen vacancies, and PVDF has a low melting point (~200 °C) and boiling point (375 °C).

Because of their wide bandgap energy, spontaneous polarization, and low electrical conductivity, III-N thin films have the potential for high-temperature operations. Particularly, it has been reported that single-crystalline gallium nitride (GaN) and aluminum nitride (AlN) piezoelectric thin films exhibit excellent output voltage up to 400 and 900 °C, respectively, indicating outstanding sensitivity, quick response time by a high electromechanical coupling factor, chemical and mechanical long-term stability, high thermal resistance, and excellent biocompatibility. The benefit is anticipated to be extended to greater temperatures with broader bandgap III-N materials. III-N materials have been also reported to have high resistance to radiation. In this work, we have developed and demonstrated a piezoelectric AlN thin film sensor with high flexibility for sensing gas pressure at very high temperatures. The crack-free AlN epitaxial layers were grown by metal-organic chemical vapor deposition. Flexible III-N thin-film-based sensors were fabricated by a layer transfer process from rigid silicon to flexible copper foil substrates. They were analyzed by X-ray diffraction and showed excellent crystalline quality without secondary phases or defects. A single sensor was attached to the membrane with a fitting tool and placed in the electric furnace. The working condition of the sensor was controlled from low to high temperature with different gas pressures. The long-term stability of the sensor was evaluated using the specified temperature and pressure levels. Simulations were performed by the software to support the results at each temperature and pressure. The flexible III-N piezoelectric sensors with high durability under harsh conditions can be used in various applications such as aerospace and defense. In addition, we compared sensing performance after exposing the sensor to radiation.

11:40 AM U10

(Student, Late News) Demonstration of 0.7 Ω.mm MOCVD-Grown Reverse Graded Contacts on Al0.85Ga0.15N Channel Yinxuan Zhu[1], Andrew Allerman[2], Chandan Joishi[1], Gabriel A. Calderon Ortiz[1], Hsien-Lien Huang[1], Jinwoo Hwang[1] and Siddharth Rajan[1,1]; [1]The Ohio State University, United States; [2]Sandia National Laboratories, United States

We report on the use of reverse-graded heterojunction contacts to ultra-wide bandgap AlGaN to enable contact resistivity as low as 3.1 x 10^{-6} Ω.cm^2 to a $Al_{0.85}Ga_{0.15}N$ layers. This represents almost 1000X lower contact resistivity than that obtained in similar MOCVD-grown structures.

Lateral transistors based on ultra-wide bandgap Al-rich AlGaN channels are promising for high frequency power amplifier applications as their higher electric breakdown fields enable improved Johnson Figure of Merit when compared with the GaN-based high electron mobility transistors [6][7]. However, a major challenge in the past has been the high contact resistance to ultra-wide bandgap AlGaN, a consequence of the significantly lower electron affinity for high Al-content AlGaN, which increases the Schottky barrier. The contact resistance leads to a lower current density and transconductance. Reverse graded top contacts have been shown to be a very promising approach to realize low contact resistance to AlGaN

channels in recent studies [1][4][5][8][11]. In this work, we report on the design and demonstration of MOCVD-grown reverse graded AlGaN contact layer to achieve record low contact resistance – 0.7 Ω.mm on $Al_{0.85}Ga_{0.15}N$ channel and analyze the contact resistance components based on two types of transfer length measurement (TLM) structures. Highly doped reverse graded contact layers were grown by MOCVD following $Al_{0.85}Ga_{0.15}N$ channel, on which two types of TLM structures were fabricated.

The epitaxial structure consists of 400 nm doped $Al_{0.85}Ga_{0.15}N$ channel, 100 nm highly doped reverse graded contact layer – grading from $Al_{0.85}Ga_{0.15}N$ to $Al_{0.14}Ga_{0.86}N$ and 30 nm highly doped $Al_{0.14}Ga_{0.86}N$ layer. Heavy doping in the reverse graded layer not only compensates the polarization-induced holes, but also enables good n+ ohmic contact on $Al_{0.14}Ga_{0.86}N$ surface. Cross-sectional scanning transmission electron microscopy (STEM) images show very linear grading of composition and growth matches our design very well with energy dispersive spectroscopy (EDX) mapping. The fabrication flow started with ohmic metal deposition – Ti/Al/Ni/Au (20 nm/120 nm/30 nm/100 nm) by e-beam evaporator followed by rapid thermal annealing in N_2 ambient for 30s. Mesa isolation was carried out after annealing.

To understand the contact resistance from such structure, we fabricated two different types of structures for TLM – with and without recessing the contact layer by ICP/RIE dry etch. The components of contact resistance include metal-semiconductor (MS) resistance, sheet resistance of contact layer, and contact-to-channel resistance. From TLM results, the estimated MS resistance, sheet resistivity of contact layer and specific contact resistance are 0.023 Ω.mm, 181 Ω/sq, and 2.8×10^{-8} Ω.cm^2 and the total contact resistance on recessed structure, sheet resistivity of doped $Al_{0.85}Ga_{0.15}N$ channel and specific total contact resistance are 0.7 Ω.mm, 1.7 kΩ/sq and 3.14×10^{-6} Ω.cm^2. Based on these estimates, we estimate a resistance of 0.59 Ω.mm between the reverse-graded contact layer and the channel layer, making it the dominant component in the total contact resistance.

In summary, we have demonstrated MOCVD-grown reverse graded AlGaN contact layer on $Al_{0.85}Ga_{0.15}N$ channel. Our work shows the promise of MOCVD-grown reverse graded contact structure on Al-rich AlGaN channel.

References: [1] S. Bajaj et al., APL, 109, 133508 (2016). [2] H. Okumura et al., Jpn. J. Appl. Phys. 57, 04FR11 (2018). [3] A. M. Armstrong et al., Jpn. J. Appl. Phys. 57, 074103 (2018). [4] P. S. Park et al., IEEE EDL, 36, 226 (2015). [5] S. Bajaj et al., IEEE EDL, 39, 256 (2018). [6] X. Hu et al., IEEE EDL, 39, 1568 (2018). [7] H. Xue et al., 76th DRC, CA, June 24–27, 2017. [8] S. Muhtadi et al., APL, 110, 171104 (2017). [9] S. Muhtadi et al., APL, 110, 193501 (2017). [10] J. Lemettinen et al., IEEE EDL. 40, 1245 (2019). [11] T. Razzak et al., Electron. Lett. 54, 1351 (2018). [12] A. M. Armstrong et al., APL, 114, 052103 (2019).

SESSION V: Growth of Gallium Oxide and Other Ultrawide-Bandgap Oxides
Session Chairs: Hari Nair and Xiuling Li
Thursday Morning, June 29, 2023
MCC Theater

8:20 AM V01
(Student) Si Doping of β-Ga_2O_3 by Disilane via Hybrid Plasma-Assisted Molecular Beam Epitaxy Zhuoqun Wen, Elaheh Ahmadi, Kamruzzaman Khan and Xin Zhai; University of Michigan, United States

Obtaining uniform silicon concentration, especially with low concentrations (ranging from $1x10^{16}$ cm^{-3} to $1x10^{18}$ cm^{-3}) by molecular beam epitaxy (MBE) has been challenging due to the oxidation of silicon solid source in the oxide environment. In this work, Si doping of β-Ga_2O_3 (010) films by diluted disilane as the Si source is investigated using a hybrid plasma-assisted molecular beam epitaxy (hybrid-PAMBE). The impact of growth temperature, disilane source concentration, and disilane flow rate on Si incorporation was studied by secondary ion mass spectrometry. Uniform Si concentrations ranging from 3×10^{16}cm^{-3} to 2×10^{19}cm^{-3} are demonstrated. Si-doped β-Ga_2O_3 films with different silicon concentrations were grown on Fe-doped β-Ga_2O_3 (010) substrates. The electron concentration and mobility were determined using Van De Pauw Hall measurements. A high mobility of 135cm^2/Vs was measured for an electron concentration of 3.4×10^{17}cm^{-3} at room temperature.

8:40 AM V02
(Student) Epitaxial Growth of α-$(Al_xGa_{1-x})_2O_3$ by Suboxide Molecular-Beam Epitaxy at 1 µm/h Jacob Steele[1], Kathy Azizie[1], Jonathan McCandless[1], Huili Grace Xing[1,1,2], Debdeep Jena[1,1,2], Takeyoshi Onuma[3] and Darrell G. Schlom[1,2,4]; [1]Cornell University, United States; [2]Kavli Institute at Cornell For Nanoscale Science, United States; [3]Kogakuin University, Japan; [4]Leibniz-Institut für Kristallzüchtung, Germany

Ga_2O_3 has garnered significant interest due to its ultra-wide bandgap, high electron mobility, and large breakdown field. These properties exceed the current benchmarks set by state-of-the-art materials such as SiC and GaN and make it optimal for next-generation power devices. Still, it has been proposed that the properties of Ga_2O_3 can be extended further by alloying with Al to form $(Al_xGa_{1-x})_2O_3$ which could raise the bandgap up to 8.6 eV. This goal presents a challenge for the most commonly researched phase, β-$(Al_xGa_{1-x})_2O_3$, as it is structurally unstable at higher Al concentrations and transitions to the corundum structure that is favored for Al_2O_3. This structural mismatch limits the compositional range, thereby limiting the range of attainable bandgaps. In contrast, α-phase Ga_2O_3 has been shown to allow alloying over the full range of *x*, unlocking tunable bandgaps over the range of 5.3 - 8.6 eV. One of the techniques available for growing α-$(Al_xGa_{1-x})_2O_3$ is molecular-beam epitaxy (MBE). MBE is a powerful and highly controllable growth technique for thin films with one drawback being its relatively slow growth rate. For high-quality β-Ga_2O_3 films grown by conventional MBE the growth rate may approach 0.2 µm/h. One method to circumvent the kinetic limitations of conventional MBE is the technique of suboxide MBE, which has been used to grow β-Ga_2O_3 thin films at rates exceeding 1 µm/h. This work investigates the application of suboxide MBE to the growth α-$(Al_xGa_{1-x})_2O_3$ thin films. We show that suboxide MBE leads to improved growth kinetics for III-O compounds, and enables the epitaxial growth of high-quality α-Ga_2O_3 and α-$(Al_xGa_{1-x})_2O_3$ thin films. This is demonstrated by the suboxide MBE growth of epitaxial α-$(Al_xGa_{1-x})_2O_3$ with high structural quality over the full range of x at growth rates exceeding 1 µm/h. For this suboxide MBE study, gallium suboxide and elemental aluminum were the MBE sources and A-plane sapphire was used as the substrate. During each growth the distilled ozone pressure (5 x 10^{-6} Torr) was held constant while the gallium suboxide flux and aluminum flux were varied to control the film composition. We show that the film composition can be controlled directly by the relative ratios of the Ga_2O and Al fluxes. Our films are shown to have high structural quality as revealed by the full width at half maximum (FWHM) of rocking curves of the α-$(Al_xGa_{1-x})_2O_3$ films ranging from 11 - 15 arcseconds; these FWHMs are identical to those of the underlying sapphire substrates. The surfaces of the films are also demonstrated to be smooth with RMS roughnesses measured by atomic force microscopy ranging from 0.3 - 1.1 nm on α-$(Al_xGa_{1-x})_2O_3$ films with thicknesses in the 17.8 - 47.8 nm range. Lastly, we confirm that the aluminum content of the α-$(Al_xGa_{1-x})_2O_3$ films cover the full range of $0 < x < 1$ with vacuum ultraviolet transmittance measurements showing that the bandgaps of our films shift with composition over the entire range of α-Ga_2O_3 to α-Al_2O_3.

9:00 AM V03

Optimizing Si Dopant Control in n-type β-Gallium Oxide Brenton A. Noesges[1,2], Yunjo Kim[2], Adam T. Neal[2], Shin Mou[2] and Thaddeus J. Asel[2]; [1]Azimuth Corporation, United States; [2]Air Force Research Laboratory, United States

Ultra-wide band gap (UWBG) materials such as β-Gallium Oxide (β-Ga_2O_3) are promising for high power electronic devices since breakdown voltage scales with band gap size. Within this material class, β-Ga_2O_3 is unique since β-Ga_2O_3 can be grown from the melt and demonstrates n-type conductivity with carrier concentration controllable between 10^{16} and 10^{20} cm^{-3} using shallow donors Ge, Si, or Sn [1]. However, achieving uniform doping profiles is not trivial in plasma-assisted molecular beam epitaxy (PAMBE). In this work, we will focus on optimizing uniform dopant profiles in the low Si doping regime of β-Ga_2O_3 films since Si doping occasionally shows gradient, increasing toward the surface of β-Ga_2O_3 thin films. We will also look at another aspect of Si incorporation in β-Ga_2O_3 that needs consideration when using traditional effusion cells as a Si dopant source. Previous work in β-Ga_2O_3 PAMBE growth demonstrated the importance of oxygen plasma power on controlling the background amount of Si present in β-Ga_2O_3 films [2]. This background Si reduction to the low 10^{17} cm^{-3} allows for greater control over doping concentration in the drift region of β-Ga_2O_3 devices. However, achieving uniform doping profiles has been challenging. In O- rich conditions with low Si cell temperatures (T_{Si}), Si concentrations ~$3x10^{17}$ cm^{-3} are achievable as demonstrated by time-of-flight secondary ion mass spectroscopy (TOF-SIMS). Capacitance-voltage (CV) measurements to extract carrier concentrations agree well with Si concentrations observed in TOF-SIMS. At these low concentrations, the Si concentration profile is not flat with a slight upward trend in Si content toward the film surface. The upward trend in Si content is even more apparent in Ga-rich conditions. This increase in dopant concentration toward sample surface may be problematic for electronic applications and we explored variations in growth parameters and post-growth treatments to create more uniform doping profiles. Another aspect of Si that we examined were sources of unintentional Si accumulation during the growth process. The presence of Si at the interface between β-Ga_2O_3 substrate and film provides a parasitic conduction channel which is problematic for device performance. Attempts have been made to remove this Si at β-Ga_2O_3 interfaces via etching. Our results indicate that removing interfacial Si may not be so simple since Si can re-accumulate in the PAMBE growth process which limits the effectiveness of pre-growth surface treatments. We created a test sample for TOF-SIMS simulating the effects of exposing clean β-Ga_2O_3 surfaces to potential sources of Si in a PAMBE including quartz plasma bulb and dopant Si effusion cells. Exposure to only quartz plasma bulb did not produce Si accumulation at the surface. On the other hand, a growth interrupt that exposed a fresh β-Ga_2O_3 to the hot Si source for several minutes produced Si accumulation equal to that of the interfacial Si between substrate and film. These results demonstrate that removing Si prior to loading into PAMBE may be inadequate to remove interfacial Si since Si can be re-introduced from the Si dopant cell during pre-deposition stages like plasma stabilization. This work and results point toward important challenges and potential solutions when creating Si-doped β-Ga_2O_3 thin films.

[1] Neal, A. T. et al. *Donors and deep acceptors in β-Ga_2O_3.* Appl. Phys. Lett. **113**, 062101 (2018).

[2] Asel, T. J., Steinbrunner, E., Hendricks, J., Neal, A. T. & Mou, S. *Reduction of unintentional Si doping in β -Ga_2O_3 grown via plasma-assisted molecular beam epitaxy*. J. Vac. Sci. Technol. A **38**, 043403 (2020)

9:20 AM V04

Demonstration of MOCVD Based *In Situ* Ga Etching of β-Ga_2O_3 Using TEGa Abishek Katta[1], Fikadu Alema[2], Will Brand[2], Andrei Osinsky[2] and Nidhin Kurian Kalarickal[1]; [1]Arizona State University, United States; [2]Agnitron Technology, United States

In this work, we report on the use of Triethyl Gallium for 'in-situ Ga etching' of β-Ga_2O_3 inside an MOCVD reactor. We demonstrate a maximum etch rate of ~8.5 μm/hr at a substrate temperature of 1000 °C and Ga flux of 140.47 μmol/min. In addition, low surface roughness of 2.9 nm was also obtained at a Ga flux of 6.05 μmol/min and substrate temperature of 800 °C.

The ultra-wide band gap semiconductor β-Ga_2O_3 (band gap=4.7 eV, breakdown field=8 MV/cm) has made rapid strides in terms of substrates, material quality and device performance over the last decade. Ga_2O_3 devices with performance exceeding that of SiC has already been demonstrated [ref]. Several promising device structures in β-Ga_2O_3 require the use of 3-D structures like fins and trenches. For fabrication of such structures in β-Ga_2O_3, dry etching using BCl_3/Ar has been widely used as the standard process. However, a key challenge when using dry etching is the induced subsurface damage. This has been shown to be significant in Ga_2O_3 resulting in charge depletion, reduction in channel mobility and increased sidewall roughness. In addition to dry etching, wet etching using HF, H_3PO_4 and KOH has also been reported. However, wet etching is found to mostly result in angled sidewalls which are not ideal. A promising etch technique for Ga_2O_3 is the use of suboxide formation upon exposure to Ga (Ga (s)+ Ga_2O_3 (s) Ga_2O (g)) at sufficiently high temperatures. Suboxide based etching of β-Ga_2O_3 performed in an MBE chamber was previously shown to result in low damage etching of Ga_2O_3 along with vertical sidewalls for fins and trenches [1]. In this work, we studied 'in-situ Ga etching' performed inside an MOCVD reactor using Triethyl Gallium (TEGa) precursor. At sufficiently high substrate temperature, TEGa undergoes cracking resulting in the deposition of Ga on the substrate surface while the remaining hydro-carbon group (C_xH_y) get pumped out of the chamber. The deposited Ga reacts with Ga_2O_3 forming volatile suboxide, resulting in etching. We studied the effects of various parameters like TEGa flow rate, substrate temperature (T_{sub}) and substrate orientation ((001) and (010)) on etch characteristics like etch rate and surface roughness. Substrate temperatures ranged from 650 °C to 1000 °C to determine the effect on etch rate and surface roughness. Pressure was held constant at 15 Torr throughout the experiments. Samples with a constant etch depth of ~300 nm was used to measure surface roughness using AFM. Gallium flux spanned from 3.63 μmol/min to 140.47 μmol/min to determine its effect on the previously stated etch characteristics. The etch rate was found to increase with substrate temperature from 1.8 m/hr at T_{sub}=700 to 3.7 m/hr at T_{sub}=1000 . The surface roughness of etched surfaces also decreased with increase in T_{sub} for both (010) and (001) Ga_2O_3 surfaces. As expected, etch rate was found to monotonically increase with TEGa flow rates both at T_{sub}=800 and T_{sub}=1000 . At a substrate temperature of 1000 and TEGa molar flow of 140.5 μmol/min, etch rates exceeding 8.5 m/hr was achieved. However, RMS roughness ((010) β-Ga_2O_3 surface) was also found to increase at high TEGa flow rates. Lowest surface roughness was obtained at low TEGa flow rates (<12 μmol/min) and T_{sub}=800 with the lowest obtained RMS roughness of ~2.8 nm. Patterned etching using SiO_2 hard mask was also demonstrated with a total etch depth of 2 m.

In conclusion, we demonstrate MOCVD-based 'in-situ Ga etching' using TEGa as the Ga source. Etch rates as high as 8.5 μm/hr was obtained at a substrate temperature of 1000 and TEGa flow rate of 140.47 μmol/min. In addition, low surface roughness <3 nm and patterned etching using SiO_2 as the hard mask is also demonstrated.

This work was supported by faculty startup fund from Arizona State University.

References: [1] Kalarickal, N. K., Applied Physics Letters, 119(12), 123503.

9:40 AM V05
Controllable Doping of MOCVD Ga_2O_3 with Nitrogen Using Ammonia Precursor Fikadu Alema[1], Takeki Itoh[2], Will Brand[1], Andrei Osinsky[1] and James S. Speck[2]; [1]Agnitron Technology, United States; [2]University of California, Santa Barbara, United States

The availability of various donor dopants to enable n-type conductivity in β-Ga_2O_3 has contributed to the fast-paced development seen over the last decade in epilayer growth and the realization of β-Ga_2O_3 based power devices. However, the possibility for p-type doping in Ga_2O_3 is bleak due to the small energy dispersion of the valance band and large effective masses in the valance band states[1]. Impurities such as magnesium (Mg), iron (Fe), and Nitrogen (N) were explored for p-type conductivity in Ga_2O_3, but all resulted in deep acceptors with ionization energies >1eV below the conduction band [2]. However, deep acceptors are also beneficial in engineering Ga_2O_3 power devices, and controllable and reproducible doping of these impurities into the films is vital. Fe and Mg have received considerable attention partly because of their success in GaN. However, one challenge both have in common is the surface riding and diffusion issue during the film growth, leading to their extension (tailing) into active layers that are not intended to be doped [3]. Less affected by thermal diffusion, nitrogen is an alternative to Mg and Fe deep acceptor dopants [4]. In the past, we extensively studied the MOCVD growth of nitrogen-doped Ga_2O_3 by using nitrous oxide (N_2O) as a source of nitrogen [5]. N_2O is used mainly as a source of oxygen to grow Ga_2O_3, but it can also dope the Ga_2O_3 layers with N. The incorporation efficiency of N depends on process conditions. Despite the two-fold benefit of N_2O, the sensitivity of the N incorporation to the growth process makes it challenging to realize the controllable doping of N into Ga_2O_3. Besides, the H impurity accompanies N in the N_2O-grown layers, which is undesirable as H potentially compensates N.
In this work, we report on controllable doping of N into Ga_2O_3 using ammonia diluted in nitrogen (NH_3/N_2) as a source for N. Ammonia (NH_3) is commonly used as a nitrogen precursor for the growth of nitride materials. It decomposes at a relatively low substrate temperature (~600 ºC), producing active nitrogen species that react with the metalorganic sources to deposit the nitride films. The requirement of low cracking temperature also makes ammonia a good candidate for its use in the nitrogen doping of Ga_2O_3. The incorporation efficiency, reproducibility, and controllability of N doping into Ga_2O_3 films were studied by varying the molar flow rates of NH_3/N_2. The concentration of N incorporated into the films was measured by SIMS. With the increase in the NH_3/N_2 molar flow rate from ~1.8×10^{-8} mol/min to 1.45×10^{-6} mol/min, the N impurities incorporated into the β-Ga_2O_3 layers increased from ~1×10^{18} cm^{-3} to ~2×10^{20} cm^{-3}. The doping of N into Ga_2O_3 using an ammonia source is found to be controllable through the molar flow rate and reproducible, as confirmed by repeated processes. Nonetheless, similar to the N_2O-based doping of Ga_2O_3, H incorporation into the film along with N was observed in ammonia-based doping when the film growth is conducted at a low substrate temperature (<800 ºC). But, the electrical characterization performed on N and H co-doped films showed no effect of H on the compensative behavior of N as the co-doped films remained resistive, with a resistance of > 100 MΩ. Increasing the growth temperature by ~150 ºC, the hydrogen incorporation in the films has reduced by ~10× with no effect on the incorporation of N. In this paper, we will also discuss the use of NH_3/N_2 to nitride the surface of the Ga_2O_3 substrate and compensate for the Si impurity commonly observed at the film/substrate interfaces.
[1] H. Peelaers *et.al.* Phys.Status solidi (b) **252**, 828 (2015)
[2] A.T. Neal *et al.* Appl. Phys. Lett.**113**, 062101 (2018).
[3] A. Mauze *et.al.* Appl. Phys. Lett. **115** 052102 (2019).
[4] M.H. Wong *et.al.* Appl. Phys. Lett. **113** 102103 (2018)
[5] F. Alema *et.al.* etal APL Materials **8**, 021110 (2020).

10:00 AM BREAK

10:20 AM V06
Vertically Aligned β–$Ga_{2-X}W_XO_3$ Nanocomposites for Ultrafast Deep-UV Photodetectors Debabrata Das, Francelia S. Escobar and Ramana Chintalapalle; The University of Texas at El Paso, United States

There is an ever-increasing demand for energy-efficient multifunctional sensors or transducers based on low-cost and environmentally acceptable material systems. This demand is a direct result of the remarkable improvement of current technology, which has led to an increase in energy consumption. In this context, we describe a self-assembled vertically aligned β–$Ga_{2-X}W_XO_3$ nanocomposite (GWO-VAN) architecture-assisted ultrafast deep-ultraviolet (DUV) photodetection on a silicon platform. Silicon has traditionally served as the core of traditional electronics. By carefully controlling the growth settings, it was possible to demonstrate the growth of W-enriched vertical β–$Ga_{2-X}W_XO_3$ nanocolumns contained within a W-deficient β–$Ga_{2-X}W_XO_3$ matrix on a silicon substrate. The presence of a nanocomposite of β–$Ga_{2-X}W_XO_3$ with a high structural and chemical quality has been confirmed by detailed structural and morphological investigations. In addition, absorption and photoluminescence spectroscopy are able to describe photo-absorption dynamics as well as the recombination process through the use of various donor-acceptor energy levels. The GWO-VAN architecture makes it possible to have equally scattered nanoregions with asymmetric donor energy state distribution, which ultimately results in the formation of build-in potential at those vertical β–$Ga_{2-X}W_XO_3$ interfaces. Under UV irradiation, the heterostructure displays the characteristics of a photovoltaic cell. A responsivity of ~30 A/W is seen alongside an ultrafast response time of ~350 microseconds under transient triggering. The corresponding detectivity and efficiency values are 7.9×10^{12} Jones and 1.4×10^{4} %, respectively. The implications of the aforementioned approach are enormous in terms of designing electronic devices for extreme environment applications and have immense potential to demonstrate a significant improvement in low-cost UV photodetector technology.

10:40 AM V07
(Student) Investigation of Phase Transition and Bandgap Engineering in $(Mg_xGa_{1-x})_2O_3$ Thin Films Grown by Molecular Beam Epitaxy Tianchen Yang, Chengyun Shou, Abdullah Almujtabi, Yuan Li, Quazi S. Mahmud and Jianlin Liu; University of California, Riverside, United States

$(Mg_xGa_{1-x})_2O_3$ alloys with bandgap energy from ~5.0 to ~6.0 eV can provide opportunities for optoelectronics in deep ultraviolet spectral range and electronics with extremely high critical field strength. It is important to grow high-quality $(Mg_xGa_{1-x})_2O_3$ alloys with varied Mg compositions and understand their structural, optical and electrical properties. In this project, $(Mg_xGa_{1-x})_2O_3$ ternary alloy thin films of different Mg concentrations were grown by using oxygen plasma assisted molecular beam epitaxy (MBE). The atomic ratios of Mg and Ga from sample 1 to sample 20 were recorded from 0 at.%/100 at.% to 100 at.%/ 0 at.% separately, which were measured by energy-dispersive X-ray spectroscopy (EDX). The lattice structures, which have transformed from β-phase in Ga-rich materials, to beta and rock salt mixture phase in high-Ga high-Mg alloys, and to pure rock salt phase in Mg-rich alloys, were investigated by high resolution x-ray diffraction (HR-XRD) and reciprocal space mapping (RSM). The change of film quality and lattice parameter with different Mg at.% was revealed. Surface morphology was characterized by atomic force microscopy (AFM), and the change of surface roughness with Mg at.% was recorded. Ultrawide bandgap absorption and transmittance spectra were measured using a high-performance UV-Vis-NIR spectrophotometer. Bandgap tuning from 5.03 eV to 5.89 eV was achieved, and all samples have the transmittance over 90% in the visible spectral range.

11:00 AM V08
(Student) Improving Quality of β–Phase MgGaO Thin Films by Using Low-Temperature Homo-Buffer Layer Chengyun Shou[1], Tianchen Yang[1], Abdullah Almujtabi[1], Theodore Yang[2], Yuan Li[1] and Jianlin Liu[1]; [1]University of California Riverside, United States; [2]Martin Luther King Jr.high school, United States

Ultra-wide bandgap semiconductors are promising for many applications such as power electronics and deep-UV photonics. With a bandgap of ~4.9 eV, Gallium Oxide (Ga_2O_3) has drawn much attention recently. To improve film quality, a low-temperature buffer layer is commonly used. In this research, wider bandgap β-phase Magnesium Gallium Oxide (MgGaO) alloys were grown in a plasma-assisted molecular beam epitaxy system. The relationship between growth temperature and thickness of low-temperature buffer layer and the quality of active layer was studied by X-ray diffraction (XRD) and by analyzing metal-semiconductor-metal (MSM) photodetector devices based on these films. Low-temperature homo-buffer layers with a growth temperature of 300-500 °C and a thickness of 0-40 nm, respectively, were deposited on *c*-sapphire substrates, followed by two-hour active layer growth at a temperature of 650 °C. Scanning electron microscope (SEM) and atomic force microscope (AFM) were used to analyze the surface morphology. Energy dispersive X-ray spectroscopy (EDX) was used and the average composition for Ga and Mg is 85 at. % and 15 at. %, respectively. Bandgaps were extracted from the Tauc plot with a value of 5.1 eV for all samples. X-ray diffraction results show all samples are oriented -phase MgGaO. The X-ray rocking curve measurement shows that the full width at half maximum (FWHM) increases as the buffer layer thickness increases, and this may be due to the poor quality of the buffer layer. Current-voltage measurement for the interdigitated electrode photodetectors shows that the current increases as the low-temperature buffer layer increases. Photocurrent decay time increases as the buffer layer thickness increases, indicating that the quality of the active layer improves. Recombination of photo-generated electrons and holes is reduced with fewer defects in the active layer, resulting in a larger current under illumination and a longer photocurrent decay time.

11:20 AM V09
(Student) Effect of Post-Deposition Annealing on Crystal Structure of RF Magnetron Sputtered Germanium Dioxide Thin Films Ahmad M. Abed and Rebecca L. Peterson; University of Michigan–Ann Arbor, United States

Germanium dioxide (GeO_2), an ultra-wide bandgap (UWBG) oxide semiconductor, has recently gained attention for high-power applications due to its excellent thermal and electrical properties [1]. GeO_2 has two polymorphs (hexagonal and tetragonal phases), both of which are UWBG semiconductors. Recently it has been reported that rutile (tetragonal) GeO_2 has a high thermal conductivity and ambipolar doping capability [2,3]. These make *r*-GeO_2 a great candidate for efficient heat management and device applications. However, the synthesis of GeO_2 has been challenging due to its polymorphism, with multiple phases having a similar free energy of formation, which increases the formation of deeply metastable states [4]. In this work, we establish methods to grow and phase stabilize hexagonal or tetragonal polycrystalline GeO_2. GeO_2 thin films were deposited using radio frequency magnetron sputtering (RFMS) on *r*-plane Al_2O_3 substrates. Following sputtering, post-deposition annealing (PDA) was performed at temperatures between 650ºC and 950ºC in an oxygen or nitrogen ambient. To study the chemical, optical, and structural nature of the films, x-ray diffraction (XRD), scanning transmission electron microscopy (STEM), energy-dispersive X-ray spectroscopy (EDS), atomic force microscopy (AFM), and optical spectroscopy (UV−vis) were performed. For the annealing ambient and deposition conditions explored, annealing at temperatures from 750ºC to 950ºC resulted in polycrystalline films of mixed phases of tetragonal GeO_2, hexagonal GeO_2, and/or cubic (diamond) Ge. Grazing angle XRD showed a preferred orientation of (220) *r*-GeO_2 aligned to the (1-102) Al_2O_3 for all conditions in this anneal temperature range. When nitrogen was used as the anneal ambient, mixed GeO_2 phases result for all annealing temperatures studied. In contrast, oxygen annealing promoted stabilization of the tetragonal GeO_2 phase. The combination of O_2 annealing and O_2 flux of 20% during growth resulted in tetragonal GeO_2 films with highly preferential alignment, the best out of all samples studied. Hexagonal-oriented GeO_2films were observed with epitaxial alignment to the *r*-plane sapphire substrate. We observed that an epitaxial hexagonal GeO_2 film at the interface helped stabilize a top polycrystalline tetragonal GeO_2 film. These results show that fine-tuning the oxygen flux during growth and PDA in O_2 ambient facilitates the stabilization of phase-pure tetragonal GeO_2 film. This work provides a path to achieving stable tetragonal phase GeO_2 thin films for future UWBG devices.
[1] S. Chae, J. Lee, K.A. Mengle, J.T. Heron, and E. Kioupakis, Appl. Phys. Lett. 114, 102104 (2019).
[2] S. Chae, K.A. Mengle, R. Lu, A. Olvera, N. Sanders, J. Lee, P.F.P. Poudeu, J.T. Heron, and E. Kioupakis, Appl. Phys. Lett. 117, 102106 (2020).
[3] S. Chae, K. Mengle, K. Bushick, J. Lee, N. Sanders, Z. Deng, Z. Mi, P.F.P. Poudeu, H. Paik, J.T. Heron, and E. Kioupakis, Appl. Phys. Lett. 118, 260501 (2021).
[4] S. Chae, H. Paik, N.M. Vu, E. Kioupakis, and J.T. Heron, Appl. Phys. Lett. 117, 072105 (2020).

SESSION W: III-Nitrides—Late News
Session Chairs: Russell Dupuis and Jimy Encomendero
Thursday Afternoon, June 29, 2023
Music Building, Lotte Lehmann

1:50 PM W01
(Late News) Impact of Cap Layer Thickness on Ga- and N-Polar Microstructure Photocathodes Emma Rocco[1], Shadi Omranpour[1], Vincent E. Meyers[1], Benjamin McEwen[1], Alireza Lanjani[1], L. D. Bell[2] and Fatemeh (Shadi) Shahedipour-Sandvik[1]; [1]SUNY Polytechnic Institute, Colleges of Nanoscale Science and Engineering, United States; [2]California Institute of Technology, United States

Photocathodes are commonly employed as detectors for astronomy and defense applications, as well as in high-energy physics as high-brightness electron sources. The III-nitride material system is ideal for such applications due to the wide and tunable bandgap energy, radiation hardness and chemical stability. III-nitride photocathodes, consisting of a p-type bulk, are commonly activated with cesium (Cs) to achieve effective negative electron affinity (NEA) and high device quantum affinity (QE). In our initial demonstration of Cs-free GaN photocathodes, we showed that a highly doped thin n++ GaN layer is necessary to achieve a narrow surface potential well and large downward band bending. To achieve such high doping in a thin (1-2nm) GaN results in degradation in quality and increase in carrier scattering, resulting in substantial drop in QE. We have shown that this limitation can be overcome by utilizing N-polarity of GaN. In this case, the aligned polarization and depletion charges at the surface allow for an unintentionally doped GaN cap layer to be utilized to achieve a theoretically predicted effective NEA. Experimental studies of N-polar GaN photocathodes show improved QE for samples grown on GaN templates with a high density of hexagonal hillock structures. Atom probe tomography reveals improved Mg-incorporation efficiency within the semi-polar facets of the hillock structures, leading to increased p-type characteristics.
To investigate the dependency of photocathode QE on Mg incorporation in semi-polar planes, along Ga- and N-polar directions, we have developed selective area grown GaN photocathodes. Photocathodes are hot carrier devices. Previously we have shown cap layer thickness trending with emission intensity in planar Ga-polar photocathode devices, due to higher scattering in thicker cap layers [1]. Here we investigate the cap layer thickness on the varied planes of

Ga- and N-polar microstructure photocathodes grown by metal organic chemical vapor deposition (MOCVD) and the impact on device performance. Flat top pyramid structures with semi-polar sidewalls were grown by a selective area growth (SAG) technique on Ga- and N-polar GaN templates. For the SAG growth, a 50 nm SiO_2 mask was utilized and 9 µm circles opened by photolithography. Following SAG the SiO_2 mask was removed by buffered oxide etch. Photocathode structures were then grown conformally over the microstructures. Three photocathode structures were studied; (1) GaN:Mg, (2) GaN:Mg with 30 sec of UID GaN cap growth and (3) GaN:Mg with 60 sec of UID GaN cap growth. Both Ga-polar and N-polar GaN:Mg microstructure photocathodes achieved a maximum QE of 2.7% at 6 eV photon energy. The addition of a thin UID GaN cap (30 s) on the N-polar GaN:Mg increased the QE to 3.16%, with thicker UID GaN cap (60s) leading to a further increase of 3.40% at 6 eV, representing the highest reported QE for Cs-free III-nitride microstructure photocathode. In SEM, evolution of v-pits is observed with increasing cap layer growth time. We will discuss the photocathode device performance including QE and threshold energy, and the relation with cap layer growth time.
[1] N. Tripathi, *et al.*, *Appl. Phys. Lett.*, **97**, 052107 (2010).

2:10 PM W02
(Student, Late News) Investigation of Si Doping in N-Polar AlN by Plasma Assisted Molecular Beam Epitaxy Md Irfan Khan and Elaheh Ahmadi; University of Michigan–Ann Arbor, United States

In this study, we present the investigation of Si doping of N-polar AlN films grown on single crystal AlN substrate by plasma assisted molecular beam epitaxy (PAMBE). Through optimization of growth condition, we obtained high quality N polar AlN films at 950ºC. However, to our surprise, our studies revealed that Si incorporation dramatically decreases at such high growth temperature, making it impossible to obtain doping concentrations beyond $5x10^{17}$ cm^{-3}. To enable higher silicon incorporation, low-temperature growth of high quality AlN films was developed using Ga as surfactant. By lowering the growth temperature of AlN to 750ºC we were able to incorporate Si with concentrations as high as $1x10^{20}$ cm^{-3} and demonstrate an electron concentrations as high as $1.4x10^{18}$ cm^{-3}. This work is the first demonstration of conductive N-polar AlN films.

2:30 PM W03
(Late News) Nanometer-Resolution Piezoelectric Probing for Vertical Top-Down GaN Nanowire Field Emitter Devices with Integrated Leveling Georgios Doundoulakis and Dimitris Pavlidis; Florida International University, United States

Nanoscale vacuum field emission (FE) devices based on GaN nanowires (NWs) are expected to combine the advantageous features of solid-state semiconductor devices with those of vacuum electronics [1-4], in conjunction with the high aspect ratio and reduced dimensionality of NWs and the advanced material properties of GaN [1-2]. Their performance relies on NW formation with minimum surface damage and well-defined cylindrical shape, while their accurate evaluation requires nanometer resolution probing. This paper reports the nanometer-resolution probe characterization of FE NW devices with a leveling structure made of the same material. Details on test structure design and fabrication are also provided.
The FE devices (FEDs) used for nanoscale characterization were designed based on previously established design rules reported by the authors [4]. An epitaxial 2 µm thick n+ GaN (10^{18} cm^{-3}) structure grown on a sapphire substrate was used. NW formation started by EBL patterning using a Ni etch-mask. Then photolithography was used for forming a 4-segment circular reference structure (inner and outer diameter of 0.9 mm and 1.3 mm, respectively), with the FE device enclosed in it. A key to the successful nanometer characterization is monitoring of electric conduction through the 4-segments, which provides the possibility of controlling the X-Y orientation of the FEDs and leveling it with respect to the anode probe. The 500 nm height GaN trapezoidal structures and the 4-segment circular "mesa" structure were formed by RIE. In order, to reduce RIE surface damage and obtain the desired cylindrical shape of NW, a TMAH-based wet etching was performed. Uniform GaN NWs of 170 nm diameter were obtained. Afterwards, the Ni-based masks were removed by wet etching and Ti/Al/Ni/Au Ohmics were deposited as the Cathode contacts. Finally, 100 nm thick Ni/Au was deposited on the 4-segment circular "mesa" structures and vertical top-down GaN NW FEDs with Integrated Leveling could be realized in this way.
The devices were characterized in a vacuum chamber (~5 x 10^{-5} Torr) equipped with a custom-made nanoresolution piezoelectric stage controller for probe control. A special procedure was established to "calibrate" the system for nanometer capability. First, a conventional probe tip was placed in contact with the Cathode. Then, a 1 mm diameter cylindrical probe tip was moved downwards to reach the reference "mesa" structure. The presence of electrical conduction allowed to find the reference value at which the cylindrical probe tip was in contact with the 100 nm thick Ni/Au metal. One could in this way position the probe acting as anode at 100 nm above the GaN NWs. 4-segment electrical control allowed at this point leveling verification and adjustment while protecting the GaN NWs from damage upon testing. Finally, the piezoelectric controlled probe tip was moved 1.9 µm upward and placed 2 µm above the GaN NWs. The I-V characteristics of the GaN NWs with Anode to NW distance of 2 µm exhibit a maximum current density of ~0.6 A/cm^2 at 100 V using a total number of 22500 (150x150) NWs with 1 µm pitch. The device turn-on voltage was ~70 V. The obtained results demonstrate the feasibility of evaluation of GaN NW-based FE devices using a new integrated leveling approach for nanometer-resolution piezoelectric controlled probing. The technique can also be utilized for the characterization of other materials and devices at the nanoscale.
The AFOSR support through the FERVIN Award FA9550-19-1-0349 is greatly acknowledged. The authors would like to thank T. Mirabito and Prof. J.M. Redwing from Penn State University for their assistance with RIE processing.
References: [1] N. Chowdhury et al., IEEE Elec. Dev. Lett., vol. 38, no. 7, p. 859 (2017); **[2]** G. Doundoulakis et al., Nanotech., vol. 30, no. 28, p. 285304 (2019); **[3]** A. Evtukh et al., Vac. Nanoelec. Dev., Hoboken, NJ, USA: Wiley (2015); **[4]** G. Doundoulakis and D. Pavlidis, IEEE TED vol. 68, no. 6, pp. 3034 (2021)

2:50 PM W04
(Late News) Characterization of the Space-Charge Region of a GaN *pn*-Junction and *pin*-Drift-Diode Using EBIC and CL Holger Eisele[1], Konstantin Wein[1], Frank Bertram[1], Gordon Schmidt[1], Juergen Christen[1], Armin Dadgar[1], Christoph Berger[1], André Strittmatter[1], Arne Debald[2,3], Michael Heuken[2,3], Thorsten Zweipfennig[3], Holger Kalisch[3], Andrei Vescan[3], Samuel Faber[4] and Bernd Witzigmann[4]; [1]Otto von Guericke Universität Magdeburg, Germany; [2]Aixtron SE, Germany; [3]RWTH Aachen University, Germany; [4]Friedrich-Alexander-Universität, Germany

GaN is currently emerging as the semiconductor of choice for energy efficient power devices in power-grid and electro-mobility applications. GaN based power devices exhibit faster switching and lower on-resistance than conventional silicon and silicon-carbide based ones. Significant progress has been achieved for the unipolar limit of breakdown voltage and on-resistance of GaN material. Nevertheless, the investigation of the local electronic and optical properties is of vital importance to comprehensively understand and improve such devices and their specific designs. Here, combined cathodoluminescence (CL) and electron beam induced current (EBIC) measurements on fully processed GaN diodes are applied to probe the internal electrical fields and to characterize carrier transport dynamics. Further insight is gained from correlating them to the growth and the process parameters of the GaN diodes. Such (Al,In)GaN homo- and heterostructures are based on polar materials with strong internal electric fields generated by their spontaneous polarization and by the doping profiles of the ionized acceptors and donators. These studies complemented by physical modelling techniques will generate a deep

understanding of how novel device designs work as well as the impact of defects and processes on the macroscopic material, interface and device properties will lead to novel strategies to fabricate high-performance junctions for GaN-based power devices.
As a first example for EBIC analysis on GaN homojunctions, temperature dependent EBIC measurements of a *pin*-diode with very long drift region are compared with a regular GaN *pn*-diode as a reference. While the doping concentration of the *pn*-diode is of about 7 x 10^{17} cm^{-3} in the n^--region, it is only 1 x 10^{16} cm^{-3} in the *i*-GaN of the *pin*-diode. The low-temperature CL linescan across the active region of the sample layer stack directly determine the exact vertical position of the p^+ and low-doped n^--drift regions. Different temperatures lead to a specific ionization of dopants and impurities, which determine the space charge region and therewith the distribution of the internal electric field. The transport of excess carriers (drift and diffusion) is dominated by temperature dependent diffusion length of the minority carriers. At room temperature the *pn*-junction exhibits a cross-sectional EBIC profile determined mainly by a broad Bethe excitation range of the scanning electron microscope (SEM) as well as transport of the minority charge carriers on both sides of the junction. While the primary excitation range results in a peak for the EBIC signal at the *pn*-junction with a lateral extension of 186 nm, the additional diffusion lengths of both charge carriers is of about 50 nm on both sides. For the *pin*-junction with a drift region thickness of about 12 µm we achieve similar results for the EBIC peak. Here, an additional second peak is visible in the p^+-region, originating from the Schottky-like contact of the p^+-region with the metallic contact layer on top. More important, in contrast to the *pn*-diode reference, a long tail of the EBIC signal is present, exponentially decaying across the almost intrinsic, extremely low n^--doped drift region of the *pin*-diode. From the slope of this tail, decay lengths of 1.8 µm and 2 µm for temperatures of 300 K and 180 K are determined, respectively.
We demonstrate that the EBIC signal of GaN *pn*-junctions and *pin*-diodes, correlated with CL measurements, exhibits detailed local device parameters, especially the diffusion lengths of the minority charge carriers and the Debye-length within the extremely low *n*-doped *i*-GaN drift region. The decay of the EBIC signal in the low n^--doped *i*-GaN region with doping concentrations of around 10^{16} cm^{-3} is consisted with the carrier lifetimes

SESSION X: Group III–Nitrides—Growth and Characterization
Session Chairs: Matthew Hardy and Brian Rummel
Thursday Afternoon, June 29, 2023
UC, Corwin East

1:30 PM X01
Computational Fluid Dynamics Modeling of a Novel High-Pressure Spatial Chemical Vapor Deposition Reactor (HPS-CVD) Design for Growth of Indium-Containing Nitrides Hooman Enayati and Siddha Pimputkar; Lehigh University, United States

Epitaxial growth of high-indium-content nitrides, such as $In_{1-x}Ga_xN$ or $Al_xIn_{1-x}N$, is challenging due to the relatively low dissociation temperature of InN into indium metal and nitrogen gas necessitating growth temperatures which are sub-optimal for growth of device-quality films.[1] Increasing the gas pressure (up to 15 atm) within a horizontal flow metal-organic chemical vapor deposition (MOCVD) tool has been shown to be effective at increasing the growth temperature of InN and at increasing the indium incorporation at a certain growth temperature.[2] Unfortunately, higher pressures and resultingly higher fluid densities result in fluid dynamic and heat transfer challenges which result in turbulence and loss of group-III source material prior to incorporation on the substrate.
To address the fluid dynamic challenges associated with high-pressure MOCVD growth of (nitride) materials, a new MOCVD reactor has been proposed which carries the potential to operate at super-atmospheric pressures (up to 100 atm).[3] Key to this innovative design is the spatial separation of precursors prior to mixing in the boundary layer immediately above the substrate.
This contribution will discuss the current state of development of this tool via a discussion of computational fluid dynamic simulations performed using the computational fluid dynamics software, COMSOL Multiphysics. Fully coupled flow and thermal studies of this novel high-pressure spatial chemical vapor deposition (HPS-CVD) tool will be presented and suitable operating windows for super-atmospheric conditions discussed to highlight the viability of this platform.
References:
[1] Yamamoto, A., Sugita, K. & Hashimoto, A. Elucidation of factors obstructing quality improvement of MOVPE-grown InN. *J Cryst Growth* **311**, 4636–4640 (2009).
[2] Dietz, N. *et al*. The growth of InN and related alloys by high-pressure CVD. *Proceedings of SPIE* **5912**, 59120E-59120E–8 (2005).
[3] Yousefian, P. & Pimputkar, S. Computational fluid dynamics modeling of a new high-pressure chemical vapor deposition reactor design. *J Cryst Growth* **566**, 126155 (2021).

1:50 PM X02
Characterization of Growth Sectors in Patterned HVPE Gallium Nitride Substrate Wafers Yafei Liu, Shanshan Hu, Qianyu Cheng, Zeyu Chen, Balaji Raghothamachar and Michael Dudley; Stony Brook University, The State University of New York, United States

Gallium Nitride (GaN) is one of the most promising wide band gap semiconductor materials that are replacing silicon (Si) in power electronic applications. However, the quality of the material is limiting its application in high performance power electronic materials. Several bulk crystal growth methods have been developed including physical vapor transport (PVT) method [1, 2], Na-flux method [3], ammonothermal method [4, 5], and hydride vapor phase epitaxy (HVPE) method [6]. Moreover, patterned HPVE growth methods template [7] have been developed to further lower the dislocation densities. The patterned growth method can concentrate dislocations to small areas leaving the remaining regions relatively dislocation-free (< 102 cm-2), which makes it very promising in the application of power device fabrication.
The microstructures of ammonothermal and HVPE grown GaN substrates have been characterized in our previous studies [8-10]. In patterned HVPE grown method, it is reported that growth sectors exist due to growth along different directions [11]. The shape of growth sectors matches the domain regions observed in patterned hydride vapor phase epitaxy (HVPE) GaN substrate by synchrotron X-ray topography (XRT) (Figure 1(a)). Information on the nature of these domain areas is important as these regions are low dislocation density regions in which the devices are supposed to be fabricated.
In this study, synchrotron X-ray plane-wave topography (SXPWT, previously known as synchrotron X-ray rocking curve topography), scanning electron microscopy (SEM), and transmission electron microscopy (TEM) are adopted to investigate the nature of the growth sectors visible as area contrast in patterned HVPE grown GaN wafers. The same domain features observed in XRT images can be correlated in the strain map generated by SXPWT (Figure 1(b)) as well as in the SEM image using a Robinson detector (RBSD) (Figure 1(c)). This result suggests that the domains have relative compressive strain values caused by different impurity incorporation rate in different growth sectors. SIMS measurements are currently being carried out to compare the impurity concentrations in these domains. These results will be discussed to confirm the origin of the strain.
[1] H. Wu, J. Spinelli, P. Konkapaka, M. Spencer, MRS Online Proceedings Library Archive 892 (2005).
[2] D. Siche, D. Gogova, S. Lehmann, T. Fizia, R. Fornari, M. Andrasch, A. Pipa, J. Ehlbeck, Journal of crystal growth 318 (2011) 406-410.

[3] M. Aoki, H. Yamane, M. Shimada, S. Sarayama, F.J. DiSalvo, Journal of crystal growth 242 (2002) 70-76.
[4] R. Dwilinski, R. Doradzinski, J. Garczynski, L. Sierzputowski, A. Puchalski, Y. Kanbara, K. Yagi, H. Minakuchi, H. Hayashi, Journal of Crystal Growth 310 (2008) 3911-3916.
[5] T. Hashimoto, F. Wu, J.S. Speck, S. Nakamura, Journal of Crystal Growth 310 (2008) 3907-3910.
[6] H.P. Maruska, J. Tietjen, Applied Physics Letters 15 (1969) 327-329.
[7] T. Nakamura, K. Motoki, GaN substrate technologies for optical devices, IEEE, vol 101, 2013, p. 2221.
[8] B. Raghothamachar, Y. Liu, H. Peng, T. Ailihumaer, M. Dudley, F.S. Shahedipour-Sandvik, K.A. Jones, A. Armstrong, A.A. Allerman, J. Han, H. Fu, K. Fu, Y. Zhao, Journal of Crystal Growth 544 (2020) 125709.
[9] Y. Liu, B. Raghothamachar, H. Peng, T. Ailihumaer, M. Dudley, R. Collazo, J. Tweedie, Z. Sitar, F.S. Shahedipour-Sandvik, K.A. Jones, Journal of Crystal Growth 551 (2020) 125903.
[10] Y. Liu, H. Peng, T. Ailihumaer, B. Raghothamachar, M. Dudley, Journal of Electronic Materials 50 (2021) 2981-2989.
[11] K. Motoki, T. Okahisa, S. Nakahata, N. Matsumoto, H. Kimura, H. Kasai, K. Takemoto, K. Uematsu, M. Ueno, Y. Kumagai, Journal of Crystal Growth 237 (2002) 912-921.

2:10 PM X03
(Student) Wing Tilt in ELO-Grown GaN Jack Almeter[1], Ronny Kirste[1,2], Seiji Mita[1,2], J. Houston Dycus[3], James Tweedie[1,2], James Loveless[1], Pramod Reddy[1,2], Ramón Collazo[1] and Zlatko Sitar[1,2]; [1]North Carolina State University, United States; [2]Adroit Materials, United States; [3]Eurofins EAG Advanced Imaging, United States

Epitaxial lateral overgrowth (ELO) is an established technique for the reduction of the high threading dislocation density of GaN grown on sapphire substrates. ELO is typically carried out via a selective area growth process with stripes of SiO_2 as a mask. While the benefits of ELO were instrumental in the development of early GaN optoelectronics, the phenomenon known as "wing tilt" is a longstanding drawback. So-named due to the crystallographic tilt induced in the "wing" regions above the SiO_2 mask, the effect is associated with a tilt boundary at the coalescence boundary. While various approaches have been suggested to mitigate the impact of wing tilt, there is not currently a scheme to eliminate the effect.
In this study, we demonstrate that wing tilt is a direct result of the use of the SiO_2 mask, and that the tilt occurs even before coalescence. We also demonstrate GaN layers free of wing tilt using a mask-free facet-controlled ELO (FACELO) scheme. For this investigation, ammonothermally grown bulk GaN substrates were used. One template was prepared for traditional ELO with SiO_2 stripes of 2 µm separated by windows of 2 µm for a period of 4 µm; another template was prepared with a mask-free pattern by etching trenches of 2 µm width and depth, leaving behind 2 µm stripes. Both templates had stripes oriented along the *m*-direction of GaN. As the first step in the ELO growth scheme, these templates were grown at a low temperature (950 °C) to promote the evolution of semipolar facets, resulting in triangular cross-sections over the stripes. The second growth step to achieve *c*-plane coalescence was then performed at a higher temperature (1100 °C). The samples were characterized at both steps via SEM and XRD, as well as TEM after coalescence. The (002) ω-rocking curve of the SiO_2-grown triangles shows symmetric satellite peaks about the main peak characteristic of wing tilt. Additionally, the FWHM of the peak has increased from 40 arcsec for the substrate to 150 arcsec for the regrown structure. This result shows that even before coalescence, the growth of GaN over SiO_2 results in a change in crystalline quality. After coalescence, the FWHM of the peak increases to 180 arcsec, a value suggesting a threading dislocation density in the high 10^8 cm^{-2} range. By contrast, the maskless sample shows no satellite peaks in the (002) ω-rocking curve, and at both steps the FWHM of the original template is maintained. The findings of the XRD are confirmed via TEM. In epitaxial layers above the SiO_2 patterned sample, a significant density of dislocations can be seen. By contrast, the maskless sample showed no visible dislocations. We therefore conclude that wing tilt and its associated dislocations are caused by the presence of the SiO_2 mask, and that by use of a maskless etched template, these deformations and defects can be avoided.

2:30 PM X04
(Student) Structural Analysis and Observation of Tilts, Twists and Crystallographic Orientation of High-Quality, Metal Rich Grown $Sc_{0.2}Al_{0.8}N$ Keisuke Motoki, Zachary Engel, Christopher M. Matthews, Sangho Lee, Emily N. Marshall and W. Alan Doolittle; Georgia Institute of Technology, United States

ScAlN alloys are promising due to their high spontaneous and piezoelectric polarizations and ferroelectric properties for various technologies including high electron mobility transistors (HEMTs), acoustic devices, etc. Despite the common belief that Molecular Beam Epitaxy (MBE) synthesis requires N-rich conditions to avoid metallic phase inclusions, our previous studies[1,2] have demonstrated that the metal modulated epitaxy (MME) allows growth of state-of-the-art structural quality ScAlN in metal-rich conditions at a low substrate temperature (T_{sub}) of 400 °C by using precise control of metal adlayer buildup. Additionally, these previous studies found an extremely unusual feature wherein, a significant catalytic effect of Sc leads to more available nitrogen and thus, ~3x faster growth rates when Sc is present in large coverages on the surface. Accounting for this critical new feature, MME allows improved crystal quality by x-ray diffraction (XRD) figures of merit and surface roughness as low as 250 arcsec and 0.73 nm, respectively. The HEMT structure in the previous studies have shown an improved sheet resistance of 152 W/■, a mobility of 700 cm^2/Vs, and a sheet charge of 5.9 x 10^{13} cm^{-2} which is near the theoretical limit, exhibiting MME's great potential for ScAlN HEMT applications. Although the optimization of III/V ratio and growth temperature was done in the previous studies[1,2], the structural properties of ScAlN are not well investigated yet especially for the MME grown films which involves low-growth temperature. The present transmission electron microscopy (TEM) study contrasts the unique characteristics of MME grown $Sc_{0.2}Al_{0.8}N$ at low T_{sub} of 400 °C, and 650 °C without metallic inclusions and 600 °C samples that showed the metallic inclusions. Significant twist is present in the 600 °C grown sample that is absent in the 400 °C sample.
MME $Sc_{0.2}Al_{0.8}N$ were grown on MME GaN on hydride vapor phase epitaxy (HVPE) GaN templates on c-plane sapphire substrates as described elsewhere[1,2], using plasma-assisted molecular-beam-epitaxy (PA-MBE). TEM and four-dimensional scanning TEM (4D-STEM) are employed to evaluate the structural properties. The cross-sectional sample is prepared by focused ion beam (FIB) under cryogenic temperature. TEM images close to the zone axis, and for the sample with T_{sub} = 400 °C show better film quality than the two higher temperature samples, having distinctive contrasts of dislocations. The 600 °C sample showed complicated and dense contrasts. This fact correlates with the previous results in XRD 2θ-ω scans indicating that the 600 °C sample had inclusions of Al_3Sc phases, which are not present in the other two samples. AFM also showed smoother surface roughness for the 400 °C sample other samples.[1,2] Local diffraction patterns (DPs) obtained from 4D-STEM taken for the 600 °C sample shows ScAlN is twisted ~5° along c-axis from underlying GaN, which is confirmed by twisting the sample around the c-axis in the measurement. Some local DPs show additional crystalline tilt by ~6° off the c-axis. These twist and tilt features are supported by the existence Moire fringes in the bulk of the film from TEM images observed in 600 °C sample, but not in 400 °C sample. In addition, multiple DP spots outside the wurtzite DPs are found in some regions, implying the inclusion of multiple phases, *e.g.*, possibly rock-salt or Al_3Sc phases, which could be from phase separation as revealed in XRD 2θ-ω scan in the previous studies.[1,2] These features in 4D-STEM are not observed in 400 °C sample. The present study helps to understand the mechanisms of better crystal quality in the epitaxially grown ScAlN under low substrate temperatures.
[1]Z. Engel, *et. al.*, J. Appl. Phys., 132, 185302, 2022.

[2] Z. Engel, Doctoral Dissertation, Georgia Institute of Technology, Approved on Dec. 5th, 2022.

2:50 PM X05
Microscale Surface Electronic Properties of Defects in Gallium Nitride Epitaxial Layers Andrew J. Winchester[1], Michael Mastro[2], Travis Anderson[2], Jennifer K. Hite[2] and Sujitra Pookpanratana[1]; [1]National Institute of Standards and Technology, United States; [2]U.S. Naval Research Laboratory, United States

Wide bandgap GaN is a desired material for next-generation high power electronics. However, the vertical structures needed for scalable devices suffer from issues related to dislocations, which propagate from the substrate into the epitaxially grown device area. Dislocations can significantly affect device performance (e.g., leakage current) and ultimately reliability. However, different types of dislocations and defects have been found to affect device performance in different ways. For example, threading dislocations with screw components are known to exhibit leakage current[1] and are predicted to have mid-bandgap states[2,3]. Therefore, determining the electronic properties of dislocations and defects at the microscale will provide valuable information for identifying "killer" defects.
Here, we use laboratory-based photoemission electron microscopy (PEEM) to investigate the local surface electronic properties of defects and dislocations in epitaxially grown GaN. We use a novel laser-based deep-ultraviolet light source to generate intense and tunable light for high-resolution PEEM imaging, which provides information about work function and valence changes from micrometer or smaller areas. Surface defects located near the stain centers in MOCVD-grown p-GaN on dot-core patterned substrates were identified using PEEM. We observe triangular regions of rough surface morphology, as well as "star"-shaped defects. These defects show a larger work function than the surrounding GaN, indicating a more p-type character. Further, these defects have a significantly shifted valence band maximum position, suggesting an altered valence band structure. Our results provide evidence for defective sites which could be related to dislocations. These sites could potentially act as leakage pathways under reverse bias conditions, which we are planning to investigate using conductive atomic force microscopy (cAFM) along with other characterization to determine their relation to dislocations.
References
1. Usami, S. *et al.* Correlation between dislocations and leakage current of p-n diodes on a free-standing GaN substrate. *Appl. Phys. Lett.* **112**, (2018).
2. Wang, J. *et al.* Do all screw dislocations cause leakage in GaN-based devices? *Appl. Phys. Lett.* **116**, 062104 (2020).
3. Nakano, T. *et al.* Screw dislocation that converts p-type GaN to n-type: Microscopic study on Mg condensation and leakage current in p–n diodes. *Appl. Phys. Lett.* **117**, 012105 (2020).

3:10 PM BREAK

3:30 PM X06
Luminescence Studies of Bulk GaN Crystals Grown by the Low-Pressure Acidic Ammonothermal Method Kohei Shima[1], Kouhei Kurimoto[2], Quanxi Bao[2], Yutaka Mikawa[3], Toru Ishiguro[1] and Shigefusa F. Chichibu[1]; [1]Tohoku University, Japan; [2]The Japan Steel Works, Japan; [3]Mitsubishi Chemical Corp., Japan

GaN is one of the promising candidates for use in high-power electronic devices operating at high frequencies because of its large bandgap energy (3.4 eV), high breakdown field (3.3 MV×cm^{-1}), and high saturation electron velocity (2.5×10^7 cm×s^{-1}). The vertically current flowing GaN devices fabricated on low threading dislocation (TD) density GaN wafers can offer high breakdown voltage and compact chip area simultaneously. To commercialize such GaN-on-GaN devices, low-cost manufacturing of large-diameter GaN wafers with low TD density is required, which can be achieved by slicing large-diameter bulk single crystals. The acidic ammonothermal (AAT) method enables the growth of bulk GaN by dissolving polycrystalline GaN in supercritical NH_3 with the assistance of ammonium halides as mineralizers and recrystallizing it on seed crystals in an autoclave. One of the advantages of AAT method is the capability of crystal growth at a pressure of approximately 100 MPa when NH_4F is used as the mineralizer. Since the pressure of 100 MPa is nearly half value of conventional AAT method, the method has been categorized as the low-pressure acidic ammonothermal (LPAAT) method. The reduced pressure allows the use of autoclaves with larger inner diameters, which are expected to significantly reduce the cost of GaN wafers. Recently, seeded growth of 2-inch-diameter GaN crystals via the LPAAT method has been demonstrated. Nearly bowing- and mosaic-free GaN crystals were achieved on high lattice coherency *c*-plane AAT seeds with gross TD densities in the order of 10^4 cm^{-2}. The next concern for the LPAAT GaN is the management of impurities, vacancy-type defects, and their complexes that could inhibit compensation-free and stable carriers. On the basis of the positron annihilation method, AAT GaN crystals have been elucidated to contain complexes of Ga-vacancies (V_{Ga}) with O on a N site (O_N) or H impurities, namely, $V_{Ga}(O_N)_n$ and $V_{Ga}(H)_n$ (n is an integer), respectively. In this study, the influences of such defect complexes are studied using steady-state and time-resolved photoluminescence (PL) methods.
GaN was grown by the LPAAT method on *c*- and *m*-plane AAT seed crystals at 580 - 625 °C in 110 MPa of supercritical NH_3 under the presence of NH_4F mineralizer. Steady-state PL was excited using the 325.0 nm line of a cw He-Cd laser. Time-resolved PL measurement was carried out using approximately 100 fs pulses of a frequency-tripled mode-locked Al_2O_3:Ti laser (λ = 267 nm). All the measurements were carried out under weak-excitation conditions to underline the nonradiative recombination processes. Steady-state PL spectra at 12 K of the LPAAT GaN taken from the -*c* plane exhibited predominant near-band-edge (NBE) emissions. The intensity was approximately three orders of magnitude higher than those of lower-energy broad emission bands originating from deep energy states at around 2.8 eV, 2.2 eV, and 1.8 eV, which are called blue, yellow, and red luminescence, respectively. Here, divacancies consisting of V_{Ga} and a N vacancy (V_N), namely $V_{Ga}V_N$, have been revealed to be the major nonradiative recombination centers (NRCs) in n-type GaN while $V_{Ga}(O_N)_n$ have been assigned as one of the origins of deep radiative recombination centers (DRCs) that give rise to the yellow luminescence. The existence of such vacancy complexes is plausible in the present LPAAT GaN. However, at 295 K, the NBE emission remained dominant, indicating that the concentrations of NRCs and DRCs in the LPAAT GaN are lower than those of the conventional AAT GaN. The NBE PL decay signals were recorded from -*c* planes of the LPAAT GaN. A record-long room-temperature PL lifetime for the NBE emission of AAT GaN crystals (~40 ps) was obtained from the -*c* plane of LPAAT GaN. These results support the progressive decrease in the concentrations of NRCs and DRCs. In the presentation, the effects of crystallographic planes and growth conditions on the luminescent properties of LPAAT GaN will also be discussed.

3:50 PM X07
(Student) Pulsed-Mode Metalorganic Vapor-Phase Epitaxial Growth of GaN on Graphene/c-Sapphire for Freestanding GaN Thin Films Seokje Lee[1], Dongha Yoo[1], Keundong Lee[2], Fabunmi T. Grace[1], Eunsu Lee[1], Imhwan Kim[1], Muhammad S. Abbas[3], Daniel Jang[3], Sangmin Lee[1], Jusang Lee[1], Miyoung Kim[1], Changgu Lee[3] and Gyu-Chul Yi[1]; [1]Seoul National University, Korea (the Republic of); [2]University of California San Diego, United States; [3]Sungkyunkwan University, Korea (the Republic of)

Manufacturing high-quality inorganic thin films on large-area flexible substrates is a key technology to utilize for flexible devices such as wearable sensors, flexible displays, and electronic devices. For the device fabrications, epitaxial thin films were grown on two-dimensional (2-D) layered materials such as graphene and *h*-BN. Since the 2-D materials offer weak bonding to the as-grown films, the exfoliation of epilayers from 2-D materials is easily feasible. In

particular, remote epitaxy has recently been reported by molecular beam epitaxial growth of GaN thin films on the graphene buffer layer (GBL) on SiC substrates. This remote epitaxial growth method enables to grow the single-crystal thin films on graphene-coated polar substrates by maintaining the epitaxial relationship between the substrate and the epilayer because the graphene does not wholly screen the electrostatic potential of the substrate. However, metalorganic vapor-phase epitaxy (MOVPE), commercially used for manufacturing GaN devices, could not be used for the remote epitaxial growth and exfoliation of high-quality GaN thin films on graphene. During the MOVPE growth, graphene substrates are affected by H_2 and NH_3 ambient gases at high growth temperatures, resulting in the failure of GaN exfoliation from the graphene substrate. Here, we report a new strategy for MOVPE growth of transferable single-crystal GaN thin films on graphene/*c*-sapphire by using pulse operation of NH_3 flow to prevent deterioration of graphene substrates during GaN growth.
The basic strategy for epitaxial growth of transferable single-crystal GaN thin films on graphene/*c*-sapphire is to use pulse operation of NH_3 flow to prevent deterioration of graphene substrates during GaN growth. In the NH_3 pulsed-flow growth, the NH_3 injection into the reactor was periodically interrupted while the trimethylgallium (TMGa) was continuously injected. By a controlled V/III ratio under the pulsed NH_3 injection, the lateral growth of the GaN buffer islands was enhanced merging into a continuous film. By optimizing the growth parameters, including the duration and period of the pulsed ammonia flow, high-quality GaN films were grown on the graphene-coated sapphire substrates, easily lifted off, and transferred onto a foreign substrate by simple mechanical exfoliation using a tape. Furthermore, we investigated the role of the pulsed operation of ammonia flow as a critical factor for the fabrication of high-quality free-standing GaN films. The freestanding GaN films, exhibiting excellent single crystallinity and electrical and optical characteristics, were also applied for transferrable GaN LEDs by heteroepitaxially growing $In_xGa_{1-x}N$/GaN multiple quantum wells and *p*-type GaN layers on the GaN films and transferring them onto Cu foil.

4:10 PM X08
(Student, Late News) Molecular Beam Epitaxy and Characterization of N-Polar AlGaN on C-Face 4H-SiC Shubham Mondal, Ding Wang, Ping Wang, Mingtao Hu, Reddeppa Maddakka and Zetian Mi; University of Michigan–Ann Arbor, United States

Nitrogen polar (N-polar) III-Nitride semiconductors have received considerable attention for applications in high-power, high frequency electronics as well as optoelectronic devices. The N-polar GaN/AlGaN heterostructure forms a natural back barrier in HEMTs which helps to achieve better carrier confinement whereas for optoelectronic devices (e.g., LEDs and laser diodes), the N polar configuration offers significantly reduced electron overflow and improved electrical efficiency compared to their M-polar counterparts. For example, N-polar Aluminum Gallium Nitride (AlGaN), with its direct tunable bandgap from 3.4 eV to 6.2 eV, has shown tremendous promise to break the efficiency bottleneck of UV-C and far UV-C LEDs. To date, however, the realization of high-quality N-polar AlGaN has remained challenging. Previous reports of N-polar Al(Ga)N grown on sapphire is plagued with the presence of very high density of dislocations, due to the large lattice mismatch, and the formation of inversion domains and poor surface morphology. Direct epitaxy of N-polar Al(Ga)N on AlN bulk substrate, on the other hand, is severely limited by the prohibitively high substrate cost. In this context, we have performed a detailed study of the epitaxy of N-polar AlN/AlGaN grown on C-face silicon carbide (4H-SiC), which has a small (~1%) lattice mismatch with AlN, a small difference of thermal expansion coefficients, and excellent thermal conductivity. We have demonstrated superior quality N-polar AlGaN with precisely controlled alloy compositions across the UV-A, UV-B and UV-C bands. A high internal quantum efficiency of 72% and electron mobility of 65 cm^2 / V.s at room temperature were measured for an ultrathin (200 nm) $Al_{0.65}Ga_{0.35}N$ epilayer grown on C-face 4H-SiC. The samples were grown using a Veeco GENXplor MBE system equipped with an RF plasma-assisted nitrogen source. Initially, a 200 nm AlN buffer layer was grown on C-face 4H-SiC following which a 200 nm AlGaN layer was grown at 800° C. Such a high-temperature growth enhances the adatom migration which results in atomically smooth surface morphology. This was confirmed by the AFM imaging of the AlGaN surface which shows an r.m.s. roughness of 0.8 nm across a 4 x 4 μm^2 scan area. Bright and streaky RHEED patterns were observed during the epitaxy of these N-polar AlGaN thin films. Also, the SEM image after 10 wt.% TMAH etching in room temperature confirms the N-polarity of the AlGaN thin films. The Al composition in the N-polar AlGaN films could be controllably tuned all the way from AlN (100% Al) to GaN (0% Al) and was confirmed by the shift in emission spectrum from photoluminescence spectroscopy measurements. An extremely high IQE ~ 72% was observed for the $Al_{0.65}Ga_{0.35}N$ sample which suggests the excellent optical quality of the high Al content N-polar AlGaN thin films. We have further studied the charge carrier transport properties of AlGaN. Room temperature Hall measurements reveal that the carrier concentration could be modulated from 10^{17} cm^{-3}, with an associated mobility of 65 cm^2 / V.s, to as high as 3×10^{19} cm^{-3}, with an associated mobility of 15 cm^2/V.s, for the Si-doped $Al_{0.65}Ga_{0.35}N$ epilayers. The charge carrier transport properties of N-polar AlGaN HEMT structures, together with the realization of high-efficiency N-polar deep UV LEDs are being studied and will be reported.

4:30 PM X09
(Student) N-Polar GaN Deep Recess HEMTs with ALD HfO_2 as Gate Dielectric Oguz Odabasi, Subhajit Mohanty, Kamruzzaman Khan and Elaheh Ahmadi; University of Michigan, United States

A combination of high electron saturation velocity, high electron mobility, large breakdown field, and high electron density can be simultaneously achieved in GaN high electron mobility transistors (HEMTs), making them attractive for high-power, high-frequency power amplifiers. N-polar GaN epi-structures offer scaling of the gate-to-channel distance without losing 2DEG density and a built-in back-barrier for better pinch-off performance. Additionally, N-polar GaN enables the implementation of a thick in-situ GaN-cap layer, which keeps surface states away from the channel and minimizes their effect on device performance. By using N-polar HEMT epi-structure with a GaN cap (deep recess HEMT) 8 W mm^{-1} output power with 27.8% power added efficiency (PAE) at 94 GHz has been demonstrated, which is more than twice the output power and efficiency of conventional Ga-polar AlGaN/GaN HEMTs [1].
Despite numerous benefits, there are challenges associated with N-polar deep recess HEMTs. Dry etching used in recess etching causes surface damage in the gate area and the trench sidewalls leading to high gate leakage and low breakdown voltage. These issues are currently addressed by inserting SiN_x gate dielectric deposited via metal organic chemical vapor deposition (MOCVD), a high temperature deposition technique that could be a limiting factor in device fabrication and integration. Moreover, inserting a thick dielectric layer under the gate increases the gate-to-channel distance, which is not desirable in scaled devices. Therefore, there is a need for developing a gate insulator with a high dielectric constant with low bulk and interface trap density. Moreover, a low-temperature deposition technique such as ALD allows for more flexibility in the fabrication process and is more desirable for manufacturing. Recent studies in our group have shown the successful application of ALD-HfO_2 as gate dielectric in N-polar planar GaN HEMTs. [2]
In this work, for the first time, a thermal-ALD HfO_2 was used as the gate dielectric in N-polar deep recess GaN HEMTs. DC, pulsed IV, and small signal measurements were conducted to evaluate the device performance. Results show low gate leakage current, high transconductance, high dielectric breakdown field, and low dispersion, which indicates a high quality dielectric and dielectric/GaN interface. This work shows the potential for HfO_2 as a gate insulator in N-polar deep recess HEMTs with a scaled channel.
MOCVD-grown N-polar deep recess GaN HEMT structure with a 12

nm thick GaN channel and a 47.5 nm thick GaN-Cap was used for this study. The devices presented here have a 100 μm gate width, and 1.75 μm source to drain distance. The etched region length for the gate recess is 200 nm and placed 650 nm away from the source. Ti/Au gate metal has 450 nm thickness, 900 nm length, and 300 nm away from the source. DC measurements showed 0.9 A/mm maximum drain current, 2 Ohm.mm on-resistance, and 2.2 V knee voltage at 1 V gate bias. The threshold voltage was -1.5 V. The maximum transconductance of 420 mS/mm was measured at V_G of -0.75 V and V_D of 3 V. Gate leakage current of 140 nA/mm, and a 6.2 MV/cm dielectric breakdown field. More importantly, near zero hysteresis was observed in DC measurements. Pulsed IV measurements revealed less than 5% dispersion. Unity current gain frequency (f_T) of 30.5 GHz and 53 GHz maximum oscillation frequency (f_{MAX}) were measured. These results show the potential of using HfO_2 as the gate dielectric in the future ultra-scaled N-polar deep recess GaN HEMTs.

[1] B. Romanczyk et al., "W-band N-polar GaN MISHEMTs with high power and record 27.8% efficiency at 94 GHz," 2016 IEEE International Electron Devices Meeting (IEDM), 2016, pp. 3.5.1-3.5.4, doi: 10.1109/IEDM.2016.7838339.

[2] S. Mohanty, A. Jian, K. Khan, and E. Ahmadi, “Demonstration of N-polar GaN MIS-HEMT with high-k atomic layer deposited HfO 2 as gate dielectric,” Accepted to appear in Journal of Electronic Materials (JEMS).

4:50 PM X10
Mechanisms for Polytype Selection During the Growth of Self-Catalyzed GaN Nanowires Liang Qi, Abby Liu and Rachel S. Goldman; University of Michigan, United States

Semiconductor polytype heterostructures, which consist of chemically homogeneous structures formed via an abrupt change in crystal structure, offer opportunities for performance exceeding those of composition-based semiconductor heterostructures. Of particular interest are heterostructures formed via an abrupt change in atomic plane stacking sequence, such as the transition from the wurtzite (WZ) polytype, with AB stacking, to the zincblende (ZB) polytype, with ABC stacking. At a fixed chemistry WZ/ZB heterojunction, the lattice mismatch and thermal expansion coefficient mismatch are typically < 0.1%, leading to a negligible interfacial defect concentration. Meanwhile, the WZ/ZB band offset and polarization discontinuity are expected to lead to the confinement of a two-dimensional electron gas (2DEG) at the interface, without the need for impurity doping and/or alloying. Depending on the type I (nested) vs. type II (staggered) band offset at the WZ/ZB polytype junction, such heterostructures would also be promising for high power electronics and single photon emitters.

It has been hypothesized that metastable NW polytype selection is governed by surface/interface energies, surface diffusivities, and/or droplet angles that determine ABC vs. AB stacking of atomic planes, resulting in zincblende (ZB) or wurtzite (WZ) polytypes. For ZB-polytype-preferring materials, such as III-As and III-P, ZB vs. WZ polytype selection has been described by empirical “contact angle” models [Panciera, 2020], enabling the design and fabrication of NW polytype superlattices. However, for GaN, a WZ-polytype preferring material, the “contact angle” models for NW polytype selection, using literature values for WZ and ZB GaN surface energies, predict ZB polytype formation, across contact angles, even though WZ GaN NWs are most frequently reported in the literature [Lu, 2021].

We are developing kinetic Monte Carlo (kMC) simulations based on a general lattice framework that can be used for both WZ and ZB polytypes, In these kMC simulations, the adsorption and desorption of Ga and N atoms are determined by the Ga chemical potential and temperature, and the polytype selection for an NW segment is automatically determined by the nucleation events occurring at the NW edges. Together, these thermodynamic and kinetic approaches will be utilized to unravel the mechanisms for polytype selection during the growth of self-catalyzed GaN nanowires.

Lu, H., S. Moniri, C. Reese, S. Jeon, A. Katcher, T. Hill, H. Deng, and R.S. Goldman. 2021. “Influence of gallium surface saturation on GaN nanowire polytype selection during molecular-beam epitaxy.” Appl. Phys. Lett. 119:031601.

Panciera, F., Z. Baraissov, G. Patriarche, V.G. Dubrovskii, F. Glas, L. Travers, U. Mirsaidov, and J.-C.Harmand. 2020. “Phase selections in self-catalyzed GaAs nanowires.” Nano Lett. 20:1669.

SESSION Y: Plasmonics, Photonics for Detection and Emission
Session Chairs: Daniel Ewing and Kurt Eyink
Thursday Afternoon, June 29, 2023
UC, Flying A Studios

1:30 PM Y01
Critical Coupling in Phonon Polariton Organ Pipe Resonance for Infrared Sensing S. Maryam Vaghefi Esfidani and Thomas G Folland; The University of Iowa, United States

Polar dielectric materials such as Silicon Carbide (SiC) have attracted much attention due to the ability to support low loss surface phonon polaritons (SPhPs) in the mid-infrared. As a consequence, SPhPs resonators have been reported with a high resonance quality factor, and have been leveraged for strong coupling to polar liquids. It would be highly useful to leverage SPhP modes to create surface enhancement infrared absorption (SERIA) sensors for phosphide containing molecules. However, so far there have only been a few demonstrations of surface enhancement from SPhP modes, and the results are relatively weak compared to more conventional metal SIRA sensors. This is because there is a lack of detailed models optimize the coupling between free space light, SPhPs modes, and the chemical under analysis. A framework for generalized design of SPhP resonators would solve this issue and provide the knowledge to design SEIRA sensors. Crucially, unlike in previous works, this model must be relatively simple, and quantitatively explain modal quality factors, which is missing from existing models.

In the present work, we investigate the impact of geometric parameters in SPhPs resonances that are excited in periodic trenches etched into a SiC surface. Resonances for high aspect ratio grating of 4H-SiC form between the walls of the trenches, and a vertical standing waves that are comparable with resonances in an organ pipe. To model mid-infrared resonant behavior of this structure, we develop two different approaches. The simplest consists of a cavity model which considers the structure as a metal-insulator-metal waveguide, coupled to waves in free space. The second consists of a full transmission line model, which accounts for propagation of the waves in and out of the structure. For both approaches we calculate the impedance of the SPhP mode, using a new approximation which accounts for the electric field concentration inside the SiC. Our results are compared against the 3D electromagnetic solution to Maxwell equations using CST Studio Suite and we observe excellent correspondence between full wave simulations and both our models. In both analytical models, SPhPs resonance, quality factor and absorbance are in good agreement with numerical simulation and follow the same trends, which is not possible to observe using previous models in the literature. Whilst our model is only highly accurate for relatively narrow openings of organ pipe resonators, the general trends match with experimental data. Crucially, our results show the applicability of simplified cavity and transmission line models can be used to design SPhP resonators. The extension to including both SEIRA and strong coupling phenomena is relatively trivial in this domain, which will accelerate the design of SPhP based SEIRA sensors.

1:50 PM Y02
(Student) Decoupling Mid-Wave Infrared Absorption and Long-Wave Infrared Radiative Cooling in Bolometric Elements
Alexander Ware[1], Morgan Bergthold[1], Noah Mansfield[1], Zarko Sakotic[1], Ethan Scott[2], Charles T. Harris[2] and Daniel Wasserman[1]; [1]The University of Texas at Austin, United States; [2]Sandia National Laboratories, United States

The bolometer has long been one of the most sensitive devices for detecting infrared radiation. Recent advances in nanofabrication have enabled new approaches to bolometric detection where response can be manipulated by engineering the optical and thermal behavior of the detecting element [1,2]. The ability to engineer absorbance (η) offers the possibility of bolometers with polarimetric or narrow-band spectral sensitivity for a range of applications, including thermography or molecular sensing.
Simultaneously, these advances have also enabled the engineering of effective thermal conductance (G) in nano-electromechanical (NEMS) bolometers by effectively isolating the absorbing pixel from the heat sink [3,4]. The ability to minimize thermal conductance has the interesting side effect of more tightly linking G to the bolometer absorptivity η. This is because heat dissipation from the pixel is increasingly dependent on radiative thermal emission, which, via Kirchhoff's law of thermal radiation, is equivalent to absorptivity (scaled by the blackbody spectral radiance at the bolometer temperature). Such coupling constrains the design of uncooled, narrow-band bolometers operating outside of the long-wave infrared (LWIR) as necessary radiative cooling features equate to enhanced η outside of targeted wavelengths. This can be circumvented by designing the bolometric element to absorb normally incident light in some spectral band and emit thermal radiation in a different band and different angle.
We present a spectrally selective, passively cooled mid-wave infrared (MWIR) bolometric absorber engineered to spatially and spectrally decouple infrared absorption and thermal emission. It consists of a Si substrate layered with Molybdenum, Aluminum Nitride, and Germanium and patterned with gold line gratings. The structure's MWIR TM-polarized response leverages a metal-insulator-metal mode formed by the grating, dielectric spacer, and reflective backplane. The normal incidence antenna-coupled cavity modes are completely absent from the LWIR enabling independent engineering of the optical structure's radiative properties. The strong, high energy phonon of AlN results in the real part of the AlN permittivity crossing zero at the AlN longitudinal optical phonon wavelength (λ_{LO} = 11.1 μm), providing the opportunity to exploit epsilon-near-zero physics and facilitate a second, separate absorption mechanism through the Berreman mode [5]. This results in a strong feature present only at grazing angles for TM-polarized light in the LWIR [6]. Due to Kirchhoff's law this feature could enable passive (radiative) cooling of the element in the LWIR without disrupting MWIR detection. We demonstrate these features experimentally using reflection spectroscopy from the surface of the fabricated sample and compare with simulated reflection and absorption calculated using rigorous coupled wave analysis [7]. Strong MWIR absorption and the lack of any significant LWIR absorption for normally incident light, combined with strong LWIR absorption at grazing angles, demonstrates our ability to decouple and independently engineer the absorption and emission features of the structure.
[1] J. J. Greffet, R. Carminati, K. Joulain, J.-P. Mulet, S. Mainguy, and Y. Chen, Nature 416, 61 (2002).
[2] M. A. Gritz, M. Metzler, D. Malocha, M. Abdel-Rahman, B. Monacelli, G. Zummo, and G. D. Boreman, J. Vac. Sci. & Technol. B: Microelectron. Nanometer Struct. Process. Meas. Phenom. 22, 3133 (2004).
[3] B. Cole, R. Higashi, and R. Wood, Proc. IEEE 86, 1679 (1998).
[4] A. Cleland, D. Schmidt, and C. S. Yung, Phys. Rev. B 64, 172301 (2001).
[5] S. Vassant, J.-P. Hugonin, F. Marquier, and J.-J. Greffet, Opt. Express 20, 23971 (2012)
[6] L. Nordin, O. Dominguez, C. M. Roberts, W. Streyer, K. Feng, Z. Fang, V. A. Podolskiy, A. J. Hoffman, and D. Wasserman, Appl. Phys. Lett. 111, 091105 (2017)
[7] From V. A. Podolskiy's research group, see http://viktor-podolskiy-research.wiki.uml.edu/RCWA.

2:10 PM Y03
Massively Degenerate Coherent Perfect Absorber Using a Single Optic Minho Choi, Christoper Munley, Johannes Fröch and Arka Majumdar; University of Washington, United States

Coherent perfect absorbers (CPA) are devices in which a weak absorber, which does not have sufficient absorption coefficient or thickness, can obtain a near-unity absorption owing to the cavity resonance. Using a CPA, we can achieve significant absorption from even thin-film semiconductors or dielectrics, so it is highly applicable in the fields of photodetection, photovoltaics, and optical processing. However, the fact that only a certain wavevector can be satisfied and completely absorbed in the CPA condition severely hinders the absorption efficiency in the general case where multiple wavevectors are incident at the same time. Recently, researchers have used a telescopic arrangement to allow incident light with different wavevectors to satisfy the CPA condition simultaneously. But still, the wavevector degeneracy of the system is sorely restricted to a numerical apertural (NA) of 0.015, and the residual reflection within multiple optics intrinsically limits the performance of the CPA. Here, we realize a photonic flatband structure with a single metasurface, and demonstrate a massively degenerate CPA over a wide range of incident wavevectors. The one-dimensional metasurface is made of crystalline silicon which intrinsically has absorption in the near-infrared; therefore, the guided-mode resonance inside the metasurface acts as a photonic cavity and a weak absorber at the same time (Figure 1A). Since the metasurface has an identical resonance frequency over a wide range of wavevectors – NA of 0.3 – we can significantly increase the absorption efficiency in general (Figure 1B). Moreover, since the single metasurface optic is operating as the massively degenerate CPA system, it is free from residual reflection or alignment imperfection. In application, we make use of the flatband-based massively degenerate CPA for optical switching. We are able to turn on and off the one-dimensional image by changing either the laser wavelength or polarization with respect to the resonance mode of the photonic flatband. Furthermore, it is possible to actively tune the resonance frequency of the metasurfaces by adding thin phase-change materials on top. In addition, from two-dimensional photonic flatband structures with advanced metasurfaces, we can build degenerative nonlinear optical networks.

2:30 PM Y04
(Student) Property Control of ErAs:InGaAlBiAs Materials for Terahertz Emitters and Detectors Pumped at 1550 nm Wilder Acuna, Weipeng Wu, James Bork, Benjamin Jungfleisch, Lars Gundlach and Joshua Zide; University of Delaware, United States

We present our latest work in optimizing properties of ErAs:InGaAlBiAs digital alloy materials for terahertz applications. In these materials, dark resistivity and carrier lifetime are controlled primarily by ErAs nanoparticles; ErAs self assembles into nanoparticles when the amount of Er incorporated is above the solubility limit. These nanoparticles behave as carrier traps, decreasing the lifetime to subpicosecond values and strongly influencing the carrier concentration in the material. On the other hand, the material's bandgap – and band alignment to the ErAs Fermi level – is tuned primarily by the matrix, which offers many degrees of freedom for band engineering; however, it is grown at low temperatures (280 °C) to allow the incorporation of Bi in the structure. All these properties must be controlled and optimized for emitter and detector devices compatible with 1550 nm pump excitation wavelength. Of these properties needed for good devices, maintaining high dark resistance while achieving material with 1550 nm pump compatibility may be the biggest challenge. Here we show the impact on carrier concentration of co-depositing Er at low temperatures

versus using interrupt growth with migration-enhanced epitaxy. These materials were characterized by different techniques to measure structure quality (high-resolution x-ray diffraction), composition (Rutherford Backscattering Spectrometry), electrical properties (Hall effect and conductivity), optical properties (spectrophotometry and optical pump-THz probe spectroscopy). Finally, we present our progress in control of material properties and performance of these structures as emitters of THz frequencies.

2:50 PM Y05
(Student) Large-Scale Inversely Designed Metasurfaces for Broadband LWIR Optical Edge Detection Brandon Swartz[1], Quan Liu[1], Yuankai Huo[1], Gregory Forcherio[2] and Jason Valentine[1]; [1]Vanderbilt University, United States; [2]Naval Surface Warfare Center Crane, United States

Convolutional neural networks (CNNs) are a powerful tool in computer vision, commonly used for image segmentation and classification. The accuracy and scope of CNNs can generally be improved be increasing the complexity of the network, such as the number of layers, channels, or fully connected layers. However, increasing CNN complexity comes at the cost of increased power consumption and calculation time. The first layer of a CNN detects low level features, such as edges. If an optical system was designed to perform low level feature detection, that task could be offloaded from the computer, allowing for faster, lower-power consumption CNNs, without sacrificing accuracy.
Optical edge detection has been explored previously, though current methods have limitations that prevent their use in many practical applications, such as requiring polarized or coherent illumination, requiring bulky 4f systems, or being limited to small apertures. We have designed and experimentally demonstrated systems which overcome these limitations, allowing for broadband optical edge detection of incoherent thermal emission with optimized signal to noise ratio. Further, UNet image segmentation networks trained using our simulated models as an optical front end demonstrated an improved Dice coefficient (from 0.877 to 0.899) with 4 times fewer FLOPs compared to a similar UNet architecture trained on raw images.
Our optical edge detection system combines the design flexibility of metasurfaces with the broadband focusing capability of refractive optics. Using gradient descent based inverse design, the metasurface is designed to modify the point spread function (PSF) of the combined optic system to emulate an edge detection kernel. Edge detection kernels have both positive and negative values, which cannot normally be achieved in an incoherent PSF; this can be circumvented by splitting the PSF into positive and negative components, which produce two images that are digitally subtracted produce a single edge image. This is achieved with a single polarization sensitive metasurface which, in conjunction with a refractive lens, forms independent images corresponding to the positive and negative PSF components using two orthogonal polarization states, which can be simultaneously captured using a polarimetry enabled LWIR camera.

3:10 PM BREAK

3:30 PM Y06
(Student) Flexible Metastructure Graded-Index Lens as a Quantum Algorithm Emulator Ashley Blackwell, Riad Yahiaoui, Yi-Huan Chen, Pai-Yen Chen, Thomas A. Searles and Zizwe A. Chase; University of Illinois Chicago, United States

Optical computers offer advantages over the commonly used electronic computers including higher speeds, lower power consumption, higher efficiency, and operation at multiple frequencies [1,2]. Metamaterials are of great importance for achieving optical computing systems and for integration into the current computing infrastructure by scaling down the size and number of on-chip transistors. Therefore, a gradient index (GRIN) lens is proposed as one part of a Quantum Algorithm Emulator (QAE) to realize the Deutsch-Jozsa (DJ) algorithm in the terahertz (THz) region. In the DJ problem, an oracle block implements a binary function f. The function, f, takes n-bit binary values as input and produces either 0 or 1 as output. If the value of f is 0 or 1 on all outputs, f is called constant function. However, if the value of f is 0 and 1 for half of the output domain, f is called a balance function. The oracle subblock is made of 500 μm thick Silicon and a Fourier subblock made of 127 μm thick polyamide film. The oracle subblock modulates the phase of the transmitted THz wave with a factor $k_0 n(y) d_0$ by encoding the function f(y) and assigning a phase shift of 0 or π on each spatial position along transversal direction. The Fourier subblock film acts as the gradient GRIN lens which displays the results of the output signal. We evaluated the structure using numerical simulations and applied inverse design machine learning to validate/improve the structure and signal output. Figure 1(a) shows the ML process used on the GRIN lens. First, the data for training the proposed neural network (NN) model is generated using numerical simulation software. The geometric configuration is randomly generated using MATLAB then ML uses the optimized output peak parameters (amplitude and full width half maximum (FWHM)) to output the optimized radii and thickness for the GRIN lens. This is done iteratively until the input peak parameters are matched as close as possible. Figure 1(b) shows the original and optimized results for both the constant (left) and balanced function (right from an input frequency of 0.8 THz. The use of ML has helped produce a QAE that has an optimal distribution of the output wave intensity that creates a device that can be better equipped to handle a greater number of database inputs [3].
Fig. 1: (a) Schematic of the Machine Learning process. (b) Comparison of the original and optimized results for both constant and balanced function at 0.8 THz.
References
[1] A. C. Arsenault et al., J. Mater. Chem., **14** (2004).
[2] J. Touch et al., Nanophotonics, **6** (2017).
[3] K. Cheng et al., Opt. Express, **28** (2020).

3:50 PM Y07
(Student) Taming Mid-IR Resonances with Hexagonal Boron Nitride Haonan Ling[1], Milad Nourbakhsh[2], Vincent Whiteside[2], Joseph Tischler[2] and Artur Davoyan[1]; [1]University of California, Los Angeles, United States; [2]The University of Oklahoma, United States

Taming mid-IR resonances with hexagonal boron nitride
Hexagonal boron nitride (hBN), a naturally hyperbolic material, has been used to achieve subwavelength light manipulation in the mid-infrared (mid-IR) frequency band. Due to the phonon polaritonic resonance, hBN exhibits a very sharp peak in permittivity along in-plane orientation around 7.3 um (Fig. 1a) [1, 2]. Previous studies have shown ultra-confined polaritonic resonances within hBN patterned into nano-disk arrays with thickness < λ/100 and diameter < λ/15 [2]. In this work we expand on these studies and examine pathways for resonant control of subwavelength fields in nanostructured hBN structures. Specifically, we show that light can be efficiently confined within ultra-narrow channels yielding a greatly enhanced electric field intensity (Fig. 1b). We then examine infrared radiation emission control with nanostructured hBN metasurfaces.
We begin our analysis with analytical solution of optical confinement in a 1D slot hBN waveguide (Fig. 1b). We find that over 70% of the optical power can be squeezed into a channel with width smaller than λ/50 at ~7 micron wavelength. In this case the optical field intensity is enhanced over 10000 times [3]. These results show that great promise for enhancing light-materials interaction at deeply subwavelength scales.
Next, we study thermal radiation emission spectra as a function of hBN metasurface structure. Specifically we design hBN disk arrays and examine emission spectra as a function of disk size and thickness. Of a particular interest for us is understanding resonance evolution near the TO phonon-polariton resonance. With variation of parameters we observe a complex interaction of geometric resonances with materials resonance. To better understand the dynamics we design and fabricate structures. We fabricate the nano-disk arrays by patterning

bulk hBN flakes ~ 350 nm thick (λ/20) exfoliated on carefully designed substrates (Fig. 1c) and perform the far-field measurements to collect reflection and transmission. We find good match between the simulation and experimental results. These results show the promise of creating metasurfaces and thermal emitters using this unique hyperbolic material for various applications.
In summary, we study theoretically and experimentally light interaction with naturally hyperbolic material, hexagonal boron nitride, in the vicinity of TO phonon polariton resonances. We show that this material platform is well suited for deeply subwavelength optical field confinement and guiding. Our study of nanodisk arrays reveals that multiple strong resonances can be sustained across a broad wavelength band.
[1] Caldwell, Joshua D., et al. "Sub-diffractional volume-confined polaritons in the natural hyperbolic material hexagonal boron nitride." Nat. Comm. 5.1 (2014): 1-9.
[2] Tamagnone, Michele, et al. "Ultra-confined mid-infrared resonant phonon polaritons in van der Waals nanostructures." Sci. Adv. 4.6 (2018): eaat7189.
[3] Ling, Haonan., et al. "Atomic-void van der Waals channel waveguides." Nano Lett. 22. 15 (2022): 6254-6261

4:10 PM Y08
(Student) Topological Spin-Valley Coupling in 2-D Photonic Crystals Madeline Brown[1], Zarko Sakotic[1], Sukrith Dev[2], Monica Allen[2], Jeffery Allen[2] and Daniel Wasserman[1]; [1]The University of Texas at Austin, United States; [2]Air Force Research Laboratory, United States

Topological 2-D photonic crystals are of great interest for the realization of topological edge modes in photonic systems, where light travels robustly and unidirectionally with long propagation lengths along an interface between two photonic crystals. Waveguides composed of these photonic crystals have allowed for the observation of various optical phenomena such as the photonic quantum spin Hall effect (QSHE) and the photonic valley Hall effect (VHE). These phenomena support topological edge modes by preserving time reversal symmetry for QSHE photonic crystals with spin degree of freedom (DOF), or by lifting spatial inversion symmetry for VHE photonic crystals with valley DOF. Crystals on either side of an interface must possess equal but opposite Chern numbers for the mode to be verified as topological [1]. Each phenomenon has its respective limitations and tradeoffs regarding coupling and propagation lengths but may be utilized together to further improve the robust and unidirectional behavior of light in topological systems. The coupling of the photonic QSHE and VHE has been proposed and demonstrated experimentally at microwave frequencies [2-4] and demonstrating such structures at optical frequencies adds additional challenges associated with the dramatic reduction of length scale required for the much shorter wavelength light. In this abstract, we propose a topological photonic waveguide at the interface of photonic QSHE and VHE crystals, operating in the mid-wave infrared wavelength range (MWIR, 3-5 μm).
Here we present unique designs for 2-D QSHE and VHE photonic crystals with the purpose of coupling the two photonic crystals in order to support a topological edge mode forming a waveguide operating in the MWIR. Simulations in this work are done within the finite-element method software COMSOL Multiphysics. All photonic crystals in the spin-valley system are simulated to have lattice constants of 1.4 μm and contain Si pillars with varying radii in air. The band structures and z-component of the electric field profiles for both photonic crystal designs are analyzed (Fig. 1). The band gap for the QSHE photonic crystal coincides with the band gap between band 4 and band 5 of the band structure for VHE photonic crystal, enabling a possible coupling. Using the photonic crystals in Fig. 1, a very robust and unidirectional topological edge mode can be seen propagating around a 120-degree bend in the interface between QSHE and VHE photonic crystals within a waveguide in Fig. 2. In this waveguide, light is excited near the left edge of the device at the interface, simulating right-hand circularly polarized (RHCP) light as required for the photonic QSHE. It is evident that a topological edge mode may be supported through this design and this model will be used as a platform for future device fabrication.
The simulations within this work show excellent agreement with the trends of available literature, with a topological edge mode observed in simulations in the MWIR at approximately 2.7 μm (roughly 105-110 THz). It is found that the presented photonic crystal designs for both the photonic QSHE and VHE are capable of coupling and supporting a very robust and unidirectional edge mode at their interface. In future work we aim to further optimize the spin-valley device for the purpose of fabrication and characterization. The work to be presented already offers a viable option for the design of 2-D topological photonic devices operating at optical frequencies.
References
[1] M.Z. Hasan et al., *Rev. Mod. Phys.* vol. 82, p. 3045–3067 (2010).
[2] X. Ni et al., *Sci. Adv.*, vol. 4, no. 5, p. 1-9 (2018).
[3] B. Yan et al., *Adv. Optics Lett*., vol. 47, no. 8, p. 2044-2047 (2022).
[4] Y. Kang et al., *Nat. Comm*, vol. 9, no. 3029, p. 1-7 (2018).

4:30 PM Y09
(Late News) Localized Phonon Polariton Modes in GaN/AlN Nanowiresx Abhilasha Kamboj[1], Matt Brubaker[2], Noah Mansfield[3], Alexana Roshko[2], Viktor Podolskiy[4], Kris Bertness[2] and Daniel Wasserman[3]; [1]University of Delaware, United States; [2]National Institute of Standards and Technology, United States; [3]University of Texas at Austin, United States; [4]University of Massachusetts Lowell, United States

The mid-infrared wavelength range (MIR: 3-30 μm) is of significant technological importance. Many of its applications are well-served by leveraging techniques capable of enhancing light-matter interaction. Phononic systems, which leverage excitations of the crystal lattice coupled to electromagnetic modes, offer one potential approach. The negative real permittivity of a phononic material, in the material's Reststrahlen Band, results in an optical response similar to that of plasmonic materials, though with lower loss (small imaginary permittivity). In the MIR, strongly polar AlN, with a high-energy longitudinal optical (LO) phonon at a free-space wavelength of 11.2 μm, is an intriguing phononic system, with negative permittivity extending from LO phonon wavelength to the transverse optical (TO) phonon wavelength of 15.9 μm[1].
In this work, we investigate periodic arrays of AlN-capped nanowires supporting a variety of unique phononic modes. We demonstrate localized surface phonon resonances (LSPhR) in the AlN nanostructures, in the frequency range bounded by AlN's LO and TO phonon energies. We also demonstrate that the nano-pillar growth regime allows for normal incidence coupling to the Berreman mode which is observed in thin films at epsilon-near-zero (ENZ) permittivity (at LO phonon energy) for light incident at large grazing angles. The nanowires are grown by plasma-assisted MBE[2] on a patterned silicon wafer, which serves as the template for GaN nanowire growth, upon which AlN caps are grown. On a silicon wafer, after a series of buffer layer growths, a 70 nm Si_3N_4 growth mask is deposited on the top GaN buffer layer, and the growth mask is then patterned (by e-beam lithography) and etched to provide apertures to the underlying GaN with 1 μm period and varying diameters. GaN nanowires 1.8 μm in height are grown in the apertures, followed by an AlN cap of 210 nm, above the GaN nanowires. Periodic arrays of AlN-capped GaN nanowires were grown with varying aperture dimensions, resulting in nanowires with diameters of ~ 210, 300 and 390 nm, During the growth of the AlN cap, a thin cylindrical shell of AlN with thickness in few 10s of nms (decreasing thickness from top to bottom) is deposited on the sidewalls of the GaN nanopillar. The result of the patterned growth are subwavelength AlN phononic resonators that effectively 'float' above the substrate, supported by the dielectric GaN nanowire bases. We measure near normal incidence reflectance (±3.5°) of the nanowire arrays using a nitrogen-purged Bruker vertex 70 FTIR with an output beam collimated and reduced to ~ 6 mm through an external double-

aperture. The reflectance data is compared to the reflection simulated with a corresponding TM-polarized 2-D model in COMSOL assuming a 20 nm thick uniform AlN shell around GaN nanopillar.
In this work, we study representative data from the nanowires with diameter of 390 nm. The reflectance spectra show three prominent resonant dips. The longest wavelength features at 13.3 μm wavelength can be thought as a dipole mode at the top and bottom corner GaN/AlN interface. The next longest wavelength features at wavelengths λ = 12.3 μm corresponds to the LSPhR of the AlN caps that are confirmed via simulation of the nanowire structures. The LSPhR spectrally red-shifts with increasing nanowire diameters. Even more interesting is a sharp reflectance dip in AlN nanowires at wavelength, λ = 11.2 μm (AlN LO phonon energy). The fields at λ = 11.2 μm are calculated with 2-D COMSOL model, which indicate a strong field confinement in the AlN shell surrounding the GaN nanowire. While such a resonance would not typically be seen in a planar AlN film (or even a patterned AlN film) at normal incidence, the vertical orientation of the thin (~20 nm) AlN shell offers strong coupling to the Berreman mode.
1. L. Nordin et al. ... D. Wasserman. Applied Physics Letters, 111(9):091105, 2017.
2. M. Brubaker et al. … K. Bertness, Nanotechnology 30, 234001, 2019.

4:50 PM Y10
(Student, Late News) Prospects of Dilute Bismuth in InGaBiAs Alloys for e-SWIR Photodetectors Md Toriqul Islam, Sheikh A. Razi, James Bork, Nuha A. Babikir, Mrudul S. Parasnis, Joshua Zide and Jamie Phillips; University of Delaware, United States

Dilute bismuth (Bi) incorporation in InGaBiAs is a promising material for extended short-wave infrared (e-SWIR, 1.7-2.5 μm wavelength) detection with a lattice match to InP-based materials. The InGaBiAs alloy is a highly mismatched semiconductor, where small concentrations of localized Bi states have a dramatic impact on the valence band electronic structure and the corresponding decrease in the bandgap energy. The use of InGaBiAs as an active material for e-SWIR photodetectors offers a means to overcome limitations of current approaches, including high dark current associated with relaxed InGaAs and low quantum efficiency of InGaAs/GaAsSb type-II superlattices on InP substrate. The epitaxial growth of InGaBiAs alloys has been previously demonstrated, with a bandgap energy shift of 56 meV/Bi% in $In_xGa_{1-x}Bi_yAs_{1-y}$ [1,2]. However, the details of optical absorption strength and minority carrier properties of key importance for photodetectors have not been explored in detail. In this work, the optical and electronic properties of InGaBiAs alloys and their relationship to epitaxial growth conditions will be reported. InGaBiAs materials were grown on InP at variable temperatures (265 and 490 °C) and V/III flux ratios. The growth parameters have a major influence on the tradeoff between efficient bismuth incorporation in the lattice and point defect density that influence the electronic properties of the material. The low temperatures (LT) grown samples are highly mismatched alloys with higher Bi incorporation. In the high temperatures (HT) grown samples, Bi acts as a surfactant. Optical absorption coefficient data were extracted from infrared transmission measurements, where the absorption edge was extended beyond 1.9 μm for Bi incorporation of 1.5% in comparison to an $In_{0.53}Ga_{0.47}As$ reference sample while maintaining a high absorption coefficient ($>10^4$ cm^{-1}) in the 1.5-1.85 μm spectral range.
The minority carrier electronic properties have been investigated by temperature-dependent microwave-detected photoconductive decay (μ-PCD) measurements. For LT samples, μ-PCD measurements exhibit time constants less than 500 ns, corresponding to fast minority carrier recombination. Long-time constants of >100 μs are observed for the HT samples, which are attributed to carrier capture and re-emission from trap states with activation energies of 0.07 eV and 0.14 eV. The long photoconductive decay time constants are indicative of material with favorable minority carrier properties for photodetectors. Diode p-i-n junction devices incorporating InGaBiAs active layers were grown and fabricated into mesa devices using standard photolithography, chemical etching, and metallization processes. Dark current-voltage characteristics correlate with photoconductive decay measurements, where materials exhibiting long-time constants exhibit low dark current density ($8.46x10^{-6}$ A/cm^2) similar to InGaAs reference samples, while materials exhibiting short-time constants show high dark current density and/or significantly degraded diode rectification. Further development of InGaBiAs e-SWIR detectors will require a focus on co-optimization of bismuth incorporation and minority carrier properties, and continued exploration of optoelectronic device characterization.
References:
J. P. Petropoulos, Y. Zhong, and J. M. Zide, "Optical and electrical characterization of InGaBiAs for use as a mid-infrared optoelectronic material," *Applied Physics Letters*, vol. 99, no. 3, p. 031110, 2011.
R. Kudrawiec, J. Kopaczek, J. Misiewicz, J. P. Petropoulos, Y. Zhong, and J. M. Zide, "Contactless electroreflectance study of E0 and E0+Δso transitions in $In_{0.53}Ga_{0.47}Bi_xAs_{1-x}$ alloys," *Applied Physics Letters*, vol. 99, no. 25, p. 251906, 2011.

SESSION Z: Emergent Materials and Devices for Microelectronics
Session Chair: Angel Yanguas-Gil
Thursday Afternoon, June 29, 2023
UC, State Street

1:30 PM #Z01
(Student) Origins of Nonvolatility in Resistive Switching Memory Jingxian Li, Anirudh Appachar, Wei Lu, Wenhao Sun and Yiyang Li; University of Michigan–Ann Arbor, United States

Resistive memory or memristor is a highly potential memory and computing unit for next-generation information storage, in-memory computing, and neuromorphic computing. Valence change memory (VCM) is a promising memristor using transition metal oxides, and changes electronic resistance by moving oxygen vacancies under applied electric fields and joule heating to form or break the conducting filaments. Amorphous TaO_X ($0<X<2.5$) has been widely used in the VCM due to its outstanding performance of fast switching, high endurance and long retention time. The LRS retention failure is consistent with the standard Fickian diffusion model that oxygen vacancies in the conducting filaments will diffuse out, which cannot explain the HRS retention failure results.
In this work, we show that the Fickian diffusion model is inadequate and fails to account for "uphill" diffusion against the concentration gradient in VCM. To do so, we combine experimental measurements and first-principles thermodynamic calculations to investigate phase separation in amorphous TaOX. Experimentally, we use reactive sputtering to deposit TaOX thin-film bilayers with different oxygen:metal ratios (X). We use Auger depth profiling to measure how the thickness and composition (X) of the two layers evolve after annealing at 300C. Our results show that, while the composition and thicknesses of each layer changed during annealing, the bilayer interface persists even after long annealing times and one phase composition is ~$TaO_{1.9}$. We complement the experimental measurements with ab initio thermodynamic calculations of the amorphous formation energies, and identify the two stable phases are $TaO_{1.9}$ and Ta. The 1D phase field simulation with chemical potential from the calculated formation energy matches the Auger depth profile results to further confirm the phase separation in the amorphous Ta-O system. We also build a 2D phase separation model to simulate the retention behavior of TaO_X VCM devices, which confirms that retention failure types can be modulated by the filament width and gaps. Our results reconcile unexplained discrepancies and enable predictive design of key performance indicators such as retention stability.

1:50 PM Z02
(Student) Controlling Response Time and Synaptic Behavior of Ion-Gated Transistors Through Modulating Different Aspects of Input Biases Ramin Karimi Azari, Tian Lan and Clara Santato; Polytechnique Montréal, Canada

High-performance and low-power consumption neuromorphic computing (i.e., brain-like computing) is attracting increasing attention in materials science, device engineering, green electronics, and bioelectronic research communities. Ion-gated transistors (IGTs) as synaptic transistors, by perceiving the environment in real-time, can be studied and exploited as neuromorphic devices.
Depending on the permeability of the semiconducting channel to ions, IGTs undergo volumetrics (three-dimensional) or electrostatic (field-effect, two-dimensional) doping, which leads to a wide range of response times. Long-term memory and high-speed data processing are essential for neuromorphic computing.
We propose a method to modulate the response time and synaptic plasticity of IGTs made up of poly (3-hexylthiophene, P3HT) gated by the [EMIM][TFSI] ionic liquid. We report on the effect of the frequency of the gate-source voltage (V_{gs}) pulses, the number of applied V_{gs} pulses, and the pulse duration time on IGT response time. With increasing drain-source voltage (V_{ds}) from -0.2 V to -1 V, we observed that the response time was half using a 200 ms-long square step V_{gs} = -0.5 V pulses. Moreover, with increasing V_{gs} from -0.5 V to -1 V the response time increases by 27% at V_{ds} = -1 V.
Our results shed light on the impact of various aspects of the input voltages on governing the transistor response time and synaptic functions in organic IGTs to reach low-power and fast-switching neuromorphic devices. The methodology also includes the effect of the V_{gs} sampling time on the accuracy of electric measurements of this study.

2:10 PM Z03
(Student) Effect of the Counter Electrode Material on the SET Kinetics of Ag/HfO_2-Based Diffusive Memristors Solomon Amsalu Chekol[1,2], Richard Nacke[1,2], Stephan Aussen[1,2] and Susanne Hoffmann-Eifert[1]; [1]Forschungszentrum Jülich GmbH, Germany; [2]RWTH Aachen University, Germany

Diffusive memristors, also known as volatile electrochemical metallization memory cells (ECMs), are recognized as extremely interesting devices for various applications in emerging memories and neuromorphic computing areas. For non-volatile ECM cells, it has been shown that the counter-electrode (CE) material plays a crucial role in the switching process by affecting the reactions at the CE/electrolyte interface. This is due to the different electrocatalytic activity of the CE material towards reduction-oxidation reactions, which determines the metal ion concentration in the electrolyte and ultimately impacts the switching kinetics.
In this work, we look at the switching behavior of diffusive memristors and how this is affected by different CE materials with a special focus on (i) the understanding of the influence of the CE material on the volatile switching process of diffusive memristors and (ii) device engineering and optimization towards industrially used and CMOS-compatible materials. To that end, we used inert Pt metal and two non-noble metals widely used in semiconductor technology, namely, W and TiN, as CE materials in Ag/HfO_2/CE-based diffusive memristor cells. Rectangular voltage pulses of different amplitudes were applied and the SET times were analyzed from the transient curves. The results show that the CE material has a significant effect on the SET kinetics, with interesting differences being observed depending on the voltage regime. It is found that non-noble CE materials such as TiN and W form a native oxide either during ambient transfer or during the ALD process of the HfO_2 electrolyte film. This has been confirmed by the XPS analysis of different stacks with and without the HfO_2 layer. Furthermore, the formation of interfacial oxides at the CE/electrolyte interface in the case of non-noble metals is also discussed in relation to the observed differences in the SET kinetics. The findings of this work highlight the significant role of the CE material in the switching process of Ag/HfO_2-based diffusive memristors and the importance of considering interfacial oxide formation in the design of these devices.
This work was in part funded by the German Research Foundation (DFG) under Grant No. SFB 917, in part by the Federal Ministry of Education and Research (BMBF, Germany) in the project NEUROTEC (Project No. 16ME0398K) and NeuroSys (Project No. 03ZU1106AB) and are based on the Jülich Aachen Research Alliance (JARA-FIT).

2:30 PM Z04
(Student) Realizing a Linear Synaptic Weight Update in Electric-Double-Layer Gated Transistors for Achieving Spike-Timing-Dependent Plasticity in Neuromorphic Computing Nithil Harris Manimaran[1], Cori Sutton[1], Shubham Sukumar Awate[2] and Ke Xu[1,1,1]; [1]Rochester Institute of Technology, United States; [2]University of Pittsburgh, United States

To overcome the von Neumann bottleneck and increase power efficiency in computation, neuromorphic computing has been considered which has the capability for parallel computing, long-term potentiation, and adaptive learning for developing energy efficient neural networks.[1] Electric double layer (EDL) gated transistor uses ions within an electrolyte to induce high carrier density (10^{14} cm^{-2}) in the channel, and its short term and long term ionic responses resemble a biological synapse, making it a promising platform for synaptic applications such as artificial synapses and neurons.[2] The accuracy, computational demands, and simplicity of training neural networks depend significantly on a linear synaptic weight response (or plasticity), i.e. a proportionate synaptic weight update in response to input signals.[3-6] However, achieving linear weight update in EDLT based synaptic devices have proven to be challenging with fixed magnitude input pulses.[7-9] In this study, we first discussed the fundamental cause for nonlinear synaptic weight update in the aforementioned EDLT synaptic devices. With fixed magnitude input voltage pulses, while the amount of EDL build up during each pulse is constant, the amount of EDL dissipation in between pulses is dependent on the instantaneous EDL concentration and follows an exponential decay with respect to time. This leads to increasing amount of dissipation as pulses progress and EDL builds up nonlinearly. This behavior was confirmed with finite element modeling using modified Nernst-Poisson-Planck equations.[10,11] A train of 10 pulses with frequencies ranging from 10 – 100 Hz (V_G = 1 V) was applied to a parallel plate capacitor geometry consisting of PEO:$LiClO_4$ as the electrolyte, and the ion concentration was calculated. As expected, the linear input pulses resulted in a non-linear response, where the maximum EDL concentration at 100 Hz eventually saturated at 9 x 10^{13} ions/cm^2, more than 2 times smaller than the maximum EDL concentration at a steady 1 V (1.9 x 10^{14} ions/cm^2). Then, we demonstrated that linear weight update can be achieved with varying input pulse widths and/or magnitudes (i.e., nonlinear inputs). A challenge for this approach is that the EDL concentration at the end of each pulse needs to be evaluated to predict the input voltage or width of the subsequent pulse. Based on the instantaneous change in EDL concentration with respect to time (dc/dt), we obtained an empirical relationship relating dc/dt, voltage, concentration, and time. Coupling this relation with the original COMSOL model, the input signals for a linear synaptic response can be predicted in a single computation. For a series of pulses with magnitude between 0.25 V and 3 V at a fixed frequency of 100 Hz, a linear synaptic weight update was obtained with R^2 = 0.996. After 10 pulses the improved model resulted with a 13% increase in EDL concentration (to 1.02 x 10^{14} ions/cm^2) and can continue to increase with subsequent pulses. These preliminary results provide insights into extending this model for an FET and developing an EDL gated synaptic network. As part of ongoing work, the group is currently working on experimentally demonstrating the model using parallel plate capacitors (metal-electrolyte-metal) and Graphene-based EDL transistors.
1. Schuman et al. arXiv abs/1705.06963, 2017; 2. Zhu et al. Adv.

Mat., 2018, 30 (21); 3. Sung et al. Nanotech., 2018, 29 (11); 4. Lee at al. Adv. Fun. Mat., 2020, 30 (45); 5. Yang et al. Small Science, 2022, 2 (1); 6. Jacobs-Gedrim et al. IEEE (ICRC), 2017; 7. Jiang et al. Nanoscale, 2019, 11 (3); 8. Wan et al. Adv. Mat., 2016, 28; 9. Wen et al. ACS App. Mat. & Int., 2017, 9 (42); 10. Woeppel et al. ACS App. Mat. & Int., 2020, 12 (36); 11. Kilic et al. Phy. Rev., 2007, 75 (2)

2:50 PM Z05

(Student) Highly Stable and Controllable Quantum Conductance States up to 100 G_0 in TiO_2 Memristor Mousam C. Sahu[1], Sameer K. Mallik[1], Pankaj Misra[2] and Satyaprakash Sahoo[1]; [1]Institute of Physics, Bhubaneswar, India; [2]Raja Ramanna Centre for Advanced Technology, India

Memristors are simple two terminal devices in which an insulating layer is sandwiched between top and bottom metal electrodes. Under applied bias, the reversible formation and dissolution of conducting filament (CF) inside the insulator results in switching of the device resistance.[1,2] When the diameter of the CF is narrowed down to one atomic radius the electron moves ballistically inside the memristors. As a result, instead of a sharp jump, the device conductance evolves through plateaus of quantum of conductance ($G_0 = 2e^2/h$). However, with the increase in diameter of the CF several phenomena evolves such as joule heating, oxidative corrosion effect, mechanical stress, Gibbs-Thomson effect that results in unstable Quantum Conductance (QC) states.[3] In this regard, an oxygen vacancy engineered $Ag/TiO_2/Pt/Ti/SiO_2/Si$ memristor is fabricated that could able to exhibit stable and controllable QC states up to 100 G_0, for the first time. Under DC cyclic voltage measurements, the device exhibit compliance current (CC) controlled volatile (VS) and non-volatile (NVS) resistive switching behaviour. The VS switching of the device signifies that, the CF in our memristors are due to Ag atoms. During the NVS, following the CF formation, when a negative voltage is applied to the memristor instead of a sharp jump the device exhibit several transitions at fraction or integer multiples of G_0. Interestingly, during the CF formation when a CC of 1mA is applied, the device exhibits QC states ranging from 1-8 G_0. However, when the CC is increased to 2mA, and 3mA the exhibits higher integer multiple of QC states ranging from 2-20 G_0 and 5- 37 G_0, respectively. Statistical data from more than thousands of resistive switching cycles showing QC is collected over 50 devices. Such CC control of QC states in memristors may be attributed to the oxygen vacancy stoichiometry inside the TiO_2 layer. A possible CF formation/dissolution model is proposed to explain the experimental results. More importantly, not only in DC mode the higher order QC states can also be achieved in ultrafast pulse voltage operation mode, which is very important for practical read-write memory operations. Highly stable, readily controllable QC states up to 100 G_0 can be achieved in our memristor in pulse operation mode by manipulating the pulse amplitude, width, number etc. This demonstration of CC controlled QC states with higher integer values up to 100 G_0 could instigate a new horizon in the multi-bit high density memory storage devices.

References:

1. Sahu, M. C. *et al.* Effect of Charge Injection on the Conducting Filament of Valence Change Anatase TiO2 Resistive Random Access Memory Device. *J. Phys. Chem. Lett.* **12**, 1876–1884 (2021).
2. Jena, A. K. *et al.* Bipolar Resistive Switching in TiO2 Artificial Synapse Mimicking Pavlov's Associative Learning. *ACS Appl. Mater. Interfaces* **15**, 3574–3585 (2023).
3. Milano, G. *et al.* Quantum Conductance in Memristive Devices: Fundamentals, Developments, and Applications. *Advanced Materials* **34**, 2201248 (2022).

3:10 PM BREAK

3:30 PM #Z06

(Student) Multi-Weight Magnetic Artificial Synapses with Geometry-Dependent Neuromorphic Functionality Thomas Leonard, Samuel Liu, Mahshid Alamdar, Harrison Jin and Jean Anne Incorvia; The University of Texas at Austin, United States

Spintronic devices offer a more efficient hardware-based alternative to digitally simulated neural networks (NNs) on conventional CMOS devices[1]. This is because spintronic devices have the potential to emulate individual biological neurons and synapses which allows for one-to-one hardware mapping of NNs[2]. Domain wall (DW) based magnetic tunnel junction (MTJ) devices offer a highly tunable way to emulate many neuromorphic functionalities on a monolithic platform. The device relies on the switching of a MTJ to change state. The MTJ is composed of a fixed ferromagnetic (FM) layer and a freely switching FM layer separated by a thin tunnel barrier[3]. The resistance across the barrier is low when the magnetizations of the FM layers are parallel (P) and high when the magnetizations are antiparallel (AP). We have previously shown that if the free layer is replaced with an DW track, the device can be switched by moving the DW back and forth with current[4]. Now, we present prototypes demonstrating the tunability of these devices for neuromorphic functionalities.

The logic devices had a long DW track and a small MTJ along the track. As the DW passed under the MTJ, the resistance through the junction would switch. However, artificial synapses benefit from a higher number of states. To open more resistance states between P and AP, the MTJ was lengthened and pinning notches were patterned in the DW track beneath it. This allows for the DW to be caught under the MTJ, such that the junction is in a mixture of P and AP states. The DW can be depinned by current pulses or left in a nonvolatile state to store a weight. This allows the devices to be efficiently set during NN training and remember their weights during NN inference.

Two prototypes were explored here, a rectangular and a trapezoidal DW track[5]. The rectangular device had 5 lithographically defined pinning locations along the DW track, 3 of which were under the MTJ. This allowed for 5 repeatable and stable resistance states using one MTJ. For the trapezoidal device the asymmetry of the track allows for directional switching. Higher input current is required for wider regions to maintain current density. This allows for distinct switching voltages, since each notch has a different depinning energy depending on its location in the track. When the DW is pushed from the narrow end to the wide end, stronger pulses are needed to depin it from each notch. Pushing the DW from the wide end to the narrow end is not MW, since the DW starts in the notch with the strongest depinning energy. This behavior was shown by pushing the DW back and forth for 3 complete write/reset cycles without reinitialization.

We performed simulations of NN training and inference using experimental device data. To take advantage of the state-dependence of the trapezoidal device, a stream-learning task was implemented, where the FMNIST training dataset was separated into 60 subsets of 1000 images. The NN is then trained on one subset at a time for 30 epochs. For standard full-batch training on FMNIST, the trapezoidal device performed worse than a rectangular linear device, but when the information was provided in subsets the trapezoidal device outperformed the linear device. The trapezoidal device network was also able to reach the full accuracy of 85.6% for both training types. For inference, CIFAR-100 was used to evaluate the rectangular device, accounting for the experimental variability and stability of the states. Near-ideal accuracy was achieved, though quantization due to notches limits the attainable accuracy. Future advances for the DW-MTJ platform can enable tunable and efficient neuromorphic computing on the edge.

[1]J. Grollier et al., *Nat. Electron.* **3** (2020).
[2]A. Kurenkov et al., *Adv. Mater.* **31** (2019).
[3]S.Z. Peng et al., *Magnetic Tunnel Junctions for Spintronics: Principles and Applications.* (2014).
[4]T. Leonard et al., *Appl. Phys. Lett.* **118** (2021).
[5]T. Leonard et al., *Adv. Electron. Mater.* **8** (2022).

3:50 PM Z07
(Student) Impact of Single Molecule Magnets (SMM) on Magnetic Properties of a Cross-Junction-Shaped Magnetic Tunnel Junction
Marzieh Savadkoohi, Eva Mutunga, Hayden Brown, Andrew C. Grizzle, Pius Suh, Christopher D'Angelo and Pawan Tyagi; University of the District of Columbia, United States

Magnetic molecules can make a fundamental link between spintronic and molecular electronics. Using molecular components, electronics can reach its ultimate scale limit with properties of bulk magnetic materials while exploiting quantum effects. Single Molecule Magnets (SMM) can manipulate spins and charges and enhance memory devices and information processing capacities due to their slow relaxation time at low temperatures. According to the literature, molecular devices show other interesting phenomena such as switchability with light and magnetic fields, current suppression, and negative differential conductance [1-3]. This Research investigates a magnetic tunnel junction-based molecular spintronic device (MTJMSD) in which SMM molecules are attached to the exposed edges of ferromagnetic electrodes (FMEs) and act as conducting bridges.
Molecules can be coupled to the FMEs weakly or strongly based on the energy difference at the barrier between molecules and contacts. FME-molecule coupling strength and nature can affect the spins' polarization within FMEs. However, the experimental study of all possible cases is a daunting task due to the complexity of magnetic interaction between different elements of the device. Moreover, a proper experimental strategy needs to be set based on some prior understanding of MTJMSD behavior. This research focuses on I) using Monte Carlo simulation to investigate MTJMSD's magnetic behavior under a variety of molecule-FM electrode Heisenberg exchange coupling conditions II) studying the effect of 9 different parameters (i.e., spinning speed, baking temperature, etc.) to optimize our photolithography step before deposition of the bottom electrode and III) fabricating MTJMSD experimentally (Ta(5nm)/ NiFe(6nm)/ AlOx(2nm)/ NiFe(4nm)/Ta(5nm)) based on the insight gained from step 1 and 2. We investigated MTJMSD's magnetic characteristics before and after molecular treatment in our computational and experimental studies. Our computational result showed the optimal values corresponding to each parameter for getting the minimum and maximum magnetic moment. In the experimental study, we observed several interesting phenomena such as the photovoltaic effect and unprecedented Tunneling Magnetoresistance (TMR) at room temperature.
1-Bogani, L., Wernsdorfer, W. Molecular spintronics using single-molecule magnets. *Nature Mater* **7,** 179–186 (2008). https://doi.org/10.1038/nmat2133
2-Heersche, H. B. et al. Electron transport through single Mn12 molecular magnets. *Phys. Rev. Lett.* **96**, 206801 (2006)
Jo, M.-H. et al. Signatures of molecular magnetism in single-molecule transport spectroscopy. *Nano. Lett.* **6**, 2014–2020 (2006).
3- P. Tyagi and C. Riso, "Molecular spintronics devices exhibiting properties of a solar cell," Nanotechnology, vol. 30, p. 495401, 2019/09/19 2019.
4-P. Tyagi and C. Riso, "Magnetic force microscopy revealing long range molecule impact on magnetic tunnel junction based molecular spintronics devices," Organic Electronics, vol. 75, p. 105421, 2019/12/01/ 2019.

4:10 PM Z08
(Student) Vertical Spin Valves Architectures Based on Screw Dislocations in Semiconductor Nanomembranes Finley Haines, Emma J. Renteria, Mengistie Debasu and Francesca Cavallo; The University of New Mexico, United States

We report our initial results on the fabrication and characterization of a vertical spin valve (VSV) based on semiconductor nanomembranes (NMs) engineered with arrays of screw dislocations (SDs) throughout their thickness. These novel devices comprise dislocated NMs sandwiched between two ferromagnetic contacts on a substrate surface. The operation of the VSV will rely on the injection of polarized spin from a hard ferromagnetic contact into a 2D array of SDs in a semiconductor NM. Spin polarization resulting from SD-induced spin-orbit coupling (SOC) promises long coherence times at room temperature and above. The unique symmetry of a SD generates a helical electric field and a magnetic field that interact with spin-polarized electrons by restricting any changes in spin polarization (due to changes in the momentum of the electrons) between 0 and 90°. Additionally, the energy of spin-orbit-coupled electrons near the dislocation core is expected to lay in the semiconductor bandgap, i.e., far from electrons with unpolarized spin. This feature will potentially prevent hybridization between polarized and unpolarized electrons in the semiconductor [1]. After transport along the SDs, polarized spins reach the second ferromagnetic contact. Only spins that are aligned with magnetic moments in the ferromagnetic material are transmitted. Therefore, if both ferromagnetic contacts are polarized in the same direction, the VSV has relatively low electrical resistance. In contrast, if the applied magnetic field is reversed and the soft ferromagnet polarity also reverses, the device has a high resistance.
We have fabricated VSVs based on 1D SOC in SDs via a scalable process. The first step is patterning single-crystalline semiconductor NMs into a 2D array of pixels onto a sacrificial layer-coated bulk substrate. The NM pixels have a lateral size of a few hundred micrometers and can be made of group IV and III-V compound semiconductors (e.g., Si, SiC, and GaAs). Next, NM pixels are released in place onto the bulk substrate by selective erosion of the sacrificial layer. Photoresist anchors prevent the pixels from floating off the substrate or twisting. An adhesive stamp is used to remove NMs from the native substrate and transfer them onto a second array of patterned pixels. In this step, the NM/stamp combination adheres to a second array of pixels at a twist angle q controlled by a mask aligner. The stamp is released in solvent, and the twisted NM pairs or twisted bicrystals undergo high-temperature furnace annealing in N_2 atmosphere. During annealing, the disregistry at the NM-NM interface seeds the growth of SDs in ultra-thin semiconductors. Selected area electron diffraction and high-resolution transmission electron microscopy show that the twist angle q controls the spacing between the SDs. After annealing, the twisted bicrystals are transferred to a bulk substrate coated with a soft ferromagnetic layer. Hard ferromagnetic contacts are created on the top surface of the twisted bicrystal by photolithography, evaporation, and lift-off. The coercivity of the ferromagnetic films used for the contacts is extracted from measured magnetization curves on a Quantum Design Magnetic Properties Measurement System 3(QD-MPMS3). Variable temperature magneto-transport measurements characterize the resistance of the VSV at different orientations and magnitudes of magnetic induction (B).
ACKNOWLEDGEMENT. Work at the University of New Mexico was supported by the NSF CAREER award No. 2144944. his work was performed, in part, at the Center for Integrated Nanotechnologies, an Office of Science User Facility operated for the U.S. Department of Energy (DOE) Office of Science by Los Alamos National Laboratory (Contract 89233218CNA000001) and Sandia National Laboratories (Contract DE-NA-0003525).
[1] L. Hu, H. Huang, Z. Wang, W. Jiang, X. Ni, Y. Zhou, V. Zielasek, M. G. Lagally, B. Huang and F. Liu, Phys. Rev. Lett., 2018, 121, 66401.

4:30 PM *Z09
(Student) Methodology for Mitigation of the Reliability of a Resistive RAM Memory Array Caused by Thermal Cross-Talk Between the Memory Cells Marius Orlowski, Amrita Chakraborty and Mohamad Al-Mamun; Virginia Tech, United States

A switching of resistive memory cells leads to a local accumulation of Joules heat in the device. In resistive RAM (ReRAM) arrays of memory cells, the heat generated in one cell spreads via common electrode metal lines to the neighboring cells and may cause their performance degradation. In our study, we used a baseline Cu/TaOx/Pt cell with a variety of alternative inert electrode cells

replacing the inert Pt electrode. The performance degradation results in a reduced number of switching cycles and, in extreme cases, even in a loss of a bit, caused by the rupture of the nanofilament. We propose a thermal analysis of the thermal cross-talk, describe its impact on cells' electric performance, and identify three major mechanisms for the ReRAM reliability: (i) thermal conductivity, (ii) the specific heat capacity, and (iii) geometry of the electrodes. Several ReRAM arrays are manufactured to vary the thermal conductivity, specific heat, and geometry of the electrodes by depositing eight different inert electrodes: Pt(50 nm)/Ti(30 nm), Ru(50 nm)/Ti(30 nm), Co(50 nm)/Ti(30 nm), Pt(50 nm/Cu(100 nm)/Ti(30 nm), Pt(50 nm)/ Cu(200 nm)/Ti(30 nm), Ru(50 nm/Cr(30 nm), Ru(50 nm)/Ti(50 nm), and Rh(50 nm)/Cr(30 nm). The analysis handles the heat generation in nanostructures and its transfer to the nano-sized or micrometer-sized electrodes and how the heat transfer over the electrodes is transferred to nanofilaments of other memory cells sharing one common electrode. Using the proposed methodology, the experimentally found differences in the degradation of electric performance of the array cells performed under identical circumstances can be correctly predicted by the proposed thermal analysis using the material properties and geometry parameters of the electrodes. The analysis starts from the observation that the heat, Q, generated - typically between 3 μJ to 60 μJ - in a metallic nanofilament of a resistance R_{on}, - typically in the 1 kΩ to 100 kΩ range - if it were absorbed in the filament itself, it would lead according to the heat absorption equation of a body of mass m and specific heat capacity c_s, $Q=m\times c_s\times\Delta T$, to a temperature higher than the temperature inside the sun of 2.7×10^7 °K. Temperature ΔT, this high is the result of the tiny volume of nanofilament of typically 5×10^{-18} cm^{-3}. Since such a high temperature is impossible, the heat has to be accommodated in the ReRAM array otherwise, as it spreads to the more massive electrodes, depending on their mass (i.e. on their volume) and their specific heat capacity, and by the Newtonian losses which largely depend on the surface areas of the electrodes including the contact pads. Our analysis shows that the heat spreads across the electrodes w very quickly in the μs range due to the high thermal diffusivity, k, of the metallic electrodes. It can be shown that the typical time scale is given by $\tau=\sqrt{(k\times L)}$, where L is e.g. the distance between two neighboring cells. Thus, within less than a second a steady state of temperature distribution is established resulting in linear dependence of the temperature distribution along the electrode when evaluating the heat conduction equation. The solution of the equation allows for determining the temperature of the passive neighboring cells when heated by an active memory cell. We have confirmed experimentally that the heat from the same heated filament spreads more efficiently and quickly along the Cu electrode than along the Pt electrode, caused by the thermal conductivity of Cu being 5.8 higher than that of Pt. In fact, we have confirmed experimentally that the reliability of the passive neighboring cells disposed along the Cy electrode is much worse than the reliability along the Pt electrode. The proposed thermal analysis allows predicting ReRAM critical switching voltages, the degradation of electrical performance, and the reliability of ReRAM devices contingent on the choice of the electrode materials and the total volume of the electrodes.

4:50 PM Z10
(Student) Micromagnetic Simulations for Deterministic Switching in SOT-MRAM Cell with Additional Heavy Metal Capping Strip
Kuan-Hao K. Chiao and Yuh-Renn Wu; National Taiwan University, Taiwan

Spin-orbit torque magnetic random-access memory (SOT-MRAM) has received extensive interest in the memory industry. Recent efforts have focused on a heavy metal (HM)/ferromagnet (FM) bilayer with an additional HM capping strip to deterministically switch the magnetization [1]. This paper investigates the switching behaviors of SOT-MRAM utilizing this structure with micromagnetic simulations coupled to the drift-diffusion spin transport model [2]. The three-dimensional spin transport solver self-consistently calculates the charge currents, spin currents, and spin accumulations for arbitrary geometries and multi-layer structures without importing a computed current density [2]. This work uses a simple W/CoFeB/MgO structure to realize deterministic magnetization switching based on the HM capping strip method, which can be readily adopted in magnetic tunnel junctions. Figure 1(c) shows the simulated structure. In the simulations, the FL magnetization starts from an initial state of Mz/Ms = +1. The pulse current density J is injected into the HM along the negative x-direction with a duration of 2 ns. After the pulse, the magnetization switches to the negative z-axis through the relaxation process. In a conventional HM/FM, there is no additional HM capping strip. The My/Ms approaches 0 and My/Ms approaches +1 after the current pulse, which leads to a non-deterministic state when the current is removed. However, Mz/Ms crosses over 0 and reaches a negative remnant value. After removing the current, Mz/Ms proceeds toward a downstate Mz/Ms=-1 and causes deterministic magnetization.

We investigate the mechanism behind the HM-capping-strip-induced deterministic magnetization switching [2]. The spin accumulation distribution on the bottom HM interface is the key to understanding deterministic switching. With an HM strip capping on the HM layer, some non-negligible negative Sz is observed near the center y position, which is immediately above the FL. This negative Sz induces an additional negative z-direction spin torque when Mx/Ms=0, My/Ms=+1, and Mz/Ms=0 is reached. Therefore, a negative is observed under sufficiently large J. This is the critical factor of deterministic magnetization switching for the proposed structure.

To understand the origin of this non-negligible Sz on the bottom HM interface, Figs. 3 show the origination from the negative z-direction spin on the edge of the HM capping strip. By characterizing the system with an accurate spin-flip length of tungsten, the drift-diffusion spin transport solver with a negative z spin on the edge of the HM capping strip leads to a non-negligible negative Sz on the bottom HM interface. Further, the spin accumulation along the y-axis on the bottom HM interface has an opposing polarity when applying the opposite direction of J. Thus, the magnetization switches from Mz/Ms = -1 to Mz/Ms = 1 by changing the polarity of the current.

Mz/Ms reaches different under various J. This depends strongly on the current direction and magnitude, which indicates that deterministic bipolar switching can be achieved by changing the polarity of the current. A larger m_r results in improved switching behaviors because it prevents the magnetization from stochastically switching under the interference of thermal fluctuations. Furthermore, Fig. 4(a) indicates that a larger m_r induces a faster relaxation process when the current is removed, which gives a faster operating speed for the MRAM cell. Therefore, a larger current does not guarantee a higher switching speed. Instead, J with a magnitude slightly larger than Jc gives the ideal results. The relationship between Jc and w is also established, where Fig. 6(a) shows the SOT switching loops with different w. As w increases, Jc decreases. Instead of choosing the HM strip edge at the middle of the FL, the Jc minimum occurs near w=35 nm.

[1] 35Y. Li, N. Zhang, and K. Wang, Sci. China Inf. Sci. 65, 122404 (2022)
[2] S. Lepadatu, J. Appl. Phys. 128, 243902 (2020).

SESSION AA: Semiconducting Oxide Thin Films and Transistors
Session Chairs: Rebecca Peterson and Sarah Swisher
Thursday Afternoon, June 29, 2023
UC, Lobero

1:30 PM AA01
Optical, Structural and Electrical Properties of Al and in Donor Doped ZnO Films for TCO Applications Tetyana V. Torchynska[1], Brahim El Filali[2], Jorge L Ramirez Garcia[2], Georgiy Polupan[2] and Lyudmyla Shcherbyna[3]; [1]National Polytechnic Institute, Mexico; [2]Instituto Politecnico Nacional, Mexico; [3]V. Lashkaryov Institute of Semiconductor Physics at NASU, Ukraine

Zinc oxide films attracted great attention for decades due to its important optical, electrical, chemical and microstructural properties, interesting for optoelectronic applications in light emitting devices, transparent conduction oxide (TCO) for solar cells, gas sensors, flat screens and touch panel displays. However, the n-type conductivity of non-doped ZnO films is not high enough to be used in TCO applications. In work presented the influence of double donor doping with Al and In elements on morphology (Fig.1a, b, c), optical, structural and electrical characteristics of ZnO nanocrystal films has been investigated. The films were prepared by spray pyrolysis with an In content of 2.0 at% and different concentrations of Al atoms from 0.5 to 3.5 at.%. The crystal structure of the ZnO:Al:In films was wurtzite for all Al/In concentrations studied (Fig.2a) and a transmittance level about 90-95% has been detected in the visible spectral range (Fig.3). Using co-doping by Al and In atoms with lower (Al) and higher (In) ionic radii compared to the Zn ions, it is expected to lower the stresses in the films and gain insight into the factors favored to the limit of electrical conductivity in ZnO films.
The residual stresses were calculated in ZnO films with the hexagonal crystal lattice and the preferential orientation (002). The changes of crystal lattice parameters and the estimated values of the residual stresses in the ZnO:2.0%In: Al films with different Al contents are presented in figure 2b, c. For the Al concentration of 1.5-2.0 at%, the ZnO lattice parameters of highly doped ZnO films are closer (Fig.2b) to the lattice parameters of un-doped bulk ZnO, along with the minimum residual stresses estimated in this ZnO film (Fig.2c). However, the further increase of Al contents to 3.0-3.5 at% significantly modifies the crystallinity of ZnO films (Fig.1c), together with the decrease of the crystal lattice parameters, the increase of the compressive residual stresses (Fig.2c), and the changes of the film morphology (Fig.1c). By Al+In co-doping the residual stresses were reduced that allows reaching the minimum electrical resistivity of ZnO:2.0%In: Al films about 4.0×10^{-3} Ω cm (Fig.4). Conditions for the growth of ZnO NC films with the wurtzite crystal structure, flat surface morphology, and low electrical resistivity have been revealed. The reasons for change non-monotonically of characteristics have been analyzed and discussed.

1:50 PM AA02
Atomic Layer Deposition of Highly Conductive Highly Transparent Indium Gallium Doped Zinc Oxide Thin Films David Winarski[1] and Farida Selim[1,2]; [1]Bowling Green State University, United States; [2]Bowling Green University, United States

Transparent conductive oxides (TCOs) are essential elements for photovoltaics and optoelectronic devices. In this work thin films of ZnO co-doped with In^{3+} and Ga^{3+} (IGZO) were deposited by atomic layer deposition onto various commercial and homegrown substrates to develop TCOs and characterized by X-ray diffraction, scanning electron microscopy, transmission electron microscopy, atomic force microscopy, optical spectroscopy, and Hall-effect measurements. The thin films exhibit structural stability, remarkable conductivity at room temperature, high visible range transparency, and a band gap near 3.42 eV. Optical and electrical characterization revealed a TCO figure of merit $\Phi = 8.66 \times 10^{-2}\ \Omega^{-3}$ for IGZO with a thickness of 164 nm surpassing Al-doped ZnO (AZO) TCOs and rivalling the industry standard ITO. Temperature-dependent electrical transport measurements of IGZO films revealed a fully degenerate semiconductor behavior.

2:10 PM AA03
Atomic Layer Deposition (ALD) and Sol-Gel Techniques Comparison from the Perspective of TiO_2 Thin-Films Fabrication Luz A. Rincon Baron[1,2], Guoduan Liu[1], Camilo Velez Cuervo[1], Juan Carlos Salcedo Reyes[2], Aura Marina Pedroza Rodriguez[2] and Augusto Enrique Mejia[2]; [1]University of California, Irvine, United States; [2]Pontificia Universidad Javeriana, Colombia

Titanium Dioxide (TiO2) is a semiconductor that can be found under Brookite, Rutile and Anatase phases, where the former has gained relevance due to its photocatalytic features, high chemical stability, low toxicity/cost, and strong oxidizing capacity under UV light [1]. Exposing TiO2 to UV light leads to the production of indirect electronical transition that enables the formation of reactive species, with free radical hydroxyl (HO) and superoxide (O2) that promotes decomposition of organic contaminants [2].
Two techniques will be compared. Atomic Layer Deposition (ALD) is physical and requires two vapor precursors injections inside a chamber separated by the purge of an inert gas, and each precursor saturates the surface of the substrate leading to the formation of the TiO2 thin film. Hence, the ALD methodology is considered a stepped self-limiting technic [3], where the thickness of the thin film relies on the number of deposited cycles under half vacuum pressure conditions (0.1 torr).
Sol-Gel is a chemical technique applied at room temperature and atmospheric pressure conditions, where simultaneous reactions are produced: hydrolysis and condensation [4]. Initially, the hydrolysis requires a metallic precursor (titanium alkoxide), solvents and acidification of the solution, which results in the formation of Titanium Hydroxides and the condensation process finally leads to the Titanium Dioxide synthesis [5].
In this work, TiO2 thin films are generated over glass substrates previously cleaned through DI water, 2propanol and acetone. For ALD the Titanium Alkoxide Tetraisopropyl Orthotitanate (Ti[OCH(CH3)2]4) was taken as precursor, and vaporized water for the formation of TiO2; under a Ni atmosphere at 20 sccm, with 1100 cycles (20 nm thick), a working temperature fixed at 200 C and pressure of 2.45x10-1 torr. For Sol-Gel, the solution was also prepared using Ti[OCH(CH3)2]4, but with ethanol (CH3CH2OH), acetic acid (CH3COOH), H2O2 and DI water, as explored in [5-7]. Solution is spin coated over hydrolyzing substrate (H2SO4 + H2O2 in 3:1 concentration. Manufactured films from both techniques, were taken to an annealing process at 450 C and 550 C, under a Ni atmosphere with a gas flux of 4000 sccm during 1 hour.
The characterization of TiO2 thin films was realized before and after the annealing process, starting from X-Ray Diffraction (XRD) to the crystallin phase of the TiO2 anatase on each treatment, in order to measure the intensity of the phase in the plane (101) with an angle of 25.16±0.2° (Fig. 1) [2]. Also, the absorption spectrum was measured using the Lambert-Beer Law [8] and the bandgap energy by direct gap of the semiconductor was estimated as a function of temperature (Fig. 2); moreover, the morphology of the films surface was observed with the Scanning Eletron Microscopy (SEM) technique and the elemental analysis of the films by energy dispersive X-ray spectroscopy (EDX). Finally, the resistivity was measured using the Van der Pauw 4-point technique and the charge mobility was analyzed with Hall effect (Fig. 2).

References

[1] A. Ibrahim, W. Phoohinkong, W. Mekprasart, and W. Pecharapa, *Mater. Today Proc.*, vol. 5, no. 5, pp. 10903–10909, 2018.
[2] R. Katal, S. Masudy-Panah, M. Tanhaei, M. H. D. A. Farahani, and H. Jiangyong, *Chem. Eng. J.*, vol. 384, no. October 2019, p. 123384, 2020.
[3] V. Pore, A. Rahtu, M. Leskelä, M. Ritala, T. Sajavaara, and J.

Keinonen, *Chem. Vap. Depos.*, vol. 10, no. 3, pp. 143–148, 2004
[4] Brinker C. Jeffrey, p. 462, 1990.
[5] M. B. Tahir, K. Nadeem, M. Hafeez, and S. Firdous, *Indian J. Pure Appl. Phys.*, vol. 55, no. 10, pp. 716–721, 2017.
[6] M. Urbonavicius, S. Varnagiris, S. Sakalauskaite, E. Demikyte, S. Tuckute, and M. Lelis, *Catalysts*, vol. 11, no. 7, 2021.
[7] C. Villanueva Jaramillo, A. M. Pedroza, J. C. Salcedo, A. K. Carrascal Camacho, and A. E. Florido Cuellar, pp. 1–125, 2011.
[8] G. L. Tian, H. B. He, and J. Da Shao, *Chinese Phys. Lett.*, vol. 22, no. 7, pp. 1787–1789, 2005.

2:30 PM AA04
(Student) Donor Activation in Boron and Phosphorus Implanted Self-Aligned Bottom-Gate IGZO TFTs Eli Powell[1], Muhammad S. Kabir[1], Rahnuma Chowdhury[1], Karl D. Hirschman[1], Robert Manley[2] and Bin Zhu[2]; [1]Rochester Institute of Technology, United States; [2]Corning Incorporated, United States

Self-aligned channel regions in thin-film transistors (TFTs) have advantages in reduced parasitic capacitance and stage delay, and a reduction in overhead real estate. A common method used to fabricate self-aligned a-Si:H TFTs is to utilize a through-glass exposure of photoresist which is blocked by the opaque metal bottom-gate electrode [1,2]. This process does not require an additional photomask or lithographic alignment, and thus supports low production cost. Sputtered IGZO has been introduced into flat panel display product manufacturing, exhibiting a channel mobility of approximately an order of magnitude higher than a-Si:H. The working source/drain electrodes in IGZO TFTs can be direct metal contact regions to the IGZO, without the need for additional processes such as doping to render the IGZO conductive. Proper metallurgy and annealing processes can provide ohmic behavior with minimal series resistance, however this usually requires several microns of gate-to-source/drain overlap to ensure such behavior.
This work provides an interpretation of donor activation in self-aligned bottom-gate IGZO TFTs with ion-implantation of boron ($^{11}B^{+}$) and phosphorus ($^{31}P^{+}$) species as the source/drain treatment. In previous investigations of boron implantation, utilizing an anneal-implant sequence resulted in self-aligned devices with transfer characteristics comparable to non-self-aligned TFTs. A left shift in transfer characteristics was observed following thermal stress at 175 °C which is not consistent with recent work from alternate sources which have shown boron implanted devices temperature stable at 200 °C [3,4]. It is hypothesized that this is the result of implant species contamination due to the presence of hydrogen in the implant gas distribution system. In contrast, following an implant-anneal sequence at 400 °C did not support an electrically active species. The implant-anneal strategy seems to result in a different bonding arrangement which does not support donor-like behavior related to boron. Self-aligned phosphorus implants present promising behavior using the implant-anneal strategy, potentially serving as a lightly doped drain (LDD) structure for sub-micron scaled devices.

2:50 PM AA05
(Student, Late News) Optimized Heterojunction Metal-Oxide Semiconductor Structures for High Performance Indium-Tin-Oxide TFTs Dong Hyuk Kim, Seong-Pil Jeon, Dongwon Kang, Jee Young Kwak, Seung-Han Kang and Sung Kyu Park; Korea University, Korea (the Republic of)

Metal oxide (MO) thin film transistors (TFTs) are widely studied to improve their performance. One way is to use a conductive metal-oxide, such as indium-tin-oxide (ITO), as the channel layer to achieve high mobility. However, the ITO semiconducting layer can cause a significant negative shift of threshold voltage (V_{th}) and an increase of off-current, possibly due to its high conductive properties. To mitigate this, we investigated a method of optimized heterojunction ITO semiconducting layers, changing the band alignment of the channels with less conductive materials, such as amorphous indium gallium zinc oxide (a-IGZO) as double or triple-channels with ITO layer.
To fabricate the heterogenous ITO TFTs, we deposited thin ITO and a-IGZO layers on glass and Si/SiO2 substrates. An Al_2O_3 dielectric layer was deposited through atomic layer deposition (ALD), and the channel layer of ITO and IGZO was fabricated through RF magnetron sputter and annealed at 300 °C in air ambient. Finally, ITO source/drain electrodes were sputtered and patterned by lift-off process.
The heterogeneous TFTs implemented using this process exhibited better performance than those with conventional single-layer channels. Thin ITO layers increased electron concentration and improved mobility, while adjustments to the ITO thickness allowed for the manipulation of band alignment through the quantum confinement effect. Moreover, the a-IGZO layer onto the ITO helped to properly adjust the threshold voltage of the device, resulting in low off-state current. The ITO/*a*-IGZO TFTs optimized via the thickness-dependent carrier concentration of ITO and band alignment manipulation in the bilayer considerably improved the device performance in terms of saturation mobility, V_{th}, and off-current. The saturation mobility was 〉 90 cm^2/V-sec (average 89.0 ± 1.0 cm^2/V-sec), subthreshold swing was 〈 95.3 mV/decade (average 95.3 ± 8.7 mV/decade), and current on/off ratio was 〉 1.87×10^{10}.
We performed computer-aided design simulation (TCAD) to analyze the underlying mechanism of the device's electrical and material characteristics. And this showed that the threshold voltage can be properly adjusted while having high mobility through band bending created by moving the ITO's electrons to IGZO. Also, PBS, NBS and NBIS test were conducted to evaluate the stability of the device, and it was found to be less shifted than the existing IGZO, resulting in better stability. Lastly, we investigated X-ray photoelectron spectroscopy (XPS) data, which showed that the stability was enhanced by reducing oxygen vacancy defects, possibly due to the diffusion of Sn ions of ITO into the heterogeneous interfaces.
In conclusion, heterojunction MO TFTs demonstrated high saturation mobility with alleviation of V_{th} shift and good operational bias stability. The results obtained through TCAD simulation provide insight into the mechanism underlying the performance improvement and could serve as the basis for future improvements of the metal-oxide TFTs.

3:10 PM BREAK

3:30 PM AA06
(Student) Accurate Field-Effect Mobility Estimation with Gate Voltage-Dependent Mobility in Linear Region for IGZO Thin-Film Transistors Yuchen Zhou, Xiao Wang and Ananth Dodabalapur; University of Texas at Austin, United States

Carrier mobility is an essential figure of merit for transistors used in various electronic applications. High mobilities are generally desired for thin-film transistors (TFTs) with amorphous metal oxide and organic/polymer semiconducting channel materials, as it enables faster operating speeds for various applications including displays, RFID tags, and integrated circuits. However, the reported linear mobility calculated using transconductance is often overestimated under the gradual channel approximation. In this abstract, we introduce a more robust method to obtain accurate mobilities by explicitly considering the gate voltage-dependence of the mobility in the linear region for metal oxide semiconductor.
Transfer curves in the linear region often exhibit superlinear or sublinear behavior, as shown in **Figure 1**. Therefore, using the gradual channel approximation results in inaccurate mobility value, since it assumes a constant mobility independent of carrier density. To obtain a more accurate mobility, the gate-dependence must be considered. After modifying the conventional transconductance method (**Equation 1**), the resulting equation consists of three terms: the transconductance term on the left-hand side, the differential mobility term with respect to gate voltage, and the modified field effect mobility on the right-hand side (**Equation 3**). The inclusion of the second term or the differential mobility term often results in calculated mobility values larger by a factor of between one and two, as shown in

Figure 2. Average mobility, the mobility of all mobile carriers at a given drain and gate voltage, is also proposed (**Equation 3**), which should be identical to the field effect mobility.
Accurate threshold voltage values must also be considered for an improved mobility extraction. While threshold voltage (conventional V_{TH}) has been estimated using the linear extrapolation method on the drain current, it can also be determined using the voltage at which drift currents start to dominate over diffusion currents in the subthreshold regime for TFTs (corrected V_{TH}).
Amorphous indium-gallium-zinc-oxide (a-IGZO) TFTs was fabricated and used to illustrate the corrected field effect mobility and threshold voltage calculation process. Shown in **Figure 3 (c)**, the conventional threshold voltage, onset voltage, and the corrected threshold voltage are compared. The corrected field effect mobilities (**Equation 4**) are calculated using three different threshold voltages and compared with the conventional field effect mobility. In one sample TFT, the conventional field effect mobility calculation yields a value of 2 cm^2/V-sec while the corrected field effect mobility is approximately 1.2 cm^2/V-sec, resulting in at least an overestimation of ~ 67% (**Figure 3 (d)**). Our calculation also shows that the average mobility is virtually identical to the corrected field effect mobility.
Given that the average mobility is unambiguous and can be obtained through a simple calculation, it is better suited for estimating mobilities in samples with severe contact resistance. Due to the presence of contact resistance, the channel voltage (V_{CH}) is significantly less than the applied drain voltage (**Figure 4 (b)**). Average mobilities excluding the contact resistance can be calculated by replacing the drain voltage in linear square law model with the channel voltage (**Equation 5**), which is significantly higher than average mobility obtained using the applied drain voltage, as shown in **Figure 4 (c)**.
This mobility calculation process can be applied to transistors with any semiconducting materials that exhibit non-constant mobilities in the linear region. It is a robust tool when it comes to accurately characterizing the device performance of thin-film transistors in the linear region.

3:50 PM AA07
IGZO Synaptic Thin-Film Transistors Using Embedded AlOx Charge-Trapping Layer Hongseok Oh; Soongsil University, Korea (the Republic of)

In this presentation, fabrication and characterization of a synaptic thin film transistors using indium gallium zinc oxide (IGZO) is discussed. Here, IGZO thin film was deposited by the radio-frequency (RF) magnetron sputtering method. Importantly, a thin and defective aluminum oxide (AlOx) film was embedded in the IGZO thin film by RF sputtering, which serves as a charge trap layers providing synaptic behaviors. From the as fabricated devices, a typical output and transfer characteristics were observed. Importantly, electrical voltage pulses introduced to the gate electrode evoked synaptic behaviors such as excitatory post-synaptic currents (EPSC), pair pulse facilitation (PPF), and potentiation and depression (PD), similar to that of the biological synapses. The main mechanism was explained as a trapping or de-trapping of electrons in the embedded AlOx layer which modulates the current in the IGZO film. Furthermore, such synaptic behaviors is found to be useful when employed in the artificial neural network, suggested by simulation study. This work provides a scalable method in developing synaptic transistors which can serve as a synapse in hardware implemented artificial neural network, which is expected to achieve energy efficient artificial intelligence (AI) technology.

4:10 PM AA08
(Student) Tuning Threshold Voltage in Ultrathin Channel Flexible Amorphous InGaZnOx TFTs Reem Alshanbari, Megan Noga, Oliver Durnan, Rajinder Deol and John Kymissis; Columbia University, United States

TFTs with ultrathin channels are promising for monolithic 3D technology for advanced CMOS scaling and integration beyond planar CMOS to extend Moore's law lifetime and have devices with low power consumption and leakage. Amorphous InGaZnOx (α-IGZO) TFT is one of the most promising candidates for replacing amorphous silicon (α-Si). α-IGZO has higher charge carrier mobility than α-Si, resulting in higher current and other advantageous properties. Because of their high field-effect mobility (10 cm^2/Vs), high uniformity, low-temperature process, and low leakage current (10^{-18} A/μm), α-IGZO TFTs are now used in panel displays. Furthermore, α-IGZO has a low fabrication cost and high transparency. However, because of their high carrier density, α-IGZO TFTs have a negative threshold voltage (Vth). Annealing could be used to optimize the Vth of α-IGZO TFTs. Despite this, tuning Vth in flexible α-IGZO TFTs via annealing is difficult due to the polymer substrate's limited thermal budget. In this work, we fabricated multiple flexible α-IGZO TFTs with bottom gate and top contacts structure with different channel thicknesses. The devices were fabricated on 15μm thick PI, followed by a 500nm thick layer of Si_3N_4 deposited on the PI side by PECVD to improve the adhesion of the subsequent layers. Then evaporated Ti/Au/Ti (5nm/50nm/5nm) as gate electrodes and alignment marks patterned by photolithography and lift-off followed by dielectric deposition via PECVD. An α-IGZO was sputtered at room temperature, followed by e-beam evaporated Ti/Au (5nm/50nm) source/drain electrodes. In addition to optimizing the Vth, we investigated electrical key metrics such as field effect mobility (μ_{EF}), on/off current ratio (I_{ON}/I_{OFF}), and subthreshold swing (*SS*). We demonstrated that the flexible α-IGZO TFT with a 10 nm-thick channel has the highest field effect mobility, with a low threshold voltage value, a small subthreshold swing, and a high on/off current ratio. The interface between the channel and the dielectric and the channel's bulk quality impact the electrical performance of *the* TFT. The electrical conductivity of the channel layer is primarily affected by tail states, oxygen defects, and deep states. Finally, we discovered that the flexible α-IGZO TFT with a 5 nm thick channel had performance degradation due to non-uniformity in the IGZO film. These findings will benefit the development of flexible ultrathin α-IGZO TFTs for logic devices, vertical memory, and monolithic 3D devices for advanced scaling.

4:30 PM AA09
(Student) Improved Electrical Performance of $InGaZnO_4$ Thin-Film Transistors with UV Ozone Treatment Guoduan Liu; University of California, Irvine, United States

We report the successful fabrication and characterization of thin film transistors (TFTs) with a significant ~95.7% reduction on the saturation currents thanks to ultraviolet ozone (UVO) and controlled annealing treatments. Such TFTs (Figure 1) were designed for autonomous microrobotic applications. On this specific study we exposed the TFTs to a 3 min ultraviolet ozone (UVO) with 184.5 nm (17%) and 253.7 nm (83%) UV light emissions at a constant light intensity (28-32 mW cm^{-2}), together with 1 hour annealing treatment at 300 °C to yield contact resistance of 74.5±1.16 Ω and sheet resistance of 5.376 Ω/square. Although, defects and uniformity of materials usually affect the performance of TFTs such as threshold voltage, contact resistance, and output current [4,5], the consistent reduction of saturation currents (~252 μA @ Vg=50 V) obtained after UVO treatment (Figure 2) are evidence that oxygen vacancies were reduced, and metal-oxygen bonding were increased.
TFT are versatile semiconductor devices with wide applications, ranging from liquid crystal displays to flexible and transparent electronic devices [1-3] expected to have low drain-source currents during saturation to reduce de energy consumption, especially critical in autonomous small scale robotic applications. The proposed TFTs were fabricated over insulated (100 nm SiO_2) P-type (100) silicon substrate with bottom-gate/top-contact architecture. The device cross section shown in Figure 1a, contains 50 nm semiconductor layer of amorphous Indium-gallium-zinc oxide ($InGaZnO_4$) via sputtering; 10 nm/50 nm Cr/Au electrode layers deposited by electron beam evaporation for drain, source and gate; and 10 nm of Al_2O_3 grown via atomic layer deposition as dielectric.
We also designed and array of TFTs with different sizes (channel with

and length) and test features, to extract important parameters for compact modeling. Lengths ranges between 8 µm to 160 µm and widths between 10 µm to 1000 µm. Test features include transfer length method (TLM), capacitance extraction, and four-point van der Pauw for hall probe measurements to extract mobility. The fully fabricated chip and TFT are shown in Figure 1b-1c. I-V curves were measured for all channel dimensions and saturation currents are summarized in Figure 3. As expected, the saturation current decreases with the length and increases with TFTs width, useful relationships that provide reference for designing specific power on future TFTs generations with improved performance after UVO and annealing technique.

Acknowledgement: The authors would like to thank the support from the Mechanical and Aerospace Engineering Department. University of California, Irvine.

References:

[1] Hays, D. C., Gila, B. P., Pearton, S. J., & Ren, F. (2017). Energy band offsets of dielectrics on InGaZnO4. *Applied Physics Reviews*, *4*(2), 021301.

[2] Zhou, X., Cao, H., Zhou, Z., Cao, J., & Yu, J. (2017). Structural, electrical and optical properties of $InGaZnO_4InGaZnO_4$ and $In_{29}Sn_3O_{48}In_{29}Sn_3O_{48}$: a first-principles study. Journal of Computational Electronics, 16(2), 280-286.

[3] Nomura, K., Takagi, A., Kamiya, T., Ohta, H., Hirano, M., & Hosono, H. (2006). Amorphous oxide semiconductors for high-performance flexible thin-film transistors. *Japanese journal of applied physics*, *45*(5S), 4303.

[4] McDonnell, S., Addou, R., Buie, C., Wallace, R. M., & Hinkle, C. L. (2014). Defect-dominated doping and contact resistance in MoS2. *ACS nano*, *8*(3), 2880-2888.

[5] Suemori, K., Uemura, S., Yoshida, M., Hoshino, S., Takada, N., Kodzasa, T., & Kamata, T. (2008). Influence of fine roughness of insulator surface on threshold voltage stability of organic field-effect transistors. *Applied Physics Letters*, *93*(3), 264.

4:50 PM AA10

Continuous Liquid Metal Printing of High-Performance 2D Oxide Heterostructures William J. Scheideler, Youxiong Ye, Andrew B. Hamlin and Simon Agnew; Dartmouth College, United States

Two-dimensional (2D) van der Waals transparent conducting metal oxides (TCOs) have recently emerged as a promising platform for fabricating flexible optoelectronic devices, offering high mobility, high transparency, and improved mechanical flexibility. This class of 2D oxides can be synthesized at low temperatures (< 180 °C) without vacuum by utilizing the unique physics of liquid metal surface oxides. Here we report continuous liquid metal printing for scalable fabrication of high-performance 2D TCOs compatible with polymer substrates. We apply a spontaneous Cabrera Mott growth at low-temperatures afforded by the low melting point of In, Ga, Sn, and their alloys. In our continuous liquid metal printing (CLMP) method, these metal droplets serve as the source material for simultaneously growing and depositing these films via adhesion of the 2-3 nm thick solid oxide skin over large areas (~ 100 cm^2). The high speed of this roller-based deposition method (> 6 meters/minute) is also particularly promising because Cabrera Mott synthesis naturally yields high conductivity, sub-stoichiometric oxides via their oxidation from the metallic phase. This allows the use of a rapid process, eliminating thermal post-annealing steps otherwise necessary for low-temperature metal oxides, opening up greater opportunities for utilizing lower cost plastic substrates.

In this presentation, we demonstrate a new class of layered TCO heterostructures exploiting modulation doping interactions between 2D InO_x and 2D GaO_x. We characterize the crystallinity of these 2D oxide films as a function of deposition temperature within the range of plastic substrates (160 °C to 240 °C) by XRD and apply TEM to observe the large plate-like cubic InO_x grain structure. These overlapped grain morphologies lead to high conductivity (up to 600 S/cm) despite the exceptionally low total processing time (3s per layer) and low temperatures (180 °C). Through XPS, UV-Vis, and Hall characterization, we examine the modulation doping effect induced by the InO_x / GaO_x interface in these multilayer TCOs. UV-Vis absorption spectroscopy reveals the impact that modulation doping can enhance visible range transparency through a Burstein Moss effect-induced optical bandgap widening. We characterize the flexibility of these 2D TCOs in comparison with sputtered ITO electrodes on plastic substrates, showing how the ultrathin nature provides substantially greater strain tolerance under cyclic bending. These results show how interfacial modulation doping interactions can be used to control and enhance the electronic properties of 2D oxides beyond the state of the art for low-temperature processed metal oxides.

SESSION BB: Group III–Nitrides—P-Type Doping and Characterization
Session Chairs: Theeradetch Detchprohm and Luke Yates
Thursday Afternoon, June 29, 2023
UC, Santa Barbara Harbor

1:30 PM BB01

Achieving Technologically Relevant P-Type Conductivity in Al-Rich (>70% Al) AlGaN Using Impurity Band Conduction Shashwat Rathkanthiwar[1], Cristyan E. Quiñones García[1], Pegah Bagheri[1], Dolar Khachariya[2], Seiji Mita[2], Pramod Reddy[2], Ronny Kirste[2], Ramón Collazo[1] and Zlatko Sitar[1,2]; [1]North Carolina State University, United States; [2]Adroit Materials Inc., United States

In this study, we demonstrate the utility of impurity band conduction in overcoming the limitations of conventional p-type doping in Al-rich aluminum gallium nitride (AlGaN). First, a model is developed to understand the impurity band conduction mechanism in Mg-doped AlGaN. It is hypothesized that at high Mg doping concentrations (mid-10^{19} cm^{-3}) -below the Mott transition-, the overlap of the Mg dopant states can cause the dopant energy level to split into a quasi-continuous impurity band. This provides an alternate route for conduction, where the carriers can propagate through the impurity band with a much-reduced activation energy as compared to the relatively large Mg ionization energy required for the valence band transport. It is worthwhile to note that the presence of compensating point defects can disrupt the overlap of the Mg orbitals and, hence, impede the formation of the impurity band. Mg-doped Al-rich AlGaN epilayers were grown on sapphire and single-crystal AlN substrates by metalorganic chemical vapor deposition. In accordance with the model, relatively heavy Mg doping in conjunction with compensation control was found to be critical to induce the impurity band formation. Record-low p-type resistivities of 9.7 and 37 Ωcm were achieved in $Al_{0.7}Ga_{0.3}N$ and $Al_{0.8}Ga_{0.2}N$ films grown on the native substrate. The resistivity exhibited shallow activation energy of ~30 meV for a wide temperature range of 150-500K. Valence band conduction associated with a large Mg ionization energy was observed to dominate above 500K. Interestingly, the Hall coefficient data was found to deviate from classical semiconductor physics. The apparently anomalous results were attributed to the fact that the Hall effect associated with the carriers propagating in the impurity band differs qualitatively from the quasi-free motion of holes in the valence band leading to a fundamentally different Hall scattering factor. This work demonstrates the utility of impurity band conduction to achieve technologically relevant p-type conductivity in Al-rich AlGaN.

Al-rich AlGaN devices are poised to enable a host of optoelectronic applications owing to their desired properties such as low size, weight, and potential operating power. While Si doping has been demonstrated to be effective in achieving n-type Al-rich AlGaN films, efficient p-type doping remains a significant challenge. Mg, the most explored p-type dopant in AlGaN presents a rather high ionization

energy of >400 meV. This creates a fundamental bottleneck as only a small fraction of the Mg atoms ionizes at room temperature to generate free holes. This results in a high resistivity >100 Ωcm in Mg-doped Al-rich AlGaN grown via the conventional Mg doping approach. While alternate doping approaches such as short-period superlattices, composition modulation, and Mg delta doping allow for low lateral resistivity in p-AlGaN the vertical conduction is limited due to the barriers associated with the periodic oscillation of the energy bands. The polarization-graded AlGaN approach, on the other hand, necessitates the grading toward Ga-rich compositions to achieve high hole concentration and to favor the Ohmic contact formation. This approach suffers from UV-C absorption loss in the p-type layer, significantly decreasing the light extraction efficiency in optoelectronic devices. Therefore, it is of significance to devise techniques for achieving low p-type resistivity in Al-rich AlGaN without modulating the composition or the doping profile.

1:50 PM BB02
(Student) Modelling Self-Compensation in Heavily Mg-Doped GaN Cristyan E. Quiñones García[1], Masahiro Kamiyama[1], Shashwat Rathkanthiwar[1], Pegah Bagheri[1], Ronny Kirste[2], Pramod Reddy[1], Seiji Mita[1], Erhard Kohn[1], Ramón Collazo[1] and Zlatko Sitar[1,2]; [1]North Carolina State University, United States; [2]Adroit Materials, United States

Despite more than 30 years of research, the nature of self-compensation in heavily Mg-doped GaN is still not well understood. Native compensating (point and extended) defects have been identified as the main cause for the rapid drop in hole concentration after a critical Mg concentration of about $2x10^{19}$ cm^{-3}. Some reports[1] have suggested that pyramidal inversion domains (PIDs), which bind and inactivate the Mg atoms, is the main cause behind this self-compensation. Others, in turn, have argued that the amount of Mg bound at PIDs is insufficient to account for the change in electrical properties.[2,3] In this case, the existence of the nitrogen-vacancy (V_N) and its complexes with Mg are invoked as the main cause of compensation.[4–6] However, the exact structure and charge state of these defects, as well as which of these is the dominant effect is still under debate.
In this study, we investigate $(nMg\text{-}V_N)^q$ complexes as the compensating defects in Mg-doped GaN. Using the charge balance equation in conjunction with the grand canonical formalism for defect complexes, a semi-empirical model for the hole concentration as a function of [Mg] is developed. Room temperature hole concentration for MOCVD-grown Mg-doped GaN samples of varying Mg concentration is analyzed by fitting the model to the experimental data. This allows the estimation of compensating complex concentrations along with effective acceptor density (N_A-N_D) and ionization energy. Charge balance fitting of temperature-dependent carrier concentration data (Hall) is used to extract the effective acceptor and compensating donor densities, as well as the ionization energy. Good agreement between both models is found in predicting the ionization energy as well as N_A-N_D as a function of Mg concentration. The experimental N_A-N_D values measured using capacitance-voltage measurements were found to be comparable to the model predictions.
Based on the shape of the knee behavior, as well as the fittings, the proposed model can distinguish between different complex charge states. This has important implications for the application of established point defect management methods, where knowing the charge state is useful in choosing a strategy for compensation control. For all growth conditions studied here, the main compensating complex is identified as the neutral charge state with three Mg bound to one vacancy($(3Mg\text{-}V_N)^0$). By using the chemical potential control technique, we demonstrate that the critical Mg concentration for self-compensation can be systematically increased from $2x10^{19}$ cm^{-3} to $7x10^{19}$ cm^{-3}.
References
[1] N. Tetsuo, I. Nobuyuki, T. Kazuyoshi, K. Keita, and K. Tetsu, J. Appl. Phys. **124**, 165706 (2018).
[2] T. Remmele, M. Albrecht, K. Irmscher, R. Fornari, and M. Straßburg, Appl. Phys. Lett. **99**, 141913 (2011).
[3] A. Papamichail, A. Kakanakova-Georgieva, E.Ö. Sveinbjörnsson, A.R. Persson, B. Hult, N. Rorsman, V. Stanishev, S.P. Le, P.O.Å. Persson, M. Nawaz, J.T. Chen, P.P. Paskov, and V. Darakchieva, J. Appl. Phys. **131**, 185704 (2022).
[4] G. Miceli and A. Pasquarello, Phys. Rev. B **93**, 165207 (2016).
[5] M.L. Nakarmi, N. Nepal, C. Ugolini, T.M. Altahtamouni, J.Y. Lin, and H.X. Jiang, Appl. Phys. Lett. **89**, 152120 (2006).
[6] Q. Yan, A. Janotti, M. Scheffler, and C.G. Van de Walle, Appl. Phys. Lett. **100**, 142110 (2012).

2:10 PM BB03
MOCVD GaN Co-Doped with Mg and Be Benjamin McEwen[1], Emma Rocco[1], Vincent Meyers[1], Alireza Lanjani[1], Oleksandr Andrieiev[2], Mykhailo Vorobiov[2], Denis Demchenko[2], Michael Reshchikov[2] and Fatemeh (Shadi) Shahedipour-Sandvik[1]; [1]SUNY Polytechnic Institute, United States; [2]Virginia Commonwealth University, United States

Recently, beryllium has regained attention as a potential *p*-type dopant in III-Nitrides due to its shallower acceptor level than magnesium. We recently reported the first systematic investigation of GaN:Be grown using metal-organic chemical vapor deposition (MOCVD) [1]. Despite the successful incorporation of Be into GaN grown by MOCVD, conductive *p*-type GaN:Be has yet to be realized. This may be in part due to poor incorporation efficiency of Be under normal growth conditions where [Be] saturates at about $1–5×10^{18}$ cm^{-3}. Techniques to increase [Be] such as using a pulsed growth method have been successful, but result in material degradation and *p*-type conductivity was still not achieved. Furthermore, a prominent YL_{Be} band in photoluminescence studies indicates the presence of a deep donor, which may be responsible for the compensation of activated Be.
Co-doping GaN with Be and Mg has been suggested as a possible way to increase Be incorporation and suppress YL_{Be}, and initial studies using MBE-grown GaN:Be+Mg showed promise [2,3]. However, no comprehensive studies were performed, and this technique has never been attempted using MOCVD. Because Be and Mg induce local tensile and compressive strains, respectively, due to their atomic sizes relative to Ga, co-doping may improve solid solubility of both species and encourage incorporation of acceptors into electrically active Ga sites. In this work, we investigate the effects of Be+Mg co-doping in GaN. Several different doping conditions are studied, including Be+Mg continuous co-coping and layered Be and Mg doped layers. The effects of co-doping on Be and Mg incorporation, material quality, activation efficiency, and conductivity are discussed and compared to the results of singly doped GaN.
[1] B. McEwen, *et al.*, MOCVD Growth and Characterization of Be-Doped GaN. *ACS Appl. Electron. Mater.*, *4*(8), 3780-3785 (2023).
[2] F. B. Naranjo, *et al.*, Study of the Effects of Mg and Be Co-Doping in GaN Layers. *Phys. Stat. Sol. (a)*, *180*(1), 97-102 (2000).
[3] A. Kawaharazuka, Be and Mg co-doping in GaN. *J. Cryst Growth*, *301*, 414-416 (2007).

2:30 PM BB04
(Student) Compensation Mechanism in Mg-Doped N-Polar GaN Masahiro Kamiyama[1], Shashwat Rathkanthiwar[1], Cristyan E. Quiñones García[1], James Loveless[1], Seiji Mita[2], Pramod Reddy[2], Ronny Kirste[2], Ramón Collazo[1] and Zlatko Sitar[1,2]; [1]North Carolina State University, United States; [2]Adroit Materials, United States

Nitrogen-polar (N-polar) GaN has attracted significant interest for the development of next-generation power devices. The reversed polarization direction in N-polar GaN as compared to the Ga-polar orientation allows for device designs with improved performance. For example, in AlGaN/GaN high electron mobility transistors, it improves the confinement in the two-dimensional electron gas channel. Furthermore, by taking advantage of the inherent polar doping selectivity, lateral polar junctions realized on side-by-side

grown Ga- and N-polar domains allow for the fabrication of novel device structures such as GaN-based superjunctions (SJ), lateral p-n homojunctions, and depletion-mode MOSFETs. The performance of these devices is limited by the ability to achieve controllable p-type doping in N-polar GaN. High hole concentration and low p-type resistivity are also critical for optimal band alignment and steep device turn-on in polarization-engineered tunnel field-effect transistors. Achieving efficient p-type doping in GaN is challenging due to a combination of a relatively high Mg acceptor ionization energy (150-220 meV) and the enhanced incorporation of compensating point defects and complexes during epitaxial growth. N-polar GaN offers additional material challenges, for example, without any control, N-polar GaN grows with a rough surface with hexagonal hillocks and incorporates high oxygen concentration, on the order of 10^{19} cm^{-3}. Oxygen on the nitrogen site (O_N) acts as a shallow donor with an activation energy of 29 meV in N-polar GaN, which poses significant difficulties in achieving p-type conductivity. While much work to date has focused on the p-doping of Ga-polar GaN, there have only been limited reports on p-type N-polar GaN. Comprehensive electrical characterization and compensation control in p-type N-polar GaN are lacking in the literature.

In this study we investigate the hole concentration, mobility, and Mg-related photoluminescence (PL) peaks in N-polar GaN epilayers grown by metalorganic chemical vapor deposition. Series of samples were grown by varying the Mg doping concentration and the nitrogen chemical potential (μ_N) during the growth process. The latter was controlled through controlling the process supersaturation by varying the precursor flow rates and switching the process diluent gas between nitrogen and hydrogen. Similar to the phenomenon typically reported for Ga-polar GaN, a knee behavior was observed at a Mg doping concentration of ~10^{19} cm^{-3}. At higher doping levels, a drop in hole concentration was observed, and the PL revealed a strong defect luminescence at 2.8 eV. To understand the mechanism behind this compensation, the temperature dependency of the carrier concentration was fit using the charge balance approach. The fittings revealed that the acceptor concentration (N_A) was equal to the doping concentration up to the knee point followed by a drastic drop. Interestingly, N_D was observed to be ~10^{18} cm^{-3} for all doping concentrations. These results suggest that the knee behavior is not related to an increase in the concentration of compensating defects, but instead, a large fraction of Mg atoms incorporate in a non-acceptor configuration. This rules out the presence of compensating defects such as isolated nitrogen-vacancy V_N^{+3}, or complex between Mg and nitrogen-vacancy with charged configurations, i.e., $(Mg\text{-}V_N)^{+2}$ and $(2Mg\text{-}V_N)^{+1}$. For a constant Mg concentration of ~10^{19} cm^{-3}, N_A was found to depend strongly on μ_N confirming that the knee behavior is related to the formation of neutral $3Mg\text{-}V_N$ complex. This study sheds light on the compensation mechanism in Mg-doped N-polar GaN and is expected to further the development of next-generation power devices based on N-polar GaN.

2:50 PM BB05
Observation of Spontaneous Intercalation of Interstitial Mg into GaN Jia Wang, Wentao Cai, Shun Lu, Yoshio Honda and Hiroshi Amano; Nagoya University, Japan

Intercalation is an important nanotechnology for the fabrication of artificial layered structures which has found a wide range of applications, such as exfoliation of 2D materials, energy storage, superconductors, and tuning of thermal conductivity. In general, 2D material is chosen as the host material for intercalation process by virtue of the weakly van der Waals-bonded layers which allow for easy insertion of foreign atom, ion, and molecule sheets without causing excessive strain. By the same token, it is considered extremely difficult to intercalate atomic sheets interstitially into a singlecrystalline ceramic having strong ionic and covalent bonds, such as semiconductor materials with wide bandgap and high bonding strength.

Here we observed an unusual intercalation of interstitial magnesium (Mg_i) into hexagonal gallium nitride (h-GaN) forming superlattice structure in which every monoatomic Mg_i layer is intercalated into a few monolayers of h-GaN. This is the first-of-its-kind observation of intercalation of 2D-metal into bulk semiconductor. A more intriguing aspect lies in that the formation of the 2D Mg-intercalated GaN superlattice (MiGs) nanostructure occurs spontaneously between the two dissimilar materials under moderate temperature and atmospheric pressure. The possible reason to form suchunusual superlattice structure is discussed and testified.

Since these 2D-Mg layers are interstitially inserted into h-GaN lattice, an unprecedented high uniaxial strain along c-axis (over 10%) is observed in the h-GaN layers by the drift-compensated atomic resolution HAADF-STEM images, making it the record high elastic strain value ever reported amongst thin film materials. The ultra-high strain and resulting ultra-small c/a ratio modify the valance band structure of h-GaN, leading to the reduced effective mass and enhanced mobility of holes. On the other hand, the intercalated Mg sheets also cause periodically polarity inversion of h-GaN in which the nearest h-GaN atomic layers below and above the 2D-Mg sheet feature opposite polarity (i.e., N-polar, and Ga-polar), confirmed by the integrated differential phase contrast (iDPC)-STEM imaging technology. We assume that the transition of N-polar to Ga-polar GaN within a pair of Mg sheets also generates electrically field-induced two-dimensional hole gas, leading to the increased hole concentration of p-type GaN which could not be explained by the incorporation of large amounts of electrically inactive interstitial Mg.

These unique features may shed light on the doping and conductivity enhancement of semiconductors as well as the elastic strain engineering of nanomaterials. The observed layered structure also provides a novel probe for studying the band structure and transport properties of metal/semiconductor superlattices.

3:10 PM BREAK

3:30 PM BB06
Investigation of Diffusion of Be and Mg Acceptor Dopant Implanted in GaN and the Impact of Annealing Method and Temperature Emma Rocco, Vincent E. Meyers, Benjamin McEwen, Alireza Lanjani, Shadi Omranpour and Fatemeh (Shadi) Shahedipour-Sandvik; SUNY Polytechnic Institute, Colleges of Nanoscale Science and Engineering, United States

The III-nitride material system is actively employed in next-generation high-power and high-frequency electronics. Realizing devices such as power diodes requires control of high conductivity p- and n-type III-nitrides. Achieving high p-type conductivity III-nitride materials remains a challenge. The only commercially viable p-type dopant in III-nitrides is Mg, with a relatively deep level at ~160 meV above the valence band in GaN. Be has also been shown as a p-type dopant in the III-nitride material system, with p-type AlN:Be achieved by molecular beam epitaxy (MBE). Additional studies of GaN:Be have focused on doping by ion implantation or *in situ* doping by metal organic chemical vapor deposition (MOCVD). The implantation process induces significant lattice damage and concentrations of point defects. To remove implant-induced damage and activate acceptors, the required activation-anneal temperatures frequently result in significant out-diffusion from the designed dopant profile. In some cases, the lattice damage and point defects created by implantation lead to defect-mediated pathways for increased diffusivity.

Here we study the diffusion pathways of implanted Be and Mg in GaN during thermal and gyrotron microwave annealing. Unintentionally doped GaN was grown by MOCVD with a background n-type carrier concentration of $2x10^{16}cm^{-3}$ and thickness of 4.5 µm on HVPE GaN substrate. For both Be and Mg species, co-implantation was performed with N to compensate the large $[V_N]$ created during implantation. Implantation profiles in a box profile were achieved in the MOCVD GaN layer to a depth of 250 nm with $[Be]=[N]=10^{19}$ cm^{-3}, or $[Mg]=[N]=10^{19}$ cm^{-3}. To protect the surface during high temperature annealing, all samples were capped with AlN by MOCVD and sputtering. Samples were then subjected to either thermal annealing at temperatures between 1000 °C and 1200 °C for 2

min, or gyrotron microwave annealing at temperatures between 1000 °C and 1450 °C. Secondary ion mass spectrometry (SIMS) depth profiles of [Be] and [Mg] were completed before and after annealing. The diffusion of the species is modeled based on SIMS measurements to interrogate the diffusion mechanism. The impact of lattice damage on the diffusion behavior is studied through high-resolution x-ray diffraction (HR-XRD). The resulting electrical characteristics will be discussed via temperature-dependent Hall effect measurements.

3:50 PM BB07
(Student) Photocathode Characteristics Dependency on Mg Incorporation in (N-polar) Semi-Polar and Non-Polar 3D Microstructures by Selective Area Epitaxy Shadi Omranpour[1], Emma Rocco[1], Vincent Meyers[1], Benjamin McEwen[1], Alireza Lanjani[1], L. D. Bell[2] and Fatemeh Shahedipour-Sandvik[1]; [1]SUNY Polytechnic Institute, United States; [2]California Institute of Technology, United States

Photocathode detectors are an important technology with applications in astronomy and military and are commonly used in image intensifiers [1] [2]. The III-nitride material system is a promising candidate for photocathodes due to the wide and tunable band gap which allows wavelength detection spanning from infrared to ultra-violet is noticeable for photon detection [3] [4] [5]. In utilizing the nitrogen polar (N-polar) orientation of III-nitrides, the polarization and depletion charge are aligned at the surface. This results in improved band alignment and increased device quantum efficiency (QE) reported theoretically and experimentally [6]. Hexagonal pyramid hillock structures are common on the N-polar surface. In studies of the impact of hillocks on photocathode performance, photocathodes with high hillock density exhibited 2x QE compared to low hillock density samples [7]. Further investigation of Mg p-type dopant incorporation within hillock structures reveal increased Mg incorporation efficiency within the semi-polar facets resulting in improved optical and electrical characteristics [8].
Hillock structures commonly observed in N-polar GaN can have semi-polar or non-polar sidewalls and are difficult to precisely control during growth. The present study aims to investigate potential differences in Mg incorporation in semi-polar sidewalls compared to the non-polar sidewalls of such microstructures, and the impact on photocathode device performance. The selective area growth (SAG) technique was used during metal-organic chemical vapor deposition (MOCVD) to establish controlled 3D microstructures overgrown on unintentionally doped (UID) N-polar templates. Microstructures with non-polar sidewalls were achieved using a low V/III ratio of 2,000 during SAG growth on sample 1. To stabilize semi-polar sidewall N-polar microstructures SAG was performed on Sample 2 using high V/III ratio of 3,350. Following SAG, the SiO_2 mask was removed, GaN:Mg films grown conformally over the microstructures and activated *in situ* following growth, at 700 ºC for 30 minutes. The QE of the photocathodes was investigated using internal photoemission spectroscopy. Sample 2, N-polar microstructures with semi-polar facets achieved a maximum QE of 2.71%. However, the GaN: Mg film grown on the N-polar SAG seed with non-polar sidewalls exhibited a lower QE of 1.16%. Both N-polar SAG seeds with non-polar and semi-polar sidewalls indicated similar threshold energy (E_{th}) of 4.8 eV. In addition, the optical characteristics of these microstructures were investigated and will be discussed.
[1] M. P. Ulmer, *Quantum Sensing and Nanophotonic Devices VI*, 2009.
[2] Peter D. Townsend, *Contemporary Phys*, vol. 44, no. 1, 2010.
[3] E Muñoz *et al*., *J. Phys*, vol. 13, 2001.
[4]C. Rivera, *et al*.,*The Open Electrical & Electronic Engineering Journal*, vol. 4, 2010.
[5] B. Alshehri, *et al*., *IEEE Photonics Journal*, vol. 9, no. 4, 2017.
[6] J. Marini, *et al*., *J. Appl Phys*, 2018.
[7] E. Rocco, *et al*., *IEEE*, vol. 14, no. 2, 2022.
[8] E. Rocco, *et al*., *Sci, Rep*, 2020.

4:10 PM BB08
Dissolution of Mg Segregated Defects in Mg-Implanted GaN After Ultra-High-Pressure Annealing Kenny Huynh[1], Yekan Wang[2], Michael E. Liao[3], James Tweedie[4], Dolar Khachariya[4], Pramod Reddy[4], Mathew H. Breckenridge[5], Ramón Collazo[5], Zlatko Sitar[5], Michael Bockowski[6] and Mark Goorsky[1]; [1]University of California, Los Angeles, United States; [2]Intel Corporation, United States; [3]National Research Council Postdoctoral Fellow at U.S. Naval Research Laboratory, United States; [4]Adroit Materials, United States; [5]North Carolina State University, United States; [6]Institute of High Pressure Physics Polish Academy of Sciences, Poland

In this work, we addressed implant-induced strain recovery and the formation of extended defects during annealing in Mg-implanted GaN. Previous results showed that annealing at 1400 C led to higher dopant activation than 1300 C. To address the microstructural causes for this behavior, we studied Mg-implanted (box profile dose of 1 x 10^{15} cm^{-2}) in homoepitaxial GaN grown on high quality ammonothermal GaN substrates. Post-implantation annealing was performed at 1000 C, 1300 °C, 1400 °C, and 1500 °C for a duration of either 10 minutes or 100 minutes. Additionally, a sample annealed at 1300 °C was further annealed at 1450 °C for 10 minutes. An ultra-high N_2 pressure of 1 GPa was applied to prevent GaN from decomposition without using a dielectric cap.
The triple axis x-ray ω:2θ scans near GaN (0004) peak shows that the implant-induced strain is fully relieved after annealing at 1300 °C for 10 min. Annealing at higher temperatures and longer time does not have any further impact on the strain state. Two beam condition STEM bright field images show residual defects, after annealing at 1300 °C for 10 min, which consist of inversion domains. The inversion domains show up in two morphologies, pyramidal and trapezoidal. High resolution TEM image shows that the pyramidal inversion domain (PID) has its base along the GaN basal plane and facets along on the {11$\underline{2}$3} planes. Energy Dispersive X-Ray analysis (EDX) maps and line scans at the PID show an increase in Mg signal close to the base of PID, where an extra layer of atoms is located, with a decrease in the Ga signal at the same position. The trapezoidal inversion domains (TID) also show base and facets that are similar to the PID. EDX maps and line scans at the TID also reveal Mg segregation near the base. The center part of a TID consists of a series of small pyramids aligned in a line. We speculate that the TIDs are the initial stages of development and will eventually evolve into the PIDs. Thus, both the PIDs and TIDs trap and make inactive Mg atoms and cause a degradation in Mg activation efficiency.
However, the PIDs and TIDs are not observed in any of the samples annealed at and above 1400 °C. This suggests that the PIDs and TIDs are thermodynamically unstable or would not form at such high temperatures (≥ 1400 °C). This provides insight for improving dopant activation efficiency with annealing temperature ≥ 1400 °C. The prominent residual defects after annealing at and above 1400 °C are dislocation loops. EDX at the dislocation loops shows no sign of Mg segregation. Meanwhile, an overall decreasing trend in the dislocation loop density is observed after annealing at a higher temperature or for a longer time. The loop density measured decreased from 3.8 x 10^9 cm^{-2} for 1400 °C 10 min, to 1.5 x 10^9 cm^{-2} for the 1400 °C 100 min, and further to 1.1 x 10^9 cm^{-2} for 1500 °C 10 min.
Samples that were initially annealed at 1300 °C, which revealed Mg segregation at PIDs, were further annealed at 1450 °C for 10 minutes. Cross sectional TEM revealed that the PIDs which had originally formed, had been dissolved and the defect structure was indistinguishable from the samples that were annealed at above 1400 °C only. This result confirms that while the PIDs may be metastable below 1400 °C, they can be successfully dissolved with high enough temperature and time even once they are formed. Results from this work are expected to bring the understanding of the key processing steps to achieve high activation efficiency p-type doping for planar, vertical device structures in a scalable framework.

4:30 PM BB09
(Late News) Tunnel Junction Enabled AlGaN/GaN Heterojunction Bipolar Transistor with All n-Type Contacts
Chandan Joishi[1], Sheikh Ifatur Rahman[1], Dan Ritter[2] and Siddharth Rajan[1,1]; [1]The Ohio State University, United States; [2]Technion–Israel Institute of Technology, Israel

AlGaN/GaN NPN heterojunction bipolar transistors (HBT) could enable excellent performance for RF/mm-wave applications, but their performance is limited by challenges related to p-type base contact and sheet resistance. In this work, we demonstrate an AlGaN/GaN HBT that employs tunnel junctions (TJ) to realize all-n-type contacts for the emitter, collector, and base layers, thus removing the need for a p-type contact to the base, with output collector current (I_C) ~ 28kA/cm^2. This is the first report of TJ-based GaN HBTs.
Motivation: GaN HBTs are favored over lateral GaN transistors for high-power handling at RF/mm-wave frequencies due to their wideband gap, high electron velocity, absence of peak electric field at the device surface/edges, as well as better linearity [1]. However, GaN-based HBTs developed so far have achieved Johnson FoMs close to 500 GHz-V, significantly lower than the theoretical JFoMs (9THz-V) [2]. The performance of GaN HBTs is currently restricted by the high sheet resistance and contact resistivity of the p-type base with difficulty in realizing low-resistance p-type base contact being the main factor limiting device performance in all these designs. To further reduce the contact resistivity, we propose a TJ-integrated HBT design which eliminates the need to fabricate the difficult p-type ohmic base contact since all metal-semiconductor contacts are n-type. Low contact resistivities using TJ have been previously demonstrated for GaN-based LEDs [3]. The proposed TJ-HBT design features a heavily doped p^+/ n^+ junction [4] that functions as an emitter-base diode for HBT operation under forward bias and as a base contact under reverse bias. The TJ-HBTs' epitaxial stack ensures low contact resistivity to the p-GaN base via the TJ. Besides, no base/emitter etch/regrowth is needed which typically degrades electrical performance in current GaN-based HBTs.
Experimental: The TJ-HBT epilayers were grown on a (0001) c-plane bulk GaN substrate in a PAMBE system (Fig. 1 (a)). The TJ consists of heavily doped n^+-GaN/p^+-GaN sandwiched between the p-GaN base and graded AlGaN emitter. Device fabrication commenced with collector definition followed by emitter/base interdigitated stripes patterning using BCl_3/Cl_2-based dry etch. The emitter/base/collector contacts were then simultaneously deposited using Al/Ni/Au as the ohmic metal stack, with Al_2O_3 as the isolation dielectric for bond pads.
Results: Using the TJ approach, n-type ohmic behavior was obtained for all the contacts. The HBT curves measured on an interdigitated emitter-base stripe pattern (9 stripes, each 3x1.4 μm_2 in area) are shown in Fig. 4. At low forward V_{BE}, interband tunneling results in a high base current with electrons being injected from the emitter conduction band (CB) to the base valance band (VB). At high forward bias, thermionic injection of electrons to the base CB dominates thereby increasing I_C. A low current gain of ~ 3-4 was obtained at high I_C (> 10 kA/cm^2), likely due to a shorter electron lifetime in the base for these MBE-grown layers. The I_C-V_{CE} curves displayed a maximum I_C of 28kA/cm^2 with a V_{CE} offset due to a high V_{BE} for I_C/I_B crossover in the Gummel plot and voltage drop in the lateral p-base layer between the emitter/base terminal. While further optimization is needed to mitigate the high knee voltage and increase the current gain and current density of the device, the reported results show that continued research on TJ-HBTs could enable new flexibility in high-power GaN RF device design.
Conclusions: We demonstrated TJ-enabled GaN HBT with all n-type contacts for improvement in device characteristics. The results demonstrated here are promising for the future development of III-Nitride HBTs. We acknowledge funding from ONR under Grant No. N00014-22-1-2260 (Dr. Paul A. Maki).
Ref.: [1] W. Liu, Wiley & Sons., (1999). [2] *IEEE EDL*, vol. 32, p. 1065-67, (2011). [3] APL, vol. 102(11), 113503 (2013) [4] IEEE EDL, vol. 32, p. 21-23, (2011).

SESSION CC: Characterization of Gallium Oxide-Based Materials and Devices II
Session Chairs: Ramana Chintalapalle and Michael Scarpulla
Thursday Afternoon, June 29, 2023
MCC Theater

1:30 PM CC01
(Student) Temperature-Dependent Calculations of β-Ga_2O_3 Defect Concentrations for Equilibrium, Full Quenching and Generalized Quenching Scenarios Khandakar Aaditta Arnab[1], Isaac Maxfield[1], Channyung Lee[2], Elif Ertekin[2,2], Joel Varley[3] and Michael Scarpulla[1,1]; [1]The University of Utah, United States; [2]University of Illinois at Urbana-Champaign, United States; [3]Lawrence Livermore National Laboratory, United States

β-gallium oxide (β-Ga_2O_3) is of intense current interest because of its ultra-wide bandgap, high critical field, and availability of melt-grown substrates. Point defects and complexes determine the properties of bulk crystals as well as epitaxial layers, thus, predictive models of defect concentrations under various impurity and processing scenarios are of very high value. First-principle calculations of defect energetics have provided critical insights into the defect system in β-Ga_2O_3, but translating computed enthalpies into defect concentrations corresponding to real-world crystal growth requires additional steps. Growth or annealing experiments typically control the sample trajectory in terms of temperatures and partial pressures, while computation papers frequently present results holding chemical potentials constant.
Here we report our quantitative modelling of equilibrium defect concentrations in Ga_2O_3, taking into account especially the temperature dependence of the bandgap and temperature-dependent chemical potentials from the Ga-O system's known thermochemistry. Additionally, we compute results for realistic sample types such as Fe- or Sn-doped wafers accounting for the fixed concentrations of these impurities as opposed to their fixed chemical potentials. Results are presented for various background n-type doping and for equilibrium and quenching, corresponding respectively to 0 or infinite cooling rates. We find significant departures from prior simpler predictions, especially in the case of the bandgap temperature dependence. We compare our predicted results to empirically-known cases, such as annealing in O_2 or Ga_2O vapors.
Finally, to give semi-quantitative insight into defect concentrations expected in finite-sized samples subjected to finite cooling rates without full-fledged multidimensional defect reaction-diffusion simulations, we introduce the concept of generalized quenching as a 3rd type of computation. At the heart of generalized quenching is the insight that, because of their different diffusion constants, different types of defects located at different distances from free surfaces will be "frozen-in" at different temperatures. Essentially by combining equilibrium and quenching calculations, it is thus possible to predict the defect concentrations present following cooling as a function of radius within a boule or within thin films of different thicknesses. We compare these results to the known phenomena from bulk crystal growth, indicating differences in carrier density between the center and periphery of CZ-grown boules.

1:50 PM CC02
Phase Transformation of β-Ga_2O_3 to Ga_2O_3-Based γ-Phase Spinels on (100) $MgAl_2O_4$ Substrate Kunyao Jiang[1], Jingyu Tang[1], Stephen D. House[2], Chenchao Xu[1], Kelly Xiao[1], Robert Davis[1,1] and Lisa Porter[1]; [1]Carnegie Mellon University, United States; [2]University of Pittsburgh, United States

Gallium oxide (Ga_2O_3), an emerging ultra-wide bandgap semiconductor material with a bandgap ~ 4.8 eV, occurs in the

trigonal , monoclinic , cubic and orthorhombic polymorphs. The thermodynamic stable phase of β-Ga_2O_3 has been the primary focus for future power electronic devices due to the availability of semi-insulating to n-type doped free-standing substrates. Although γ-Ga_2O_3 has been identified as the least stable phase, γ-Ga_2O_3 inclusions have been found in many β-Ga_2O_3 films, particularly when Al or Mg is present. [1–3] These γ-phase inclusions are recognized as a potential problem for devices based on β-Ga_2O_3.[1] In this study, Ga_2O_3 films were deposited on (100) $MgAl_2O_4$ in the temperature range of 550 °C to 850 °C via metal-organic chemical vapor deposition (MOCVD). Post-deposition thermal treatments were conducted in air at temperatures between 800 °C to 1000 °C. The phase composition and nanostructure of the as-grown and annealed films were investigated using X-ray diffraction and transmission electron microscopy (TEM). Phase-pure β-Ga_2O_3 was observed in the films deposited at 550°C and 650 °C, whereas γ-Ga_2O_3 -based solid solutions (hereafter referred to as γ-phase) were formed at 850°C, and a mixture of β-Ga_2O_3 and γ-phase were observed in the films grown at 750°C. The transformation of β-Ga_2O_3 to γ-phase originated at the film/substrate interface and was accompanied by interdiffusion of Al and Mg from the substrate. The minimum atomic percent of Al + Mg associated with the phase transformation was determined to be ~ 4.6 at%. Atomic scale TEM characterization indicates that Al and Mg have a strong preference for octahedral sites whereas Ga prefers the tetrahedral sites, to form an inverse spinel structure. It is postulated that the octahedral site preference of Al and Mg drives the β-Ga_2O_3 to γ-phase transition and, as a result, enhances the observed thermal stability of the γ-phase at elevated temperatures.

[1] C.S. Chang, N. Tanen, V. Protasenko, T.J. Asel, S. Mou, H.G. Xing, D. Jena, and D.A. Muller, APL Mater. **9**, (2021).
[2] A.F.M.A.U. Bhuiyan, Z. Feng, J.M. Johnson, H.L. Huang, J. Sarker, M. Zhu, M.R. Karim, B. Mazumder, J. Hwang, and H. Zhao, APL Mater. **8**, (2020).
[3] Q. Hou, K. Liu, X. Chen, J. Yang, Q. Ai, Z. Cheng, Y. Zhu, B. Li, L. Liu, and D. Shen, Physica Status Solidi - Rapid Research Letters **16**, (2022).

2:10 PM CC03

Characterization Analysis of Extended Defects in β-Ga2O3 and AGO Jacqueline Cooke[1], Praneeth Ranga[2], Jani Jesenovec[3], Arkka Bhattacharyya[2], Xueling Cheng[1], Yunshan Wang[1], John S. McCloy[3], Sriram Krishnamoorthy[2], Michael Scarpulla[1] and Berardi Sensale Rodriguez[1]; [1]The University of Utah, United States; [2]University of California, Santa Barbara, United States; [3]Washington State University, United States

Gallium oxide (Ga_2O_3) is a conducting transparent semiconducting oxide and ultra-wide bandgap material which allows for a large critical electric field that maximizes frequency and voltage operation. Due to its large Baliga's figure of merit (3200 * Si) and inexpensive melt-growth methods, Ga_2O_3 is of interest in electrical and optical applications [1, 2, 3]. β-Ga_2O_3 is the most chemically and thermally stable phase with an anisotropic bandgap between 4.5 and 4.9 eV, depending on orientation [1, 2, 3]. To control the electrical and optical properties of Ga_2O_3 and aluminum gallium oxide alloy (AGO) within devices, understanding where their defects come from and how they develop is important. For example, although point defects can be used to control their properties, e.g. doping, extended defects tend to negatively impact their operation. As such, identifying the types of defects caused by growth or fabrication processes is important for developing those processes and reducing undesirable defects.
One method to characterize defects is through photoluminescence (PL) which is a noninvasive process. For β-Ga_2O_3, the PL spectrum is broad over the UV, blue, and green wavelengths making deconvolving the spectra extremely difficult [1, 2]. There have been studies in the literature to determine the origin of the β-Ga_2O_3 spectra, but those studies typically focus on point defects as a cause [1]. Here, the correlation between sample quality and extended defects is possible with PL and PL Microscopy (PLM).
Comparing β-Ga_2O_3 or AGO films and bulk samples shows that extended defects have an essential role in the PL emission. Homogeneous films with no extended defects and bulk crystals will yield a UV dominant PL emission. Samples of poor film quality that have extended defects throughout will have a dominant blue PL emission. This means the quality of a sample, in terms of the density or extended defects, can be determined through PL [1].
Furthermore, sample topography and extended defects can be identified through PLM [2]. Single crystal samples have uniform UV emission. That said, any topography can alter the emission intensity due to refraction and diffraction. Furthermore, any topography that is altered due to defects also causes a contrast in emission intensity. As such, PLM tends to match AFM and SEM images. But, there are cases where PLM can diverge from AFM and SEM due to other extended defects within the film, which are more luminescent than surface defects/topography. Some defects identified using PLM include cracks running along [001] on AGO films, rotational domains found in β-Ga_2O_3 grown on sapphire, incoherent stacking faults from (-201) β-Ga_2O_3 grown on Fe-doped β-Ga_2O_3, and sympetalous defects which are a newly discovered defect [2].
The sympetalous defect is found on metalorganic vapor-phase epitaxy (MOVPE) films grown on (010) Ga_2O_3. This defect generally grows out from underlying line defects in the substrate, such as nano-pipes, which is similar to v-defects found in GaN. The defect creates a polycrystalline region in the film, expanding out from the initial starting line defect seed [3]. PL shows that the sympetalous defects are polarization-dependent. Furthermore, circular polarization also shows luminescence likely caused by the defect grains having a semi-helix growth with themselves and/or bulk crystal surrounding the defect [3]. Lastly, the quality of a sample can be determined by looking at the density and surface size range of defects on the surface of a sample. Sympetalous defects are similar in size and have the same density as substrate etch-pits. Nodular defects, on the other hand, have a wide variety of sizes and density that increases with thickness [3].

[1] J. Cooke, *et al.*, *Scientific Reports*, 12, 3243 (2022).
[2] J. Cooke, *et al.*, *Optical Material Express*, 12 (11), 4341 (2022).
[3] J. Cooke, *et al.*, *J. Vac. Sci. Technol. A*, 41 (1), 013406 (2023).

2:30 PM CC04

(Student) Temperature Dependence of Bandgap and Anisotropy in Urbach Tails in β-Ga_2O_3 Ariful Islam, Nathan D. Rock and Michael Scarpulla; The University of Utah, United States

Gallium oxide (Ga_2O_3) has an extremely wide bandgap, predicted high breakdown field, and can be produced from melt crystal growth techniques making it attractive for next-generation high-power electronics. It is well-known that the optical transitions in monoclinic β-Ga_2O_3 are anisotropic; the threshold energies for carrier generation using linearly polarized light depend on crystallographic direction. Using transmission optical spectroscopy, which probes subtly differently than e.g. ellipsometry, we have investigated the optical transitions of Fe doped [100] β-Ga_2O_3 as function of elevated temperature and have documented the dramatic bandgap narrowing with temperature which was recently explained using density functional theory [1]. Here we also report on the anisotropy and doping dependencies of the disorder-induced Urbach tails in the optical absorption coefficient for β-Ga_2O_3. Band tails in semiconductors depend on both static disorder and the dynamic disorder induced by phonons mediated by the electron-phonon coupling. Given the low symmetry of β-Ga_2O_3 and its strong electron-phonon coupling, we predicted that the Urbach tails should also exhibit significant anisotropy. We show that this is indeed the case, and also provide results for UID- and Fe-doped crystals both of which exhibit larger band tails as expected.

References

[1]. Lee, C., Rock, N.D., Islam, A., Scarpulla, M.A. and Ertekin, E., 2023. Electron–phonon effects and temperature-dependence of the electronic structure of monoclinic β-Ga2O3. *APL Materials*, *11*(1), p.011106.

2:50 PM CC05
Crack Formation in Strained β-$(Al_xGa_{1-x})_2O_3$ Films Grown on (010) β-Ga_2O_3 Substrates Kenny Huynh[1], Michael E. Liao[2], Marko Tadjer[3], James Lundh[2], Kohei Sasaki[4], Keita Konishi[4], Hannah Masten[2], Jennifer K. Hite[3], Michael Mastro[3], Nadeemullah Mahadik[3], Akito Kuramata[4], Karl Hobart[3] and Mark Goorsky[1]; [1]University of California, Los Angeles, United States; [2]National Research Council Postdoctoral Fellow at U.S. Naval Research Laboratory, United States; [3]U.S. Naval Research Laboratory, United States; [4]Novel Crystal Technology, Japan

Relaxation in the form of cracking is observed in a systematic study of epitaxially grown (010) β-$(Al_xGa_{1-x})_2O_3$ films ranging from 50 – 400 nm thick with varying composition (x = 0.10 to 0.15). Generally, cracking was observed in samples with higher Al content or in thicker films, where the films can no longer accommodate the strain and the thickness. Cracks were primarily formed along the [001] direction across the sample with a few cracks also observed in the [100] direction. (010) β-$(Al_xGa_{1-x})_2O_3$ films were grown by ozone assisted molecular beam epitaxy with a reactor temperature at 555 °C, and with a Ga cell temperature of 760 °C and Al cell temperature of 890–900 °C. High resolution x-ray diffraction (XRD) and transmission electron microscopy (TEM) were used to investigate β-$(Al_xGa_{1-x})_2O_3$ films to assess the chemical and mechanical stability.
Triple axis x-ray (020) line scans were used to verify the aluminum content after growth. To assess the effects of cracking, symmetric (020) reciprocal space maps (RSM) were taken such that x-ray beam was either parallel or perpendicular to the (100) cleavage plane. For samples that exhibited cracking, when the x-ray beam was aligned with the [100] direction, perpendicular to the dominant crack direction, diffuse scattering is observed in large arcs around the substrate and epilayer. However, the diffuse scattering is minimized when the x-ray beam is aligned parallel to the dominant crack direction. Samples that did not exhibit cracking did not show this behavior. From this we infer that the cracking causes lattice tilt and strain in both the epilayer and substrate. Additionally, asymmetric ($\underline{4}22$) RSMs reveal that the epilayer remains fully strained with respect to the substrate, indicating that the crack formation, at these levels, does not release significant strain.
In a sample where cracking was observed (x = 13.6, 200 nm), cross sectional transmission electron microscopy measurements were taken perpendicular to the dominant crack direction along the [10$\underline{2}$] zone axis. Cracks were observed to penetrate into the substrate between 300 to 400 nm from the surface of the film. This supports the RSM data that revealed diffuse scattering from cracking in both the epilayer and substrate peaks. Additionally, phase separation was observed in the β-$(Al_xGa_{1-x})_2O_3$ film, where the top ~40 nm of the film had transformed into the γ phase. The γ-$(Al_xGa_{1-x})_2O_3$ surface layer observed is single crystal and uniformly thick across the TEM sample, which may indicate nonuniform Al incorporation in the out of plane direction. Phase transformation from the β to γ phase has been observed previously when Al incorporation exceeds 27%.

3:10 PM BREAK

SESSION DD: Gallium Oxide Materials Processing
Session Chairs: Esmat Farzana and Nidhin Kurian Kalarickal
Thursday Afternoon, June 29, 2023
MCC Theater

3:30 PM DD01
Improvement of Ga_2O_3 Schottky Barrier Diode Characteristics by Nitrogen Radical Treatment Zhenwei Wang[1], Sandeep Kumar[1], Takahiro Kitada[1,2] and Masataka Higashiwaki[1,2]; [1]National Institute of Information and Communications Technology, Japan; [2]Department of Physics and Electronics, Osaka Metropolitan University, Japan

In the last decade, β-Ga_2O_3 has been extensively studied as a strong contender for future high-power electronics applications, owing to a large Baliga's figure of merit and the availability of melt-grown single-crystal bulks. Vertical Ga_2O_3 fin field-effect transistors (FETs) attract much attention due to their high-voltage and high-current handling capacity. The quality of the sidewall surface on which a gate electrode is formed strongly affects the FET performance; therefore, it is important to develop technical procedures for recovering the Ga_2O_3 surface condition. In this work, we found that nitrogen (N) radical irradiation to a damaged Ga_2O_3 surface is effective to improve electrical properties of Ga_2O_3 Schottky barrier diodes (SBDs).
Vertical SBD structures were fabricated using unintentionally doped Ga_2O_3 (010) and (100) substrates with net donor concentrations of 1 ~ 2 × 10^{17} cm^{-3}. The substrate orientations correspond to typical sidewall planes of vertical fin FETs fabricated on Ga_2O_3 (001) and (010) substrates, respectively. The bottom grinding surfaces of the (010) substrates were first planarized by lapping and chemical mechanical polishing. Both surfaces of the Ga_2O_3 (100) substrates had been prepared by cleavage and thus were used as received. To fabricate good ohmic contacts, the bottom surfaces were degenerately doped by Si-ion implantation (box profile, Si = 5 × 10^{19} cm^{-3}), followed by activation annealing. Then, the samples were loaded into a molecular-beam epitaxy growth chamber to perform N radical irradiation to the top surfaces for 2 hours. The RF plasma power, N_2 flow rate, and substrate temperature were 500 W, 0.6 sccm, and 700ºC, respectively. After the nitridation process, Ti/Au ohmic and Pt/Ti/Au Schottky electrodes were fabricated on the bottom and top surfaces, respectively. Control SBD structures without the nitridation were simultaneously fabricated under the same procedures for comparison.
Current density–voltage (*J*–*V*) measurements were performed for the Ga_2O_3 (010) and (100) SBDs with and without the nitridation treatment. Note that we evaluated characteristics of various devices fabricated on the substrates. The Ga_2O_3 (010) SBDs showed small changes in *J*–*V* characteristics; only the ideality factors (*n*) were improved from 1.14 ± 0.01 to 1.06 ± 0.01 by the nitridation. On the other hand, the Ga_2O_3 (100) SBDs exhibited more noticeable differences. The nitridated (100) SBDs showed nearly ideal and homogeneous *J*–*V* characteristics. In contrast, kinks and/or drifts of the turn-on voltage were observed in the *J*–*V* curves of the control SBDs without the nitridation, and the characteristics varied across the devices. The *n* of the nitridated and non-nitridated (100) SBDs were 1.07 ± 0.01 and 1.18 ± 0.04, respectively. The poor and non-uniform *J*–*V* characteristics of the non-nitridated (100) SBDs were probably caused by high-density surface defects formed during wafer production and/or device fabrication procedures. On the other hand, all of the nitridated (100) SBDs demonstrated reasonably good device characteristics. These results indicate that the N radical treatment is effective to remove Ga_2O_3 surface damage and improve the Schottky diode characteristics. Therefore, we consider that the nitridation technique should be useful for development of various types of Ga_2O_3 FETs and diodes.
This work was supported in part by the Ministry of Internal Affairs and Communications (MIC) research and development (JPMI00316).

3:50 PM #DD02
(Student) Enhancing the Dielectric Performance of Al_2O_3 on β-Ga_2O_3 Using Temperature Modulated *In Situ* Dielectric Deposition Saurav Roy, Arkka Bhattacharyya, Carl Peterson and Sriram Krishnamoorthy; University of California, Santa Barbara, United States

We report on the growth and characterization of in-situ Al_2O_3 on (010) β-Ga_2O_3 deposited using metalorganic chemical vapor deposition (MOCVD) to enhance the dielectric quality and lifetime. The growth of Al_2O_3 is performed after the growth of β-Ga_2O_3 without breaking the vacuum in an Agnitron MOVPE reactor with far injection showerhead design using Trimethylaluminum (TMAl) and Oxygen as precursor gas. The interfacial dielectric layer (First 5 nm) is grown at 800 °C to crystallize the interface to have reduced interface trap density and the rest of the dielectric (17 nm) is grown at 600 °C. Thickness of the grown Al_2O_3 layer was extracted to be ~22 nm using Xray reflectivity measurements. Grazing incident Xray diffraction analysis was performed and polycrystalline inclusions were observed in the grown Al_2O_3 films. The dielectrics grown at 600 °C exhibited higher interface trap densities ($D_t = 3.2\times10^{12}$ cm^{-2}) and lower breakdown fields (E_{BR}=6 MV/cm) when compared to the dielectrics grown at 800 °C (E_{BR}= 10 MV/cm, $D_t=5.4\times10^{11}$ cm^{-2}) as is evident from the hysteresis and the trap density vs energy characterization which were determined using deep-UV assisted CV measurements and the current-voltage characteristics of the MOS capacitor test structures. The temperature-modulated dielectric sample (interfacial layer grown at 800 °C, and the bulk dielectric grown at 600 °C) has higher breakdown strength (E_{BR}=7.7 MV/cm) and lower trap density ($D_t = 1.1\times10^{12}$ cm^{-2}) compared to the dielectric grown at 600 °C. This is possibly due to the interfacial crystallization of the hybrid dielectric due to the initial growth at higher temperature. Time dependent dielectric breakdown (TDDB) (current vs stress time) was performed to characterize the long-term reliability of the grown dielectrics. From the Weibull distribution plots of the time to breakdown for four different TDDB stress conditions, a shape factor of β > 1 is observed which indicates good statistical uniformity and intrinsic breakdown behavior. The TDDB distribution is much tighter (higher β value) for the 600 °C dielectric, compared to the 800 C grown dielectric. This is possibly due to the short-range ordering of the 800 °C dielectric compared to the 600 °C dielectric, which reduces the long-term reliability of the dielectric. However, for the hybrid dielectric, the time to breakdown is found to be more tightly distributed when compared to both 600 °C & 800 °C dielectric. Based on the E-model (field-based model), the lifetime of the 800 °C can be extended to 10 years if the dielectrics are stressed at 0.7 MV/cm, whereas the lifetime of the hybrid dielectric can be extended to 10 years if it is stressed at 3.1 MV/cm. Thus although the static breakdown voltage and trap densities of the hybrid dielectric are a little inferior compared to the 800 °C dielectric, the long term reliability of the hybrid dielectric is much superior. This approach of in-situ dielectric deposition on β-Ga_2O_3 can pave the way for promising robust gate dielectrics for future β-Ga_2O_3 based high performance MOSFETs due to its promise of improved interface and bulk quality and long-term reliability compared to other conventional dielectric deposition techniques.
We acknowledge funding from AFOSR MURI program under Award No. FA9550-21-0078 (PM: Dr. Ali Sayir).

4:10 PM DD03
(Student) SIMS Study of the Accumulation of Si on the Surface of Gallium Oxide and Its Mitigation Cameron A. Gorsak[1], Jonathan McCandless[1], Vladimir Protasenko[1], Darrell G. Schlom[1,1,2], Huili Grace Xing[1,1,1], Michael O. Thompson[1], Debdeep Jena[1,1,1] and Hari Nair[1]; [1]Cornell University, United States; [2]Max-Born-Str. 2, Germany

The unique properties of β-Ga_2O_3 such as its ultra-wide bandgap of ~4.8 eV, critical breakdown field of ~8 MV/cm, the availability of large-area native substrates, and controllable n-type doping have enabled rapid development in both its growth and device processing. One of the major challenges yet to be addressed is the commonly observed parasitic Si donors at the substrate-epitaxial interface because this parallel conducting channel contributes to buffer leakage and adversely affects the performance of lateral field-effect transistors [1]. This interfacial Si peak observed in secondary ion mass spectrometry (SIMS) data often varies widely and is theorized to originate from a combination of substrate polishing as well as exposure to laboratory ambient settings, warranting a systematic study.
To investigate the surface Si accumulation due to the laboratory ambient as well as methods to remove the Si after ambient exposure, we grew a single SIMS stack in which we grew multiple ~150 nm UID β-Ga_2O_3 epitaxial layers, using metal-organic chemical vapor deposition (MOCVD). After the growth of each layer, the sample was removed from the MOCVD reactor and exposed to the laboratory ambient for 2 hours. Before returning the sample to the MOCVD reactor, various chemical treatments were performed to remove the Si, such as HF etching. SIMS results show that a 30-minute HF etch effectively reduces the surface Si concentration by ~1 order of magnitude as compared to the controls which received no chemical treatment. However, the Si content returns to the non-etched levels if the sample is held in laboratory ambient conditions for 10 minutes between etching and loading into the MOCVD reactor. We used atomic force microscopy (AFM) to evaluate the effect of HF etching on the surface morphology of the Fe-doped (010) β-Ga_2O_3 substrates. The HF etched substrate exhibited a surface roughness RMS value of ~95 pm while that of the untreated substrate was ~170 pm, illustrating that this etching has a negligible effect on the surface roughness of the substrates. Subsequently, we grew ~550 nm thick β-Ga_2O_3 films using MOCVD on these two substrates. The surface roughness values were determined as ~663 pm and ~677 pm RMS for the substrates with and without the HF treatment, respectively, which confirms that HF etching of the substrate before growth does not adversely affect the surface morphology of the epitaxial film.
This work illustrates the importance of HF etching to prevent parasitic conduction channels due to Si accumulation at the substrate-epitaxial film interface and verifies that the HF etching step does not negatively affect film surface morphology. We further confirm the need for minimizing ambient air exposure after etching to prevent a reemergence of the Si contamination layer by quantifying the time it takes for Si to accumulate on the gallium oxide surface. This systematic study addressing the accumulation and subsequent mitigation of silicon contamination on β-Ga_2O_3 surfaces will help in pushing the performance of β-Ga_2O_3 based devices toward the theoretical limits.
Reference
[1] S. Kumar, T. Kamimura, C.-H. Lin et al., Applied Physics Letters **117**, 193502 (2020).

4:30 PM DD04
(Student) Optimizing Si Implantation and Annealing in β-Ga_2O_3 Katie Gann[1], Naomi Pieczulewski[1], Thaddeus J. Asel[2], Brenton Noesges[2,3], Cameron A. Gorsak[1], Karen N. Heinselman[4], Kathleen Smith[1], Jonathan McCandless[1], Huili Grace Xing[1], Debdeep Jena[1], Hari Nair[1], David Muller[1] and Michael O. Thompson[1]; [1]Cornell University, United States; [2]Air Force Research Laboratory, United States; [3]Azimuth Corporation, United States; [4]National Renewable Energy Laboratory, United States

Optimizing thermal activation anneals for silicon ion implantation in β-Ga_2O_3 is critical for achieving low resistance contacts and selective area doping for advanced device structures. While activation has been widely reported, annealing conditions vary significantly and systematic annealing studies have not yet been reported. We report the impact of time, temperature, and especially the annealing ambient, on the activation of Si in β-Ga_2O_3 at concentrations from 5×10^{18} cm^{-3}, to 1×10^{20} cm^{-3}, and in β-$(Al_xGa_{1-x})_2O_3$ ($x\leq15\%$) at concentrations 5×10^{19} cm^{-3}. Under optimized conditions, nearly full activation (>90%) and high mobility (>70 cm^2/V-s) are achieved in β-Ga_2O_3 at implant concentrations to $5x10^{19}$ cm^{-3}, with contact resistances measured below 0.16 Ω-mm Extending optimized anneal conditions to β-

$(Al_xGa_{1-x})_2O_3$ shows promising initial results with limited activation (>5×10^{18} cm^{-3} carriers) but high mobility recovery (60-80 cm^2/V-s). Unintentionally doped (UID) β-Ga_2O_3 films (>400 nm) were grown by plasma assisted molecular beam epitaxy, and β-$(Al_xGa_{1-x})_2O_3$ layers by metal-organic chemical vapor deposition, on Fe-doped (010) β-Ga_2O_3 substrates. Samples were ion implanted with Si at multiple energies to yield 65 or 100 nm box profiles with concentrations of 5×10^{18} cm^{-3}, 5×10^{19} cm^{-3}, or 1×10^{20} cm^{-3}. Dopant activation was achieved by annealing as-implanted films in a load-locked ultrahigh vacuum compatible quartz tube furnace at 1 bar pressure with precisely controlled gas ambient.

The impact of O_2 (to 10^{-2} bar) and H_2O (to 25 ppm) in the annealing ambient condition was determined by mixing with research plus grade nitrogen (<1 ppm total impurities). P_{O2} below 10^{-5} bar ensures Si activation (>85%) at 5×10^{19} cm^{-3}, while lower concentration implants (5×10^{18} cm^{-3}) maintain high carrier activation up to ~10^{-2} bar. To maintain the stability of the β-Ga_2O_3, P_{O2} must be greater than 10^{-9} bar, with annealing in vacuum or forming gas result in poor activation or decomposition. Water vapor is critical as even ppm concentrations significantly reduce activation, with 25 ppm H_2O reducing active carriers by an order of magnitude. The effect is reversible, and activation can be recovered with a subsequent anneal in a “dry” ambient. Optimal results were consistently obtained with the gas ambient intentionally dried below 10 ppb of H_2O.

Recovery of the mobility requires annealing temperatures above 900 °C, with increasing carrier activation and mobility to temperatures as high as 1050 °C, though SIMS shows substantial Si diffusion at temperatures above 1000 °C. 950 °C is identified as an optimized temperature with minimal Si diffusion. The optimal time at 950 °C is between 5 and 20 minutes, with shorter times showing lower mobilities and longer times showing carrier deactivation; this “over-annealing” behavior is observed at all temperatures.

Lattice damage and recovery were also determined using Rutherford Backscattering Channeling (RBS/C), scanning transmission electron microscopy (STEM), and x-ray diffraction. No evidence of any second phase transformation was observed. RBS/C and STEM show only partial amorphization from 5×10^{19} cm^{-3} implants, with remnant β-Ga_2O_3, likely seeding rapid lattice recovery after thermal annealing. At higher implant doses, phase transformations have been reported in literature, which we believe is related to increasing lattice damage during implants. Varying implant dose and implant temperatures (from liquid nitrogen cooled to 650 °C) were used to assess the impact of amorphization on lattice recovery.

In conclusion, we demonstrate the importance of optimizing anneal conditions to activate implanted Si carriers in β-Ga_2O_3 and extend this understanding to higher concentration Si implants and to activating implants in β-$(Al_xGa_{1-x})_2O_3$ and ultimately a-$(Al_xGa_{1-x})_2O_3$.

4:50 PM DD05

Silicon Ion Implant Activation in β-$Al_{0.4}Ga_{1.6}O_3$ Alan G. Jacobs[1], Joseph Spencer[1,2], Marko Tadjer[1], Boris N. Feigelson[1], Ming-Hsun Lee[3], Rebecca L. Peterson[3], Fikadu Alema[4], Andrei Osinsky[4], Yuhao Zhang[2], Karl Hobart[1] and Travis Anderson[1]; [1]US Naval Research Lab, United States; [2]Virginia Tech, United States; [3]University of Michigan–Ann Arbor, United States; [4]Agnitron Technology, Inc, United States

Gallium oxide (GO) devices have generated great interest for next generation power and RF devices, in no small part due to the availability of large area, high quality, melt grown bulk substrates in multiple orientations. Many structures take advantage of heteroepitaxial growth of aluminum gallium oxide (AlGO) pseudomorphically for heterjunction AlGO/GO devices. A key challenge for HFET and similar devices remains in obtaining low contact resistance, enabling high drain-source current density with minimal contact self-heating.

Here we focus on the activation of ion implanted silicon donors by rapid thermal annealing of AlGO grown by metalorganic chemical vapor deposition on a bulk GO substrate by varying the implant concentration, anneal duration, and anneal temperature in expansion of last year’s presented work. Films were ion implanted with silicon concentrations of 5e18, 3e19, and 1e20 cm^{-3} approximating box profiles ~60nm deep into the ~100nm thick AlGO films. Anneals were performed from 900 to 1140 C with varying nominal durations from 6 to 600 seconds. Standard Ti/Au contacts were used with a short ohmic anneal for 60 seconds at 470 C.

Linear transmission line measurements (LTLMs) indicate that ohmic contact was achievable at all implantation doses tested, with the broadest anneal process latitude available at the highest silicon concentration of 1e20. At this concentration, the specific contact resistance was at or below 10^-3 ohm-cm^2 for most anneal conditions and achieving a minimum measured value of 5e-5 ohm-cm^2 for a 6 second anneal at 1100 C, however, the minimum sheet resistance was measured for anneals near 1000C for 6-60seconds at ~3 kohm/sq. At 3e19 silicon concentration, optimal annealing conditions again centered around 1000C for 6-60 seconds achieving sheet resistances of 5-10 kohm/sq with specific contact resistances of ~3e-2 ohm-cm^2. At the lowest silicon concentration of 5e18, longer and lower temperature anneals were favored at 900C 1-10 minutes or 1000C for 1 minute achieving optimal performance at 900C for 1 minute at 10-20 kohm/sq and specific on resistance of 2e-3 ohm-cm^2.

Hall effect on samples annealed at 1000C for 1 minute showed a mobility of ~22 cm^2/Vs with approximately 3% of implanted species actively generating carriers, while annealing for a shorter duration of 6 seconds shows an improved mobility of 30-35 cm^2/Vs and 4-7% of implanted species generating carriers. This preference of shorter anneals agrees with LTLMs indicating degradation for long duration or higher temperatures at the same duration showing that over-annealing can have a significant impact. This effect could be the consequence of excessive diffusion, coalescence into inactive aggregates, or other effects, but is as of yet unknown in cause. This successful activation of donors in AlGO yielding lower contact resistance and controllably conductive films provides an easy route to device integration for greater reliability, higher performance, and lower thermal loading.

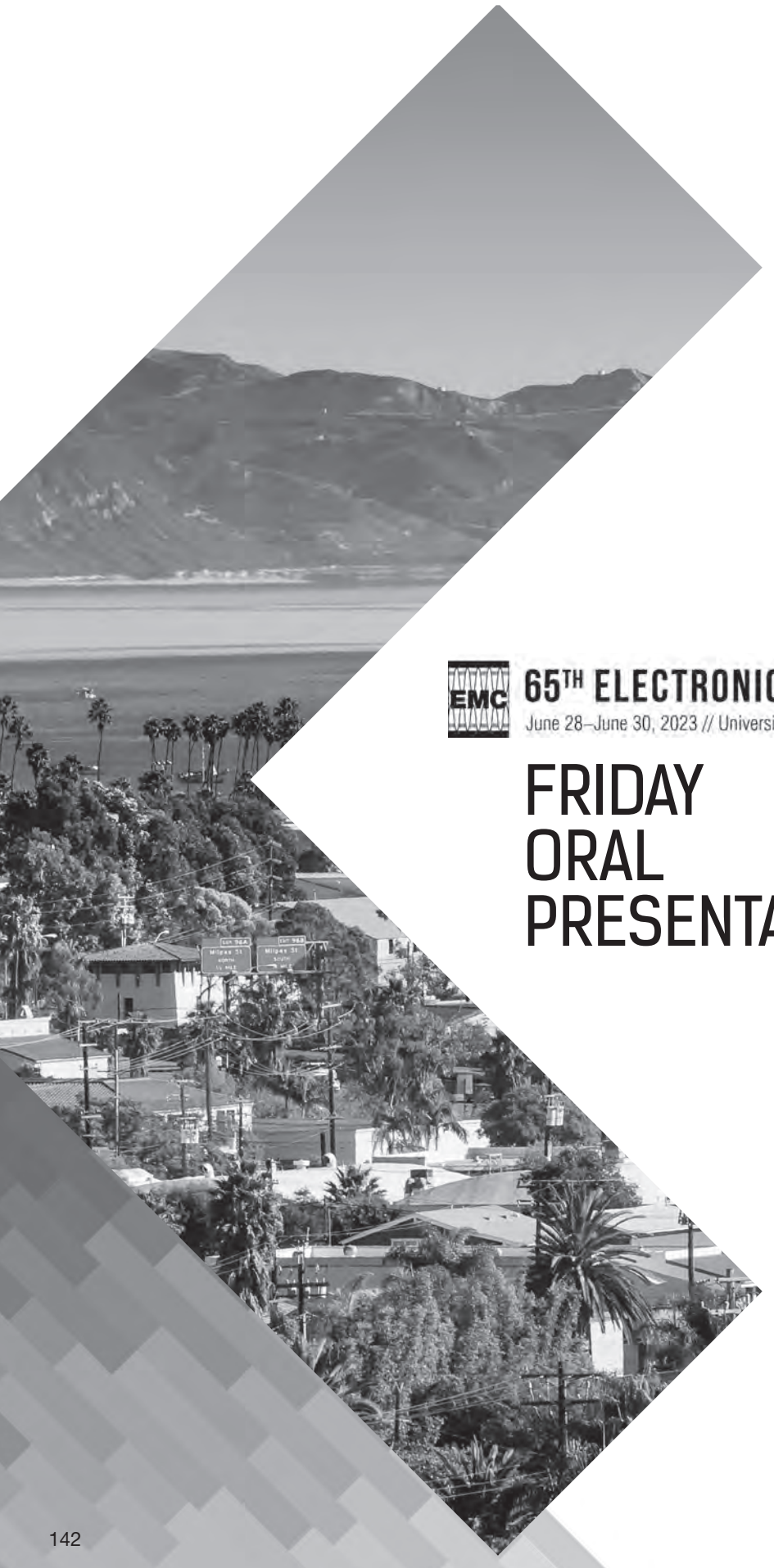

EMC 65TH ELECTRONIC MATERIALS CONFERENCE

June 28–June 30, 2023 // University of California, Santa Barbara // Santa Barbara, California

FRIDAY ORAL PRESENTATIONS

SESSION EE: Diamond and Related Materials
Session Chairs: Mark Goorsky and Patrick Shea
Friday Morning, June 30, 2023
UC, Corwin East

8:20 AM EE01
(Student) Synthesis of Free-Standing Polycrystalline Diamond Nanomembrane Dmitry Shinyavskiy[1], Matthias Muehle[2] and Jung-Hun Seo[1]; [1]University at Buffalo, The State University of New York, United States; [2]Fraunhofer USA, Inc., Center Midwest, United States

Polycrystalline diamond has excellent material properties such as high carrier mobility, excellent thermal and mechanical properties. Although polycrystalline diamond has been widely used as a surface protection layer, its practical use in electronic applications has been limited due to an unfavorable synthesis conditions. Polycrystalline diamond nanomembrane (PCD NM) is a different format of polycrystalline diamond film that is a free-standing form. The PCD NM is also a transferable diamond film that has a wide range of freedom in their thicknesses (a few tens of nm to hundreds of microns), size (micron-size to a full wafer scale), doping type/concentration, therefore, PCD NMs can be heterogeneously integrated with other foreign substrates or platform easily. In this talk, we will present our recent development of transferrable PCD NMs, including the NM synthesis and manipulation processes and their electrical properties.
Fig.1(a) shows a schematic illustration of the creation of PCD NMs from the bulk PCD substrate. A 3um thick boron doped PCD thin-film was originally grown on a 2-inch SiO_2/Si substrate via microwave plasma assisted chemical vapor deposition (MPACVD) growth reactors. In order to achieve a high-quality PCD thin-film, the pre-seeding process with diamond powder was performed prior to the growth. Once the PCD growth was completed, an array of etching holes was formed to access the underlying SiO2 layer, thus enabling a selective removal of the SiO2 layer using hydrofluoric acid. Then, the top PCD thin-film was separated from the substrate and formed a PCD NM. This PCD NM can be manipulated using various micro-transfer-printing techniques. Fig. 1(b)-(d) show the optical and scanning electron microscopy (SEM) images of free-standing PCD NMs after the process step (v) in Fig. 1(a). Fig. 1(e) presents transfer-printed PCD NM onto PET substrate using a micro-transfer-printing method. The free-standing nature of PCD NM allows us to access both top and bottom surfaces. Fig.2 shows a statistical distribution of grain sizes of the top (Fig. 2(a)) and bottom (Fig. 2(b)). Interestingly, the average grain size of the top and bottom sides of PCD NM were measured to be ~1.2um and 0.17um, respectively. This is due to a growth mechanism of the PCD thin-film (seed-to-crystalization), therefore, this result gives a possibility to engineer the size of the PCD grain larger.
As shown in Fig.3, changes in a structural property of PCD thin-film and NM were investigated using Raman spectroscopy with the following three surfaces: (i) top surface of as-grown PCD on SiO2/Si sample, (ii) top surface of PCD NM, (iii) bottom surface of PCD NM. Strong sp3 peaks at 1332 cm-1 were obsevered from all three conditions. Noticebly, a relative intensity of carbon-boron vibrational modes at 1220 cm-1 is higher on the top surface than the bottom surface, suggesting that boron incorporation in the carbon lattice was poor in the beginning.
To further investigate the doping quality in PCD NM, a transmission line method (TLM) method was employed. Total six TLM ohmic metal (Ti/Au=30nm/150nm) pads were deposited using an electron-beam evaporator. Fig.4 indicates I-V curves measured from TLM pads, showing a good linear I-V characteristic. Contact resistance and sheet resistance values were calculated from Resistance-Distance curve in Fig. 4(b), yielding 27 ohm and 37 ohm/sq, respectively.
In summary, high-quality PCD NMs were successfully created and their manipulation methods were demonstrated. Various material properties of top and bottom surfaces of PCD NMs can be investigated and reveals differences in grain size, surface morphology and doping. PCD NMs can readily be implemented in various ways in electronics to improve the performance or to create new applications. For example, PCD NMs can be used to demonstrate 3D-stackable electronics, highly reliable bioelectronics, less-corrosive electrodes, heat dissipator and flexible electronics

8:40 AM EE02
Characterization of Inch-Sized Diamond Wafer Grown on Misoriented Sapphire Makoto Kasu, Jacques Dagbeto and Niloy Chandra Saha; Saga University, Japan

Diamond is an ultra-wide bandgap (5.47 eV) semiconductor material with exceptional physical features that enables energy-efficient high-power and high-frequency devices. We have demonstrated extremely high-power output (875 MW/cm^2) [1] and high off-state breakdown voltage (3659 V) [2] of diamond MOSFETs. Recently, two-inch diameter diamond wafers were achieved on misoriented sapphire substrates [3] with a low XRC FWHM 004 of 89 arcsec and dislocation density of 1.4×10^7 cm^{-2}, which are the lowest among heteroepitaxial diamonds. By using the misoriented substrate, the 2-inch diameter free-standing diamond wafer was successfully achieved without any cracking.
An A-plane (11-20) sapphire misoriented by 7.0 º towards [0001] c-direction was used as the substrate. 1-μm-thick iridium (Ir) buffer layer was deposited on it. The diamond nucleation on the Ir buffer layer was performed using the bias-enhanced nucleation (BEN) process. Next, the diamond thick layer was grown on BEN-treated Ir buffered misoriented sapphire substrates by the microwave plasma CVD method. Each layer of the sample was characterized by XRD, AFM, and cross-sectional TEM.
Crystal curvature occurred in the misorientation direction, however, no crystal curvature in the perpendicular direction was found. This is the key factor to relax the strain in the grown diamond thick layer induced by Ir/sapphire substrate and to obtain an inch-sized diamond wafer without any cracking.
The misorientation angles of the diamond layer, Ir buffer layer, and sapphire substrate were measured by XRC measurements. The misorientation angles of the sapphire α_{sapp} showed negligible variation from 6.92 to 6.94º. Surprisingly, Ir misorientation angles α_{Ir} were found to be lower than α_{sapp} and varied from 5.69 to 5.81º. Diamond misorientation angles α_{Dia} were varied from 6.66 to 6.82º. In addition, nitrogen-doped (N-doped) diamond showed α_{Dia} of 6.25~6.38º which are lower than that of N-free diamond. This investigation showed a as $\alpha_{Ir} < \alpha_{Dia} < \alpha_{sapp}$ and this phenomenon could be caused by lattice relaxation during diamond, Ir growth.
In conclusion, we investigated how an inch-sized diamond thick layer can be grown without any cracking on Ir/misoriented sapphire substrates. This study revealed the initial growth mechanism of the diamond on the Ir buffered misoriented sapphire and their variation of misorientation angles which determined a relation as $\alpha_{Ir} < \alpha_{Dia} < \alpha_{sapp}$.
[1] N. C. Saha, M. Kasu, et al., IEEE Electron Dev. Lett. 43, 777 (2022).
[2] N. C. Saha, M. Kasu, et al., IEEE Electron Dev. Lett. 44, 112 (2023).
[3] S. -W. Kim, M. Kasu, et al., Appl. Phys. Express 14, 115501 (2021).

9:00 AM EE03
(Student) Chemical Mechanical Polishing of Polycrystalline Diamond Films for Integration as High Thermal Conductivity Layers Kaicheng Pan, Michael E. Liao, Lezli Matto and Mark Goorsky; University of California, Los Angeles, United States

Polishing of polycrystalline diamond thin films with sub-nanometer roughness is demonstrated with subsequent transfer of the diamond film to other substrates. Direct growth of diamond on a substrate or device layer necessitates a barrier layer to protect the underlying substrate and the small diamond nuclei that form at the interface reduce the thermal transport of the diamond layer. However, the high

surface roughness of polycrystalline diamond films also poses a challenge for integration (transfer via bonding) of such diamond films with other materials. Polycrystalline diamond-on-silicon films with large average grain size (0.7 µm) and a thickness of 2.7 µm were lapped and chemical mechanical polished (CMP). By the means of lapping and CMP, the r.m.s roughness decreased from 61 nm to 8 nm on a 40 x 40 μm^2 scale, and r.m.s roughness of 0.5 nm was achieved over 1 μm^2 with only small indentations (no protrusions). This low roughness paves the way for integration of the diamond film, such as thin film transfer by wafer bonding for heat dissipation of high-performance semiconductor devices. The short polishing time (2 hours) and low r.m.s. roughness shows our procedure to be successful and efficient. First, a mechanical lapping step was performed using diamond paste. The surface roughness reduction plateaued at 30 nm. However, due to the strong interface strength between the diamond layer and the silicon substrate, up to 80 kPa pressure can be used without the diamond film peeling. Additionally, the lapping step was determined to significantly save the subsequent chemical mechanical polishing time as well as the slurry usage. Scanning electron microscopy (SEM) shows that the lapping step can induce cracks on top of the grains. These cracks actually assisted their subsequent removal and were polished away during the CMP process. Scanning electron microscopy after the CMP process was used to study the surface morphology as well as diamond layer thickness before and after the polishing. We found that the surface is smooth with crevices (valleys), which is the primary causes for the roughness observed using AFM. On the plateaus between these valleys, the r.m.s. roughness reached as low as 0.5 nm, which is sufficient for wafer bonding purposes. The slurry particles and diamond debris that were deposited in the depressions during the CMP step were removed with subsequent cleaning steps. The available bonding area was around 80% percent, as determined from SEM images. The removal rate of most of the diamond layer is negligible, demonstrating that only the peak diamond protrusions were being polished and not the bulk of the diamond layer. Examples of this diamond film bonded to other substrates and the silicon substrate removed will be presented.

9:20 AM EE04
Electronic and Optical Characterization of Bulk and Epitaxial Single Crystals of Cubic Boron Nitride (cBN) Peker Milas[1,1], Sheikh Mathab[1,1], Jahangir Alam[1,1], MVS Chandrashekhar[2], Birol Ozturk[1] and Michael Spencer[1,1]; [1]Morgan State University, United States; [2]University of South Carolina, United States

Cubic boron nitride (cBN) is a relatively less studied wide bandgap semiconductor despite its many promising mechanical, thermal, and electronic properties. We report on the electronic, structural, and optical characterization of commercial cBN crystal platelets and single crystal epitaxial films grown on silicon and diamond substrates. Temperature dependent transport measurements on the bulk substrates revealed the charge limited diode behavior of the cBN crystals. The equilibrium Fermi level of the bulk material was determined to be 0.47 eV below the conduction band and the electron conduction was identified as n-type. Unirradiated dark and amber color bulk cBN crystals displayed broad photoluminescence emission peaks centered around different wavelengths. RC series zero phonon line defect emission peaks were observed at room temperature from electron beam irradiated and oxygen ion implanted cBN crystals, making this material a promising candidate for high power microwave devices, next generation power electronics and future quantum sensing applications. Epitaxial films were grown using a plasma assisted CVD process using BF_3 and Nitrogen as gas precursors on silicon substrates. Preliminary analysis of these films showed them to be a mixture of hexagonal and cubic polytypes. Photoluminescence on these films revealed a board luminescence spectrum. Additional data on these samples as well as material grown on diamond will be presented.

9:40 AM EE05
(Student) Two-Dimensional Spin Systems in PECVD-Grown Diamond with Tunable Density and Long Coherence for Enhanced Quantum Sensing and Simulation Lillian B. Hughes[1], Zhiran Zhang[1], Simon Meynell[1], Weijie Wu[2], Bingtian Ye[2], Zilin Wang[2], Emily Davis[2], Norman Yao[2], Kunal Mukherjee[3] and Ania Jayich[1]; [1]University of California Santa Barbara, United States; [2]Harvard University, United States; [3]Stanford University, United States

Solid-state spins constitute a powerful platform for quantum technologies. Dense ensembles of coherent spins provide a starting point for investigating strongly interacting spin systems in which novel, many-body states can arise with applications in both quantum simulation and sensing. Dimensionality plays a critical role in the nature of many-body states, with reduced dimensionality giving access to unique phases and phenomena such as interaction-driven localization or dipolar-driven spin squeezing. For sensing applications, a dense 2D layer of sensors in close proximity to a sensing target exhibits enhanced spatial resolution (set by the depth of the layer) compared to a 3D ensemble at the same volumetric density, while benefiting from either $1/\sqrt{N}$ classical sensitivity enhancements or entanglement-driven enhancements. Lastly, dense 2D ensembles could serve as a starting point for targeted, on demand formation of individual, optically resolvable defects at specific locations, such as inside nanostructures. Altogether, creating thin spin layers with tunable density is of intense current interest but has been minimally explored in solid-state electronic spin systems to date.
Defects in diamond, such as nitrogen-vacancy (NV) centers and substitutional nitrogen (P1 centers), are particularly promising solid-state platforms to explore. However, the ability to controllably create coherent, two-dimensional spin systems and characterize their properties, such as density, depth confinement, and coherence has been an outstanding materials challenge. We present a refined approach to engineer dense (≥1 ppm*nm), 2D nitrogen and NV layers in (100) diamond using delta-doping during plasma-enhanced chemical vapor deposition (PECVD) epitaxial growth. We employ both traditional materials techniques, *e.g.,* secondary ion mass spectrometry (SIMS), alongside NV spin decoherence-based measurements to characterize the density and dimensionality of the P1 and NV layers. We present depth confinement of the spin layer down to 1.6 nm, high (up to 0.74) ratios of NV to P1 centers, and reproducibly long NV coherence times which are dominated by dipolar interactions between the engineered P1 and NV spin baths. Altogether, the results of our joint materials and qubit-based approach are key elements in the engineering of solid-state-spin systems for the next generation of quantum technologies.[1-2]
References
[1] L. B. Hughes, Z. Zhang, C. Jin, S. A. Meynell, B. Ye, W. Wu, Z. Wang, E. J. Davis, T. E. Mates, N. Yao, K. Mukherjee, A. C. B. Jayich, "Two-dimensional spin systems in PECVD-grown diamond with tunable density and long coherence for enhanced quantum sensing and simulation," (2022), arXiv:2211.02282.
[2] E. Davis, B. Ye, F. Machado, S. Meynell, T. Mittiga, W. Schenken, M. Joos, B. Kobrin, Y. Lyu, D. Bluvstein, S. Choi, C. Zu, A. C. B. Jayich, and N. Y. Yao, "Probing many-body noise in a strongly interacting two-dimensional dipolar spin system," (2021), arxiv:2103.12742.

10:00 AM BREAK

SESSION FF: Group III–Nitrides—Thermal Transport
Session Chairs: Ramón Collazo and Andrew Winchester
Friday Morning, June 30, 2023
UC, Corwin East

10:20 AM FF01
Thermal Considerations in Co-Designed III-Nitride Transistors
MVS Chandrashekhar, Md Didarul Alam, Richard Floyd, Abdullah Mamun, Mohammad Hussain, Grigory Simin and Asif Khan; University of South Carolina, United States

Compact power electronics have now approached a thermally limited performance regime. In response to this, the materials and device communities have adopted the paradigm of "co-design" where electrical and thermal design constraints are considered holistically. In this paper, we present an electro-thermal lumped element framework to quantify co-design constraints in the design of III-Nitride power devices. The key elements are the electrical and thermal analogs of resistance and capacitance, the interplay between which determines the time constants associated with overall system performance. Ideally, active channels should cool down quickly with the electrical transient after a fast voltage pulse to operate with passive cooling, and scale to higher switching frequencies for compact power systems. This also requires a heat sink with large heat capacity and small thermal resistance.

We begin with a technique we call "thermal titration" to measure static steady-state thermal resistance $R_{thermal.}$ Thermochromic paint, dispensed on a transmission line model (TLM) structure, changes its color at a given temperature under steady state electrical power, P, from which the thermal resistance $R_{thermal}$ is $\Delta T=R_{thermal}$ P is measured. Thermal titration was performed on GaN channel HEMTs grown by MOCVD on 16 µm thick AlN templates on sapphire with record thermal conductivity.[1] $R_{thermal}$ improved from ~30 W/mK for standard 2 µm thick AlN templates to 16 W/mK for 16um thick AlN. By removing the sapphire substrate by laser liftoff (LLO)[2], and subsequent transfer/soldering to a copper heat sink, $R_{thermal}$ decreased further still to 8 W/mK, with a corresponding elimination of thermal current droop. Thermal titration on record BFOM=460 MW/cm^2 ultra-wide bandgap AlGaN (87/64 Al-mol fraction) channels grown on bulk AlN substrates yielded $R_{thermal}$~10W/m-K[3], which also showed elimination of thermal droop.

To further investigate this issue using dynamic heating measurements, we performed pulsed I-V from 0.3 µs-1 ms pulse duration with 2 ms period on GaN-channel HEMTs on 16um AlN on sapphire and LLO soldered to copper. The longer the voltage pulse, the longer the duration of joule heating in the channel, leading to a temperature-induced decrease of current. Clear exponential regimes consistent with the thermal diffusivity (α_i) picture of heat transport were seen, in excellent agreement with the thermal conductivities k_i and heat capacities $C_{p,i}$ of the various constituents. For GaN 2 µm thick, a time constant ($L_{GaN}^2/2\alpha_{GaN}$) ~0.2-0.3 µs was observed regardless of substrate, while that for AlN 16 µm thick, $L_{AlN}^2/2\alpha_{AlN}$increased from 3 µs to 7 µs, while the final substrate time constants were >100 µs for both sapphire and copper heat sinks. The $k_{sapphire}<k_{Copper}$ leads to higher steady-state temperature for sapphire, consistent with the observed current droop in the output curves. The current for both structures should normally be identical before the heat reaches the heat sink, leading to the insight that LLO ablates ~0.5 µm of the poorer quality nucleation layer on sapphire that was identified in thermoreflectance[1]. In other words, electro-thermal transients enabled the identification and quantification of an interfacial issue in real devices.

In summary, we demonstrate strategies to measure and interpret the static and dynamic electro-thermal performance of III-Nitride channel transistors under real operating conditions to enable true co-design optimization strategies by identifying key performance limiters not possible using purely electrical means. The techniques described here are applicable to other emerging ultra-wide bandgap materials/devices such as cBN, AlGaN, diamond, and Ga_2O_3.

[1] Cheng at al., *Phys. Rev. Mat. 4, 044602(2020).*
[2] Alam et al., *Appl. Phys. Lett.,119, 132106 (2021).*
[3] Mamun et al., "$Al_{0.64}Ga_{0.36}N$ Channel MOSHFET on Single Crystal Bulk AlN Substrate" (*Manuscript in progress*).

10:40 AM FF02
Thermal Mapping of AlGaN/GaN High Electron Mobility Transistors Using Mechanically Exfoliated MoS_2 Flakes
James Spencer Lundh[1,2], Hsun Jen Chuang[2], Joseph Spencer[2,3], Karl Hobart[2], Travis Anderson[2] and Marko Tadjer[2]; [1]National Research Council, Postdoctoral Fellow, United States; [2]U.S. Naval Research Laboratory, United States; [3]Virginia Tech, United States

During device operation, self-heating occurs that is detrimental to electrical performance, causes reliability issues, and can lead to premature failure. Accordingly, it is critical to be able to acquire the device temperature distribution, identify the peak temperature rise, and quantify device thermal resistance in order to develop and assess thermal management solutions and prevent device degradation and failure. Previously, gravity drop coating was used to deposit MoS_2 flakes in 200-400 nm thick films on device structures for thermal imaging. [1] In this work, we present the use and transfer of mechanically exfoliated (~30 nm thick) MoS_2 flakes in conjunction with thermoreflectance thermal imaging (TTI) in order to measure the surface temperature rise of devices based on wide and ultrawide bandgap semiconductors, specifically AlGaN/GaN high electron mobility transistors (HEMTs).

MoS_2 flakes were mechanically exfoliated and transferred onto GaN transmission measurement line (TLM) structures fabricated on SiC substrates. A photomicrograph of the as-transferred MoS_2 flake is shown in Fig. 1. The thickness of these flakes is typically on the order of ~30 nm. The TLM structure has a channel length of 20 µm and a channel width of 100 µm. To assess the viability of using the flake as a surface temperature transducer, LEDs with two different wavelengths (365 nm, 470 nm) were used and compared. TTI was performed using a TMX Scientific T°Imager with a 100X objective. For all measurements, the stage temperature was maintained at 20 °C. Additionally, an oscilloscope was used to ensure accurate assessment of the operating power density. First, TTI calibrations were performed and maps with uniform thermoreflectance coefficients were obtained (Figs. 2(a),(b)). Subsequently, thermal measurements were performed using both wavelengths at power densities ranging from 2-10 W/mm. Figs. 2(c) and (d) show exemplary thermal maps of the MoS_2 flake acquired at power densities of (c) 7.51 W/mm (365 nm) and (d) 7.61 W/mm (470 nm). The temperature distribution along the flake was extracted for measurements using both LEDs and compared in Fig. 2(e). As shown, when the TLM was operated at approximately the same power density, the temperature distributions along the MoS_2 flake were the same. Subsequently, the temperature distribution (Fig. 3(a)) and peak temperature rise (Fig. 3(b)) of the MoS_2 flake was measured as a function of power density. Based on this, the device-level thermal resistance of the GaN TLM structure is ~3.5 W/mm. While this is lower than those typically reported for GaN-on-SiC HEMTs, the heat generation in the TLM structures is vastly different than in HEMTs. The TLM structure can be approximated as a uniform heater; this is in contrast to the HEMT structure where the vast majority of heat generation occurs at the drain-side corner of the gate electrode. To further confirm the accuracy of the method, MoS_2 flakes have been transferred to metal heater structures deposited on poly-Si to simultaneously obtain the temperature rise of both the MoS_2 flake and the underlying poly-Si. Additionally, this method is being applied to measure the surface temperature rise and assess the thermal performance of AlGaN/GaN HEMTs. The AlGaN/GaN HEMTs have a 2DEG mobility of 1946 cm^{2}V^{-1}s^{-1}, sheet carrier concentration of 9.25E-12 cm^{-2}, and sheet resistance of 345 Ω/sq, and specific contact resistivity of 1.18E-5 Ωcm^2. This work also has important implications for the assessment of thermal performance of devices based on ultrawide bandgap semiconductors (Ga_2O_3, AlGaN, diamond) as they are transparent to the IR, visible, and near-UV wavelengths on which other techniques rely (i.e., IR thermography,

standard TTI, Raman thermography).
J.S.L. gratefully acknowledges support by the NRC postdoctoral fellowship program. Research at the NRL was supported by the ONR.
[1] R. Hanus *et al., ACS Appl. Mater. Interfaces* 2021, 13, 42195-42204.

11:00 AM FF03
(Student) Understanding of Multi-Way Heat Extraction Using Peripheral Diamond in AlGaN/GaN HEMT by Electrothermal Simulations Khush Mahendrakumar Gohel, Swarnav Mukhopadhyay, Linhui Zhou, Shubhra Pasayat and Chirag Gupta; University of Wisconsin–Madison, United States

High Electron Mobility Transistors (HEMTs) are widely used in telecommunication, aerospace, and military for RF and power electronic applications[1]. High power operation of the AlGaN/GaN HEMT is significantly limited by self-heating effects caused due to inadequate heat extraction from the localized hotspot generated near high electron mobility channel [2]. Unoptimized design for heat extraction and high thermal boundary resistance at the GaN/Substrate interface are the primary causes of poor heat extraction [3]. Integration of diamond heat spreaders with high thermal conductivity has shown promising results in the thermal performance of the device[4]. However, several factors like GaN/Diamond thermal boundary resistance (TBR), optimal distance from the hotspot, and heat spreader configuration can lead to the sub-optimal thermal performance of the device. Consequently, in this work, we implement a multi-way heat extraction strategy for improving the thermal performance of the AlGaN/GaN/Diamond HEMT using a cohesive understanding of TBR and distance from hotspot to diamond heat dissipators.
AlGaN/GaN HEMT with a GaN substrate (Fig 1a), is simulated to set a baseline performance, which showed a thermal resistance of ~80 K.mm/W (fig 2). Upon replacing the GaN substrate with a Single Crystalline Diamond at the bottom of the device (fig 1b), its thermal resistance reduced by ~13 times. Despite of remarkable performance improvements, the device still suffers at high power density due to low thermal conductivity of GaN layer and high TBR at GaN/SCD interface. Device with SCD at bottom operating at 40W/mm is simulated for varying values of GaN thickness (50 -2000 nm) and GaN/SCD TBR values (3.1-20 m^2K/GW). Simulation output showed reducing GaN thickness provides a better heat extraction from the bottom of the device, however, only up to an optimum thickness, going thinner leads to higher device temperature (fig 3a). The optimum thickness has a positive correlation with GaN/SCD TBR, i.e., as the TBR value increases the GaN layer optimal thickness also increases. For very thin GaN layer, a steep increase of ~ 200K is recorded near the hotspot in the Lateral temperature profile of the device (Fig 3b), going from the edge of the device (~500 K) towards the hotspot (~700 K). This demonstrates as the thickness reduces heat in unable to spread in the GaN layer before reaching the thermal interface and increases the device temperature.
Owing to 500 K temperature at the side edge, further enhancements to the device are made by adding Poly-Crystalline Diamond (PCD) side walls at the edge of the device (Fig 1c) along with SCD at the bottom. The device is simulated for the same GaN layer thicknesses and TBR values (Fig 4a). For the optimized value of GaN layer (200 nm) and lowest TBR (3.1 m^2K/GW) a significant drop of ~ 150 K is observed in the device temperature due to 3-way heat extraction. Lateral temperature profile (fig 4b) recorded ~330 K at GaN/PCD-sidewall interface and ~550 K at the hotspot which still showed a steep rise of ~200K, which illustrates that, lateral thermal resistance of GaN layer limits maximum heat extraction plausible from the edge of the device. Therefore, to extract heat from the hotspot region, an additional PCD layer with associated interface TBR layer is added on top of the device. The additional heat extraction path led to a temperature reduction of 70 K. Consequently, using side, top, and bottom heat extraction pathways and optimization of GaN layer in correlation with TBR, an AlGaN/GaN HEMT operating at a power density of 40W/mm are simulated with temperature ~470-500 K.
[1] Fletcher, A. *Superlattices and Microstructures* vol. 109 519–537 (2017). [2] Gaska, R. *et al. IEEE ELECTRON DEVICE LETTERS* vol. 18 (1997) [3] Chen, G. PhD. *et. al. Annual review of heat transfer. Volume 18* [4] Jessen, G. H. *et al. IEEE Compound Semiconductor Integrated Circuit Symposium, CSIC* 271–274 (2006)

11:20 AM FF04
Visualizing and Quantifying Thermal Conductance and Strain at Compression Bonded GaN-Diamond Interfaces via Optical Methods Luke Yates, William Delmas, Amun Jarzembski, Anthony McDonald, Matthew Bahr, Brian Rummel, Wyatt Hodges, Zachary Piontkowski and Robert Kaplar; Sandia National Laboratories, United States

Vertical gallium nitride (GaN) power devices have demonstrated excellent potential to enhance the efficiency of power conversion circuits and reduce system sizes. Enhanced mobilities and high critical electric fields allow for low on-resistance devices with high voltage blocking and avalanche breakdown capabilities. However, these material benefits lead to exceptionally high-power densities during the operation of vertical GaN power devices (MOSFETs and PN diodes), which in turn impacts device reliability, lifetime, and electrical performance. To this end, the heterogeneous integration of diamond with vertical GaN devices is pursued as an effective means of heat removal within the device assembly. This work expands on previous diamond incorporation with lateral device structures to include a metal compression bonding interface that allows for backside electrical contact to the vertical device. This necessary requirement precludes the ability to perform a direct GaN/diamond bond. Here we will discuss current efforts that have demonstrated a GaN/diamond intermetallic bonding process for bulk material systems. Investigation of the GaN/diamond bond quality/interface is performed via hyperspectral frequency domain thermoreflectance (FDTR) imaging to quantify the bond quality of buried interfaces. By raster scanning the sample, a 3-dimensional data cube containing spatial and depth dependent thermal property information is obtained. This information is evaluated via standard radial phase lag thermal models, typically employed with FDTR, in addition to the use of a k-means clustering algorithm to allow for quick identification of unbonded, partially bonded, and intimately bonded regions. The interfaces are compared to confocal scanning acoustic microscopy (CSAM) and vibrational (Raman) spectroscopy maps to obtain additional thermomechanical information. It is shown that “poor” or partially bonded regions cannot be quantified via traditional CSAM approaches, and thermal/optical methods allow for higher fidelity and quantification of these regions. Substantial changes in the GaN/diamond thermal boundary conductance are identified on the same scale as a would-be power device. This indicates an increased need for high fidelity, high throughput analysis techniques to identify thermomechanical inconsistencies in bonded heterogenous integration schemes.
This research was supported by the Laboratory Directed Research and Development program at Sandia National Laboratories, a multimission laboratory managed and operated by National Technology & Engineering Solutions of Sandia, LLC, a wholly owned subsidiary of Honeywell International Inc., for the U.S. Department of Energy’s National Nuclear Security Administration under contract DE-NA0003525

SESSION GG: Epitaxy of Structured and Quantum Materials
Session Chair: Seth Bank
Friday Morning, June 30, 2023
UC, Flying A Studios

8:20 AM GG01
(Student) Dark Current Reduction by MBE Selective Area Growth in III-V Semiconductor PIN Photodetectors Alec M. Skipper[1], Adam A. Dadey[2], Ashlee Garcia[1], Moaz Waqar[3], Huaixun Huyan[3], Chaojie Du[3], Xiaoqing Pan[3], Joe Campbell[2] and Seth R. Bank[1]; [1]University of Texas at Austin, United States; [2]University of Virginia, United States; [3]University of California, Irvine, United States

High sensitivity photodetectors are required for numerous modern applications in communications, imaging, and biological sensing. These applications often utilize a high density of devices employed in a two-dimensional array, emphasizing the need for improved performance and yield at smaller device sizes. However, many material systems are plagued by dark currents caused by surface and bulk defects in the device [1]. These defects can arise due to damage from etch processes during post-growth fabrication, often requiring complicated passivation schemes and cryogenic cooling to keep dark currents low [2].
Selective area growth presents a potential solution to these fabrication-induced defects by removing the etch process entirely. By performing selective area growth on a patterned template on a III-V wafer, devices are defined without requiring post-growth etching. Prior work in selectively grown InGaN micro-LEDs using a similar technique suggests that this may result in dark current reduction due to the lack of etch damage [3]. The size and density of the devices can be easily controlled by setting the dimensions of the growth template, shifting the fabrication to straightforward SiO_2 etches rather than III-V etches.
We demonstrate dark current reduction in GaAs PIN photodetectors grown by selective-area molecular beam epitaxy. In this work, we used periodic supply epitaxy, a growth technique which employs periodic pauses in group-III flux to enhance adatom desorption and diffusion to allow for both selective area growth and lateral epitaxial overgrowth [4], to grow GaAs PIN photodetectors in patterned silicon dioxide templates on n-type GaAs substrates. The devices consisted of a 70 nm n-type contact region doped with Si to ~$1x10^{18}$ per cm^3, a 200 nm intrinsic region, and a 70 nm p-type contact region doped with Be to ~$1x10^{18}$ per cm^3. A control sample was grown under identical growth conditions on an unpatterned n-type GaAs wafer. Control devices were patterned using UV photolithography and a phosphoric acid etch. Both the control and selective growth devices were metallized and dark current was measured on devices ranging from 20 µm in diameter to 100 µm in diameter.
Fitting the dark current and device diameter to a quadratic function showed a significant reduction in bulk dark current for the selective area growth device. However, the inverse of the zero bias resistance-area product against the perimeter to area ratio shows a significantly flatter curve for the control device. According to the variable area diode array method [5], this suggests that surface defects dominate the dark current for the selective area growth devices and bulk defects dominate for the control devices. While scanning transmission electron microscope studies of GaAs regrowth initially suggested high-quality interfaces between the GaAs and SiO_2 template, further growth optimization of this interface may be necessary to further reduce surface component of dark current. Investigations into the nature of this interface and the temperature dependence of the dark current are currently underway and will be reported at the conference.
[1] B. Marozas et al., "Surface dark current mechanisms in III-V infrared photodetectors," Optical Materials Express (2018)
[2] E. Pils et al., "Passivation techniques for InAs/GaSb strained layer superlattice detectors," Laser Photonics (2013)
[3] J. Bai et al., "A Direct Epitaxial Approach to Achieving Ultrasmall and Ultrabright InGaN Micro Light-Emitting Diodes (µLEDs)," ACS Photonics (2020)
[4] D. Ironside et al., "High-Quality GaAs Planar Coalescence over Embedded Dielectric Microstructures Using an All-MBE Approach," ACS Cryst. Growth Des. (2019)
[5] V. Dhar and V. Gopal, "Dependence of zero-bias resistance–area product and quantum efficiency on perimeter-to-area ratio in a variable-area diode array," Semicond. Sci. Technol. (2001)

8:40 AM GG02
(Student) InP Lateral Epitaxial Overgrowth by Solid-Source Molecular Beam Epitaxy Yiteng Wang[1,2], Ryan D. Hool[1,2], William K. North[2,2], Sanat Pandey[2,2], Erin M. Raftery[2,2], Kent D. Choquette[2,2] and Minjoo L. Lee[2,2]; [1]University of Illinois Urbana-Champaign, United States; [2]University of Illinois at Urbana-Champaign, United States

Lateral epitaxial overgrowth (LEO) enables lithographically patterned dielectric features to be embedded within single-crystal semiconductor materials. InP-based photonic crystal surface-emitting lasers (PCSELs) take advantage of the index contrast created by periodic arrays of encapsulated voids while avoiding the challenges of growing distributed Bragg reflectors at this lattice constant [1]. LEO on photonic crystals (e.g., arrays of triangles) requires coalescence from multiple crystal fronts, which can introduce pits, as well as threading dislocations (TDs) and stacking faults (SFs) [2]. In this work, we demonstrate selective InP nucleation and coalescence on patterned InP substrates with designed feature sizes of 266-1110 nm by solid-source molecular beam epitaxy (SS-MBE). Despite the lack of lattice mismatch, we find that extended defects form before the completion of coalescence in all cases and that LEO on smaller features with sides aligned away from [0 -1 1] and [0 1 1] directions favors lower defect densities.
InP substrate patterning started with 40 nm of SiN deposited by PECVD and patterned by e-beam lithography. Reactive ion etching left arrays of SiN isosceles-right triangles with side lengths of 465-1110 nm and polygons with a side length of 266 nm. The sides of the triangles were aligned along [0 -1 1] and [0 1 1] crystallographic directions, while the sides of the polygons spanned a wide range of directions. We found a pre-growth cleaning procedure consisting of O_2 plasma ashing and wet cleaning in uncut (98 wt%) H_2SO_4 to enable InP surface morphologies matching those on epi-ready wafers. Samples consisting of 20 and 350 nm of Be-doped InP (10^{18} cm^{-3}) were grown on patterned n-InP at an elevated substrate temperature (Tsub) of 500°C and a low growth rate of 0.2 µm/hr to encourage selectivity [3]. Thicker samples of 1300 nm p-InP were initiated using the same conditions for the first 500 nm, followed by a second growth step at more typical InP MBE growth conditions of 440°C, 1 µm/hr. InP growths of 20 and 350 nm at Tsub = 500°C show good selectivity, as no polycrystalline nucleation was found on the dielectric regions. After 350 nm of growth, coalescence was completed over the 266 nm polygons, while an array of small pits was observed over the 1110 nm triangles. After 1300 nm growth, the InP surface was fully coalesced, regardless of feature size, with small, enclosed voids above the SiN patterns. Despite the excellent selectivity, we have found that Tsub = 500°C leads to rough InP surfaces, and the rms roughness of the coalesced films was ~30 nm due to high densities of hillocks.
Using electron channeling contrast imaging (ECCI), we find that InP LEO on the 266 nm polygons shows the lowest density of extended defects. 1300 nm overgrown InP on the 266 nm polygons had a TDD of 5.0×10^6 cm^{-2}, which is an order of magnitude lower than on the 465 and 1110 nm triangle patterns. Stacking fault density (SFD) decreases by nearly 10× as the feature size decreases from 1110 to 266 nm. At a pattern size of 1110 nm, ECCI reveals an unexpectedly asymmetric distribution of SFs with [0 -1 1]-oriented SFs over every buried triangle and virtually no [0 1 1]-oriented SFs. Consistent with the ECCI results, we find that overgrown InP on 266 nm polygonal patterns exhibits 3.9 and 1.6× greater photoluminescence intensity than on 465 and 1110 nm patterns, respectively. Future work will

focus on reducing surface roughness while maintaining selectivity and on better understanding the effect of pattern geometry on the formation of extended defects.

References
[1] K. Hirose, Y. Liang, Y. Kurosaka, A. Watanabe, T. Sugiyama and S. Noda, Nat. Photon **8**, 406–411 (2014)
[2] D. J. Ironside, A. M. Skipper, A. M.García and S. R. Bank, Prog. Quantum. Electron. **77**, 110316 (2021)
[3] M. Fahed, L. Desplanque, C. Coinon, D. Troadec and X. Wallart, Nanotechnology **26**, 295301 (2015)

9:00 AM #GG03
(Student) SiO_2 Surface Planarization for Molecular Beam Epitaxy Selective Area Regrowth of High Aspect Ratio Microstructures
Ashlee Garcia, Alec M. Skipper, Morgan Bergthold and Seth R. Bank; The University of Texas at Austin, United States

A molecular beam epitaxy (MBE) approach to selective area epitaxy (SAE) of III-V semiconductors could enable the seamless integration of metals, dielectrics, and high-quality crystalline semiconductors. This technique has the potential to advance novel optoelectronic structures, such as high-contrast photonics, site-controlled quantum emitters, stacked pixel detectors, and photonic integrated circuits. While SAE by metal organic chemical vapor deposition has been widely successful due to its high material deposition selectivity, an SAE MBE method could enable further advances through its high layer precision and access to non-equilibrium growth conditions[1,2]. SAE is difficult to achieve with conventional MBE due to III-V nucleation on the amorphous mask even at temperatures as high as 700°C. As a result, Allegretti et al. developed periodic supply epitaxy (PSE), a method to inhibit polycrystal formation by cycling group III deposition under a constant group V flux[2,3]. Combined with high growth temperatures and low growth rates, PSE enables SAE by mitigating the nucleation of poly-GaAs through increased Ga adatom diffusion to seeding windows and desorption off the mask surface[3-4]. While this all-MBE approach has been demonstrated to achieve selective growth and embedding of features up to ~2 µm wide and ~300 nm tall, applications requiring larger dielectric features such as mid- and long-wave infrared high-contrast photonics[5] and aspect ratio trapping of threading dislocations for metamorphic growth[6], are more difficult to access due to increased surface roughness of micron-scale features.[7] Increased roughness and defects on the mask surface lowers the barrier for nucleation further restricting the selective growth regime.[8]
Hydrogen silsesquioxane (HSQ) is an inorganic flowable oxide that has been utilized to create high quality planar SiO_2 interfaces that are vacuum and high temperature stable once cured.[9,10] In this study, we explore the use of HSQ surface planarization and curing process to restore the surfaces of micron-scale films for fabrication of high aspect ratio SiO_2 features with surfaces comparable to that of thin films. Integrating surface planarization with a 100 nm layer of HSQ in the fabrication of 1.5 µm tall features demonstrated a significant decrease in film roughness from a root-mean-square roughness of 3.95 nm to 0.75 nm. Furthermore, selectivity studies on cured HSQ films have demonstrated selectivity equivalent to that of SiO_2 deposited by plasma-enhanced chemical vapor deposition. Experiments are underway to utilize the surface planarization technique to achieve MBE selective area growth of high aspect ratio microstructures.
[1] D.J. Ironside et al., *J. Cryst. Growth* (2019). [2] A.M. Skipper et al., 2019 MRS EMC. [3] F.E. Allegretti et al., *J. Cryst. Growth* (1995). [4] S.C. Lee et al. *J. of Appl. Phys.* (2002). [5] Jun Wang *et al.* 2017 *Laser Phys. Lett.* 14 125801. [6] J.Z. Li et al. Appl. Phys. Lett. 91 (2) (2007). [7] M. R. Amirzada et al. *Appl Nanosci* 6, 215–222 (2016). [8] M. Ohring, The Material Science of Thin Films, *Academic Press* (1992). [9] F. Salmassi et al, *Applied Optics*, Vol. 45, No. 11 (2006). [10] C.-C. Yang and W.-C. Chen, J. *Mater. Chem.*, 2002,12, 1138-1141
This research was partly done at the Texas Nanofabrication Facility (NSF grant NNCI-1542159) and was supported by Lockheed Martin and NSF via the UT CDCM: an NSF MRSEC under Cooperative Agreement DMR-1720595, as well as CCF-1838435, DMR-1839175 and ECCS-1926187.

9:20 AM GG04
(Student) Light-Emitter/Superconducting Stack Within the Nitride Family
Mikolaj Chlipala[1], Henryk Turski[1,2], Marcin Siekacz[1], Krzesimir Nowakowski-Szkudlarek[1], Anna Feduniewicz-Zmuda[1], Anand Ithepalli[2], Chandrashekhar P. Savant[2], Huili Grace Xing[2], Debdeep Jena[2] and Czeslaw Skierbiszewski[1]; [1]Institute of High Pressure Physics Polish Academy of Sciences, Poland; [2]Cornell University, United States

Superconductors and semiconductors have separately revolutionized modern technology and both can be obtained within the nitride family. Transmission metal nitrides (TMNs) exhibit high durability, low resistance and superconductivity. Among these materials NbN exhibits a rather high critical temperature (T_c) of ~17 K. Group III nitrides, on the other hand, are renowned for their superior optical and electrical qualities used in LEDs and transistors. Given that III-nitrides and TMN each have distinctive features, the ability to integrate them on a single monolithic platform gives a device like this a significant advantage.
Recently, this subject draw attention of the community. For example a combination of III-nitride devices (i.e. high electron mobility transistor and tunnel diode [1,2]) with NbN superconductor have been presented. Here, we report on the first monolithic stack of III-nitride LED with the superconducting member of TMN with highest T_c, which is NbN. Both LED and NbN parts were obtained using a high-purity technique of plasma-assisted MBE.
Emitter needed for the application is required to operate at extremely low temperatures, below NbN T_c, where standard blue LEDs suffer from low injection and increased forward voltage. To overcome this, we used a Ge-Mg doped bottom tunnel junction (TJ). This construction presents: enhanced operation at low temperatures, provides a nitrogen-polar-like built-in field in quantum well on a gallium-polar substrate and terminates with low resistivity n-type layer, which allows for a good contact with NbN [3].
Initial results show good crystal quality of the bottom TJ LED part and the NbN part. T_c, extracted from electrical resistance, is 13.4 K. At temperatures below T_c, an increase in electroluminescence intensity is observed at different driving currents, which as reported before [4] can be a fingerprint of copper pair injection into the active region. These results show a successful epitaxial growth of the light-emitting/superconducting device stack within the nitride material system.
References
[1] Yan, R., et al., Nature 555, 183–189 (2018)
[2] Balasubramanian, K., et al., Opt. Mater. Express 10, 1724 (2020)
[3] Chlipala M., et al. Appl. Phys. Lett. 120, 171104 (2022)
[4] Panna, D., et al. Nano Lett. 18, 6764–6769 (2018)
Acknowledgments: This work is carried out within National Science Centre Grant, UMO-2018/31/B/ST5/03719, UMO-2019/35/N/ST7/04182, and project of the Foundation for Polish Science co-financed by the European Union under the European Regional Development Fund TEAM-TECH POIR.04.04.00-00-210C/16-00.

9:40 AM GG05
(Student) Manipulating the Opto-Electronic Properties of $Al_xIn_{1-x}As_ySb_{1-y}$ Digital Alloys by Adjusting the Period Thickness
J. A. McArthur[1], Ann K. Rockwell[1], Adam A. Dadey[2], Seth R. Bank[1] and Joe Campbell[2]; [1]The University of Texas at Austin, United States; [2]University of Virginia, United States

$Al_xIn_{1-x}As_ySb_{1-y}$ (referred to as AlInAsSb) grown as a digital alloy strain-balanced to GaSb substrates has recently emerged as a promising material system for photodetectors operating at near- to mid-infrared wavelengths. AlInAsSb possesses a broadly tunable compositional range which leads to a flexible IR bandgap, as well as advantageous band offsets and low-noise impact ionization properties

at room-temperature. [1-3] These factors make AlInAsSb an exciting alternative to other low-noise detector materials, like Si, which lacks the bandgap flexibility for spectral response at telecom and mid-IR wavelengths, or HgCdTe, which suffers from challenging growth and fabrication. [4] A number of advanced detectors have been realized with AlInAsSb, such as 2-µm separate absorption, charge multiplier avalanche photodiodes, (APDs) [3] staircase APDs, [4,5] and n-Barrier-n (nBn) photodetectors. [8,9]

Despite this success, the complex growth space of AlInAsSb digital alloys remains relatively underexplored. For example, the strain-balanced period stack offers a wide design space owing to its digital alloy nature. Generally, the material has been grown at a fixed period thickness of 10 monolayers (ML), primarily adjusting the aluminum molar fraction to access different material properties and bandgap energies. This has been sufficient for devices thus far; however, to reach longer absorption wavelengths and to potentially improve device performance metrics like dark current and bandwidth, adjusting the period thickness is then a clear and suitable development in the material platform. With detectors that already exhibit low-noise and high gain performance, even modestly expanding the materials design space could yield outsized benefits at the device and systems levels.

We report the structural and optical characteristics of AlInAsSb digital alloys with varying period thicknesses. An initial sample set of AlInAsSb films (Fig. 1a) with aluminum molar compositions of 70% were grown via molecular beam epitaxy with period thicknesses varying from 5ML (1.5nm) to 20ML (6.1nm). High resolution X-ray diffraction ω-2θ scans (Fig 1b) confirmed the crystal quality of the films with nearly lattice-matched AlInAsSb peaks. The satellite peaks indicate the superlattice periods were within 5% of the intended thicknesses. Photoluminescence (PL) spectra were also measured at room temperature. As expected, a blueshift in the PL emission was observed as the digital alloy period thickness was decreased. This shift indicates that significantly broader bandgap tunability can be achieved by varying the period thickness in digital alloy devices. Carrier mobilities, dark current densities, and impact ionization characteristics are currently being studied and will be presented at the conference.

This research was supported by Lockheed Martin and the National Science Foundation through DMR-1839175, CCF-1838435, and ECCS-1926187.

References:

[1] Maddox, et al. Crystal Growth 2016
[2] Woodson, et al. APL 2016
[3] Ren, et al. JLT 2017
[4] Martyniuk, et al. App Phys Rev 2014
[5] Jones, et al. Nature Photonics 2020
[6] Ren, et al. APL 2016
[7] March, et al. Nature Photonics 2021
[8] Wang, et al. JLT 2021
[9] Wang, et al. JLT 2022

10:00 AM BREAK

10:20 AM GG06

(Student) Growth and Characterization of Multigrain SmB_6 Thin Films by Chemical Vapor Deposition Brendan Jordan, Daniel Lewis and Kevin Daniels; University of Maryland, United States

In 2010, Dzero et. al predicted that samarium hexaboride (SmB_6) could exhibit a topological insulating phase [1]. At room temperature, SmB_6 is a metal with no bandgap. However, at temperatures below 10 K, a band gap forms due to the Kondo effect [3]. The Kondo effect can only be explained by electron-electron interactions and cannot be explained by band theory alone. It was proposed that a topological insulating phase can form along this bandgap creating a topological Kondo insulator. Verification of this, however, has proven difficult due to issues involving polarized surfaces and the small Kondo gap of only ~20meV that cannot be resolved by most ARPES measurements [3]. SmB_6 possesses properties that can be useful for spintronic applications.

Spin-polarized STS measurements have been reported suggesting spin momentum locking [2]. Strong spin-orbit-torque has also been shown by thin films of SmB_6 although the same study highlighted possible issues with a solely surface conduction picture [4].

This research focuses on the scalable synthesis of SmB_6 by chemical vapor deposition (CVD) and electrochemically grown films. Most research has been done on bulk crystals grown through Al-based flux or float zone methods [3]. Thin films of 50-500nm have also been grown using magnetron sputtering [4].

Recently, CVD-grown nanostructures were developed which consisted of single crystal rectangular rods roughly a few hundred nanometers thick [5].

We report the CVD growth and optical, structural, and electrical characterization of thin film SmB_6 on silicon and the recreation of previously reported nanostructures. Thorough Raman and XPS analysis of SmB_6 with and without various impurities have not been reported in-depth, which could prove useful as surface termination can greatly affect measurements to determine topological nature. Additionally, the possible effects of grain boundaries in thin films of SmB_6 have been largely ignored [4]. While grain boundaries shouldn't affect the topological phase assuming they are larger than a characteristic length, they can still have an effect on the local electronic structure thus affecting transport properties. These growth properties will also be controlled by CVD to be studied along with their effect on Raman spectra and low-temperature transport.

After measurements of the thin films, devices are patterned using traditional lithography. A focus will be on making non-local spin valves to measure the spin transport properties of the film and its performance in spintronic applications. Additionally, heterostructures with graphene and various ferromagnetic materials can be fabricated and studied.

[1] Dzero, M., Sun, K., Galitski, V., & Coleman, P. (2010). Topological kondo insulators. Physical Review Letters, 104(10), 106408–106408.
[2] Aishwarya, A., Cai, Z., Raghavan, A., Romanelli, M., Wang, X., Li, X., Gu, G. D., Hirsbrunner, M., Hughes, T., Liu, F., Jiao, L., & Madhavan, V. (2022). Spin-selective tunneling from nanowires of the candidate topological kondo insulator smb6. Science, 377(6611), 1218–1222.
[3] Li, L., Sun, K., Kurdak, C., Allen, J. W., & Univ. of Michigan, Ann Arbor, MI (United States). (2020). Emergent mystery in the kondo insulator samarium hexaboride. Nature Reviews Physics, 2(9).
[4] Li, Y., Ma, Q., Huang, S. X., & Chien, C. L. (2018). Thin films of topological kondo insulator candidate smb6: strong spin-orbit torque without exclusive surface conduction. Science Advances, 4(1), 8294.
[5] Gan, H., Zhang, T., Xu, N., Deng, S., Liu, F., Ye, B., & He, H. (2019). A controllable solid-source cvd route to prepare topological kondo insulator smb6 nanobelt and nanowire arrays with high activation energy. Crystal Growth and Design, 19(2), 845–853.

10:40 AM GG07

(Student) Quasi van der Waals Epitaxy of Magnetic Topological Insulator on a GaAs (111) Substrate Yuxing Ren, Lixuan Tai, Yaochen Li and Kang-Lung Wang; University of California, Los Angeles, United States

Magnetic topological insulator could achieve quantum anomalous Hall (QAH) effect and spin-orbit torque (SOT) switching in the same structure. This is promising for its future applications in memory or switching applications with its robust surface properties by topological protection. In this work we have grown Cr:(BixSb1-x)2Te3 and MnBi2Te4 on GaAs (111) substrate through modulation doping by MBE (Molecular Beam Epitaxy). The doping level and the thickness of each layer is examined to tune the bandgap and the Fermi level of the whole sample. In this way, we can tune the Fermi level into the bandgap and optimize the total resistivity to achieve quantization. Considering the van der Waals nature of the epitaxial layers, it has very weak van der Waals bonding with the substrate. This gives rise to

a quasi Van der Waals epitaxial growth mode at the interface of GaAs (111) and epitaxial layers. In this growth mode strain relaxes quickly within the 1st epitaxial layer. Growth mechanism and the influence on its transport properties are also discussed.

11:00 AM GG08
(Student) Electrical and Optical Properties of Sputtered SnTe Tri Nguyen, Leland J. Nordin and Kunal Mukherjee; Stanford University, United States

Tin Telluride (SnTe), a rocksalt-structured IV-VI narrow-bandgap semiconductor (E_g = 0.18 eV at 300K), is a promising candidate to engineer the optical space in epitaxial mid-infrared optoelectronics [1,2]. Since SnTe is always unintentionally Sn-deficient [3], a native defect, SnTe films are always heavily doped, specifically degenerate p-type semiconductor with hole concentrations on the order of 10^{20} – 10^{21} cm^{-3}. Such a high concentration of holes leads to high free carrier reflectivity of SnTe in the mid-infrared wavelengths [1,4]. SnTe also undergoes a cubic-rhombohedral ferroelectric transition at cryogenic temperatures (T_c < 90K), although the Curie temperature is raised significantly in few atomic layer thick SnTe [5]. We aim to harness these unique properties of SnTe towards integrated tunable epitaxial mirrors with applications in imaging and sensing.
We prepare thin films of SnTe (60-290 nm) via radio frequency (RF) sputtering on silicon for this initial investigation, as it is unclear to what extent UHV-based growth is necessary for such heavily doped samples. Structural analysis of SnTe films using high-resolution x-ray diffractometry shows that the films are polycrystalline across a wide range of growth parameters despite in-situ and ex-situ Si native oxide removal. Atomic force microscopy (AFM) measurements indicate that the global root mean squared (RMS) surface roughness is on the order of a few nanometers. Nevertheless, we find some degree of control over native defect induced doping and obtain Hall mobilities only slightly worse than those reported for single-crystalline bulk samples at these very high doping levels. Optical measurements of sputtered SnTe thin films confirm their high reflectance in the mid-infrared and we will present a systematic study of this property across our samples. In summary, we find promise for SnTe in integrated and tunable reflectors for active mid-infrared optoelectronic devices with future work geared towards to achieving epitaxial films and thickness control down to the few atomic layer limit.
References
1. J. N. Zemel et al. *Phys. Rev.*140 (1965)
2. R. B. Schoolar and J. R. Dixon. *J. Opt. Soc. Am.* 58 (1968)
3. N. Wang et al. *Phys. Rev. B* 89 (2014)
4. R. F. Bis and J. R. Dixon. *Phys. Rev. B* 1004 (1970)
5. K. Chang et al. *Science* 353 (2016)

11:20 AM GG09
(Student) Self-Limiting Formation of Bismuth-Induced Nanostructures on the InSb(111) Surface Rohit Yadav, Yi Liu, Sandra Benter, Yen-Po Liu, Austin Irish and Rainer Timm; Lund University, Sweden

Bismuth (Bi)-containing III-V semiconductor materials are attracting considerable interest due to their predicted non-trivial topological surface states and band inversion. These topological surface states (TSSs) have their spin locked with orbital momentum because of large spin-orbit coupling, presenting the high charge to spin conversion efficiency and application in spintronics. [1, 2] Previously, either Bi1-xSbx bulk growth was studied, [3] which is hampered by low Bi incorporation, or the focus was set on the growth of metallic Bi films on top of semiconductor substrates, [4] without highlighting the Bi-substrate interaction. However, it is vital to experimentally investigate the Bi-semiconductor interface and the potential formation of Bi-induced topological surface states, not just for spintronics application but also from the fundamental physics point of view.
Here, we investigate the incorporation of Bi atoms into the semiconductor surface, thus increasing the local Bi content in the semiconductor and forming atomic-scale heterostructures in a controlled way. We will present multiple steps of Bi incorporation in the InSb(111)B surface using a combined study of scanning tunneling microscopy (STM), X-ray photoemission spectroscopy (XPS), and low energy electron diffraction (LEED). After cleaning the InSb(111)B surface from native oxide using atomic hydrogen, STM shows a 3X3 reconstruction, in agreement with previous studies. [5] We observe that Bi incorporation on a heated InSb(111)B substrate (Ts=250 C) initiates by forming a buckled triangular atomic arrangement. XPS of the Bi 5d core-level shows that Bi interacts with Sb by forming Bi-Sb bonds. Interestingly, the incorporation is self-limiting, i.e., the amount of Bi in a Bi-Sb configuration remains unchanged irrespective of deposition cycles for the heated sample. Further deposition of Bi at room temperature (RT) instead results in multi-layer thick Sierpinski-type defective triangles [6] comprising mainly metallic Bi.
However, the Bi incorporation under the before-mentioned conditions occurs predominantly at random sites on the surface, hindering the formation of a large-scale symmetric surface layer. However, when Bi was deposited at RT, followed by an annealing step at 250 C for 15 minutes, a periodic (2X2) reconstructed surface was observed. XPS indicates that also this ordered 2X2 surface is characterized by Sb-Bi bonding, similar to the chemical state of the surface that results from Bi deposition at Ts=250 C (as mentioned above). Similar 2X2 reconstruction can be obtained if the sample is annealed (at Ts= 250 C) in-between any Bi deposition conditions. That shows that Bi bonded to Sb tends to stabilize in a 2X2 periodic surface structure of self-limiting bonding configuration. In summary, we present the formation of a controllable and ordered, atomically thin Bi-Sb layer on InSb which is highly promising for realizing 2D topological insulators on III-V semiconductor substrates.
References:
[1] S. Fragkos et al., Phys. Rev. Materials 5, 014203 (2021)
[2] T. Campos et al., Phys. Rev. B 97, 245402 (2018)
[3] D. Hsieh et al., Nature 452, 970 (2008)
[4] Z. Liu, et al., Phys. Rev. Lett. 107, 136805 (2011)
[5] J. Wever et al., Surf. Sci., 321, L225 (1994)
[6] C. Liu et al., Phys. Rev. Lett., 126, 176102 (2021)

11:40 AM GG10
(Student) Magnetotransport Studies of Two-Dimensional Cd_3As_2 Heterostructures Binghao Guo, Alexander Lygo and Susanne Stemmer; University of California, Santa Barbara, United States

Topological semimetals are defined by characteristic, linear band crossings at the Fermi level, around which their electronic states can be described by the Weyl or the Dirac equations. A decade ago, cadmium arsenide (Cd_3As_2) was classified as a symmetry-protected, 3D Dirac semimetal, with two such crossing points along Γ−Z [1]. Cd_3As_2 is also of particular interest because of its stability and its high intrinsic carrier mobility [2]. Here, we use the high mobilities to our advantage (typical μ_H ~25 × 10^3 cm^2/Vs at 2 K) and report on electronic transport studies of a controlled thickness series of (001) Cd_3As_2 films, grown by molecular beam epitaxy (MBE), under out-of-plane and in-plane magnetic fields. In these quantum-confined Cd_3As_2 films (13 nm to 22 nm), the relative positions of Γ point subband energies are expected to evolve with layer thickness. Consequently, thickness controls the occurrence of subband inversion that determines non-trivial electronic structure topology [1]. To understand the low-energy band structure in thin films, we developed a gate-tunable (001) Cd_3As_2 heterostructure that allows access to the states around the charge neutrality point. In the first study on a 20 nm Cd_3As_2 film [3], we observed a prominent ν = 0 quantum Hall state that is fully developed at ~6 T, but with a zero conductance plateau that continues to broaden with increasing out-of-plane magnetic field. The highly insulating ν = 0 region is attributed to a widening energy gap between two zeroth Landau levels that disperse with magnetic field. Furthermore, for higher mobility Cd_3As_2 of the same thickness, grown on closely lattice-matched III-antimonide buffer layers ($Al_xIn_{1-x}Sb$), we resolve a characteristic crossing of the two zeroth Landau levels at a critical magnetic field, which is indicative of an ideal two-

dimensional topological insulator (2D TI) [4]. Increasing the film thickness raises the critical magnetic field, following a similar trend as earlier works on HgTe/HgCdTe quantum wells. In even thinner films (13 nm), normal band ordering is restored, and the result is a trivial band insulator. Lastly, directing an external magnetic field in the film plane provides another level of control over the topological phase, with preliminary results suggesting a field-driven transition from a 2D TI state to a semimetallic state. Additionally, the in-plane magnetic field can be used study the complex evolution of helical edge states under broken time-reversal symmetry. In summary, our results aim to establish epitaxial (001) Cd_3As_2 thin films as a material platform for realizing tunable topological states, which now includes the 2D TI.

[1] Z. Wang, H. Weng, … Z. Fang, Phys. Rev. B 88, 125427 (2013)
[2] A. J. Rosenberg, T. C. Harman, J. Appl. Phys. 30, 1621 (1959)
[3] B. Guo, A. C. Lygo, … S. Stemmer, APL Mater. 10, 091116 (2022)
[4] A. C. Lygo, B. Guo, … S. Stemmer, Phys. Rev. Lett. 130, 046201 (2023)

We acknowledge support from the Air Force Office of Scientific Research (Grant No. FA9550-21-1-0180), the Graduate Research Fellowship Program of the National Science Foundation (NSF) (Grant No. 2139319), the UCSB Quantum Foundry, which is funded via the NSF Q-AMASE-i program (Grant No. DMR-1906325), and the MRL Shared Experimental Facilities, which is funded by the NSF MRSEC Program (Award No. DMR 1720256).

SESSION HH: Materials Processing and Integration
Session Chair: Robert C Roberts
Friday Morning, June 30, 2023
UC, State Street

8:20 AM HH01
(Student) Fabrication of SU-8 Microstructures on Bulk Molybdenum Substrates for Cryogenic Applications Archit Shah[1], Bhargav Yelamanchili[1], Sherman Peek[1], Vaibhav Gupta[1], David B. Tuckerman[2], John Sellers[1] and Michael Hamilton[1]; [1]Auburn University, United States; [2]Tuckerman & Associates, United States

SU-8 is widely used in a variety of applications for fabricating micro-scale or millimeter-scale structures due to its high viscosity, high optical transmission in the UV range, and excellent mechanical properties. The use of SU-8 for cryogenic applications has been limited because of possible internal stress in SU-8 films due to CTE mismatch with Si, the most commonly used material as a substrate, which can cause adhesion-related problems. We have developed a fabrication process of micro-scale SU-8 structures on a molybdenum (Mo) substrate using polyimide as an interfacial layer. Fabricated SU-8 structures showed good adhesion to the substrate from room temperature to cryogenic temperatures down to 4.2 K. Mo was chosen as a substrate due to its robustness, excellent mechanical strength, and compatibility with laser and CNC machining.
SU-8 fabrication was done on 500-micron thick commercially available Mo wafers. The wafers were cleaned using an H_2O_2/H_2SO_4 "piranha" solution to remove organic material from the substrate. Atomic force microscopy (AFM) and scanning electron microscopy (SEM) was done before and after cleaning. SU-8 2075 was used to fabricate 250-micron tall structures with different aspect ratios on the Mo substrate. HD-4100 series polyimide was evaluated as an interfacial layer to improve the adhesion of SU-8 to Mo. Thermal shock tests were done using LN_2 to test the adhesion of SU-8 with and without the interfacial layer. Shear tests were performed to characterize the adhesion of the SU-8 pillars to the substrate.
The Mo wafers were laser-cut using a femtosecond laser to singulate them into pieces with SU-8 structures. These pieces were used as part of a superconducting interconnection scheme for multi-channel DC superconducting flexible cables, wherein the SU-8 structures provided self-alignment and distributed mechanical pressure over the contact area of the flexible cables. This interconnect scheme was demonstrated to be functional over multiple thermal cycles from room temperature to 4.2 K. The results of these experiments provide guidelines and motivation for using SU-8 with a polyimide interfacial layer in cryogenic system applications.
Acknowledgment: We gratefully acknowledge funding and technical guidance from Microsoft for this work. We thank the Alabama Micro/Nano Science and Technology Center (AMNSTC) for providing access to fabrication and characterization facilities used in this work.<gwmw style="display:none;"></gwmw>

8:40 AM HH02
Growth of Patterned Diamond Using High Seeding Density and Hot-Filament Chemical Vapor Deposition (HFCVD) Florence A. Nugera[1], Dipa Devkota[2,1], Anupam KC[1], Anival Ayala[2], Ganesh Aryal[2], Chris Engdahl[3], Edwin L. Piner[1,2] and Mark W. Holtz[1,2]; [1]Texas State University, United States; [2]Materials Science, Engineering, and Commercialization Program, Texas State University, United States; [3]Crystallume Inc., United States

A bottom-up method is reported to grow patterned diamond using polymer-assisted high seeding and standard contact photolithography. The pattern consists of features extending from millimeters to microns in size. The high seeding densities achieved range between 1.5×10^{11} and 1.5×10^{12} cm^{-2} for all samples studied here. A systematic study is carried out on the effects of CH_4 concentration on the growth of patterned diamond using hot-filament chemical vapor deposition (HFCVD). CH_4 concentrations studied are 1.5, 2.0, 2.5, and 3.0 % in H_2. The study focuses on the early growth regime, including coalescence, following 30 min, 45 min and 2 h of HFCVD process times. Scanning electron microscopy (SEM) and atomic force microscopy (AFM) measurements are used to study thickness, growth rate, grain size, and grain morphology of the polycrystalline diamond. The study compromise of 12 samples at different growth times (30 min, 45 min and 2 h) at each CH_4 concentrations (1.5%, 2%, 2.5 and 3%). Material quality is checked using micro-Raman spectroscopy including area images. Steady state thermoreflectance (SSTR) is used to investigate the thermal properties. The results show that higher concentration leads to improvements in the diamond properties, for this seeding, and some local variation in the growth rates within the pattern.

9:00 AM HH03
Experimental Characterization and Modification of Silicon Nitride Crystallization Reaction Kinetics for Microelectronics Applications Christopher Bishop, Jennie Podlevsky, Calvin Parkin, Khalid Hattar, Carlos Chacon, Paul Kotula, Andrea Rodarte, J. Matthew D. Lane, Tesia Janicki, Hojun Lim, Scott Grutzik, Aashique Rezwan, Edwin Chiu, Brian Homeijer, T.A. Friedmann and Paul Resnick; Sandia National Laboratories, United States

Anomalous silicon nitride (SiN) crystallization in the presence of phosphorous dopants and other surface imperfections is a recurring yield-limiting material defect in microelectronics fabrication, impacting device development. Understanding of fundamental physical mechanisms for this SiN phase formation is lacking, resulting in tailored process flows using workarounds to suppress defects. In this work, we aim to form the building blocks necessary to unravel the fundamental physical mechanisms of this phenomenon by experimentally determining SiN crystallization nucleation and growth kinetics in various processing conditions, ultimately leading to more reliable device designs. Furthermore, we aim to use this understanding to unlock new material properties by tailoring reaction kinetics of SiN crystallization in favorable ways for microelectronics development. For example, understanding these mechanisms could enable the ability to strategically fabricate different crystalline phases of SiN at temperatures compatible with microelectronics processing, unlocking a suite of material properties not previously accessible.
We fabricate SiN films in common microelectronics film stacks on

silicon using low pressure chemical vapor deposition (LPCVD) and perform multiple experiments aimed at characterizing the crystallization behavior as a function of temperature, dopant profiles, and local stress perturbations at film interfaces. Experiments primarily focus on thermal cycling from 1000°C to 1150°C coupled with image processing to determine the percent amorphous phase versus time and temperature, from which Arrhenius constants are calculated and reported. Other experiments, such as laser heating and intentional surface imperfections from heavy ion irradiation are discussed. Crystallization and dopant diffusion profiles are characterized using SEM and TEM imaging with selected area diffraction pattern analysis and automated crystal orientation mapping (ACOM). These experiments result in (1) calculations of the nucleation and growth kinetics of crystalline SiN with determined values for activation energies and rate constants; (2) structural analysis of crystallized SiN films showing a nearly single crystal α-Si_3N_4 structure along with insight into nucleation physics and dopant diffusion in the crystallized material; (3) demonstration of crystallization behavior as a function of various film modifications aimed at intentionally raising/lowering nucleation/growth activation barrier heights, showing methods of engineering the films for microelectronics processing applications; and (4) initial quantitative inputs for future atomistic, meso, and continuum scale modeling of the SiN crystallization phenomena. Sandia National Laboratories is a multimission laboratory managed and operated by National Technology & Engineering Solutions of Sandia, LLC, a wholly owned subsidiary of Honeywell International Inc., for the U.S. Department of Energy's National Nuclear Security Administration under contract DE-NA0003525.

9:20 AM HH04
Investigation of Bonded GaN-Si p-n Junction Interface Properties
Eric Blanton[1,2], Nicholas R. Glavin[3] and Michael Snure[1]; [1]Sensors Directorate, AFRL, United States; [2]KBR Inc, United States; [3]Materials and Manufacturing Directorate, AFRL, United States

The need for higher power RF and energy conversion electronics has motivated the search for new device heterojunctions beyond what can be grown using conventional techniques. Instead, we can conceive of new material layer combinations that result in higher performance transport characteristics, e.g., channel conductivity, breakdown voltage, and heat dissipation. However, realizing a high-quality bonded interface has several challenges including the production and processing of low-defect thin material layers and reducing the interface trap density. Here, we have fabricated bonded n^--GaN/p^+-Si diodes to investigate the dependence of interface quality on surface pretreatments and post-bond annealing. Si-doped GaN films were grown on BN-sapphire templates [1] before being exfoliated using stressed Ni-spalling [2]. The GaN films were bonded top (Ga-polar)-side down onto (100) P-doped Si. IV and CV measurements were performed to characterize the transport across and the charge at the interface. Conducting scanning probe measurements were performed on the GaN surface to characterize the bond areal uniformity. These results are generally applicable to the optimization of interface properties for novel bonded junctions.
[1] M. Snure, G. Siegel, D. C. Look, and Q. Paduano, *J. Cryst. Growth* **464**, 168 (2017).
[2] E. W. Blanton, M. J. Motala, T. A. Prusnick, A. Hilton, J. L. Brown, A. Bhattacharyya, S. Krishnamoorthy, K. Leedy, N. R. Glavin, and M. Snure, *Small* **17**, 2102668 (2021).

9:40 AM HH05
(Student) Thin-Film Layer Transfer of 128° Y-Cut $LiNbO_3$ on (0001) Al_2O_3 Through Ion Implantation and Exfoliation
Lezli Matto, Michael E. Liao, Kenny Huynh, Patricia Barron, Kaicheng Pan and Mark Goorsky; University of California, Los Angeles, United States

Successful direct wafer bonding and thin film layer transfer of 128° Y-cut (01$\underline{1}$4) $LiNbO_3$ on to (0001) sapphire (Al_2O_3) substrates was achieved through He^+ ion implantation with a dose of 2.3×10^{16} cm^{-2} and 250 keV ion energy. While there have been some reports of using implantation-induced exfoliation of $LiNbO_3$ to oxidized silicon wafers, neither the transfer of this orientation nor transfer to sapphire has been reported. The $LiNbO_3$ substrates were implanted with He^+ prior to bonding. Both the $LiNbO_3$ and sapphire substrates were cleaned using standard cleaning procedures prior to bonding. The wafers were then brought face-to-face and bonded using an applied pressure of only a few ~kPa. The bonded structure was then annealed at 200° C for 10 h. During annealing, a ~850 nm layer of $LiNbO_3$ (matching the projected range of the 250 keV implant energy) transferred to the Al_2O_3 substrate. Subsequent chemical mechanical polishing (CMP) was performed in order to reduce the surface r.m.s. roughness of the transferred layer from 8.3 nm to 0.5 nm. Different polishing parameters were tested in order to achieve sub nanometer roughness and remove the lattice damage associated with the implantation. Triple axis x-ray rocking curves show FWHM of 59" for a polishing pressure of 1 kPa, comparable to commercially available thin film samples. The results presented in this work are leading towards the fabrication of multilayer complementary oriented thin $LiNbO_3$ layers on Al_2O_3, as opposed to layers obtained through grinding and polishing of full wafers where polishing damage is commonly observed, and the thin film layers are not uniform in those cases whereas the exfoliated layers are uniform. The appealing electromechanical properties of thin $LiNbO_3$ layers on sapphire make it a promising candidate for achieving novel high piezoelectric and low loss 50 GHz surface acoustic wave devices [1]. We also note that this process has been reproduced for $LiNbO_3$ on oxidized silicon wafers, demonstrating that our process can be applied to that material combination, which is a top candidate for photonic integrated circuits and quantum sensing applications.
References: [1] R. Lu, et al., J. Microelectro. Systems, 29(3), 313 (2020).

10:00 AM BREAK

10:20 AM HH06
(Student) Realization of Vapor-Phase MacEtch: Mechanism, Programmability and Scalability
Lukas L. Janavicius[1], Julian A. M[1], Clarence Y. Chan[1], Dane J. Sievers[1] and Xiuling Li[1,2]; [1]University of Illinois, United States; [2]The University of Texas at Austin, United States

Defying the isotropic nature of the conventional chemical etch, metal-assisted chemical etching (MacEtch) has allowed spatially defined anisotropic etching by using patterned metal catalyst films to locally enhance the etch rate of various semiconductors [1]. Significant progress has been made on achieving unprecedented aspect ratio nanostructures using this facile approach, mostly in solution. However, the path to manufacturing scalability remains challenging, because of the difficulties in controlling etch morphology including the minimization of porosity and aggregation, and etching uniformity. Taking MacEtch from liquid phase to vapor phase completely will eliminate surface tension, allow independent control of the partial pressure, injection timing and pattern of each etchant, while preventing the movement of the metal-catalyst films. Prior demonstrations of VP-MacEtch utilize thermally generated vapor by suspending the sample over a heated bath of either HF/H_2O_2 or HF with atmospheric O_2 as the oxidant [2-4]. However, the presence of H_2O_2 in the vaporized solution serves to increase porosity with little impact on the etch rate compared to ambient oxygen [2,4]. The use of O_2 as the oxidant limits the range of etching control, as the molar ratio may only be controlled through the dilution of HF. This approach leads to etch rates substantially lower (0.1-0.4 µm/min [1-3]) compared to the liquid phase (>3 µm/min [5]). Although increasing the concentration of HF does improve the etch rate, because of the fixed oxidant supply as the vapor flows across the sample the O_2 becomes depleted leading to non-uniform etching and failure in pattern transfer.
Here, we demonstrate a programmable vapor-phase MacEtch (VP-MacEtch) approach, with independent control of the etchant flow

rates, injection and pulse time, chamber pressure and temperature, as well as UV irradiation. Silicon (Si) nanostructures are demonstrated with each of these parameters systematically varied synchronously or asynchronously, moving MacEtch closer to a manufacturing technique for versatile arrays of 3D Si micro and nanostructures.[6] Figure 1 presents a fully computer-controlled programmable VP-MacEtch system that operates under vacuum with an N_2 carrier gas and representative structures produced, with unprecedented features.
This work was supported in part by United States Army Research Office Award No. W911NF2110337 , National Science Foundation ECCS #2200651, and a gift from Lam Research.
[1] X. Li and P.W. Bohn, "Metal-assisted chemical etching in HF/H2O2 produces porous silicon," ***Appl. Phys. Lett.***, 77, 2572 (2000).
[2] Hildreth, O. J., & Schmidt, D. R. (2014). Vapor Phase Metal-Assisted Chemical Etching of Silicon. Advanced Functional Materials, 24(24), 3827–3833.
[3] Kim, J. D., Kim, M., Chan, C., Draeger, N., Coleman, J. J., & Li, X. (2019). CMOS-Compatible Catalyst for MacEtch: Titanium Nitride-Assisted Chemical Etching in Vapor phase for High Aspect Ratio Silicon Nanostructures. ACS Applied Materials and Interfaces, 11(30), 27371–27377.
[4] Romano, L., Kagias, M., Vila-Comamala, J., Jefimovs, K., Tseng, L. T., Guzenko, V. A., & Stampanoni, M. (2020). Metal assisted chemical etching of silicon in the gas phase: A nanofabrication platform for X-ray optics. Nanoscale Horizons, 5(5), 869–879.
[5] Balasundaram, K., Sadhu, J. S., Shin, J. C., Azeredo, B., Chanda, D., Malik, M., Hsu, K., Rogers, J. A., Ferreira, P., Sinha, S., & Li, X. (2012). Porosity control in metal-assisted chemical etching of degenerately doped silicon nanowires. Nanotechnology, 23(30), 305304.
[6] Janavicius, L. L, Michaels, J. A, Chan, C., Sievers, D. J, Li, X. (2023). "Programmable Vapor-Phase Metal-Assisted Chemical Etching for Versatile High-Aspect Ratio Silicon Nanomanufacturing," Apph. Phys. Rev. **accepted.**

10:40 AM HH07
(Late News) Substrate-Removed GaAs Photovoltaic Cells for Microscale Energy Harvesting Abhilasha Kamboj[1], Bhavika Mani[1], Jungho Lee[2], Eunseong Moon[2], David Blaauw[2] and Jamie Phillips[1]; [1]The University of Delaware, United States; [2]University of Michigan–Ann Arbor, United States

Wireless interconnected devices have become ubiquitous, with many transformative applications emerging as sensor nodes that scale to smaller dimensions and higher node density. Energy harvesting for sensor systems at the millimeter-scale and microscale has become paramount, where functionality and system lifetime is determined by available power. Energy can be harvested through optical, radio-frequency, mechanical, piezo, thermoelectric and many diverse means [1]. Optical energy harvesting via photovoltaic cells scales efficiently down to the microscale, including sources from outdoor sunlight, indoor lighting, and near-infrared illumination (NIR ~ 850 nm, particularly for biomedical implantable sensors[2]). GaAs/AlAs photovoltaics (PV) provide high power conversion efficiencies for these sources across a broad range of optical spectra Furthermore, GaAs-based PV provides a platform for integrated optoelectronic devices that can be used for low-power optical communications. In this work, we present thin (<8 µm) GaAs PV cells for energy harvesting in microscale systems and heterogeneous integration approaches with low-power CMOS electronics.
The PV cell structures consist of a single or dual-junction devices that were grown epitaxially by external foundries. Single junction devices are designed for optical response ranging from outdoor sunlight to 850 nm monochromatic illumination, where lateral series-connected devices may be fabricated to step up voltage output for energy harvesting. Dual junction "segmented" PV devices are designed for monochromatic illumination at 850 nm with target applications for bio-implantable systems. Devices were fabricated using previously established etching, photolithography, and metallization technologies. SiN_x passivation layers are used on mesa devices, which also serve as electrical isolation for bonding pads metal interconnects. Fabricated devices are mounted epi-side down on glass substrates for substrate removal using wet chemical etching facilitated by an InGaP etch stop layer. A substrate transfer process is used to flip substrates to a sapphire substrate for device testing or flip chip bonding to silicon CMOS. Single junction and dual-junction PV devices show power density on the order of 1 µW/mm^2 under mild 850 nm irradiation with an efficiency >20 %. Experiments using substrate removal utilized a new dual-junction epitaxial growth run where devices exhibited a diode blocking behavior attributed to an improper tunnel junction. Nevertheless, substrate removed devices exhibit power generation and integrity of electrical behavior for both frontside and substrate removed backside illumination. Further progress on substrate removed microscale PV harvesters and flip-chip bonding for device integration will be presented.
The authors gratefully acknowledge the National Science Foundation award CBET-2129817 and the National Institute of Health award 1RF1NS128667.
J. D. Phillips, *Frontiers in Nanotechnology*, *3*, 633931, 2021
E. Moon et al, … J. D.Phillips, *ACS Photonics* 8, no. 5 (2021)

11:00 AM HH08
(Late News) Anionic Engineering and 3D Integration of 2D $Ti_3C_2T_x$ MXene for Electrocatalysis and Energy Storage William J. Scheideler, Anand P. Tiwari and Julia E. Huddy; Dartmouth College, United States

2D-layered metal-carbide MXenes have emerged as promising earth-abundant materials for electrocatalysis and energy storage due to their exceptional combination of high conductivity and high surface area. Large scale synthesis of MXenes offers the potential for low-cost device applications, but this goal demands integration with advanced manufacturing approaches such as 3D printing and methods for tuning MXenes' electrical properties. Here we present two complementary strategies to address these practical limitations of MXenes.
The low chemical activity of pristine MXenes such as $Ti_3C_2T_x$, and limited active site density inhibit MXenes as practical electrocatalysts for hydrogen evolution reaction (HER). We present a simple and scalable nitrosulfurization method for overcoming these limitations via interfacial doping and structural modification with nonmetallic electron donors (N and S) by heat treatment of 2D titanium carbide ($Ti_3C_2T_x$) MXene with thiourea. XPS measurements show substitution of N and S occurs at the basal plane with controllable compositions ranging from 2 - 4 at. % (Sulfur), and 5-15 at. % (Nitrogen) depending on the thermal annealing conditions. HRTEM, SEM, and AFM characterization illustrate simultaneous structural changes from planar nanosheets to hexagonal-nanoplate-decorated nanosheets. XRD reveals increased interlayer spacing after N,S doping, which is expected to increase the diffusivity of electrolytes into the layers and enhance electrocatalytic activity. The optimally N,S doped $Ti_3C_2T_x$ MXene exhibits a high concentration of Ti-S and Ti-N bonds , yielding a low overpotential of –260 mV and a Tafel slope of 85 mV/dec at a current density of 10 mA/cm^2 in 0.5 M H_2SO_4—3X lower than pristine $Ti_3C_2T_x$. This strategy to improve electrocatalytic activity of $Ti_3C_2T_x$ MXene for hydrogen evolution could open the possibility for manipulating the electrocatalytic performance of a broad range of MXenes.
Finally, towards the goal of facilitating device integration of MXenes, we have developed MXene coatings that, when applied on 3D printed conductive lattices, can significantly enhance the specific capacity of microscale porous carbon supercapacitor electrodes. Electrochemical impedance spectroscopy illustrates the capacity for these 3D MXene structures to offer high areal capacitance will delivering low electrode resistance for fast charging and discharge. Mechanical measurements of these electrodes show that integration of 2D MXenes with 3D lattices provides a means for enhancing the electrochemical performance while precisely controlling mass and device geometry.

11:20 AM HH09
(Student, Late News) Development of Sustainable Non-Toxic TiO_2/Sb_2Se_3 Solar Cells for Renewable Energy Applications Bailey Garfield; University of the District of Columbia, United States

The urgent need for high-efficiency, low-cost, and environmentally friendly solar cell technology compels new research into innovative solar materials that are stable, earth-abundant, and benign for the development of sustainable thin-film photovoltaics (PVs). Antimony selenide (Sb_2Se_3) is one such solar-absorbing material that has recently emerged as a promising alternative to CdTe (cadmium telluride) solar cells. CdTe solar cells represent the second-largest PV technology on the market, but contain toxic compounds that have been demonstrated to leach toxins into the soil and water table when left to decompose in landfills.
In moderate quantities, the constituent components of Sb_2Se_3 are inexpensive to source and are non-toxic to humans and the ecosystem [2-3]. Similar to CdTe, Sb_2Se_3 is a simple binary compound with just one stable phase and stoichiometry – unlike the multivalent copper selenide (CuSe) or tin selenide (SnSe) binary systems. Sb_2Se_3 exhibits a direct bandgap of 1.1-1.3eV, which approaches the ideal Shockey-Queisser value for single-junction solar cells and demonstrates efficient light harvesting with an absorption coefficient of $10^5 cm^{-1}$ in the near-infrared region below about 1000 nm. The >30% theoretical efficiency of Sb_2Se_3 cells suggests a comparable efficiency to existing CIGS and CdTe solar cells.
Other research shows the efficiency of Sb_2Se_3 thin-film solar cells has improved from 0.66% in 2009 (Nair et al) to 6.6% and 7.6% in 2018 by improving the crystallinity of Sb_2Se_3 films (Choi et al, Zhou et al). In 2019, the implementation of a one-dimensional (1D) crystal structure improved construction of Sb_2Se_3 solar cells and resulted in an efficiency of 9.2%. However, these Sb_2Se_3 solar cells typically use CdS as a n-type partner and therefore are not environmentally friendly due to the toxicity of cadmium.
For this reason, we developed and implemented a titanium dioxide (TiO_2) n-type partner for the Sb_2Se_3 solar cells. This paper explores the process of spin-coating fabrication for TiO_2 as an n-type partner using three different solutions on FTO-coated soda-lime glass substrates, the deposition of Sb_2Se_3 for the absorption layer, and nickel deposition by thermal evaporation to construct the complete solar cell. In addition to fabrication processes, we conducted optical-electrical and materials characterization of these TiO_2/Sb_2Se_3 cells to determine their efficiency and investigate their effects on the solar cell performance.

11:40 AM HH10
(Student, Late News) Probing Nonstoichiometry and Local Atomic Environments in $GaAs_{1-x-y}N_xBi_y$ Alloys Jared Mitchell[1], Christian Greenhill[1], Tao-Yu Huang[1], Kyle Hammond[1], Timothy Jen[1], Alexander Chang[2] and Rachel S. Goldman[1]; [1]University of Michigan, United States; [2]Northwestern University, United States

Due to the significant bandgap narrowing induced by incorporation of dilute fractions of N and Bi, dilute nitride-bismide alloys are of interest for optoelectronic devices operating in the near- to mid-infrared range. Bi incorporation into $GaAs_{1-x-y}N_xBi_y$ alloys during molecular-beam epitaxy requires low substrate temperatures, which also promote the incorporation of excess As. This work aims to quantify the nonstoichiometry related to these excess As defects and to assess the influence it has on the solute distribution and optical properties in $GaAs_{1-x-y}N_xBi_y$ alloys. We investigated the stoichiometry and spatial distribution of N and Bi solute atoms in MBE-grown $GaAs_{1-x-y}N_xBi_y$ films using a combination of atom probe tomography (APT), high-resolution x-ray diffraction (XRD), and ion beam analysis. We determined optimal APT parameters to obtain nearly stoichiometric compositions for GaAs, which can be generalized broadly to other III-As-based alloys, including those expected to incur non-stoichiometries. Both APT and XRD reveal an increase in the excess As concentration with decreasing growth temperature in low-temperature grown GaAs layers. By calibrating the APT measurements to the XRD results for GaAs, excess As content in $GaAs_{1-x-y}N_xBi_y$ alloys was also quantified and shown to increase with decreasing growth temperature. APT data also show an increase in the excess As concentration with Bi fraction up to $y_{Bi} = 0.044$ due to the surfactant behavior of Bi on the $GaAs_{1-x-y}N_xBi_y$ surface, beyond this Bi surface coverage outcompetes chemisorbed As for surface sites. Global measurements of N and Bi solute fractions agree with those from XRD and ion beam analysis and show a monotonic increase in Bi fraction with increasing Bi flux and a stable N fraction with increasing Bi flux below 1E-7 torr. A quantitative analysis of solute atom pair correlations suggests a random distribution of Bi ions. Using the structural data obtained from APT, we have shown that low photoconductivity lifetimes and mobilities observed in Thz pump-probe measurements of the $GaAs_{1-x-y}N_xBi_y$ alloys are correlated with the presence of excess As related defects.
*NSF-DMR#1810280

SESSION II: Flexible, Printed and Wearable Electronics and Sensors
Session Chairs: Shayla Sawyer and William Wong
Friday Morning, June 30, 2023
UC, Lobero

8:20 AM II01
3D Printable Polymer Matrix Synthesis with UV-Curable Polyurethane for Wearable Electronics Jung-Bin Ahn[1,2], Kyung-Seok Kang[3] and Soaram Kim[1,2]; [1]Texas A&M University, United States; [2]Center for Remote Health Technologies and Systems, United States; [3]Department of Chemistry and Biochemistry, United States

Organic polymers can be fabricated into various forms such as film, membranes, and fibers. By controlling the chemical structure of the polymers, the flexibility of the products can be easily achieved, ensuring the application of the polymers as a matrix for wearable electronics. A solidified polymer can be obtained through the coagulation of polymer solutions through a solvent exchange method, or by solidifying the melt polymer. However, this method is unsuitable to fabricate the purpose-oriented 3-D structured form. In this context, the 3-D printing technique for polymers is essential for wearable electronics. Fused deposition modeling type 3D printers are the most commonly accessible printing technology. Mostly, molten PLA is deposited on a plate layer by layer and solidified. It can be used at a low price but has a low surface resolution of the 3D printed sculpture. Due to this problem, digital light processing (DLP) type 3-D printing technology using photo-curing reaction by light irradiation to the resin, has been actively researched and developed.
Polyurethane (PU) is the representative elastic polymer. It is composed of hard and soft segments, which enables control of the mechanical properties of the product by changing the chain length of the soft segment, or the ratio of the hard and soft segments. In this work, acrylate-terminated PU (A-PU) was synthesized to utilize PU as a resin for DLP-type 3-D printer. The acrylate end group on the PU prepolymers allowed for photo-polymerization to be carried out.
A-PU was synthesized by the following steps (Fig. 1). 4,4`-methylenebis (phenyl isocyanate) (MDI) and poly (tetramethylene glycol) (PTMG1000) were used as diisocyanate and polyol, respectively, to fabricate the pre-polymer. After synthesizing the pre-polymer, 2-hydroxyethyl methacrylate (HEMA) was added and further reacted to obtain acrylate-terminated PU. The chemical structure of A-PU was measured and analyzed by NMR and FT-IR, as shown in Fig. 2-3. According to ^{1}H-NMR spectra, the urethane prepolymer composed of MDI and PTMG1000 was successfully synthesized (Fig. 2). The acrylate group by HEMA was also observed, meaning that HEMA successfully reacted to the end of the PU prepolymer. The chemical structure of the A-PU was confirmed again

by FT-IR spectra (Fig. 3).
The viscosity of the polymer is an important parameter for the application of 3-D printable resin. The viscosity of the resin should be low enough to induce a fast light-curing reaction. The apparent viscosity of A-PU was measured and shown in Fig. 4. The solution of A-PU dissolved in HEMA had low apparent viscosity, showing the possibility of being utilized as DLP resin. Fig. 5 shows the digital images of the A-PU cured by light irradiation. The A-PU/HEMA solution was fully cured within 7 min. The obtained A-PU object was further immersed in DMSO for 12 h. The cured A-PU maintained its shape without any crack, showing the successful photo-polymerization of the polymers.

8:40 AM II02
(Student) Characterization and Fabrication of 3D Inkjet Printed Flexible Copper Electrodes Annatoma Arif, Ryan M Price and Robert C Roberts; The University of Texas at El Paso, United States

In this research, multiple commercially available copper (Cu) nanoparticle conductive inks have been investigated, both as received and in modified form, for future flexible printed electronic device fabrication and its applications. This work reports the characterization and fabrication of the inkjet printed flexible Cu electrodes. Different fluid properties such as viscosity, surface tension, particle size measurement, and pH values were investigated along with their temperature dependance. Three commercial formulations, Ink 1: DM-CUI-5002 (Dycotec Materials Ltd. UK), Ink 2: Metalon® CI-004 (NovaCentrix, USA), Ink 3: Metalon® CI-005 (NovaCentrix, USA), and a fourth custom diluted version of the Dycotec ink (Ink 4) were investigated. The mean particle sizes of the different Cu nanoparticle inks are 56.2 nm for Ink 1/ Ink 4, 8.62 nm for Ink 2, and 11.5 nm for Ink 3. The viscosities at 25°C for Inks 1 through 4 are 17.14, 31.30, 13.52, and 15.02 cPs, respectively. The resistivity obtained for each nanoparticle ink (Ink 1-4) varied from 1.01× Ω/cm to 2.31× Ω/cm. Different fluid properties of the nanoparticle inks have been investigated and optimized for inkjet printing using Fujifilm Dimatix Materials Printer - DMP 2850. All the jetting recipes are developed based on both legacy printheads and recently launched (2021) Samba G3L printheads. This new printhead requires a lower ink viscosity which potentially renders all commercially available Cu inks unsuitable for use without modification. Hence, the optimized diluted Dycotec Cu ink has been modified with diethylene glycol monoethyl ether (5:1) to achieve the viscosity within the range of Samba G3L operating parameters.
Inkjet printing parameters varied based on different printheads and formulations of inks i.e. platen temperature for both printheads were chosen as 35°C, cartridge temperature varied from 40 - 50°C, jetting voltage ranged from 28 to 35 V, jetting frequency and meniscus set point for legacy and Samba printheads were chosen as 5 kHz and 0.5 as well as 3.5 kHz and 5 respectively. The drop spacing used for printing different patterns with both print heads and all the types of Cu inks was chosen as 15 mm (1693.3 DPI) to ensure 70% overlapping of the two adjacent ink droplets. Polyimide has been chosen as a printing substrate as it offers excellent adhesion characteristic, mechanical stability, and flexibility over a wide range of temperature i.e., -269 °C to 400 °C. The optimization of the sintering process has also been investigated thoroughly. The required temperature to sinter the printed Cu films was settled at 300-400 °C. To remove oxidation 3% hydrogen gas in 97% argon was flowed in the vacuum chamber with ~4 Torr.
Electrochemical impedance spectroscopy (EIS) measurement was performed for the inkjet printed Cu electrodes to evaluate their performance in terms of impedance. This process was performed using phosphate buffer saline with pH 7.43. The EIS was performed for two different designs (plain and interdigitated electrodes) for the chosen (based on their compatibility with Samba G3L printheads – DMP 2850) ink solutions (Ink 2 – plain: 575 Ω & interdigitated: 400 Ω and Ink 4 – plain: 418 Ω & interdigitated: 380 Ω).
Based on our experiments/investigation (fluid properties) and reported optimized inkjet printing parameters (waveforms, platen temperature, and cartridge temperature), this research indicates the potential viability of utilizing commercially available Cu ink – Ink 3 for printing flexible electronics with both legacy and newly commercialized Samba G3L printheads. However, Ink 4 showed excellent performance with the lowest impedance (resistivity and EIS) making it a promising formulation for flexible inkjet printed Cu electronics.
Honeywell Federal Manufacturing and Technologies, LLC operates the Kansas City National Security Campus for the United States Department of Energy / National Nuclear Security Administration under Contract Number DE-NA0002839.

9:00 AM II03
(Student, Late News) Carbon Based Omnidirectional Wearable Strain Sensor Arrays with Optimized Multi-Output Neural Networks Jee Young Kwak[1], Jun Ho Lee[1], Dong Hyuk Kim[1], Seong Hwan Yang[1], Su Jae Lee[2] and Sung Kyu Park[1]; [1]Chung-Ang University, Korea (the Republic of); [2]Electronics and Telecommunications Research Institute, Korea (the Republic of)

Recently, stretchable strain sensor is considered as the promising technology for various application, such as wearable electronics, healthcare monitoring, and robotic skin/arms, due to its mechanical stretchability and multi-axial sensing capabilities. The recent research for stretchable strain sensors have made tremendous efforts to significantly improve key deterministic parameters, including sensitivity, durability, sensing range, and response time. Although various high-performance strain sensors have been demonstrated using a range of mechanistic device structures, most conventional strain sensors are only capable of detecting uniaxial strain and lack the ability to measure directional variable motions. In order to overcome this challenge, novel sensor devices with geometrically engineered architectures, composed of multidimensionally stacked channels or cross-shaped detecting electrodes have been developed. These architectures were developed to address the challenge of achieving multidirectional strain sensing, by employing isotropic conducting pathways. While these advancements are significant, the complicated and intermixed pathways in the channel region can cause unsatisfactory linearity and make it difficult to determine the strain direction under complex stimulation environments. In addition, it is worth noting that many recent studies have utilized machine learning techniques, such as Neural network to classify data obtained by strain sensor. However, in order for Neural network to be applied effectively in industry, optimization processes such as model lightweighting are necessary.
Here, we propose a simply designed array of wearable strain sensor capable of detecting and interpreting the direction and intensity of strain through a neural network algorithm trained through cognitive learning. The wearable strain sensor arrays comprises a heterogeneous surface architecture consisting of a stretchable substrate made of polydimethylsiloxane (PDMS), strain-insensitive rigid electrode regions made of polyethylene terephthalate (PET) film, and a strain-sensing channel region composed of multi-walled carbon nanotube (MWCNT) with carbon black (CB) nanofiber dispersed in a PDMS matrix. We utilized a mechanism based on the change in the number of conducting pathways between MWCNT and CB depending on the direction of strain. The use of a heterogeneous device architecture can reduce the negative effects of electrode strain on electrical interruptions, resulting in more reliable strain sensing characteristics. This wearable strain sensor arrays exhibited high sensitivity with a gauge factor of approximately 8, a wide strain sensing range of 0 to 35%, and excellent reliability after 3,000 stretching cycles. To detect strain from any direction, Strain sensor array was made using three sensors arranged at 45-degree tilted angles. Furthermore, to achieve high-accuracy detection of both the intensity and direction of strain, a machine learning algorithm known as a multi-output neural network was employed. A neural network was constructed for strain sensing, which showed an accuracy of over 95% for both strain intensity and direction. In addition, optimization of the strain sensing system's neural network was done by adjusting the number of sensors and input

data dimension to achieve a lightweight model. By employing this method, not only data obtained from the wearable strain sensor arrays be efficiently handled, but also the strain intensity and direction can be accurately classified.

9:20 AM II04
(Student) Electrochemical Detection of the LuxR Protein Using the Metabolic Activity of *Shewanella oneidensis* MR-1 for the Development of a Modular Bioelectronic Interface Lauren Kelly, James Dylan Rees and Shayla Sawyer; Rensselaer Polytechnic Institute, United States

This work focuses on developing a modular bioelectronic interface using the dissimilatory metal reducing bacteria *Shewanella oneidensis* MR-1, with the long-term goal of improving low-cost real time nutrient sensors for aquatic ecosystems. *S. oneidensis* MR-1 is used to initiate extracellular electron transfer (EET) and produce a measurable current in response to a LuxR protein that is generated by *Escherichia coli*. The goals of the system are to adjust the gain by adjusting the amount of quorum sensing signal, in this case the LuxR protein, produced by *E.coli*, thereby increasing the current produced by *Shewanella*. The bioelectronic interface uses genetically engineered *S. oneidensis* MR-1 to trigger EET that preferentially engages in the generation of bacterial nanowires, promoting nanowire growth to the electrode. The creation of this bioelectronic interface between *E.coli* and *Shewanella* would allow for the ability to have a modular bioelectronic sensing system, with the ability to change the desired sensing target through the genetic engineering of *E.coli* at the front end of the system, while leaving the back end of the system unchanged as it is always sensing the quorum sensing signal generated by the *E.coli*. Additionally, this system could allow for greater stability by using positive and negative genetic regulatory feedback systems to help modulate the speed of the response, and improve the switch like behaviour by improving the bistability and enhancing the resistance to fluctuations.
Previous literature has demonstrated the successful creation of genetic Boolean circuits using *S. oneidensis* MR-1, including AND and NOT gates to control extracellular electron transport [1]-[3]. This project will work to improve the gain and stability of the existing AND gate circuitry using synthetic biology [4]. *S. oneidensis* MR-1 was grown in 800mL batch culture jars where Cyclic Voltammetry and biocurrent measurements were performed using a three-electrode system to electrochemically investigate the electron transfer processes within the system. Batches containing wildtype *S. oneidensis* MR-1 and genetically modified *Shewanella* strain J.G. 1453 that is missing all Mtr related components, were compared to a sterile control. A -0.2V DC bias was applied and ammonium nitrate was introduced as an electron acceptor. Preliminary results show the magnitude of biocurrent generation is on the order of microamps in the wildtype sample compared to nanoamps in the genetically modified strain, confirming the reduction of biocurrent with genetically modified Mtr deleted *S. oneidensis* MR-1. Scanning Electron Microscopy images of carbon felt electrodes were taken to compare the response of biofilm development in wildtype *S. oneidensis* MR-1 with genetically modified *Shewanella* strain J.G. 1453. There is significant bacterial nanowire and biofilm growth present on the wildtype electrode which is significantly minimized in the genetically modified strain confirming the control of the EET mechanisms using genetic engineering. The same experimental techniques will be utilized to confirm biocurrent generation with recognition of the LuxR protein using engineered *S. oneidensis* MR-1.
References
[1] Y. Hu, Y. Yang, E. Katz, and H. Song, “Programming Quorum Sensing-based AND Gate in *Shewanella oneidensis* for Logic Gated-Microbial Fuel Cells,” *J. Chem. Soc., Chem. Commun.*, vol. 51, no. 20, pp. 4184-4187, Feb. 2015.
[2] F. Li *et al.*, "Developing a population-state decision system for intelligently reprogramming extracellular electron transfer in *Shewanella oneidensis*," *Proc. Natl. Acad. Sci. U. S. A.*, vol. 117, no. 37, pp. 23001-23010, Sept. 2020.
[3] C. M. Dundas, D. J. F. Walker, and B. K. Keitz, "Tuning Extracellular Electron Transfer by *Shewanella oneidensis* Using Transcriptional Logic Gates," *ACS Synth. Biol.*, vol. 9, no. 9, pp. 2301-2315, July 2020.
[4] A. Graham *et al.*, “Transcriptional Regulation of Synthetic Polymer Networks,” 2021, *bioRxiv 2021.10.17.464678*.

9:40 AM II05
Highly Sensitive and Selective Cortisol Detection from Sweat Using Piezoelectric Single-Crystalline Flexible GaN Thin-Film Sensor Nam-In Kim, Asad Ali and Jae-Hyun Ryou; University of Houston, United States

In biomedical applications, such as the personal healthcare monitoring of physical and physiological signals, wearable and skin-attachable electronics, particularly sensors, are becoming more and more significant. The general health of people is greatly impacted by stress. When a person is under stress, their adrenal gland releases cortisol and adrenaline into the bloodstream. These chemicals are then expelled through various bodily fluids, such as sweat, saliva, and tears. Long-term stress can damage homeostasis, which is activated across the body and includes the immunological, renal, skeletal, cardiovascular, and endocrine systems. Additionally, the imbalance of homeostasis may lead to chronic illnesses. Monitoring cortisol levels in body fluids is crucial for maintaining healthy conditions as a result. Since they are reliant on the physical detection of skin sweat, conduction, heart rate, and body temperature, the majority of the present stress sensors in the literature have limitations. These impulses can come from both stress and the surrounding environment.
Organic electrochemical transistors type cortisol sensing and field-effect transistor-based cortisol sensors with cortisol antibody embedding technology to create the sensing layer have recently been designed and investigated. Both also have drawbacks including susceptibility to interference from other ions found in the target body fluids. Additionally, applying a voltage to the gate and drain electrodes might hasten the absorption of off-target analytes (such as serotonin and dopamine) onto the detecting region, leading to sensor malfunction. Another obstacle to commercialization is the transistor-based sensors’ need for an external electric supply to monitor cortisol. The cortisol monoclonal antibody may readily functionalize the piezoelectric-based quartz crystal microbalance (QCM)-type sensors to produce the sensing layer because they have a certain resonant frequency. The force that the target substance (cortisol) exerts on the sensing layer is caused by its mass, and the Sauerbrey equation then causes the initial resonant frequency to be altered in the opposite direction. Furthermore, due to the quick antigen-antibody interaction process, QCM-type piezoelectric sensors have outstanding response times. The initial resonant frequency's position affects the sensitivity, therefore a higher beginning frequency can pick up on low cortisol levels. The QCM-type sensor’s selectivity is virtually assured because the single attraction of bonding energy between the analyte and antibody serves as the interaction’s driving force. Because of this, only a very small amount of other substances or hormones can react. When it comes to using III-N thin films with single-crystalline properties as QCM-type sensors for cortisol detection, many different piezoelectric materials show great promise. The remarkable detection capabilities of III-N materials are made possible by their initial resonance frequency, which is relatively high at several GHz.
In this study, a III-N thin film-based QCM-type sensor for the detection of cortisol under diverse conditions was designed and shown. The layer transfer process was used to create III-N thin-film sensors. They were discovered to be single-crystalline and free of second phase or flaws by X-ray diffraction analysis. The sensor was exposed to the controlled cortisol solutions, and the concentration affected the resonance frequency. The selectivity of our sensor was then confirmed using diluted versions of several hormones. For comparison, synthetic bodily fluid and actual sweat were both taken from volunteers who had participated in both exercise and sauna sessions.

10:00 AM BREAK

10:20 AM II06
(Student) Optimizing Dual-Gate IGZO TFTs for Long-Term Flexible Neural Interfaces Andrew Bourhis[1], Hongseok Oh[1,2], Ritwik Vatsyayan[1], Shadi Dayeh[1] and Ian Galton[1]; [1]University of California, San Diego, United States; [2]Soongsil University, Korea (the Republic of)

Consisting of nearly 80 billion neurons and hundreds of trillions of synapses, the human brain is one of the most complex information-processing systems in the known universe. To understand how the brain functions, it is crucial to be able to measure the spatiotemporal dynamics of the generation and propagation of signals between each of these neurons. Measuring these signals can provide insight into normal function as well as shed light into the signatures or root causes of diseases such as epilepsy or Parkinson's disease. However, measuring the electrical activity of neurons at such a large scale has proven to be an extremely challenging endeavor. Electrocorticography is one method that is commonly used in the clinic to measure aggregate neural activity. Cutting-edge electrocorticography systems may employ thin-film fabrication of flexible microelectrode arrays with dense wiring schemes to achieve higher channel-count systems. These microelectrode arrays are typically fabricated using polymers such as parylene-C and the microelectrodes are routed individually and conductively bonded to rigid silicon-based acquisition circuits for digitization and downstream signal processing. Recent efforts have demonstrated high-density microelectrode arrays which can achieve thousands of channels; however, it is a major challenge to form reliable interconnects over one thousand channels between the flexible microelectrodes and the rigid acquisition electronics.
Taking inspiration from the high-definition flexible display industry, we have developed a 16x16 array of actively multiplexed microelectrodes using dual-gate thin film transistors made of indium gallium zinc oxide and fabricated on flexible polyimide substrates at low temperature. These neural interfaces use on-site multiplexing to help drastically reduce the interconnect bottleneck and thus improve the scalability of the system towards higher channel counts. Furthermore, this marriage of flexible substrates with active electronics is accomplished in a monolithic fashion, allowing for superior performance in a soft and wet biofluid environment. A major challenge with achieving reliability in such a system is the hermeticity of the encapsulation. Active electronics require biasing and control signals, thus any failure in encapsulation, if not properly designed for, can cause charge injection directly into cortical tissue. Thus, we have incorporated conformal atomic-layer-deposited ceramic biofluid barriers in addition to polymer encapsulation layers to help improve the operation of our active electronics in biofluid mediums. We are currently evaluating this encapsulation strategy in accelerated aging soak tests in elevated saline chambers, and have observed functional TFT microelectrode arrays after several weeks of soaking in saline. We expect that this strategy should be compatible with chronic experimental lifetimes of several months and plan to perform animal testing in the rat model after completing benchtop characterization. Another crucial aspect of this work is ensuring that the TFTs are robust over long periods of time. We have found that the contact resistance, mobility, and threshold voltage are all very sensitive to annealing and surface preparation conditions. By incorporating fluorine-based plasma treatment to the IGZO contact areas, and by optimizing the metal deposition conditions, we have found that we can lock in dopants in the IGZO film such that after curing the encapsulating polyimide films in nitrogen ambient, the annealing of these films results in stable and time-invariant electrical properties.

10:40 AM II07
(Student) Integration of ZnO Thin-Film Transistor Array with Surgical Forceps for Minimally Invasive Robotic Surgery Jing Gu[1], Hyunsoo Kim[2], Hongseok Oh[2] and Shadi Dayeh[1]; [1]University of California, San Diego, United States; [2]Soongsil University, Korea (the Republic of)

Minimally Invasive Robotic Surgery (MIRS) offers many advantages, including smaller incisions, faster recovery, less trauma to the patient, and the potential to be conducted from a distance. Currently, surgeons rely solely on the endoscope video without direct assessment of the surgical sites through the sense of touch or grasp. However, tactile feedback is crucial for surgeons to characterize and manipulate various kinds of healthy tissue with different mechanical properties, manipulate tumors, and suture incisions with arbitrary geometries aiming at improving patient outcomes. The difficulty of integrating touch sensors onto the surgical forceps lies in the small dimensions of the jaw (less than 5mm in width and less than 15mm in length). Additionally, the sensation of shear force to obtain information on grasp strength, tissue type and properties has not been demonstrated thus far. Our group utilized piezoelectric Zinc Oxide (ZnO) thin-film transistor (TFT) arrays with integrated pillars to measure shear and close the loop for robotic grasping without optical feedback for the first time (Oh et al., Science Advances, 6, eabd7795, 2020). In this work, we exploit ZnO TFTs to develop a compact tactile module for integration on surgical forceps to provide real-time tactile feedback to the operating surgeons with the da Vinci surgical forceps. Our TFTs for this application have pitch dimensions of 500µm, covering the jaw surface with 6 or 24 TFT elements which can detect normal force from a single TFT unit and shear force from a cell composed of 4 TFTs, respectively. The total thickness of the sensor array is around 13µm, which makes our device conform to the forceps. The device is well-passivated by a Parylene C coating and can operate in dry or wet environments. A 6TFT/24TFT array was fabricated by an RF sputtering system on a Polyimide substrate. The array was gently released from the silicon carrier wafer after laser cutting the outline. The fabricated array was attached to the surgical forceps with Polydimethylsiloxane (PDMS). We developed customized data acquisition circuits to receive the pressure response at 150Hz frame rate and generate a real-time heatmap. Additionally, we developed a visualization and wearable wrist module to deliver the tactile information with light and vibration. We integrated our free-standing GaN LEDs on flexible substrates to the surgeon's googles and controlled the number of LEDs lit with the magnitude of the pressure. For the wearable module, we integrated off the shelf vibrotactile stimulator disk whose amplitude of vibration is controlled by the magnitude of the shear force. We have tested the overall integrated system in benchtop and are currently conducting animal studies. This research, once adapted by surgeons, can be beneficial in informing the surgeons during robotic surgeries for short and effective surgical decisions and tasks and for improving patient outcomes.

11:00 AM II08
(Student) Ultrathin Skin-Attachable TiO_2 Synaptic Array Integrated with an Organic Proximity Sensor for Finger Gesture Recognition Haein Cho[1], In Ho Lee[2], Jingon Jang[1], Jae-hyun Kim[2], Hanbee Lee[2], Sungjun Park[2] and Gunuk Wang[1,3]; [1]Korea University, Korea (the Republic of); [2]Ajou University, Korea (the Republic of); [3]Korea Institute of Science and Technology, Korea (the Republic of)

Human gestures and motions recognition technology have attracted great attention with the growing industry of Metaverse platforms and robot technology that requires in-depth human-computer interaction. Among them, especially, finger gesture recognition has been becoming important due to its high degree of freedom for effective and direct communication between human and computer. To accelerate the realization of real-time gesture recognition and to promote seamless communications, one of the suggestions is integrating recognition function with sensory devices that can be adhered to skin and tissue surfaces, proving their long-term

operational stability under mechanical and environmental changes. However, unlike ultra-flexible organic sensory devices that have long proven their moderate tolerance to mechanical changes, the unstable performances of artificial synapse under mechanical deformation has been an obstacle to developing the integration. Here, we realize finger gesture recognition in free space via integration between artificial synapse array and proximity sensors attached on skin surface. We integrated organic photodiodes used as proximity sensors with 8 × 8 crossbar array titanium oxide (TiO_2) based artificial synaptic device and on a one-micrometre-thick ultra-flexible substrate. It is revealed that synaptic array was stably maintained under severe mechanical deformation at 60 % strain with 6400 repeated input pulses. Via device-to-device integration, the finger motion to draw numeral with an Eulerian trail in the free space of 100 cm^2 was successfully recognized with maximum accuracy of ~ 90.1%. Also, the arbitrary motion gestures at generalized sensing condition of organic proximity sensor device were well recognized presenting accuracy of ~82.5 % even in interpreting of different persons. Our finds suggest a future avenue of interacting wearables for human-machine interactions in extended reality.

11:20 AM II09
(Late News) Integrated Graphene FET Array for High Sensitive Detection of New Corona Virus with Automated Solution Exchange System Kaori Yamamoto and Kazuhiko Matsumoto; Osaka University, Japan

1. Introduction
By integrating the 32 graphene FET with antibody modified channel, the new corona virus was detected with 100~1000 times higher sensitivity than the conventional antigen detection kits. The detection time is ~10~20 minutes, which is ~10 times shorter than the PCR system. By using the graphene FET with and without the antibody modification for detecting the signal of virus and for the reference signal, the problems of the signal drift and the physical adsorption of virus were solved. Also by adapting the micro-TAS and automated washing system, the restriction of the Debye length was solved and the impurity such as a saliva could be washed away and the pure signal only from the virus which bind to antibody could be detected.
2. Experimental Process
The channel length and width of the fabricated graphene FETs are 10mm and 100mm, respectively, and 32 graphene FET's are integrated. The 13FET's in the half of left hand side are modified by antibody through PBASE, and the 13FET's in the half of right hand side are without antibody modification and used as reference FET. Onto this integrated graphene FET array, the micro total analysis system (m-TAS) made by PDMS was set to introduce the phosphate-buffered saline (PBS) solution from the right hand side inlet and through the graphene FET channel, and to drain from the left hand side outlet. PBS solution was introduced from the reservoir by the computer controlled micropump. In order to control the Debye length, the different concentration of PBS solution should be used for the introduction of virus and for the detection of the charge of virus.
3. Results & Discussions
The time dependence of the average of the Dirac point of 13 graphene FET's with and without the antibody modification was measured using the 0.01xPBS and its Debye length is 7nm. There is the difference I n the Dirac point between with and without the antibody modification, which is attributed by the positive charge of the antibody modified on the graphene surface.
2 time of 1xPBS was introduced into the system without virus to confirm the no influence by the exchange of the high concentration of PBS.
Then, the new corona virus with $1x10^8$FFU/mL in high concentration of 1xPBS solution was introduced to the graphene FET. Virus combines well to the antibody in the high concentration of 1xPBS solution. The Debye length at 1xPBS solution is as short as 0.7nm, and the charge of virus could not be detected by the graphene FET as the height of the antibody is as large as ~10nm. Again, the low concentration of 0.01xPBS was introduced to extend the Debye length. Then, the negative charge of the virus was detected and the Dirac point increased positively.
The detail of this Dirac point shift was analyzed. Dirac point of the 13FETs with antibody modification shift as large as ~20mV , while that without antibody as small as ~3.5mV after the introduction of virus. The large shift of Dirac point with antibody FET is attributed to three reasons as (1)charge of virus which combine to antibody, (2)charge of the physical adsorbed virus on the graphene, and (3)Drift characteristic of the total measurement system. While the small shift of Dirac point without antibody FET is attributed to two reasons as (2) and (3). The difference of these value, i.e., ~16.5mV(20mV – 3.5mV) is due to the net charge of virus which combined to only antibody. Using the SEM, the new corona virus on the graphene FET channel could be counted. About 10 times larger number of virus binds to graphene surface with antibody modification than without antibody modification. The number of the virus on the channel is linearly proportional to the Dirac point shift.
3. Conclusions
Using the integrated graphene FET array and automated washing systems, the new corona virus was detected with the 100~1000times higher sensitivity than the conventional antigen test.

SESSION JJ: Low-Dimensional Structures – Quantum Dots, Wires and Wells
Session Chair: Thomas Searles
Friday Morning, June 30, 2023
UC, Santa Barbara Harbor

8:20 AM JJ01
Carrier Capture into Individual InP Quantum Dots Directly Imaged by Nanoscale Cathodoluminescence Microscopy Frank Bertram[1], Gordon Schmidt[1], Juergen Christen[1], Peter Veit[1], Julie Kernchen[1], Hannes Schuermann[1], Michael Jetter[2], Ana Cutuk[2] and Peter Michler[2]; [1]University of Magdeburg, Germany; [2]University of Stuttgart, Institut für Halbleiteroptik und Funktionelle Grenzflächen, Center for Integrated Quantum Science and Technology (IQST) and SCoPE, Germany

We present a nanoscopic investigation of the carrier capture into individual InP quantum dots (QDs) by means of highly spatially resolved cathodoluminescence spectroscopy directly performed in a scanning transmission electron microscope (STEM-CL). Single dot spectroscopy using low temperature STEM-CL provides a detailed insight into the energy structure of individual QDs and directly correlates those properties with the real structure on a nanoscale. We characterize the vertical and lateral transfer of carriers within a 7-fold stack of layers containing high-density InP quantum dots.
Grown by metal-organic vapor-phase epitaxy, the sample consists of 7 InP QD layers embedded in 20.0 nm $Al_{0.1}GaInP$ barriers sandwiched between 31.6 nm $Al_{0.55}GaInP$ cladding layers and topped by an AlInP layer of 12.0 nm thickness used as electron blocking layer. The cladding layer at the very bottom and the very top of the stack is slightly thicker (64.8 nm) than the others. A 12.0 nm AlInP and subsequently a 10.0 nm thick $Al_{0.1}GaInP$ layer encloses the complete QD stack. The QD layers were grown via Stranski-Krastanov growth mode achieving a high QD density of $10^{10}/cm^2$.
A STEM high-angle annular dark field image (HAADF) discloses the complete sample structure in cross-section. The overall total thickness of all epitaxial layers is 968.6 nm. Starting from the GaAs substrate, a 200 nm thick AlGaAs sacrificial layer (for later lift-off of the QD sandwich) is followed by the clearly resolved periodic structure of the 7-fold QD stack. The STEM-HAADF contrast reveals the embedded InP quantum dots as a thin line within the $Al_{0.1}GaInP$ barriers as well as the surrounding $Al_{0.55}GaInP$ cladding layers. The AlInP electron-blocking layer positioned in between the QD layer packages as well as

at the top and bottom of the structure is also visible. Furthermore, the thick $Al_{0.55}GaInP$ cladding layers positioned at the top and bottom of the QD stack is visible as well. No extended defects can be found.
Low-temperature CL imaging and spectroscopy was performed to correlate the structural and optical properties of the separate confinement heterostructure. Three distinct emission lines can be observed in CL spectra: For the AlGaAs sacrificial layer, intense narrow luminescence at $\lambda = 594$ nm is detected. Exclusively from the top and bottom cladding, an extremely weak - yet detectable - emission evolves at a wavelength around $\lambda = 540$ nm.
STEM-CL performed at a relatively thick specimen region averages in the depth of the sample slice over a large number of QDs, i.e., representing ensemble properties. This ensemble luminescence of the seven quantum dot layers exhibits a broad and intense emission band, which is composed of overlapping sharp emission lines in the spectral range from $\lambda = 610$ to 680 nm, with an overall maximum around $\lambda = 627$ nm.
STEM-CL measurements in thinner parts of the TEM lamella exciting fewer dots within the specimen depth take advantage of the ultra-high spatial resolution of our STEM-CL setup ($\delta x < 5$ nm). This allows to perform spectroscopy on a single dot and image its different excitonic transitions. The nanoscopic lateral transport is investigated by a spectrum linescan across an isolated single InP QD. A characteristic change of the excitonic lines during this linescan is observed. This directly correlates to the change of the numbers of excess carriers reaching the dot and accordingly altering the QD population, while moving the electron beam excitation towards the QD. The observed shift of emission energies originates from the renormalization of the ground-state energy of the single dot. The intensity ratio evolution of the excitonic recombination is caused by and directly visualizes the change of occupation probability of the QD states.

8:40 AM JJ02
(Student) Electronic and Structural Properties of Rare-Earth Mono-Pnictide (RE-V) Nanoparticles in III-V Matrices Ruiqi Hu[1], Quoc Dai Ho[1], Quang To[1], Garnett Bryant[2] and Anderson Janotti[1]; [1]University of Delaware, United States; [2]National Institute of Standards and Technology, United States

Embedding semi-metallic rare-earth mono-pnictide (RE-V) nanoparticles into III-V semiconductors enables nanocomposites with a wide range of optical, electrical, and thermoelectric properties. It decreases carrier lifetime, and increases the phonon scattering, leading to lower thermal conductivity but enhanced electrical conduction through electron filtering mechanisms. The common group-V sublattice offers an interesting matching across interfaces of the rock-salt semimetal RE-V (e.g. ErAs) to the zinc-blende semiconductor III-V (e.g. GaAs, AlAs) matrices with similar lattice parameters. Density functional theory (DFT) calculations with the modified Becke-Johnson meta-GGA (MBJ) functional are used to describe the electronic properties of ErAs nanoparticles embedded in GaAs and AlAs. We investigate the stability of different nanoparticle shapes and sizes, from cubic to spherical, deriving a direct correlation between the electron density and atomic density associated with excess metal atoms at the interface. Four different sizes of spherical ErAs nanoparticle embedded in different sizes of two III-V matrices are studied. According to the formation energy calculations, spherical shape is the most energetic favorable among all shapes. We discuss the band alignment between the RE-V and the III-Vs, finding the Fermi level pinned near mid-gap of the semiconductor for the 1.73 nm size ErAs nanoparticle, explaining previous experimental measurements. Our predictions serve to guide the design of nanocomposite materials with targeted properties.

9:00 AM JJ03
MBE Growth for Wafer Scale Uniformity in Low Density InAs Quantum Dots Yuanchang Zhang and Kurt Eyink; AFRL, United States

Low density ($\leq$10 dot/μm^2) of InAs QDs is required for single photon emitters. Such a low density QD can be achieved by depositing less than the critical coverage for InAs QD formation followed by an in-situ annealing.[1] However, to achieve a repeatable density from growth to growth and high uniformity across the wafer is challenging. In a recent study by Huang et al,[2] only a few percent variation in indium flux caused over an order of magnitude changes in the QD density and could completely eliminate the QDs. In order to routinely hit a target density and size of QDs we need to improve control beyond the simply repeating standard growth conditions (In BEP, As cell settings, growth temperature and rotation rate…). A typical flux variation across a sample can be near 15-20% without rotation. However, by locking the rotation rate to give nearly a complete number of rotations during the deposition, this variation can be reduced to near zero and leaves only the 1-2% variation across the sample. We implemented this strategy by changing the indium cell temperature so that we had 15 rotations during a 54 second InAs growth which minimizes these transient nonuniformities. In addition we measured the time for the 2-3D transition, $t_{2\text{-}3D}$, during post annealing after ~1.5 ML InAs growth in analogy with Li et al,[3] who looked at a continuous InAs deposition condition. This gives us an in-situ indication of the In coverage. Prior to modifying our growth procedure our QD densities varied from 20 to 100 dot/μm^2 with nominally the same growth conditions and clearly showed an off-center PL maximum. After implementing our strategy we have the maximum PL signal at the center of the wafer. We found we were able to adjust the densities from run to run by varying $t_{2\text{-}3D}$. We observed $t_{2\text{-}3D}$ varied from ~16 to >120 sec corresponding to ~0.03ML change in coverage. The corresponding PL for these different transition times is shown in Figure 1. The PL intensity changes by a factor of 6 indicating a 6X higher QD density for $t_{2\text{-}3D}$ of 16s vs 60s. We measured the PL across the wafers and show the variation from the center to the edge in Figure 2. The PL mapping shows one order of magnitude intensity variation in a 1 cm range which is also consistent with the QD density variation observed using the AFM. This work enables us to control the QD density in the center of the wafer, but clearly indicates more effort is needed in order to achieve wafer scale uniformity.
[1] Song, H. Z., T. Usuki, Y. Nakata, N. Yokoyama, H. Sasakura, and S. Muto. "Formation of In As_Ga As quantum dots from a subcritical InAs wetting layer: A reflection high-energy electron diffraction and theoretical study." Physical Review B 73, no. 11 (2006): 115327.
[2] Huang, Xiaoying, Rongbin Su, Jiawei Yang, Mujie Rao, Jin Liu, Ying Yu, and Siyuan Yu. "Wafer-scale epitaxial low density InAs/GaAs quantum dot for single photon emitter in three-inch substrate." Nanomaterials 11, no. 4 (2021): 930.
[3] Li, Mi-Feng, Ying Yu, Ji-Fang He, Li-Juan Wang, Yan Zhu, Xiang-jun Shang, Hai-Qiao Ni, and Zhi-Chuan Niu. "In situ accurate control of 2D-3D transition parameters for growth of low-density InAs/GaAs self-assembled quantum dots." Nanoscale research letters 8, no. 1 (2013): 1-6.

9:20 AM JJ04
Quantum Dot Morphology and Defect Configuration Anisotropy for III-V Laser Material Grown on Patterned Si Photonic Wafers Chen Shang[1], Eamonn T. Hughes[1], Rosalyn Koscica[1], Kunal Mukherjee[2], Kaiyin Feng[1] and John Bowers[1]; [1]University of California, Santa Barbara, United States; [2]Stanford University, United States

Over the last few years, tremendous improvements of device performance and reliability have been demonstrated in devices grown on blanket Si substrates. Recently, electrically pumped QD lasers deposited in narrow oxide pockets in a butt-coupled configuration and on-chip coupling have been realized on patterned Si photonic wafers.

However, the device yield and reliability, which ultimately determines the scalability of such technology, are limited by the material uniformity. Here, we perform the detailed analysis on the material anisotropy induced by the pocket geometry. Both the QD morphology and defect configuration anisotropy suggest that all pockets should be aligned to the [1 -1 0] direction of the III-V crystal.
The 300 mm growth template consists of rectangular oxide pockets both “parallel” and “orthogonal” with respect to the Si substrate step edges, shown in Figure 1(a) and (b). The room temperature photoluminescent (PL) spectra of the as-grown in-pocket QD laser material, shown in Figure 1(d), indicate that QD quality is higher in the “orthogonal” and wider pockets. The corresponding laser performance, shown in Figure 1(e), suggesting the gain from the QDs in the narrower “parallel” pockets is not high enough for lasing. Representative PL intensity maps of a “half-laser” structure and the corresponding atomic force microscopy (AFM) image of the exposed active region dots are shown in Figure 1(f). The drastic discrepancy of the emission uniformity and QD density between the materials in the wider “orthogonal” pocket and the narrower “parallel” pockets are attributed to asymmetric indium adatom diffusion, with [1 -1 0] being the fast diffusion direction. To map the crystal orientation onto the pocket orientation, faceted trenches (FTs), which would form when a GaAs layer experience abrupt tensile relaxation, were introduced in the pocket with the test structure shown in Figure 2(a). Nomarski images show that FTs elongate along the “orthogonal” pocket, confirming that “orthogonal” pockets are in the [] orientation with respect to the III-V crystal, shown in Figure 2(b) and (c). Thus, aligning the pocket to the fast diffusion orientation would prevent indium adatoms from diffusing onto the edges.
Since the edge of the III-V strip is stress free, it is also expected that the residual thermal stress state of the in-pocket materials would also be highly anisotropic with the direction along the short edge of the strip experiencing lower residual tension. It has previously been confirmed that the misfit dislocations (MDs) generated from the residual thermal stress is responsible for device degradation. Such stress anisotropy introduced by the pock geometry could then be utilized to reduce the MD density. Two TEM foils were prepared parallel (“∥”) and perpendicular (“⊥”) to a 20 μm [1 -1 0] oriented pocket, shown in Figure 2(d). Comparing to Figure 2(e) where foil oriented parallel to the pocket, the foil perpendicular to the pocket, shown in Figure 2(f), has a significantly lower density of misfit dislocations, even much lower than those measured in blanket substrate materials. It has previously been found that the MDs in the [1 -1 0] direction formed via tensile relaxation have a Ga-core structure, which resides closer to the middle of the GaAs/AlGaAs bandgap than the MDs in the [1 1 0] direction Though the MDs along the long edge of the pocket would be reduced regardless of the alignment of the pocket with respect to the III-V crystal, all pockets should be aligned to the [1 -1 0] direction to effectively lower the density of the most detrimental defects. The in-pocket devices would then potentially surpass the performance of the state-of-the-art devices grown on blanket Si substrate.

9:40 AM JJ05
(Student) Gradual Degradation via Dislocation Microloop Formation in InAs Quantum Dot Lasers on Si and GaAs Eamonn T. Hughes[1], Chen Shang[1], Jennifer Selvidge[1], Daehwan Jung[1], Yating Wan[1], Robert Herrick[2], John Bowers[1,1] and Kunal Mukherjee[3]; [1]University of California, Santa Barbara, United States; [2]Intel Corporation, United States; [3]Stanford University, United States

Recent research efforts have unlocked substantial improvements in the performance and reliability of InAs quantum dot lasers on silicon by mitigating the effects of active-region-adjacent misfit dislocations through the introduction of defect trapping layers (TLs). These TLs enable lifetimes of lasers on silicon comparable with those grown on native GaAs substrates. Even so, current state-of-the-art lifetimes still fall somewhat short of requirements for more widespread adoption as both types of lasers exhibit gradual degradation in performance with aging. In this work, we demonstrate that this gradual degradation is a result of the generation of point defect populations during aging, which, over time, coalesce into dislocation microloops which we characterize using scanning transmission electron microscopy (STEM).
We selected a single high-performing laser from each of three large aging sets of QD lasers (1) on silicon with TLs, (2) on silicon without TLs (no-TL)), and (3) on native GaAs. Each selected device was aged for between 8700 and 12,000 h at 80 °C at a current density between 1050 and 1900 A cm^{-2}, depending on the initial threshold current and output power. After 2700 h, the no-TL device had doubled its initial threshold current (a common metric for device failure), and after 5700 h it failed to lase entirely. The TL device and the GaAs device, however, show threshold current increases of just 35% and 46% respectively after 8700 h with extrapolated lifetimes of 45,000 h and 75,000 h. Note, however, that these numbers are not directly comparable due to somewhat harsher aging conditions for the GaAs device.
After aging, the devices were imaged using backside electroluminescence to check for signs of inhomogeneous degradation. For all lasers, degradation appeared largely homogeneous aside from dark line defects associated with misfit dislocations in the devices on silicon. There are also regions of decreased luminescence throughout the structure for the two devices on silicon, which we attribute to misfit dislocations lying parallel to the laser ridge for the no-TL device and to misfit dislocations escaped from the TL for the TL device, as confirmed by plan-view STEM of these regions.
With sufficient thinning of the plan-view foils, dislocation microloops with diameters ranging from 5 to 20 nm are visible both in the [001] zone imaging condition overlaid with the QD contrast and more clearly in various g-3g STEM weak beam imaging modes where competing QD contrast is minimized. In the no-TL device in regions within 100-150 nm of the heavily climbed misfit dislocations, there is a dramatic increase in loop density on the order of 10^{10} cm^{-2}. We believe this to be the result of a large density of point defects expelled by the misfit dislocations as they undergo climb. Thus, degradation caused by climbing misfit dislocations is multifold: first an increase in total misfit length and second the generation of a high density of point defects which coalesce into microloop defects surrounding the misfit dislocation, all of which substantially enhance non-radiative recombination processes.
Meanwhile, the TL and GaAs device active regions, though largely or entirely free of climbed misfit dislocations, are still observed to contain microloop densities on the order of 10^{8}–10^{9} cm^{-2}, which likely accounts for the gradual, homogeneous degradation observed in these devices. These microloops coalesce from elevated point defect populations in the active region, and while there are many remaining questions, such as whether these point defects are pre-existing or are generated during aging, this work points the way for future routes to improve device and material quality.

10:00 AM BREAK

SESSION KK: Micro-LEDs
Session Chairs: Ding Wang and William Wong
Friday Morning, June 30, 2023
UC, Santa Barbara Harbor

10:20 AM KK01
(Student) Impact of Barrier Thickness and Doping on the Carrier Transport in MQW P-Down Green LEDs Sheikh Ifatur Rahman[1], Xuefeng Li[2], Andrew M. Armstrong[3], Daniel Feezell[2], Rob Armitage[4] and Siddharth Rajan[1,1]; [1]The Ohio State University, United States; [2]The University of New Mexico, United States; [3]Sandia National Laboratories, United States; [4]Lumileds LLC, United States

Introduction: The development of InGaN/GaN LEDs has led to significant advances in the field of solid-state lighting with a wide range of potential applications, such as in microLED displays, wearable displays, general lighting, etc. However, while blue/violet emitting InGaN/GaN LEDs have near-theoretical efficiency, emitters in the longer wavelength (>500 nm) suffer from lower optical and electrical performance due to the large average polarization sheet charges in high composition InGaN QWs. One way to overcome the challenges associated to large electrostatic barrier is to reverse the relative electric field of the p-n junction and the QWs. Such reversed polarization LEDs reduce electrostatic barriers significantly and enable diodes to operate with at lower voltages (V_f)[1-4]. There have been few reports on p-down LEDs, and the impact of design of barrier(QB)/QWs is still not well-understood. ***In this work, we explore the impact of barrier thickness and doping on the electrical and optical properties of reversed-polarization Ga-polar p-down green LEDs. We show that carrier transport plays a critical role in the performance of p-down LEDs and demonstrate state-of-art performance for p-down green emission LEDs.***
Experimental: The LED epitaxial structures were grown on a non-patterned n-type GaN on sapphire template without any surface texturing or encapsulation. A bottom tunnel junction with n^{++}/p^{++} configuration was grown before the active region. The active region is composed of three InGaN QWs (3nm), which are sandwiched between GaN barriers. The QB thickness (18 nm and 5 nm) and doping ($1x10^{18}$ cm^{-3} Si doping) conditions were varied to study their impact on transport in these LEDs. The reported data here are obtained from 100µm by 100µm square devices.
Impact of barrier thickness: First, we investigated how the thickness of the QBs impacts the properties of LEDs by comparing LEDs with two QB thickness of 5 nm and 18 nm. Due to the reversed polarization direction, barriers in p-down LEDs present a larger barrier to carrier transport. We find that devices with 5 nm QBs showed a lower V_f (3.71 V @ 20 A/cm^2) compared to thicker 18 nm QB (3.91 V at 20 A/cm^2). The thin QB reduces the initial injection barrier lowering the diode operation voltage. On-wafer measurements showed an increased EQE for the thin QB device over the thick QB device, however the wavelength was significantly shorter for the thin QB devices.
Impact of barrier doping: In case of a doped thick barrier the V_f was reduced (3.61 V @ 20 A/cm^2) when compared to the sample with undoped barriers (3.91 V @ 20 A/cm^2). Furthermore, the device with doped barriers showed increased peak EQE at a lower current density.
Defect spectroscopy and small-signal electroluminescence: To understand the impact of having highly doped Si and Mg layers before the active region DLOS measurements were performed. When compared to a standard green LED, the p-down active region showed a broadened near band gap absorption spectra which is possibly related to Mg impurities in the active region. Small-signal electroluminescence measurements for thin QB p-down LEDs also showed a shorter recombination lifetime compared to a standard p-up green LED [5].
Conclusion: In summary, we have investigated the effect of QB barrier thickness and doping in the unconventional p-down MQW green LEDs. The results indicate that with proper epitaxial design, p-down LEDs can show favorable voltage and optical performance. This demonstration of high efficiency p-down LED provides a framework to improve the efficiency of other designs including longer wavelength LEDs and novel multiple active region LEDs.
This work is supported by the U.S. Department of Energy's Office of EERE under the BTO award no. DE-EE0009163. SNL is managed and operated by NTESS under DOE NNSA contract DE-NA0003525.
Ref.: 1. APL **121**, 021102 (2022). **2.** JAP **125**, 203104 (2019) **3.** APL **100**, 111118 (2012) **4.** JJAP. **50** 052101 **5.** JAP **122**, 035706 (2017)

10:40 AM KK02
(Student) Carrier Dynamics in Blue, Cyan and Green Commercial InGaN/GaN LEDs Measured by Small-Signal Electroluminescence Xuefeng Li[1], Nick Pant[2], Elizabeth DeJong[1], Rob Armitage[3], Emmanouil Kioupakis[2] and Daniel Feezell[1]; [1]University of New Mexico, United States; [2]University of Michigan–Ann Arbor, United States; [3]Lumileds LLC, United States

Blue and green InGaN/GaN light-emitting diodes (LEDs) are crucial for solid-state lighting and display applications. Violet–blue LEDs have achieved a high EQE of ~80%. However, InGaN/GaN LEDs still suffer from strong efficiency loss in the green region, which is usually referred to as the "green gap." The green gap issue has been related to Auger recombination, the quantum-confined Stark effect (QCSE), carrier leakage, random alloy fluctuations, and defects and carrier localization, among other causes. To achieve longer emission wavelengths, the indium composition must be increased, leading to several problems. First, high indium content increases lattice mismatch and introduces additional point defects during metalorganic chemical vapor deposition (MOCVD). High indium content also leads to strong polarization-related electric fields in the quantum wells (QWs), lowering the wave function overlap and decreasing the radiative and non-radiative recombination rates (i.e., from the QCSE). An important question is how much of the change in efficiency reduction from blue to green is due to intrinsic effects (i.e., wave-function overlap and phase-space filling (PSF)) vs. extrinsic effects (i.e., material degradation).
In this work, we use small-signal electroluminescence (SSEL) to study the carrier dynamics in commercial *c*-plane LEDs with various emission wavelengths ranging from blue (~470 nm), to cyan (~500 nm), to green (~530 nm). The LED series consists of three wafers grown by Lumileds with identical active region designs (3X, 3 nm QWs) but different indium compositions. LEDs with mesa diameters of 100 µm and ground-signal-ground electrodes were fabricated. SSEL was then used to study the carrier dynamics of the LEDs. Each element in an equivalent circuit model was acquired via simultaneous fitting of the impedance and modulation responses, leading to the injection efficiency and total carrier recombination lifetime. Combining the total carrier lifetime with internal quantum efficiency (IQE) enables the separation of the radiative and non-radiative recombination lifetimes and rates as a function of carrier density (n) and current density (J). The results reveal that efficiency loss at longer wavelength is related to reductions in injection efficiency and radiative recombination, and an increase in Auger recombination. The interplay between the QCSE and carrier-current density relationship is shown to determine the relative importance of the radiative ($B(n)*n^2$) and non-radiative recombination rates ($A(n)$ and $C(n)*n^3$) as the indium content is increased. Both the SSEL experiment and Schrödinger-Poisson calculations showed $C(n)/B(n)$ is similar for the three wafers at high n, indicating that intrinsic material degradation is not significant. In addition, compared with QCSE, PSF, and material degradation, the increase of the carrier density at a given J for longer wavelengths is the dominant reason for the green gap. Thus, methods to decrease the carrier density in each QW are suggested to increase the EQE of green LEDs.

11:00 AM KK03
(Student) Trap-Assisted Auger Recombination in Commercial Green InGaN/GaN LEDs Xuefeng Li[1], Elizabeth DeJong[1], Rob Armitage[2], Andrew M. Armstrong[3] and Daniel Feezell[1]; [1]University of New Mexico, United States; [2]Lumileds LLC, United States; [3]Sandia National Laboratories, United States

Nonradiative recombination centers (NRCs) are known to negatively affect the efficiency of light-emitting diodes (LEDs). NRCs contribute not only to Shockley–Read–Hall (SRH) recombination, but also to trap-assisted Auger recombination (TAAR). The relationship between NRCs and the TAAR processes has been predicted theoretically and observed experimentally to a limited degree. However, some details about TAAR are still under debate, including its magnitude relative to intrinsic Auger and SRH recombination, its dependence on carrier density (e.g., $\propto n^2$ or $\propto n^3$), and its role in the green gap, particularly in high-quality commercial-grade LEDs. TAAR is typically assumed to be linearly dependent on trap density, directly tying the magnitude of TAAR to the quality of the sample. Previous studies have examined TAAR using time-resolved photoluminescence and optical differential lifetime measurements, which do not capture certain effects related to electrical injection.
In this work, we report a quantitative study of TAAR in *c*-plane commercial-grade green LEDs grown by metal-organic chemical vapor deposition (MOCVD). We investigate a series of three wafers with identical active regions (3X, 3-nm-thick quantum wells) but different NRC trap densities ($4.4e14\ cm^{-3} < N_t < 1.5e15\ cm^{-3}$). We use small-signal electroluminescence (SSEL) and deep-level optical spectroscopy (DLOS) to study the carrier dynamics and density of NRCs in the samples, respectively. SSEL is used to determine the carrier lifetime, which is used in conjunction with the internal quantum efficiency (IQE) to decouple the radiative and nonradiative recombination rates. The total recombination lifetime in higher quality growth is found to be longer than that in lower quality growth and is attributed to the longer nonradiative recombination time in higher quality samples. On the other hand, the radiative recombination rates for different growth qualities at a given carrier density (n) are identical, as expected from samples with the same active region design. We extract the relationship between the density of NRCs and the corresponding nonradiative recombination rates at a given carrier density (n). The difference in nonradiative recombination between the samples offers information about both SRH and TAAR with respect to growth quality. The linear dependence between the SRH recombination rate and the density of NRCs at low n was confirmed. However, TAAR was found to be sublinear with the density of NRCs, possibly due to the relatively small changes (~3X) in defect density (N_t) in these samples. We find that TAAR is best fit to an n^2 dependence on carrier density. This is supported by the observation that all three samples have similar IQE at high carrier density, which would not be consistent with an n^3 process. We also show that the TAAR recombination coefficients (D) are on the order of ~1e13 $cm^3\ s^{-1}$, which is similar to that reported for violet LEDs and shows the weak dependence of TAAR on bandgap. Using the extracted TAAR coefficients, we calculate that TAAR accounts for about 10% of the total nonradiative recombination rate at moderate carrier densities. Thus, intrinsic Auger dominates the nonradiative recombination and TAAR is not a major contributor to the green gap in these commercial LEDs.
SNL is managed and operated by NTESS under DOE NNSA contract DE-NA0003525.

11:20 AM KK04
The Role of Zn-Precursor in the Formation of Environment-Friendly Highly Luminescent Colloidal Quantum Dots and R/G/B QLEDs with Inverted Structure Yujin Kim and Seonghoon Lee; Seoul National University, Korea (the Republic of)

During the past decades, colloidal quantum dots (CQDs) have gained enormous attention as an alternative photostable emitting material. Using the quantum confinement effect, the emitting color of CQDs can be easily tuned through a change in their size and shape (.i.e. the control of excitons). Cd-based CQDs have been studied widely and found to have useful photonic properties. However, under the restriction of hazardous substances (RoHS) regulation, the commercialization of toxic Cd-based CQDs has been limited. In order to develop Cd-free CQDs, some researches on InP CQDs have been carried out. The emitting color of $In_{1-x}Ga_xP$@ZnS (alloy-core@outer shell) CQDs can be tuned from red to shorter wavelengths such as blue. Yet, it is difficult to synthesize blue-emitting InP CQDs. Some used a zinc precursor in the core-synthesizing step to produce blue-emitting CQDs. The role of zinc is not clear. We investigated the role of Zn precursor based on hard and soft acids and bases theory and we found that the roles of Zn precursor are as a reaction suppressant, a size regulator, and a dopant. Furthermore, we discovered which role was primarily played by Zn precursor at different concentrations. Environmentally benign highly luminescent R/G/B emitting $In_{1-x}Ga_xP$@ZnS CQDs were produced with bis(trimethylsilyl) phosphine and new metal complex precursors (Indium-trioctylphosphine, In-TOP; Ga-TOP; Zn-TOP). To achieve high photoluminescence quantum yield (PLQY), the surface states associated with surface atoms on CQDs were passivated with ZnS shell. Furthermore, we realized R/G/B-emitting quantum dot light-emitting devices (QLEDs) with the efficiency of 26, 66, or 4 cd/A, respectively. The nontoxic R/G/B-emitting $In_{1-x}Ga_xP$@ZnS, CQD-based QLEDs with inverted structure are shown in Figure below.

11:40 AM KK05
(Student, Late News) Electron Emission Microscopy of an Electrically Driven III-Nitride-Based LED: Evidence of Lateral Electron Injection at V-Defect Sidewalls Tanay Tak[1], Cameron W. Johnson[2], Wan Ying Ho[1], Feng Wu[1], Mylène Sauty[3], Alejandro Quevedo[1], Andreas K. Schmid[2], Jacques Peretti[3], Claude Weisbuch[1,3] and James S. Speck[1]; [1]University of California, Santa Barbara, United States; [2]Lawrence Berkeley National Laboratory, United States; [3]Ecole Polytechnique, France

GaN-based light emitting diodes (LEDs) for white light illumination are one of the biggest technological achievements in energy efficiency. However, challenges remain with GaN-based LEDs such as efficiency droop and low efficiency for longer wavelengths. Auger-Meitner recombination, a three-carrier process, has been identified as the dominant mechanism for efficiency droop via electron emission spectroscopy (EES). In EES, LEDs were activated to negative electron affinity (NEA) to allow for the emission of hot electrons from the surface which were quantitatively correlated to Auger-Meitner recombination processes. In recent years, V-defects have been proposed as the solution to the excess driving voltage of long wavelength nitride-based LEDs, one of the sources of their diminished efficiency. One way to image the effects of V-defects is using electron emission microscopy (EEM). EEM is a newly developed technique analogous to EES that allows for spatially resolved microscopy of hot electrons. EEM uses a low energy electron microscope with its illumination column turned off, such that only internally generated electrons escaping out the surface during electrical driving of the device are observed.
Commercial blue ($\lambda \approx 460$ nm) and green ($\lambda \approx 525$ nm) LED wafers from Seoul Viosys were acquired and processed into LEDs. The diodes were formed by Pd/Au (20/30 nm) *p*-contacts with open circular and hexagonal apertures lithographically defined with known dimensions. A C-shaped *n*-contact partially surrounding the *p*-contact was formed by reactive ion etching into the *n*-region and contacted with Ti/Au (30/300 nm). EEM was performed in an ELMITEC LEEM III system modified to allow for electrical biasing of devices from the sample stage, where Cs was deposited onto the sample using a SAES Getters Cs source to activate the sample to NEA.
For LEDs, EEM images the non-radiatively-recombined electrons that cross the diode junction and diffuse through the *p*-GaN and escape out the surface, which can include overflow, Auger-Meitner, and trap-assisted Auger-Meitner electrons. EEM images of blue and green LEDs show non-electron emitting regions (dark spots) with densities

of ~2 × 10^7 cm^{-2} and ~3 × 10^8 cm^{-2}, respectively, which we identify as V-defects. This is confirmed through the corresponding dark spots of panchromatic CL measurements of the same samples, as well as SEM and plan-view TEM for V-defect densities.
Since the density and dimensions of the non-electro-emitting and non-illuminating regions are identical, we attribute our measured lack of electron emission directly from the V-defect areas to electrons fast traveling through the sidewalls of the V-defects and being injected laterally and efficiently into planar quantum wells without any Auger-Meitner recombination or overflow within the sidewalls. This is supported by the stronger electron emission observed at the ridge of the V-defects due to larger carrier densities there and thus increased hot electrons generation. Our results agree with simulations that electrons travel up the sidewalls of V-defects that have been nucleated prior to the active region and directly inject themselves into the quantum wells in the active region, so the carrier density in these sidewalls is negligible [1].
Support at UCSB was provided by U.S. Department of Energy under the Office of Energy Efficiency & Renewable Energy (EERE) Award No. DE-EE0009691.
[1] C.-H. Ho, J. S. Speck, C. Weisbuch, and Y.-R. Wu. Phys. Rev. Appl. **17**, 014033 (2022).

SESSION LL: Dielectrics, Ferroelectrics and Multifunctional Oxides
Session Chairs: Doug Hall and Patrick Lenahan
Friday Morning, June 30, 2023
MCC Theater

8:40 AM LL01
Molecular Beam Epitaxy and Strain Engineering of KTaO3 Kaveh Ahadi; North Carolina State University, United States

Complex transition metal oxides exhibit an incredible variety of orders and instabilities. Growth of high quality, epitaxially strained thin films and heterostructures promises tuning of the unique properties of these materials. KTaO3 is an incipient ferroelectric, in which superconductivity emerges at low temperatures in electron-doped samples. The KTaO3 conduction band is derived from the Ta 5d states and shows highly anisotropic electronic transport. Furthermore, charge carriers in KTaO3 have smaller effective mass and larger spin–orbit coupling compared to SrTiO3. High quality thin films and heterostructures of KTaO3 allow for control and understanding of these phenomena. Molecular beam epitaxy (MBE) growth of KTaO3, however, has not been demonstrated.
The main challenge to MBE growth of KTaO3 is the stability of tantalum and potassium fluxes. Tantalum is a refractory metal, requiring an e-beam source, while potassium is highly volatile at growth temperatures. Furthermore, the reflective nature of the Ta metal leads to uneven melting and evaporation in the Ta e-beam sources. Successful MBE growth of tantalates remain elusive and limited to the use of e-beam Ta source. Recent thermodynamic calculations, however, suggest Ta2O5 as a potential source for the MBE growth of tantalates. Potassium, is highly unstable and readily oxidizes in air. Potassium sources typically show very large and unstable flux. Intermetallic compounds of alkali metals with relatively low vapor pressure elements, e.g., LiSn4 and CsIn3, have been recently explored as the MBE source.
I will discuss the MBE growth of high quality KTaO3. We used both suboxide and Ta e-beam sources. Potassium was evaporated from an In4K intermetallic compound source, to improve its flux stability. We used a combination of ozone and oxygen (10 % O3 + 90 % O2) to control oxygen stoichiometry. The structural quality of the epitaxial $KTaO_3$ films grown in multiple strain states was assessed using a wide range of characterization techniques. Laue fringes suggest that the films are smooth with an abrupt film/substrate interface. Cross-sectional scanning transmission electron microscopy does not show any extended defects and confirms that the films have an atomically abrupt interface with the substrate. Atomic force microscopy reveals atomic steps at the surface of the grown films. Reciprocal space mapping demonstrates that the films, when sufficiently thin, are coherently strained to the $SrTiO_3$ (001) and $GdScO_3$ (110) substrates.

9:00 AM LL02
Semiconductor-Oxide Interfaces of InAs-Based Ferroelectric and RRAM Devices Austin Irish, Anton Persson, Robin Athle, Mamidala S. Ram, Rohit Yadav, Mattias Borg, Lars-Erik Wernersson and Rainer Timm; Lund University, Sweden

Devices based on ferroelectric field effect transistors (FeFET) or resistive random access memory (RRAM) stacks are currently in the focus of academic and industrial research towards steep-slope transistors, neuromorphic networks, and computation-in-memory application. Especially promising are RRAM HfO_2 or ultrathin (below 5 nm) ferroelectric $Hf_{1-x}Zr_xO_2$ (HZO) layers. Their combination with III-V semiconductor substrates such as InAs offers superior charge carrier mobility compared to Si. Our InAs/HZO/TiN devices have shown an unexpectedly high remanent polarization of the ferroelectric film [1]. We have developed InAs nanowire-based gate-all-around FeFET [2] and RRAM [3,4] devices including 1 transistor 1 resistor structures integrated in a single nanowire [4]. These novel devices have in common that their performance critically relies on the quality of the semiconductor-oxide interface and that the structure and chemical composition of this interface provides additional functionality.
Previously, we performed various synchrotron X-ray photoemission (XPS) studies of InAs/HfO_2 and InAs/Al_2O_3 interfaces of MOSFET devices, where we analyzed the role of different As sub-oxides and defect states, obtained As-oxide and In-oxide interface depth profiles, and also looked at interfacial thermal oxides [5,6]. It turned out that best device performance was reached with as little interfacial oxide as possible.
Here, we present XPS results from InAs/HZO [7] and HZO/TiN [8] interfaces of ferroelectric MOS devices. We observe an interface layer consisting of both In- and As-oxides at the semiconductor/oxide interface. This interface layer with a significant amount of InAs-oxides is assumed to form during the annealing of the InAs/HZO/TiN stack, which is essential to transform the HZO layer into the non-centrosymmetric orthorhombic phase and thus obtain ferroelectric behavior. However, a millisecond short annealing process with reduced heat load, which resulted in less interface oxide and less As^0 defects, was found to improve the endurance of the FE devices [7].
For InAs/HfO_2 RRAM devices, we find that the existence of a sufficiently thick As-oxide interface layer, obtained through extended oxygen plasma pulses, below the HfO_2 film with oxygen vacancies is crucial for enabling resistive switching [4]. This is contrary to the case of conventional InAs-based MOSFETs where we previously were aiming for the perfect self-cleaning [9]. Furthermore, also the structure of the HfO_2/TiN top metal interface of RRAM devices is relevant, where substantial band-bending can result in strong Schottky barriers [3].
These results show that the previous “the cleaner the better” paradigm for interfaces between III-V semiconductors and high-k oxides seems not to be valid anymore when it comes to novel MOS-based device structures. Instead, a combined and interactive materials science and electrical device processing approach is needed to optimize these complex interface requirements. Our observations provide important insight for understanding the superior performance of III-V/HZO

based devices.
[1] A. E. Persson et al., Appl. Phys. Lett. **116**, 062902 (2020).
[2] A. E. Persson et al., IEEE El. Dev. Lett. **43**, 854 (2022).
[3] Z. Yong et al., Appl. Surf. Sci. **551**, 149386 (2021).
[4] M. S. Ram et al., Nature Electronics **4**, 914 (2021).
[5] R. Timm et al., Appl. Phys. Lett. **97**, 132904 (2010).
[6] A. Troian et al., AIP Advances **8**, 125227 (2018).
[7] R. Athle et al., Adv. Mater. Interfaces **2022**, 2201038 (2022).
[8] R. Athle et al., ACS Appl. Mater. Interf. **13**, 11089 (2021).
[9] G. D'Acunto et al., ACS Appl. Electr. Mater. **2**, 3915 (2020).

9:20 AM LL03

(Student) Pushing the Limits of Switching Voltage, Leakage in Ultrathin $BaTiO_3$ Thin Films Harish Kumarasubramanian[1], Prasanna V. Ravindran[2], Mythili Surendran[1], Jayakanth Ravichandran[1,1] and Asif I. Khan[2,2]; [1]University of Southern California, United States; [2]Georgia Institute of Technology, United States

Over the last fifty years, miniaturization has been the primary driver in improving efficiency, facilitating higher speed and reduced cost in MOSFETs while enabling an exponential increase in computational and storage capabilities. The discovery of stable ultra-thin ferroelectric and other high K dielectric gate oxides have provided an additional impetus in lowering the threshold voltage and the power dissipation in FETs [1] . However, despite the scaling down in physical dimensions of the gate oxide, the power supply voltage or the physical voltage has been stuck around 1 V or above for the last 15 years [2]. Even though fluorite oxides like Hafnia and Zirconia show ferroelectricity at a few unit cells of thickness, their extremely high coercive fields (>1 MV/cm) impede the reduction in switching voltage. It has thus become imperative to develop and investigate leakage free, low voltage technological platforms. The more conventional ferroelectric systems like perovskite oxides have recently shown much lower switching voltages (<0.1 V) [3]. But they have also been simultaneously plagued by high leakage currents and depolarizing fields.

In this work, we have achieved ultra-low coercive voltages (<50mV) [4] in ferroelectric thin films based on epitaxial oxide perovskites in the Metal-Insulator-Metal geometry. More specifically we have deposited epitaxial $BaTiO_3$ (BTO) thin films on $GdScO_3$ substrates using Pulsed Laser Deposition (PLD). We have minimised depolarization effects in our thin films by sandwiching the BTO with an epitaxial conductive oxide perovskite ($SrRuO_3$) on either sides. Our BTO films have also shown leakage currents at least 3 orders of magnitude lower than HfO_2 and SiO_2 at sub 1 nm equivalent oxide thicknesses [4].

In order to satisfy a broader set of applications, it is essential to achieve a similar or better set of ferroelectric/leakage properties on Metal-Insulator-Semiconductor (MOS) structures. Even though Si has been the workhorse of the semiconductor industry for at least half a century, the scaling requirements have increasing eaten into its primary advantages, namely its thermally grown dielectric native oxide. There is an urgent need to replace SiO_2 with other high k oxides and hence there is an impetus towards replacing Si with other commercially viable semiconductors. Ge in particular has many advantages as the channel material. It has higher electron and hole mobilities than Si. There is also an additional advantage in that the native germanium oxides are much less stable and hence are easier to remove, thereby rendering a low switching voltage platform. Moreover, Ge provides an excellent epitaxial template for BTO (<0.5 % strain).

The primary challenge in a MOS structure would be achieving a defect free and abrupt semiconductor-oxide interface. On that account, all oxides of Ge have to be removed from the surface with little or no change in roughness. There could also be trap states and dead layers at the interface due to the structural dissimilarity of BTO and Ge. In addition, although BTO has a reasonable valence band offset with Ge, the conduction band offset is negligible. In order to minimise leakage currents and trap states, sufficient band and interface engineering is necessary. We have employed thin blocking layers of epitaxially compatible perovskite dielectric oxides such as $BaZrO_3$ and $CaZrO_3$ with high enough valence and conduction band offsets at the Ge interface to help on that front.

REFERENCES :

1. Böscke, T. S., J. Müller, D. Bräuhaus, U. Schröder, and U. Böttger. "Ferroelectricity in hafnium oxide thin films." *Applied Physics Letters* 99, no. 10 (2011): 102903.
2. Andrew Danowitz et al. "CPU DB: recording microprocessor history". In: *Communi- cations of the ACM* 55.4 (2012), pp. 55–63.
3. Jiang, Y., E. Parsonnet, A. Qualls, W. Zhao, S. Susarla, D. Pesquera, A. Dasgupta et al. "Enabling ultra-low-voltage switching in $BaTiO_3$." *Nature Materials* (2022): 1-7
4. Extended Abstract figure 2

9:40 AM LL04

Frequency-Dependent Conductivity of Mo-SiN_X Granular Metals Michael P. McGarry, Simeon Gilbert, William Bachman, Peter Sharma, Jack Flicker, Michael Siegal and Laura Biedermann; Sandia National Laboratories, United States

We have evaluated the frequency-dependent conductivity (σ) of granular metals (GMs) from DC to MHz. GMs are 3D structured composites of nanoscale metal islands homogenously dispersed within an insulating matrix. By controlling the metal volume fraction (φ), we can tune the GM to have desired electrical properties for a range of applications. At high metal fractions (metallic regime) the GM is a disordered metal with limited insulator inclusions. At low metal fractions (dielectric regime) and low frequencies, the electrical conduction is driven primarily by thermally-assisted electron tunneling at high E fields. When we progress into higher frequencies (ω), the capacitive transport dominates the electrical conduction. This capacitive transport has a conductivity-frequency dependency that follows Jonscher's universal power law, $\sigma(\omega)= \sigma_{DC} + A\omega^n$ where A and n are constants [1]. We have synthesized low-metal fraction, thermally stable Mo-SiN_X GMs [2].

We have optimized Mo-SiN_X for electron tunneling between the metal islands in the low frequency regime. The Mo island sizes range from 1 – 2 nm in diameter with sub-nanometer spacing between the islands. The Mo and SiN_X were co-deposited by RF sputtering onto a sapphire substrate with an average GM thickness of ~200 nm. The metal fraction dependency has been well studied with noble metals (Au, Ag, Pt) in oxide insulators; for example $\sigma=10^{-5}$ S/cm for Au-Al_2O_3 at $\varphi=0.25$ [3]. GMs sputtered in a pure Ar environment had an undesirable $\sigma=10^{-2}$ S/cm at $\varphi=0.25$. SiN_X sputtered in pure argon is known to be nitrogen deficient. XPS analysis showed interfacial defects, Mo-silicides and Mo-nitrides, in our GMs [2]. By sputtering the GMs in a partial nitrogen environment we achieved $\sigma=10^{-7}$ S/cm at $\varphi=0.25$.

The frequency response was measured for these improved Mo-SiN_X GMs as a function of φ. We define the on/off ratio as the real part of the impedance (Z) at DC over Z at 1 MHz, Z_{DC}/Z_{MHz}. The highest on/off ratio of 10^5 was achieved for a $\varphi=0.25$ Mo-SiN_X sample. The more conductive samples had lower on/off ratios, decreasing to an on/off ratio of 10^1 for $\varphi=0.35$. This range of frequency-dependent behavior is greater than previously reported for GMs. For Pb-ZrO_2 and Pt-C, on/off ratios of 10^1 [4] to 10^2 [5] respectively, have been reported. Similarly, our GMs sputtered in a pure Ar environment had only an on/off ratio of 10^2 . Due to this large on/off ratio as well as the high thermal stability of the GM components, Mo-SiN_X are a promising high-pass filter material for electrical grid applications.

This work was supported by the Laboratory Directed Research and Development program at Sandia National Laboratories, a multimission laboratory managed and operated by National Technology and Engineering Solutions of Sandia LLC, a wholly owned subsidiary of Honeywell International Inc. for the U.S. Department of Energy's National Nuclear Security Administration under contract DE-NA0003525.
[1] Abeles *et al*., Adv. in Phys. **24**, 407 (1975).
[2] S. Gilbert *et al*., "*Granular Metals with SiNx Dielectrics*", submitted.
[3] C. Grimaldi, Phys. Rev. B, **89**, 214201 (2014).
[4] H. Bakkali *et al*., Sci. Rep. **6**, 29676 (2016).
[5] M. Hanefeld *et al*., Sci. Rep. **11**, 15163 (2021).

10:00 AM BREAK

10:20 AM LL05
Porous Dielectric Thin Films for Advanced Dielectrics Using Molecular and Atomic Layer Deposition Nicholas C. Strandwitz; Lehigh University, United States

Atomic and molecular layer deposition (ALD, MLD) techniques boast precise control of film thickness, conformal growth, and a wide range of material compositions. Generally, ALD and MLD thin films are non-porous, yet introduction of porosity would enable a wide range of uses ranging from catalysis to low-k dielectrics for electronics. Here, we have examined the purposeful inclusion of organic molecules including bifunctional and monofunctional alcohols during the MLD/ALD process and their subsequent removal using thermal and/or UV treatment to induce porosity. We examined the evolution of various physical and electrical properties with thermal treatment as well as the composition of these films. We found that the density and dielectric constant of these materials are smaller than the parent dense ALD oxides. This strategy is thus promising for tailor made dielectrics based on sequential self-limiting surface reactions characteristic of the ALD and MLD processes. This development parallels other methods for forming porous inorganic oxides such as terpinene inclusion in silicon-based dielectrics or block copolymer templating of inorganic solids.

10:40 AM LL06
Impact of Annealing Conditions on Structural and Optical Properties of Si – Rich Hafnia-Based Thin Films Doped with Pr Elements Tetyana V. Torchynska[1], Jose Luis Casas Espinola[1], Leonardo G. Vega Macotela[1], Jose Oliveros[1], Georgiy Polupan[1], Manuel Alejandro Garcia Andrade[1], Yevgen Venger[2], Fabrice Gourbilleau[3] and Larysa Khomenkova[2]; [1]Instituto Politecnico Nacional, Mexico; [2]V. Lashkaryov Institute of Semiconductor Physics at NASU, Ukraine; [3]CIMAP Normandie Univ, ENSICAEN, UNICAEN, CEA, CNRS, France

HfO_2 based materials offer high refractive index and high transparency in UV-NIR spectral range that are promising for photonic applications. HfO_2 is an ionic material, and for stabilizing its amorphous structure and minimizing the optical losses the use of silicon is preferable due to the flexibility of covalent Si-O bonds. It is known that stabilization of the tetragonal structure can be achieved via HfO_2 doping with trivalent elements, such as rare earth (RE) atoms. In this case, the electrical neutrality is achieved via formation of oxygen vacancies. However, the interaction between different ions and their redistribution upon high temperature annealing were not well addressed.
In this report the structural transformation of HfO_2 thin films codoped with silicon and rare earth elements is considered in terms of the evolution of optical and light emitting properties of these materials at annealing. The films were grown on Si substrates by radio frequency magnetron sputtering in argon plasma and annealed at T_A=800-1100ºC for t_A=15-60 min in inert atmosphere. The transformation of film properties was studied by means of SEM, EDX, XRD, XPS, TEM and photoluminescence (PL) techniques.
For HfO_2 films doped with Pr ions, the stabilization of the tetragonal HfO_2 phase in annealed films was observed contrary to the monoclinic structure of pure HfO_2 films. The main reason responsible for this phenomenon is the formation of oxygen vacancies. For Pr-doped HfSiOx films, phase separation between SiOx and HfO_2 occurs upon annealing at 1100ºC. The Pr ions appeared in the HfO_2 phase mainly. The shape of RE-related PL spectra followed the structural transformation. Narrow RE-related PL peaks were detected in the samples annealed at 1000-1100°C that confirms the location of RE ions in the phase with a high crystal field. The peculiarities of PL spectra and the mechanism of RE-emission excitation in tetragonal HfO_2 phase are discussed.
Hereafter, some experimental results obtained for Si-rich Pr-doped HfO_2-based films are presented as an example of additional information for the abstract.

11:00 AM LL07
Anion Stoichiometry Modulation and *In Situ* Compositional Analysis of Functional Metal Oxide Thin Films Rajeswari M. Kolagani[1], Ryan Paxson[1], Benjamin Moore[1], R. Shipra[1], Jeonggoo Kim[2] and Mikhail Strikovski[2]; [1]Towson University, United States; [2]Neocera LLC, United States

Cation and oxygen stoichiometry of mixed-valent functional metal oxide thin films control electronic properties relevant for technology applications. While there has been significant research on modulating properties through cation stoichiometry, effects of oxygen stoichiometry variation and substitution of other anions at the oxygen site have been much less explored. Oxygen stoichiometry variation in thin films grown by Pulsed Laser deposition is generally achieved by varying the oxygen pressure in the growth ambient. However, varying the oxygen growth pressure is also known to result in cation stoichiometry offsets which convolute the results. In an effort to address this problem, we have studied the cation composition of $La_{0.67}Ca_{0.33}MnO_{3-y}$(LCMO) thin films grown in varying oxygen pressures using the novel in-situ Low Angle X-ray Spectroscopy (LAXS) technique. We will present compositional analysis of LCMO thin films grown in oxygen pressures ranging from 10^{-6} Torr to 100 mTorr. In addition, we will also present the results of our recent investigations that show remarkable changes in the structural and electrical properties of LCMO thin films resulting from a topotactic fluorination process designed to incorporate Fluorine at oxygen vacancy sites.

11:20 AM LL08
(Student, Late News) Effect of HfO_2 Dielectric Thickness on the DC-RF Dispersion in N-Polar GaN HEMTs Subhajit Mohanty[1], Zhe Ashley Jian[1], Oguz Odabasi[1], Md Irfan Khan[1], Kamruzzaman Khan[2] and Elaheh Ahmadi[1,2]; [1]University of Michigan, Ann Arbor, United States; [2]University of Michigan–Ann Arbor, United States

GaN-based high electron mobility transistors (HEMTs) are the de-facto standard for RF power amplifiers in radars and high-frequency applications due to high power efficiency over a wide range of frequency range. Recently, N-polar GaN offers many advantages over Ga-polar such as better 2DEG confinement, improved ohmic contact, output resistance and pinch-off characteristics [2]. Moreover, gate length can be reduced to boost up the frequency of operation, however, this requires reducing GaN channel thickness proportionately to maintain the aspect ratio to suppress short-channel

effects. This scaling down typically leads to a higher gate leakage current which can be suppressed by inserting a thick insulator layer between the channel and gate metal. High-k dielectrics such as HfO_2 with thick dielectric can be deposited without altering the gate capacitance because of small effective oxide thickness (EOT). In this work, the results show that traps in the bulk HfO_2 dielectric under gate region contribute to the DC-RF current collapse which disappears at thinner thickness.

In this study, MOCVD-grown N-polar deep recessed GaN HEMT structure commercially available from Transphorm Inc., was used to fabricate three samples with three different thicknesses (10.1, 7.1, 4 nm) of HfO_2 together. SiO_2 and Al_2O_3 were used as the hard mask and etch stop to define the regrown area and a UID-GaN/n^+ GaN was regrown in source/drain regions after selective etching of the thick GaN cap to minimize ohmic contact resistance. Device isolation was achieved by ion implantation with Aluminum to form a high-resistive region between devices. Then, the sample was recessed etched using selective etch under the gate area for better gate control. The sample then underwent a sequence of wet cleaning, UV-ozone conditioning and in-situ ALD plasma treatment prior to the deposition of thermal ALD HfO_2. The deposited HfO_2 was removed under the contact area using a BCl_3-based dry etch and a hydrochloric acid wet etch was performed immediately before 30/200 nm of Ti/Au deposition by electron-beam evaporation. A very low Metal-to-GaN contact resistance of 0.1 Ω-mm was measured from the un-passivated Transfer Length Method (TLM) with sheet resistance (R_{sh}) of ~250 Ω/sq. Finally, 30/420 nm of Ti/Au optical gate and contact pads were patterned via liftoff.

All three samples exhibited a charge density of 1.6-1.8x10^{13} cm^{-2}. The regrown contact resistance was 0.25-0.3 ohm-mm. C-V hysteresis was measured to be 0.46V, 0.3V and <0.05V for samples with 10.1 nm (sample A), 7.1 nm (sample B), and 4.4 nm (sample C) HfO_2 thickness, respectively. Similarly, the I_D-V_G hysteresis decreased with HfO_2 thickness. Despite being deep recessed HEMT, pulsed-IV measurements revealed the presence of DC-RF dispersion in all devices which also reduces HfO_2 thickness. Drain saturation current in the on-state (I_{DSS} at Vg=0V), dynamic Ron, peak transconductance at V_D=3V (g_m) and change in threshold voltage (DV_{th}) was observed in the pulsed-IV measurement with gate-drain electric field and dielectric thickness. Pulsed IV measurements reveal that the amount of current collapse is independent of the surface electric field which proves the effectiveness of the deep-recessed HEMT architecture. However, the current collapse varies significantly across the HfO_2 thickness. The current collapse was ~30%, 20% and <10% for the samples with 10.1, 7.1, 4 nm of HfO_2 respectively. Moreover, most of the current collapse occurs during gatelag when devices are under pinch-off. This indicates the effect of traps under the gate which is apparent from the negative shift in threshold voltage. This shift is proportional to the HfO_2 thickness suggesting the role of bulk traps present in the dielectric. The dynamic Ron did not change across samples which indicates that the channel resistance in the access region remains unaffected by the surface electric field indicating no effect of surface traps on 2DEG channel.

11:40 AM LL09
(Late News) Magnetic Tunnel Junction Molecular Spintronics Based Chemical Sensing Device Pius Suh and Pawan Tyagi; University of the District of Columbia, United States

The Magnetic Tunnel Junction (MTJ) was first successfully fabricated and tested in the 90s. it consist of a Tri-layer of two ferromagnet, sandwiching a 2nm ultra-thin layer of dielectric or insulator called the tunneling barrier. If a voltage is applied to the ferromagnets, electrons can tunnel across the barrier in the process called quantum mechanical tunneling. The tunnelling current in this case is maximum if the direction of magnetization of the two electrodes are parallel to each, and minimum when the two electrodes are anti parallel to the direction of magnetization. The tunnelling current and resistance of this device will therefore change in response to changes in the magnetic orientation of the two ferromagnetic electrodes.

When we introduce an organo-metallic molecule to the exposed edges of the ferromagnetic electrodes, the molecule covalently bonds to two ferromagnetic electrodes creating a molecular channel through which electrons can spin through. The Magnetic Tunnel Junction Molecular spintronic device (MTJMSD) can transform ferromagnetic and materials and produce intriguing spin transport characteristics with high sensitivity, low power consumption, very small in size and less expensive.

This disclosure is directed toward a new MTJ based spintronics device for converting chemical absorption into a change in magnetoresistance. The magnetic material used is dependent on the organic structure of the thin film electrodes for its absorption at cross junction of the MTJMSD and thus modify its magnetic properties. A change in the magnetic property will lead to a change in the resistance of a magneto resistive structure allowing a standard electrical detection of the chemical change in the sensor surface.

Due to its high sensitivity, excellent scalability, and low power consumption, MTJMSD based sensors can be widely implemented in different applications. In our investigation, we tested some commonly used chemical in the lab on our device, both at the excited state (with light) and at the ground state (in the dark) We tested Acetone (CH3COCH3), Ethyl Alcohol (CH2CHOH) and Dichloromethane (CH2Cl2) and studied the trend. The IV measurements were conducted before and after molecular attachment. There was no clear distinction in the detectivity between the measurement done under the light and in the dark, however, a general observation before and after molecular attachment showed a significant increase in the current. In the present work, we fabricated a metal/insulator/semiconductor MTJ as a testbed for our MTJMSD based chemical sensing device. This paper is part of an ongoing investigation with the aim of fabricating a MTJMSD based sensor for detection dopamine concentration and other chemicals.

EMC INDEX

This index lists session chairs, presenters and co-authors.

- Session chairs will have the session letter code. (eg: AA)
- Plenary speaker will have an * before the paper number in bold type. (eg: ***A01**)
- Presenters of Student Finalist for Oral Presentation will have a # before the paper number in bold type. (eg: **#H07**)
- All other Presenters will have the session letter code followed by the paper number in bold type. (eg: **II02**)
- Co-authors will have the session letter code followed by the paper number in regular type. (eg: B02)

D

E

F

M

S

Z

NOTES

EMC 2023 Program Grid

UC = University Center; MCC = MultiCultural Center
Registration opens on Tuesday, 8:00 am–5:00 pm, UC, Corwin Lobby

Location	Wednesday AM	Wednesday PM	Thursday AM	Thursday PM	Friday AM
UC, Corwin Lobby	**EMC Registration:** 7:30 am – 5:00 pm		**EMC Registration:** 8:00 am – 5:00 pm		**EMC Registration:** 8:00 am – 12:00 pm
UC, Lagoon Plaza	**Exhibit Hours:** 10:00 am – 8:00 pm **Refreshment Breaks:** 9:20 am – 10:00 am 3:10 pm – 3:30 pm **General Poster Viewing:** 3:10 pm – 3:30 pm **Welcome Reception:** 6:00 pm – 8:00 pm **Poster Reception:** 6:00 pm – 8:00 pm		**Exhibit Hours:** 10:00 am – 4:00 pm **Refreshment Breaks:** 10:00 am – 10:20 am 3:10 pm – 3:30 pm **General Poster Viewing:** 10:00 am – 10:20 am 3:10 pm – 3:30 pm **Poster Tear Down by 5:30 pm**		**AM Break:** 10:00 am – 10:20 am
Music Building, Lotte Lehmann	**EMC Awards Ceremony & Plenary Session 8:20 am – 9:20 am** **A: Group III-Nitrides—Devices**	**G: Group III-Nitrides—Vertical Power Devices**	**O: Group III-Nitrides—Novel Nitride Growth**	**W: Group III-Nitrides—Late News**	
UC, Corwin East	**B: 2D Materials Properties and Interfaces**	**H: 2D Materials, Devices and Sensors**	**P: 2D Materials Synthesis and Characterization**	**X: Group III-Nitrides—Growth and Characterization**	**EE: Diamond and Related Materials** **FF: Group III-Nitrides—Thermal Transport**
UC, Corwin West	**DRC Session 11: Memory**	**DRC Session 12: Devices for Extreme Conditions**			
UC, Flying A Studios	**C: Photonic Devices**	**I: Novel IR Detector Materials** **J: Novel Materials Epitaxy**	**Q: Optical Materials on Si** **R: Epitaxial Materals Design and Properties**	**Y: Plasmonics, Photonics for Detection and Emission**	**GG: Epitaxy of Structured and Quantum Materials**
UC, State Street	**D: Nanoscale Characterization**	**K: Energy Materials and Devices** **Student Finalists for Oral Presentation Award—Part A**	**S: SiC Materials Characterization, Processing and Devices**	**Z: Emergent Materials and Devices for Microelectronics**	**HH: Materials Processing and Integration**
UC, Lobero		**L: Organic and Hybrid Materials for Optoelectronic Devices** **Student Finalists for Oral Presentation Award—Part B**	**T: Organic Devices and Molecular Electronics**	**AA: Semiconducting Oxide Thin Films and Transistors**	**II: Flexible, Printed, and Wearable Electronics and Sensors**
UC, Santa Barbara Harbor	**E: Hetero-Integration, Interconnects and Packaging**	**M: Group III-Nitrides—Optical Emitters**	**U: Group III-Nitrides—Contacts and Special Topics**	**BB: Group III-Nitrides—P-Type Doping and Characterization**	**JJ: Low-Dimensional Structures—Quantum Dots, Wires and Wells** **KK: Micro-LEDs**
MCC Theater	**F: Gallium Oxide Devices**	**N: Characterization of Gallium Oxide-Based Materials and Devices I**	**V: Growth of Gallium Oxide and Other Ultrawide-Bandgap Oxides**	**CC: Characterization of Gallium Oxide-Based Materials and Devices II** **DD: Gallium Oxide Materials Processing**	**LL: Dielectrics, Ferroelectrics and Multifunctional Oxides**
Manzanita Village Las Encinas Quad Lawn				**EMC Dinner Reception 6:30 pm – 8:30 pm**	